Comptes Rendus de l'Académie des sciences

1878-1543 (electronic)

Chimie

Special issue / ***Numéro thématique***

Women Chemists in France in 2026 / ***Femmes chimistes en France en 2026***

Coordinated by / ***Coordonné par***

Janine Cossy

INVENIT ET PERFICIT 1666 ACADÉMIE DES SCIENCES INSTITUT DE FRANCE

CENTRE MERSENNE

Comptes Rendus

Chimie

Objective of the journal

Comptes Rendus Chimie is an international peer-reviewed electronic journal, covering all areas of chemistry.
It publishes special issues, original research articles, review articles, accounts, historical perspectives, pedagogical texts or conference proceedings, of unlimited length, in English or in French and in as flexible a format as necessary (figures, associated data, etc.).

Comptes Rendus Chimie has been published since 2020 with the centre Mersenne pour l'édition scientifique ouverte (Mersenne Center for open scientific publishing), according to a virtuous Diamond Open Access policy, free for authors (no author processing charges nor publishing fees) as well as for readers (immediate and permanent open access. Since 1 January 2026, it is coedited by the Académie des sciences and the Centre national de la recherche scientifique (CNRS).

About the journal

Comptes Rendus Chimie is published exclusively in electronic format. All information on the journal, as well as the full text of all articles, is available on its website at:
https://comptes-rendus.academie-sciences.fr/chimie.

Authors enquiries

For any inquiries about submitting a manuscript, please refer to the journal's website:
https://comptes-rendus.academie-sciences.fr/chimie.

Contact

Académie des sciences
23 quai de Conti
75006 Paris (France)
cr-chimie@academie-sciences.fr

To cite this issue:
Janine Cossy (ed.). Women Chemists in France in 2026. *Comptes Rendus. Chimie* (2026). https://doi.org/10.5802/crchim.sp.3

ACADÉMIE DES SCIENCES
INSTITUT DE FRANCE

Comptes Rendus. Chimie
2025, Vol. 28, p. 755-769
https://doi.org/10.5802/crchim.417

Review article

High specificity is a key parameter for copper ligands as future therapeutic agents for Alzheimer's, Wilson's, and cancer diseases

Anne Robert [*, a], **Yan Liu** [*, b], **Michel Nguyen** [a], **Françoise Benoit-Vical** [a] and **Bernard Meunier** [*, a, b]

[a] Laboratoire de Chimie de Coordination du CNRS, LCC-CNRS, Inserm ERL 1289 MAAP, Université de Toulouse, 205 route de Narbonne, 31077 Toulouse cedex, France

[b] School of Chemical Engineering and Light Industry, Guangdong University of Technology, Higher Education Mega Center, Guangzhou 510006, PR China

E-mails: anne.robert@lcc-toulouse.fr, yanliu@gdut.edu.cn, michel.nguyen@lcc-toulouse.fr, francoise.benoit-vical@lcc-toulouse.fr, bmeunier@lcc-toulouse.fr

This review is dedicated to Dr. Marguerite Pitié, † 2011, in memoriam

Abstract. The loss of copper homeostasis is considered a characteristic feature of several major human diseases such as Alzheimer's, Wilson's, or cancer diseases. Consequently, the design of new efficient ligands targeting copper regulation is a major concern of therapeutic bioinorganic chemistry and should take in consideration the chelator structures for being copper-specific and the redox properties of the corresponding complexes to obtain suitable pharmacological activities. As an improvement of previously developed amine ligands, N4-tetradentate 8-aminoquinoline chelators, are able to inhibit memory and behavior impairment in Alzheimer mice, by generating square planar Cu(II) complexes suitable for the efficient extraction of copper ions from metallated amyloid peptides, leading to a reduction of the neurotoxic oxidative stress in the brain. These chelators also reverse the hepatotoxic accumulation of copper in animals with Wilson's disease and inhibit the proliferation and migration of human cancer cell lines. This review summarizes the gradual and logical development of twenty-five years of research in our group on copper-specific chelators and their promising development as potential therapeutic tools against diseases in which copper is involved.

Keywords. Alzheimer's disease, Cancer, Chelator, Copper, Medicinal chemistry, Redox metal, Wilson's disease.

Funding. CNRS, Inserm, GDUT.

Note. Article submitted by invitation.

Manuscript received 20 August 2025, revised 30 August 2025, accepted 1 September 2025.

1. Introduction: copper in human health and disease

After iron and zinc, copper is the third essential metal ion in living systems [1]. The highest concentrations of copper are found in liver and brain. The copper concentration in human frontal lobe and cerebellum is ranging from 60 to 110 μM [2]. In living organisms, copper exists in the oxidized Cu(II) and reduced Cu(I) forms. In biological conditions, the interconversion between these two oxidation states is easy and facilitates the role of this metal as catalytic co-factor in various copper enzymes involved in electron transfers and oxidations.

Copper ions are found in many different metalloenzymes (laccases, tyrosinase, superoxide dismutase, ascorbate oxidase, cytochrome-c oxidase

* Corresponding authors

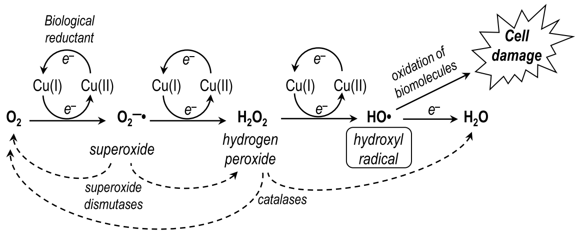

Scheme 1. Step-by-step reduction of dioxygen catalyzed by low-valent transition metals such as Cu(I) or Fe(II).

to cite a few ones) and metalloproteins (hemocyanin, ceruloplasmin) [3,4]. Among these copper proteins involved in vital processes, cytochrome-c oxidase is a large transmembrane terminal heme/copper oxidase of the respiratory electron transport chain. Its redox centers involved in electron transport consist of two heme moieties and two copper centers that catalyze the reduction of dioxygen to water with the concomittant pumping of four protons through the mitochondrial membrane [5] (Equation (1)).

$$O_2 \xrightarrow{4e^-,4H^+} 2H_2O \qquad (1)$$

Since the air-stable oxidation state +II of copper can be easily reduced to the highly reactive state (+I) by endogenous reducing agents (e.g., ascorbate, glutathione, NADPH) [6], its acquisition, distribution and regulation in living systems is strictly controlled by copper carriers and chaperone proteins [7]. As a low-valent transition metal ion, Cu(I) behaves in the same way as Fe(II), being able to induce the *electron-by-electron* reduction of dioxygen to water in all aerobic organisms (Scheme 1). This catalytic reaction is potentially deleterious because it produces superoxide radical anion $O_2^{\bullet-}$, then hydrogen peroxide H_2O_2 and finally hydroxyl radical $HO^{\bullet}$, the most aggressive form among the reactive/reduced oxygen species (ROS).

Superoxide is a relatively mild reductant and hydrogen peroxide is the required cofactor of the ubiquitous peroxidases. In healthy organisms, the concentrations of superoxide and hydrogen peroxide are strictly controlled by metallo-enzymes. The efficient superoxide dismutases (SODs), Cu/Zn-superoxide dismutase (= SOD-1), to name one of them, have a key role in the regulation of this metabolic pathway, by converting two superoxide radical anions to molecular oxygen and hydrogen peroxide through the redox activity of its copper centre, while zinc plays a structural role (Equation (2)).

Cu/Zn-SOD (= SOD-1) is present in nearly all compartments of human cells, nucleus, mitochondria, cytosol, and peroxisomes.

$$2O_2^{\bullet-} \xrightarrow{2H^+} O_2 + H_2O_2 \qquad (2)$$

Hydrogen peroxide is used as cofactor by peroxidases, but any excess of production of this peroxide is controlled by catalases that are highly efficient at H_2O_2 disproportionation. In the case of H_2O_2 overproduction, the three-electron reduction product of dioxygen, hydroxyl radical $HO^{\bullet}$, is produced. This radical is the strongest oxidizing agent (standard redox potential = 2.8 V/NHE) after fluorine gas (2.9 V/NHE) and, unlike $O_2^{\bullet-}$ or H_2O_2, no specific detoxifying enzymes exist for $HO^{\bullet}$. At diffusion-controlled rates, $HO^{\bullet}$ hydroxylates aliphatic C–H bonds, or performs the one-electron oxidation of rather inert molecules, or modifies unsaturated compounds by addition [8]. All biomolecules of living organisms can be quickly oxidized by $HO^{\bullet}$, leading to extensive damage up to cell death. The only way to prevent the formation of this deleterious radical is to control the upstream reduction of molecular oxygen. Involvement of an oxidative stress induced by misregulated copper in the brain has been documented as a key feature of Alzheimer's disease and proposed to be important for the development of the brain pathology [9–11]. It is also well known that the deregulation of copper homeostasis is involved in other inherited or sporadic neurodegenerative pathologies like Parkinson's disease, amyotrophic lateral sclerosis that is caused by mutations of SOD-1 [12], or prion-mediated encephalopathies [13]. Copper ions are also essential for the function of several brain metalloenzymes like tyrosinase [14] or dopamine β-hydroxylase [15].

In addition, any deficiency of a human copper carrier protein involved in the regulation of copper uptake, may generate a pathology. This is the case for Wilson's disease, a genetic condition caused by mutations of the *Atp7b* gene coding for the copper carrier ATP7B in charge of excreting copper from liver to bile. Impairment of ATP7B causes massive accumulation of copper in liver, brain, and other organs, resulting in liver disease and neurological disorders [16–18]. Moreover, copper is essential for efficient iron and zinc trafficking in mammals. The major copper transporter ceruloplasmin exhibits a ferroxidase activity that promotes the Fe(II) oxidation to facilitate the iron loading into ferritin, and Zn(II) is a substrate of ferroportin [19]. So it should be noted that the roles of these three vital metal ions, copper, zinc, and iron, are often interconnected in different proteins or enzymes. Consequently, any metal chelator, if considered as drug candidate, should be specific for one of these metal ions to avoid as much as possible perturbations of metalloproteins dependent on the two other metal ions. This is a prerequisite point in the rational design of a copper ligand for being beneficial in the therapy of a copper-related disease.

As bioinorganic chemists initially involved in DNA cleavage by metal complexes, our group became interested by using copper complexes as DNA cleavers (Section 2 of the present review article), then some copper ligands were designed for antitumor activity (Sections 3 and 6). Different series of specific copper chelators were then developed as potential drugs to treat Alzheimer's disease (Section 4) and Wilson's disease (Section 5). In relation to the state of the art, the present review is therefore focused on the last twenty-five years of research on copper ligands with potential therapeutic interest performed in our research group, especially on the step-by-step rational design of metal-selective and biologically efficient drugs.

2. Copper complexes as DNA cleavers

Among the various metal complexes developed over the last three decades as artificial nucleases, copper complexes of 1,10-phenanthroline (Phen) have been widely used as DNA cleavers [20–24]. The versatile Phen ligand is able to chelate copper ions as redox-active Cu(Phen) and Cu(Phen)$_2$ complexes (for a general review on the chemistry of phenanthrolines, see Ref. [24]). Interaction of the redox-active Cu(I)/Cu(II)–phenanthroline complexes in the minor groove of double-stranded DNA in the presence of H_2O_2, triggers the oxidation of C1′ and C4′ of 2-deoxyribose units, resulting in single-strand DNA cleavage [20,21]. This cleavage can also be achieved by aerobic oxidation in the presence of a reducing agent. Cu(Phen)$_2$ was found significantly more active than Cu(Phen), but the association constant for the second Phen ligand onto the copper ion is too low to

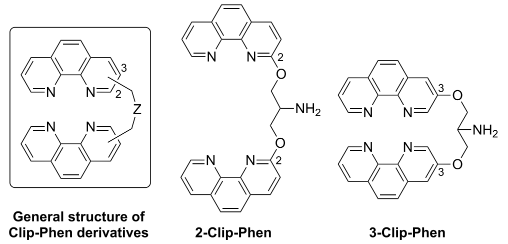

Figure 1. Structures of the covalently linked bis-phenanthroline ligands, 2-Clip-Phen and 3-Clip-Phen.

enhance DNA oxidation at submicromolar concentrations ($\log K_{\text{app}} = 5.5$) [25]. Consequently, chelators named "Clip-Phen" were prepared, containing two Phen residues linked through their C2 or C3 positions by an adjustable bridge, to favor the coordination of two Phen units around a single copper ion (Figure 1) [26,27]. The efficiency of oxidative DNA cleavage by Cu–Clip-Phen complexes, under aerobic and physiological conditions in the presence of a reductant, was evaluated by quantification of the cleavage of supercoiled circular bacteriophage ΦX174 DNA (form I) into relaxed (form II) and circular (form III) forms. In these conditions, Cu–Clip-Phen complexes exhibited a nuclease activity that was dramatically higher than that of Cu–1,10-phenanthroline [26].

The DNase activity of Clip-Phen was higher when the bridge was linked at the C3 position of the Phen moiety (3-Clip-Phen series) compared to the C2 position (2-Clip-Phen series) and when the bridge contained three methylene units [27,28]. The most efficient chelator of this series was 3-Clip-Phen (Figure 1) with a serinol bridge at C3 position of the Phen rings, being 20–30 times more active as DNA cleaver than its 2-Clip-Phen analog [27,28]. In fact, 2-Clip-Phen in the presence of $CuCl_2$ (1:1 molar ratio) resulted in an incomplete (70%) cleavage of ΦX174 form I into relaxed form II (30% of remaining form I) whereas, in the same conditions, 3-Clip-Phen resulted in the complete cleavage of form I into form II (35%) and circular form III (65%), with an intense smear corresponding to smaller DNA fragments.

In addition, the serinol bridge between the two Phen units allowed, via its primary aliphatic amine, the vectorization and modulation of the binding domain in these DNA cleavers. As expected, the attachment of spermine, which has high affinity for the minor groove of double helix DNA, to 2-Clip-Phen afforded a new spermine–phenanthroline conjugate with an enhanced nuclease efficacy [29].

The electrochemical study of the 2- and 3-Clip-Phen series indicated that the 2-Clip-Phen ligands are better to stabilize the tetrahedral Cu(I) state of their complexes in comparison to the Cu(II) state. On the other hand, 3-Clip-Phen derivatives facilitate the stabilization of the corresponding Cu(II) complexes with a quasi-irreversible Cu(II) → Cu(I) reduction, suggesting that the reduced DNA cleavage efficacy of Cu–2-Clip-Phen complexes might be correlated with the higher stabilization of the cuprous oxidation state. However, the absence of strict correlation between the redox properties of the copper complexes and their DNA cleavage efficacy suggests that steric or electrostatic parameters of the DNA interactions also take part in the modulation of the nuclease activity of these copper complexes.

Noteworthy, several complexes of 2- or 3-Clip-Phen with Cu(II) crystallized as a double-helical structure of stoichiometry Cu_2L_2, while monomeric CuL species, with various geometries, were predominant in solution [28]. The structure and reactivity of these copper complexes appear to be particularly versatile, a feature that opens the way for potential uses as biological tools.

3. Copper ligands/complexes with antitumor activity

Since the registration of cisplatin in the early 1980s, the role of metal ligands and complexes in cancer research has been the subject of many studies until now (for a recent review, see Ref. [30]). The efficacy of the copper complexes of Clip-Phen as DNA cleavers suggested that these chelators might also be considered as therapeutic agents against cancer. In fact, research on the cytostatic and potential antitumor activities of substituted Phen derivatives or related ligands metalated with copper or other various metals has been investigated in parallel to their DNase activity [31–34] and has remained an active research field until recent years, with the aim of developing novel metal-based anticancer drugs [35–37].

In this context, the cytostatic properties of a series of 3-Clip-Phen derivatives were evaluated on the classic L1210 murine leukemia cell line. The concentration inhibiting the cell growth by 50% after 48 h (IC_{50}) of 3-Clip-Phen was close to that of Phen itself

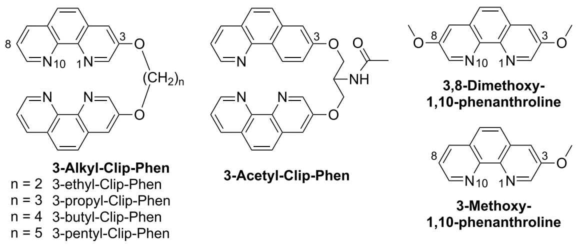

Figure 2. Structures of alkyl substituted 3-Clip-Phen ligands, and 3,8-substituted-1,10-phenanthrolines.

(1.15 and 2.5 μM, respectively), although Cu–3-Clip-Phen was a better DNA cleaver than $Cu(Phen)_2$ [33]. This result suggested that the cytostatic activity was not strictly correlated to the DNase activity.

Conversely, 3-propyl-Clip-Phen, with a simple aliphatic linker (Figure 2), exhibited a significantly higher activity against L1210 cells (IC_{50} = 0.25 μM) compared to 3-Clip-Phen (Figure 1). Analogs of 3-propyl-Clip-Phen containing two to five methylene units in the linker (3-alkyl-Clip-phen series) (Figure 2), were also evaluated. Their activity was significantly correlated to their number of methylene units in the linker, itself correlated to hydrophobicity (Figure 3). The longer the linker, the more active the compound was, with an IC_{50} value of 0.13 μM for 3-pentyl-Clip-phen. In order to investigate whether the hydrophilic primary amine of the linker of 3-Clip-phen ($\log P_{calc}$ = 2.47, IC_{50} = 1.15 μM) could hamper its biological activity, this ligand was compared to the slightly more hydrophobic 3-acetyl-Clip-Phen ($\log P_{calc}$ = 2.80). However, the antiproliferative activity of 3-acetyl-Clip-Phen was lower at 5 μM, indicating that the correlation between biological activity and $\log P_{calc}$ was limited to the 3-aliphatic-Clip-Phen series [33].

The putative role of the alkoxy substituent at the C3-position in the phenanthroline of Clip-Phen derivatives was evaluated by comparing their activities to that of monomeric Phen derivatives, 3-methoxy- and 3,8-dimethoxy-1,10-phenantholine. The IC_{50} values of 3-methoxy- and 3,8-dimethoxy-1,10-phenantholine were 1.5 μM and 1.4 μM, respectively, in the same range as for Phen itself (2.5 μM), suggesting that the alkoxy substituents at the C3- and C8-position were not responsible for the higher cytostatic activity of 3-alkyl-Clip-Phen. On the other hand, the attachment position of the linker on the

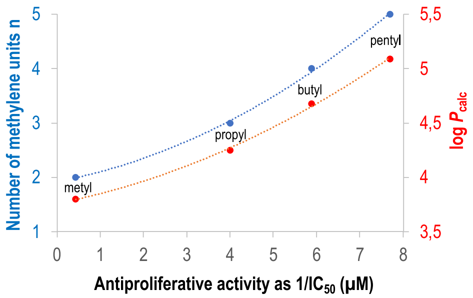

Figure 3. Antiproliferative activity of 3-alkyl-Clip-Phen derivatives measured as $1/IC_{50}$ value with respect to the number of methylene units in the linker (n, blue trace) or to the hydrophobicity ($\log P_{calc}$, red trace). The dotted lines stand for polynomial trend curves of degree 2.

phenanthroline units is an important parameter, since 2-propyl-Clip-Phen exhibited a much poorer activity (IC_{50} value > 100 µM) than its regio-isomer 3-propyl-Clip-Phen (1.15 µM) [33].

The conjugation of 3-Clip-Phen with DNA binders and/or cell penetration agents such as spermine or polyarginine $(Arg)_9$ did not increase the antiproliferative activity. The IC_{50} values of 3-Clip-Phen–spermine and 3-Clip-Phen–$(Arg)_9$ were 12 µM and 1.9 µM, respectively, against L1210 cells [33], despite the fact that 3-Clip-Phen–spermine exhibited a much higher nuclease activity than 3-Clip-Phen on supercoiled ΦX174 DNA [29].

Importantly, Cu(II) complexes of Clip-Phen derivatives were prepared, and their cytostatic activities were evaluated. While complexation of copper failed to improve the activity of 3-Clip-Phen derivatives regardless of the composition of the linker, the activity of 2-propyl-Clip-Phen dramatically increased with copper complexation (IC_{50} = 2 µM, compared to IC_{50} > 100 µM for the free ligand). These results confirmed that the attachment position of the linker induced large variations in the biological properties of Clip-Phen derivatives [33].

4. Copper chelators against Alzheimer's disease

Among the various putative targets involved in Alzheimer's disease (AD), the loss of metal ion homeostasis in AD brain is well documented [38–41]. Post-mortem analyses of the brain of patients with AD indicated that amyloid plaques contain an excess of copper, iron, and zinc by a factor of 5.7, 2.8, and 3.1, respectively, compared to the levels of normal brains [9]. Copper–amyloid complexes, in the presence of endogenous reductants, catalyze the reduction of dioxygen to generate reduced ROS (Scheme 1) [40,42]. Production of ROS is the molecular signature of chronic inflammation reported in AD brain and involved in neuronal death [43]. In addition, copper ions sequestered in amyloid plaques may be responsible for a deficit in copper for cerebral copper-dependent enzymes, like superoxide dismutase-1, [44] or copper oxidases involved in the biosynthesis of neurotransmitters. Therefore, restoration of copper homeostasis in the brain is a multifunction drug target that requires the design of specific chelators [11,38,45,46]. Because of the deleterious oxidative stress catalyzed by out-of-control redox-active metal ions, this approach should be considered an essential strategy among all various attempts in AD drug design.

4.1. *Clioquinol (CQ) and PBT2*

The 8-hydroxyquinoline derivatives clioquinol (CQ) and PBT2 (Figure 4) have been the first copper/zinc ligands considered as potential anti-AD agents to limit the interactions between metal ions and amyloid peptide (Aβ). Clioquinol was able to decrease Aβ deposits in brain and to improve learning and memory abilities of transgenic AD mice [47,48]. Unfortunately, this simple chelator, previously used as antifungal and antiprotozoal drug, was withdrawn from the market in 1983, due to its neurotoxicity attributed to zinc chelation [15,49]. In fact, the 8-hydroxyquinolines are non-specific metal chelators [50,51], and the affinity constant of CQ for Cu(II) is only one order of magnitude higher than that for Zn(II) ($\log K$ = 10 and 9, respectively) [38,52]. In this series, PBT2 [38] was less toxic [48]. However, phase II clinical trial of PBT2 as anti-AD drug was stopped due to its lack of efficacy [53].

In fact, CQ and PBT2 are bi- or tridentate ligands. Consequently, their corresponding Cu(II) complexes have a 1:2 metal/ligand stoichiometry [38,54]. Moreover, addition of stoichiometric amounts of CQ or PBT2 to Cu(II)–Aβ in vitro does not efficiently remove Cu from Cu(II)–Aβ, but generates stable ternary CQ– or PBT2– Cu(II)–Aβ complexes [54,55]. Since

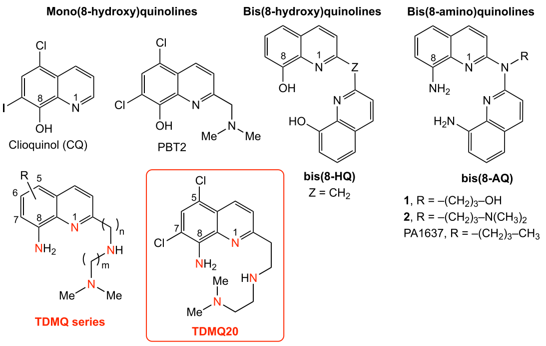

Figure 4. Structures of copper chelators developed as drugs against Alzheimer's disease. Z stands for an adjustable linker.

8-hydroxyquinolines are unable to extract copper(II) from soluble amyloids, these ligands should not be considered as regulators of the copper homeostasis in AD brains. Moreover, their flexible coordination properties allow them to accommodate either Cu(II) or Cu(I), reducing their capacity to inhibit the oxidative stress induced by Cu–Aβ [56].

Additionnally, copper is a required cofactor for several essential metalloenzymes, for example, for the tyrosinase that produces L-DOPA from tyrosine and catecholamine neurotransmitters [14]. Circadian rhythm dysfunction occurs in AD, and copper was recently reported to modulate rest–activity cycles via norepinephrine produced by copper enzyme dopamine β-hydroxylase [15]. These data indicate that the chance to get an efficient copper ligand from the shelves to treat copper-related disease are limited, due to the necessity of understanding the whole picture of the various parameters in copper coordination chemistry. Specific copper chelators should result from a rational design in order to create drugs as specific as possible. These ligands should not disrupt the regular activity of copper enzymes or proteins and must have suitable pharmacological and safety profiles. Moreover, they should be able to cross the blood–brain barrier after an oral administration, to avoid any painful mode of administration. The following sections are reporting our successive works to reach this goal.

4.2. *Bis(8-hydroxyquinolines)*

In line with our expertise on Clip-Phen as copper chelators endowed with nuclease and cytostatic activities (see above), we prepared a series of chelators using two 8-hydroxyquinoline motifs covalently linked at their C2 position. Contrary to mono(8-hydroxy)quinolines, bis(8-hydroxy)quinolines (Figure 3) offer tetradentate N_2O_2 binding sites to form copper complexes with a ligand/metal ratio = 1:1. The affinity of bis(8-hydroxyquinolines) for Cu(II) is higher than that of mono(8-hydroxy)quinolines by 4 to 6 orders of magnitude, with $\log K_{app}$ of 15.5–16.6 at physiological pH [57,58]. However, their selectivity for copper with respect to zinc is only 100 to 1000 [$\log K_{app}$ for Zn(II) = 12.5–14.2]. These ligands are efficient at solubilizing Aβ peptides and are able to inhibit H_2O_2 production by the Cu–Aβ/ascorbic acid system. These results were superior to those obtained with the corresponding 8-hydroxyquinoline monomers, thus validating the strategy of tetradentate chelators. However, their affinity for Zn(II) is still too high to consider these ligands as biologically pertinent copper regulators [59].

4.3. *Bis(8-aminoquinolines)*

To proceed to the transfer of copper from Aβ to glutathione (an efficient copper carrier) and, therefore, to restore the copper homeostasis in AD brains, we designed a series of tetradentate ligands L based on a bis(8-aminoquinoline) scaffold, which are specific for copper coordination (Figure 4, PA1637, 1, 2) [11]. These ligands have a high affinity for Cu(II) ions, with $\log K_{app}$ values ranging from 14 to 16 at pH 7.4, and a low affinity for Zn(II), resulting in very high selectivity for Cu(II) with respect to Zn(II), with a log [K_{app}(Cu–L)/K_{app}(Zn–L)] value over 12 [60]. In vitro, at micromolar concentrations, they efficiently extract Cu(II) from Cu(II)–Aβ, to provide the Cu(II)–L complex (Scheme 2) [54]. The presence of an amino function at the C8-position of the quinoline skeleton is required for the specific chelation of copper.

Importantly, this series of chelators offers a well-defined square planar coordination suitable for Cu(II) but not for Cu(I). So, in the presence of glutathione (GSH), a reducing agent and a competitive ligand for copper, the Cu(II)–L complex readily releases its copper ion to glutathione to generate a Cu–GSH complex that will be able to transfer copper to regular metal carriers (Scheme 2) [61].

In such conditions, the bis(8-AQ) ligand is released and should be able to act as a catalyst

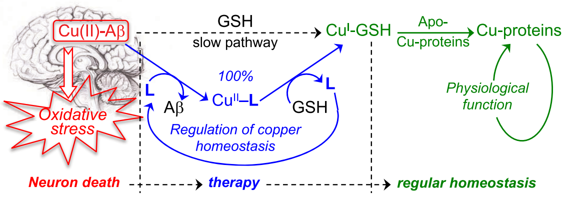

Scheme 2. Transfer of copper from Cu–Aβ to Cu-proteins, assisted by a specific Cu(II) chelator. L stands for TDMQ20; GSH stands for glutathione. Reprinted with permission from Ref. [41]. Copyright 2019 American Chemical Society.

(Scheme 2). Bis(8-AQ) ligands may therefore be considered as suitable copper regulators of the copper homeostasis. Conversely, it was also shown that the copper complex of the mono(8-hydroxyquinoline) derivative PBT2 was unable to release copper in the presence of GSH.

On the basis of these in vitro studies, the pharmacological activity of PA1637 (Figure 4) was evaluated on a murine model of AD. The preclinical evaluation of drug candidates against AD has usually been carried out on transgenic mice [48,62,63]. However, AD is not a condition determined by a single gene mutation but a multi-parameter pathology in which a large number of age-related genes are involved. The fact that these transgenic mouse models do not accurately reflect human pathogenesis is probably one of the reasons for the failures during preclinical selection of drug candidates [64,65]. To enlarge the panel of predictable mice models, we developed a non-transgenic mouse model of AD. In regular mice (much cheaper than transgenic ones), a memory impairment similar to the early stage of AD is triggered by a single injection of $A\beta_{1-42}$ oligomers in the mouse cerebral lateral ventricles (intracerebroventricular [icv] model) [66]. The animal model is validated by the fact that injection of the control antisense peptide $A\beta_{42-1}$ has no effect on mouse memory and behavior. The ability of PA1637 to inhibit the episodic memory loss was evaluated on this non-transgenic murine model. After a short oral treatment with PA1637 (8 doses of PA1637, 25 mg/kg each, over a 3-week period), the episodic memory of AD mice was completely restored, similar to that of healthy animals, while that of untreated AD mice was significantly impaired [66]. These results clearly validated the oral administration of PA1637 to fully inhibit the cognitive impairment induced by icv injection of amyloid oligomers, a way to mimic the early stage of AD. At the moment, there is no treatment able to regenerate functional neurons in the late stages of AD. An efficient drug able to stop the development of AD in the early stages will be welcome.

4.4. *Tetradentate mono-8-aminoquinolines (TDMQ) against Alzheimer's disease*

In spite of the capacity of PA1637 to extract copper from copper–amyloid in vitro and to inhibit the catalytic production of H_2O_2 by Cu(II)–amyloid, its development was stopped due to its rather low bioavailability. To enhance the efficiency and druggability of such copper chelators, a new series of tetradentate amine ligands (named TDMQs) was designed. TDMQs were based on a mono(8-amino)quinoline motif substituted at the C2 position by a nitrogen-containing side chain, able to offer a N4-tetradentate square planar coordination site for Cu(II) complexes, similar to that of bis(8-AQ) (Figure 4) [67,68]. Structural modulation of the polyamine chain allowed tuning the geometry of the coordination site and, consequently, the copper selectivity and the ability to inhibit oxidative stress.

In this TDMQ series, the ligands having a side chain with $n = m = 2$ $(2+2$ methylene groups), exhibited the highest affinity values for Cu(II), with log K_{app} [Cu–L] values in the range 15–17, and also the highest selectivity for Cu(II) with respect to Zn(II) (ratio > 11 log units) [68]. These chelators were also able to transfer copper from Cu–Aβ to glutathione, and to inhibit the aerobic production of ROS induced by Cu–Aβ in the presence of a reductant [56]. These features are clearly related to the capacity of these N4-tetradentate ligands to offer a tetradentate square planar coordination sphere around the copper(II) ion, generating copper complexes with four nitrogen ligands in a N4 equatorial plane coordination sphere [69]. Noteworthily, bis(8-AQ) derivatives (structures depicted in Figure 4) offered the same coordination, resulting in similar correlations between the structures of the Cu(II)–L complexes and their physicochemical properties such as high affinity for Cu(II) and ability to inhibit ROS production [60].

Based on these results, TDMQ20 (Figure 4) was selected for evaluation of its anti-AD activity on three different mouse models. An oral treatment with TDMQ20 was used to check the possibility of reversing the cognitive and behavior impairments in two non-transgenic models mimicking the early stage of AD and in a transgenic one modeling a more advanced stage of AD. In the non-transgenic mice, memory deficits were triggered by a single injection of the copper complex of amyloid $A\beta_{1-42}$ in the lateral ventricles (icv-CuAβ model) or hippocampus (hippo-CuAβ model) of regular mice. The third model was the classical transgenic mouse 5XFAD model [70,71].

A short oral treatment with TDMQ20 of icv-CuAβ or hippo-CuAβ mice (10 mg/kg, 8 doses over 16 days) fully restored the cognitive status evaluated by the short-term novel object recognition (NOR) assay [72], in comparison to untreated AD mice (Figure 5) [73].

By comparison, the 8-hydroxyquinoline derivative clioquinol (CQ) did not significantly improved the short-term memory of icv-CuAβ- and hippo-CuAβ mice. The level of malondialdehyde, the signature of an oxidative stress, in the cortex of icv-CuAβ was also reduced by TDMQ20. The three-month oral treatment of transgenic 5XFAD mice with TDMQ20 also resulted in behavioral improvements. Pharmacokinetic studies in rats indicated that TDMQ20 has a good bioavailability and efficiently crosses the blood–brain barrier after oral administration [74]. Noteworthily, TDMQ20 did not exhibit significant acute or chronic toxicity [73].

In addition, a three-month oral treatment of 5XFAD mice with TDMQ20 remarkably reduced the plaque loading in the cortex by about 70%, suggesting a beneficial role of TDMQ20 in clearing pathological Aβ deposits in AD mice. The treatment also significantly increased the expression of the ChAT enzyme and the CHRM4 receptor, two proteins involved in the cholinergic system [75]. All these results strongly suggest that TDMQ20 is acting on several pathways of this multifactorial disease.

Due to their reliability and easy use, the icv-CuAβ and hippo-CuAβ mice should be considered as robust non-transgenic models to evaluate the activity of potential drugs in the early stages of memory deficits. Moreover, among other possible assays [76,77], the short-term NOR test was found particularly robust to evaluate the impairment of declarative memory in mice, making it easy to select molecules for the treatment of the early stages of AD.

One should keep in mind that the few current AD therapies are not curative and provide at best a short-term improvement in symptoms, with potentially serious side effects. Moreover, their efficiency/cost ratios are questionable. Despite intensive efforts on AD over the last two decades in genetics, biochemistry, and cell biology, the pipeline of new drugs is rather unproductive. As a reference point, lecanemab, approved in the United States for the treatment of AD, is an anti-amyloid monoclonal antibody administered intravenously every other week with a post-infusion observation period with monitoring of the effect by magnetic resonance imaging. In addition to these rather strong constraints, treatment with lecanemab results in frequent and potentially severe anticoagulation side effects, and this treatment is not recommended for patients with a wide range of comorbidities, a very frequent condition in aging patients [78]. In addition, the European health agency (EMA) initially refused this treatment (July 2024) [79]. Donanemab, another antibody targeting amyloids recently approved by the FDA (June 2024), also induces fatal brain bleeding in a few patients [80]. These facts strongly suggest that efforts should be made to support the discovery of new "small molecules", namely chemical agents, designed for an easy crossing of the blood–brain barrier in order to produce an efficient pharmacological effect on the early stages of AD, without strong constraints or potentially severe adverse effects.

So the efficacy of TDMQ20 by oral administration at low doses on three different AD mouse models with a very low toxicity, is an encouragement for a future development of this specific copper chelator, maybe in parallel with research of other molecules targeting different mechanisms. However, considering that the introduction of a new drug candidate in the pipeline of AD treatments is rather challenging, we decided to investigate the correlation between the copper chelating activity of TDMQ20 and its therapeutic interest in a well-known copper-related disease, namely the Wilson's disease.

5. Tetradentate mono-8-aminoquinoline TDMQ20 and Wilson's disease

Wilson's disease (WD) is a genetic disease caused by mutations on the *Atp7b* gene coding for the copper carrier ATP7B, an ATPase in charge of incorporating

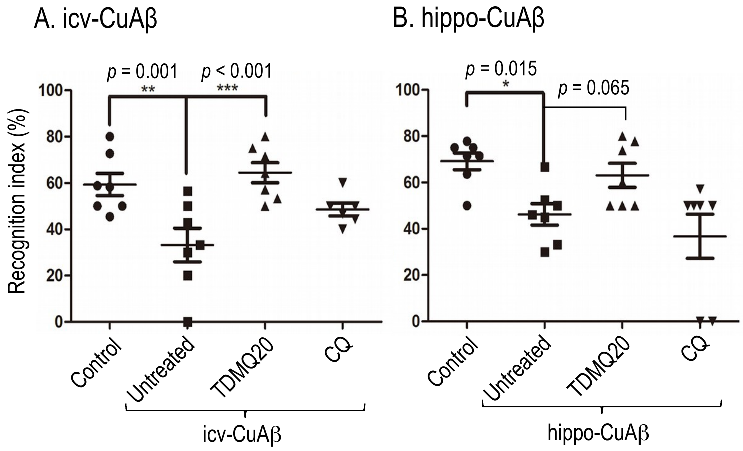

Figure 5. Declarative memory evaluated by the short-term novel object recognition task (NOR). The recognition index for short term memory in the icv-CuAβ and the hippo-CuAβ non-transgenic mouse models are reported in panels A and B, respectively. In each case, the recognition index of AD mice which received no drug-treatment (untreated group) was compared to that of healthy mice (control group), and to the recognition index of AD mice treated with TDMQ20 or clioquinol (CQ) (8 × 10 mg/kg in 16 days). Each mark represents the result obtained with a single mouse; horizontal lines represent mean values ± SEM. $^{***}p < 0.001$, $^{**}p < 0.01$, $^{*}p < 0.05$ vs. the untreated AD group (ANOVA). Adapted with permission from Figure 2 of Ref. [73]. Copyright 2020 American Chemical Society.

copper in apoceruloplasmin in the liver, leading to the elimination of this metal ion in bile and then in feces. Deficiency in this copper carrier causes accumulation of copper in the liver, generating acute or chronic hepatitis and liver cirrhosis, potentially leading to a fulminant hepatic failure. Copper is partially released in the bloodstream and slowly eliminated in urine. In advanced stages of the disease, neurological symptoms such as seizures or Parkinsonism appear, along with psychiatric disorders. Accumulation of copper in various organs, resulting especially in renal and cardiac pathologies as well as hypoparathyroidism and osteoarticular damages, are correlated with a fatal prognosis [17,18]. Lifelong treatment is therefore necessary, using copper chelators to facilitate the excretion of copper. The first-line drugs for WD treatment via oral administration are currently D-penicillamine (DPA) and, to a lesser extent, trientine, a non-selective polyamine chelator (Figure 6) [81].

These two drugs are given at very high doses (1–2 g per day for an adult) and exhibit adverse effects that may be serious enough to require discontinuation of the treatment (in approximately 30% of patients for DPA) [82,83]. The efficacy of DPA in neurologic

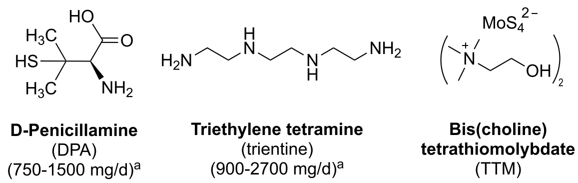

Figure 6. Structures of copper chelators currently used in the treatment of Wilson's disease (DPA and trientine), or in development (TTM). [a] Daily oral dosage for an adult [82].

WD is only moderate (55% of improvement rate), and both DPA and trientine induce a severe and irreversible neurological worsening in 10–50% of patients with previous neurological symptoms [84]. So there is a real medical need for a specific copper chelator able to efficiently regulate the copper excess, at lower doses than those used for DPA or trientine and with lower side effects in the long term. Ammonium tetrathiomolybdate has been proposed for more than 30 years [85], recently replaced by bis-choline tetrathiomolybdate (TTM, Figure 6) [86]. The MoS_4^{2-} ion chelates copper to form very stable and highly insoluble sulfur-bridged Mo–Cu clusters [87,88] detected in the liver of WD rat models [87], resulting in accumulation of molybdenum in major organs (spleen, liver, adrenal glands, kidney, and brain) following administration of TTM [89,90]. The high affinity of TTM for copper is also responsible for inhibition of major copper enzymes such as ceruloplasmin, ascorbate oxidase, cytochrome oxidase, Cu/Zn-superoxide dismutase and tyrosinase [91].

The main drawback of DPA and trientine as ligands is their lack of selectivity in metal chelation. In fact, both drugs coordinate with high affinities a wide variety of metal ions and oxidation states [92] (see footnote[1]). For example, DPA coordinates Cu^{2+} with $\log K_1 = 16.5$, but also Cu^+ ($\log K_1 = 19.5$), Zn^{2+} ($\log K_1 = 9.6$ and $\log \beta_2 = 19.6$) [92], as well as Fe^{2+}, Fe^{3+}, Co^{2+}, and Co^{3+} [93]. In addition, the structures of DPA–metal complexes can be diverse, including ternary complexes involving another amino acid such as histidine or methionine [94,95], or mixed valence Cu(I)/Cu(II) cluster complexes [96]. Moreover, the ability of DPA to act as a reductant due to its thiol functionality, in addition to its capacity to coordinate both Cu(II) and Cu(I) [or Fe(III) and Fe(II)], may confer to DPA complexes the ability to trigger deleterious Fenton-like reaction damages.

Due to the specificity of TDMQ20 for chelation of Cu(II) and the oral bioavailability of this ligand , we decided to evaluate its activity for the treatment of WD. In TX mice, a genetic model of WD [97], the overload of copper in the liver was reduced in a dose-dependent manner by a short oral treatment with TDMQ20 at doses ranging from 12.5 to 50 mg/kg/day (Figure 7a). This decrease in hepatic copper was correlated to an increase in fecal copper excretion (Figure 7b) [98]. These studies indicate that such low doses of TDMQ20 are more efficient at improving the physiological excretion pathway of copper in TX mice than DPA at 200 mg/kg/day. TDMQ20 also increases the serum concentration of ceruloplasmin (Figure 7c). Such an effect is particularly important since this concentration is a biomarker clinically used to evaluate the efficency of chelation therapy in patients with WD.

In addition, TDMQ20 up to 300 μM does not disturb the activity of Cu/Zn-SOD, in contrast with DPA, which inhibits Cu/Zn-SOD at a 50 μM concentration. In addition, the DPA–copper complex produces damaging ROS in vitro in the presence of a reducing agent, which is not the case with TDMQ20. In fact, DPA inhibits catalase in vitro and could be responsible for chronic inflammation through chronic disruption of H_2O_2 redox homeostasis in vivo [99]. In conclusion, TDMQ20 should be considered as a first-in-class drug candidate able to challenge DPA in the treatment of WD.

6. TDMQ20 copper chelator as anticancer agent

The possibility of using metal ligands in anticancer chemotherapy to regulate metal homeostasis has not been extensively explored, although it is known that the metal ion content is significantly higher in cancer cells compared to normal ones [100]. In particular, copper ions are involved in angiogenesis [101,102], which is essential for tumor growth and dissemination of cancer metastases [103,104]. It has been evidenced that copper depletion inhibits angiogenesis in cancer cells [105]. A few clinical trials have been reported with copper chelators such as DPA, trientine, or TTM, three ligands that have been documented for WD (see above, Figure 6). However, these attempts have not been successful, probably due to their lack of metal selectivity and/or potential toxicity [106]. So having TDMQ20 at hand as specific copper chelator, preliminary evaluation of its activity against different cancer cell lines was carried out. TDMQ20 was found cytotoxic against non-small cell lung carcinoma (A549), cervix cancer HeLa and hepatocarcinoma HepG2 cells, with IC_{50} values ranging from 14 to 16 μM in vitro, lower than the reference drug 5-Fluorouracil (5-FU), and the selectivity index of TDMQ20 was higher than that of 5-FU when using non-cancer human cells as comparators. TDMQ20 also exhibited a significant anti-migration activity on HeLa cells in vitro. Mechanistic studies indicated that the activity of TDMQ20 probably involves the overproduction of ROS, with the collapse of the inner transmembrane potential in mitochondria and the induction of apoptosis [107].

---

[1] $$M + L \underset{K_1}{\rightleftharpoons} ML \underset{K_2}{\overset{L}{\rightleftharpoons}} ML_2$$

$$K_1 = \frac{[ML]}{[M][L]} \quad K_2 = \frac{[ML_2]}{[ML][L]} \quad \beta_{1,2} = \frac{[ML_2]}{[M][L]^2} = K_1 K_2$$

(usually noted β_2)

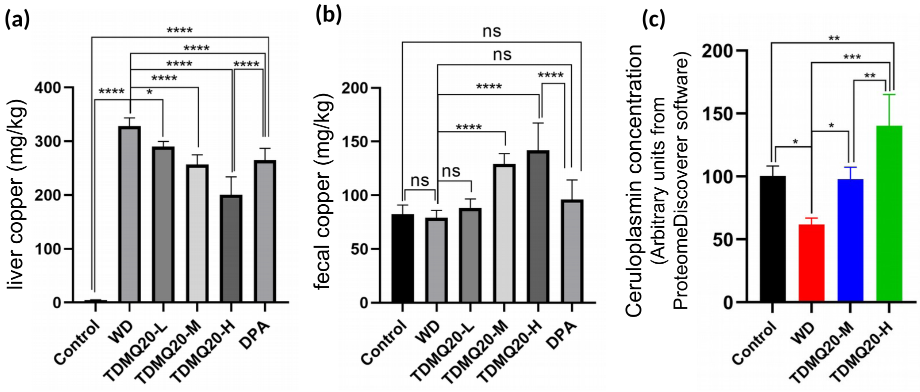

Figure 7. Concentration of copper in liver (a) and feces (b) in mg/kg, and of ceruloplasmin in serum (c) of TX mice (WD) after oral treatment with TDMQ20 at 12.5 mg/kg/d (TDMQ20-L), 25 mg/kg/d (TDMQ20-M), or 50 mg/kg/d (TDMQ20-H). WD mice orally treated by DPA at 200 mg/kg/d are given for comparison. Control mice are healthy C57BL/6 mice bearing no mutation on ATP7B. *$p < 0.05$, **$p < 0.01$, ***$p < 0.001$ and ****$p < 0.0001$. Adapted from Ref. [98].

7. Conclusion

Since copper plays essential functions in human body, this metal ion can be considered as a promising therapeutic target in several diseases. A twenty-five-year review of the state of the art in rational chelator design has led us from phenanthroline derivatives to the N4-tetradentate mono-8-aminoquinoline series, especially the TDMQ20 as a suitable copper(II) chelator for therapeutic use. Due to its optimized coordination properties, this specific Cu(II) ligand exhibits a promising activity on murine models of Alzheimer's and Wilson's diseases, two diseases involving copper dyshomeostasis and copper accumulation, respectively. Clinical development of TDMQ20 as a therapeutic alternative to DPA for normalizing copper levels in WD patients is currently under discussion. In addition, this chelator is more active than the reference drug 5-FU on several human cancer cell lines. Future clinical developments will be necessary to evidence which therapeutic domain will be best tackled by TDMQ20.

As a concluding remark, the specificity for copper chelation and the structure and properties of the corresponding copper complex are prerequesite parameters in the design of pharmacological ligands suitable for targeting diseases triggered by the pathological disruption of copper homeostasis.

Data availability

All data presented in this review article have been reported in the cited articles of our group and in the associated supporting information.

Acknowledgments

Authors gratefully acknowledge all colleagues, postdoctoral fellows, PhD and master students, and collaborators who have been involved in the research of specific metal regulators as potential drugs.

Declaration of interests

The authors do not work for, advise, own shares in, or receive funds from any organization that could benefit from this article, and have declared no affiliations other than their research organizations.

Funding

Financial support was received from the CNRS, Inserm, and GDUT.

References

[1] J. J. R. Frausto da Silva and R. J. P. Williams, *The Biological Chemistry of the Elements: The Inorganic Chemistry of Life*, Oxford University Press: Oxford, 2001.

[2] E. D. Gaier, B. A. Eipper and R. E. Mains, "Copper signaling in the mammalian nervous system: synaptic effects", *J. Neurosci. Res.* **91** (2012), pp. 2–19.

[3] J. J. P. Perry, D. S. Shin, E. D. Getzoff and J. A. Tainer, "The structural biochemistry of the superoxide dismutases", *Biochem. BioPhys. Acta* **180** (2010), pp. 245–262.

[4] E. I. Solomon, U. M. Sundaram and T. E. Machonkin, "Multicopper oxidases and oxygenases", *Chem. Rev.* **96** (1996), pp. 2563–2605.

[5] G. Babcock, L. E. Vickery and G. Palmer, "The electronic state of heme in cytochrome oxidase II", *J. Biol. Chem.* **253** (1978), pp. 2400–2411.

[6] D. A. Rowley and B. Halliwell, "Formation of hydroxyl radicals from NADH and NADPH in the presence of copper salts", *J. Inorg. Biochem.* **23** (1985), pp. 103–108.

[7] B. E. Kim, T. Nevitt and D. J. Thiele, "Mechanisms for copper acquisition, distribution and regulation", *Nature Chem. Biol.* **4** (2008), pp. 176–185.

[8] W. Lai, Q. Wei, J. Zhuang, M. Lu and D. Tang, "Fenton reaction-based colorimetric immunoassay for sensitive detection of brevetoxin, B", *Biosens. Bioelectron.* **80** (2016), pp. 249–256.

[9] M. A. Lovell, J. D. Robertson, W. J. Teesdale, J. L. Campbell and W. R. Markesbery, "Copper, iron and zinc in Alzheimer's disease senile plaques", *J. Neurol. Sci.* **158** (1998), pp. 47–52.

[10] C. S. Atwood, R. C. Scarpa, X. Huang, R. D. Moir, W. D. Jones, D. P. Fairlie, R. E. Tanzi and A. I. Bush, "Characterization of copper interactions with Alzheimer amyloid β-peptides: identification of an attomolar-affinity copper bonding site on amyloid β_{1-42}", *J. Neurochem.* **75** (2000), pp. 1219–1233.

[11] A. Robert, Y. Liu, M. Nguyen and B. Meunier, "Regulation of copper and iron homeostasis by metal chelators: a possible chemotherapy for Alzheimer's disease", *Acc. Chem. Res.* **48** (2015), pp. 1332–1339.

[12] J. S. Valentine, P. A. Doucette and S. Z. Potter, "Copper-zinc superoxide dismutase and amyotrophic lateral sclerosis", *Ann. Rev. Biochem.* **74** (2005), pp. 563–593.

[13] D. J. Waggoner, T. B. Bartnikas and J. D. Gitlin, "The role of copper in neurodegenerative disease", *Neurobiol. Dis.* **6** (1999), pp. 221–230.

[14] M. Rios, B. Habecker, T. Sasaoka, G. Eisenhofer, H. Tian, S. Landis, D. Chikaraishi and S. Roffler-Tarlov, "Catecholamine synthesis is mediated by tyrosinase in the absence of tyrosine hydroxylase", *J. Neurosci.* **19** (1999), pp. 3519–3526.

[15] T. Xiao, C. M. Ackerman, E. C. Carroll, et al., "Copper regulates rest-activity cycles through the locus coeruleus-norepinephrine system", *Nat. Chem. Biol.* **14** (2018), pp. 655–663.

[16] O. Bandmann, K. H. Weiss and S. G. Kaler, "Wilson's disease and other neurological copper disorders", *Lancet Neurol.* **14** (2015), pp. 103–113.

[17] A. Lucena-Valera, D. Perez-Palacios, R. Muñoz-Hernandez, M. Romero-Gómez and J. Ampuero, "Wilson's disease: revisiting an old friend", *World J. Hepatol.* **13** (2021), pp. 634–649.

[18] J. R. Forbes, G. Hsi and D. W. Cox, "Role of the copper-binding domain in the copper transport function of ATP7B, the P-type ATPase defective in Wilson disease", *J. Biol. Chem.* **274** (1999), pp. 12408–12413.

[19] B. X. Wong, A. Tsatsanis, L. Q. Lim, P. A. Adlard, A. I. Bush and J. A. Duce, "β-Amyloid precursor protein does not possess ferroxidase activity but does stabilize the cell surface ferrous iron exporter ferroportin", *PLoS One* **9** (2014), article no. e114174.

[20] D. S. Sigman, A. Mazumder and D. M. Perrin, "Chemical nucleases", *Chem. Rev.* **93** (1993), pp. 2295–2316.

[21] G. Pratviel, J. Bernadou and B. Meunier, "DNA and RNA cleavage by metal complexes", *Adv. Inorg. Chem.* **45** (1998), pp. 251–312.

[22] G. Pratviel, J. Bernadou and B. Meunier, "Carbon-hydrogen bonds of DNA sugar units as targets for chemical nucleases and drugs", *Angew. Chem. Int. Ed.* **34** (1995), pp. 746–769.

[23] J. M. Veal, K. Merchant and R. L. Rill, "The influence of reducing agent and 1,10-phenanthroline concentration on DNA cleavage by phenanthroline + copper", *Nucleic Acids Res.* **19** (1991), pp. 3383–3388.

[24] C. Queffélec, P. Baran Pati and Y. Pellegrin, "Fifty shades of phenanthroline: synthesis strategies to functionalize 1,10-Phenanthroline in all positions", *Chem. Rev.* **124** (2024), pp. 6700–6902.

[25] B. James and R. J. P. Williams, "The oxidation–reduction potentials of some copper complexes", *J. Chem. Soc.* (1961), pp. 2007–2019.

[26] M. Pitié, B. Donnadieu and B. Meunier, "Preparation of the new bis(phenanthroline) ligand "Clip-Phen" and evaluation of the nuclease activity of the corresponding copper complex", *Inorg. Chem.* **37** (1998), pp. 3486–3489.

[27] M. Pitié, B. Sudres and B. Meunier, "Dramatic increase of the DNA cleavage activity of Cu(Clip-phen) by fixing the bridging linker on the C3 position of the phenanthroline units", *Chem. Commun.* (1998), pp. 2597–2598.

[28] M. Pitié, C. Boldron, H. Gornitzka, C. Hemmert, B. Donnadieu and B. Meunier, "DNA Cleavage by copper complexes of 2- and 3-Clip-Phen derivatives", *Eur. J. Inorg. Chem.* (2003), pp. 528–540.

[29] M. Pitié and B. Meunier, "Preparation of a spermine conjugate of the bis-phenanthroline ligand Clip-Phen and evaluation of the corresponding copper complex", *Bioconjugate Chem.* **9** (1998), pp. 604–611.

[30] A. Casini and A. Pothig, "Metals in cancer research: beyond platinum metallodrugs", *ACS Centr. Sci.* **10** (2024), pp. 242–250.

[31] A. De Vizcaya Ruiz, A. Rivero-Muller, L. Ruiz-Ramirez, G. E. N. Kass, L. R. Kelland, R. M. Orr and M. Dobrota, "Induction of apoptosis by a novel copper-based anticancer compound-Casiopeina II in L1210 murine leukaemia and CH1 human ovarian carcinoma", *Tox. In Vitro* **14** (2000), pp. 1–5.

[32] I. Gracia-Mora, L. Ruiz-Ramirez, C. Gomez-Ruiz, et al., "Knight's move in the periodic table, from copper to platinum, novel antitumor mixed chelate copper compounds, casiopeina, evaluated by an in vitro human and

murine cancer cell line panel", *Met. Based Drugs* **8** (2001), pp. 19–28.

[33] M. Pitié, A. Croisy, D. Carrerz, C. Boldron and B. Meunier, "Cytostatic activity of 1,10-phenanthroline derivatives generated by the Clip-Phen strategy", *ChemBioChem* **6** (2005), pp. 686–691.

[34] C. Deegan, B. Coyle, M. McCann, M. Devereux and D. A. Egan, "In vitro anti-tumour effect of 1,10-phenanthroline-5,6-dione (phendione), $[Cu(phendione)_3](ClO_4)_2{\bullet}4H_2O$ and $[Ag(phendione)_2]ClO_4$ using human epithelial cell lines", *Chem. Biol. Interact.* **164** (2006), pp. 115–125.

[35] J. C. García-Ramos, G. Vértiz-Serrano, L. Macías-Rosales, R. Galindo-Murillo, Y. Toledano-Magaña, J. P. Bernal, F. Cortés-Guzmán and L. Ruiz-Azuara, "Isomeric effect on the pharmacokinetic behavior of anticancer Cu^{II} mixed chelate complexes: experimental and theoretical approach", *Eur. J. Inorg. Chem.* (2017), pp. 1728–1736.

[36] P. H. Alves Machado, D. A. Paixão, R. Campos Lino, et al., "A selective Cu^{II} complex with 4-fluorophenoxyacetic acid hydrazide and phenanthroline displays DNA-cleaving and pro-apoptotic properties in cancer cells", *Sci. Rep.* **11** (2021), article no. 24450.

[37] M. A. Uvarova, I. A. Lutsenko, M. A. Shmelev, S. E. Nefedov, O. B. Bekker, A. I. Lashkin, V. O. Shender and I. L. Eremenko, "Research of the influence of anions in complexes $[CuPhen(Hpz)_2X_2]$ ($X = CF_3\ COO^-$, Otf^-, Cl^-) on the structure and bioactivity", *New J. Chem.* **48** (2024), pp. 717–723.

[38] K. J. Barnham and A. I. Bush, "Biological metals and metal-targeting compounds in major neurodegenerative diseases", *Chem. Soc. Rev.* **43** (2014), pp. 6727–6749.

[39] K. P. Kepp, "Alzheimer's disease: How metal ions define β-amyloid function", *Coord. Chem. Rev.* **351** (2017), pp. 127–159.

[40] L. Guilloreau, S. Combalbert, A. Sournia-Saquet, H. Mazarguil and P. Faller, "Redox chemistry of copper-amyloid-beta: the generation of hydroxyl radical in the presence of ascorbate is linked to redox-potentials and aggregation state", *ChemBioChem* **8** (2007), pp. 1317–1325.

[41] Y. Liu, M. Nguyen, A. Robert and B. Meunier, "Metal ions in Alzheimer's disease: a key role or not?", *Acc. Chem. Res.* **52** (2019), pp. 2026–2035.

[42] S. J. C. Lee, E. Nam, H. J. Lee, M. G. Savelieff and M. H. Lim, "Towards an understanding of amyloid-beta oligomers: characterization, toxicity mechanisms, and inhibitors", *Chem. Soc. Rev.* **46** (2017), pp. 310–323.

[43] E. G. McGeer and P. L. McGeer, "Brain inflammation in Alzheimer disease and the therapeutic implications", *Curr. Pharm. Des.* **5** (1999), pp. 821–836.

[44] T. A. Bayer, S. Schäfer, A. Simons, et al., "Dietary Cu stabilizes brain superoxide dismutase 1 activity and reduces amyloid Abeta production in APP23 transgenic mice", *Proc. Natl. Acad. Sci. USA* **100** (2003), pp. 14187–14192.

[45] P. Faller and C. Hureau, "A Bioinorganic View of Alzheimer's Disease: when misplaced metal ions (re)direct the electrons to the wrong target", *Chem. Eur. J.* **18** (2012), pp. 15910–15920.

[46] L. R. Perez and K. J. Franz, "Minding metals: tailoring multifunctional chelating agents for neurodegenerative disease", *Dalton Trans.* **39** (2010), pp. 2177–2187.

[47] R. A. Cherny, C. S. Atwood, M. E. Xilinas, et al., "Treatment with a copper-zinc chelator markedly and rapidly inhibits beta-amyloid accumulation in Alzheimer's disease transgenic mice", *Neuron* **30** (2001), pp. 665–676.

[48] N. G. Faux, C. W. Ritchie, A. Gunn, et al., "PBT2 rapidly improves cognition in Alzheimer's Disease: additional phase II analyses", *J. Alzheimer's Dis.* **20** (2010), pp. 509–516.

[49] D. A. Andersson, C. Gentry, S. Moss and S. Bevan, "Clioquinol and pyrithione activate TRPA1 by increasing intracellular Zn^{2+}", *Proc. Natl. Acad. Sci. USA* **109** (2009), pp. 8374–8379.

[50] A. Takeda, S. Takada, M. Ando, K. Itagaki, H. Tamano, M. Suzuki, H. Iwaki and N. Oku, "Impairment of recognition memory and hippocampal long-term potentiation after acute exposure to clioquinol", *Neuroscience* **171** (2010), pp. 443–450.

[51] J. P. Phillips, "The reactions of 8-quinolinol", *Chem. Rev.* **56** (1956), pp. 271–297.

[52] E. Ferrada, V. Arancibia, B. Loeb, E. Norambuena, C. Olea-Azar and J. P. Huidobro-Toro, "Stoichiometry and conditional stability constants of Cu(II) or Zn(II) clioquinol complexes; implications for Alzheimer's and Huntington's disease therapy", *Neurotoxicology* **28** (2007), pp. 445–449.

[53] A. Therapeutics, *Prana Biotechnology Announces Top-Line Results of Phase 2 IMAGINE Trial of PBT2 in Alzheimer's Disease*, 2014. Online at https://alteritytherapeutics.com/investor-centre/news/2014/03/31/prana-biotechnology-announces-top-line-results-phase-2-imagine-trial-pbt2-alzheimers-disease/ (accessed on September 18, 2025).

[54] M. Nguyen, A. Robert, A. Sournia-Saquet, L. Vendier and B. Meunier, "The necessity of having a tetradentate ligand to extract copper(ii) ions from amyloids", *ChemistryOpen* **4** (2015), pp. 27–31.

[55] M. Nguyen, L. Vendier, J.-L. Stigliani, B. Meunier and A. Robert, "Structures of the copper and zinc complexes of PBT2, a chelating agent evaluated as potential drug for neurodegenerative diseases", *Eur. J. Inorg. Chem.* (2017), pp. 600–608.

[56] W. Zhang, Y. Liu, C. Hureau, A. Robert and B. Meunier, "N4-Tetradentate chelators efficiently regulate copper homeostasis and prevent ROS production induced by copper-amyloid-β_{1-16}, even in the presence of an excess of zinc", *Chem. Eur. J.* **24** (2018), pp. 7825–7829.

[57] C. Deraeve, M. Pitié, H. Mazarguil and B. Meunier, "Bis-8-hydroxyquinoline ligands as potential anti-Alzheimer agents", *New J. Chem.* **31** (2007), pp. 193–195.

[58] C. Deraeve, C. Boldron, A. Maraval, H. Mazarguil, H. Gornitzka, L. Vendier, M. Pitié and B. Meunier, "Preparation and study of new poly-8-hydroxyquinoline chelators for an anti-Alzheimer strategy", *Chem. Eur. J.* **14** (2008), pp. 682–696.

[59] S. Noël, S. Bustos Rodriguez, S. Sayen, E. Guillon, P. Faller and C. Hureau, "Use of a new water-soluble Zn sensor

to determine Zn affinity for the amyloid-β peptide and relevant mutants", *Metallomics* **6** (2014), pp. 1220–1222.

[60] M. Nguyen, A. Robert, A. Sournia-Saquet, L. Vendier and B. Meunier, "Characterization of new specific copper chelators as potential drugs for the treatment of Alzheimer's disease", *Chem. Eur. J.* **20** (2014), pp. 6771–6785.

[61] M. Nguyen, C. Bijani, N. Martins, B. Meunier and A. Robert, "Transfer of copper from an amyloid to a natural copper-carrier peptide with a specific mediating ligand", *Chem. Eur. J.* **21** (2015), pp. 17085–17090.

[62] J. F. Quinn, C. J. Harris, K. E. Cobb, C. Domes, M. Ralle, G. Brewer and T. L. Wadsworth, "A copper-lowering strategy attenuates amyloid pathology in a transgenic mouse model of Alzheimer's disease", *J. Alzheimer's Dis.* **21** (2010), pp. 903–914.

[63] P. A. Adlard, L. Bica, A. R. White, et al., "Metal ionophore treatment restores dendritic spine density and synaptic protein levels in a mouse model of Alzheimer's disease", *PLoS One* **6** (2011), article no. e17669.

[64] K. R. Zahs and K. H. Ashe, ""Too much good news" – are Alzheimer mouse models trying to tell us how to prevent, not cure, Alzheimer's disease?", *Trends Neurosci.* **33** (2010), pp. 381–389.

[65] "Editorial. "Why are drug trials in Alzheimer's disease failing?", *The Lancet* **376** (2010), pp. 658–658.

[66] J. Ceccom, F. Coslédan, H. Halley, B. Francès, J.-M. Lassalle and B. Meunier, "Copper chelator induced efficient episodic memory recovery in a non-transgenic Alzheimer's mouse model", *PLoS One* **7** (2012), article no. e43105.

[67] Y. Liu, X. Liu, D. Huang, M. Huang, D. Wang, M. Nguyen, A. Robert and B. Meunier, Four-tooth chelating single quinoline derivative, preparation method thereof and application as metal ion regulator for neurodegenerative disease, CN patent, 201610369550.X, 2016.

[68] W. Zhang, D. Huang, M. Huang, et al., "Preparation of tetradentate copper chelators as potential anti-Alzheimer agents", *ChemMedChem* **13** (2018), pp. 684–704.

[69] Y. Li, M. Nguyen, M. Baudoin, L. Vendier, Y. Liu, A. Robert and B. Meunier, "Why is tetradentate coordination essential for potential copper homeostasis regulators in Alzheimer's disease?", *Eur. J. Inorg. Chem.* (2019), pp. 4712–4718.

[70] H. Oakley, S. L. Cole, S. Logan, et al., "Intraneuronal β-amyloid aggregates, neurodegeneration, and neuron loss in transgenic mice with five familial Alzheimer's disease mutations: potential factors in amyloid plaque formation", *J. Neurosci.* **26** (2006), pp. 10129–10140.

[71] S. Jawhar, A. Trawicka, C. Jenneckens, T. A. Bayer and O. Wirths, "Motor deficits, neuron loss, and reduced anxiety coinciding with axonal degeneration and intraneuronal Aβ aggregation in the 5XFAD mouse model of Alzheimer's disease", *Neurobiol. Aging* **33** (2012), 196.e29–196.e40.

[72] B. Grayson, M. Leger, C. Piercy, L. Adamson, M. Harte and J. C. Neill, "Assessment of disease-related cognitive impairments using the novel object recognition (NOR) task in rodents", *Behav. Brain Res.* **285** (2015), pp. 176–193.

[73] J. Zhao, Q. Shi, H. Tian, et al., "TDMQ20, a specific copper chelator, reduces memory impairments in Alzheimer's disease mouse models", *ACS Chem. Neurosci.* **12** (2021), pp. 140–149.

[74] L. Huang, Y. Zeng, Y. Li, Y. Zhu, Y. He, Y. Liu, A. Robert and B. Meunier, "Distribution in rat blood and brain of TDMQ20, a copper chelator designed as a drug-candidate for Alzheimer's disease", *Pharmaceutics* **14** (2022), article no. 2691.

[75] F. Sun, J. Zhao, H. Zhang, Q. Shi, Y. Liu, A. Robert, Q. Liu and B. Meunier, "System and synaptic transmission in a mouse model of Alzheimer's disease", *ACS Chem. Neurosci.* **13** (2022), pp. 3093–3107.

[76] A. K. Kraeuter, P. C. Guest and Z. Sarnyai, "The Y-maze for assessment of spatial working and reference memory in mice", *Methods Mol. Biol.* **1916** (2019), pp. 105–111.

[77] A. A. Walf and C. A. Frye, "The use of the elevated plus maze as an assay of anxiety-related behavior in rodents", *Nat. Protoc.* **2** (2007), pp. 322–328.

[78] J. Cummings, L. Apostolova, G. Rabinovici, et al., "Alzheimer's disease and related disorders therapeutics work group, Lecanemab: appropriate use recommendations", *J. Prev. Alzheimers Dis.* **10** (2023), pp. 362–377.

[79] E. M. Agency, *Questions and Answers on the Approval and Marketing Authorisation of Leqembi (Lecanemab)*, 2024. Online at https://www.ema.europa.eu/en/documents/medicine-qa/questions-answers-approval-marketing-authorisation-leqembi-lecanemab_en.pdf (accessed on October 7, 2025).

[80] J. Couzin-Frankel, "New Alzheimer's drug clears FDA advisory vote despite unknowns", *Science* **384** (2024), pp. 1164–1165.

[81] J. M. Walshe, "The conquest of Wilson's disease", *Brain* **132** (2009), pp. 2289–2295.

[82] K. H. Weiss, F. Thurik, D. N. Gotthardt, et al., "EUROWILSON Consortium. Efficacy and safety of oral chelators in treatment of patients with Wilson disease", *Clin. Gastroenterol. Hepatol.* **11** (2013), pp. 1028–1035.

[83] E. A. Roberts and M. L. Schilsky, "American Association for Study of Liver Diseases (AASLD), diagnosis and treatment of Wilson disease: an update", *Hepatology* **47** (2008), pp. 2089–2111.

[84] G. J. Brewer, "Neurologically presenting Wilson's disease: epidemiology, pathophysiology and treatment", *CNS Drugs* **19** (2005), pp. 185–192.

[85] G. J. Brewer, R. D. Dick, V. Johnson, Y. Wang, V. Yuzbasiyan-Gurkan, K. Kluin, J. K. Fink and A. Aisen, "Treatment of Wilson's disease with ammonium tetrathiomolybdate", *Arch. Neurol.* **51** (1994), pp. 545–554.

[86] K. H. Weiss, F. K. Askari, A. Czlonkowska, et al., "Bischoline tetrathiomolybdate in patients with Wilson's disease: an open-label, multi-centre, phase 2 study", *Lancet Gastroenterol. Hepatol.* **2** (2017), pp. 869–876.

[87] G. N. George, I. J. Pickering, H. H. Harris, J. Gailer, D. Klein, J. Lichtmannegger and K.-H. Summer, "Tetrathiomolybdate causes formation of hepatic

copper-molybdenium clusters in an animal model of Wilson's disease", *J. Am. Chem. Soc.* **125** (2003), pp. 1704–1705.

[88] G. R. Helz and B. E. Erickson, "Extraordinary stability of copper(I)-tetrathiomolybdate complexes: possible implication for aquatic ecosystems", *Environ. Toxicol. Chem.* **30** (2011), pp. 97–102.

[89] Y. Plitz and L. Boyling, "Metabolic disposition of WTX101 (bis-choline tetrathiomolybdate) in a rat model of Wilson's disease", *Xenobiotica* **49** (2019), pp. 332–338.

[90] J. R. Foster, K. Billimoria, M. E. del Castillo Busto, S. Strekopytov, H. Goenaga-Infante and T. J. Morley, "Accumulation of molybdenum in major organs following repeated oral administration of bis-choline tetrathiomolybdate in the Sprague Dawley rat", *J. Appl. Toxicol.* **42** (2022), pp. 1807–1821.

[91] H. M. Alvarez, Y. Xue, C. D. Robinson, et al., "Tetrathiomolybdate inhibits copper trafficking proteins through metal cluster formation", *Science* **327** (2010), pp. 331–334.

[92] A. E. Martell (ed.), in *Stability Constants of Metal-ion Complexes*, 2nd edition, Royal Society of Chemistry: London, 1971.

[93] L. G. Stadtherr and R. B. Martin, "Iron(II) and iron(III) complexes of penicillamine", *Inorg. Chem.* **11** (1972), pp. 92–94.

[94] P. de Meester and D. J. Hodgson, "Model for the binding of D-penicillamine to metal ions in living systems: synthesis and structure of L-histidinyl-D-penicillaminatocobalt(III) monohydrate, [Co(L-His)(D-Pen)]•H_2O", *J. Am. Chem. Soc.* **99** (1977), pp. 101–104.

[95] B. B. Tewari, "Studies on complexation in solution with a paper electrophoretic technique [The system copper(II)/cobalt(II)-methionine-penicillamine]", *J. Chem. Eng. Data* **55** (2010), pp. 1779–1783.

[96] P. J. M. W. L. Birker and H. C. Freeman, "Structure, properties, and function of a copper(I)-copper(II) complex of D-penicillamine: Pentathallium(I) 8-chloro-dodeca(D-penicillaminato)-octocuprate(I)hexacuprate(II) n-hydrate", *J. Am. Chem. Soc.* **99** (1977), pp. 6890–6899.

[97] M. B. Theophilos, D. W. Cox and J. F. B. Mercer, "The toxic milk model is a murine model of Wilson disease", *Human Mol. Genet.* **5** (1996), pp. 1619–1624.

[98] Y. Zhu, Y. Tang, L. Huang, M. Nguyen, Y. Liu, A. Robert and B. Meunier, "The specific copper(II) chelator TDMQ20 is efficient for the treatment of Wilson's disease in mice", *Pharmaceutics* **15** (2023), article no. 2719.

[99] D. Padovani and E. Galardon, "Molecular basis for the interaction of catalase with D-penicillamine: rationalization of some of its deleterious effects", *Chem. Res. Toxicol.* **35** (2022), pp. 412–421.

[100] D. Yoshida, Y. Ikeda and S. Nakazawa, "Quantitative analysis of copper, zinc and copper/zinc ratio in selected human brain tumors", *J. Neurooncol.* **16** (1993), pp. 109–115.

[101] E. Urso and M. Maffia, "Behind the link between copper and angiogenesis: established mechanisms and an overview on the role of vascular copper transport systems", *J. Vasc. Res.* **52** (2015), pp. 172–196.

[102] L. Chen, J. Min and F. Wang, "Copper homeostasis and cuproptosis in health and disease", *Signal Transduct. Target. Ther.* **7** (2022), article no. 378.

[103] S. Ishida, P. Andreux, C. Poitry-Yamate, J. Auwerx and D. Hanahan, "Bioavailable copper modulates oxidative phosphorylation and growth of tumors", *Proc. Natl. Acad. Sci. USA* **110** (2013), pp. 19507–19512.

[104] E. J. Ge, A. I. Bush, A. Casini, et al., "Connecting copper and cancer: from transition metal signalling to metalloplasia", *Nat. Rev. Cancer* **22** (2022), pp. 102–113.

[105] L. Finney, S. Vogt, T. Fukai and D. Glesne, "Copper and angiogenesis: unravelling a relationship key to cancer progression", *Clin. Exp. Pharmacol. Physiol.* **36** (2009), pp. 88–94.

[106] C. Santini, M. Pellei, V. Gandin, M. Porchia, F. Tisato and C. Marzano, "Advances in copper complexes as anticancer agents", *Chem. Rev.* **114** (2014), pp. 815–862.

[107] Y. Guan, M. Nguyen, A. Robert, Y. Liu and B. Meunier, "Copper selective 8-aminoquinoline based tetradentate chelators as anticancer agents", *RSC Med. Chem.* **15** (2024), pp. 3048–3056.

ACADÉMIE
DES SCIENCES
INSTITUT DE FRANCE

Comptes Rendus. Chimie
2025, Vol. 28, p. 911-924
https://doi.org/10.5802/crchim.426

Research article

2-Deoxystreptamine as a platform to design original inhibitors of oncogenic miRNA biogenesis

Thi Phuong Anh Tran [a], Nadia Patino [a], Audrey Di Giorgio [a] and Maria Duca [*, a]

[a] Université Côte d'Azur, CNRS, Institut de Chimie de Nice (ICN), 28 avenue Valrose, 06100 Nice, France

E-mail: maria.duca@univ-cotedazur.fr (M. Duca)

Abstract. MicroRNAs are small non-coding RNAs playing a key role in the regulation of gene expression. The overexpression of microRNAs in cancer has been recognized not only as a specific biomarker but also as a potential target to inhibit cancer cell proliferation or increase their sensitivity to chemotherapy. In this work, we present 2-deoxystreptamine as an ideal platform for the design and synthesis of selective RNA binders directed against the biogenesis of an oncogenic microRNA: miR-372. The developed compounds have been designed to bind to the structured precursor of this microRNA and block its processing toward the mature miRNA (miR-372). The performed affinity and selectivity studies revealed that one of the prepared binders is particularly selective for the targeted miRNAs and shows a very promising activity in inhibiting the production of the mature miRNAs.

Keywords. RNA ligands, RNA targeting, MicroRNAs, 2-Deoxystreptamine, Carbamates.

Note. Article submitted by invitation.

Manuscript received 19 September 2025, revised 6 October 2025, accepted 8 October 2025.

1. Introduction

Targeting RNA using synthetic small molecules has become an important field of medicinal chemistry [1]. Indeed, the targeting of biologically relevant RNAs is an interesting approach for the discovery of innovative therapies because of the essential role that RNA plays in all major biological processes [2]. Noteworthy, RNA bears a tridimensional structure associating single-stranded and double-stranded regions and leading to the formation of stem-loop structures containing internal loops and bulges that create ideal binding sites for small-molecule ligands due to the distortion of the RNA double helix [3]. A number of RNA binders has been reported in the literature during the last twenty years against viral, bacterial and oncogenic RNAs [4]. Furthermore, drugs acting as RNA binders are already on the market, such as the antibiotic aminoglycosides or mRNA splicing modulators, such as risdiplam [5]. However, methods to rationally design ligands specific to a particular RNA structure remain underdeveloped because of a lack of knowledge about the tridimensional structure of most RNA targets as well as about the interactions formed by the reported ligands [1].

During the last years, our group has focused on the targeting of non-coding RNAs, such as microRNAs (miRNAs or miRs). These small non-coding RNAs are responsible for the regulation of gene expression [6]. They are produced in the cell starting from two precursors: primary miRNAs (pri-miRNAs) followed by precursor miRNAs (pre-miRNAs) upon processing by intracellular ribonucleases called Drosha and Dicer, respectively (Figure 1A). These precursors are stem-loop–structured RNAs and have been reported as targets for small molecules. In this context, we reported various series of compounds whose synthesis was performed using a focused design [7–14] based on the conjugation of various RNA-binding domains that act cooperatively to bind the RNA target with both affinity and selectivity.

* Corresponding author

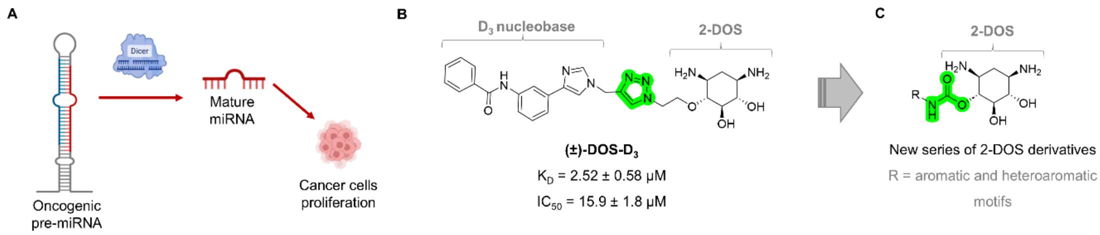

Figure 1. (A) General process of pre-miRNA cleavage by Dicer to produce the mature miRNA. When the miRNA is oncogenic, its production induces the proliferation of cancer cells, and the pre-miRNA represents a potential target for small molecules to block cancer cell proliferation. (B) Chemical structure of a previously identified pre-miR-372 binder based on 2-DOS conjugated via a triazole linker to a heteroaromatic motif to form **DOS-D$_3$**. (C) General chemical structure of the 2-DOS conjugates prepared in this study.

More specifically, several binding domains such as aminoglycosides, heteroaromatic compounds, and amino acids [10,11,13,14] were combined to synthesize ligands directed against the production of miR-372, an oncogenic miRNA involved in various cancers [15,16], such as gastric cancer. This work allowed us to develop optimized compounds with a specific antiproliferative activity in gastric adenocarcinoma cells overexpressing miR-372. The mechanism of this inhibition was clearly identified as resulting from the binding to pre-miR-372 and the inhibition of Dicer processing leading to mature miRNA. Among these ligands, there were a series of conjugates containing the 2-deoxystreptamine (2-DOS) core linked to various heteroaromatic compounds via a triazole linker [17]. This led us to the discovery of compound **DOS-D$_3$** (Figure 1B), which showed a low micromolar affinity for pre-miR-372 as well as a low micromolar IC_{50} for the inhibition of Dicer processing. This compound is composed of a 2-DOS structure, present in most of the aminoglycoside antibiotics that act by binding to prokaryotic ribosomal RNA thus impairing protein synthesis in bacteria, coupled via a triazole linker to an artificial nucleobase called D$_3$. While 2-DOS is known to strongly interact with RNA but lacks selectivity, the heteroaromatic moiety D$_3$ is known to selectively interact with A•U base pairs via the formation of specific hydrogen bonds to form a base triplet [18]. Thus, derivatives combining 2-DOS and more selective substructures (such as D$_3$ for example) have the advantage of bearing more favorable physicochemical properties than their aminoglycoside counterpart while maintaining a similar affinity for RNA. In this work, we decided to explore the carbamate linker as a replacement for the triazole one to modify the properties of the compounds (Figure 1C). Indeed, while both triazole and carbamate are commonly employed in medicinal chemistry, the carbamate linker is more flexible and could improve affinity and binding properties [19]. Carbamates can serve as both hydrogen-bond donors and acceptors and, since they are geometrically and electronically closer to amides than triazoles, they can better mimic peptide-like motifs, peptides being the RNA binders chosen by Nature.

We thus prepared a series of nine derivatives where 2-DOS was conjugated with a carbamate linker to aromatic and heteroaromatic compounds. These new derivatives have been studied against our primary target, pre-miR-372, but also against other miRNAs that could represent potential targets or competitors. The study of the affinity, selectivity and inhibition activity for the processing of these miRNAs revealed a promising selectivity profile for some compounds that could be exploited for future intracellular studies.

2. Results and discussion

2.1. *Synthesis of 2-deoxystreptamine derivatives*

2-DOS represents an ideal platform for the development of RNA binders since it bears two *cis*-amino groups recognized as very important for RNA binding and hydroxyl groups that can be functionalized [20,21]. We thus decided to substitute one of the hydroxyl groups with various aromatic and heteroaromatic substituents via the formation of

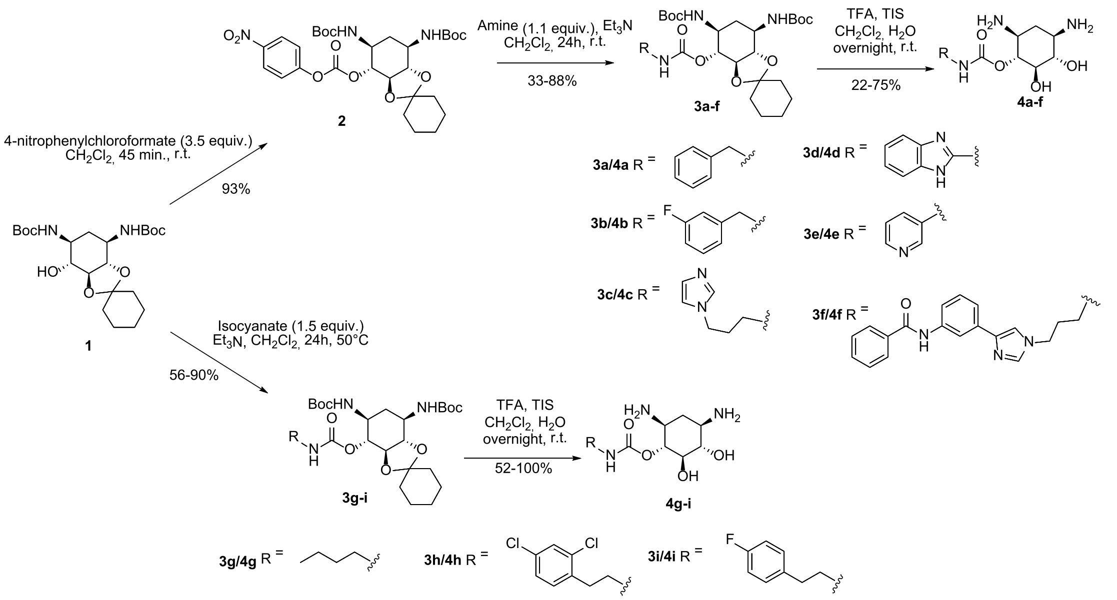

Scheme 1. Synthesis of new carbamate derivatives of 2-DOS **4a–i**.

a carbamate linker. Carbamates show many advantages, such as the ability to permeate the cell membrane as well as a particular chemical stability. For these reasons, carbamates have been used in the design of various drugs, such as β- and γ-secretase inhibitors, carbamate-based Hepatitis C virus (HCV) therapeutics or cysteine-protease inhibitors [19]. To prepare new conjugates with 2-DOS, we chose to conjugate various aromatic and heteroaromatic compounds (R in Figure 1B). First, we chose phenyl substituents containing or not fluorine atom(s) because this kind of substituent could interact with RNA by forming hydrophobic interactions or through unusual hydrogen bonds mediated by the fluorine atoms. Then, we chose heteroaromatic compounds such as imidazole, benzimidazole, pyridine, and the previously employed D_3 nucleobase [*N*-(3-(1-(3-aminopropyl)-1*H*-imidazol-4-yl)phenyl)benzamide]. To obtain a novel series of ligands with high RNA binding affinity and miRNA inhibitory activity, we thus employed commercially available substrates as well as starting materials prepared using straightforward synthetic pathways. To synthesize the carbamate compounds, we decided to start from the previously prepared protected racemic compound **1** [17] and to use two approaches (Scheme 1): (i) preparation of the activated carbonate **2** followed by amine substitution leading to compounds **3a–f**, and (ii) reaction of the free alcohol of **1** with various isocyanates leading to compounds **3g–i**.

Following the first strategy, compound **1** was converted into its corresponding activated carbonate **2** in the presence of 4-nitrophenyl chloroformate in CH_2Cl_2. Compound **2**, obtained in 93% yield, was then coupled with suitable (hetero)aromatic compounds bearing amine groups in order to form the desired carbamate derivatives. We selected five commercially available amines for the synthesis of compounds **3a–e** and an artificial nucleobase that we had previously prepared for the synthesis of neomycin and 2-DOS derivatives, e.g., the *N*-(3-(1-(3-aminopropyl)-1*H*-imidazol-4-yl)phenyl)benzamide [22] also called D_3 for the preparation of compound **3f** and to achieve structural diversity of synthesized ligands (Figure S1, Supporting Information for the chemical structures of amine derivatives). The reaction of the amines with carbonate **2** was carried out in the presence of Et_3N in CH_2Cl_2 at 50 °C leading to the protected carbamate derivatives **3a–f** in 33–88% yields. Removal of the Boc and acetal protecting groups of compounds **3a–f** was performed in one step under acidic conditions (TFA in a mixture of CH_2Cl_2/water 2:1) and in the presence of tripropylsilane (5%) as a scavenger.

The final compounds **4a–f** were obtained in 22–67% yields.

Concomitantly to the preparation of carbamate derivatives **4a–f**, we also decided to prepare new conjugates upon reaction of commercially available isocyanates with compound **1**. As illustrated in Scheme 1, treatment of three isocyanates, whose chemical structures are illustrated in Figure S2, with protected 2-DOS **1** in the presence of Et_3N at 50 °C, led to the desired carbamates **3g–i** in 56–90% yields. The final deprotection of these conjugates using TFA and TIS (5%) in a mixture of CH_2Cl_2/H_2O (2:1) allowed the obtention of the final compounds **4g–i**, which were isolated in 52–100% yield after purifications using semi-preparative HPLC. All conjugates were fully characterized by NMR, HRMS, and HPLC.

2.2. *Evaluation of the affinity and inhibition activity of the synthesized 2-DOS conjugates*

Once the compounds synthesized and characterized, we evaluated their affinity for pre-miR-372 but also for other microRNAs to assess the extent of selectivity that could be reached by these compounds. For this, pre-miR-17 as well as pre-miR18a, pre-miR-148a, and pre-miR-210 were chosen. The corresponding miRNAs are overexpressed in different types of cancers thus representing interesting RNAs to assess selectivity but also as potential targets. The evaluation of the affinity was performed using established assays where the target RNA is 5′-labeled with a fluorophore (fluoresceine) and incubated with increasing concentrations of the synthesized compounds. If a compound binds to the RNA target, the environment of the fluorophore changes and induces a dose-dependent variation in fluorescence. This allows the measurement of dissociation constants (K_D) for all compounds against the five chosen pre-miRNAs. The results reported in Table 1 demonstrated that among all tested compounds, only three displayed an affinity for the pre-miRNAs studied: compounds **4c**, **4f**, and **4h**. Compounds **4c** and **4h** showed affinity only for one pre-miRNA each, i.e., pre-miR-210 for **4c** (K_D = 42.3 μM) and pre-miR-372 for **4h** (K_D of 38.4 μM). These results, although moderate, suggest that these compounds could be further studied to optimize them in order to obtain selective compounds for one targeted RNA structure. Compound **4f** strongly binds to both pre-miR-372 (K_D of 2.36 μM) and pre-miR-17 (K_D = 1.88 μM), while the affinity decreases at least ten times when tested on other pre-miRNAs. To further confirm the selectivity of compound **4f**, we tested it in competition with other nucleic acids, i.e., a large excess (100 equiv) of tRNA and DNA, and the obtained results showed that **4f** maintains its affinity for pre-miR-372 in both cases (data not shown).

Interestingly, compound **4f** exhibits the same affinity as the previous hit of the triazole series **DOS-D$_3$** (Figure 1A) suggesting that the linker does not affect the affinity. We thus wondered if the modification of the linker from triazole to carbamate was affecting the inhibition activity. To assess this parameter, we employed a FRET-based assay that we had previously validated to measure the ability of a compound to block Dicer processing by binding to a pre-miRNA.

Compounds **4f** (Figure 2A) and **DOS-D$_3$** (Figure 2B) exhibit similar affinity for both pre-miR-372 and pre-miR-17. In contrast, compound **4f** shows a 11.3 μM IC_{50} for the inhibition of pre-miR-372 processing but cannot inhibit Dicer processing of pre-miR-17 (Figure 2C). Derivative **DOS-D$_3$** can inhibit the processing of pre-miR-372 and pre-miR-17 with similar IC_{50}s of 15.9 and 17.6 μM, respectively (Figure 2D). So, while **DOS-D$_3$** does not show selectivity between pre-miR-372 and pre-miR-17 in binding and inhibition activities, compound **4f**, while binding both, inhibits only the processing of pre-miR-372. This could be due to differences in the binding site that could be much more favorable for inhibition in the case of pre-miR-372 than in pre-miR-17 and this result further supports the selectivity of compound **4f** for the targeted miRNA.

2.3. *Study of the binding site of compound **4f***

To gain a better understanding of differences in the inhibition activity between pre-miR-372 and -17 for compound **4f**, we employed molecular docking and explored what could be the site of interaction of **4f** on the two RNA structures. MC-Fold/MC-Sym, a program allowing RNA-structure prediction, was previously employed to predict the structural organization and the double-helix region of multiple pre-miRNAs [23]. Here, we employed the pre-miR-372 and pre-miR-17 structures obtained by integrating the MC-Fold/MC-Sym and AutoDock programs [24].

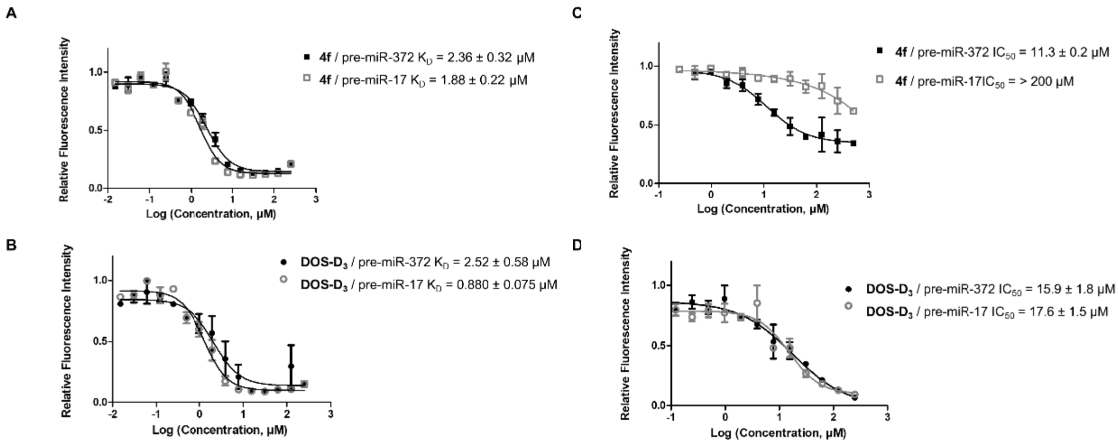

Figure 2. (A) Dissociation constants curves for compound **4f** against pre-miR-372 (full black squares) and pre-miR-17 (empty grey squares) with the associated K_D values. (B) Dissociation constants curves for compound **DOS-D$_3$** against pre-miR-372 (full black circles) and pre-miR-17 (empty grey circles) with the associated K_D values. (C) Inhibition curves for the processing of pre-miR-372 (full black squares) and pre-miR-17 (empty grey squares) by Dicer in the presence of compound **4f** and the associated IC_{50} values. (D) Inhibition curves for the processing of pre-miR-372 (full black circles) and pre-miR-17 (empty grey circles) by Dicer in the presence of compound **DOS-D$_3$** and the associated IC_{50} values.

Table 1. Dissociation constants (K_D, μM) for synthesized compounds **4a–i** and for reference **DOS-D$_3$** against pre-miR-372, -17, -18a, -148a, and -210

ID	K_D (pre-miR-372)	K_D (pre-miR-17)	K_D (pre-miR-18a)	K_D (pre-miR-148a)	K_D (pre-miR-210)
4a	No binding	>50	No binding	No binding	No binding
4b	>50	>50	No binding	No binding	No binding
4c	No binding	>50	No binding	No binding	42.3 ± 7.5
4d	No binding	>50	No binding	No binding	No binding
4e	No binding	No binding	No binding	No binding	No binding
4f	**2.36 ± 0.32**	**1.88 ± 0.22**	**20.2 ± 1.85**	**33.5 ± 0.35**	**35.7 ± 0.42**
4g	No binding	No binding	No binding	No binding	No binding
4h	38.4 ± 11	No binding	No binding	No binding	No binding
4i	>50	>50	No binding	No binding	No binding
DOS-D$_3$	2.52 ± 0.58	0.880 ± 0.075			

Binding studies were performed on 5′-FAM-pre-miR-372 in 20 mM Tris-HCl buffer (pH 7.4), 12 mM NaCl, 2.5 mM $MgCl_2$, and 1 mM DTT.

The exploration of the binding site of compound **4f** on pre-miR-372 showed that this compound likely interacts with residues A11–G14 and U49–C51 where a G-bulge as well as an internal G-loop open the duplex region offering a favorable binding site (Figure 3). Compared to our previous study about the **DOS-D$_3$** compound, the binding site has changed. This highlights how minor changes in the chemical structure of an RNA ligand unexpectedly modify its binding site, rendering unpredictable which modifications should be performed to improve binding.

The results described above, however, support a selective binding to pre-miR-372. While the binding site of **4f** on pre-miR-372 was confirmed in

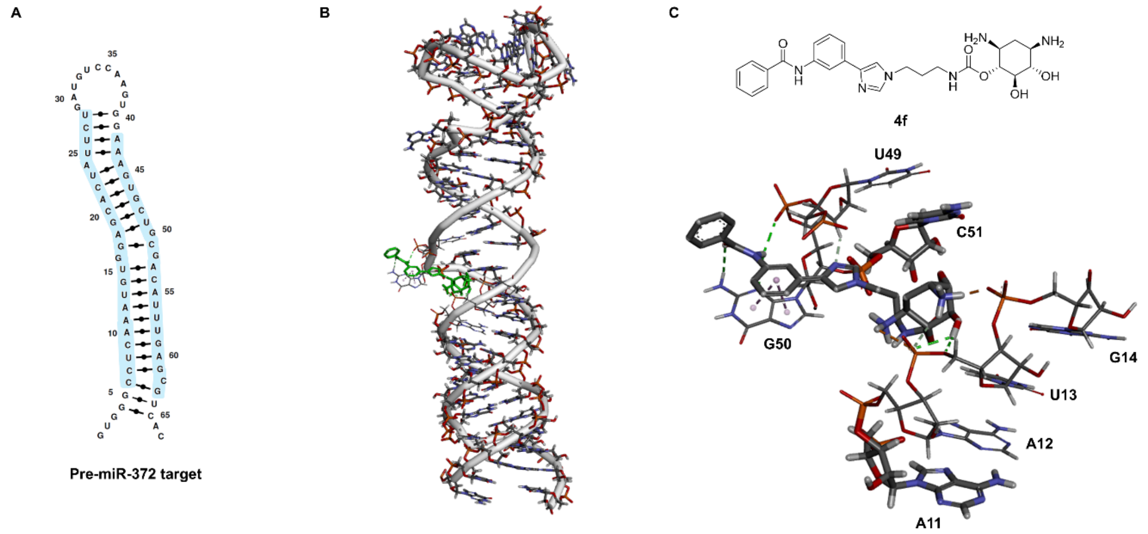

Figure 3. (A) Primary and secondary structures of pre-miR-372 RNA target. (B) Docking of compound **4f** with the pre-miR-372 hairpin loop performed using Autodock 4 in which the grid boxes were fixed on the entire RNA sequence. (C) Chemical structure of compound **4f** and detail of the binding pocket and interactions formed.

all binding poses obtained after docking, we found many possible binding sites in the case of pre-miR-17 binding. The one that occurs most frequently is located in the internal loop CA/GUA located in the lower-stem part of the pre-miRNA (Figure S4). These results suggest that binding to pre-miR-372 is much more efficient than to pre-miR-17 in inhibiting Dicer processing, due to differences in the binding site and interactions.

3. Conclusion

In this work, we successfully synthesized a new series of 2-DOS conjugates using a divergent synthetic method that led to nine new compounds. Some of these compounds can bind to the desired target pre-miR-372, the precursor of oncogenic miR-372, with low micromolar affinities making them interesting compounds, especially compound **4f**, able to inhibit Dicer processing of this pre-miRNA. Interestingly, compound **4f** is also selective since the comparison of its affinity with pre-miR-17, -18a, -148a, and -210 showed that **4f** binds to pre-miR372 and pre-miR-17 with similar activities but not to the other pre-miRNAs. Furthermore, compound **4f** showed a specific inhibition of pre-miR-372 processing while the other pre-miRNAs were not affected. Molecular docking showed that the binding site of **4f** on the pre-miR-372 structure is much more favorable for inhibition than the one on pre-miR-17 thus explaining the specificity observed in inhibition activity. It is important to note that compound **4f** derives from the conjugation of 2-DOS with an artificial nucleobase via a carbamate linker and that we previously studied the same conjugate but containing a triazole linker: compound **DOS-D$_3$**. Both compounds show similar activity on pre-miR-372 but only **4f** shows a specific inhibition activity. Furthermore, the modification from a triazole to a carbamate linker induced a major change in the binding site on the pre-miR-372 structure. This further supports an observation that we made for many series of RNA ligands before: what could be considered minor changes in the chemical structure of an RNA binder induces major modifications in the binding site and eventual biological activity. This represents one of the major limitations when designing RNA binders since it hampers our ability to predict the chemical modifications that should be introduced to improve binding based on the structure of the target. The study presented here contributes to a better understanding of the binding and inhibition activity of this kind of 2-DOS derivatives and more generally to the rules that govern RNA binding to small molecules.

4. Experimental section

4.1. *Chemistry*

Reagents and solvents were purchased from Merck or Carlo Erba and used without further purification. All reactions that involved air- or moisture-sensitive reagents or intermediates were performed under an argon atmosphere. Flash column chromatography was carried out on silica gel (Merck; SDS 60 Å, 40–63 µM, VWR). Analytical TLC was conducted on precoated silica gel plates (60F254; Merck) and compounds were visualized by irradiation (λ = 254 nm) or by staining with ninhydrin. ^{1}H and ^{13}C NMR spectra were recorded on Bruker AC 200 and 500 MHz spectrometers. Chemical shifts are reported in parts per million (ppm, δ) referenced to the residual ^{1}H resonance of the solvent ($CDCl_3$ δ 7.26; CD_3OD δ 3.31; DMSO-d_6 δ 2.50; acetone-d_6 δ 2.05 ppm). Splitting patterns are labeled as follows: s (singlet), d (doublet), t (triplet), m (multiplet), and br s (broad singlet). Coupling constants (J) are listed in hertz (Hz). High resolution mass spectrometry (HRMS) was carried out on an LTQ Orbitrap hybrid mass spectrometer with an electrospray ionization probe (Thermo Fisher Scientific, San Jose, CA) by direct infusion from a pump syringe, to confirm the correct molar mass and high purity of the compounds. HPLC analyses were performed using a Waters Arc HPLC pump coupled to a Waters 2998 photodiode array detector and Waters Cortex® C18+ column (50 × 4.6 mm, 2.7 µm). Analyses were run at room temperature by using a gradient of CH_3CN containing 0.1% formic acid (eluent B) in water containing 0.1% formic acid (eluent A) at a flow rate of 1.5 mL/min. The gradient of elution employed was 5 to 40% eluent B over 5 min and 40 to 100% eluent B over 2 min.

1,3-Bis-*N*-(*tert*-butyloxycarbonyl)-5,6-*O*-cyclohexylidene-2-deoxystreptamine (**1**) was prepared following a previously published procedure [17].

4.2. *General protocol of carbamate synthesis starting from the activated carbonate of **2** (General procedure A)*

To a stirred solution of compound **2** (100 mg, 0.16 mmol) in CH_2Cl_2 (5 mL), were added triethylamine (25 µL, 0.18 mmol, 1.1 equiv) and the appropriate amine (commercially available benzylamine, 3-fluorobenzylamine, 1-(3-aminopropyl)imidazole, 2-aminobenzimidazole, 3-aminopyridine and the prepared *N*-(3-(1-(3-aminopropyl-1*H*-imidazol-4-yl)phenyl)benzamide (see below) (0.18 mmol, 1.1 equiv) at room temperature. After stirring for 24 h at rt or at 50 °C, the reaction mixture was evaporated under reduced pressure, and the crude residue was purified by flash chromatography on a silica gel column.

4.3. *General protocol of carbamate synthesis starting from protected **1** (General procedure B)*

To a solution of compound **1** (100 mg, 0.23 mmol) in CH_2Cl_2 (5 mL), were added triethylamine (47.4 µL, 0.34 mmol, 1.5 equiv) and the appropriate isocyanate (butyl isocyanate, 2,4-dichloro-1-(2-isocyanatoethyl)benzene and 1-fluoro-4-(2-isocyanatoethyl)benzene, 0.34 mmol, 1.5 equiv). After stirring for 24 h at 50 °C, the reaction was concentrated in vacuo, and the residue was purified by silica gel column chromatography.

4.4. *General procedure for cleavage of the Boc and acetal groups (General procedure C)*

To a solution of protected compounds **3a–i** in CH_2Cl_2 and H_2O (3:1), was added TFA (50 equiv). The reaction mixture was stirred at rt overnight. Solvent and residues of TFA were then removed under reduced pressure by co-evaporating twice with toluene. Ether precipitation led to pure compounds as white solids (TFA salts).

4.5. *N-3-(1-(3-aminopropyl-1H-imidazol-4-yl)phenyl)benzamide (D_3)*

To a solution of the previously described *N*-(3-(1*H*-imidazol-4-yl)phenyl)benzamide (250 mg, 0.95 mmol) in dry THF (10 mL), were added sodium hydride (45.6 mg, 1.9 mmol, 2 equiv) and 3-(Boc-amino)propyl bromide (317 mg, 1.42 mmol, 1.4 equiv), and the reaction mixture was stirred overnight at 60 °C. After evaporation of the solvent, the crude residue was dissolved in EtOAc and washed three times with H_2O. The organic phase was dried over reduced pressure. The residue was then purified by flash chromatography on a silica gel column using a mixture of CH_2Cl_2/MeOH 98:2 leading to the desired protected compound as a light yellow solid. This compound was then deprotected using TFA (61 μL, 0.79 mmol, 10 equiv) in CH_2Cl_2 (0.6 mL) at rt for 3 h. After evaporation of the solvent and removal of the residual TFA by co-evaporation with toluene, the crude product was purified by flash chromatography on a silica gel column using a mixture of CH_2Cl_2/MeOH 9:1 leading to the desired protected compound as a light yellow solid in 73% yield (300 mg) over two steps. R_F = 0.20 (CH_2Cl_2/MeOH 8:2); ^{1}H NMR (200 MHz, CD_3OD) δ (ppm): 8.10–7.90 (m, 3H), 7.80–7.70 (m, 2H), 7.65–7.50 (m, 5H), 7.40–7.30 (m, 1H), 4.20–4.10 (t, J = 6.0 Hz, 2H), 2.70–2.60 (m, 2H), 2.10–1.95 (m, 2H); ^{13}C NMR (50 MHz, CD_3OD) δ (ppm): 161.5, 157.9, 148.3, 144.9, 140.2, 138.9, 136.1, 132.8, 129.6, 128.6, 121.9, 120.7, 118.3, 117.1, 45.6, 38.1, 34.7; MS (ESI) m/z = 321.2 $[M+H]^+$ (theoretical *m/z* 321.0).

4.6. *1,3-Bis-N-(tert-butyloxycarbonyl)-5,6-O-cyclohexylidene-2-deoxystreptamine-4-O-[p-nitrophenyl] carbonate (**2**)*

To a solution of commercially available *p*-nitrophenyl chloroformate (980 mg, 4.86 mmol, 3.5 equiv) in CH_2Cl_2 (5 mL), were added pyridine (461 μL, 5.72 mmol, 4 equiv) and compound **1** (633 mg, 1.43 mmol). The reaction mixture was stirred for 45 min at rt and then washed twice with H_2O (2 × 20 mL). The organic phase was dried over $MgSO_4$. Concentration under reduced pressure followed by flash chromatography on a silica gel column using a mixture cyclohexane/EtOAc 6:4 led to desired compound **2** as a white solid in 93% yield (807 mg). R_F = 0.52 (cyclohexane /EtOAc 6:4); ^{1}H NMR (200 MHz, CD_3OD) δ (ppm): 8.33 (d, J = 10.2 Hz, 2H), 7.47 (d, J = 10.2 Hz, 2H), 5.02–4.92 (m, 1H), 3.84–3.50 (m, 4H), 2.18–2.09 (m, 1H), 1.60–1.50 (m, 10H), 1.45 (br s, 18H), 1,31–1.29 (m, 1H); ^{13}C NMR (50 MHz, CD_3OD) δ (ppm): 157.7, 157.0, 153.5, 146.9, 126.27, 123.1, 113.8, 80.5, 79.7, 79.0, 51.7, 37.4, 37.2, 28.7, 26.1, 24.7; MS (ESI) m/z = 630.4 $[M+Na]^+$ (theoretical *m/z* 630.3).

4.7. *1,3-Bis-N-(tert-butyloxycarbonyl)-5,6-O-cyclohexylidene-2-deoxystreptamine-4-N-benzylcarbamate (**3a**)*

General procedure A was employed for the reaction between compound **2** (100 mg) and commercially available benzylamine (20 μL). Compound **3a** was obtained after purification by flash chromatography on a silica gel column using a mixture cyclohexane/EtOAc 6:4 as a white solid in 88% yield (81 mg). R_F = 0.25 (cyclohexane/EtOAc 8:2); ^{1}H NMR (200 MHz, $CDCl_3$) δ (ppm): 7.34–7.24 (m, 5H), 4.30 (br s, 2H), 3.68–3.33 (m, 5H), 2.57–2.51 (m, 1H), 1.60–1.50 (m, 8H), 1.42–1.10 (m, 21H); ^{13}C NMR (50 MHz, $CDCl_3$) δ (ppm): 156.2, 155.3, 138.1, 128.8, 127.7, 127.6, 112.9, 80.0, 79.0, 74.6, 51.8, 36.4, 31.1, 29.8, 28.5, 25.1, 23.8; MS (ESI) m/z = 576.5 $[M+H]^+$ (theoretical *m/z* 576.3).

4.8. *1,3-Bis-N-(tert-butyloxycarbonyl)-5,6-O-cyclohexylidene-2-deoxystreptamine-4-O-[N-m-fluorobenzyl]-N-methyl carbamate (**3b**)*

General procedure A was employed for the reaction between compound **2** (100 mg) and 3-fluorobenzylamine (24.7 μL). Purification by flash chromatography on a silica gel column using a mixture cyclohexane/EtOAc 7:3 afforded the desired product **3b** in 83% yield (80.7 mg). R_F = 0.54 (cyclohexane/EtOAc 6:4); ^{1}H NMR (200 MHz, CD_3OD) δ (ppm): two isomers (minor one in italic): 7.38–7.28 (m, 1H), 7.08–6.96 (m, 3H), 4.96–4.85 (m, 2H), 4.58–4.38 (d, J = 15.8 Hz , 2H), 4.20–4.12 (d, J = 16.0 Hz, 1H), 3.76–3.46 (m, 4H), 2.89 (s, 3H), 2.85 (s, 3H), 2.18–2.10 (m, 1H), 1.65–1.25 (m, 29H); ^{13}C NMR (50 MHz, CD_3OD) δ (ppm): 166.9, 162.0, 158.1, 157.7, 157.3, 141.7, 131.4, 124.6, 115.4, 114.9, 113.4, 80.2, 79.8, 79.6, 76.8, 53.0, 52.7, 52.2, *52.1*, 37.3, 37.1, *34.6*, 34.3, 30.7, 28.7, 26.1, 24.7; MS (ESI) *m/z* 608.5 $[M+H]^+$ (theoretical *m/z* 608.3).

4.9. *1,3-Bis-N-(tert-butyloxycarbonyl)-5,6-O-cyclohexylidene-2-deoxystreptamine-4-N-(n-propylimidazole) carbamate (**3c**)*

General procedure A was employed for the reaction between compound **2** (100 mg) and commercially available 1-(3-aminopropyl)imidazole (21.3 μL). Compound **3c** was obtained after purification by flash chromatography on a silica gel column using a mixture CH_2Cl_2/MeOH 95:5 as a white solid in 80% yield (76 mg). R_F = 0.53 (CH_2Cl_2/MeOH 9:1); ^{1}H NMR (200 MHz, CD_3OD) δ (ppm): 7.75 (br s, 1H), 7.18 (br s, 1H), 7.00 (br s, 1H), 4.83–4.79 (m, 1H), 4.07 (t, J = 6.2 Hz, 2H), 3.72–3.43 (m, 4H), 3.11 (t, J = 6.2 Hz, 2H), 2.18–2.09 (m, 1H), 1.97 (quintuplet, J = 6.2 Hz, 2H), 1.60–1.50 (m, 8H), 1.45–1.29 (m, 21H,); ^{13}C NMR (50 MHz, CD_3OD) δ (ppm): 158.5, 157.7, 135.5, 120.8, 113.3, 112.4, 80.3, 79.7, 75.5, 52.4, 45.2, 38.5, 37.3, 37.2, 32.5, 28.7, 26.1, 24.7; MS (ESI): *m/z* 594.4 [M+H]$^+$ (theoretical *m/z* 594.3).

4.10. *1,3-Bis-N-(tert-butyloxycarbonyl)-5,6-O-cyclohexylidene-2-deoxystreptamine-4-N-(benzimidazole)carbamate (**3d**)*

General procedure A was employed for the reaction between compound **2** (100 mg) and commercially available 2-aminobenzimidazole (21.3 mg). Compound **3d** was obtained after purification by flash chromatography on a silica gel column using a mixture cyclohexane /EtOAc 1:1 as a white solid in 67% yield (64.4 mg). R_F = 0.23 (cyclohexane/EtOAc 6:4); ^{1}H NMR (200 MHz, DMSO-*d6*) δ (ppm): 7.69 (br s, 1H), 7.19–7.11 (m, 4H), 7.00–6.92 (m, 1H), 5.13 (t, J = 10.3 Hz, 1H), 4.09–3.97 (m, 2H), 3.74–3.76 (m, 1H), 1.95–1.90 (m, 1H), 1.55–1.13 (m, 29H); ^{13}C NMR (50 MHz, DMSO-*d6*) δ (ppm): 155.1, 154.9, 153.3, 150.4, 142.8, 129.9, 120.0, 115.3, 114.3, 111.3, 78.0, 77.9, 77.8, 76.9, 35.9, 35.8, 28.2, 23.4, 23.3; MS (ESI) *m/z* 602.2 [M+H]$^+$ (theoretical *m/z* 602.3).

4.11. *1,3-Bis-N-(tert-butyloxycarbonyl)-5,6-O-cyclohexylidene-2-deoxystreptamine-4-N-(pyridine)carbamate (**3e**)*

General procedure A was employed for the reaction between compound **2** (100 mg) and commercially available 3-aminopyridine (16.9 mg). The reaction mixture was heated to 50 °C. Purification by flash chromatography on a silica gel column using a mixture CH_2Cl_2/MeOH 95:5 afforded desired compound **3e** as a white solid in 33% yield (29.7 mg). R_F = 0.46 (CH_2Cl_2/MeOH 98:2); ^{1}H NMR (200 MHz, CD_3OD) δ (ppm): 8.64 (br, 1H), 8.19 (dd, J = 4.1, 2.3 Hz), 8.00 (dd, J = 4.1, 2.3 Hz), 7.40 (q, J = 4.1 Hz, 1H), 5.02–4.97 (m, 1H), 3.80–3.47 (m, 4H), 2.13 (td, J = 6.3, 4.1 Hz, 1H), 1.60–1.50 (m, 9H), 1.46–1.20 (m, 20H); MS (ESI) *m/z* 563.5 [M+H]$^+$ (theoretical *m/z* 563.3).

4.12. *1,3-Bis-N-(tert-butyloxycarbonyl)-5,6-O-cyclohexylidene-2-deoxystreptamine-4-N-(D_3) carbamate (**3f**)*

General procedure A was employed for the reaction between compound **2** (100 mg) and *N*-3-(1-(3-aminopropyl-1*H*-imidazol-4-yl)phenyl)benzamide (78.1 mg). The reaction mixture was heated to 50 °C. Purification by flash chromatography on a silica gel column using a mixture CH_2Cl_2/MeOH 95:5 afforded desired compound **3e** as a white solid in 33% yield (41.6 mg). R_F = 0.45 (CH_2Cl_2/MeOH 9:1); ^{1}H NMR (200 MHz, CD_3OD) δ (ppm): 9.57 (s, 1H), 8.30 (s, 1H), 8.05 (d, J = 3.0 Hz, 2H), 7.80–7.50 (m, 8H), 7.35–7.25 (m, 1H), 6.70–6.60 (m, 1H), 6.40–6.30 (m, 1H), 6.10–6.00 (m, 1H), 5.00–4.90 (m, 1H), 4.14 (t, J = 2.5 Hz, 2H), 3.90–3.80 (m, 1H), 3.80–3.60 (m, 4H), 3.00–2.90 (m, 2H), 2.30–2.20 (m, 1H), 1.60–1.50 (m, 11H), 1.41 (s, 18H); ^{13}C NMR (50 MHz, CD_3OD) δ (ppm): 171.3, 166.3, 157.6, 157.4, 156.1, 140.5, 168.7, 136.7, 136.4, 132.3, 129.5, 129.2, 128.4, 120.9, 118.9, 117.3, 116.3, 112.2, 79.0, 74.7, 55.0, 52.5, 44.7, 38.5, 37.5, 37.0, 36.9, 25.6, 24.4; MS (ESI) *m/z* 563.5 [M+H]$^+$ (theoretical *m/z* 563.3).

4.13. *1,3-Bis-N-(tert-butyloxycarbonyl)-5,6-O-cyclohexylidene-2-deoxystreptamine-4-N-(n-butyl) carbamate (**3g**)*

General procedure B was employed for the reaction between compound **1** (100 mg) and butyl isocyanate (38.3 μL). Compound **3g** was obtained after purification of the crude product by flash chromatography on a silica gel column using a mixture cyclohexane/EtOAc 7:3 as a white solid in 90% yield (112 mg). R_F = 0.61 (cyclohexane/EtOAc 6:4); ^{1}H NMR (200 MHz, CD_3OD) δ (ppm): 4.84–4.74 (m, 1H), 3.70–3.41 (m, 4H), 3.10 (t, J = 6.1 Hz, 2H), 2.17–2.05 (td, J = 4.2, 12.4 Hz, 1H), 1.60–1.50 (m, 9H), 1.55–1.41 (m, 24H), 1.17 (t, J = 6.1 Hz, 1H), 0.95 (t, J = 6.1 Hz, 3H); ^{13}C NMR (50 MHz, CD_3OD) δ (ppm): 158.4, 157.7, 113.3, 79.7, 79.7, 75.3, 52.4, 41.5, 37.3, 33.1, 28.7, 26.1, 24.7, 20.9, 14.16; MS (ESI) *m/z* 542.4 [M+H]$^+$ (theoretical *m/z* 542.3).

4.14. *1,3-Bis-N-(tert-butyloxycarbonyl)-5,6-O-cyclohexylidene-2-deoxystreptamine-4-N-[n-ethyl-(2′,4′-dichlorophenyl)] carbamate (**3h**)*

General procedure B was employed for the reaction between compound **1** (100 mg) and 2,4-dichloro-1-(2-isocyanatoethyl)benzene (56 μL). Compound **3h** was obtained after purification of the crude product by flash chromatography on a silica gel column using a mixture cyclohexane/EtOAc 85:15 as a white solid in 56% yield (85 mg). R_F = 0.64 (cyclohexane/EtOAc 6:4); ^{1}H NMR (200 MHz, acetone-*d6*) δ (ppm): 7.46–7.30 (m, 3H), 6.57 (br, 1H), 4.92–4.82 (m, 1H), 3.77–3.53 (m, 4H), 3.39–3.29 (m, 2H), 3.00–2.89 (m, 2H), 2.31–2.24 (m, 1H), 1.60–1.50 (m, 9H), 1.62–1.28 (m, 20H); ^{13}C NMR (50 MHz, Acetone-*d6*) δ (ppm): 157.1, 156.1, 136.9, 135.4, 133.3, 133.2, 129.7, 128.1, 112.2, 79.1, 78.9, 74.7, 52.5, 49.2, 41.2, 37.4, 33.1, 28.6, 27.5, 25.7, 24.4; MS (ESI) m/z = 658.1 [M+H]$^+$ (theoretical *m/z* 658.3).

4.15. *1,3-Bis-N-(tert-butyloxycarbonyl)-5,6-O-cyclohexylidene-2-deoxystreptamine-4-N-[n-ethyl-(4′-fluorophenyl)] carbamate (**3i**)*

General procedure B was employed for the reaction between compound **1** (100 mg) and commercially available 1-fluoro-4-(2-isocyanatoethyl)benzene (49 μL). Compound **3i** was obtained after purification of the crude product by flash chromatography on a silica gel column using a mixture cyclohexane/EtOAc 8:2 as a white solid in 59% yield (82 mg). R_F = 0.53 (cyclohexane/EtOAc 6:4); ^{1}H NMR (200 MHz, acetone-*d6*) δ (ppm): 7.26–6.93 (m, 4H), 4.81–4.77 (m, 1H), 3.71–3.34 (m, 4H), 3.33–3.26 (m, 2H), 2.88–2.77 (m, 2H), 2.16–2.09 (m, 1H), 1.60–1.50 (m, 7H), 1.47–1.29 (m, 22H); ^{13}C NMR (50 MHz, acetone-*d6*) δ (ppm): 158.3, 157.7, 136.4, 133.3, 131.6, 131.4, 116.2, 115.8, 113.3, 80.3, 79.7, 75.4, 71.34, 52.4, 43.5, 37.3, 37.3, 36.2, 28.7, 26.11, 24.74, 23.94; MS (ESI): m/z = 608.1 [M+H]$^+$ (theoretical *m/z* 608.3).

4.16. *2-Deoxystreptamine-4-O-(N-phenyl) carbamate (**4a**)*

General procedure C was applied for the protection of compound **3a** (50 mg, 0.087 mmol) in the presence of TFA (323 μL, 50 equiv) and triethylsilane (TIS, 0.89 μL, 4.3 nmol, 0.05 equiv) in a mixture of CH_2Cl_2 and H_2O (2.6 mL, 3:1). Compound **4a** was obtained as a white solid in 44% yield (20 mg). t_R = 0.68 min (analytical HPLC method); ^{1}H NMR (200 MHz, CD_3OD) δ (ppm): 7.33–7.23 (m, 5H), 4.77–4.67 (m, 1H), 4.34 (q, J = 15.2 Hz, 2H), 3.68–3.38 (m, 3H), 3.25–3.22 (m, 1H), 2.48–2.41 (m, 1H), 1.90–1.69 (m, 1H); ^{13}C NMR (50 MHz, CD_3OD) δ (ppm): 156.2, 140.1, 129.5, 128.8, 128.4, 128.2, 76.2 75.2, 51.3, 45.9, 30.1; HRMS (ESI) *m/z* = 296.16061 [M+H]$^+$ ($C_{14}H_{22}O_4N_3$ requires 296.16048).

4.17. *2-Deoxystreptamine-4′-O-[N-m-fluorophenyl]-N-methyl carbamate (**4b**)*

General procedure C was applied for the deprotection of compound **3b** (80 mg, 0.13 mmol) in the presence of TFA (489 μL, 50 equiv) and TIS (1.33 μL, 6.5 mmol, 0.05 equiv) in a mixture of CH_2Cl_2 and H_2O (4.5 mL, 3:1). Compound **4b** was obtained as a white solid in 67% yield (48 mg). t_R = 0.79 min (analytical HPLC); ^{1}H NMR (500 MHz, CD_3OD) δ (ppm): two isomers (minor one in italics): 7.37–7.32 (m, 1H), 7.18–6.98 (m, 3H), 4.84–4.73 (m, 2H), 4.37 (d, J = 16.0 Hz, 2H), 4.30 (d, J = 15.5 Hz, 1H), 3.56–3.45 (m, 3H), 3.26–3.20 (m, 1H), 2.96 (s, 3H), 2.87 (s, 3H), 2.49–2.47 (m, 1H), 1.90–1.83 (m, 1H); ^{13}C NMR (125 MHz, CD_3OD) δ (ppm) two isomers (minor one in italics): 165.5, 163.6, 141.5, 131.5, 124.7, 115.6, 115.1, 76.4, 77.4, 74.9, *54.8, 53.2*, 52.9, 51.3, 51.2, 34.7, 34.4, 30.3; HRMS (ESI) m/z = 328.16681 [M+H]$^+$ ($C_{15}H_{23}O_4N_3F$ requires 328.16671).

4.18. *2-Deoxystreptamine-4-O-(N-propylimidazole) carbamate (**4c**)*

General procedure C was applied for the deprotection of compound **3c** (78 mg, 0.13 mmol) in the presence of TFA (483 μL, 50 equiv) and TIS (1.33 μL, 6.5 mmol, 0.05 equiv) in a mixture of CH_2Cl_2 and H_2O (4.2 mL, 3:1). Compound **4c** was obtained as a colorless solid in 61% yield (25 mg). t_R = 0.68 min (analytical HPLC); ^{1}H NMR (200 MHz, CD_3OD) δ (ppm): 8.96 (br s, 1H), 7.69 (br s, 1H), 7.58 (br s, 1H), 4.82–4.76 (m, 1H), 3.45 (t, J = 6.3, 2H), 3.49–3.16 (m, 4H), 3.14 (t, J = 6.3 Hz, 2H), 2.51–2.40 (m, 1H), 2.15–2.11 (m, 2H), 1.63–1.29 (m, 29H); ^{13}C NMR (50 MHz, CD_3OD) δ (ppm): 158.4, 133.2, 121.7, 111.4, 76.1, 75.2, 74.2, 51.4, 49.0, 38.1, 38.1, 31.5, 23; HRMS (ESI) *m/z* = 314.18240 [M+H]$^+$ ($C_{13}H_{24}O_4N_5$ requires 314.18228).

4.19. *2-Deoxystreptamine-4-O-[N-benzimidazole] carbamate (**4d**)*

General procedure C was applied for the deprotection of compound **3d** (50 mg, 0.083 mmol) in the presence of TFA (726 µL, 50 equiv) and TIS (0.85 µL, 4.1 mmol) in a mixture of CH_2Cl_2 and H_2O (3 mL, 2:1). Compound **4d** was obtained as a colorless solid in 30% yield (13.7 mg). t_R = 1.23 min (analytical HPLC). ^{1}H NMR (500 MHz, CD_3OD) δ (ppm): 7.38–7.25 (m, 4H), 4.81–4.68 (m, 1H), 3.59–3.45 (m, 3H), 3.29–3.16 (m, 1H), 2.51–2.40 (m, 1H), 1.94–1.81 (m, 1H); ^{13}C NMR (125 MHz, CD_3OD) δ (ppm): 163.5, 158.4, 131.0, 124.7, 112.3, 81.3 79.3, 74.7, 51.2, 29.9; HRMS (ESI) m/z = 322.15103 $[M+H]^+$ ($C_{14}H_{20}O_4N_5$ requires 322.15098).

4.20. *2-Deoxystreptamine-4-O-(N-pyridine) carbamate (**4e**)*

General procedure C was applied for the deprotection of compound **3e** (40 mg, 0.071 mmol) in the presence of TFA (264 µL, 50 equiv) and TIS (0.72 µL, 3.5 mmol) in a mixture of CH_2Cl_2 and H_2O (2.2 mL, 3:1). Compound **4e** was obtained as a colorless solid in 22% yield (8.0 mg). t_R = 0.63 min (analytical HPLC); ^{1}H NMR (200 MHz, CD_3OD) δ (ppm): 8.97 (br, 1H), 8.41 (br, 1H), 8.28 (d, J = 8.4 Hz, 1H), 7.75 (br, 1H), 4.95–4.80 (m, 1H), 3.67–3.19 (m, 3H), 3.27–3.19 (m, 1H), 2.54 – 2.43 (td, J = 12.1, 4.2 Hz, 1H), 1.97–1.78 (q, J = 12.1 Hz); HRMS (ESI) m/z = 283.14020 $[M+H]^+$ ($C_{12}H_{19}O_4N_4$ requires 283.14008).

4.21. *2-Deoxystreptamine-4-N-(D_3) carbamate (**4f**)*

General procedure C was applied to compound **3f** (100 mg, 0.127 mmol) in the presence of TFA (490 µL, 50 equiv) in a mixture of CH_2Cl_2 and H_2O (2 mL, 3:1). Compound **4f** was obtained as a colorless solid in 75% yield (70.0 mg). t_R = 1.48 min (analytical HPLC); ^{1}H NMR (500 MHz, CD_3OD) δ (ppm): 9.57 (s, 1H), 8.30 (s, 1H), 8.05 (d, J = 20 Hz, 2H), 7.80–7.50 (m, 8H), 7.35–7.25 (m, 1H), 6.60–6.50 (m, 1H), 6.35–6.25 (m, 1H), 5.00–4.90 (m, 1H), 4.20–4.10 (m, 2H), 3.70–3.50 (m, 4H), 3.00–2.90 (m, 2H), 2.35–2.25 (m, 1H), 1.70–1.50 (m, 10H), 1.40–1.50 (m, 19H); ^{13}C NMR (125 MHz, CD_3OD) δ (ppm): 168.9, 158.3, 140.9, 137.2, 135.9, 135.8, 133.0, 130.9, 129.5, 128.7, 128.5, 123.1, 122.5, 119.2, 119.0, 75.9, 75.1, 74.1, 51.1, 50.0, 47.6, 38.0, 31.2, 29.8, 23.7; HRMS (ESI) m/z = 509.25095 $[M+H]^+$ ($C_{26}H_{33}O_5N_6$ requires 509.25069).

4.22. *2-Deoxystreptamine-4-O-(N-butyl) carbamate (**4g**)*

General procedure C was applied to compound **3g** (100 mg, 0.18 mmol) in the presence of TFA (668 µL, 50 equiv) in a mixture of CH_2Cl_2 and H_2O (4.5 mL, 3:1). Compound **4g** was obtained as a colorless solid in 88% yield (77.5 mg). t_R = 0.77 min (analytical HPLC); ^{1}H NMR (200 MHz, CD_3OD) δ (ppm): 4.71–4.61 (m, 1H), 3.45–3.06 (m, 6H), 2.46–2.40 (m, 1H), 1.89–1.77 (m, 1H), 1.55–1.27 (m, 4H), 0.94 (t, J = 6.3 Hz, 2H); ^{13}C NMR (50 MHz, CD_3OD) δ (ppm): 158.4, 76.1, 75.1, 74.3, 51.3, 41.8, 40.3, 32.9, 21.0, 14.1; HRMS (ESI) m/z = 262.17624 $[M+H]^+$ ($C_{11}H_{24}O_3N_3$ requires 262.17613).

4.23. *2-Deoxystreptamine-4-O-[N-(2′,4′-dichlorophenyl)ethyl] carbamate (**4h**)*

General procedure C was applied to compound **3h** (55 mg, 0.084 mmol) in the presence of TFA (312 µL, 50 equiv) in a mixture of CH_2Cl_2 and H_2O (2.5 mL, 3:1). Compound **4h** was obtained as a white solid in quantitative yields (50.8 mg). t_R = 0.69 min (analytical HPLC); ^{1}H NMR (500 MHz, CD_3OD) δ (ppm): 7.44–7.43 (m, 1H), 7.35–7.24 (m, 2H), 4.73–4.63 (m, 1H), 3.51–3.37 (m, 3H), 3.35–3.32 (m, 3H), 2.99–2.91 (m, 2H), 2.47–2.40 (m, 1H), 1.90–1.72 (m, 1H); ^{13}C NMR (125 MHz, CD_3OD) δ (ppm): 158.3, 136.9, 135.9, 134.0, 133.3, 130.1, 76.3, 75.3, 74.1, 51.2, 41.8, 33.8, 30.2; HRMS (ESI) m/z = 378.09857 $[M+H]^+$ ($C_{15}H_{22}O_4N_3Cl_2$ requires 378.09819).

4.24. *2-Deoxystreptamine-4-O-[4′-(fluorophenyl) ethyl] carbamate (**4i**)*

General procedure C was applied to compound **3i** (45 mg, 0.079 mmol) in the presence of TFA (293 µL, 50 equiv) in a mixture of CH_2Cl_2 and H_2O (1.5 mL, 3:1). Compound **4i** was obtained as a colorless solid in 52% yield (23 mg). t_R = 0.95 min (analytical HPLC); ^{1}H NMR (500 MHz, CD_3OD) δ (ppm): 7.28–7.22 (m, 2H), 7.21–6.94 (m, 2H), 4.74–4.64 (m, 1H), 3.49–3.37 (m, 3H), 3.31–3.27 (m, 2H), 3.24–3.20 (m, 1H), 2.84–2.77 (m, 2H), 2.49–2.41 (m, 1H), 1.91–1.72 (m, 1H); 13C NMR (125 MHz, CD_3OD) δ (ppm): 158.2, 156.6, 131.6, 131.4, 116.3, 115.9, 76.0, 74.9, 74.2, 51.2, 43.8, 36.0, 30.0; HRMS (ESI) m/z = 328.16678 [M+H]+ ($C_{15}H_{23}FN_3O_4$ requires 328.16726).

Interestingly, 2D-NMR analysis of conjugate **3b** as well as its corresponding deprotected form **4b** containing 2-DOS connected to a 2-fluoro-*N*-methylbenzylamine moiety clearly showed two distinct rotamers. This could be due to the presence of the methyl group on the nitrogen atom of the carbamate linker, which probably impedes free rotation of the carbamate function. In the absence of this methyl group, no steric effect is found to restrict this free rotation, thus no observation of two conformations was detected by NMR analysis.

5. Biochemistry

5.1. *RNA and biochemicals*

The buffers and solutions used in the fluorescence experiments were filtered through Millipore filters (0.22 mm; GP ExpressPLUS membrane). Human recombinant Dicer enzyme (Genlantis) had a concentration of 0.5 U/μL. Tris(hydroxymethyl)aminomethane hydrochloride (Tris–HCl) 20 mM (pH 7.4), containing 12 mM NaCl, 3 mM $MgCl_2$, and 1 mM DTT was used for the FRET assays and K_D determination. RNA oligonucleotides were purchased from IBA GmbH (Goettingen, Germany). RNA folding was performed in TRIS buffer upon incubation at 90 °C for 2 min, 4 °C for 10 min, and slowly returning to room temperature for 15 min.

For pre-miR-372:

5′-FAM-GUGGGCCUCAAAUGUGGAGCACUAUU CUGAUGUCCAAGUGGAAAGUGCUGCGACAUUUG AGCGUCAC-3′-DABCYL (ODN1)

5′-FAM-GUGGGCCUCAAAUGUGGAGCACUAUU CUGAUGUCCAAGUGGAAAGUGCUGCGACAUUUG AGCGUCAC-3′ (ODN2)

For pre-miR-17:

5′-FAM-GUCAGAAUAAUGUCAAAGUGCUUACAG UGCAGGUAGUGAUAUGUGCAUCUACUGCAGUGA AGGCACUUGUAGCAUUAUGGUGAC-3′-DABCYL (ODN3)

5′-FAM-GUCAGAAUAAUGUCAAAGUGCUUACAG UGCAGGUAGUGAUAUGUGCAUCUACUGCAGUGA AGGCACUUGUAGCAUUAUGGUGAC-3′ (ODN4)

For pre-miR-18a:

5′-FAM-UGUUCUAAGGUGCAUCUAGUGCAGAU AGUGAAGUAGAUUAGCAUCUACUGCCCUAAGUGC UCCUUCUGGCA-3′-DABCYL (ODN5)

5′-FAM-UGUUCUAAGGUGCAUCUAGUGCAGAU AGUGAAGUAGAUUAGCAUCUACUGCCCUAAGUGC UCCUUCUGGCA-3′ (ODN6)

For pre-miR-148a:

5′-FAM-GAGGCAAAGUUCUGAGACACUCCGACU CUGAGUAUGAUAGAAGUCAGUGCACUACAGAACU UUGUCUC-3′-DABCYL (ODN7)

5′-FAM-GAGGCAAAGUUCUGAGACACUCCGACU CUGAGUAUGAUAGAAGUCAGUGCACUACAGAACU UUGUCUC-3′ (ODN8)

DNA duplex sequence:

5′-CGTTTTAAATTTTGC-3′ (ODN9) and 5′-GCTT TTAAATTTTGC-3′

5.2. *FRET Dicer assay*

The Dicer assay was performed in 384-well plates (Greiner bio-one) in a final volume of 40 μL by using a 5070 EpMotion automated pipetting system (Eppendorf). Each experiment was performed in duplicate and repeated three times. A beacon of ODN1, ODN3, ODN5, or ODN7 at 50 nM was used in each well and the reaction mixtures containing inhibitors were preincubated at rt for 30 min. Human recombinant Dicer (0.25 U; Genlantis) or *Escherichia coli* RNase III (0.25 U, Ambion) were added to the reaction mixtures. For the IC_{50} experiments, each ligand was added in 12 dilutions (0.244 pM–500 μM). The fluorescence increase was measured after 1 h incubation at 37 °C on a GeniosPro (Tecan) with excitation and emission filters of l = 485 ± 10 and 535 ± 15 nm, respectively. Each point was measured ten times with an integration time of 500 ms and then averaged. The inhibition data were analyzed using nonlinear regression in Prism 5 (GraphPad Software) following the equation: $Y = \text{bottom} + (\text{top} - \text{bottom})/(1 + 10^{[(\log(IC_{50})-X)\cdot \text{Hills Slope}]})$ where X is log(concentration) and Y the fluorescence intensity.

5.3. *Binding experiments and K_D determination*

Binding experiments were performed in 384-well plates (Greiner bio-one) in a final volume of 60 mL by using a 5070 EpMotion automated pipetting system

(Eppendorf). Each experiment was performed in duplicate and repeated at least three times. A beacon (ODN2, ODN4, ODN6 and ODN8) was used at 10 nM in each well. Each ligand was added in 15 dilutions (0.030 nM–0.5 mM). The fluorescence increase measured after 4 h on a GeniosPro (Tecan) with excitation and emission filters of $l = 485 \pm 10$ and 535 ± 15 nm, respectively. Each point was measured ten times with an integration time of 500 ms and then averaged. The binding data were analyzed using Graphpad Prism 5 software. Unless otherwise stated, the binding profiles were well fitted by a simple model that assumed 1:1 stoichiometry. In the competition experiments, 100 equiv of tRNA structured as pre-miR-372 beacon were added to the RNA solution and 100 equiv of duplex DNA (mixture of ODN9 and ODN10 incubated at 90 °C for 5 min then slowly returned at rt) were added to the RNA solution.

5.4. *Molecular modeling and docking*

The MC-Fold/MC-Sym pipeline (http://www.major.iric.ca/MC-Pipeline/) is a web-hosted service for RNA secondary and tertiary structure prediction. The pipeline consists in uploading RNA sequence to MC-Fold, which outputs secondary structures that are directly input to MC-Sym, which outputs tertiary structures. Pre-miRNA sequences were obtained from the miRBase database (http://www.mirbase.org/). The hairpin loops of pre-miR-372 and pre-miR-17 were chosen to predict the 3D structure using the MC-Fold/MC-Sym pipeline. Energy optimization was further conducted on the 3D model using the TINKER Molecular Modeling Package (http://dasher.wustl.edu/tinker/). For docking with AutoDock, polar hydrogen atoms, Kollman united charges and solvent parameters were applied to the RNA using pmol2q script. This script converts the .pdb file format of the RNA template to the .pdbqt file format that is compatible with AutoDock program version 4 (http://autodock.scripps.edu/). Pre-miR-372/**4f** and pre-miR17/**4f** molecular docking were conducted using AutoDock program version 4. The rotational bonds of the ligand were treated as flexible, whereas the receptor was kept rigid. Grid box was fixed in order to include the entire RNA sequence. RNA–ligand interactions were analyzed and visualized using Discovery Studio Visualizer version 4.1 (https://www.3ds.com/fr/products/biovia/discovery-studio).

Declaration of interests

The authors do not work for, advise, own shares in, or receive funds from any organization that could benefit from this article, and have declared no affiliations other than their research organizations.

Supplementary materials

Supporting information for this article is available on the journal's website under https://doi.org/10.5802/crchim.426 or from the author.

References

[1] S. Kovachka, M. Panosetti, B. Grimaldi, S. Azoulay, A. Di Giorgio and M. Duca, “Small molecule approaches to targeting RNA”, *Nat. Rev. Chem.* **8** (2024), pp. 120–135.

[2] J. L. Childs-Disney, X. Yang, Q. M. R. Gibaut, Y. Tong, R. T. Batey and M. D. Disney, “Targeting RNA structures with small molecules”, *Nat. Rev. Drug Discov.* **21** (2022), pp. 736–762.

[3] J. T. Koehn, S. Felder and K. M. Weeks, “Innovations in targeting RNA by fragment-based ligand discovery”, *Curr. Opin. Struct. Biol.* **79** (2023), article no. 102550.

[4] J. P. Falese, A. Donlic and A. E. Hargrove, “Targeting RNA with small molecules: from fundamental principles towards the clinic”, *Chem. Soc. Rev.* **50** (2021), pp. 2224–2243.

[5] H. Ratni, M. Ebeling, J. Baird, et al., “Discovery of risdiplam, a selective survival of motor neuron-2 (SMN2) gene splicing modifier for the treatment of spinal muscular atrophy (SMA)”, *J. Med. Chem.* **61** (2018), pp. 6501–6517.

[6] V. Ambros, “The evolution of our thinking about microRNAs”, *Nat. Med.* **14** (2008), pp. 1036–1040.

[7] C. Martin, M. Bonnet, N. Patino, S. Azoulay, A. Di Giorgio and M. Duca, “Design, synthesis, and evaluation of neomycin-imidazole conjugates for RNA cleavage”, *ChemPlusChem* **87** (2022), article no. e202200250.

[8] C. Martin, M. Panosetti, E. Tesini, et al., “Synthetic RNA ligands as activators of type I toxin-antitoxin systems: a novel antimicrobial strategy targeting Helicobacter pylori”, *Chem. Sci.* **16** (2025), pp. 13249–13255.

[9] C. Maucort, M. Bonnet, J. C. Ortuno, et al., “Synthesis of bleomycin-inspired RNA ligands targeting the biogenesis of oncogenic miRNAs”, *J. Med. Chem.* **66** (2023), pp. 10639–10657.

[10] C. Maucort, D. D. Vo, S. Aouad, C. Charrat, S. Azoulay, A. Di Giorgio and M. Duca, “Design and implementation of synthetic RNA binders for the inhibition of miR-21 biogenesis”, *ACS Med. Chem. Lett.* **12** (2021), pp. 899–906.

[11] D. D. Vo, C. Becquart, T. P. A. Tran, A. Di Giorgio, F. Darfeuille, C. Staedel and M. Duca, "Building of neomycin-nucleobase-amino acid conjugates for the inhibition of oncogenic miRNAs biogenesis", *Org. Biomol. Chem.* **16** (2018), pp. 6262–6274.

[12] D. D. Vo and M. Duca, "Design of multimodal small molecules targeting mirnas biogenesis: synthesis and in vitro evaluation", *Methods Mol. Biol.* **1517** (2017), pp. 137–154.

[13] D. D. Vo, C. Staedel, L. Zehnacker, R. Benhida, F. Darfeuille and M. Duca, "Targeting the production of oncogenic microRNAs with multimodal synthetic small molecules", *ACS Chem. Biol.* **9** (2014), pp. 711–721.

[14] D. D. Vo, T. P. Tran, C. Staedel, R. Benhida, F. Darfeuille, A. Di Giorgio and M. Duca, "Oncogenic microRNAs biogenesis as a drug target: structure-activity relationship studies on new aminoglycoside conjugates", *Chem. Eur. J.* **22** (2016), pp. 5350–5362.

[15] X. Cheng, J. Chen and Z. Huang, "miR-372 promotes breast cancer cell proliferation by directly targeting LATS2", *Exp. Ther. Med.* **15** (2018), pp. 2812–2817.

[16] W. J. Cho, J. M. Shin, J. S. Kim, et al., "miR-372 regulates cell cycle and apoptosis of ags human gastric cancer cell line through direct regulation of LATS2", *Mol. Cells* **28** (2009), pp. 521–527.

[17] T. P. A. Tran, S. Poulet, M. Pernak, A. Rayar, S. Azoulay, A. Di Giorgio and M. Duca, "Development of 2-deoxystreptamine-nucleobase conjugates for the inhibition of oncogenic miRNA production", *RSC Med. Chem.* **13** (2022), pp. 311–319.

[18] L. C. Griffin, L. L. Kiessling, P. A. Beal, P. Gillespie and P. B. Dervan, "Recognition of all four base pairs of double-helical DNA by triple-helix formation: design of nonnatural deoxyribonucleosides for pyrimidine-purine base pair binding", *J. Am. Chem. Soc.* **114** (1992), pp. 7976–7982.

[19] A. K. Ghosh and M. Brindisi, "Organic carbamates in drug design and medicinal chemistry", *J. Med. Chem.* **58** (2015), pp. 2895–2940.

[20] Q. Vicens and E. Westhof, "Molecular recognition of aminoglycoside antibiotics by ribosomal RNA and resistance enzymes: an analysis of x-ray crystal structures", *Biopolymers* **70** (2003), pp. 42–57.

[21] S. Yoshizawa, D. Fourmy, R. G. Eason and J. D. Puglisi, "Sequence-specific recognition of the major groove of RNA by deoxystreptamine", *Biochemistry* **41** (2002), pp. 6263–6270.

[22] L. L. Kiessling, L. C. Griffin and P. B. Dervan, "Flanking sequence effects within the pyrimidine triple-helix motif characterized by affinity cleaving", *Biochemistry* **31** (1992), pp. 2829–2834.

[23] M. Parisien and F. Major, "The MC-Fold and MC-Sym pipeline infers RNA structure from sequence data", *Nature* **452** (2008), pp. 51–55.

[24] C. Detering and G. Varani, "Validation of automated docking programs for docking and database screening against RNA drug targets", *J. Med. Chem.* **47** (2004), pp. 4188–4201.

ACADÉMIE
DES SCIENCES
INSTITUT DE FRANCE

Comptes Rendus. Chimie
2025, Vol. 28, p. 873-886
https://doi.org/10.5802/crchim.425

Review article

Lectins in the sweet strategy of lung pathogens: from structural glycobiology to design of glycomimetic pathoblockers

Anne Imberty[a]

[a] Univ. Grenoble Alpes, CNRS, CERMAV, 38000 Grenoble, France
E-mail: anne.imberty@cermav.cnrs.fr

Abstract. Glycan epitopes exposed on the host cell surface serve as receptors for a wide range of proteins expressed by microorganisms. Among these, lectins that are produced by viruses, bacteria, and fungi in either soluble or surface-attached forms, play key roles in infection processes. The fine specificity that many of these glycan-binding proteins display toward human glycan epitopes is the result of long-term co-evolution. Structural insights into lectin architecture, their binding sites, and the atomic details of their interactions with glycans are crucial for designing antimicrobial agents capable of competing with infectious processes and potentially supplementing antibiotics in the current fight against antimicrobial resistance. This review highlights how structural lectinology can serve as a starting point for fruitful collaborations with synthetic carbohydrate chemists in the design, synthesis, and characterization of glycomimetics acting as pathoblockers. Various strategies have been developed to target lectins, exemplified here by soluble lectins from the lung pathogens *Pseudomonas aeruginosa* and members of the *Burkholderia cepacia* complex. The affinity for monosaccharide ligands has been enhanced through heterocyclic functionalization using classical medicinal chemistry approaches, with the best results obtained by mimicking natural glycan receptors. Alternatively, the oligomeric nature of lectins allows the design of divalent or multivalent ligands, which exhibit much stronger affinity due to the cluster effect. Covalent inhibitors and non-carbohydrate glycomimetics also represent promising leads for future strategies to combat antimicrobial resistance.

Keywords. Lectins, Protein–carbohydrate interactions, Pathoblockers, Glycomimetics.

Funding. CNRS, CBH-EUR-GS (grant no. ANR-17-EURE-0003), Glyco@Alps (grant no. ANR-15-IDEX-02).

Note. Article submitted by invitation.

Manuscript received 12 September 2025, revised 23 September 2025, accepted 25 September 2025.

1. Introduction

Lectins are proteins that specifically recognize and bind to carbohydrates, including glycoconjugates present on the surface of all living cells [1]. These glycans participate in a wide range of biological processes, most of which are mediated through the recognition of the so-called *glycocode* by protein readers [2]. Indeed, the structural diversity of monosaccharides, their linkages, and conformational states provide an optimal system for signal transmission. The evolutionary expansion of glycan complexity, driven by the diversification of biosynthetic enzymes, has been paralleled by the emergence of a broad repertoire of glycan-binding proteins (GBPs), including lectins, capable of mediating both physiological and pathological functions [3].

Traditionally, lectins are defined as proteins that bind specifically to certain sugars and thereby cause agglutination of particular cell types [4]. This definition excludes both enzymes and antibodies of the adaptive immune system. Lectins can exist as soluble proteins or as modules integrated into larger proteins, where their primary function is to engage glycan targets. In pathogenic bacteria, for example, adhesins act as virulence factors by mediating attachment to host surfaces, often through pili or flagella that incorporate one or more lectin domains [5]. Similarly, many bacterial toxins, such as those responsible for cholera or tetanus, require glycan recognition for binding to host membranes prior to cell entry or membrane disruption [6]. Because lectins frequently present multiple binding sites, achieved either through oligomerization or tandem repeats, they are often called agglutinins. While the affinity of a single binding site is typically low, this is compensated by multivalency, resulting in strong avidity (the so-called Velcro effect) when glycans are presented in multiple copies [7].

Blocking lectin–glycan interactions can interfere with infection processes and biofilm formation. As such, lectins are increasingly recognized as promising targets for the development of pathoblockers [8]. These compounds are designed to inhibit virulence factors or other pathogenic mechanisms without affecting bacterial viability. By targeting processes such as adhesion, invasion, quorum sensing, and biofilm formation, pathoblockers disarm pathogens rather than kill them. This approach exerts minimal selective pressure, thereby reducing the risk of resistance development, while preserving the beneficial commensal microbiota. Pathoblockers are now considered as alternative, or more likely adjunctive, therapies alongside antibiotics, and hold significant promise in the fight against multidrug-resistant pathogens [9].

2. Structural information on lectins from pathogens involved in airway infections

The airway epithelium is covered by a dense glycocalyx composed of *O*-glycosylated mucins, *N*-glycoproteins, and glycolipids. The composition and frequency of glycan epitopes in the respiratory tract vary according to tissue type, with notable differences in the sialylated glycans expressed in the upper versus lower airways [10]. Glycan signatures are also altered in certain pathologies: for instance, cystic fibrosis is associated with abnormally thick mucus and modification of the relative abundance of sialic acid and fucose residues [11]. From the nasal epithelium to the alveoli, the respiratory tract constitutes the primary entry point for numerous airborne pathogens, which can lead to life-threatening diseases such as tuberculosis or Middle East Respiratory Syndrome. Many of these pathogens are hospital-associated and exhibit multidrug resistance, including *Pseudomonas aeruginosa* [12] and members of the *Burkholderia cepacia* complex (BCC) [13]. Emerging fungal infections further exacerbate this burden, as they are often characterized by increasing antifungal resistance and delayed diagnosis.

While mucins play a protective role by trapping pathogens, many microorganisms have evolved mechanisms to exploit host glycans in order to colonize and invade airway tissues. Lectins, in particular, play a central role in these processes, mediating specific recognition of epithelial glycans and thereby facilitating infection or biofilm formation. A summary of lectins implicated in airway infections, together with their specificities and structural data, is provided in Table 1.

The most extensively studied viral lectin is hemagglutinin (HA) from influenza A virus. Sequence variations in HA have resulted in at least 18 subtypes identified across birds and mammals. Importantly, HA specificity underlies the interspecies transmission barrier: avian influenza strains preferentially recognize sialic acid on NeuAc(α2-3)Gal epitopes, whereas human strains target NeuAc(α2-6)Gal receptors [14]. In coronaviruses, the N-terminal domain of the spike glycoprotein contains a galectin-like lectin module. Binding to sialylated glycans is well established in human coronaviruses (HCoVs) [15] and in MERS-CoV [16], where it constitutes a primary receptor-recognition mechanism. Although the lectin domain is structurally conserved in SARS-CoV-2, the sialic acid-binding activity observed in the early Wuhan strain [17] has been lost in subsequent variants [18].

Lectins from fungal opportunistic pathogens also play a central role in host–pathogen interactions. In *Aspergillus fumigatus*, lectins expressed on both conidia and hyphae bind efficiently to fucosylated glycans on epithelial cells and mucins [19]. A closely related lectin has been characterized in *Scedosporium apiospermum*, an emerging opportunistic pathogen of growing clinical concern [20]. Both fungi are associated with nosocomial infections and display increasing resistance to antifungal treatments.

Table 1. Lectins from pathogens responsible for airway infections with available structural data

Species	Lectins	Structural class	Monosaccharide specificity	PDB code
		Bacteria		
Bordetella pertussis	PTX	AB_5 toxin	NeuAc	1PTO
Burkholderia ambifaria	BambL	β-propeller	Fuc	3ZW0
Burkholderia cenocepacia	Bc2L-A, Bc2L-C-Cter	2-calcium lectin	Man	2VNV
	Bc2L-C-Nter	TNFα-like	Fuc	3WQ4
Mycoplasma pneumoniae	P40/P90 adhesin	Mycoplasma adhesin	NeuAc	6TLZ
Pseudomonas aeruginosa	Pyocin	Monocot-lectin like	Man	4LEA
	LecA/PA-IL	1-calcium lectin	αGal	1OKO
	LecB/PA-IIL	2-calcium lectin	Fuc	1GZT
Yersinia pestis	PsaA	Bacterial adhesin	Gal	2HB0
		Fungi		
Aspergillus fumigatus	AFL1/FleA	β-propeller	Fuc	4AGI
Scedosporium apiospermum	SapL1	β-propeller	Fuc	6TRV
		Viruses		
Human coronavirus (HCoV) MERS-CoV SARS-CoV-2	Spike glycoprotein	Coronavirus spike protein	9Ac-NeuAc	8OPM
			NeuAc	6Q04
			NeuAc	7QUR
Influenza virus	Hemagglutinin	Influenza hemag	NeuAc	3HTQ

Fuc: fucose; Man: mannose, Gal: galactose, NeuAc: *N*-acetylneuraminic acid; 9Ac-NeuAc: *N*-acetylneuraminic acid with acetyl group at C9.

Additional structural data are available for lectins from bacterial pathogens causing respiratory diseases, including *Bordetella pertussis* (whooping cough), *Yersinia pestis* (plague) [21] and *Mycoplasma pneumoniae* (atypical pneumonia) [22]. However, the present review focuses on *Pseudomonas aeruginosa* and species of the *Burkholderia cepacia* complex. Rather than providing a comprehensive account of efforts to develop high-affinity ligands against microbial lectins, the aim here is to illustrate how structural studies have guided the rational design of active compounds through distinct strategies. This review also highlights how structural and biophysical investigations conducted at the CERMAV center for research on plant macromolecules have fostered a productive dialogue with carbohydrate chemistry groups, ultimately advancing the synthesis of antibacterial pathoblockers effective against *P. aeruginosa* and different species of *Burkholderia*.

2.1. *Lectins from Pseudomonas aeruginosa and Burkholderia cepacia complex*

Pseudomonas aeruginosa is a ubiquitous opportunistic pathogen associated with severe infections in immunocompromised individuals, particularly in patients with cystic fibrosis and those under mechanical ventilation [24]. It is included in the World Health Organization's priority list of pathogens due to its critical role in the development of antimicrobial resistance. *P. aeruginosa* produces several soluble factors, including pyocins, i.e., short peptides with antibacterial activity, and two lectins, LecA and LecB, which are specific for galactose and fucose, respectively [25]. Both lectins are tetrameric and bind monosaccharides through interactions that involve calcium ions [26,27] (Figure 1A and 1B). LecA binds to host glycolipids, inducing rearrangements of the plasma membrane that not only exert cytotoxic effects but also promote cellular internalization of the

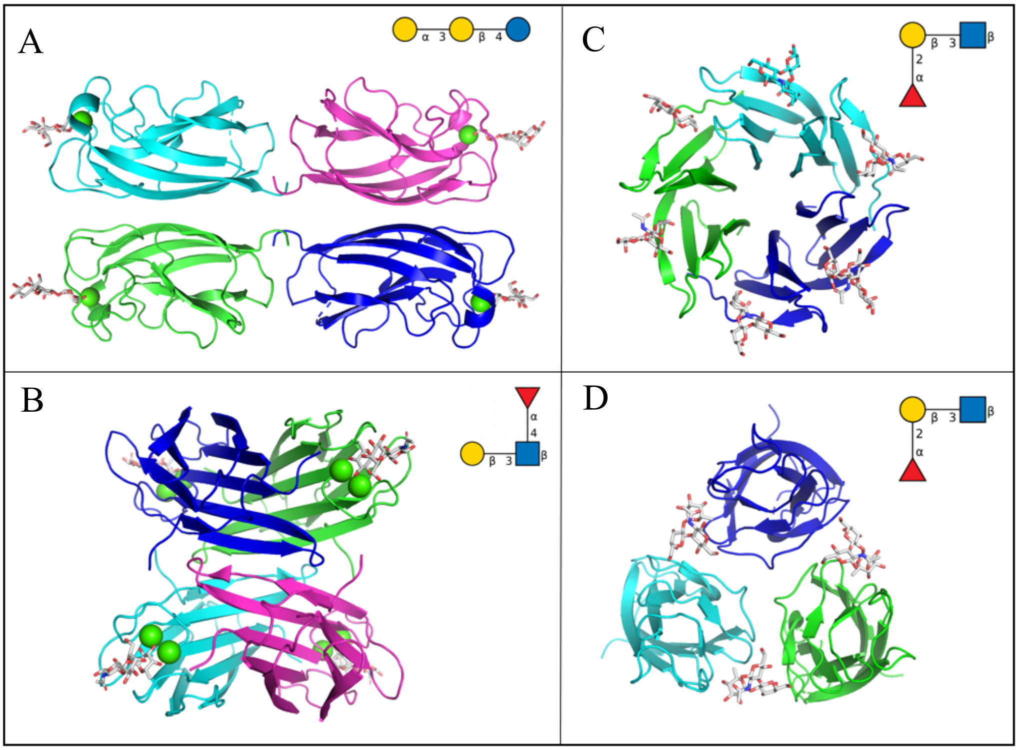

Figure 1. Crystal structures of soluble lectins from bacterial pathogens in their oligomeric form and in complex with human glycan epitopes. (A) LecA from *P. aeruginosa* complexed with iso-Gb3 trisaccharide Gal(α1-3)Gal(β1-4)Glc, PDB 2VXJ. (B) LecB from *P. aeruginosa* complexed with Lewis a trisaccharide Gal(β1-3)[Fuc(α1-4)]GlcNAc, PDB W8H. (C) BambL from *B. ambifaria* complexed with H-type 1 trisaccharide Fuc(α1-2)Gal(β1-3)GlcNAc, PDB 3ZW2. (D) Bc2LC-nt from *B. cenocepacia* complexed with H-type 1 trisaccharide Fuc(α1-2)Gal(β1-3)GlcNAc, PDB 6TID. Proteins are represented by ribbons colored by chains, glycans by sticks, and calcium ions by green spheres (Pymol, Schrödinger). Oligosaccharide ligands are also represented as cartoons using the Symbol Nomenclature for Graphical Representations of Glycans [23] (Gal: yellow circle; Fuc: red triangle; Glc: blue circle, GlcNAc: blue square).

bacterium [28]. LecB has a strong preference for Lewis a oligosaccharides but binds broadly to fucose residues on glycoproteins and glycolipids [29]. Both lectins contribute significantly to biofilm formation [30].

The *Burkholderia cepacia* complex (BCC) comprises at least twenty distinct *Burkholderia* species, many of which are clinically important opportunistic pathogens in cystic fibrosis patients [31]. *Burkholderia cenocepacia* produces several lectins with LecB-like domains, showing specificity for fucose and mannose [32]. Among them, BC2L-C is notable for its modular structure: its N-terminal domain resembles LecB, while its C-terminal domain adopts a tumor necrosis factor (TNF)-α-like fold, also with fucose specificity [33] (Figure 1D). In contrast, *Burkholderia ambifaria* produces a different lectin that assembles into a trimeric β-propeller, exposing six fucose-binding sites [34] (Figure 1C).

2.2. *Forces involved in protein–sugar interaction*

The binding sites of the four lectins discussed in this review are shown in Figure 2, and they exemplify the classical interactions typically observed in protein–carbohydrate recognition. In all cases, hydroxyl groups of the glycans participate in hydrogen bonding with amino acid side chains within the protein binding site. Statistical analyses have shown that among polar amino acids, asparagine and aspartate

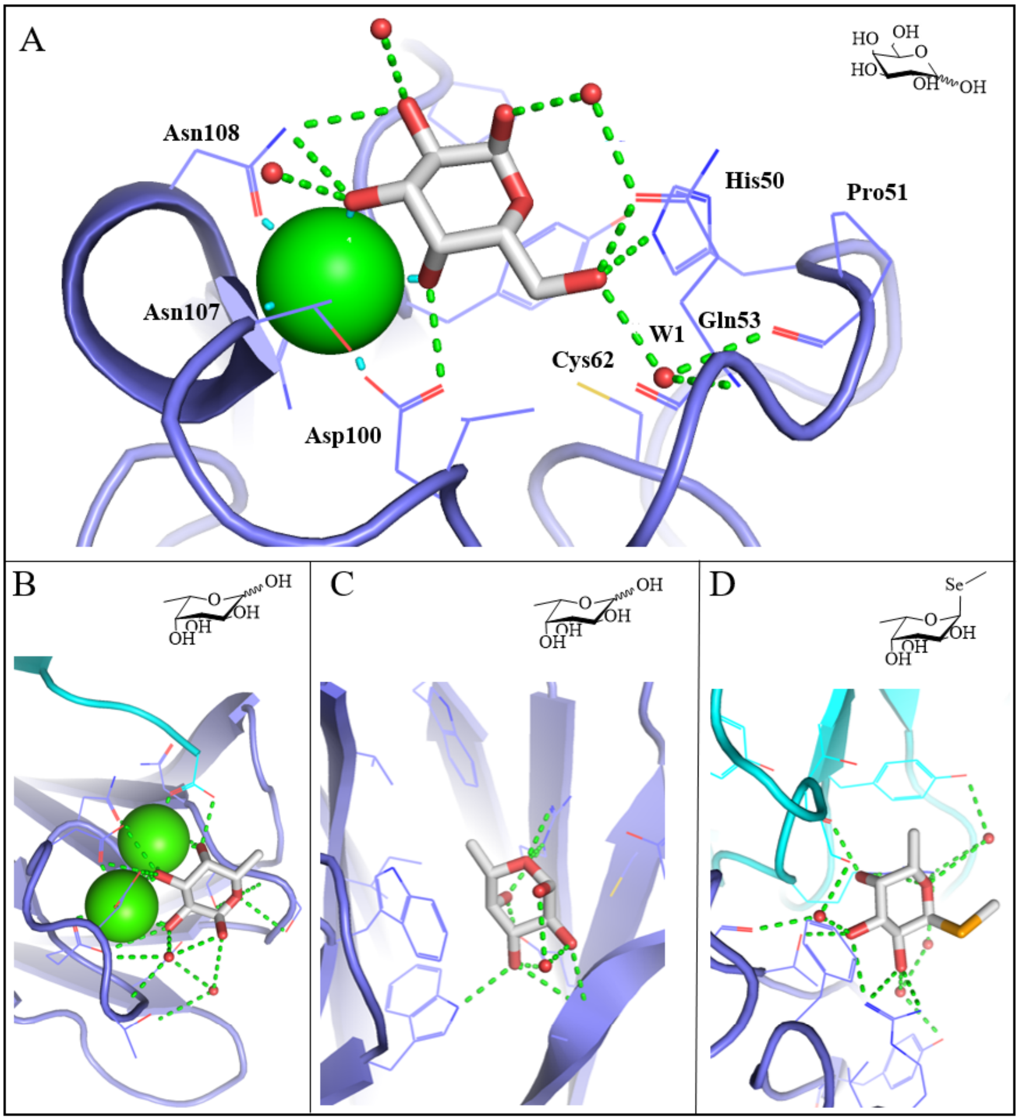

Figure 2. Details of the glycan binding sites of bacterial lectins from crystal structures. (A) LecA/galactose, PDB 1OKO. (B) LecB/fucose, PDB 1GZT. (C) BambL/fucose, PDB 3ZW0. (D) BC2LC-nt/SeMeFuc, PDB 3WQ4. Hydrogen bonds are represented by green dashed lines, calcium ions by green spheres and water molecules as small red balls. Schematic representation of ligands is displayed in the right upper corner of each panel (ChemSketch, ACD/Labs).

are preferred, occurring at approximately twice the frequency expected by chance [35]. However, aromatic amino acids are most strongly favored, with a pronounced prevalence of tryptophan, followed by tyrosine and then histidine.

This preference is attributed to CH–π interactions, whereby the CH–presenting face of monosaccharides interacts with electron-rich aromatic side chains [36]. For example, fucose interacts with tryptophan in the binding site of BambL (Figure 2C). Additional contacts are often mediated by water molecules that are integral components of the binding site; for instance, water molecule W1 in LecA is consistently observed in crystal structures and forms a hydrogen bond with O6 of the glycan within a small pocket of the protein surface (Figure 2A). The two *P. aeruginosa* lectins exhibit a nonconventional mode of glycan recognition. In these cases, calcium ions are directly involved in binding: O3 and O4 of galactose in LecA and O2, O3, and O4 in LecB are coordinated by calcium (Figure 2A and 2B). The presence of two calcium ions is unique to this latter lectin class, and a recent neutron diffraction study demonstrated their role in creating low-barrier hydrogen bonds, which contribute to the unusually high affinity of these interactions [37].

3. Strategies for designing high-affinity glycomimetics against lectins from pathogens

The structural information described above served as the basis for the development of high affinity glycomimetics that are able to compete with the binding of the lectins to the glycan targets with the aim of inhibiting the first stage of adhesion, but also biofilm formation. High-affinity glycomimetics are also a strategy for the vectorization of antibiotics [38] and other compounds or for labeling pathogen or biofilms by fluorescent compounds [39].

3.1. *Structure-based design of monovalent glycomimetics*

LecA binds to the terminal α-galactose residue present in Gb3, which belongs to the globosphingolipid group of glycolipids and consists of the Gal(α1-4)Gal(β1-4)Glc trisaccharide linked to ceramide [40]. The affinity of LecA for galactose or for its natural ligand Gal(α1-4)Gal is relatively low with dissociation constant (K_d) between 50 and 100 μM, but this limitation is compensated during infection by multivalent effects induced by the many oligosaccharide heads of glycolipids present on the membrane. An isomer of the natural ligand, the isoglobosidetrisaccharide Gal(α1-3)Gal(β1-4)Glc, displays comparable affinity and the crystal structure of the complex with LecA has been described (Figure 3A) [40], providing a basis for structure-guided design of mimetics. In the development of glycomimetics, β-galactosides with aromatic aglycones exhibit enhanced affinity, largely due to a T-shaped electronic interaction with His50 in the binding site [41]. For example, *p*-nitrophenyl-β-galactoside (PNP-Gal) binds with a K_d of 5 μM and the particular interaction is illustrated in Figure 3B. Other *O*- and *S*-linked aromatic derivatives have also been investigated [42], and the best monovalent ligand reported to date, a diarylthiogalactoside reaches an affinity of ∼1 μM [43]. This ligand adopts a binding mode closely resembling that of the natural ligand (Figure 3C), underscoring the potential of ligand design strategies that mimic the structural features of native glycans.

LecB exhibits strong affinity for natural ligands such as fucose ($K_d \approx 3$ μM) and Fuc(α1-4)GlcNAc-containing trisaccharides, with a K_d of 210 nM for the Lewis a antigen (Figure 4A) [29]. Functionalization at the reducing end of this disaccharide yielded potent inhibitors with affinities comparable to those of the natural trisaccharide (Figure 4B) [44].

The observation that D-mannose, which is stereochemically related to L-fucose, is also a ligand for LecB has inspired the design of carbohydrate ring mimics, in which the axial anomeric oxygen of fucose is replaced by an equatorial sulfonamide moiety [45] (Figure 4C). Building on this approach, β-fucosyl amides, sulfonamides, and thiourea derivatives were synthesized, among which a β-fucosyl amide diaryl derivative displayed both high affinity and notable stability in plasma [46] (Figure 4D).

BambL from *B. ambifaria* also interacts with fucose-containing oligosaccharides, exhibiting high affinity for the fucose monosaccharide [34] as well as for fucosylated glycans such as Lewis and ABO antigens (Figure 5A). The synthesis of a conformationally constrained aryl-α-*O*-fucosyl analogue produced a compound with binding affinity comparable to that of native fucose, but with substantially enhanced selectivity, as it is not recognized by either human fucose-binding lectins or LecB [47]. The crystal structure of the BambL–ligand complex further revealed that the compound acts as an effective glycomimetic of natural fucosylated glycans, engaging the protein surface at the same binding site as the blood group B oligosaccharide [48] (Figure 5B).

BC2L-C-nt from *B. cenocepacia* also binds fucose but displays a marked preference for H-type 1 (Figure 6A) and H-type 3 epitopes [49], albeit with modest affinity. An innovative fragment-based theoretical approach identified a binding pocket adjacent to the fucose-binding site, and several potential hits were subsequently validated using biophysical methods [50]. From the results of the fragment-based screening, bifunctional ligands were

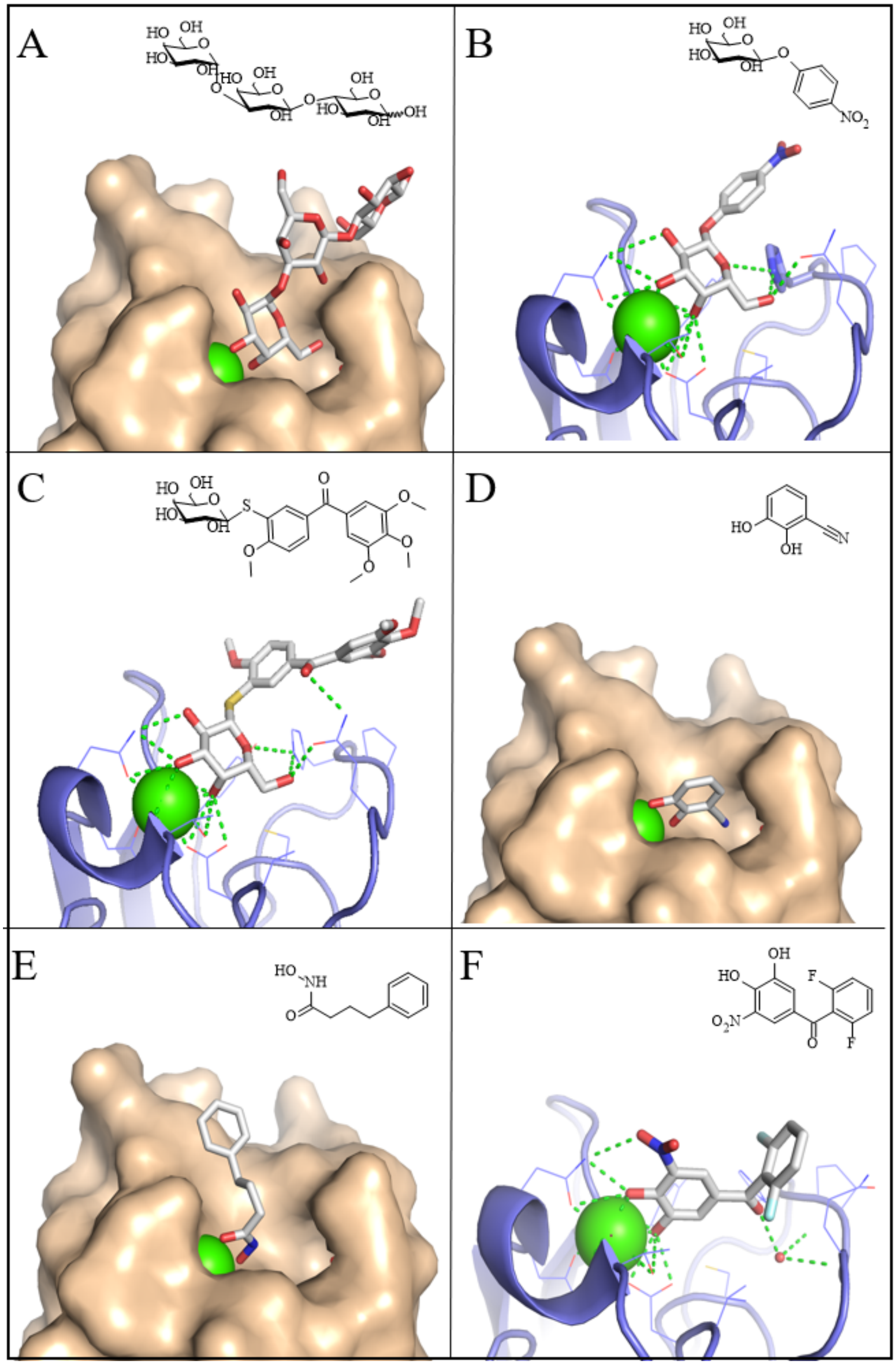

Figure 3. Crystal structures of LecA (surface in beige and ribbon in blue) complexed with natural and synthetic ligands. (A) Gal(α1-3)Gal(β1-4)Glc, PDB 2VXJ. (B) *p*-Nitrophenyl-β-galactoside, PDB 3ZYF. (C) Diarylthiogalactoside, PDB 7Z63. (D) Cyanocatechol, PDB 6YO3. (E) Phenylbutyryl hydroxamic acid, PDB 7FJH. (F) Difluoro tolcapone derivative, PDB 9I7Z. Schematic representation of ligands is displayed in the right upper corner of each panel (ChemSketch, ACD/Labs).

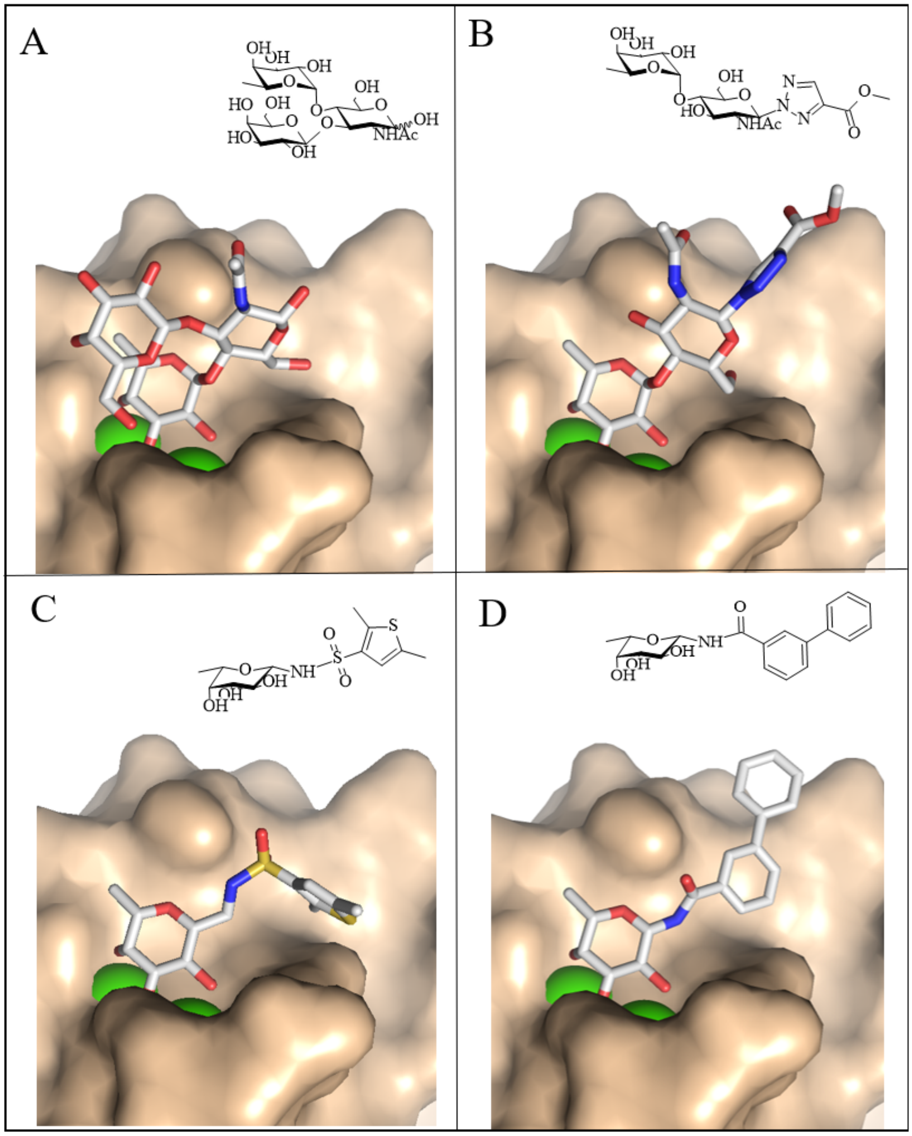

Figure 4. Crystal structures of LecB (surface in beige) complexed with natural and synthetic ligand. (A) Gal(β1-3)[Fuc(α1-4)]GlcNAc, PDB W8H. (B) Fuc(α1-4)GlcNAc triazole derivative, PDB 2JDK. (C) β-Fucopyranosyl-thiophenesulfonamide derivative, PDB 5MAZ. (D) β-Fucopyranosyl-biphenyl-3-carboxamide, PDB 8AIY. Schematic representation of ligands is displayed in the right upper corner of each panel (ChemSketch, ACD/Labs).

synthesized employing a panel of rationally selected linkers, yielding an alkene-bound glycomimetic with a tenfold increase in affinity relative to fucose (Figure 6B) [51]. Although *N*-fucosides were also synthesized, their poor aqueous solubility limited their application as antagonists. However, a subsequent generation of derivatives overcame this limitation, exhibiting both satisfactory affinity and improved solubility (Figure 6C) [52].

3.2. *Covalent glyco-derived inhibitors*

Covalent inhibitors have recently been developed to target growth factors in cancer and proteases in viral

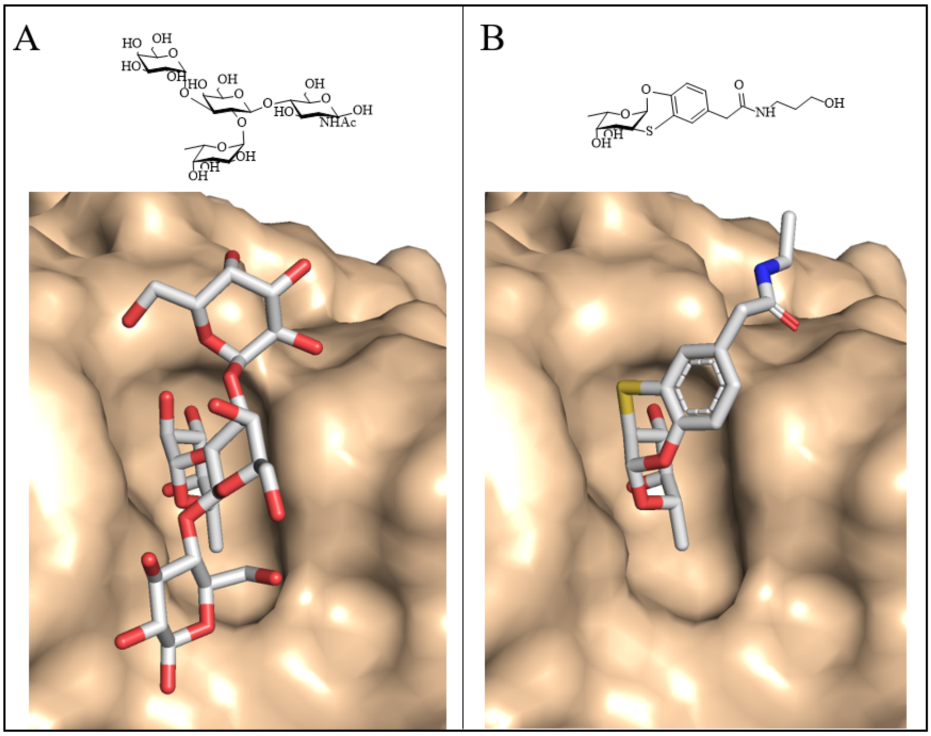

Figure 5. Crystal structures of BambL (surface in beige) complexed with natural and synthetic ligands. (A) Gal(α1-3)[Fuc(α1-2)]Gal(β1-4)GlcNAc, PDB 3ZWE. (B) Conformationally constrained fucose-based glycomimetics, PDB 6ZFC. Schematic representation of ligands is displayed in the right upper corner of each panel (ChemSketch, ACD/Labs).

infections. Because specificity represents the primary challenge in this strategy, successful design requires precise positioning of the ligand warhead in close proximity to a reactive amino acid within the lectin binding site. In the case of LecA, this was achieved by exploiting Cys62, located at the base of the binding pocket near the secondary hydroxyl group of galactose (Figure 2A) [53]. A phenyl-β-galactoside derivative bearing an epoxy group at the C6 position was synthesized, and formation of the covalent adduct was confirmed by mass spectrometry. Furthermore, a fluorescein-conjugated derivative enabled specific staining of *P. aeruginosa* biofilms.

Another warhead was used for covalent inhibition of BC2L-C-nt by fucosides connected to salicylaldehyde groups by a variety of linkers with the aim of targeting Lys108 in the binding site of the lectin [54]. Mass spectrometry conducted on the whole lectin and on digestion peptides confirmed the formation of the covalent adduct.

3.3. *Non-carbohydrate glycomimetics*

All of the inhibitors described above retain the principle of a glycan residue bound in the primary binding site of the lectin. In contrast, non-carbohydrate glycomimetics offer the potential for more straightforward synthetic routes, broader chemical diversity, and improved pharmacokinetic properties. Using a virtual screening strategy, more than 1500 compounds from the National Cancer Institute (NCI) Diversity set IV were docked into LecA, leading to the identification of promising candidates [55]. Many of these compounds contained a catechol moiety, raising the possibility of false positives due to nonspecific reactivity with the protein surface. Nevertheless, screening of catechol libraries with

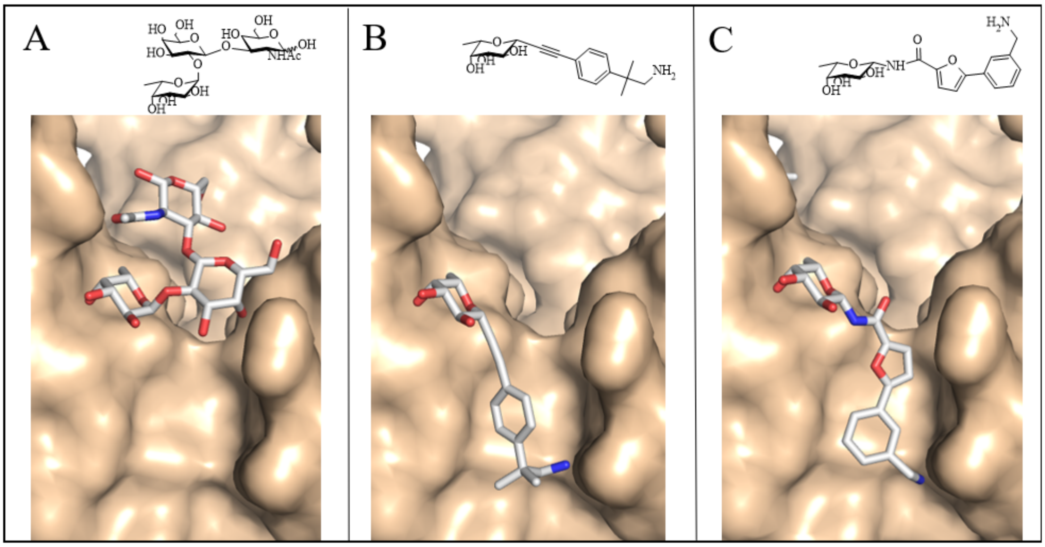

Figure 6. Crystal structures of BC2L-C-nt (surface in beige) complexed with natural and synthetic ligands. (A) Fuc(α1-2)Galβ(1-3)GlcNAc, PDB 6TID. (B) Ethynyl-phenyl derivative of fucose, PDB 7OLU. (C) Aminomethyl-phenyl derivative of fucose, PDB 8BRO. Schematic representation of ligands is displayed in the right upper corner of each panel (ChemSketch, ACD/Labs).

multiple biophysical methods confirmed that several electron-deficient catechols bind specifically to LecA. Although their affinities were only in the millimolar range, the crystal structure of LecA in complex with cyanocatechol demonstrated that its oxygen atoms mimic the roles of galactose O3 and O4 in coordinating calcium within the binding site (Figure 3D) [55]. Building on this concept of metal-binding pharmacophores as novel scaffolds for inhibiting Ca^{2+}-dependent lectins, both virtual and NMR-based screening of general and specialized compound libraries were undertaken [56]. Several hydroxamates were identified as specific LecA ligands, again with affinities in the low millimolar range, and crystal structures confirmed their calcium-coordinating interactions (Figure 3E) [56]. By contrast, malonates displayed broader activity, binding not only to LecA and LecB but also to human C-type lectins. To further develop the catechol-based scaffold, 3267 unique catechol derivatives from the Hoffmann-La Roche compound library were tested for LecA binding [57]. Among these, tolcapone, a drug used in the treatment of Parkinson's disease, and several structural analogues, emerged as potent ligands with affinities around 10 μM—approximately 5- to 10-fold stronger than galactose. The crystal structure of one representative compound (Figure 3F) revealed that these ligands not only coordinate calcium but also form hydrogen bonds with conserved water molecules and engage in hydrophobic interactions with the protein surface.

3.4. *Structure-based multivalent ligands*

Structural information on lectins can also be used for the design of multivalent ligands with appropriate linkers to reach two or more binding sites of the lectins, resulting in a chelating effect that can result in several-fold increases in affinity [7].

A substantial body of literature has described the synthesis of glycoclusters, glycopolymers, and other multivalent ligands targeting LecA and LecB (see Refs. [58–60]). In the case of *P. aeruginosa*, the present article focuses on selected examples of structure-based design of divalent ligands for LecA. The architecture of the LecA tetramer (Figure 1A), which presents two galactose-binding sites separated by approximately 29 Å on the same face, provides an optimal framework for the rational design of divalent ligands. Flexible linkers, such as those based on polyethylene glycol (PEG), proved ineffective in promoting efficient chelation due to the entropic penalty arising from their conformational flexibility. In contrast, introducing additional interactions at the protein surface, for instance, through linkers identified from a large heteroglycoconjugate library generated by nucleic-acid-encoded peptide synthesis, yielded high-affinity binders with dissociation constants as low as 82 nM [61]. Rigid spacers proved even more effective at eliciting strong avidity effects, provided they positioned the two galactose moieties at the appropriate distance while retaining adequate aqueous solubility. Subsequent optimization, involving the incorporation of alternating glucose and triazole units, resulted in a ligand with an affinity of 28 nM, corresponding to an approximately 100-fold improvement relative to the monovalent ligand [62]. Remarkably, this compound was the only divalent ligand successfully crystallized with LecA (Figure 7A), as the high protein concentrations required for crystallization typically favor ligand cross-bridging rather than intramolecular chelation. Additional potent divalent galactosides, with dissociation constants in the range of 10–40 nM, were later reported by Titz and colleagues, who also demonstrated their improved solubility and effectiveness in reducing *P. aeruginosa* invasiveness in host cells (Figure 7B) [39].

The spherical architecture of LecB, with its fucose-binding sites positioned far apart, is not favorable for the design of divalent chelating ligands. Consequently, only limited improvements in binding affinity have been achieved relative to fucose itself [60]. In contrast, the propeller-shaped architecture of BambL is more amenable to multivalent ligand design, as it allows simultaneous engagement of two or more of the six fucose-binding sites, each separated by approximately 20 Å. The glycomimetic structure depicted in Figure 5B was assembled into a hexavalent ligand using a peptide raft scaffold [63]. The resulting construct exhibited the appropriate shape and size to interact with multiple sites of the BambL propeller, as demonstrated by the structural superposition shown in Figure 7C, and achieved a K_d of 14 nM. An alternative strategy exploited ligand cooperativity through PNA–fucose conjugates, which contained only a single fucose residue but were capable of hybridizing via the PNA (peptide nucleic acid) backbone in the presence of the protein [64]. This cooperative assembly resulted in high-affinity binding, with a K_d of 11 nM.

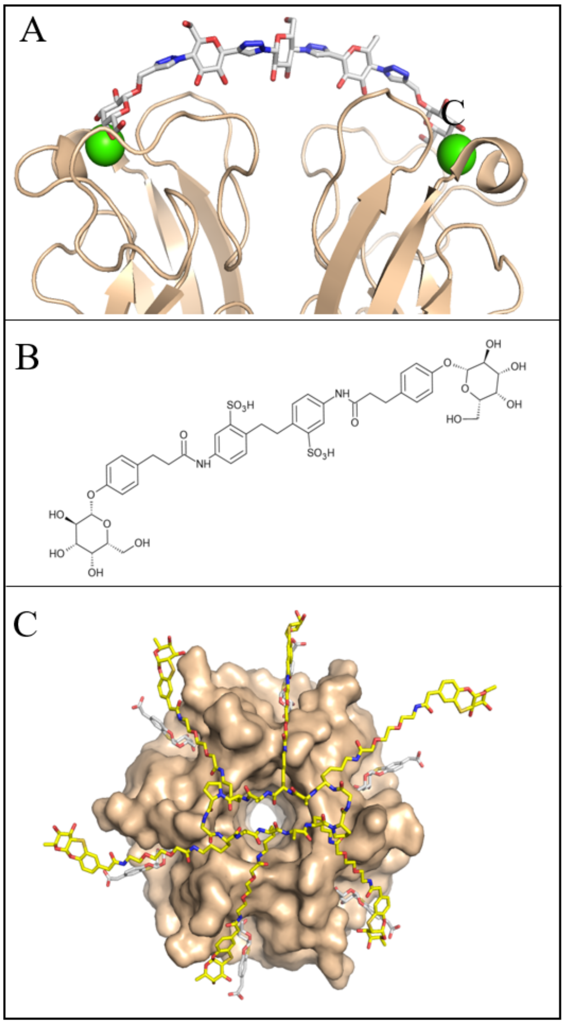

Figure 7. Some multivalent glycosides with high affinity for bacterial lectins. (A) Divalent galactoside with triazolyl–glucose-based linker in complex with LecA (surface in beige, crystal structure PDB 4YWA). (B) Divalent galactoside with aromatic-based linker also binding to LecA. (C) Pentavalent fucoside with high affinity for BambL (model superimposed on crystal structure, PDB 6ZFC).

4. Prospectives: identification of new targets

This article highlights a subset of bacterial species implicated in lung infections, yet the principles discussed are broadly applicable to other carbohydrate-dependent pathogens. Indeed, comparable strategies have already proven effective against uropathogenic *Escherichia coli*, which use FimH adhesin to bind to mannosylated epitopes on urothelial cells, a crucial step in urinary tract infections [65]. Looking forward, the identification of novel lectin targets is likely to expand considerably, as systematic data mining of genomic resources now enables the prediction of putative lectins across bacterial, viral, and fungal species [66]. Dedicated tools such as LectomeXPlore will accelerate this process, providing a framework for the rational prioritization of targets [67]. In parallel, the rapid advances of carbohydrate-based therapeutics in oncology and vaccinology underscore their untapped potential in infectious disease management. Positioned as a complementary strategy to antibiotics, these approaches could play a decisive role in addressing the dual challenges of antimicrobial resistance and the emergence of novel pathogens driven by climate change.

Acknowledgments

Pathogens in the graphical abstract are designed by Freepik (www.freepik.com).

Declaration of interests

The author does not work for, advise, own shares in, or receive funds from any organization that could benefit from this article, and has declared no affiliations other than their research organization.

Funding

Support from CNRS, CBH-EUR-GS (ANR-17-EURE-0003) and Glyco@Alps (ANR-15-IDEX-02) is acknowledged.

References

[1] H. Lis and N. Sharon, "Lectins as molecules and as tools", *Ann. Rev. Biochem.* **1986** (1986), pp. 35–67.

[2] H. J. Gabius, M. Cudic, T. Diercks, et al., "What is the sugar code?", *Chembiochem* **23** (2022), no. 13, article no. e202100327.

[3] M. E. Taylor, K. Drickamer, A. Imberty, Y. v. Kooyk, R. L. Schnaar, M. E. Etzler and A. Varki, "Discovery and classification of glycan-binding proteins", in *Essentials of Glycobiology*, fourth edition (A. Varki, J. H. Prestegard, R. L. Schnaar, et al., eds.), Cold Spring Harbor Laboratory Press: Cold Spring Harbor, NY, 2022, pp. 375–386.

[4] I. J. Goldstein, R. C. M. Hughes, T. Osawa and N. Sharon, "What should be called a lectin?", *Nature* **285** (1980), p. 66.

[5] M. Farez, A. Imberty and A. Titz, "Bacterial lectins: multifunctional tools in pathogenesis and possible drug targets", *Trends Microb.* **33** (2025), pp. 839–852.

[6] A. L. Lewis, J. J. Kohler and M. Aebi, "Microbial lectins: hemagglutinins, adhesins, and toxins", in *Essentials of Glycobiology* (A. Varki, R. D. Cummings, J. D. Esko, et al., eds.), Cold Spring Harbor Laboratory Press: Cold Spring Harbor, NY, 2022, pp. 505–516.

[7] R. T. Lee and Y. C. Lee, "Affinity enhancement by multivalent lectin–carbohydrate interaction", *Glycoconj. J.* **17** (2000), no. 7–9, pp. 543–551.

[8] M. B. Calvert, V. R. Jumde and A. Titz, "Pathoblockers or antivirulence drugs as a new option for the treatment of bacterial infections", *Beilstein J. Org. Chem.* **14** (2018), pp. 2607–2617.

[9] M. Miethke, M. Pieroni, T. Weber, et al., "Towards the sustainable discovery and development of new antibiotics", *Nat. Rev. Chem.* **5** (2021), no. 10, pp. 726–749.

[10] T. Walther, R. Karamanska, R. W. Chan, et al., "Glycomic analysis of human respiratory tract tissues and correlation with influenza virus infection", *PLoS Pathog.* **9** (2013), no. 3, article no. e1003223.

[11] A. D. Rhim, L. Stoykova, M. C. Glick and T. F. Scanlin, "Terminal glycosylation in cystic fibrosis (CF): a review emphasizing the airway epithelial cell", *Glycoconj. J.* **18** (2001), no. 9, pp. 649–659.

[12] K. Poole, "Pseudomonas aeruginosa: resistance to the max", *Front. Microbiol.* **2** (2011), article no. 65.

[13] K. A. Rhodes and H. P. Schweizer, "Antibiotic resistance in Burkholderia species", *Drug Resist. Updat.* **28** (2016), pp. 82–90.

[14] R. J. Connor, Y. Kawaoka, R. G. Webster and J. C. Paulson, "Receptor specificity in human, avian, and equine H2 and H3 influenza virus isolates", *Virology* **205** (1994), no. 1, pp. 17–23.

[15] M. F. Pronker, R. Creutznacher, I. Drulyte, et al., "Sialoglycan binding triggers spike opening in a human coronavirus", *Nature* **624** (2023), no. 7990, pp. 201–206.

[16] Y. J. Park, A. C. Walls, Z. Wang, et al., "Structures of MERS-CoV spike glycoprotein in complex with sialoside attachment receptors", *Nat. Struct. Mol. Biol.* **26** (2019), no. 12, pp. 1151–1157.

[17] C. J. Buchanan, B. Gaunt, P. J. Harrison, et al., "Pathogen–sugar interactions revealed by universal saturation transfer analysis", *Science* **377** (2022), no. 6604, article no. eabm3125.

[18] S. Kuhaudomlarp and A. Imberty, "Involvement of sialoglycans in SARS-COV-2 infection: opportunities and challenges for glyco-based inhibitors", *IUBMB Life* **17** (2022), pp. 1253–1263.

[19] J. Houser, J. Komarek, G. Cioci, A. Varrot, A. Imberty and M. Wimmerova, "Structural insights into *Aspergillus fumigatus* lectin specificity - AFL binding sites are functionaly non-equivalent", *Acta Crystallogr. D* **71** (2015), pp. 442–453.

[20] D. Martinez-Alarcon, V. Balloy, J. P. Bouchara, R. J. Pieters and A. Varrot, "Biochemical and structural studies of tar-

get lectin SapL1 from the emerging opportunistic microfungus Scedosporium apiospermum", *Sci. Rep.* **11** (2021), no. 1, article no. 16109.

[21] R. Bao, M. K. Nair, W. K. Tang, L. Esser, A. Sadhukhan, R. L. Holland, D. Xia and D. M. Schifferli, "Structural basis for the specific recognition of dual receptors by the homopolymeric pH 6 antigen (Psa) fimbriae of Yersinia pestis", *Proc. Natl. Acad. Sci. USA* **110** (2013), no. 3, pp. 1065–1070.

[22] D. Vizarraga, A. Kawamoto, U. Matsumoto, et al., "Immunodominant proteins P1 and P40/P90 from human pathogen Mycoplasma pneumoniae", *Nat. Commun.* **11** (2020), no. 1, article no. 5188.

[23] A. Varki, R. D. Cummings, M. Aebi, et al., "Symbol nomenclature for graphical representations of glycans", *Glycobiology* **25** (2015), no. 12, pp. 1323–1324.

[24] I. Jurado-Martin, M. Sainz-Mejias and S. McClean, "Pseudomonas aeruginosa: an audacious pathogen with an adaptable arsenal of virulence factors", *Int. J. Mol. Sci.* **22** (2021), no. 6, article no. 3128.

[25] N. Gilboa-Garber, " *Pseudomonas aeruginosa* lectins", *Meth. Enzymol.* **83** (1982), pp. 378–385.

[26] G. Cioci, E. P. Mitchell, C. Gautier, M. Wimmerova, D. Sudakevitz, S. Pérez, N. Gilboa-Garber and A. Imberty, "Structural basis of calcium and galactose recognition by the lectin PA-IL of *Pseudomonas aeruginosa*", *FEBS Lett.* **555** (2003), pp. 297–301.

[27] E. Mitchell, C. Houles, D. Sudakevitz, et al., "Structural basis for oligosaccharide-mediated adhesion of *Pseudomonas aeruginosa* in the lungs of cystic fibrosis patients", *Nat. Struct. Biol.* **9** (2002), pp. 918–921.

[28] T. Eierhoff, B. Bastian, R. Thuenauer, et al., "A lipid zipper triggers bacterial invasion", *Proc. Natl. Acad. Sci. USA* **111** (2014), pp. 12895–12900.

[29] S. Perret, C. Sabin, C. Dumon, et al., "Structural basis for the interaction between human milk oligosaccharides and the bacterial lectin PA-IIL of *Pseudomonas aeruginosa*", *Biochem. J.* **389** (2005), pp. 325–332.

[30] J. L. Reymond, M. Bergmann and T. Darbre, "Glycopeptide dendrimers as Pseudomonas aeruginosa biofilm inhibitors", *Chem. Soc. Rev.* **42** (2013), no. 11, pp. 4814–4822.

[31] E. Mahenthiralingam, A. Baldwin and P. Vandamme, "Burkholderia cepacia complex infection in patients with cystic fibrosis", *J. Med. Microbiol.* **51** (2002), no. 7, pp. 533–538.

[32] E. Lameignere, L. Malinovská, M. Sláviková, et al., "Structural basis for mannose recognition by a lectin from opportunistic bacteria *Burkholderia cenocepacia*", *Biochem. J.* **411** (2008), pp. 307–318.

[33] O. Šulák, G. Cioci, E. Lameignère, et al., " *Burkholderia cenocepacia* BC2L-C is a super lectin with dual specificity and proinflammatory activity", *PLoS Pathog.* **7** (2011), article no. e1002238.

[34] A. Audfray, J. Claudinon, S. Abounit, et al., "The fucose-binding lectin from opportunistic pathogen *Burkholderia ambifaria* binds to both plant and human oligosaccharidic epitopes", *J. Biol. Chem.* **287** (2012), pp. 4335–4347.

[35] K. L. Hudson, G. J. Bartlett, R. C. Diehl, J. Agirre, T. Gallagher, L. L. Kiessling and D. N. Woolfson, "Carbohydrate–aromatic interactions in proteins", *J. Am. Chem. Soc.* **137** (2015), no. 48, pp. 15152–15160.

[36] J. L. Asensio, A. Arda, F. J. Canada and J. Jimenez-Barbero, "Carbohydrate–aromatic interactions", *Acc. Chem. Res.* **46** (2013), no. 4, pp. 946–954.

[37] L. Gajdos, M. P. Blakeley, M. Haertlein, V. T. Forsyth, J. M. Devos and A. Imberty, "Neutron crystallography reveals mechanisms used by Pseudomonas aeruginosa for host-cell binding", *Nat. Commun.* **13** (2022), article no. 194.

[38] J. Meiers, E. Zahorska, T. Rohrig, D. Hauck, S. Wagner and A. Titz, "Directing drugs to bugs: antibiotic-carbohydrate conjugates targeting biofilm-associated lectins of Pseudomonas aeruginosa", *J. Med. Chem.* **63** (2020), no. 20, pp. 11707–11724.

[39] E. Zahorska, L. M. Denig, S. Lienenklaus, et al., "High-affinity lectin ligands enable the detection of pathogenic *Pseudomonas aeruginosa* biofilms: implications for diagnostics and therapy", *JACS Au* **4** (2024), pp. 4715–4728.

[40] B. Blanchard, A. Nurisso, E. Hollville, et al., "Structural basis of the preferential binding for globo-series glycosphingolipids displayed by *Pseudomonas aeruginosa* lectin I (PA-IL)", *J. Mol. Biol.* **383** (2008), pp. 837–853.

[41] R. U. Kadam, D. Garg, J. Schwartz, R. Visini, M. Sattler, A. Stocker, T. Darbre and J. L. Reymond, "CH-pi "T-shape" interaction with histidine explains binding of aromatic galactosides to Pseudomonas aeruginosa lectin LecA", *ACS Chem. Biol.* **8** (2013), no. 9, pp. 1925–1930.

[42] J. Rodrigue, G. Ganne, B. Blanchard, et al., "Aromatic thioglycoside inhibitors against the virulence factor LecA from *Pseudomonas aeruginosa*", *Org. Biomol. Chem.* **11** (2013), pp. 6906–6918.

[43] A. Bruneau, E. Gillon, A. Furiga, et al., "Discovery of potent 1,1-diarylthiogalactoside glycomimetic inhibitors of *Pseudomonas aeruginosa* LecA with antibiofilm properties", *Eur. J. Med. Chem.* **247** (2023), article no. 115025.

[44] K. Marotte, C. Sabin, C. Préville, M. Moumé-Pymbock, M. Wimmerova, E. P. Mitchell, A. Imberty and R. Roy, "X-ray structures and thermodynamic of interaction of PA-IIL from *Pseudomonas aeruginosa* with disaccharide derivatives", *ChemMedChem* **2** (2007), pp. 1328–1338.

[45] R. Sommer, S. Wagner, K. Rox, et al., "Glycomimetic, orally bioavailable LecB inhibitors block biofilm formation of *Pseudomonas aeruginosa*", *J. Am. Chem. Soc.* **140** (2018), pp. 2537–2545.

[46] P. Mala, E. Siebs, J. Meiers, K. Rox, A. Varrot, A. Imberty and A. Titz, "Discovery of N-beta-l-fucosyl amides as high-affinity ligands for the Pseudomonas aeruginosa lectin LecB", *J. Med. Chem.* **65** (2022), no. 20, pp. 14180–14200.

[47] B. Richichi, A. Imberty, E. Gillon, R. Bosco, I. Sutkeviciute, F. Fieschi and C. Nativi, "Synthesis of a selective inhibitor of a fucose binding bacterial lectin from Burkolderia ambifaria", *Org. Biomol. Chem.* **11** (2013), pp. 4086–4094.

[48] S. Kuhaudomlarp, L. Cerofolini, S. Santarsia, et al., "Fucosylated ubiquitin and orthogonally glycosylated mutant A28C: conceptually new ligands for Burkholderia ambifaria lectin (BambL)", *Chem. Sci.* **11** (2020), pp. 12662–12670.

[49] R. Bermeo, A. Bernardi and A. Varrot, "BC2L-C N-terminal lectin domain complexed with histo blood group oligosac-

charides provides new structural information", *Molecules* **25** (2020), no. 2, article no. 248.

[50] K. Lal, R. Bermeo, J. Cramer, et al., "Prediction and validation of a druggable site on virulence factor of drug resistant Burkholderia cenocepacia", *Chemistry* **27** (2021), no. 40, pp. 10341–10348.

[51] R. Bermeo, K. Lal, D. Ruggeri, et al., "Targeting a multidrug-resistant pathogen: first generation antagonists of Burkholderia cenocepacia's BC2L-C lectin", *ACS Chem. Biol.* **17** (2022), no. 10, pp. 2899–2910.

[52] S. Mazzotta, G. Antonini, F. Vasile, E. Gillon, J. Lundstrom, A. Varrot, L. Belvisi and A. Bernardi, "Identification of new L-fucosyl and L-galactosyl amides as glycomimetic ligands of TNF lectin domain of BC2L-C from Burkholderia cenocepacia", *Molecules* **28** (2023), no. 3, article no. 1494.

[53] S. Wagner, D. Hauck, M. Hoffmann, et al., "Covalent lectin inhibition and application in bacterial biofilm imaging", *Angew. Chem. Int. Ed. Engl.* **56** (2017), no. 52, pp. 16559–16564.

[54] G. Antonini, A. Bernardi, E. Gillon, A. Dal Corso, M. Civera, L. Belvisi, A. Varrot and S. Mazzotta, "Achieving high affinity for a bacterial lectin with reversible covalent ligands", *J. Med. Chem.* **67** (2024), no. 21, pp. 19546–19560.

[55] S. Kuhaudomlarp, E. Siebs, E. Shanina, et al., "Non-carbohydrate glycomimetics as inhibitors of calcium(II)-binding lectins", *Angew. Chem. Int. Ed.* **60** (2021), pp. 2–13.

[56] E. Shanina, S. Kuhaudomlarp, E. Siebs, et al., "Targeting undruggable carbohydrate recognition sites through focused fragment library design", *Commun. Chem.* **5** (2022), article no. 64.

[57] S. Leusmann, E. Siebs, A. Varrot, S. Kuhaudomlarp, A. Imberty, B. Kuhn and C. L. U. G. A. Titz, "The Parkinson's disease drug Tolcapone and analogues are potent glycomimetic lectin inhibitors of Pseudomonas aeruginosa LecA", *Angew. Chem.* (2025), article no. e202508864. (in press).

[58] A. Bernardi, J. Jiménez-Barbero, A. Casnati, et al., "Multivalent glycoconjugates as anti-pathogenic agents", *Chem. Soc. Rev.* **42** (2013), pp. 4709–4727.

[59] S. Cecioni, A. Imberty and S. Vidal, "Glycomimetics versus multivalent glycoconjugates for the design of high affinity lectin ligands", *Chem. Rev.* **115** (2015), no. 1, pp. 525–561.

[60] K. Wojtczak and J. P. Byrne, "Structural considerations for building synthetic glycoconjugates as inhibitors for Pseudomonas aeruginosa lectins", *ChemMedChem* **17** (2022), no. 12, article no. e202200081.

[61] A. Novoa, T. Eierhoff, J. Topin, A. Varrot, S. Barluenga, A. Imberty, W. Römer and N. Winssinger, "Novel LecA ligand identified from glycan array inhibits host cell invasion by *Pseudomonas aeruginosa*", *Angew. Chem. Int. Ed.* **53** (2014), pp. 8885–8889.

[62] R. Visini, X. Jin, M. Bergmann, et al., "Structural insight into multivalent galactoside binding to Pseudomonas aeruginosa lectin LecA", *ACS Chem. Biol.* **10** (2015), no. 11, pp. 2455–2462.

[63] D. Goyard, V. Baldoneschi, A. Varrot, M. Fiore, A. Imberty, B. Richichi, O. Renaudet and C. Nativi, "Multivalent glycomimetics with affinity and selecivity towards fucose-binding receptors from emerging pathogens", *Bioconjug. Chem.* **29** (2018), pp. 83–88.

[64] T. Machida, A. Novoa, É. Gillon, et al., "Dynamic cooperative glycan assembly blocks binding of bacterial lectins to epithelial cells", *Angew. Chem. Int. Ed.* **56** (2017), pp. 6762–6766.

[65] T. Klein, D. Abgottspon, M. Wittwer, et al., "FimH antagonists for the oral treatment of urinary tract infections: from design and synthesis to in vitro and in vivo evaluation", *J. Med. Chem.* **53** (2010), no. 24, pp. 8627–8641.

[66] F. Lisacek, B. Schnider and A. Imberty, "Tools for structural lectinomics: from structures to lectomes", *BBA Adv.* **7** (2025), article no. 100154.

[67] F. Bonnardel, J. Mariethoz, S. Perez, A. Imberty and F. Lisacek, "LectomeXplore, an update of UniLectin for the discovery of carbohydrate-binding proteins based on a new lectin classification", *Nucleic Acids Res.* **49** (2021), no. D1, pp. D1548–D1554.

ACADÉMIE DES SCIENCES
INSTITUT DE FRANCE

Comptes Rendus. Chimie
2025, Vol. 28, p. 849-871
https://doi.org/10.5802/crchim.423

Account

Shaping the 3D architecture of [2.2]paracyclophanes: from selective functionalization to functional luminophores

Laurent Micouin [a] **and Erica Benedetti** [*, a]

[a] Université Paris Cité, CNRS, Laboratoire de Chimie et de Biochimie Pharmacologiques et Toxicologiques, F-75006 Paris, France

E-mails: laurent.micouin@u-paris.fr (L. Micouin), erica.benedetti@u-paris.fr (E. Benedetti)

Abstract. Over the past few years, [2.2]paracyclophanes (pCps) have attracted considerable attention due to their unique three-dimensional structure and distinctive electronic properties. In this account, we explore various strategies for selective modification of these molecules, with a particular focus on controlling their planar chirality and tuning their photophysical behavior. The versatility of pCps is further illustrated through their broad scope of applications, spanning the development of organic and organometallic luminophores, advances in photocatalysis, and contributions to biochemical research. These diverse applications underscore the strong potential of pCps as key platforms for the design of innovative molecular systems.

Keywords. [2.2]Paracyclophanes, Planar chirality, 3D luminophores, Organic photocatalysts, RNA ligands.

Funding. CNRS, Paris Cité University (IdEx Dynamique Recherche pCp-Photocat - ANR-18-IDEX-0001), Agence Nationale de la Recherche (ANR JCJC PhotoChiraPhane - ANR-19-CE07-0001-01).

Note. Article submitted by invitation.

Manuscript received 11 July 2025, revised 16 July 2025, accepted 12 September 2025.

1. Introduction

[2.2]Paracyclophane (pCp) is the smallest known member of the [n.n]cyclophane family. This molecule was serendipitously discovered and first isolated in 1949 by Brown and Farthing as an unexpected byproduct of the gas-phase pyrolysis of *para*-xylene [1]. X-ray diffraction analysis revealed that pCp consists of two benzene rings, commonly referred to as decks, arranged in a cofacial orientation and connected at the *para* positions by two ethylene bridges [2]. This molecular architecture forces the decks into an unusual boat-like conformation (Figure 1), in which the bridgehead carbon atoms are displaced out of the plane defined by the remaining trigonal carbon atoms. Consequently, the distance between the carbon atoms bearing the ethylene bridges is shorter than the overall inter-ring separation (2.78 Å versus 3.09 Å, respectively, Figure 1).

These structural characteristics have a significant impact on the electronic distribution and chemical reactivity of the molecule, positioning pCp as a valuable scaffold for the design of novel aromatic compounds with a distinctive three-dimensional framework. Accordingly, significant research efforts have been dedicated to the synthesis and functionalization of pCp, as well as the modulation of its physicochemical properties and the exploration of its potential across various scientific domains [3].

* Corresponding author

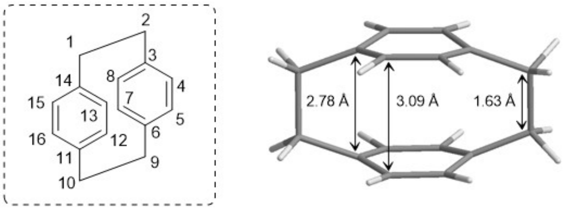

Figure 1. Structure of [2.2]paracyclophane (pCp).

In this account, we report our contributions to the chemistry of pCps, at first by placing our research in its broader context and outlining the strategies that we have developed to selectively functionalize the aromatic rings of commercially available pCp. Our methods for controlling the planar chirality inherent to these unique systems are then discussed. Finally, the synthesis of novel families of three-dimensional luminophores derived from pCp is described, and their applications across different research areas are discussed, including photocatalysis, coordination chemistry, and chemical biology.

2. Tailoring the aromatic decks of [2.2]paracyclophane

Since its discovery, numerous synthetic strategies have been developed to try and access pCp in an efficient manner. In addition to the industrial synthesis, which relies on the Hofmann elimination of *p*-methylbenzyl trimethylammonium hydroxide [4], the method reported by Brink in 1975 remains the most widely adopted and highest-yielding approach at the laboratory scale [5]. This approach involves the coupling of 1,4-bis(bromomethyl)benzene **1** with 1,4-bis(mercaptomethyl)-benzene **2** to produce dithia[3.3]paracyclophane **3**, followed by photochemical desulfurization to yield pCp in 51% overall yield (Scheme 1). This robust and reliable method has since enabled the synthesis of a broad range of pCp derivatives [6–8].

[2.2]Paracyclophanes are remarkably stable toward acids, bases, oxidants, or light, and retain their structural integrity up to 200 °C. Above this temperature, homolytic cleavage of the ethylene bridges occurs, leading to ring opening of the pCp core. This thermal behavior has been widely exploited in materials science, particularly for polymer production via chemical vapor deposition (CVD) processes [9–12]. For example, unsubstituted pCp is a key precursor in the synthesis of parylene (Scheme 1) [13], an aromatic polymer extensively used as a protective coating in electronics, optics, and biomedical devices.

Owing to its widespread industrial applications, pCp is now commercially available at low cost. As a result, functionalized pCp derivatives are nowadays most easily prepared via direct functionalization of the parent compound, rather than through de novo synthesis of substituted analogues.

Each aromatic ring of the pCp scaffold offers four accessible positions, allowing up to eight possible sites for derivatization. Monofunctionalization is typically achieved through electrophilic aromatic substitution, enabling the introduction of diverse functions such as bromine atoms, formyl, nitro, or ester motifs. Alternatively, halogen–lithium exchange from brominated precursors followed by trapping with suitable electrophiles allows the incorporation of a broader array of functional groups, including amines, hydroxyls, azides, thiols, carboxylic acids, and phosphines [14]. More recently, direct C–H activation strategies have also emerged as effective tools for regioselective modification of the pCp core [15].

From monosubstituted intermediates, various disubstituted pCps can be easily prepared (Figure 2). These are typically classified according to their substitution pattern: *ortho*, *meta*, or *para* when both substituents are on the same aromatic ring; and *pseudo-gem*, *pseudo-ortho*, *pseudo-meta*, or *pseudo-para* when the substituents are located on both decks.

Higher substituted derivatives (tri- and tetrafunctionalized pCps) are generally synthesized via sequential electrophilic substitutions on di-substituted precursors [16]. However, systems bearing more than four substituents are highly strained and remain uncommon in the literature [17].

In certain cases, the reactivity of the aromatic units in pCps can pose notable synthetic challenges due to through-space electronic delocalization between the closely positioned π systems. Interestingly, reactivity patterns resembling those of isolated double bonds have been observed in some cases [18,19]. Moreover, the introduction of substituents on one deck can significantly influence the electronic distribution across the molecule, thereby activating or deactivating specific positions on the

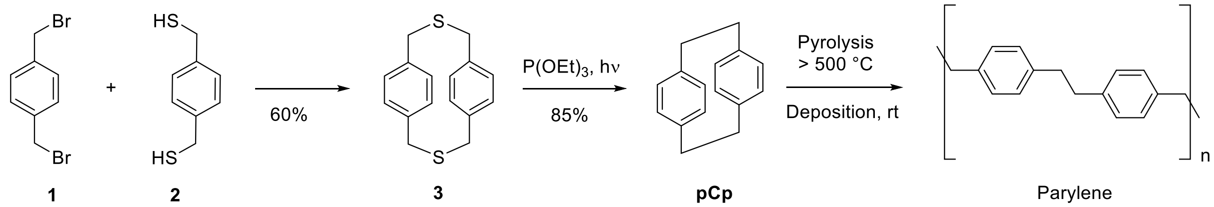

Scheme 1. Synthesis and polymerization of [2.2]paracyclophane.

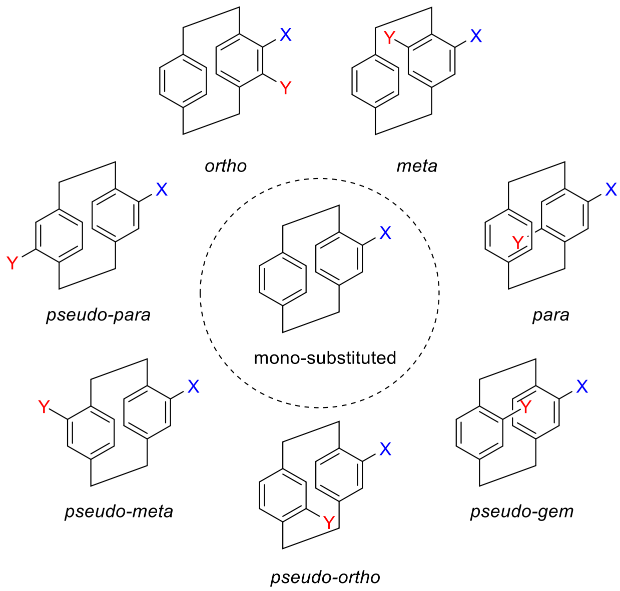

Figure 2. Substitution patterns and nomenclature of pCps.

opposite ring. For example, the introduction of electron-withdrawing groups can direct selective functionalization to the *pseudo-geminal* position, an effect well known and extensively exploited in [2.2]paracyclophane chemistry [20,21].

Despite significant progress, the selective introduction of multiple substituents onto a single aromatic ring of pCp remains a synthetic challenge. In our studies, we have developed an efficient and regioselective approach for synthesizing *para*-disubstituted pCps in a limited number of steps and with good overall yields. This strategy relies on a Vilsmeier–Haack formylation of various 4-amino[2.2]paracyclophane derivatives (**4**, Table 1), enabling the installation of a formyl group opposite to the existing electron-donating substituent.

The transformation is performed using $POCl_3$ (1 equiv.) in the presence of DMF, with the reaction mixture gradually heated from 0 to 100 °C over 3 h. These conditions exhibit broad substrate tolerance, accommodating tertiary and secondary amines bearing alkyl, allyl, or benzyl substituents on the nitrogen atom, as well as derivatives featuring mildly electron-withdrawing groups, such as a 9-fluorenylmethyloxycarbonyl (Fmoc) motif (Table 1). This method provides access to a range of functionalized aldehydes in a practical and scalable manner, generating versatile intermediates for the construction of more elaborate molecular architectures based on the pCp core [22], as detailed in the following sections of this account.

3. Controlling planar chirality in [2.2]paracyclophanes

Extensive efforts have been devoted to the investigation and rationalization of the geometry of pCps.

Table 1. Para-formylation of 4-amino[2.2]paracyclophanes

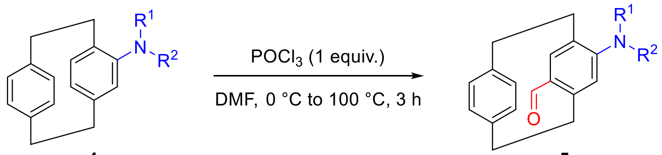

4 5

Entry	Product	R^1	R^2	Yield (%)
1	**5a**	Me	Me	90
2	**5b**	Bn	Bn	77
3	**5c**	H	Bn	72
4	**5d**	Allyl	Allyl	50
5	**5e**	H	Fmoc	42

For many years, it was believed that the unsubstituted pCp adopted a fully eclipsed conformation with D_{2h} symmetry. However, subsequent experimental and theoretical studies have shown that, at very low temperatures, the molecule favors a staggered conformation with D_2 symmetry, characterized by a torsional angle between 6 and 9°. As a result, the D_{2h} structure is now considered as a transition state between two enantiomeric D_2 conformers (Figure 3). Despite this, the unsubstituted pCp remains achiral at room temperature due to the rapid interconversion between its enantiomeric conformations [23–25].

Substituted pCps can exhibit planar chirality due to their rigid, strained structure, which prevents rotation of the aryl groups around their axes. Monosubstituted pCps are inherently nonsymmetrical, but disubstituted derivatives may or may not be chiral, depending on the nature and position of their substituents (Figure 3). Indeed, *ortho*, *meta*, *pseudo-gem*, and *pseudo-para* derivatives are achiral when both substituents are identical.

On the contrary, *para*, *pseudo-ortho*, and *pseudo-meta* pCps display planar chirality even when bearing the same substituents. A similar trend is observed for *tetra*-substituted derivatives (Figure 3) [14].

To assign the absolute configuration of pCps, specific Cahn–Ingold–Prelog rules (CIP conventions) [26] must be followed. The less substituted aromatic ring of the pCp core is positioned toward the front of the molecule, and the priority atom is identified as the carbon of the ethylene bridge bonded to the aromatic ring at the position nearest the highest-priority substituent. The configuration is assigned by numbering the ring carbons beginning at the priority atom, moving sequentially toward the highest priority substituent, and including the aromatic quaternary carbon attached to the ethylene bridge. The direction of numbering (clockwise or counterclockwise) determines the R_p or S_p configuration, respectively (Figure 3).

Planar chirality in pCps was first identified by Gram and Allinger in 1955 [27]. Early research in this domain focused on synthesizing monosubstituted pCps and determining their absolute configuration. Since the 1990s, chiral pCps have become valuable ligands in asymmetric catalysis [28] and, more recently, key components in the development of circularly polarized light-emitting materials [29,30]. However, large-scale synthesis of polysubstituted pCps with controlled chirality remains a significant challenge, which still considerably limits their broader applications.

The synthesis of structurally complex enantiopure pCps typically involves the functionalization of simpler optically active intermediates. Over the years, various strategies have been developed to obtain such compounds in an efficient manner. Techniques like high-performance liquid chromatography (HPLC) on chiral stationary phases are commonly used for enantiomer separation, although they require costly equipment and large volumes of solvents. Classical resolution methods, which rely on forming diastereoisomeric products using stoichiometric amounts of chiral resolving agents, are also frequently employed to generate enantioenriched pCps. However, these approaches often involve multi-step syntheses (i.e., formation of

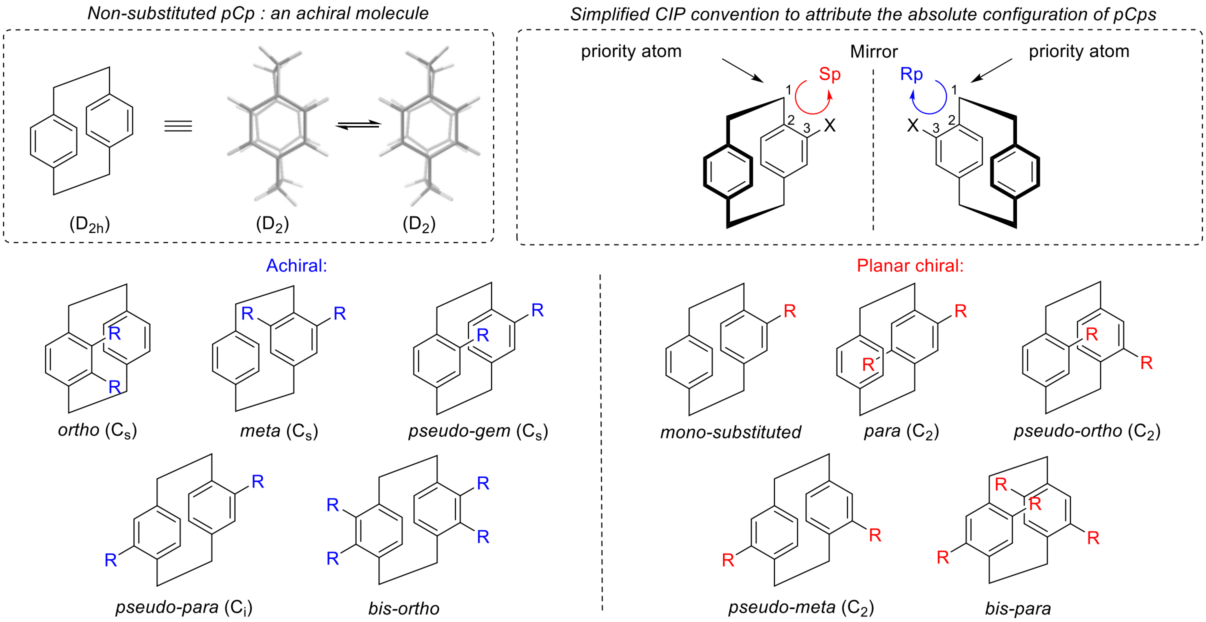

Figure 3. Achiral and planar chiral pCps.

the diastereomers, separation, and regeneration of the initial pCps), which are time-consuming [31].

In our studies, we have investigated kinetic resolution and desymmetrization strategies as effective alternatives to traditional methods for accessing optically active pCps. Kinetic resolution (KR) constitutes a powerful approach wherein racemates undergo asymmetric transformations in the presence of a chiral catalyst, with the two enantiomers reacting at different rates. Ideally, at 50% conversion, one enantiomer is recovered as unreacted starting material, while the other one is obtained as the product. In contrast, desymmetrization of *meso* derivatives enables the generation of enantiopure compounds under similar catalytic conditions in yields up to 100%, by differentiating prochiral sites within an achiral molecule.

Starting from racemic aldehydes or centrosymmetric *meso* dialdehydes derived from pCp, we employed asymmetric transfer hydrogenations (ATH) as key transformations to control planar chirality [16,32,33]. After optimizing the reaction conditions, enantioselective reductions were successfully carried out using the commercially available Noyori's catalyst RuCl(p-cymene)[(R,R)-TsDPEN] ((R,R)-**Cat**, 1 mol%) in a 1:1 iPrOH/DMF mixture at 0 °C, with t-BuOK (5 mol%) as the base. These reactions, which are operationally simple and easy to implement, delivered a wide range of optically active products in short times (Scheme 2).

The resulting molecules possess diverse substituents, including carbonyl or hydroxyl groups, and halogen atoms, on each aromatic ring of the pCp core, thereby enabling further functionalization through a variety of orthogonal transformations such as condensations, nucleophilic substitutions, Grignard additions, transition-metal-catalyzed couplings, and olefination reactions. Enantiopure pCp-based aldehydes are thus now routinely prepared in our laboratory on multigram scales, serving as valuable key intermediates.

Notably, following our work, there has been a renewed interest in controlling the planar chirality of [2.2]paracyclophanes through catalytic chemical methods, resulting in a number of compelling contributions to the field [34–38]. Among the various strategies developed in this area, our approach has proven both viable and competitive, and it has been successfully employed by other research teams worldwide [39].

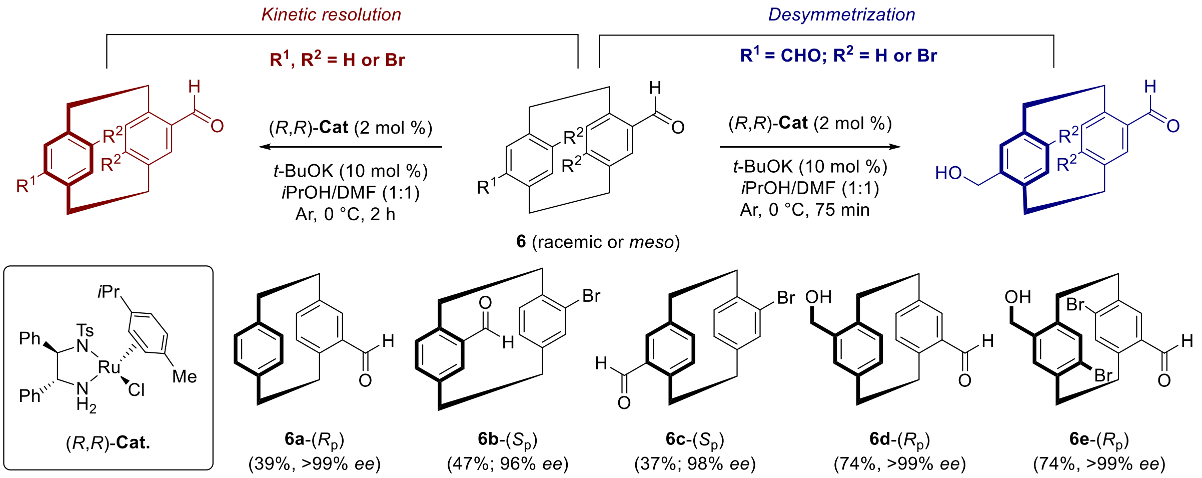

Scheme 2. Kinetic resolution and desymmetrization of aldehydes derived from [2.2]paracyclophanes.

4. Modulating the photophysical properties of [2.2]paracyclophanes

[2.2]Paracyclophanes are known to exhibit unique photophysical properties arising from electronic conjugation between their two aromatic rings, aided by both through-bond and through-space interactions. Indeed, unsubstituted pCp displays a distinctive UV–visible absorption spectrum, characterized by maxima at 225, 244, 286, and 302 nm [40,41]. The absorption band at the longest wavelength, commonly referred to as the cyclophane band, emerges in a spectral region that is atypical for standard benzene derivatives, such as xylenes. Furthermore, the molecule exhibits a broad fluorescence emission band centered around 356 nm. These characteristics have led to the widespread use of pCp as a core structure in the design of three-dimensional organic luminophores.

Pioneering studies have focused on the development of various systems that mimic excimers, transient dimers typically observed via fluorescence spectroscopy. In contrast to true excimers, which exist solely in the excited state, pCp-based analogues are stable in the ground state, making them particularly well-suited as model compounds for photophysical investigations. Notably, a variety of stilbene dimers incorporating the pCp scaffold have been isolated and thoroughly characterized [42–44]. Furthermore, di- and tetrasubstituted pCp derivatives bearing both electron-donating and electron-withdrawing groups have been designed to probe through-space charge-transfer delocalization [45]. All these systems offer valuable insight into electronic communication between stacked aromatic units within the distinctive three-dimensional architecture of the pCp framework.

More recently, numerous studies have demonstrated that the synergistic interplay between planar chirality and the distinctive spectroscopic behavior of pCps can be effectively exploited for the development of advanced circularly polarized luminescence (CPL) emitters. Research on CPL active compounds has gained momentum, driven by their promising applications in advanced optoelectronic technologies, such as 3D displays, optical data storage, and bioimaging [46]. Nevertheless, the rational design of organic luminophores that combine high emission efficiency with strong chiroptical activity remains a major challenge, spurring ongoing innovation in molecular engineering.

In this context, helicene-like structures featuring a pCp core have been synthesized and extensively investigated for their CPL properties [47]. Additionally, a variety of second-order molecular architectures, such as V-, N-, M-, triangle-, propeller-, and X-shaped frameworks, have been constructed from pCp units [48–55]. These structurally complex compounds exhibit remarkable optical properties, including high molar extinction coefficients (ε), strong fluorescence with significant quantum yields (Φ), and impressive dissymmetry factors [56]

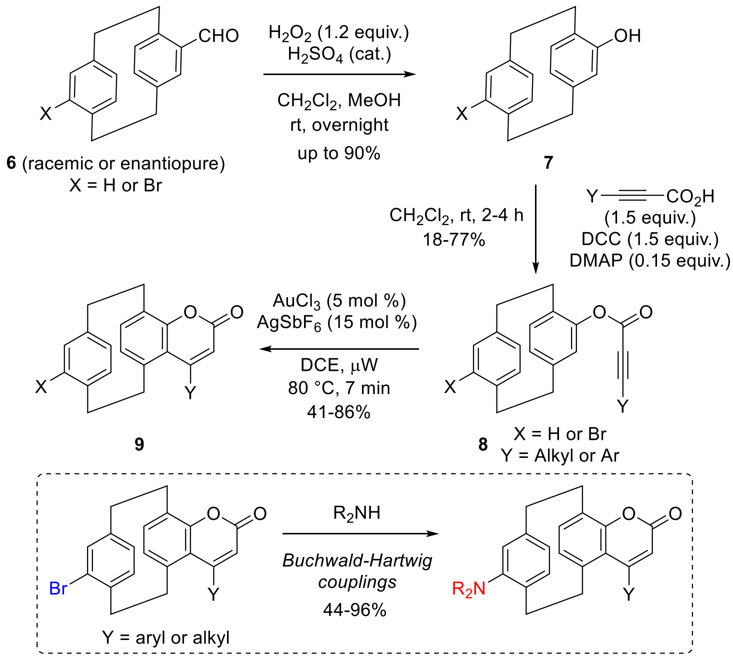

Scheme 3. Synthesis of pCp-based 3D coumarins.

in both absorption (g_{abs}) and emission (g_{lum}). Such attributes render them promising candidates for the development of advanced functional materials in the field of chiral photonics.

As a complementary strategy to modulate the (chir)optical properties of pCps we explored the possibility of expanding the pCp aromatic framework to access functionalized polycyclic (hetero)aromatic derivatives—three-dimensional analogues of classical aromatic dyes such as naphthalenes, coumarins, and cyanines [57]. This approach has led to the development of chiral luminophores with more compact molecular structures and enhanced solubility, offering key advantages for solution-phase applications, including asymmetric catalysis, supramolecular recognition, and chiral sensing in complex environments.

All the new families of 3D luminescent compounds that we developed [57] were synthesized in just a few steps, starting from aldehyde intermediates, the chirality of which can be easily controlled using the methods described earlier in this article. For example, three-dimensional coumarin dyes were synthesized in three steps, beginning with Dakin oxidation, conducted using H_2O_2 and catalytic amount of H_2SO_4 in a CH_2Cl_2/MeOH mixture, to form 4-hydroxy[2.2]paracyclophanes **7** in up to 90% yield. These molecules were then esterified with various propiolic acid derivatives under classical conditions (DCC and DMAP cat. in CH_2Cl_2). The resulting esters **8** were subjected to cyclization promoted by gold- and silver-based catalysts in 1,2-dichloroethane under microwave irradiation at 80 °C, yielding the desired coumarin core **9** (Scheme 3). In a final diversification step, starting from brominated compounds, Buchwald–Hartwig couplings were employed to introduce electron-donating amino groups on the pCp scaffold [58].

The impact of the pCp motif and its characteristic "phane" interactions on the spectroscopic properties of the synthesized coumarins was investigated using unpolarized UV–visible absorption and fluorescence spectroscopy. Overall, the three-dimensional dyes exhibited bathochromic shifts in both absorption and emission spectra compared to analogous planar structures (Table 2). Interestingly, the absorption maxima of the pCp-based coumarins remain hypsochromically shifted relative to those of planar commercial dyes such as **coumarin 6**, which possess a strong intramolecular charge-transfer character (Table 2). The luminescence properties of the 3D coumarins, which spanned the blue-to-green

Table 2. Spectroscopic properties of pCp-based coumarins and flat analogues

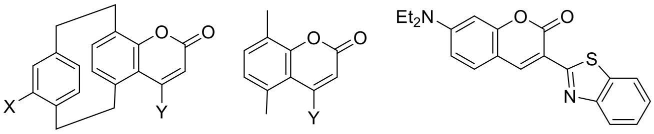

9a-o 10a,b coumarin 6

Entry	Compound	X, Y	λ_{max}^{abs} (nm)	λ_{max}^{em} (nm)[d]
1[a]	**9a**	H, Ph	265, 300, 330	460
2[a]	**9b**	H, Me	301, 319	435
3[a]	**9c**	H, *i*Pr	300, 320	432
4[a]	**9d**	H, H	304, 320	445
5[a]	**9e**	Br, Ph	307, 325	450
6[a]	**9f**	Br, Me	306, 320	425
7[a]	**9g**	H, *p*-MePh	315	455
8[a]	**9h**	H, *p*-OMePh	300, 330	455
9[a]	**9i**	H, *p*-ClPh,	288, 310, 335	465
10[a]	**9j**	H, *p*-OTfPh,	280, 330	470
11[a]	**9k**	H, *p*-CF_3Ph	270, 335	475
12[a]	**9l**	NHBoc, Ph	317	450
13[a]	**9m**	NH_2, Ph	300, 330	560
14[a]	**9n**	H, *p*-NHBocPh	317	450
15[a]	**9o**	H, *p*-NH_2Ph	330	470
16[b]	**10a**	-, Ph	294	418
17[b]	**10b**	-, Me	286	413
18[c]	**Coumarin 6**	-,-	455	498

[a] 10^{-4} M solution in 1,2-dichloroethane. [b] 10^{-5} M solution in 1,2-dichloroethane. [c] 10^{-5} M solution in CH_2Cl_2. [d] No significant effects were observed on the emission spectra while changing the excitation wavelength or the concentration of the samples.

region of the electromagnetic spectrum, were significantly influenced by the substitution pattern on the out-of-plane aromatic ring of the pCp core. In particular, the introduction of halogen atoms induced hypsochromic shifts in the emission profiles compared to their unsubstituted counterparts (Table 2, entries 5 and 6 versus entries 1 and 2). Conversely, amino-substituted derivatives bearing electron-donating groups exhibited pronounced bathochromic shifts in their emission maxima (Table 2, entry 13 versus entry 1), highlighting the effective modulation of luminescent properties through electronic effects. These findings clearly demonstrate that precise control over the photophysical behavior of these compounds can be achieved by modulating both the nature and spatial arrangement of substituents around the three-dimensional pCp framework.

All pCp-based coumarins demonstrated notable photostability, along with exceptionally larger Stokes shifts (reaching up to 43 478 cm^{-1}) in comparison with their flat analogues. However, these dyes generally exhibited modest fluorescence quantum yields ($0.1\% < \Phi < 5\%$).

In collaboration with Dr. J. Crassous's group, we carried out the chiroptical characterization of enantiopure planar chiral coumarins obtained from optically active aldehyde precursors [58]. As expected, electronic circular dichroism (ECD) spectra recorded in CH_2Cl_2 (10^{-5} M) displayed well-defined

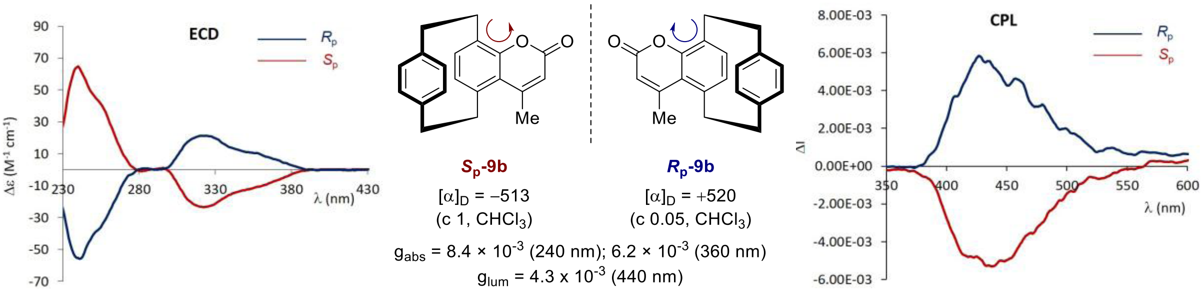

Figure 4. Chiroptical properties of pCp-based coumarins S_p-**9b** and R_p-**9b**. ECD and CPL spectra were recorded in CH_2Cl_2 (10^{-5} M, λ_{ex} = 320 nm).

mirror-image signatures for the two enantiomers of compound **9b** (Figure 4), with the S_p enantiomer exhibiting a strong positive Cotton effect at 240 nm ($\Delta\varepsilon$ = +64 $M^{-1}\cdot cm^{-1}$) and a weaker negative one at 320 nm ($\Delta\varepsilon$ = −23 $M^{-1}\cdot cm^{-1}$). Complementary CPL measurements under identical conditions (λ_{ex} = 330 nm) further revealed mirror-image emission profiles, consistent with their enantiomeric nature (Figure 4). Overall, the pCp-based coumarin derivatives showed promising chiroptical responses, with dissymmetry factors of $g_{abs} \approx 6.2 \times 10^{-3}$ at 360 nm and $g_{lum} \approx 4.0 \times 10^{-3}$ at 440 nm. These values are especially noteworthy given the compact and rigid nature of the molecular framework in contrast to the previously reported systems based on extended π-conjugation. Additionally, the g_{lum}/g_{abs} ratio of ~0.7 suggests minimal structural reorganization upon excitation, an advantageous feature for preserving chiroptical integrity in emissive applications.

Three-dimensional cyanine-type dyes based on the pCp scaffold were also readily prepared from aldehyde intermediates, particularly those obtained via the regioselective formylation strategy outlined in Table 1. In this case, key aldehyde **5a**, bearing a dimethylamino group, underwent a Wittig-type reaction with compound **11**, followed by *N*-methylation of its benzothiazole moiety. This sequence efficiently led to the formation of novel luminescent compound **12**, which exhibited emission in the red region of the electromagnetic spectrum (Scheme 4). Once again, both racemic and enantiopure products could be synthesized using the strategies developed in our laboratory [59].

The photophysical properties of three-dimensional cyanine dye **12** were investigated in both dichloromethane and an aqueous Tris-EDTA (TE) buffer, the latter containing 1% DMSO to ensure full solubilization of the organic compound. When comparing the two environments, a modest hypsochromic shift in both absorption and emission maxima was observed upon transitioning from the organic to the aqueous medium (Table 3). Additionally, both the molar extinction coefficient and fluorescence quantum yield were reduced in the TE buffer, indicating diminished brightness in the aqueous phase.

Compared to its flat analogue **13** [60], pCp-based cyanine **12** exhibited significantly red-shifted absorption and emission spectra in both organic and aqueous media (Table 3). This pronounced bathochromic shift aligns with observations made for other pCp-derived fluorophores, including the coumarin chromophores discussed earlier. This effect is attributed to the presence of the second aromatic ring in the pCp scaffold, which serves as a mild electron-donating group, thereby modulating the global electronic properties of the dyes.

Overall, these results underscore the remarkable versatility of pCp-based three-dimensional luminophores. By tailoring the functionalization of the pCp core, we can precisely tune absorption and emission profiles to cover the entire visible spectrum and develop differently colored CPL emitters from enantiopure molecules [57]. The diverse families of compounds we have isolated hold promise for a wide range of applications in different domains, including coordination chemistry, photocatalysis, and the chemistry–biology interface. Their potential in these areas will be explored in greater detail in the following sections.

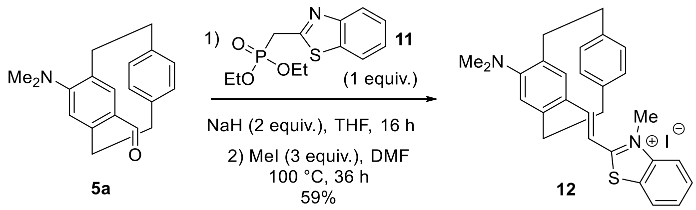

Scheme 4. Synthesis of a pCp-based 3D cyanine.

Table 3. Spectroscopic properties of cyanine dyes in different media

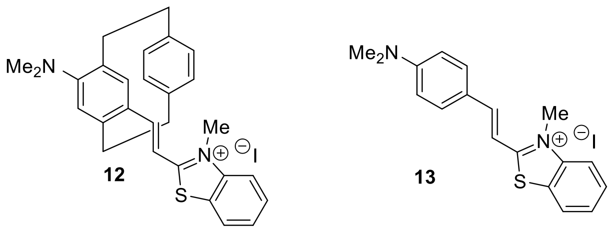

Dye[a]	Solvent	λ_{abs}^{max} (nm)	ε_{max} ($M^{-1}\cdot cm^{-1}$)	λ_{em}^{max} (nm)	Φ_f (%)[b]
12	CH_2Cl_2	597	46×10^3	645	2.0
	TE[c]	565	39×10^3	635	1.5
13	CH_2Cl_2	553	44×10^3	607	6.2
	TE[c]	510	36×10^3	600	1.3

[a] 10^{-5} M solution. [b] Absolute quantum yields. [c] 1% DMSO was added to fully solubilize the dyes.

5. Lanthanide luminescence sensitization using [2.2]paracyclophanes

In recent decades, the distinctive photophysical characteristics of lanthanide ions (Ln) have garnered considerable interest, owing to their sharp emission bands and prolonged luminescence lifetimes [61], which make them particularly attractive for imaging and photonic applications [62–64]. In addition, lanthanide-based organometallic complexes exhibit exceptional photostability, effectively addressing a major limitation of conventional organic fluorophores, namely, photobleaching under prolonged or intense light exposure. A key limitation, however, arises from the intrinsically low molar absorption coefficients of lanthanide cations ($\varepsilon < 1\ M^{-1}\cdot cm^{-1}$), which severely restricts their direct excitation. To circumvent this issue, the use of antenna ligands, chromophores capable of efficiently absorbing light and transferring the harvested energy to the lanthanide center, has become a widely adopted strategy for efficiently sensitizing lanthanide emission [65,66].

In this context, our group has investigated the potential of luminophores derived from pCp as antenna or ligands for lanthanide sensitization. While pCps have demonstrated significant utility in transition metal coordination chemistry [67], their application in lanthanide systems, either as antennas or as coordinating ligands, remains largely unexplored to date [68]. We thus identified a promising opportunity to expand the functional utility of pCp-based scaffolds by designing new Ln–pCp complexes with enhanced photophysical performance.

As part of this study, in collaboration with Dr. O. Maury's group (ENS Lyon), we successfully prepared a series of picolinate-based lanthanide complexes bearing pCp-derived coumarin antennas (Scheme 5) [69]. The synthesis of these molecular objects began with compound **15**, obtained from a 3D coumarin bearing a triple bond at its *pseudo-para*

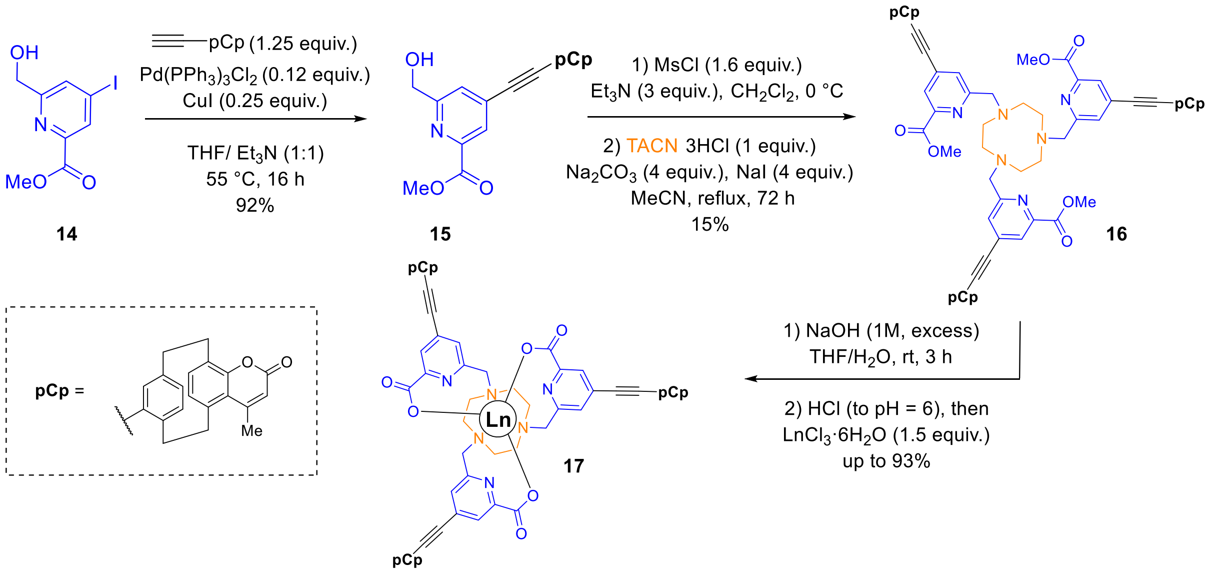

Scheme 5. Synthesis of Ln complexes incorporating pCp-based coumarins as antennas.

Table 4. Photophysical properties of Ln complexes **17a** and **17b**

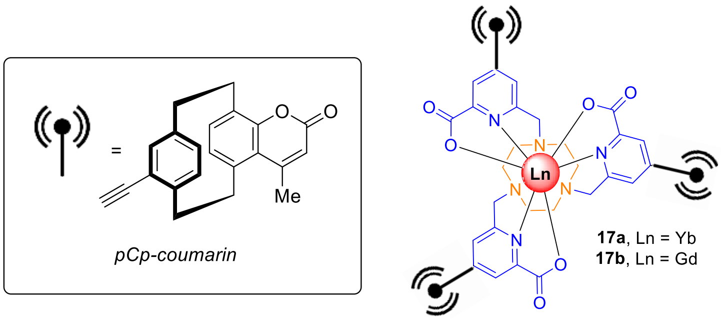

Ln	λ_{abs} (nm)[a]	ε ($L{\cdot}mol^{-1}{\cdot}cm^{-1}$)	λ_{em} (nm)[a]	τ_{obs} (μs)[a]	Φ[b]	Φ_{Δ}[c]
17a	332	48.5×10^3	980	9.48	<0.01	0.00
17b	332	61×10^3	422	-	<0.01	0.45

[a]Solution in CH_2Cl_2 (10^{-5} M); [b]fluorescence quantum yield; [c]quantum yield for singlet oxygen generation.

position, via a Sonogashira cross-coupling with iodopicolinic ester **14**. Following mesylation, the intermediate was coupled to 1,4,7-triazacyclononane (TACN), yielding target ligand **16** in 15% overall yield after purification by column chromatography. Complexation with lanthanide ions was then carried out via in-situ saponification, followed by the addition of the hydrated lanthanide chloride at pH 6 (Scheme 5).

Spectroscopic characterization revealed that the pCp–coumarin unit undergoes rapid intersystem crossing from the singlet to the triplet excited state [$E(T_1)$ = 19 500 cm^{-1}]. The triplet-state energy is well-matched for efficient energy transfer to Yb^{3+} and Gd^{3+} ions. This was confirmed by excitation of the antenna at 332 nm, which resulted in the characteristic near-infrared (NIR) luminescence of Yb^{3+} in complex **17a** (λ_{em} = 980 nm, Table 4, entry 1).

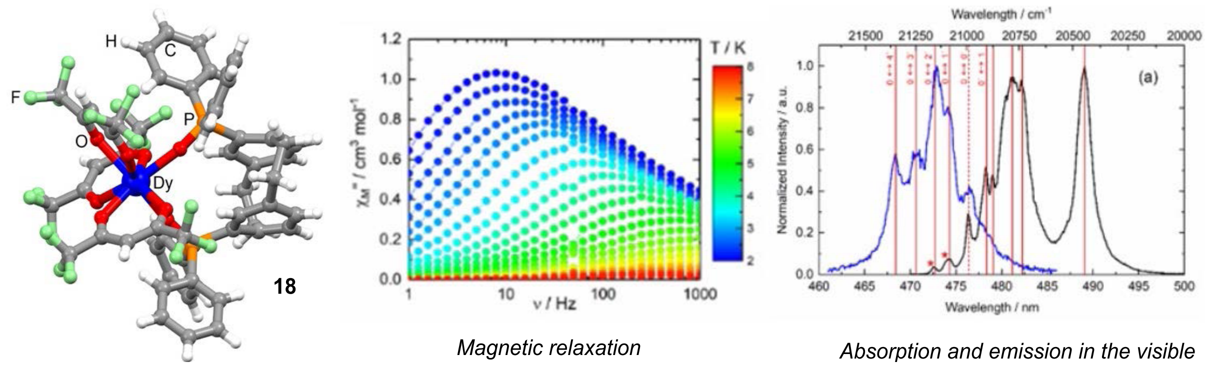

Figure 5. Luminescence and magnetic properties of a Dy(III) complex incorporating a pCp-based ligand.

Notably, under the same excitation conditions, Gd^{3+}-containing complex **17b** was found capable of generating a singlet oxygen, with a quantum yield of $\Phi_\Delta = 0.45$ (Table 4, entry 2) [69]. These findings highlight the potential of pCp-based architectures for the development of lanthanide complexes with tunable and multifunctional properties [70].

Lanthanide ions are currently the focus of extensive research in the field of molecular magnetism [71], as they are prime candidates for the design of single-molecule magnets (SMMs). Unlike traditional magnets, which consist of large assemblies of atoms, SMMs are composed of discrete mono-, di-, or polynuclear complexes capable of retaining magnetic information at low temperatures [72]. To fully harness the potential of SMMs for practical use, it is crucial to investigate their magnetic properties in relation to other physical characteristics, such as luminescence and chirality. This could pave the way for multifunctional materials in emerging technologies, such as: quantum computing, where the integration of stable magnetic states and optical properties could lead to more reliable qubits; molecular electronics, where combining magnetic and luminescent properties may improve device performance and enable further miniaturization; and high-density data storage, where the ability to manipulate and store information at the molecular level could transform data retention capabilities. In this context, luminescent SMMs based on lanthanide complexes, incorporating ligands with central, axial, or helical chirality, have been developed [73]. Embedding rare-earth ions within chiral organic frameworks facilitates chirality transfer from the ligand to the metal center, generating circular anisotropies at the lanthanide ion level. This can give rise to phenomena such as CPL and magnetochiral dichroism (MChD) [74]. Surprisingly, planar chiral ligands have yet to be utilized to modulate these intriguing properties in lanthanide complexes.

Recently, in collaboration with Dr. O. Maury (ENS Lyon) and Dr. F. Pointillart (Univ. Rennes 1), we employed racemic pCp-derived phosphine oxides as ligands to finely tune the crystal field and electronic environment surrounding Yb^{3+} and Dy^{3+} ions, thereby enabling the manifestation of slow magnetic relaxation (Figure 5). The synthesized complexes also exhibited distinct luminescence in the visible or NIR regions of the electromagnetic spectrum. A magneto-structural correlation between the emission and magnetic properties was established for these new complexes, thereby contributing to a deeper understanding of the interplay between these phenomena [75].

Our laboratory is currently exploring the use of enantiopure pCps as antennas or ligands for lanthanide ions, with the objective of developing novel multifunctional molecular systems that integrate luminescence, magnetism, and planar chirality.

6. [2.2]Paracyclophanes as building blocks for the design of organic photocatalysts

At the beginning of the last century, Ciamician recognized that visible light could serve as a renewable and cost-effective energy source for driving chemical reactions under mild and environmentally friendly conditions [76]. Since then, the fields of photochemistry and photocatalysis have unveiled numerous opportunities for reimagining established reactions and pioneering pathways to previously inaccessible products [77]. Over the years, a variety of highly performant photocatalytic systems have been developed, ranging from metal-based compounds such as ruthenium and iridium polypyridyl complexes to fully organic molecules like eosin Y or acridinium salts. Despite these inspiring advances, the quest continues for novel, more versatile molecules capable of promoting a broader range of catalytic photoreactions. Regardless of their intriguing photophysical properties and considerable potential, pCps had remained largely unexplored as catalysts in photochemical transformations until very recently [39].

As a proof of concept, and inspired by previous reports [78–80], our group demonstrated that pCp-based coumarins can serve as organic photocatalysts, effectively promoting desulfonylation reactions under light irradiation [81].

Starting from a readily accessible model substrate (**19a**, Table 5), prepared according to a reported procedure [78], coumarin derivative **9b** demonstrated effective photocatalytic activity for the reductive cleavage of the tosyl protecting group. Using a Hantzsch ester as the sacrificial electron donor, irradiation at 300 nm led to 65% conversion within 2 h (Table 5, entry 1). Prolonging the reaction time did not improve this outcome (Table 5, entry 2); however, catalyst loading could be reduced from 20 to 5 mol% without any loss in efficiency (Table 5, entries 3 and 4). A series of structurally related pCp-based coumarins was evaluated to probe structure–activity relationships. Interestingly, catalyst **9a** bearing aryl substituents proved significantly less effective (Table 5, entry 7), indicating that an alkyl group on the coumarin framework may be crucial for efficient photocatalysis in this case. Control experiments further confirmed the key roles of each component: no conversion was observed in the dark or in the absence of the Hantzsch ester (Table 5, entries 8 and 9), while reactions conducted without the pCp-coumarin—or with pCp-deprived analogue **10b**—resulted in only traces of conversion (Table 5, entries 10 and 11). These findings underscore the unique contribution of the pCp moiety to the activity of the photocatalyst. The presence of oxygen significantly suppressed the deprotection (Table 5, entry 12), and no conversion was observed when TEMPO, a well-established radical scavenger, was added to the reaction mixture (Table 5, entry 13). Alternative reducing agents were evaluated as well but did not exhibit performances comparable to the Hantzsch ester (Table 5, entries 14–16).

The scope of the reaction was subsequently examined using the conditions optimized on substrate **19a**, as illustrated in Scheme 6. The deprotection of a range of sulfonyl groups, including tosyl (Ts), phenylsulfonyl (SO_2Ph), and mesitylsulfonyl (SO_2Mes), was tested using 5 mol% of catalyst **9b**. In line with the reactivity observed for the Ts group, efficient removal of the phenylsulfonyl moiety afforded compound **20a³** in 59% yield. Conversely, sulfonamides bearing mesityl or mesyl groups proved unreactive under identical conditions, yielding only trace amounts of the desired product.

Substrates containing tosyl groups with a variety of functional motifs, such as substituted (hetero)arenes, alkyl chains, and a Boc-protected amine, were well tolerated, affording the corresponding products in good yields. The method also extended to sulfonamides incorporating alternative aroyl groups, although substrates bearing electron-donating substituents showed reduced efficiency (Scheme 6).

Notably, the protocol was compatible with stereochemically sensitive compounds. When enantiomerically enriched substrates were subjected to the reaction conditions, the corresponding products were obtained with full retention of enantiopurity. This indicates that the transformation proceeds without racemization, even in the presence of base-sensitive stereogenic centers (Scheme 6).

It is worth highlighting that the presence of an aroyl group on the sulfonamide was critical for successful cleavage. Substrates featuring alternative groups such as acetyl, Boc, or methyl failed to undergo transformation under the optimized conditions (Scheme 6).

To gain deeper insight into the mechanism of the photodesulfonylation promoted by pCp-based coumarins, we conducted a series of mechanistic studies. Computational analysis realized in collaboration with A. Maruani (LCBPT UPCité) revealed that energy transfer (EnT) from the excited state of catalyst **9b** to the lowest excited state of substrate **19a** is thermodynamically uphill (ΔG_{EnT} = +1.13 eV), rendering this pathway unlikely. Based on prior studies

Table 5. Optimization of the photodeprotection reaction

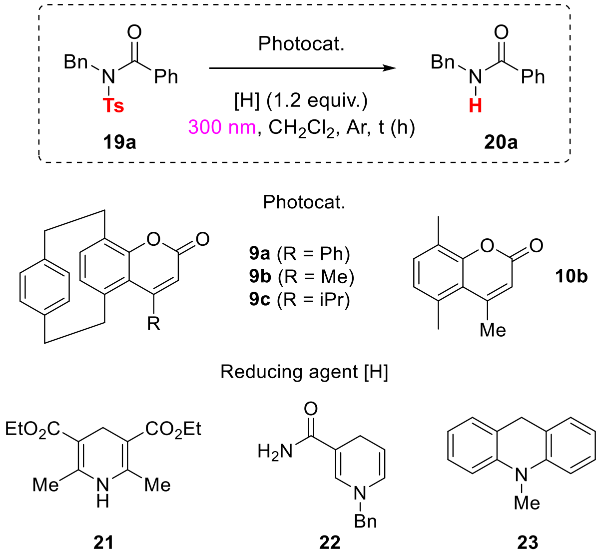

Entry	Photocat. (mol%)	[H]	t (h)	Conv. (%)[e]
1	**9b** (20)	**21**	2	66
2	**9b** (20)	**21**	16	71
3	**9b** (15)	**21**	2	63
4	**9b** (5)	**21**	2	65
5[a]	**9b** (5)	**21**	2	64
6	**9c** (5)	**21**	2	56
7	**9a** (5)	**21**	2	26
8[b]	**9b** (5)	**21**	2	-
9	**9b** (5)	-	2	-
10	-	**21**	2	9
11	**10b** (5)	**21**	2	14
12[c]	**9b** (5)	**21**	2	19
13[d]	**9b** (5)	**21**	2	-
14	**9b** (5)	**22**	2	-
15	**9b** (5)	**23**	2	-
16	**9b** (5)	n-Bu_4NBH_4	2	-

Reactions were performed in a Rayonet photochemical reactor equipped with eight 300 nm lamps (T = 29 °C, c = 0.05 M). [a]Reaction performed under more diluted conditions (c = 0.025 M); [b]reaction performed in dark (T = 25 °C, c = 0.05 M); [c]reaction performed under an oxygen atmosphere; [d]reaction performed in the presence of TEMPO (1 equiv.); [e]determined by ^{1}H NMR analysis.

involving an iridium-based photocatalyst combined with a Hantzsch ester [78], we hypothesized that the sulfonamide cleavage could proceed via a photoinduced electron transfer (ET) mechanism.

Electrochemical measurements of the redox potentials of **9b**, **19a**, and **21**, combined with the determination of the excited-state energy (E^*) of **9b** via absorption and fluorescence spectroscopy, enabled

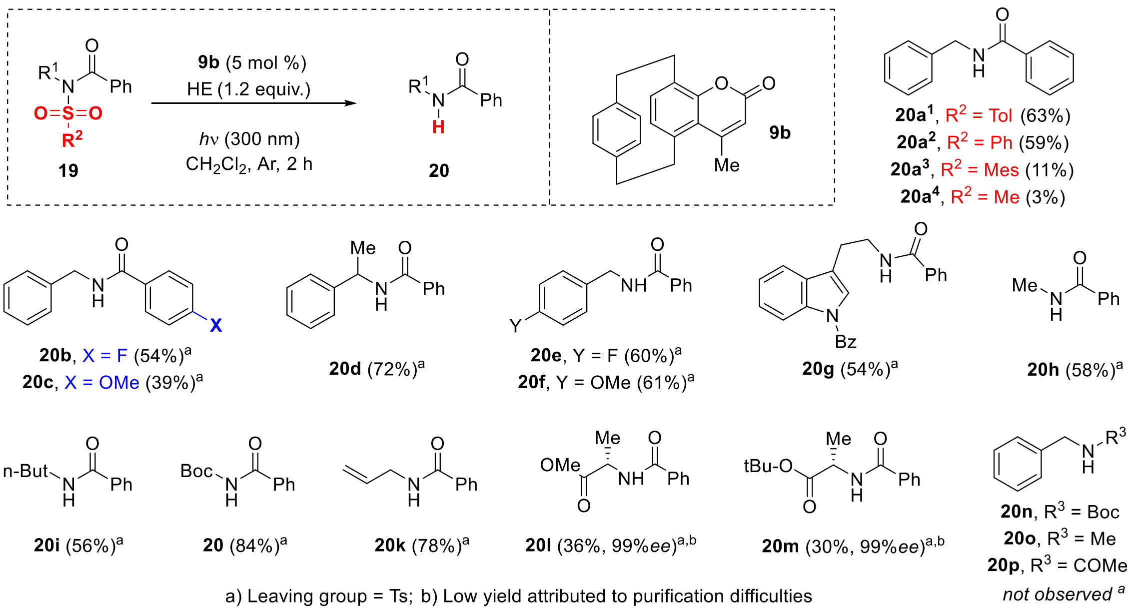

Scheme 6. Scope of the photodeprotection reaction.

the evaluation of the Gibbs free energy for potential photoinduced electron-transfer processes. According to this analysis, ET from the excited catalyst to the Hantzsch ester is thermodynamically favorable ($\Delta G_{ET} = -0.63$ eV). Conversely, direct ET from the excited state of **9b** to substrate **19a** is thermodynamically disfavored ($\Delta G_{ET} = +0.13$ eV). Furthermore, UV–Vis absorption studies excluded the formation of electron donor–acceptor (EDA) complexes, as no appreciable spectral changes were detected upon gradual addition of either **19a** or **21** to a solution of **9b**. Finally, the reaction was shown to halt immediately upon interruption of light irradiation, thereby excluding the involvement of a self-propagating radical chain process in the photocleavage mechanism.

Based on the collected experimental data, the photodesulfonylation was proposed to proceed via the mechanism illustrated in Scheme 7.

Upon irradiation at 300 nm, pCp-based catalyst **9b** is promoted to its excited state (**A**), which then undergoes a single-electron transfer (SET) with the Hantzsch ester. This step generates dihydropyridine radical cation **C** and coumarin-centered radical anion **B**. The radical anion subsequently interacts with the reaction substrate, forming radical intermediate **D** and regenerating the ground-state photocatalyst. Note that the formation of intermediate **D** aligns with analogous species previously identified in related electrochemical processes [82]. Radical **D** then undergoes homolytic cleavage of its N–S bond, yielding carboxamide anion **E** and aryl sulfonyl radical $ArSO_2^{\bullet}$. The final desulfonylated product is formed through quenching reactions between these species and dihydropyridine radical cation **C**. The proposed mechanistic pathway was further corroborated by theoretical calculations carried out in collaboration with A. Maruani (LCBPT UPCité).

Attaining precise control over chirality in photoinduced organic transformations remains one of the foremost challenges in the field of photocatalysis. While numerous reports have demonstrated satisfactory enantioselectivities using costly transition-metal-based catalysts [83], there is growing interest in metal-free strategies. These approaches often employ chiral organocatalysts that function dually as stereocontrolling agents and photosensitizers [84–86]. Despite these advances, examples of asymmetric photocatalytic reactions driven by such organocatalysts remain scarce [87]. Building on this background, our current research is focused on investigating enantiopure planar chiral pCp derivatives

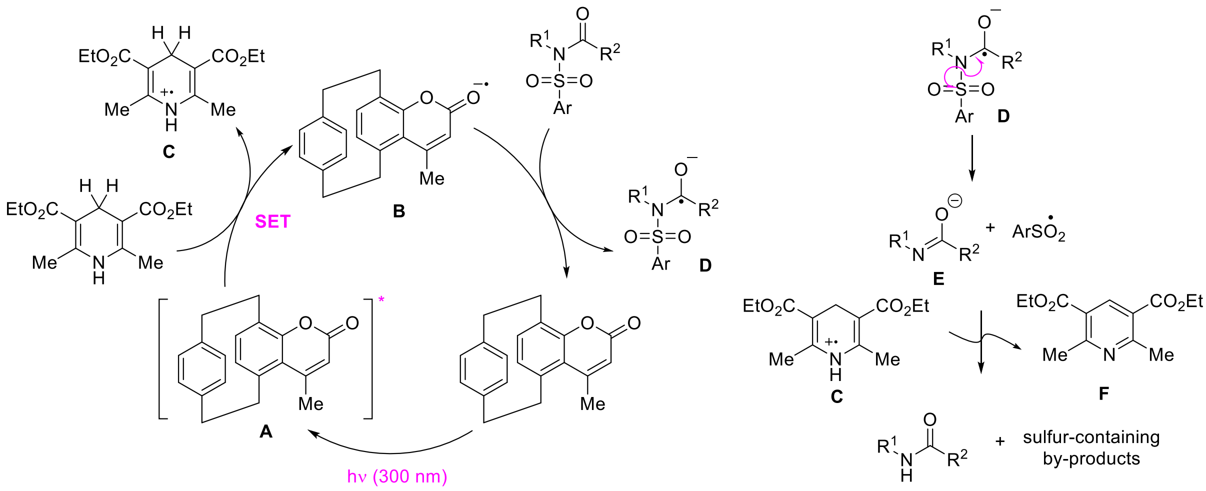

Scheme 7. Mechanistic proposal for the photodeprotection mediated by pCp-based coumarins.

as photocatalysts to promote asymmetric transformations, aiming to broaden the scope of light-driven enantioselective photocatalytic processes.

7. Developing RNA binders using [2.2]paracyclophane scaffolds

Ribonucleic acids (RNAs) are fundamental biomolecules involved in the regulation of a variety of different cellular processes, including, for instance, gene expression and protein synthesis [88]. Beyond their canonical roles, RNAs have increasingly been recognized as key actors in the onset and progression of various diseases, such as certain cancers, as well as genetic or neurodegenerative disorders [89,90]. Today, RNA is broadly recognized as a valuable therapeutic target. However, despite this acknowledged potential, developing small molecules that selectively bind to RNA and modulate its function remains a significant challenge in medicinal chemistry.

Most RNA-binding ligands identified to date are planar or rod-like molecules that may show strong binding affinity but often lack selectivity [91–95]. Their limited ability to distinguish between closely related RNA structures, or even between RNA and DNA, significantly restricts their therapeutic usefulness. Consequently, there is an increasing need to discover and develop novel molecular scaffolds that combine high specificity with strong binding to well-defined RNA targets.

Small molecules interact with nucleic acids through diverse binding modes. Cationic ligands primarily participate in electrostatic interactions with the negatively charged phosphodiester backbone, whereas flat aromatic compounds typically participate in π–π stacking interactions with nucleobases. These interactions can occur via intercalation between base pairs or by occupying the major and minor grooves of helical structures. However, these binding modes are intrinsically limited in selectivity and often fail to distinguish between RNA and DNA duplexes, owing to their similar base-pairing architectures.

To circumvent these limitations, recent studies have focused on incorporating non-planar aromatic motifs that exploit the inherent structural plasticity of RNA. Indeed, unlike DNA, RNA is predominantly found in cell as single-stranded sequences and capable of folding upon itself to generate complex secondary and tertiary architectures, including bulges, internal loops, pseudoknots, and three-way junctions. These unique structural features offer distinct molecular recognition sites for small molecules. For instance, spirocyclic compounds have demonstrated remarkable selectivity for bulged, non-canonical RNA regions (Scheme 8a) [96,97].

Similarly, triptycene-based ligands have been reported to specifically target three-way junctions (Scheme 8b) [98–100]. Notably, these last compounds exhibited potential as modulators of the

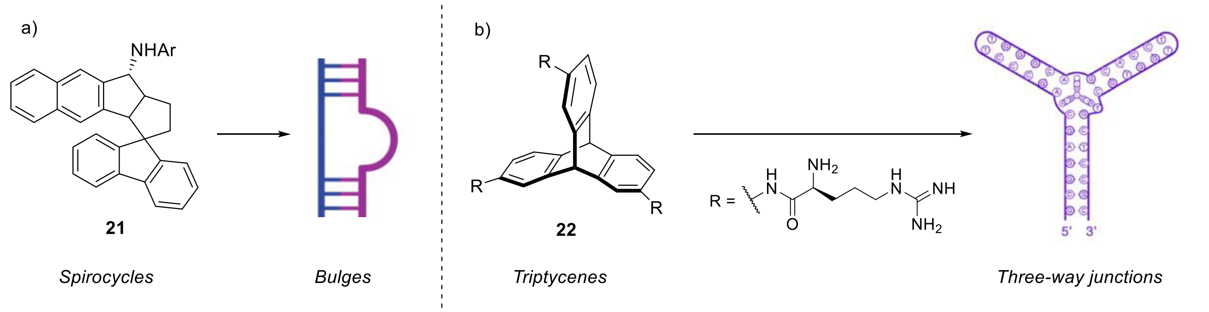

Scheme 8. Examples of three-dimensional ligands preferentially targeting non-paired RNA structures.

heat shock response in *E. coli*, highlighting their functional relevance as RNA-targeting agents. The non-planar architecture of these molecules, which arranges aromatic groups across orthogonal planes, appears to mitigate non-specific intercalation into double-helical regions. This spatial configuration enhances selectivity for non-duplex RNA motifs while minimizing off-target interactions with double-stranded DNA, thus overcoming a common limitation of planar aromatic RNA-binding compounds.

Inspired by these precedents, we hypothesized that pCps could preferentially drive recognition of non-helical RNA structural motifs. Indeed, their rigid and sterically demanding architecture, characterized by a 3.1 Å distance between the benzene moieties (Figure 1), does not match the helical rise per base pair in double-stranded RNA (2.6 Å) or DNA (3.4 Å), making intercalation unlikely and effectively limiting interactions with RNA or DNA duplexes (Figure 6).

Guided by this rationale, we explored pCp as a central core for the design of novel RNA-binding ligands. Simultaneously, we aimed to exploit the intrinsic photophysical properties of pCps to monitor ligand–RNA interactions via fluorescence spectroscopy, enabling real-time observation of binding events.

Cyanine dyes are well-established probes in chemical biology, frequently used for nucleic acid staining [60,101,102]. These dyes exhibit strong fluorescence turn-on behaviors upon target binding. We therefore set out to compare the luminescence responses of pCp-based cyanine dye **12** with those of analogous flat cyanine **13** in the presence of nucleic acids.

As described earlier in this article, both compounds exhibited low emission in aqueous buffer (Table 3). However, upon the addition of increasing amounts of tRNA, a significant fluorescence enhancement was observed for both cyanines, demonstrating that incorporation of the pCp moiety into the luminophore does not negatively impact the turn-on behavior of the cyanine (Figure 7) [59].

Digestion studies with RNase A confirmed that the observed fluorescence enhancement is attributable to the presence of RNA in solution [34]. Since cyanines are known to form aggregates [61]—a tendency also confirmed for pCp derivative **12**—, the observed turn-on responses were attributed to disaggregation processes triggered by the interaction of the dyes with RNA.

We next compared the behavior of the flat and three-dimensional cyanines in the presence of different types of nucleic acids. Interestingly, flat compound **13** exhibited comparable fluorescence turn-on responses with all tested nucleic acids (Figure 8, in red), indicating a non-selective interaction profile. In contrast, three-dimensional pCp-based derivative **12** displayed only modest fluorescence enhancements in the presence of double-stranded DNA or RNA (Figure 8, in blue), while it showed markedly stronger turn-on behaviors with nucleic acids containing multiple unpaired regions, with a clear preference for tRNA.

Fluorescence titrations performed with custom-designed hairpin loops of different sizes (**I**–**V**, Table 6) further demonstrated that pCp-based dye **12** interacts weakly with small loop structures, while exhibiting higher binding affinity—reflected by lower dissociation constants (K_d)—for larger loops. Remarkably, the dye showed a marked preference for a sequence containing eight unpaired nucleotides ($K_d \sim 0.54$ μM, Table 6). It is also worth noting that, at this

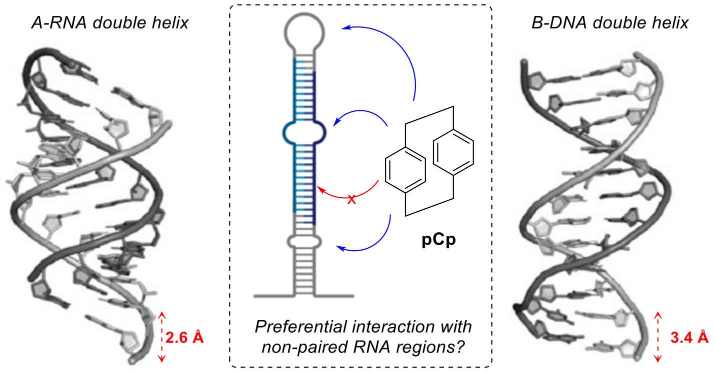

Figure 6. Rationale for targeting non-paired RNA motifs using pCp.

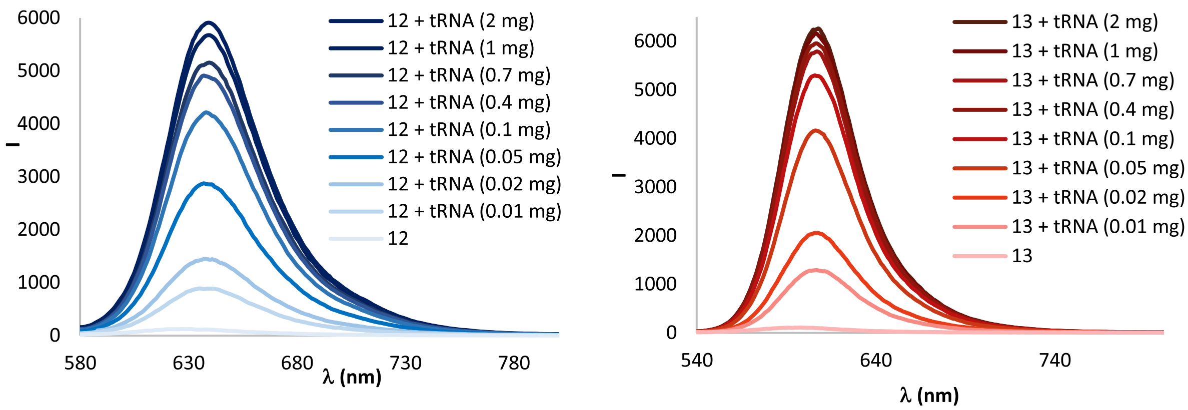

Figure 7. Turn-on fluorescence responses of cyanines **12** (in blue) and **13** (in red) in the presence of increasing amounts of tRNA.

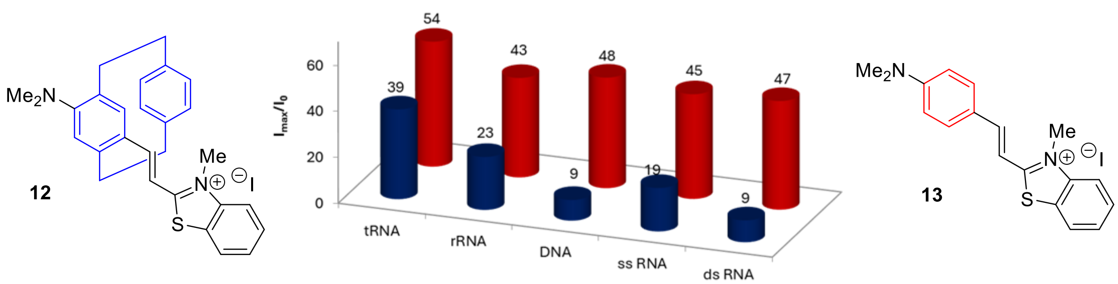

Figure 8. Turn-on fluorescence responses of cyanines **12** and **13** (10^{-6} M) in the presence of diverse nucleic acid (0.4 mg/mL) in Tris-EDTA (TE) buffer at 20 °C.

Table 6. Dissociation constants (μM) for RNA–cyanine **12** interactions

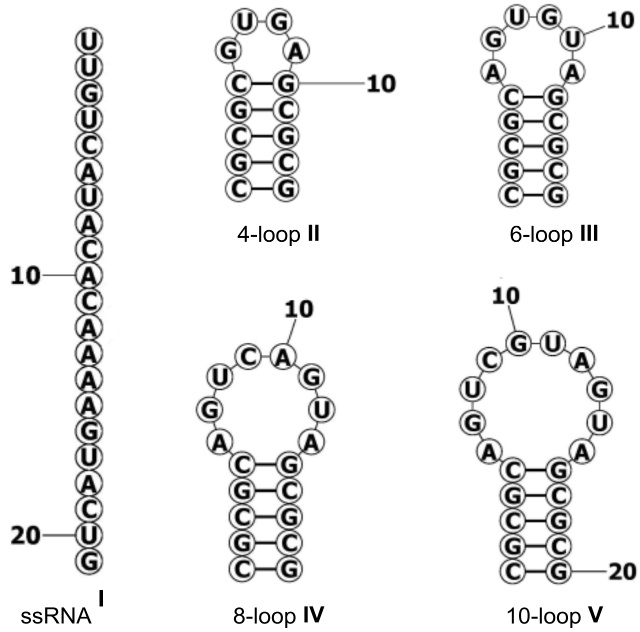

I[a]	II[a]	III[a]	IV[b]	V[b]
14.22	24.53	6.04	0.54	1.65
±14.46	±6.60	±2.05	±0.16	±1.14

[a] 10^{-6} M solution of dye **12** in Tris-EDTA (TE) buffer. [b] 10^{-7} M solution of dye **12** in Tris-EDTA (TE) buffer. Data are presented as mean of the three independent experiments ± standard deviation.

stage, both racemic and enantiopure compounds exhibited similar behavior [34].

In the future, the ability of enantiopure pCp-based luminophores to emit circularly polarized luminescence may be harnessed to monitor RNA–ligand interactions via CPL spectroscopy. This approach may offer several advantages, including enhanced sensitivity and selectivity stemming from the polarized nature of the emitted light, reduced background interference relative to conventional fluorescence methods, and the potential to provide detailed insights into the chiral environment and binding-induced conformational changes of RNA structures.

8. Conclusions

Thanks to their unique three-dimensional geometry, distinctive electronic properties, and atypical reactivity, [2.2]paracyclophanes (pCps) have emerged as versatile molecular platforms attracting growing interest across diverse areas of chemical research.

In this account, we have highlighted a variety of strategies that enable the selective functionalization of their aromatic cores, efficient control over planar chirality, and modulation of their photophysical properties. The methods developed in our laboratory have enabled access to structurally diverse pCp scaffolds with tunable spectroscopic behaviors on synthetically useful scales. These rigid π-stacked systems exhibited significant potential in fields such as organic and organometallic luminophore chemistry, photocatalysis, and chemical biology. Nevertheless, important challenges remain to be addressed. For example, the development of selective functionalization protocols targeting the ethylene bridges and the *meta* or *pseudo-meta* positions of these scaffolds could greatly broaden their chemical diversity. Strategies to further modulate the absorption and emission properties of functionalized pCps, such as attaining higher brightness and enhanced CPL efficiency, also warrant continued investigation. In lanthanide chemistry, pCp-based ligands with planar chirality may lead to the development of next-generation luminescent and multimodal metal complexes. The use of enantiopure chiral pCp derivatives as photosensitizers in photoredox catalysis also remains underexplored and could enable the design of novel light-activated asymmetric transformations. Finally, our recent efforts to incorporate the pCp motif into RNA-binding small molecules have opened promising avenues for targeting non-paired structural motifs within nucleic acids. However, further studies are required to better elucidate the precise binding mode of pCp derivatives to RNA.

In summary, pCps represent a fascinating class of molecular architectures that continue to captivate the chemistry community. Despite the significant progress already achieved in their synthesis and controlled functionalization, we are confident that ongoing research on these original compounds will continue to drive innovation across a range of disciplines, including organic synthesis, materials science, and chemical biology.

Acknowledgments

The authors extend their sincere thanks to all undergraduate, master's, and PhD students, as well as postdoctoral researchers and collaborators, for their invaluable contributions. Special thanks are due to J. Crassous, L. Favereaux, and F. Pointillart (Univ. Rennes 1); O. Maury and L. Abad-Galan (ENS Lyon); A. Maruani, S. Lajnef, F. Peyrot, C. Sagné and S. Turcaud (Paris Cité University).

Declaration of interests

The authors do not work for, advise, own shares in, or receive funds from any organization that could benefit from this article, and have declared no affiliations other than their research organizations.

Funding

The authors gratefully acknowledge the support of the CNRS and Paris Cité University (*IdEx Dynamique Recherche pCp-Photocat - ANR-18-IDEX-0001*), as well as funding from the *Agence Nationale de la Recherche* (*ANR JCJC PhotoChiraPhane - ANR-19-CE07-0001-01*).

References

[1] C. J. Brown and A. C. Farthing, "Preparation and structure of di-p-xylylene", *Nature* **164** (1949), pp. 915–916.

[2] H. Hope, J. Bernstein and K. N. Trueblood, "Trueblood, The crystal and molecular structure of 1,1,2,2,9,9,10,10-octafluoro-[2,2]paracyclophane and a reinvestigation of the structure of [2,2]paracyclophane", *Acta Cryst. B* **28** (1972), pp. 1733–1743.

[3] S. Wu, S. Felder, J. Brom, F. Pointillart, O. Maury, L. Micouin and E. Benedetti, "[2.2] paracyclophanes: From selective functionalization to optical properties", *Adv. Optical Mater.* **12** (2024), article no. 2400934.

[4] H. E. Winberg, F. S. Fawcett, W. E. Mochel and C. W. Theobald, "Dimethylenedihydroheteroaromatic compounds and heterocyclophanes by 1,6-Hofmann elimination reactions", *J. Am. Chem. Soc.* **82** (1960), pp. 1428–1435.

[5] M. Brink, "Eine verbesserte synthese von [2.2]paracyclophan und 4-formyl-[2.2]paracyclophan", *Synthesis* **12** (1975), pp. 807–808.

[6] T. Otsubo and V. Boekelheide, "An alternate route for the conversion of dithia[3.3]cyclophanes to cyclophanedienes. Reaction with benzyne followed by sulfoxide pyrolysis", *Tetrahedron Lett.* **45** (1975), pp. 3881–3884.

[7] A. Iwama, T. Toyoda, M. Yoshida, T. Otsubo, Y. Sakata and S. Misumi, "Layered compounds. LII. Syntheses of eleven anthracenophanes", *Bull. Chem. Soc. Jpn.* **51** (1978), pp. 2988–2994.

[8] M. Montanari, A. Bugana, A. K. Sharma and D. Pasini, "Mild preparation of functionalized [2.2] paracyclophanes via the Pummerer rearrangement", *Org. Biomol. Chem.* **9** (2011), pp. 5018–5020.

[9] J. Lahann, D. Klee and H. Höcker, "Chemical vapour deposition polymerization of substituted [2.2] paracyclophanes", *Macromol. Rapid Commun.* **19** (1998), pp. 441–444.

[10] H. Nandivada, H.-Y. Chen, L. Bondarenko and J. Lahann, "Reactive polymer coatings that "click"", *Angew. Chem. Int. Ed.* **45** (2006), pp. 3360–3363.

[11] H. Pu, Y. Wang and Z. Yang, "Chemical vapor deposition copolymerization of 4-carboxyl-[2, 2] paracyclophane and 4-amino-[2, 2] paracyclophane", *Mater. Lett.* **61** (2007), pp. 2718–2722.

[12] Z. Hassan, D. Varadharajan, C. Zippel, S. Begum, J. Lahann and S. Bräse, "Design strategies for structurally controlled polymer surfaces via cyclophane-based CVD polymerization and post-CVD pabrication", *Adv. Mater.* **34** (2022), article no. 2201761.

[13] D. Klee, N. Weiss and J. Lahann, in *Modern Cyclophane Chemistry* (R. Gleiter and H. Hopf, eds.), Wiley-VCH: Weinheim, 2004, pp. 463–484.

[14] Z. Hassan, E. Spuling, D. M. Knoll and S. Bräse, "Regioselective functionalization of [2.2] paracyclophanes: Recent synthetic progress and perspectives", *Angew. Chem. Int. Ed.* **59** (2020), pp. 2156–2170.

[15] J. Pu, L. Chen, R.-R. Wu, et al., "Non-directed Pd-catalysed C–H arylation of [2.2] paracyclophane", *Chem. Commun.* **59** (2023), pp. 9348–9351.

[16] M.-L. Delcourt, S. Felder, S. Turcaud, C. H. Pollok, C. Merten, L. Micouin and E. Benedetti, "Highly enantioselective asymmetric transfer hydrogenation: a practical and scalable method to efficiently access planar chiral [2.2] paracyclophanes", *J. Org. Chem.* **84** (2019), pp. 5369–5382.

[17] S. H. Eltamany and H. Hopf, "Cyclophane, XIV: darstellung polymethylierter [2.2] paracyclophane", *Tetrahedron Lett.* **21** (1980), pp. 4901–4904.

[18] Y. Zhao, X. Li, W.-H. Deng, B. Wu, R.-Z. Liao and Y.-G. Zhou, "Dearomatization of [2.2]paracyclophane-derived N-sulfonylimines through cyclopropanation with sulfur ylides", *J. Org. Chem.* **89** (2024), pp. 321–329.

[19] D. Ly, J. Bacs and H. M. L. Davies, "Rhodium (II)-catalyzed asymmetric cyclopropanation and desymmetrization of [2.2] paracyclophanes", *ACS Catal.* **14** (2024), pp. 6423–6431.

[20] N. V. Vorontsova, E. V. Vorontsov, E. V. Sergeeva and V. I. Rozenberg, "The first regioselective double electrophilic substitution of the C2-symmetric pseudo-meta-disubstituted [2.2] paracyclophanes", *Tetrahedron Lett.* **47** (2006), pp. 2357–2360.

[21] K. P. Javasundera, D. N. M. Kusmus, L. Deuilhé, L. Etheridge, Z. Farrow, D. J. Lun, G. Kaur and G. J. Rowlands, "The synthesis of substituted amino [2.2] paracyclophanes", *Org. Biomol. Chem.* **14** (2016), pp. 10848–10860.

[22] S. Felder, L. Micouin and E. Benedetti, "Para-functionalization of N-substituted 4-amino [2.2] paracyclophanes by regioselective formylation", *Eur. J. Org. Chem.* **2021** (2021), pp. 4015–4018.

[23] S. E. Walden and D. T. Glatzhofer, "Distinctive normal harmonic vibrations of [2.2] paracyclophane", *J. Phys. Chem. A* **101** (1997), pp. 8233–8241.

[24] D. Henseler and G. Hohlneicher, "Theoretical study on the molecular distortions in [2.2] paracyclophane and cyclobutene", *J. Phys. Chem. A* **102** (1998), pp. 10828–10833.

[25] S. Grimme and C. Mück-Lichtenfeld, "Accurate computation of structures and strain energies of cyclophanes with modern DFT methods", *Isr. J. Chem.* **52** (2012), pp. 180–192.

[26] R. S. Cahn, C. Ingold and V. Prelog, "Specification of molecular chirality", *Angew. Chem. Int. Ed.* **5** (1966), pp. 385–415.

[27] D. J. Cram and N. L. Allinger, "Macro rings. XII. Stereochemical consequences of steric compression in the smallest paracyclophane", *J. Am. Chem. Soc.* **77** (1955), pp. 6289–6294.

[28] S. E. Gibson and J. D. Knight, "[2.2] Paracyclophane derivatives in asymmetric catalysis", *Org. Biomol. Chem.* **1** (2003), pp. 1256–1269.

[29] Y. Morisaki and Y. Chujo, "Planar chiral [2.2] paracyclophanes: optical resolution and transformation to optically active π-stacked molecules", *Bull. Chem. Soc. Jpn.* **92** (2019), pp. 265–274.

[30] K. J. Weiland, A. Gallego and M. Mayor, "Beyond simple substitution patterns—Symmetrically tetrasubstituted [2.2] paracyclophanes as 3D functional materials", *Eur. J. Org. Chem.* **2019** (2019), pp. 3073–3085.

[31] S. Felder, S. Wu, J. Brom, L. Micouin and E. Benedetti, "Enantiopure planar chiral [2.2] paracyclophanes: Synthesis and applications in asymmetric organocatalysis", *Chirality* **33** (2021), pp. 506–527.

[32] M.-L. Delcourt, S. Turcaud, E. Benedetti and L. Micouin, "Efficient and scalable kinetic resolution of racemic 4-formyl[2.2]paracyclophane via asymmetric transfer hydrogenation", *Adv. Synth. Catal.* **358** (2016), pp. 1213–1215.

[33] M.-L. Delcourt, S. Felder, E. Benedetti and L. Micouin, "Highly enantioselective desymmetrization of centrosymmetric pseudo-para-diformyl[2.2]paracyclophane via asymmetric transfer hydrogenation", *ACS Catal.* **8** (2018), pp. 6612–6616.

[34] Z. Wu, S. Fang, J. He, J. Che, Z. Liu, X. Wei, Z. Su and T. Wang, "Desymmetrization/kinetic resolution of planar chiral [2.2] paracyclophanes by bioinspired peptide-iminophosphorane catalysis", *Angew. Chem. Int. Ed.* **64** (2025), article no. e202423702.

[35] V. Docekal, F. Koucky, I. Cisarova and J. Vesely, "Organocatalytic desymmetrization provides access to planar chiral [2.2] paracyclophanes", *Nat. Commun.* **15** (2024), article no. 3090.

[36] S. Yu, H. Bao, D. Zhang and X. Yang, "Kinetic resolution of substituted amido [2.2] paracyclophanes via asymmetric electrophilic amination", *Nat. Commun.* **14** (2023), article no. 5239.

[37] Y. Zhao, Y.-X. Ding, B. Wu and Y.-G. Zhou, "Nickel-catalyzed asymmetric hydrogenation for kinetic resolution of [2.2]paracyclophane-derived cyclic N-sulfonylimines", *J. Org. Chem.* **86** (2021), pp. 10788–10798.

[38] C. Zippel, Z. Hassan, A. Q. Parsa, J. Hohmann and S. Braese, "Multigram-scale kinetic resolution of 4-acetyl[2.2]paracyclophane via Ru-catalyzed enantioselective hydrogenation: Accessing [2.2]paracyclophanes with planar and central chirality", *Adv. Synth. Catal.* **363** (2021), pp. 2861–2865.

[39] S.-C. Huo, R. R. Indurmuddam, B.-C. Hong, C.-F. Lua and S.-Y. Chien, "The hamburger-shape photocatalyst: thioxanthone-based chiral [2.2]paracyclophane for enantioselective visible-light photocatalysis of 3-methylquinoxalin-2(1H)-one and styrenes", *Org. Biomol. Chem.* **21** (2023), pp. 9330–9336.

[40] P. Rademacher, in *Modern Cyclophane Chemistry* (R. Gleiter and H. Hopf, eds.), Wiley-VCH: Weinheim, 2004, pp. 275–310.

[41] D. J. Cram, N. L. Allinger and H. Steinberg, "Macro rings. VII. The spectral consequences of bringing two benzene

rings face to face", *J. Am. Chem. Soc.* **76** (1954), pp. 6132–6141.

[42] G. C. Bazan, W. J. Oldham, R. J. Lachicotte, S. Tretiak, V. Chernyak and S. Mukamel, "Stilbenoid dimers: dissection of a paracyclophane chromophore", *J. Am. Chem. Soc.* **120** (1998), pp. 9188–9204.

[43] G. P. Bartholomew and G. C. Bazan, "Bichromophoric paracyclophanes: models for interchromophore delocalization", *Acc. Chem. Res.* **34** (2001), pp. 30–39.

[44] W. J. Oldham, Y. J. Miao, R. J. Lachicotte and G. C. Bazan, "Stilbenoid dimers: effect of conjugation length and relative chromophore orientation", *J. Am. Chem. Soc.* **120** (1998), pp. 419–420.

[45] J. Zyss, I. Ledoux, S. Volkov, V. Chernyak, S. Mukamel, G. P. Bartholomew and G. C. Bazan, "Through-space charge transfer and nonlinear optical properties of substituted paracyclophane", *J. Am. Chem. Soc.* **122** (2000), pp. 11956–11962.

[46] Y. Liu and P. Xing, "Circularly polarized light responsive materials: Design strategies and applications", *Adv. Optical Mater.* **35** (2023), article no. 2300968.

[47] A. Yanagawa, M. Tsuchiya, R. Inoue and Y. Morisaki, "Optical resolution of pseudo-para-disubstituted [2.2]paracyclophane: a chiral building block for optically active helicene-stacked molecules emitting circularly polarized luminescence", *J. Mater. Chem. C* **11** (2023), pp. 986–993.

[48] Y. Morisaki, M. Gon, T. Sasamori, N. Tokitoh and Y. Chujo, "Planar chiral tetrasubstituted [2.2] paracyclophane: optical resolution and functionalization", *J. Am. Chem. Soc.* **136** (2014), pp. 3350–3353.

[49] Y. Morisaki, K. Inoshita and Y. Chujo, "Planar-chiral through-space conjugated oligomers: Synthesis and characterization of chiroptical properties", *Chem. Eur. J.* **20** (2014), pp. 8386–8390.

[50] Y. Morisaki, R. Hifumi, L. Lin, K. Inoshita and Y. Chujo, "Through-space conjugated polymers consisting of planar chiral pseudo-ortho-linked [2.2] paracyclophane", *Polym. Chem.* **3** (2012), pp. 2727–2730.

[51] M. Gon, Y. Morisaki and Y. Chujo, "Optically active cyclic compounds based on planar chiral [2.2] paracyclophane: extension of the conjugated systems and chiroptical properties", *J. Mater. Chem. C* **3** (2015), pp. 521–529.

[52] M. Gon, H. Kozuka, Y. Morisaki and Y. Chujo, "Optically active cyclic compounds based on planar chiral [2.2] paracyclophane with naphthalene units", *Asian J. Org. Chem.* **5** (2016), pp. 353–359.

[53] M. Gon, Y. Morisaki and Y. Chujo, "Highly emissive optically active conjugated dimers consisting of a planar chiral [2.2] paracyclophane showing circularly polarized luminescence", *Eur. J. Org. Chem.* **2015** (2015), pp. 7756–7762.

[54] M. Gon, Y. Morisaki, R. Sawada and Y. Chujo, "Synthesis of optically active, x-shaped, conjugated compounds and dendrimers based on planar chiral [2.2]paracyclophane, leading to highly emissive circularly polarized luminescence", *Chem. Eur. J.* **22** (2016), pp. 2291–2298.

[55] A. Morisaki, R. Inoue and Y. Morisaki, "Synthesis of two novel optically active#-shaped cyclic tetramers based on planar chiral [2.2] paracyclophanes", *Chem. Eur. J.* **29** (2023), article no. e202203533.

[56] X. Li, Y. Xie and Z. Li, "The progress of circularly polarized luminescence in chiral purely organic materials", *Adv. Photonics Res.* **2** (2021), article no. 2000136.

[57] S. Felder, M.-L. Delcourt, D. Contant, R. Rodríguez, L. Favereau, J. Crassous, L. Micouin and E. Benedetti, "Compact CPL emitters based on a [2.2] paracyclophane scaffold: recent developments and future perspectives", *J. Mater. Chem. C* **11** (2023), pp. 2053–2062.

[58] M.-L. Delcourt, C. Reynaud, S. Turcaud, L. Favereau, J. Crassous, L. Micouin and E. Benedetti, "3D Coumarin systems based on [2.2] paracyclophane: Synthesis, spectroscopic characterization, and chiroptical properties", *J. Org. Chem.* **84** (2019), pp. 888–899.

[59] S. Felder, C. Sagné, E. Benedetti and L. Micouin, "Small-molecule 3D ligand for RNA recognition: tuning selectivity through scaffold hopping", *ACS Chem. Biol.* **17** (2022), pp. 3069–3076.

[60] N. Akbay, M. Y. Losytskyy, V. B. Kovalska, A. O. Balanda and S. M. Yarmoluk, "The mechanism of benzothiazole styrylcyanine dyes binding with dsDNA: Studies by spectral-luminescent methods", *J. Fluoresc.* **18** (2008), pp. 139–147.

[61] J.-C. G. Bünzli, "On the design of highly luminescent lanthanide complexes", *Coord. Chem. Rev.* **293–294** (2015), pp. 19–47.

[62] J.-C. G. Bünzli, "Lanthanide luminescence for biomedical analyses and imaging", *Chem. Rev.* **110** (2010), pp. 2729–2755.

[63] G.-Q. Jin, Y. Ning, J.-X. Geng, Z.-F. Jiang, Y. Wang and J.-L. Zhang, "Joining the journey to near infrared (NIR) imaging: the emerging role of lanthanides in the designing of molecular probes", *Inorg. Chem. Front.* **7** (2020), pp. 289–299.

[64] O. Guillou, C. Daiguebonne, G. Calvez and K. Bernot, "A long journey in lanthanide chemistry: From fundamental crystallogenesis studies to commercial anticounterfeiting taggants", *Acc. Chem. Res.* **49** (2016), pp. 844–856.

[65] S. I. Weissman, "Intramolecular energy transfer the fluorescence of complexes of europium", *J. Chem. Phys.* **10** (1942), pp. 214–217.

[66] H. Uh and S. Petoud, "Novel antennae for the sensitization of near infrared luminescent lanthanide cations", *C. R. Chim.* **13** (2010), pp. 668–680.

[67] Z. Hassan, E. Spuling, D. M. Knoll, J. Lahann and S. Bräse, "Planar chiral [2.2] paracyclophanes: from synthetic curiosity to applications in asymmetric synthesis and materials", *Chem. Soc. Rev.* **47** (2018), pp. 6947–6963.

[68] R. Grykien, B. Luszczynska, I. Glowacki, et al., "Electric field tunable light emitting diodes containing europium β-diketonates with [2.2] paracyclophane moiety", *Opt. Mater.* **57** (2016), pp. 114–119.

[69] S. Wu, L. A. Galan, M. Roux, et al., "Tuning excited-state properties of [2.2] paracyclophane-based antennas to ensure efficient sensitization of lanthanide ions or singlet oxygen generation", *Inorg. Chem.* **60** (2021), pp. 16194–16203.

[70] R. Marin, G. Brunet and M. Murugesu, “Shining new light on multifunctional lanthanide single-molecule magnets”, *Angew. Chem. Int. Ed.* **60** (2021), pp. 1728–1746.

[71] K. Bernot, “Get under the umbrella: A comprehensive gateway for researchers on lanthanide-based single-molecule magnets”, *Eur. J. Inorg. Chem.* **26** (2023), article no. e202300336.

[72] D. N. Woodruff, R. E. P. Winpenny and R. A. Layfield, “Lanthanide single-molecule magnets”, *Chem. Rev.* **113** (2013), pp. 5110–5148.

[73] D. Thakura and S. Vaidyanathan, “Chiral lanthanide complexes in the history of circularly polarized luminescence: a brief summary”, *J. Mater. Chem. C* **13** (2025), pp. 9410–9452.

[74] F. Pointillart, M. Atzori and C. Train, “Magneto-chiral dichroism of chiral lanthanide complexes”, *Inorg. Chem. Front.* **11** (2024), pp. 1313–1321.

[75] H. Flichot, A. Sickinger, J. Brom, et al., “Magneto-structural correlation in lanthanide luminescent [2.2] paracyclophane-based single-molecule magnets”, *Dalton Trans.* **53** (2024), pp. 8191–8201.

[76] G. Ciamician, “The photochemistry of the future”, *Science* **36** (1912), pp. 385–394.

[77] P. Melchiorre, “Introduction: photochemical catalytic processes”, *Chem. Rev.* **122** (2022), pp. 1483–1484.

[78] J. Xuan, B.-J. Li, Z.-J. Feng, et al., “Desulfonylation of tosyl amides through catalytic photoredox cleavage of N-S bond under visible-light irradiation”, *Chem. Asian J.* **8** (2013), pp. 1090–1094.

[79] A. Gualandi, G. Rodeghiero, E. Della Rocca, et al., “Application of coumarin dyes for organic photoredox catalysis”, *Chem. Commun.* **54** (2018), pp. 10044–10047.

[80] A. Gualandi, A. Nenov, M. Marchini, et al., “Tailored coumarin dyes for photoredox catalysis: Calculation, synthesis, and electronic properties”, *ChemCatChem* **13** (2021), pp. 981–989.

[81] J. Brom, A. Maruani, S. Turcaud, S. Lajnef, F. Peyrot, L. Micouin and E. Benedetti, “[2.2] Paracyclophane-based coumarins: effective organo-photocatalysts for light-induced desulfonylation processes”, *Org. Biomol. Chem.* **22** (2024), pp. 59–64.

[82] P. Viaud, V. Coeffard, C. Thobie-Gautier, I. Beaudet, N. Galland, J.-P. Quintard and E. Le Grognec, “Electrochemical cleavage of sulfonamides: an efficient and tunable strategy to prevent β-fragmentation and epimerization”, *Org. Lett.* **14** (2012), pp. 942–945.

[83] A. J. David, R. Balaji and A. Das, “Advances of chiral metal complexes as standalone photocatalyst for asymmetric organic transformations”, *Adv. Synth. Catal.* **367** (2025), article no. e202401543.

[84] A. Bauer, F. Westkamper, S. Grimme and T. Bach, “Catalytic enantioselective reactions driven by photoinduced electron transfer”, *Nature* **436** (2005), pp. 1139–1140.

[85] C. Muller, A. Bauer and T. Bach, “Light-driven enantioselective organocatalysis”, *Angew. Chem. Int. Ed.* **48** (2009), pp. 6640–6642.

[86] J. Großkopf, T. Kratz, T. Rigotti and T. Bach, “Enantioselective photochemical reactions enabled by triplet energy transfer”, *Chem. Rev.* **122** (2022), pp. 1626–1653.

[87] C. Prentice, J. Morrisson, A. D. Smith and E. Zysman-Colman, “Recent developments in enantioselective photocatalysis”, *Beilstein J. Org. Chem.* **16** (2020), pp. 2363–2441.

[88] X. Cao, Y. Zhang, Y. Ding and Y. Wan, “Identification of RNA structures and their roles in RNA functions”, *Nat. Rev. Mol. Cell Biol.* **25** (2024), pp. 784–801.

[89] V. Bernat and M. D. Disney, “RNA structures as mediators of neurological diseases and as drug targets”, *Neuron* **87** (2015), pp. 28–46.

[90] A. Fatica, “The emerging role of RNA in diseases and cancers”, *Int. J. Mol. Sci.* **24** (2023), article no. 6682.

[91] J. L. Childs-Disney, X. Yang, Q. M. R. Gibaut, Y. Tong, R. T. Batey and M. D. Disney, “Targeting RNA structures with small molecules”, *Nat. Rev. Drug Discov.* **21** (2022), pp. 736–762.

[92] Y. Tong, J. L. Childs-Disney and M. D. Disney, “Targeting RNA with small molecules, from RNA structures to precision medicines: IUPHAR review: 40”, *Br. J. Pharmacol.* **181** (2024), pp. 4152–4173.

[93] A. E. Hargrove, “Small molecule–RNA targeting: starting with the fundamentals”, *Chem. Commun.* **56** (2020), pp. 14744–14756.

[94] S. Kovachka, M. Panosetti, B. Grimaldi, S. Azoulay, A. Di Giorgio and M. Duca, “Small molecule approaches to targeting RNA”, *Nat. Rev. Chem.* **8** (2024), pp. 120–135.

[95] K. Deigan Warner, C. E. Hajdin and K. M. Weeks, “Principles for targeting RNA with drug-like small molecules”, *Nat. Rev. Drug Discov.* **17** (2018), pp. 547–558.

[96] S. T. Meyer and P. J. Hergenrother, “Small molecule ligands for bulged RNA secondary structures”, *Org. Lett.* **11** (2009), pp. 4052–4055.

[97] C. Fleurisson, N. Graidia, J. Azzouz, et al., “Design and Evaluation of Azaspirocycles as RNA binders”, *Chem. Eur. J.* **31** (2025), article no. e202403518.

[98] S. A. Barros and D. M. Chenoweth, “Triptycene-based small molecules modulate (CAG)·(CTG) repeat junctions”, *Chem. Sci.* **6** (2015), article no. 4752.

[99] S. A. Barros and D. M. Chenoweth, “Recognition of nucleic acid junctions using triptycene-based molecules”, *Angew. Chem. Int. Ed.* **53** (2014), pp. 13746–13750.

[100] S. A. Barros, I. Yoon and D. M. Chenoweth, “Modulation of the *E. coli* rpoH temperature sensor with triptycene-based small molecules”, *Angew. Chem. Int. Ed.* **55** (2016), pp. 8258–8261.

[101] V. B. Kovalska, D. V. Kryvorotenko, A. O. Balanda, M. Yu Losytskyy, V. P. Tokar and S. M. Yarmoluk, “Fluorescent homodimer styrylcyanines: synthesis and spectral-luminescent studies in nucleic acids and protein complexes”, *Dyes Pigm.* **67** (2005), pp. 47–54.

[102] C.-Q. Zhu, S.-J. Zhuo, H. Zheng, J.-L. Chen, D.-H. Li, S.-H. Li and J.-G. Xu, “Fluorescence enhancement method for the determination of nucleic acids using cationic cyanine as a fluorescence probe”, *Analyst* **129** (2004), pp. 254–258.

ACADÉMIE
DES SCIENCES
INSTITUT DE FRANCE

Comptes Rendus. Chimie
2025, Vol. 28, p. 789-804
https://doi.org/10.5802/crchim.414

Account

Expanding heterocyclic chemical space through the reactivity of *N*-allenamides

Dorian Schutz [*,a] **and Laurence Miesch** [*,a]

[a] Equipe de Synthèse Organique et Phytochimie, Institut de Chimie, CNRS-UdS, UMR 7177, 4 rue Blaise Pascal, CS 90032, 67081 Strasbourg, France

E-mails: dorian.schutz@unistra.fr (D. Schutz), lmiesch@unistra.fr (L. Miesch)

Abstract. Over the last few decades, allenes have evolved from objects of curiosity to central elements of organic synthesis. Among them, *N*-allenamides, allenes featuring an electron-withdrawing group on the nitrogen, stand out for their great stability and versatility. Their unique reactivity has made them valuable platforms for numerous chemical transformations. Their interest is reinforced by their ability to efficiently lead to multisubstituted enamides, motifs present in many bioactive natural products but notoriously challenging to synthesize with high regio- and stereocontrol. Driven by our deep interest in the reactivity of activated *N*-allenamides, particularly those with fluorinated units, we present here new transformations leading to the construction of heterocyclic fluorinated structures and complex enamides, two motifs with significant relevance in medicinal chemistry.

Keywords. *N*-allenamides, Ene-ynamides, Tertiary enamides, γ-sultams, Hydroazidation, *N*-to-*C* [1,3]-sulfonyl shift.

Note. Article submitted by invitation.

Manuscript received 21 July 2025, revised 23 July 2025, accepted 30 July 2025.

1. Introduction

N-Allenamides, featuring an electron-withdrawing group (EWG) on the nitrogen atom, have gained significant attention among organic chemists over the past decade, surpassing their allenamine counterparts. This increased interest stems from their enhanced stability and retained distinctive reactivity. The delocalization of the nitrogen's lone pair into the allenic system imparts these compounds with dual reactivity, as depicted in their resonance structures (Figure 1). As a consequence, a range of highly regio- and stereoselective functionalizations at the α-, β-, and γ-positions of the allene moiety has been developed. These transformations enable the construction of complex and valuable N-heterocycles, often yielding either proximal or distal adducts with precise control. The extensive focus that has been dedicated to *N*-allenamides is clearly reflected in the substantial number of publications and comprehensive reviews that have emerged over the years, highlighting their diverse and powerful reactivity as versatile synthetic building blocks (for selected reviews on *N*-allenamide, see [1–5]). Over the past three years, our research group has initiated a dedicated program focused on exploring the reactivity of activated *N*-allenamides. Our initial approach involved the use of ynamides as precursors to access these valuable intermediates. We then shifted our attention to investigating their reactivity, with particular emphasis on the construction of heterocyclic frameworks which are key structural motifs commonly found in natural products.

2. Results and discussions

N-Allenamides, a subclass of allenes, have emerged as essential motifs in a myriad of transformations. Despite their growing prominence as unique and

* Corresponding authors

ISSN (electronic): 1878-1543

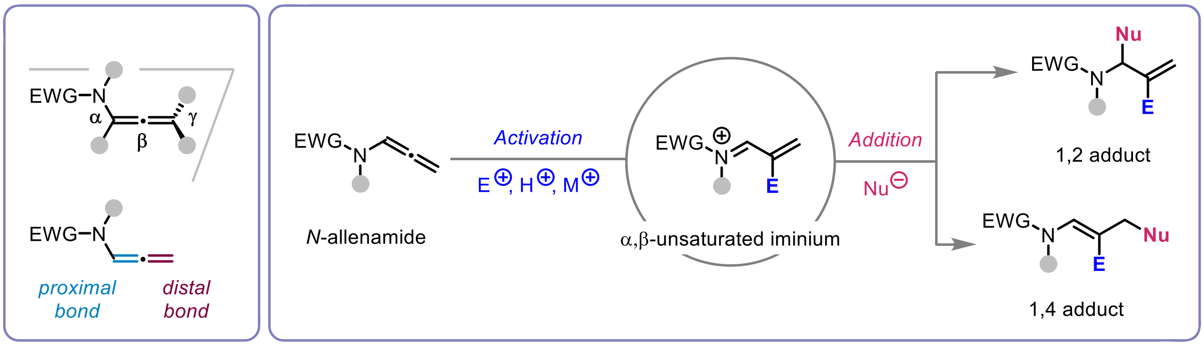

Figure 1. *N*-allenamide structure and reactivity profile.

versatile building blocks in organic synthesis, existing methods for their preparation often suffer from limited substrate scope and restricted structural diversity. Inspired by the addition of diazo compounds to alkynes [6–10], we envisioned that a coupling reaction between terminal ynamides and a readily available diazomethane surrogate, trimethylsilyldiazomethane (Me_3SiCHN_2, 2 M in diethyl ether), in the presence of tetra-*n*-butylammonium fluoride (TBAF) could offer a straightforward route to terminal *N*-allenamides. We were pleased to find that the desired coupling products were obtained in good yields, and the reaction exhibited broad functional group tolerance, such as fluorinated substituents (Scheme 1) [11].

Fluorine-containing building blocks have become essential in the development of new drug candidates [12–14]. Despite major advances in fluorine chemistry, fluorine-substituted *N*-allenamides remain scarce [15]. Building on this, we sought to explore the synthesis of fluorinated *N*-allenamides using fluorinated diazoalkanes. Addition of trifluorodiazoethane to terminal ynamides under copper catalysis in acetonitrile led to the formation of the desired *N*-allenamides in very good yields. The pentafluoroethyl group, another highly fluorinated motif, also proved compatible with this transformation, cleanly delivering the corresponding *N*-allenamides. Encouraged by these results, we turned our attention to more challenging fluorinated substituents, notably the difluoromethyl group (CF_2H). Recognized as a metabolically stable bioisostere of hydroxyl and thiol groups, the CF_2H moiety has gained prominence in pharmaceutical, agrochemical, and materials science [16,17]; for recent reviews on difluoromethylation reactions see [18–20]. When CF_2HCHN_2 was reacted with electron-deficient alkynes, we successfully obtained CF_2H-substituted *N*-allenamides from terminal ynamides under similar conditions. Remarkably, the reaction displays broad functional group tolerance, accommodating oxazolidinones, halogens (e.g., chlorine), protected aldehydes, and even unsaturated side chains that offer further opportunities for downstream functionalization (Scheme 1).

Building on our efficient access to a new class of push–pull allenes, we turned our attention to hydroaminations, an atom-economical reaction for constructing diverse heterocyclic scaffolds, which serve as valuable platforms for further functionalization. While significant progress has been made in hydroaminations targeting the proximal C=C bond [21,22] and, to a lesser extent, the distal C=C bond [23,24], additions to the central C=C bond remain comparatively rare. To address this gap, we employed our ynamide/diazo coupling method to synthesize *N*-allenamides bearing an ester substituent. Although these intermediates were highly unstable, they proved amenable to hydroamination, yielding a variety of amido-captodative enamines. Notably, the activated *N*-allenamides underwent regio- and stereoselective addition with a range of secondary amines. A counterintuitive anti-Michael addition provides a unique *E*-configured enamine. Numerous amides as well as distinct amines could be adapted (Scheme 2). Density functional theory (DFT) calculations further supported the regio- and stereoselectivity of the reaction [25].

Eight-membered heterocycles are conspicuous structural motifs found in numerous natural

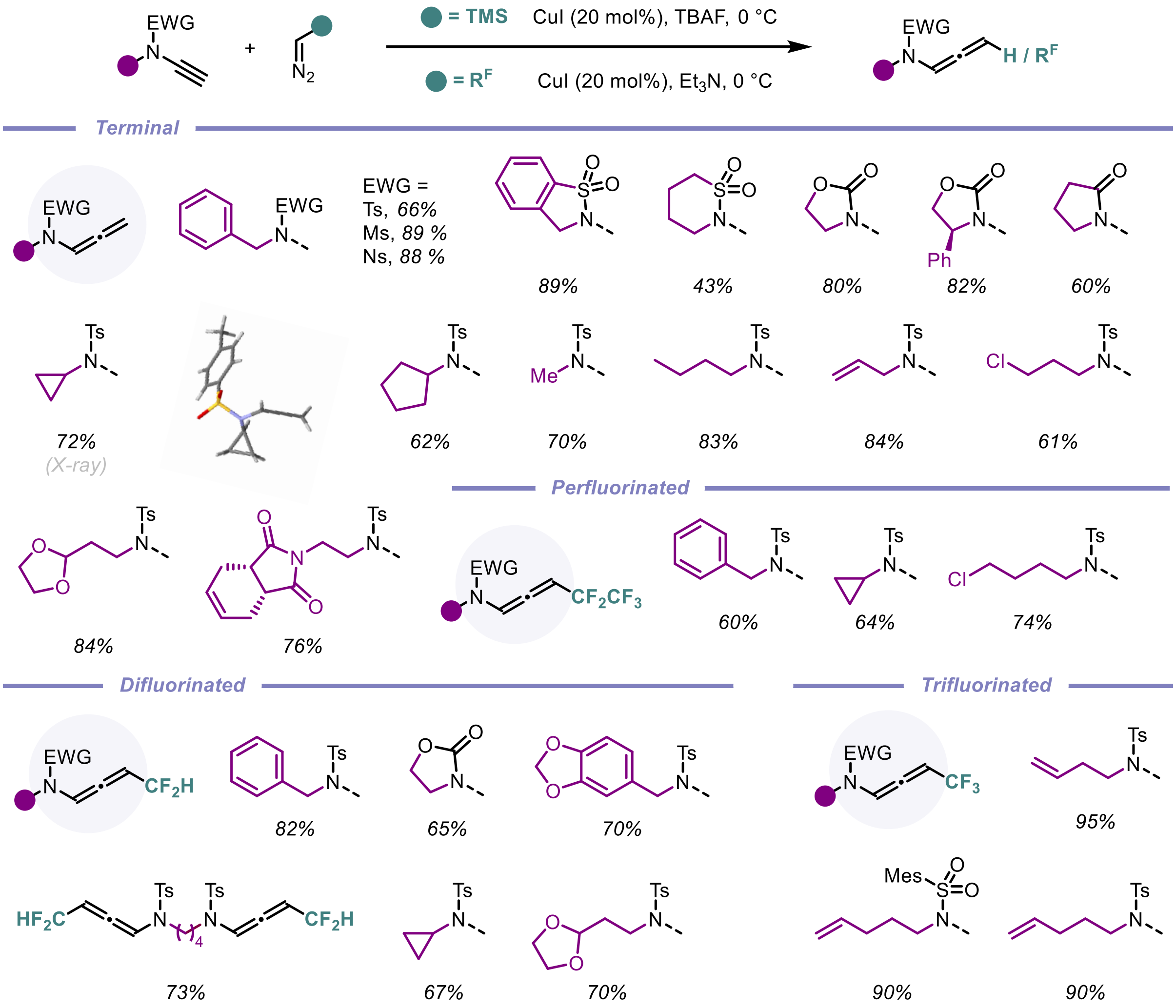

Scheme 1. Synthesis of terminal and fluorinated *N*-allenamides.

products and/or bioactive molecules. However, their synthesis remains challenging due to unfavorable enthalpic and entropic barriers associated with the transition states required for medium-size ring formation [26–28]. Among these, benzo[*b*][1,5]-dioxocines stand out as particularly valuable eight-membered heterocycles. Notable examples include penicillide [29] and a derivative discovered by Bayer [30], both exhibiting significant biological activity. These compounds act as cholesteryl ester transfer protein (CETP) inhibitors and have emerged as promising candidates for the treatment of dyslipidemia (Figure 2) [31]. Reported Conia-ene reactions of ene-ynamides remain scarce [32,33]. As part of our ongoing research on ynamide reactivity, we became interested in exploring the behavior of ynamides tethered to propargylic ethers under basic conditions [34]. Given that propargylic ethers are known to isomerize in the presence of a base, we hypothesized an enolate addition to the in-situ formed *N*-allenamide ether. Among the bases evaluated, a solution of benzyltrimethyl-ammonium hydroxide (Triton B) in methanol emerged as the optimal choice to perform this transformation. Experimental observations were supported by DFT calculations, indicating a regioselective *O*-alkylation, where the enolate adds to the proximal position of the *N*-allenamide. This transformation furnishes eight-membered rings

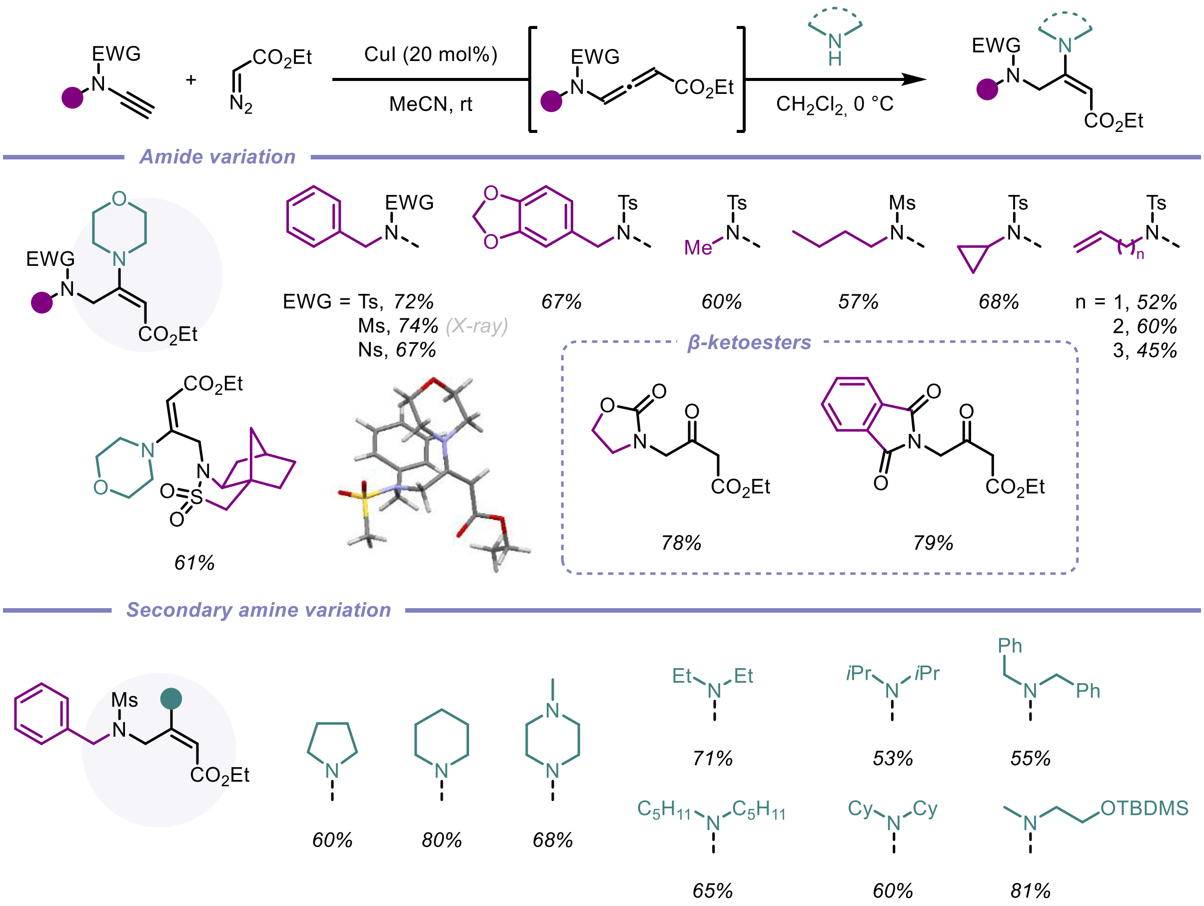

Scheme 2. One-pot hydroamination of activated *N*-allenamides.

featuring two embedded enols and a hemiaminal core. Importantly, the structure tolerates modifications at the terminal tether of the ynamide as well as both substituents on the nitrogen atom, demonstrating the versatility of this method in generating diverse, highly functionalized substructures. This approach offers a sustainable and green route to access shelf-stable eight-membered O-heterocycles, significantly expanding the accessible chemical space for this underexplored class of compounds (Scheme 3). The computed energy profiles show that the pathway involving the formation of an *N*-allenamide intermediate can be considered as the preferential one, essentially due to the lower activation energy and more favorable initial deprotonation step [35].

In light of our previous findings, we investigated whether trifluoromethylated *N*-allenamides could be leveraged to generate ene-ynamides with a particular emphasis on incorporating *gem*-difluoroalkene and monofluoroalkene motifs. These fluorinated alkenes are especially appealing: *gem*-difluoroalkenes act as carbonyl mimics, and monofluoroalkenes serve as bioisosteres of peptide and enol bonds [36]. For example, the pyrrolidone derivative seletracetam demonstrates a lack of psychomimetic effects, offering significant advantages over many conventional antiepileptic drugs [37]. In-vivo studies have shown that a difluoromethylated GABA aminotransferase inhibitor is highly effective in suppressing dopamine release following acute exposure to cocaine or nicotine [38]. The presence of a fluoroalkene transformed the opioid peptide Leu-enkephalin into an in-vivo probe with sufficient plasma and microsomal stability to provide an orally active peptide probe with central nervous system distribution (Figure 3) [39]. We found that a

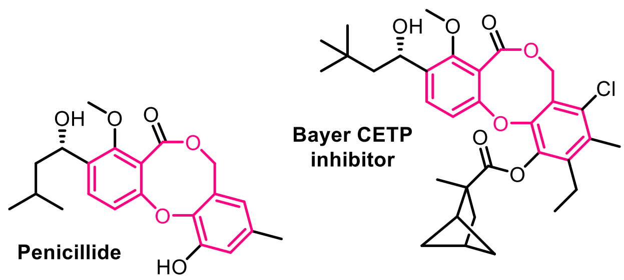

Figure 2. Bioactive benzo[b][1,5]dioxocines.

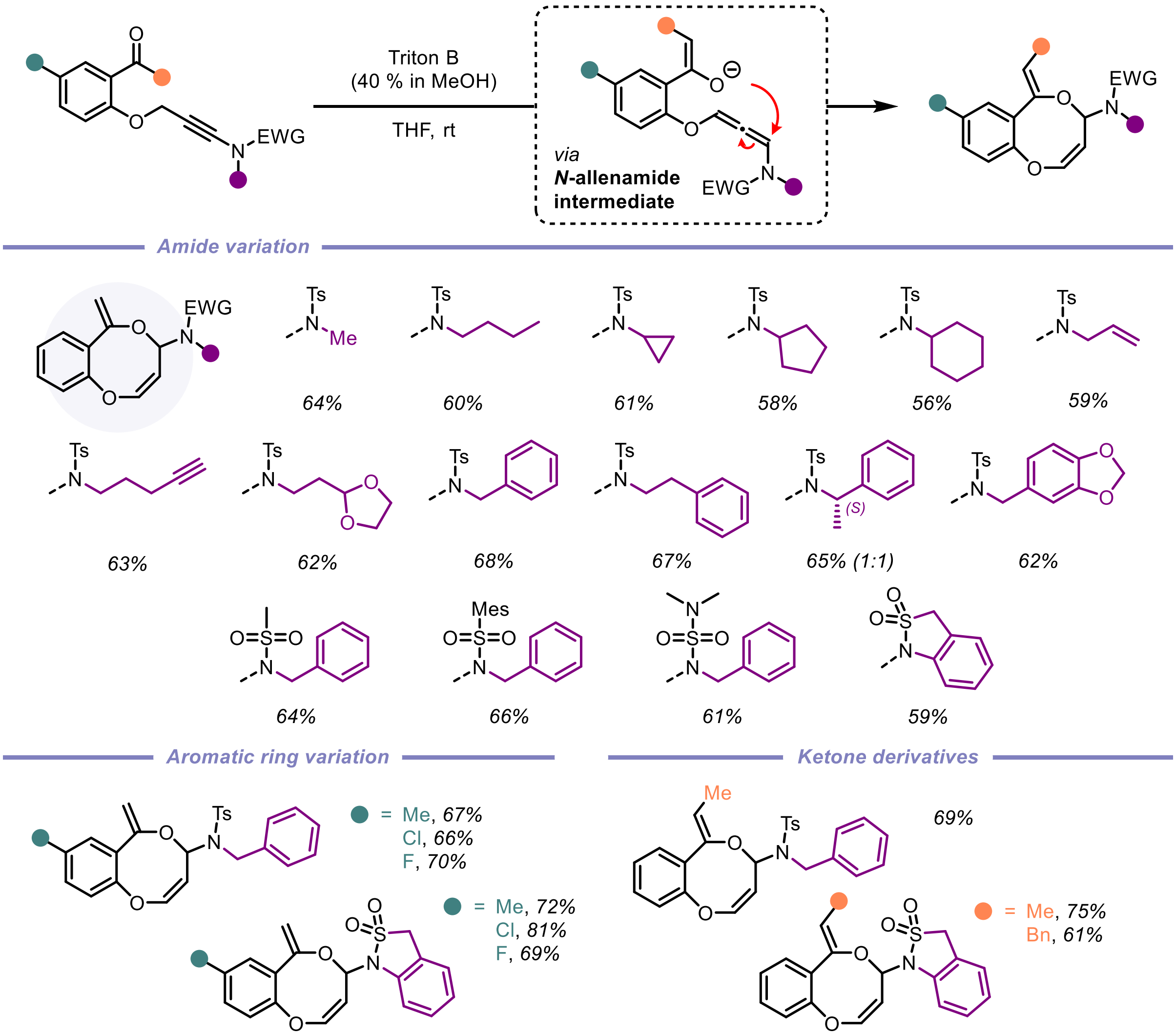

Scheme 3. Construction of eight-membered O-heterocycles from tethered ynamides.

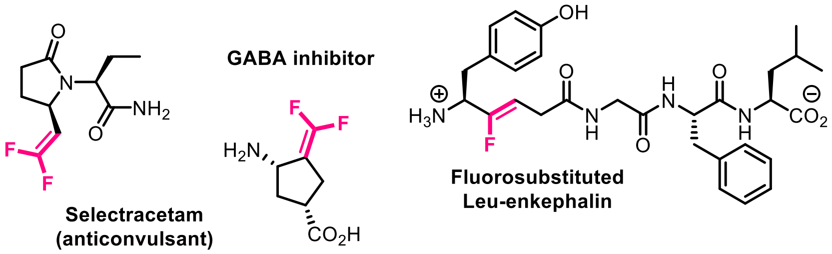

Figure 3. Bioactive mono- and difluorinated alkenes.

base-promoted δ-elimination of a fluorine atom from the CF_3-substituted *N*-allenamides efficiently afforded *gem*-difluorinated ene-ynamides. Both potassium *tert*-butoxide (*t*-BuOK) and sodium hydride (NaH) proved to be effective bases for this transformation. The reaction proceeded smoothly and exhibited a broad functional group tolerance, accommodating a variety of functionalized side chains and electron-withdrawing groups, thus highlighting the versatility of this strategy (Scheme 4) [40]. Given the polarity of the ynamides and the high electrophilicity of the α-carbon of the *gem*-difluoroalkene moiety, it was possible to tune the reactivity of these peculiar building blocks by adding nucleophiles on the ynamide moiety or on the difluoroalkenyl part. Alcoholates were directly added to the starting *N*-allenamides. Interestingly, this reaction yielded a mixture of *Z*- and *E*-monofluorinated ene-ynamides, with the alkoxy group at the carbon atom δ to the nitrogen. The overall yield was good, and the two stereoisomers could be successfully separated, affording both *Z*- and *E*-configured ene-ynamides (Scheme 5). Subsequent selective *syn*-hydroacylation and hydrochlorination promoted by $ZrCl_4$ occurred exclusively at the ynamide moiety, enabling the synthesis of tailored mono- or difluorinated dienes depending on the starting material (Scheme 6) [40].

Despite their attractive properties, only a limited number of protocols have been developed for the synthesis of fluoropyrroles. Currently, fluorinated pyrroles are predominantly obtained through the functionalization of pre-existing pyrrole frameworks [41–43]. Building on our previous results, we envisioned that *gem*-difluorinated ene-ynamides [40] could serve as suitable precursors for the synthesis of fluorinated pyrroles via hydroamination followed by an intramolecular cyclization. To explore this possibility, we investigated the use of silver catalysts to promote the regioselective addition of primary amines to ene-ynamides. In contrast to alcoholates, primary amines selectively add to the ynamide moiety of the molecule generated in situ. Upon silver-mediated activation of the *gem*-difluoroalkenyl group, a 5-*endo-trig* cyclization followed by β-fluoride elimination occurred, furnishing the desired fluorinated pyrrole scaffold (Scheme 7). This transformation exhibits high modularity, allowing straightforward access to a wide range of highly functionalized 2-amido-5-fluoropyrroles. Good yields were obtained for this operationally simple process involving a one-pot four-step sequence (Scheme 8). An intramolecular version of this process led to the synthesis of tricyclic oxazoles from monofluorinated ene-ynamides embedding a primary amine (Scheme 9) [44].

Since the discovery of sulfonamide antibacterials [45], sulfonamides have played a key role in medicinal chemistry. The cyclic counterparts of sulfonamide compounds (sultams) display enhanced biological activities compared to their acyclic congeners [46]. Our strategy aimed to exploit the electron-withdrawing substituent on the nitrogen atom in trifluorinated *N*-allenamides. Specifically, we hypothesized that deprotonation at the α-position of the sulfonyl group in *N*-sulfonyl allenamides could trigger an anionic 5-*endo-dig* cyclization, ultimately leading to the formation of cyclic sulfonamides. Although not found in nature, these amide surrogates are considered privileged motifs that have found diverse applications in drug discovery such as in sultiame, an anticonvulsant agent [47], S-2474, a non-steroidal anti-inflammatory drug [48], and an antidiabetes agent developed by Boehringer Ingelheim (Figure 4) [49]. Upon treatment with TBAF and acetic acid, CF_3-substituted *N*-allenamides were transformed into γ-sultams bearing an ene-*gem*-difluorinated tether, whereas TBAF alone provided

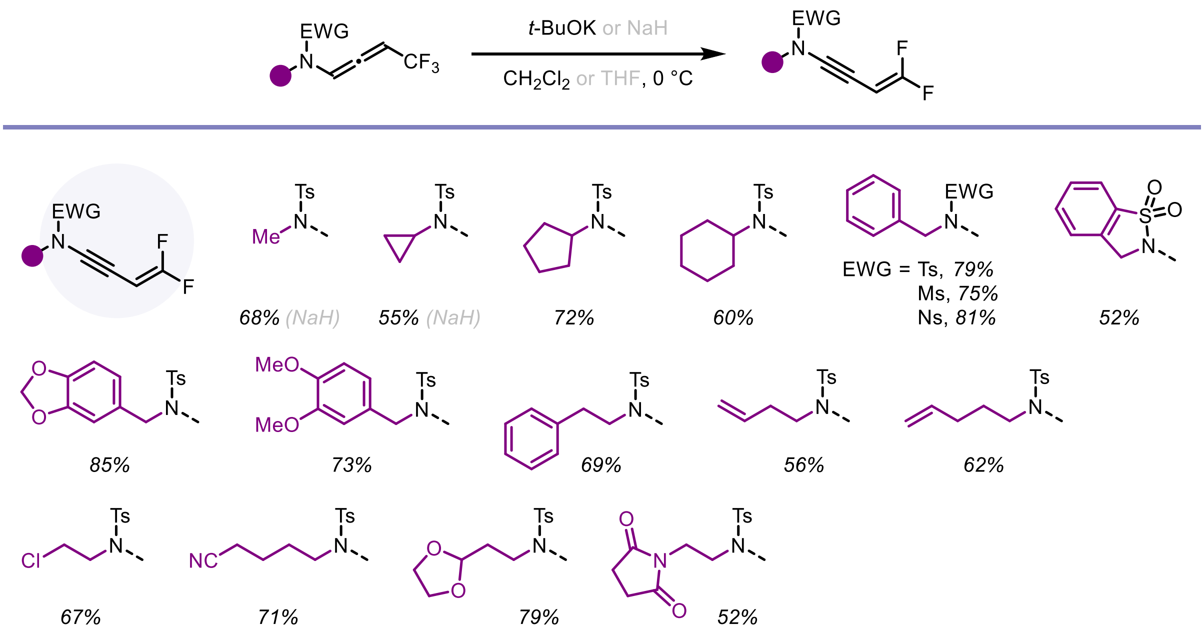

Scheme 4. Synthesis of *gem*-difluorinated ene-ynamides.

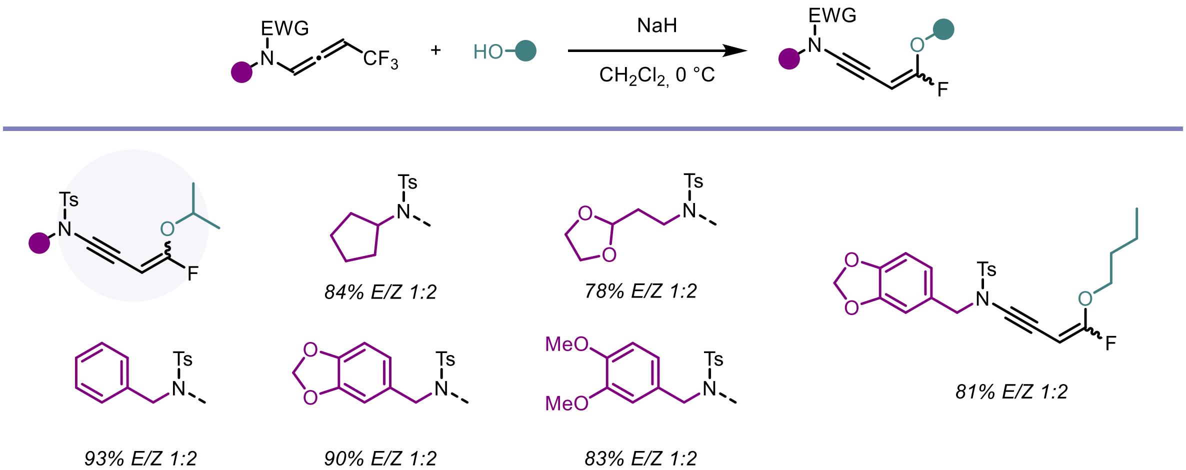

Scheme 5. Regioselective substitution on the alkenyl moiety.

the corresponding trifluorinated ethyl sultams. The developed method demonstrated broad functional group tolerance and a wide substrate scope, affording sultams featuring a *gem*-difluorinated ene moiety (Scheme 10). Moreover, DFT calculations supported a reaction pathway involving a 5-*endo-dig* cyclization on the ene-ynamide intermediate generated in situ [50].

We next considered a chemoselective, metal-free approach for the 1,2- and 2,3-semireduction of CF_3-substituted *N*-allenamides. The enamide moiety in these compounds was efficiently and regioselectively reduced using a combination of triethylsilane (Et_3SiH) and boron trifluoride etherate ($BF_3{\cdot}OEt_2$), affording the desired products with good stereoselectivity. Subsequent 1,8-diazabicyclo[5.4.0]undec-7-ene (DBU)-mediated isomerization of the resulting allyl amide proceeded cleanly, furnishing the *E*-configured enamide exclusively (Scheme 11) [51].

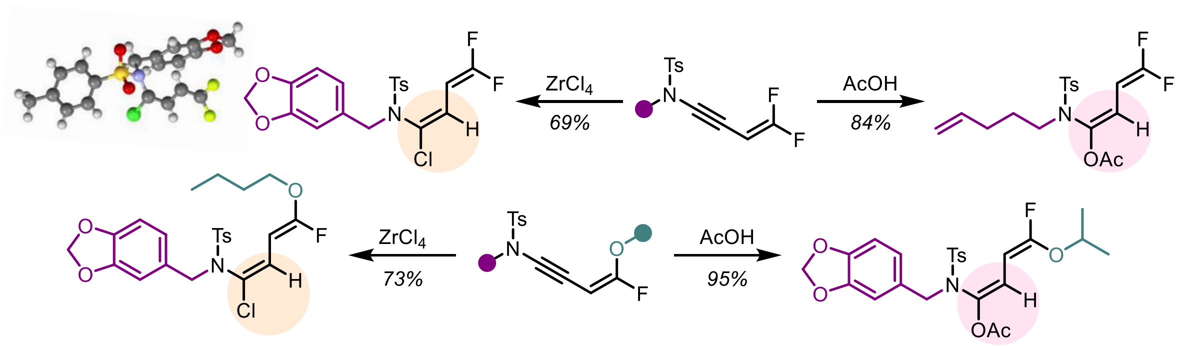

Scheme 6. Hydrofunctionalization of the ynamide moiety.

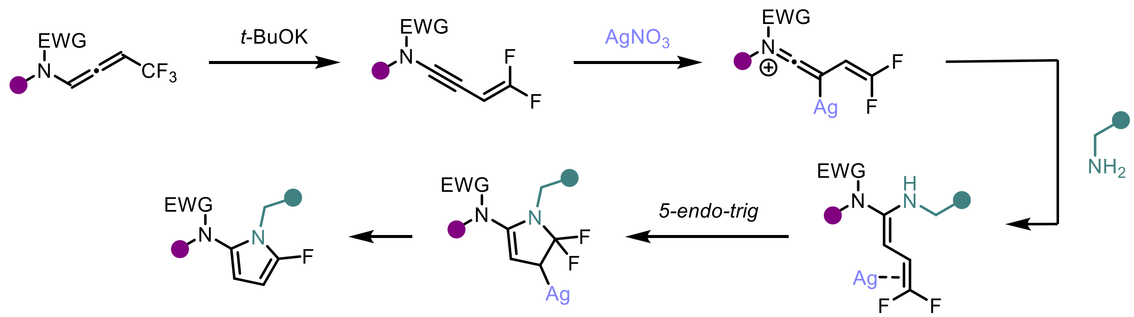

Scheme 7. Proposed reaction mechanism.

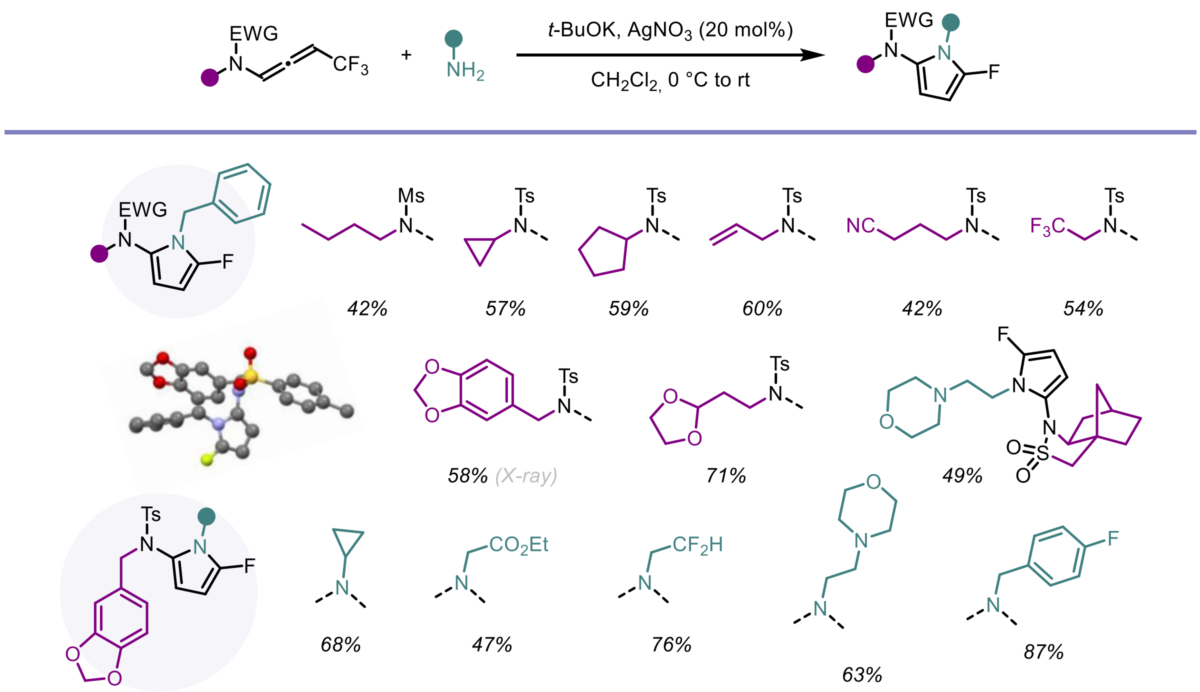

Scheme 8. Domino synthesis of fluorinated pyrroles.

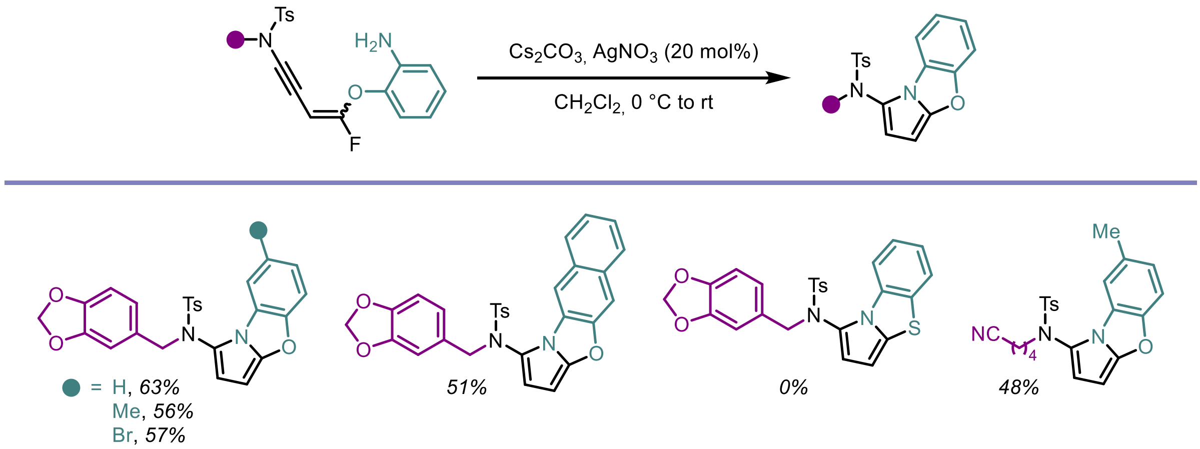

Scheme 9. Synthesis of oxazoles from monofluorinated ene-ynamides.

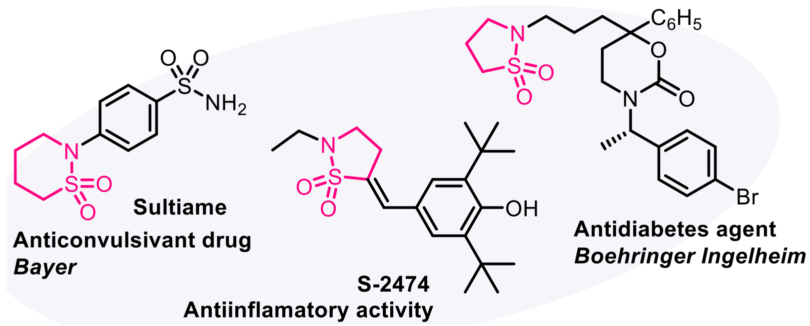

Figure 4. Bioactive sultams.

Among diverse organic azide compounds, vinyl azides represent a remarkable synthetic scaffold with their ability to act as an electrophile, an enamine-type nucleophile or a radical acceptor [52]. Given the unsaturated nature of *N*-allenamides, we envisioned that these compounds could be the perfect candidates to obtain vinyl azides via hydroazidations. We initiated our study by exploiting the reactivity of activated *N*-allenamides to achieve direct hydrofunctionalization at the central *sp*-hybridized carbon. Employing a combination of trimethylsilyl azide ($TMSN_3$) and TBAF, we achieved a smooth hydroazidation of both trifluorinated and ester-substituted *N*-allenamides. This transformation yielded vinyl azides with complete regio- and stereoselectivity (Scheme 12). In contrast, when trifluorinated *N*-allenamides were activated with trifluoroacetic acid (TFA) in the presence of $TMSN_3$, hydroazidation occurred selectively at the distal double bond. This enabled the site-specific installation of an azido group at the γ-position. While vinyl azides have found extensive utility in organic synthesis, allyl azides have often been overlooked due to their exposure to the Winstein rearrangement, typically leading to a mixture of isomers through allylic azide equilibrium [53]. In our system, the proximity of a heteroatom appears to suppress this equilibrium, enabling the exclusive formation of allyl azides featuring a conjugated system. Furthermore, treatment of these allyl azides with DBU induced a sigmatropic shift of the azido group, followed by double-bond isomerization. This process afforded vinyl azides with the azido moiety at the α-site with complete regio- and stereocontrol (Scheme 13) [54].

N-Allenamides bearing an electron-withdrawing group on the nitrogen atom have emerged as readily accessible and versatile nitrogen-containing synthons [1–5]. While their thermal reactivity—driven

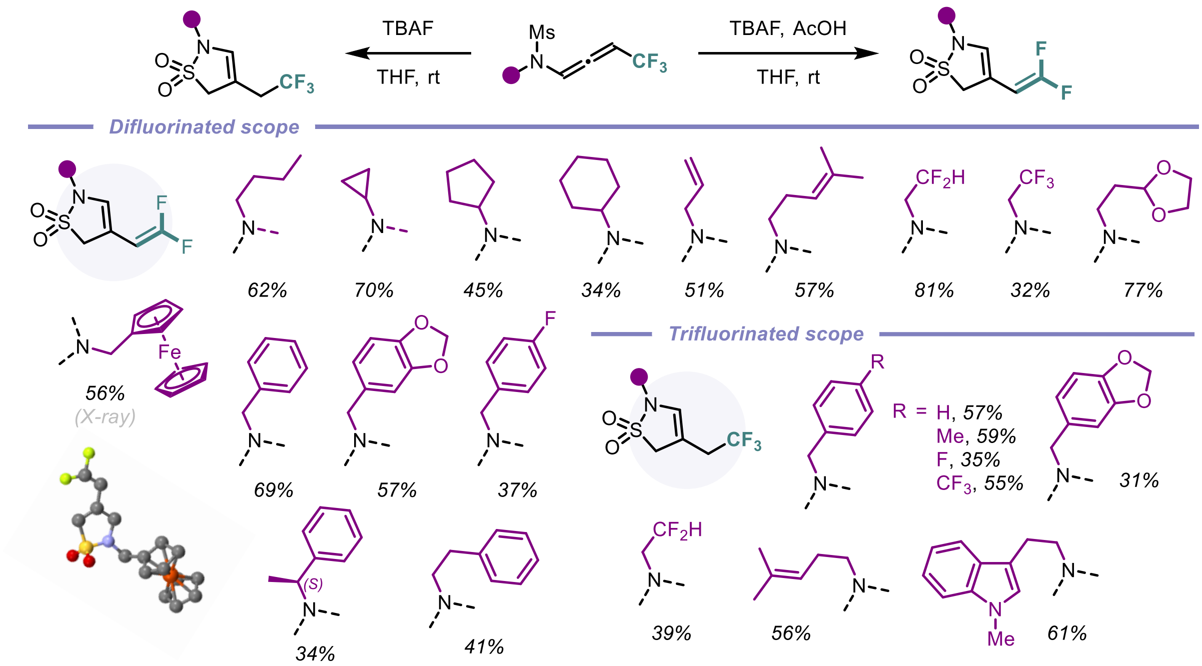

Scheme 10. Synthesis of tri- and difluorinated γ-sultams.

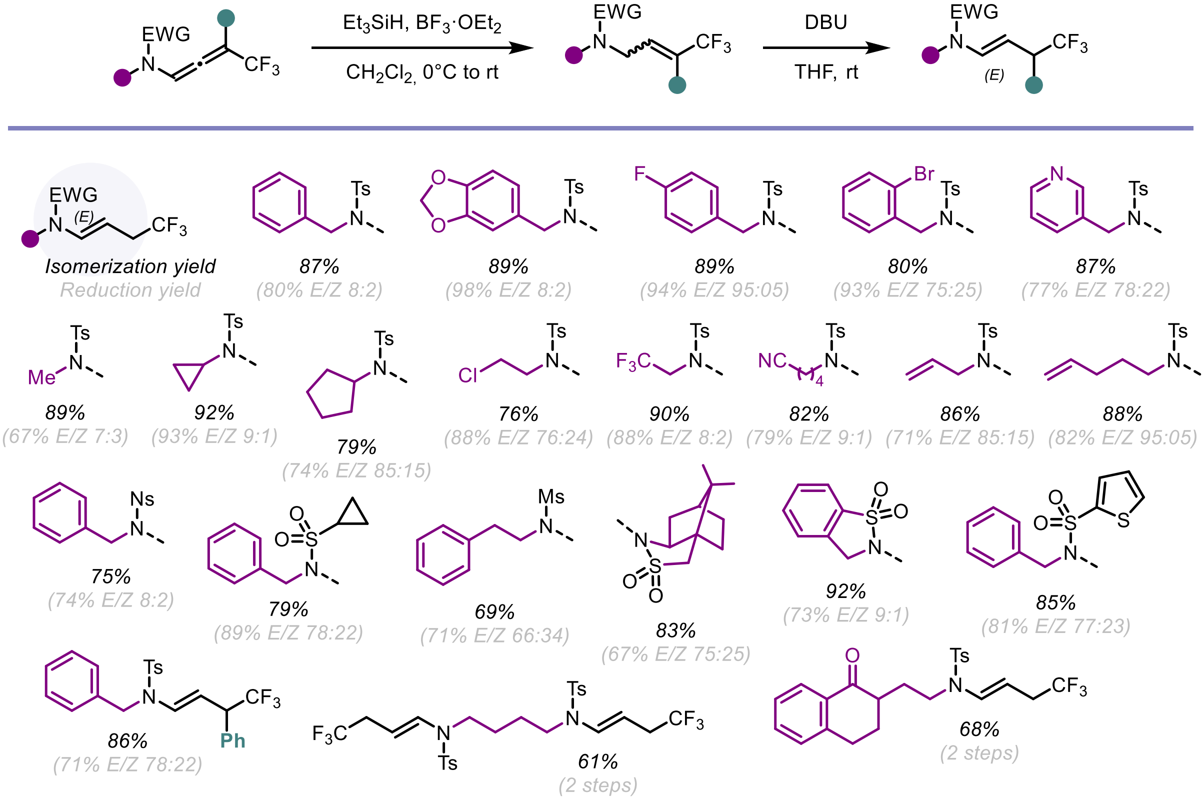

Scheme 11. Semireduction and isomerization of CF_3^- *N*-allenamides.

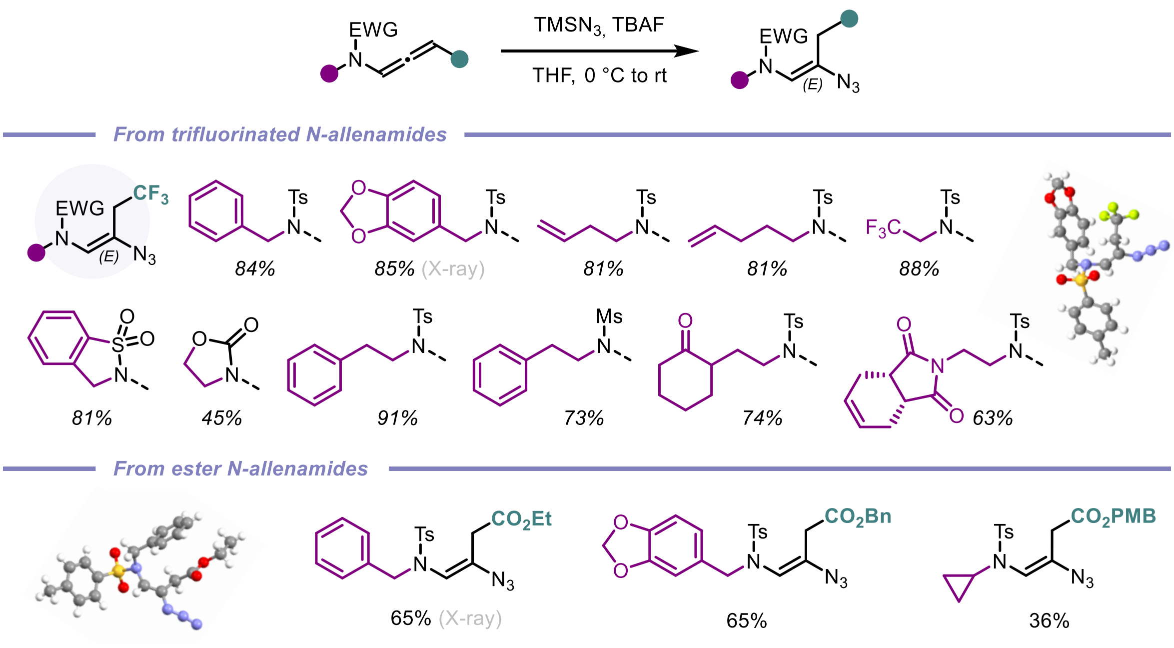

Scheme 12. β-Hydroazidation of activated N-allenamides.

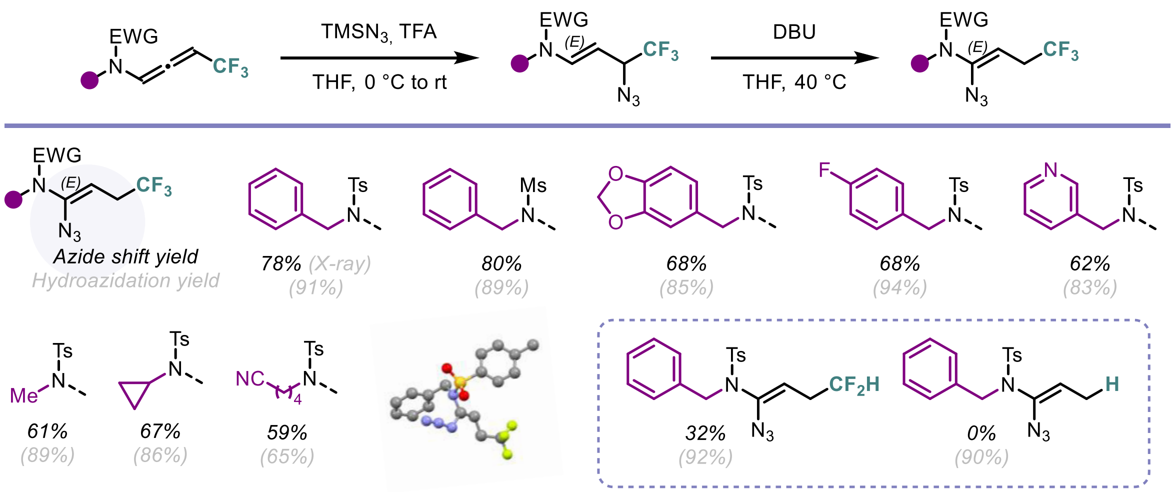

Scheme 13. γ-Hydroazidation of activated N-allenamides and base-promoted azide shift.

by electronic bias in the ground state (S_0)—is well established [55–57], their behavior and reactivity in the triplet excited state (T_1) remain largely unexplored. We were puzzled by the fact that the photochemical reactivity of N-sulfonyl allenamides remained unexplored (Figure 5) [58,59]. We hypothesized that the presence of the sulfonyl group could be strategically leveraged to control the fate of the vinyl radical intermediate, potentially unlocking new reactivity pathways. Our investigations revealed that the direct addition of H-phosphine oxide to a CF_3-substituted N-sulfonyl allenamide under visible-light irradiation led to the formation of the corresponding α-phosphorylated β-sulfonyl enamine.

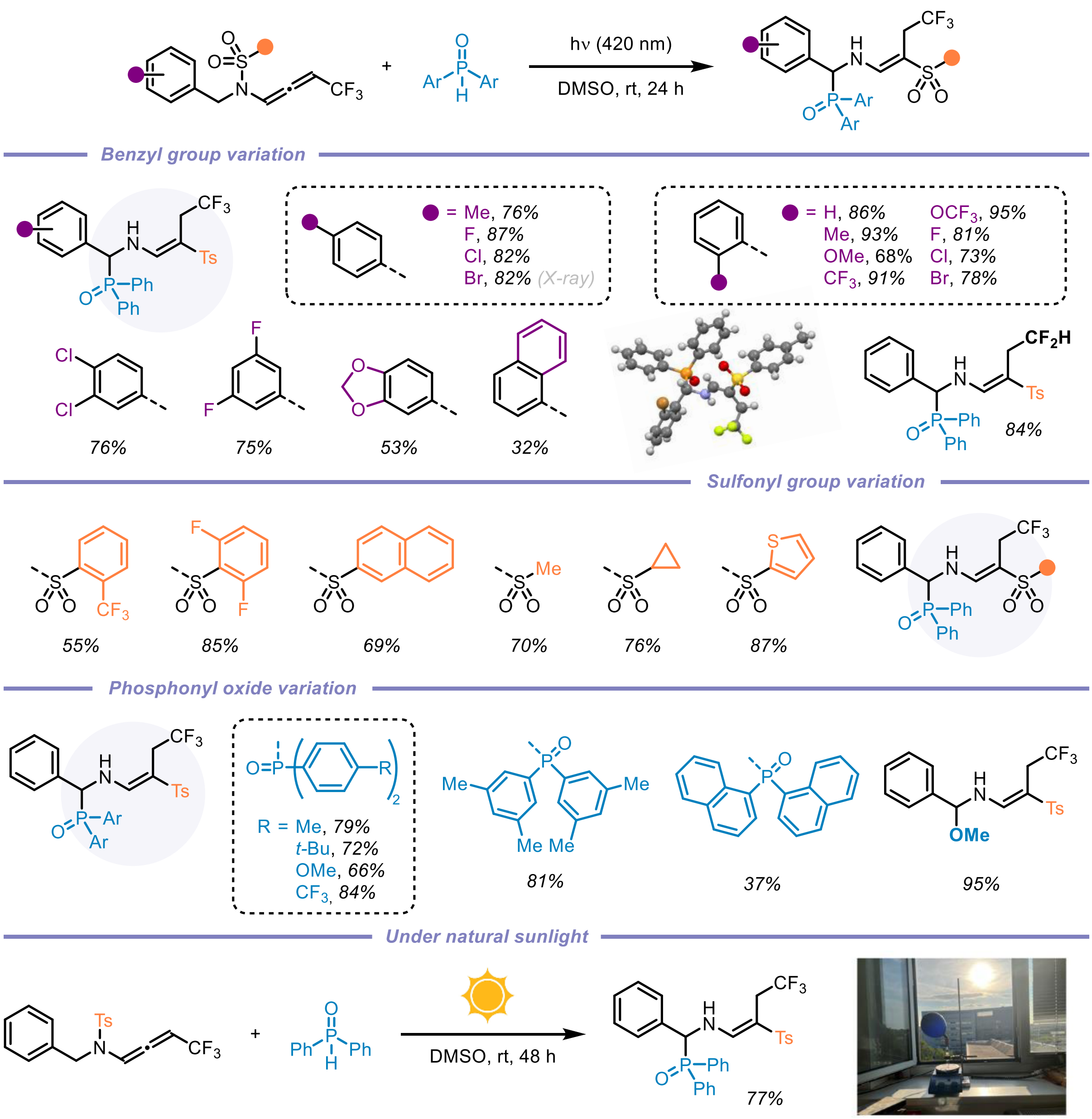

Scheme 14. Light-induced synthesis of α-phosphorylated β-sulfonyl enamines.

This transformation proved to be applicable to a broad range of substrates and demonstrated notable sustainability (Scheme 14). Remarkably, the reaction could be performed under natural sunlight over the course of two days, affording the desired phosphorylated enamine in 77% yield. Encouraged by our findings and the visible-light-induced *N*-to-*C* [1,3]-sulfonyl shift, we questioned whether this transposition could be extended beyond CF_3-substituted *N*-allenamides. When terminal *N*-allenamides were employed in the presence of *H*-phosphine oxides, a divergent reactivity was observed, leading to the formation of structurally distinct hydrophosphorylated products. In this case, we propose that an

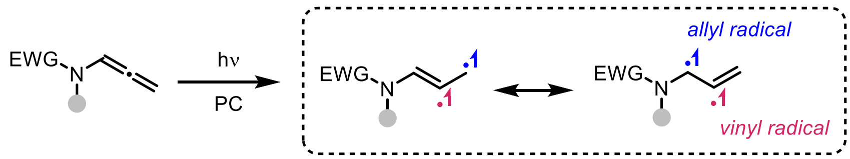

Figure 5. The reactivity of excited *N*-allenamides: a chemical challenge.

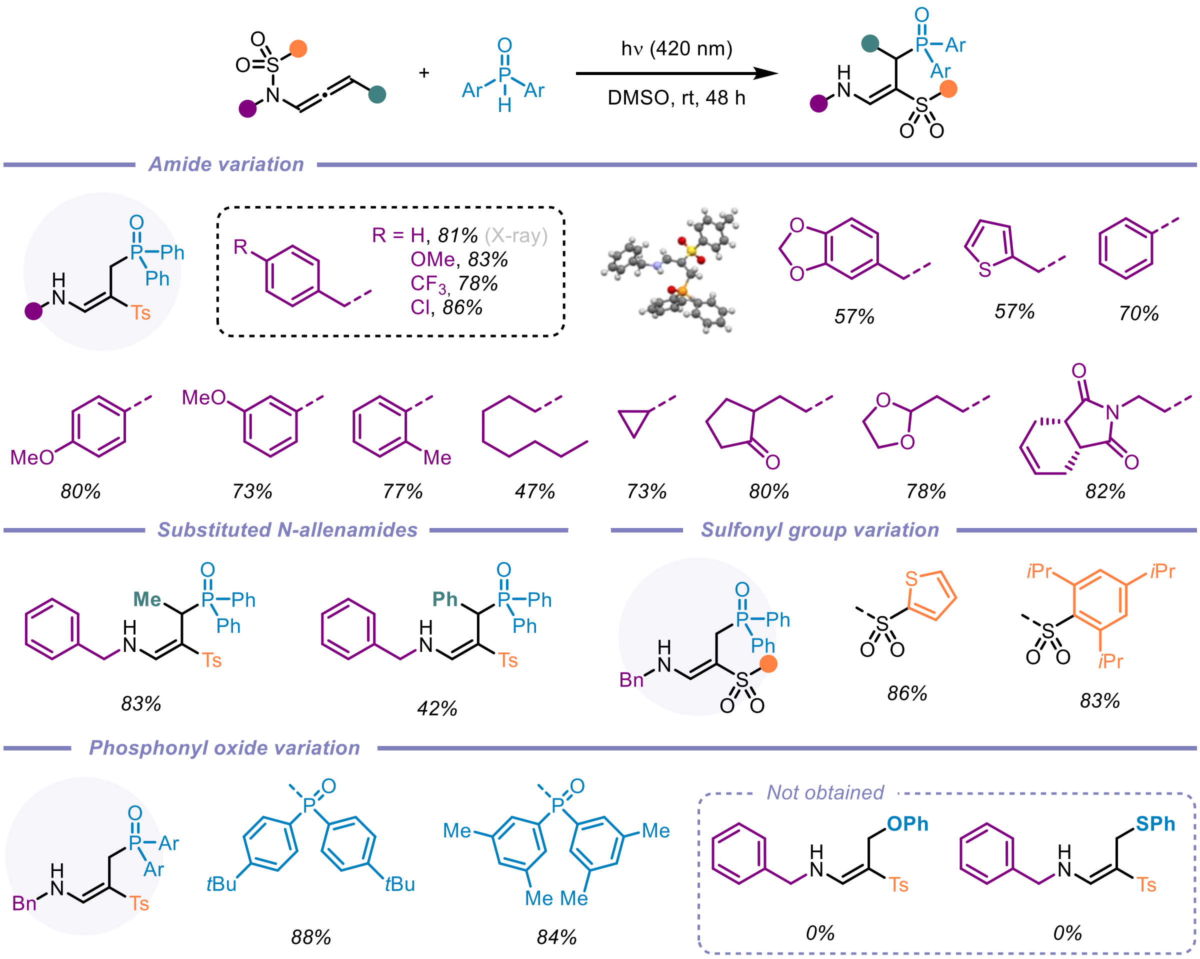

Scheme 15. Light-induced synthesis of γ-phosphorylated β-sulfonyl enamines.

intermolecular hydrogen atom transfer (HAT) occurs, followed by the addition of a phosphinoyl radical [P(O)·] to the terminal alkene moiety. This sequence furnishes γ-phosphorylated β-sulfonyl enamines. Notably, for terminal allenamides, functionalized side chains could be used and underwent a [1,3]-Ts shift, further expanding the structural diversity accessible through this approach. Additionally, terminal *N*-sulfonyl allenamides bearing various aryl and heteroaryl sulfonyl groups on the nitrogen atom were also effective substrates for this *N*-to-*C* [1,3]-sulfonyl shift reaction. This simple, efficient, and atom-economical process exhibits a broad substrate scope, excellent functional compatibility, and more importantly complete regio- and stereo-selectivity (Scheme 15) [60]. In conclusion, this account highlights our recent efforts toward the synthesis of activated *N*-allenamides and, more importantly, showcases their remarkable versatility as reactive intermediates. Under basic conditions, difluorinated ene-ynamides were efficiently generated. Nucleophilic additions to the difluorinated alkenyl moiety afforded highly functionalized, tailor-made dienes, while reactions with primary amines led to the formation of fluorinated pyrroles. Furthermore, the electron-withdrawing group on the nitrogen atom was strategically exploited to access potentially bioactive *gem*-difluorinated γ-sultams. Regio- and stereoselective reductions, as well as hydroazidations, delivered valuable fluorinated enamides, allylamides, and vinyl azides. Finally, the discovery of the first *N*-to-*C* tosyl shift in *N*-allenamides under photocatalyst-free conditions underscores the untapped potential of these compounds to unlock novel reactivity patterns and generate original phosphorylated structures.

Declaration of interests

The authors do not work for, advise, own shares in, or receive funds from any organization that could benefit from this article, and have declared no affiliations other than their research organizations.

References

[1] F. López and J. L. Mascareñas, "Gold(I)-catalyzed enantioselective cycloaddition reactions", *Beilstein J. Org. Chem.* **9** (2013), pp. 2250–2264.

[2] T. Lu, Z. Lu, Z.-X. Ma, Y. Zhang and R. P. Hsung, "Allenamides: A powerful and versatile building block in organic synthesis", *Chem. Rev.* **113** (2013), pp. 4862–4904.

[3] R. Blieck, M. Taillefer and F. Monnier, "Metal-catalyzed intermolecular hydrofunctionalization of allenes: Easy access to allylic structures via the selective formation of C–N, C–C, and C–O bonds", *Chem. Rev.* **120** (2020), pp. 13545–13598.

[4] J. L. Mascareñas, I. Varela and F. López, "Allenes and derivatives in gold(I)- and platinum(II)-catalyzed formal cycloadditions", *Acc. Chem. Res.* **53** (2019), pp. 465–479.

[5] M. Hourtoule and L. Miesch, "Construction of C–N and C–O bonds based on N-allenamide functionalization", *Org. Biomol. Chem.* **20** (2022), pp. 9069–9084.

[6] A. Suárez and G. C. Fu, "A straightforward and mild synthesis of functionalized 3-alkynoates", *Angew. Chem. Int. Ed.* **43** (2004), pp. 3580–3582.

[7] M. Hassink, X. Liu and J. M. Fox, "Copper-catalyzed synthesis of 2,4-disubstituted allenoates from α-diazoesters", *Org. Lett.* **13** (2011), pp. 2388–2391.

[8] C.-B. Liu, W. Meng, F. Li, S. Wang, J. Nie and J.-A. Ma, "A facile parallel synthesis of trifluoroethyl-substituted alkynes", *Angew. Chem. Int. Ed.* **51** (2012), pp. 6227–6230.

[9] J. Li, D. Ding, L. Liu and J. Sun, "CuI-catalyzed cross-coupling of diazoacetamide with terminal alkynes: an approach to synthesizing substituted dienamides and 3-butynamides", *RSC Adv.* **3** (2013), pp. 21260–21266.

[10] Y. Zheng, A. Perfetto, D. Luise, I. Ciofini and L. Miesch, "Direct synthesis of CF2H-substituted 2-amidofurans via copper-catalyzed addition of difluorinated diazoacetone to ynamides", *Org. Lett.* **23** (2021), pp. 5528–5532.

[11] Y. Zheng, B. Moegle, S. Ghosh, A. Perfetto, D. Luise, I. Ciofini and L. Miesch, "Copper-catalyzed synthesis of terminal vs. fluorine-substituted N-allenamides via addition of diazo compounds to terminal ynamides", *Chem. Eur. J.* **28** (2022), article no. e202103598.

[12] J.-P. Bégué and D. Bonnet-Delpon, *Bioorganic and Medicinal Chemistry of Fluorine*, Wiley: Hoboken, 2008.

[13] W. K. Hagmann, "The many roles for fluorine in medicinal chemistry", *J. Med. Chem.* **51** (2008), pp. 4359–4369.

[14] P. Kirsch, *Modern Fluoroorganic Chemistry: Synthesis Reactivity*, Wiley-VCH: Weinheim, 2013.

[15] C. Guissart, A. Dolbois, C. Tresse, S. Saint-Auret, G. Evano and N. Blanchard, "A straightforward entry to γ-trifluoromethylated allenamides and their synthetic applications", *Synlett* **27** (2016), pp. 2575–2580.

[16] Y. Zafrani, G. Sod-Moriah, D. Yeffet, et al., "CF2H, a functional group-dependent hydrogen-bond donor: Is it a more or less lipophilic bioisostere of OH, SH, and CH_3?", *J. Med. Chem.* **62** (2019), pp. 5628–5637.

[17] C. D. Sessler, M. Rahm, S. Becker, J. M. Goldberg, F. Wang and S. J. Lippard, "CF2H, a hydrogen bond donor", *J. Am. Chem. Soc.* **139** (2017), pp. 9325–9332.

[18] J. B. I. Sap, C. F. Meyer, N. J. W. Straathof, N. Iwumene, C. W. am Ende, A. A. Trabanco and V. Gouverneur, "Late-stage difluoromethylation: concepts, developments and perspective", *Chem. Soc. Rev.* **50** (2021), pp. 8214–8247.

[19] D. E. Yerien, S. Barata-Vallejo and A. Postigo, "Difluoromethylation reactions of organic compounds", *Chem. Eur. J.* **23** (2017), pp. 14676–14701.

[20] M.-C. Belhomme, T. Besset, T. Poisson and X. Pannecoucke, "Recent progress toward the introduction of functionalized difluoromethylated building blocks onto C(sp^2) and C(sp) centers", *Chem. Eur. J.* **21** (2015), pp. 12836–12865.

[21] A. M. Manzo, A. D. Perboni, G. Broggini and M. Rigamonti, "Gold-catalyzed intramolecular hydroamination of α-amino allenamides as a route to enantiopure 2-vinylimidazolidinones", *Tetrahedron Lett.* **50** (2009), pp. 4696–4699.

[22] E. M. Beccalli, A. Bernasconi, E. Borsini, G. Broggini, M. Rigamonti and G. Zecchi, "Tunable Pd-catalyzed cyclization of indole-2-carboxylic acid allenamides: carboamination vs microwave-assisted hydroamination", *J. Org. Chem.* **75** (2010), pp. 6923–6932.

[23] L. A. Perego, R. Blieck, A. Groué, F. Monnier, M. Taillefer, I. Ciofini and L. Grimaud, "Copper-catalyzed hydroamination of allenes: from mechanistic understanding to

methodology development", *ACS Catal.* **7** (2017), pp. 4253–4264.

[24] A. W. Hill, M. R. J. Elsegood and M. C. Kimber, "An intermolecular hydroamination of allenamides with arylamines catalyzed by cationic Au(I) salts", *J. Org. Chem.* **75** (2010), pp. 5406–5409.

[25] M. Hourtoule, Y. Zheng, A. Perfetto, D. Luise, I. Ciofini and L. Miesch, "One-pot anti-Michael regio- and stereoselective hydroamination of activated N-allenamides", *J. Org. Chem.* **87** (2022), pp. 5404–5411.

[26] W. Zhao, Z. Li and J. Sun, "A new strategy for efficient synthesis of medium and large ring lactones without high dilution or slow addition", *J. Am. Chem. Soc.* **135** (2013), pp. 4680–4683.

[27] T. Iwai, H. Okochi, H. Ito and M. Sawamura, "Construction of eight-membered carbocycles through gold catalysis with acetylene-tethered silyl enol ethers", *Angew. Chem. Int. Ed.* **52** (2013), pp. 4239–4242.

[28] W. Zhao, Z. Wang and J. Sun, "Synthesis of eight-membered lactones: Intermolecular [6+2] cyclization of amphoteric molecules with siloxy alkynes", *Angew. Chem. Int. Ed.* **51** (2012), pp. 6209–6213.

[29] G. M. Salituro, D. J. Pettibone, B. V. Clineschmidt, J. M. Williamson and D. L. Zink, "Potent, non-peptidic oxytocin receptor antagonists from a natural source", *Bioorg. Med. Chem. Lett.* **3** (1993), pp. 337–340.

[30] D. Brückner, F.-T. Hafner, V. Li, C. Schmeck, J. Telser, A. Vakalopoulos and G. Wirtz, "Dibenzodioxocinones—A new class of CETP inhibitors", *Bioorg. Med. Chem. Lett.* **15** (2005), pp. 3611–3614.

[31] L. S. Harikrishnan, H. J. Finlay, J. X. Qiao, et al., "Diphenylpyridylethanamine (DPPE) derivatives as cholesteryl ester transfer protein (CETP) inhibitors", *J. Med. Chem.* **55** (2012), pp. 6162–6175.

[32] C. F. Heinrich, I. Fabre and L. Miesch, "Silver-catalyzed 7-exo-dig cyclization of silylenolether-ynesulfonamides", *Angew. Chem. Int. Ed.* **55** (2016), pp. 5170–5174.

[33] Y. Xu, Q. Sun, T.-D. Tan, et al., "organocatalytic enantioselective conia-ene-type carbocyclization of ynamide cyclohexanones: Regiodivergent synthesis of morphans and normorphans", *Angew. Chem. Int. Ed.* **58** (2019), pp. 16252–16259.

[34] R. Lhermet, M. Ahmad, C. Hauduc, C. Fressigné, M. Durandetti and J. Maddaluno, "Intramolecular carbolithiation of heterosubstituted alkynes: an experimental and theoretical study", *Chem. Eur. J.* **21** (2015), pp. 8105–8111.

[35] S. Ghosh, Y. Zheng, D. Maccarone, F.-A. Korsaye, I. Ciofini and L. Miesch, "Triton B-promoted regioselective intramolecular addition of enolates to tethered ynamides for the construction of 8-membered O-heterocycles", *Org. Chem. Front.* **9** (2022), pp. 4057–4062.

[36] N. A. Meanwell, "Synopsis of some recent tactical application of bioisosteres in drug design", *J. Med. Chem.* **54** (2011), pp. 2529–2591.

[37] A. Matagne, D.-G. Margineanu, H. Potschka, W. Löscher, P. Michel, B. Kenda and H. Klitgaard, "Profile of the new pyrrolidone derivative seletracetam (ucb 44212) in animal models of epilepsy", *Eur. J. Pharmacol.* **614** (2009), pp. 30–37.

[38] J. I. Juncosa, K. Takaya, H. V. Le, et al., "Design and mechanism of (S)-3-amino-4-(difluoromethylenyl)cyclopent-1-ene-1-carboxylic acid, a highly potent γ-aminobutyric acid aminotransferase inactivator for the treatment of addiction", *J. Am. Chem. Soc.* **140** (2018), pp. 2151–2164.

[39] R. A. Altman, K. K. Sharma, L. G. Rajewski, P. C. Toren, M. J. Baltezor, M. Pal and S. N. Karad, "Tyr^1-ψ[(Z)CF=CH]-Gly^2 fluorinated peptidomimetic improves distribution and metabolism properties of Leu-dnkephalin", *ACS Chem. Neurosci.* **9** (2018), pp. 1735–1742.

[40] M. Hourtoule and L. Miesch, "Regio- and stereoselective addition to gem-difluorinated ene–ynamides: Access to stereodefined fluorinated dienes", *Org. Lett.* **24** (2022), pp. 3896–3900.

[41] B. Troegel and T. Lindel, "Microwave-assisted fluorination of 2-acylpyrroles: synthesis of fluorohymenidin", *Org. Lett.* **14** (2012), pp. 468–471.

[42] Z. Yang, Y. Liu, J. Ahn, et al., "Novel fluorinated pyrrolomycins as potent anti-staphylococcal biofilm agents: Design, synthesis, pharmacokinetics and antibacterial activities", *Eur. J. Med. Chem.* **124** (2016), pp. 129–137.

[43] K. Hiramatsu and H. Tamamura, "A mild method for the direct fluorination of pyrroles by using a lipophilic anionic phase-transfer catalyst", *Eur. J. Org. Chem.* **2016** (2016), pp. 3491–3494.

[44] M. Hourtoule and L. Miesch, "Silver-catalyzed domino reaction of CF_3-substituted N-allenamides with primary amines for the construction of 2-amido-5-fluoropyrroles", *Org. Lett.* **25** (2023), pp. 1727–1731.

[45] J. E. Lesch, *The First Miracle Drugs: How the Sulfa Drugs Transformed Medicine*, Oxford University Press: Oxford, 2007.

[46] S. Debnath and S. Mondal, "Sultams: recent syntheses and applications", *Eur. J. Org. Chem.* **2018** (2018), pp. 933–956.

[47] K. M. Gorman and A. Shahwan, "Sultiame revisited: treatment of refractory absence seizures", *Epileptic Disord.* **18** (2016), pp. 329–333.

[48] M. Inagaki, T. Tsuri, H. Jyoyama, et al., "Novel antiarthritic agents with 1, 2-isothiazolidine-1, 1-dioxide (γ-sultam) skeleton: cytokine suppressive dual inhibitors of cyclooxygenase-2 and 5-lipoxygenase", *J. Med. Chem.* **43** (2000), pp. 2040–2048.

[49] D. A. Claremon, L. Zhuang, K. Leftheris, C. M. Tice, Y. Ye, S. B. Singh and F. Immelsbach, Cyclic inhibitors of 11BETA-hydroxysteroid dehydrogenase 1, US patent, US 8592410B2, 2013.

[50] C. Gommenginger, Y. Zheng, D. Maccarone, I. Ciofini and L. Miesch, "TBAF-promoted carbanion-mediated sulfonamide cyclization of CF_3-substituted N-allenamides: an access to fluorinated γ-sultams", *Org. Chem. Front.* **10** (2023), pp. 4055–4060.

[51] C. Gommenginger, M. Hourtoule, M. Menghini and L. Miesch, "Metal free regio- and stereoselective semireduction of CF_3-substituted N-allenamides", *Org. Biomol. Chem.* **22** (2024), pp. 940–944.

[52] J. Fu, G. Zanoni, E. A. Anderson and X. Bi, "α-Substituted vinyl azides: an emerging functionalized alkene", *Chem. Soc. Rev.* **46** (2017), pp. 7208–7228.

[53] A. S. Carlson and J. J. Topczewski, “Allylic azides: synthesis, reactivity, and the Winstein rearrangement”, *Org. Biomol. Chem.* **17** (2019), pp. 4406–4429.

[54] D. Schutz, M. Hourtoule and L. Miesch, “Regio- and stereoselective azidation of activated N-allenamides: an entry to α, β, γ and δ-amido-azides”, *Org. Chem. Front.* **12** (2025), pp. 185–191.

[55] X. Zhong, J. Tan, J. Qiao, Y. Zhou, C. Lv, Z. Su, S. Dong and X. Feng, “Catalytic asymmetric synthesis of spirocyclobutyl oxindoles and beyond via [2+2] cycloaddition and sequential transformations”, *Chem. Sci.* **12** (2021), pp. 9991–9997.

[56] Y. Ning, Q. Ji, P. Liao, E. A. Anderson and X. Bi, “Silver-catalyzed stereoselective aminosulfonylation of alkynes”, *Angew. Chem. Int. Ed.* **56** (2017), pp. 13805–13808.

[57] R.-R. Liu, J.-P. Hu, J.-J. Hong, C.-J. Lu, J.-R. Gao and Y.-X. Jia, “Enantioselective [2+2] cycloaddition of N-allenamides with cyclic N-sulfonylketimines: access to polysubstituted azetidines bearing quaternary stereocenters”, *Chem. Sci.* **8** (2017), pp. 2811–2815.

[58] M. Chiminelli, A. Serafino, D. Ruggeri, L. Marchiò, F. Bigi, R. Maggi, M. Malacria and G. Maestri, “Visible-light promoted intramolecular para-cycloadditions on simple aromatics”, *Angew. Chem. Int. Ed.* **62** (2023), article no. e202216817.

[59] A. Serafino, M. Chiminelli, D. Balestri, L. Marchiò, F. Bigi, R. Maggi, M. Malacria and G. Maestri, “Dimerizing cascades of enallenamides reveal the visible-light-promoted activation of cumulated C–C double bonds”, *Chem. Sci.* **13** (2022), pp. 2632–2639.

[60] J.-D. Guo, F.-A. Korsaye, D. Schutz, I. Ciofini and L. Miesch, “Photocatalyst-free, visible-light-induced regio- and stereoselective synthesis of phosphorylated enamines from N-allenamides via [1,3]-sulfonyl shift at room temperature”, *Chem. Sci.* **15** (2024), pp. 17962–17970.

ACADÉMIE
DES SCIENCES
INSTITUT DE FRANCE

Comptes Rendus. Chimie
2025, Vol. 28, p. 831-847
https://doi.org/10.5802/crchim.421

Account

Exploring crystal-state vs. solution-based reactivity of donor–acceptor cyclopropanes

Michel Giorgi [a] **and Gaëlle Chouraqui** [*, b]

[a] Aix Marseille Univ, CNRS, Centrale Med, FSCM, 13397 Marseille, France

[b] Aix Marseille Univ, CNRS, Centrale Med, ISM2, 13397 Marseille, France

E-mails: michel.giorgi@univ-amu.fr (M. Giorgi), gaelle.chouraqui@univ-amu.fr (G. Chouraqui)

This account is dedicated to my mentor, Dr. Jean-Luc Parrain, whose intellectual integrity and scientific rigor have been a source of inspiration throughout my career.

Abstract. Donor–acceptor cyclopropanes (DACs) are highly reactive building blocks in organic synthesis due to their combination of electronic bond polarization and ring strain. This work explores three modes of activation, thermal, photochemical, and catalytic, applied to the same vinologous DAC precursor, both in solution and in the solid state.

In solution, thermal activation enables the regio- and stereoselective formation of eight-membered carbocyclic frameworks, without the need for catalysts or reagents, thanks to a rational precursor design based on electronic and steric considerations. Depending on the nature of the substituents, either a concerted or a stepwise mechanism is involved. Additionally, and still in solution, a Lewis-acid-promoted cascade reaction leads to benzocyclobutene scaffolds, with complete transfer of stereochemistry into the regioselectivity of the final product.

In the solid state, exposure to X-ray radiation induces a rare single-crystal-to-single-crystal photopolymerization, governed by precise molecular preorganization and a degree of crystal lattice flexibility.

Overall, this study highlights how DAC reactivity is modulated by both the mode of activation and the physical environment, thereby offering new strategies for the construction of complex molecules.

Keywords. Donor–acceptor cyclopropane, Rearrangement, Topochemical polymerization, Benzocyclobutene, Medium-sized ring.

Funding. Agence Nationale de la Recherche (project ANR-18-CE07-0005/Benz), French Ministère de l'Enseignement Supérieur et de la Recherche (MESR, Aix-Marseille Université (AMU), Centre National de la Recherche Scientifique (CNRS), Centrale Méditerranée.

Note. Article submitted by invitation.

Manuscript received 15 July 2025, revised 2 September 2025 and 3 September 2025, accepted 8 September 2025.

1. Introduction

Donor–acceptor cyclopropanes (DACs) are highly versatile reactive intermediates in organic synthesis, thanks to their unique combination of electronic polarization and ring strain (for seminal reports on DACs, see [1–5]). These molecules feature electron-donating and electron-withdrawing groups on adjacent carbon atoms, creating a pronounced push–pull effect that facilitates selective bond cleavage and rearrangements. At the same time, the significant strain inherent to the cyclopropane ring (~27.5 kcal/mol) contributes a powerful driving force for a variety of transformations. It is precisely the synergy between these two features, electronic

* Corresponding author

polarization and ring strain, that underpins the distinctive reactivity of DACs (for kinetic studies on the reactivity of DACs, see [6]). Consequently, they have emerged as valuable synthetic building blocks for constructing complex carbocyclic and heterocyclic frameworks, enabling access to diverse molecular architectures with high efficiency and selectivity (for selected reviews on DACs chemistry, see [7–29]; for an example on total synthesis, see [30]).

While numerous DAC-mediated transformations have been developed, the influence of the reaction environment on their reactivity remains an area of investigation. DAC activation can occur through thermal, catalytic, or photochemical methods, each offering distinct benefits and presenting specific challenges (for different modes of activation of DACs, see [31–43]).

In solution-phase reactions, factors such as solvent polarity, thermal input, and catalytic systems play a central role in governing reactivity and selectivity. In contrast, crystal-state transformations (for seminal reports on topochemical polymerization, see [44–47]; for examples of topochemical polymerization, see for instance [48–54]) introduce unique considerations, including crystal-packing effects, molecular orientation, and topochemical restrictions, which can profoundly influence reaction pathways [55–57]. A deeper understanding of how these environmental variables impact selectivity and product distribution is essential to fully harness the synthetic potential of DAC chemistry.

This account critically examines three distinct activation modes, thermal, catalytic, and photochemical, for our in-house synthesized DACs, studied across two different physical states (solution and solid). Each pathway reveals unique aspects of DAC reactivity and selectivity: thermal synthesis of eight-membered rings (solution phase), rearrangement to benzocyclobutenes (solution phase), and crystal-to-crystal photopolymerization (solid state).

By comparing these three pathways, this work aims to identify key mechanistic differences, evaluate their scope and limitations, and illustrate how both mode of activation and reaction medium contribute to the outcome. Ultimately, this comparative approach offers insights into the interplay between molecular design, reaction conditions, and functional outcomes in DAC chemistry. By bridging the gap between solution-phase and crystal-state reactivity, this study provides insights into how reaction environment dictates selectivity and efficiency in DAC transformations.

2. Solution-phase reactivity of DACs

2.1. *Solution-phase synthesis of eight-membered rings*

This section summarizes the results recently reported by our group, in which a thermally driven rearrangement of bis-cyclopropyl DACs afforded eight-membered carbocyclic systems under catalyst-free conditions [58].

Medium-sized functionalized cycles (eight- to eleven-membered rings) occupy a unique chemical space [59–66]. Their intermediate size imparts conformational rigidity and distinct three-dimensional geometry that can sometimes enhance biological activity by improving binding affinity, oral bioavailability, and/or membrane permeability compared to both acyclic analogs and rings of other sizes [62,67–73]. Despite these advantages, medium-sized rings remain underexplored in drug discovery programs, largely due to well-known kinetic and thermodynamic barriers to their synthesis.

From a synthetic standpoint, medium-sized rings are particularly difficult to access via classical cyclization of linear precursors, which is often entropically disfavored. Moreover, their ring size is small enough to experience destabilizing transannular strain. As such, innovative synthetic strategies are required to overcome these inherent limitations [74–78].

One promising approach involves ring-expansion reactions, particularly starting from small strained rings like cyclopropanes [79–88]. The substantial release of ring strain (~27.5 kcal·mol^{-1}) offers a thermodynamic driving force, while appropriate substitution can be employed to guide selectivity.

Since divinylcyclopropanes **1** undergo Cope-type rearrangements to form seven-membered rings **2** [89–93], and given that cyclopropanes can exhibit C–C double bond character[1], we aimed to extend

[1] In cyclopropane, the internal bond angles are forced to be 60°, far from the ideal 109° angle, causing severe angle strain. To relieve strain, the carbon atoms in cyclopropane adjust their hybridization toward more p-character (closer to sp^2). This gives the C–C bonds some characteristics of π-bonds, similar to those in alkenes.

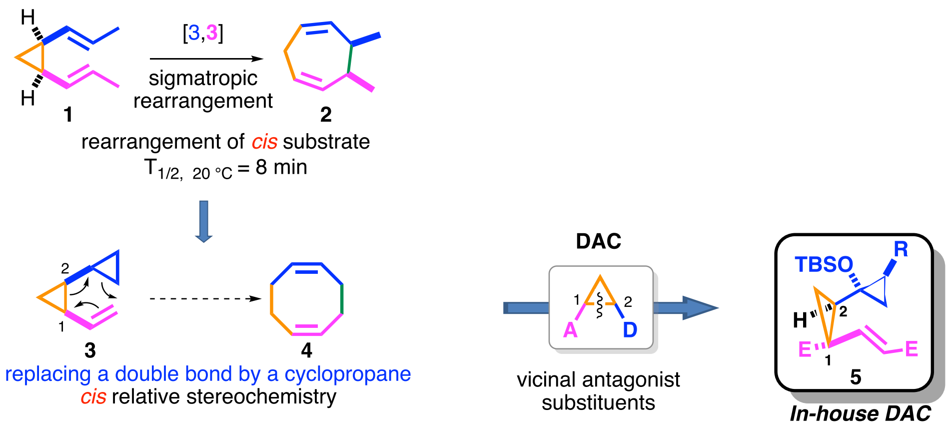

Scheme 1. Design of a strategy.

this strategy by replacing one of the alkene units with a cyclopropyl moiety (see compound **3**, Scheme 1). This modification would provide the additional carbon atom needed to access eight-membered carbocyclic frameworks.

It is also worth noting that, for this rearrangement to occur at room temperature or even below, a *cis* relationship between the two olefin partners is necessary (see compound **1**, Scheme 1) [94]. Therefore, a *cis* relationship at the C1 and C2 positions should be considered a prerequisite in the design of precursor **3**.

At the heart of this approach lies the donor–acceptor cyclopropane (DAC), a class of reactive intermediates known for their versatility (see Introduction). In our design, a *gem*-ester/vinyl ester motif was employed as the electron-withdrawing component to promote C1–C2 bond cleavage (see compound **5**). The donor moiety consisted of a cyclopropyl group, whose donor reactivity has been previously demonstrated [95–101]. To further enhance donor ability and facilitate rearrangement, an alkoxy substituent was introduced, inspired by the known behavior of vinyl cyclopropanols [102–106], (for reviews, see [107,108]).

This design merges strain-release strategies with sigmatropic rearrangement logic, as illustrated in Scheme 1. From a structural perspective, the resulting precursor **5** resembles a modified Cope system, in which one π-bond is replaced by a bent reactive cyclopropane [40]. The synthesis of biscyclopropane **5a**, obtained in only four steps, relies on a classical Rh(II)-mediated cyclopropanation reaction between a vinylcyclopropane and a di-acceptor diazo derivative (Scheme 2). Notably, after three days of reflux in xylene, the designed DAC **5a** successfully delivered the expected eight membered ring **6a** in 83% yield.

With this platform in hand, we quickly recognized that the nature of the substituent on the donor portion of the molecule (R in biscyclopropanes **5**, Scheme 1) significantly influences the reaction outcome, revealing the existence of two distinct mechanistic pathways.

Aryl-substituted biscyclopropanes **5b–j** underwent thermal cyclization at 100 °C to afford the corresponding eight-membered Z-enol ethers **7**, which were subsequently hydrolyzed to ketones **6b–j** using Dowex H^+ cation-exchange resin (Scheme 3).

Electron-rich, electron-poor, and *ortho*-, *meta*-, or *para*-substituted aryl groups all participated successfully in the cyclization (yields ranging from 54 to 92%), furnishing mixtures of *cis*-/*trans*-diastereomers (50:50 < d.r. < 95:5) but consistently yielding the same β-regioisomer of ketones **6b–j**. These results suggest that, in aryl-substituted systems **5b–j**, the C6–C8 bond is cleaved selectively during the rearrangement.

In contrast, the outcome of the cyclization for alkyl-substituted biscyclopropanes displayed a strong dependence on both the size of the R groups (Scheme 1) and the nature of the starting diastereomers **5k–p** and **5n–p′** (Scheme 4). In these cases, a temperature of 160 °C was required for the

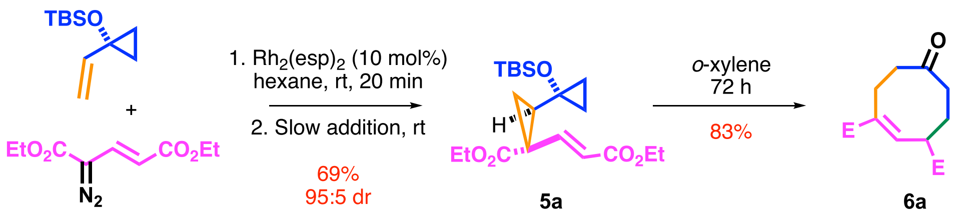

Scheme 2. Proof of concept.

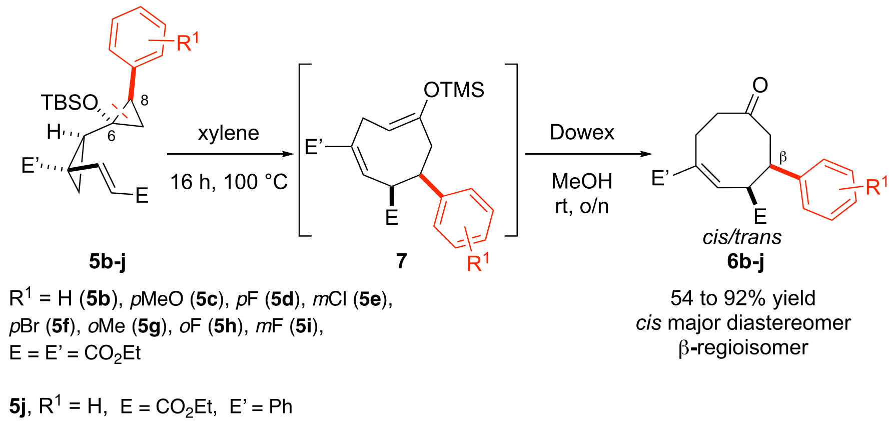

Scheme 3. Exploring the aryl scope of the Cope-type rearrangement.

reaction to proceed. For secondary alkyl groups **5k–m** (R = *i*Pr, Cy), the reactions proceeded with high regio- and diastereoselectivity (yields 70–99%, d.r. > 95:5), indicating a preferential cleavage of the C6–C7 bond, now favoring the formation of the α-regioisomer. In the case of smaller alkyl groups (e.g., R = Me, *n*-Hex), starting from a mixture of diastereomers **5n–p** and **5n–p′**, the reaction afforded mixtures of regioisomers **6n–p** and **6n–p′**, while diastereoselectivity remained excellent (yields 54–90%; d.r. > 95:5, 55:45 < α/β-regioisomer < 68:32). We showed that the diastereomeric identity of the starting material is fully retained in the regioisomeric outcome, i.e., each diastereomer yields a single regioisomer.

These results prompted a theoretical investigation using density functional theory (DFT) to clarify the origin of the observed selectivity. For both methyl **6n** and **6n′**, and phenyl **6b** derivatives, detailed energy profiles were established.

Computational analysis supported a concerted but asynchronous mechanism for both diastereomers of methyl derivatives **6n** and **6n′**, initiated by the opening of the central cyclopropane ring (Figure 1). In the case of methyl derivative **6n′** (Figure 1, right), two atropisomers of the enol ether (**A1** and **A2**) were identified. **A2** was found to exist in two conformations that differed by the equatorial or axial orientation of an ester group (see $\mathbf{rot_{A2-1}}$). The **A1**/**A2** ratio depends on the reaction temperature: **A1** was favored at 160 °C, while **A2** predominated at 120 °C. This axial chirality arose from restricted rotation around the C2–C3 bond. Computational data indicated that **A2** corresponds to the kinetic product, formed more rapidly and preferentially at lower temperature, whereas **A1** was the thermodynamic one (*Trans*-cyclooctenes are known to display atropisomerism. The transient *trans*-enol ether in a 1,5- or 1,3-cyclo-octadiene has been reported before but as far as our knowledge goes, never in the 1,4 cyclooctadiene case [109–113]), (for detailed computational studies on (*E*,*Z*)-cycloocta-1,4-diene conformers see [114]).

For phenyl derivative **6b**, the mechanism diverged. We proposed a stepwise biradical pathway involving the ring opening of the two cyclopropane moieties (Figure 2, Intermediate **I**), and low-barrier conformational changes (Figure 2, intermediates **II** and **III**) before ring closure. This pathway

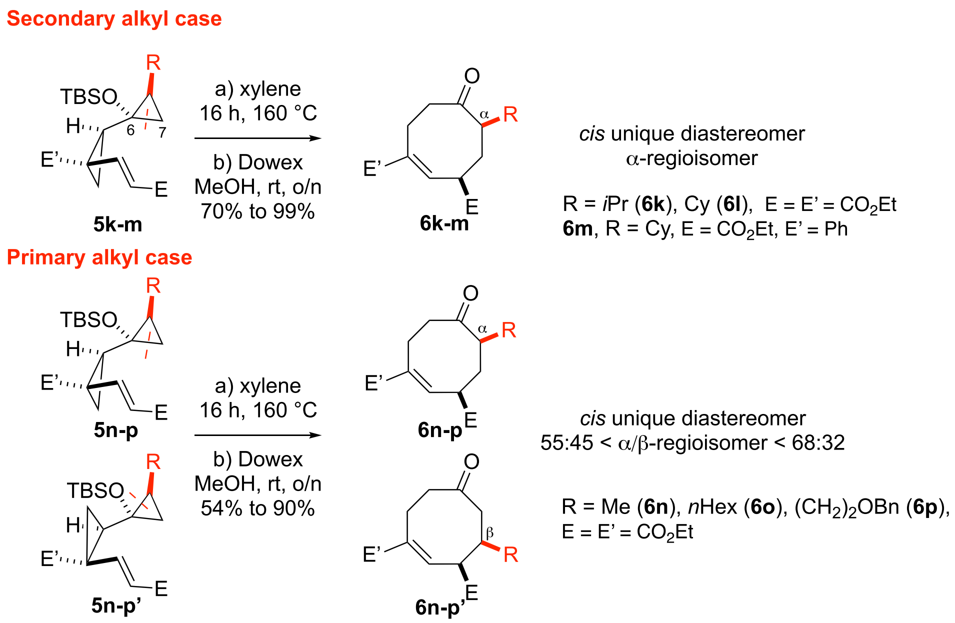

Scheme 4. Exploring the alkyl scope of the rearrangement.

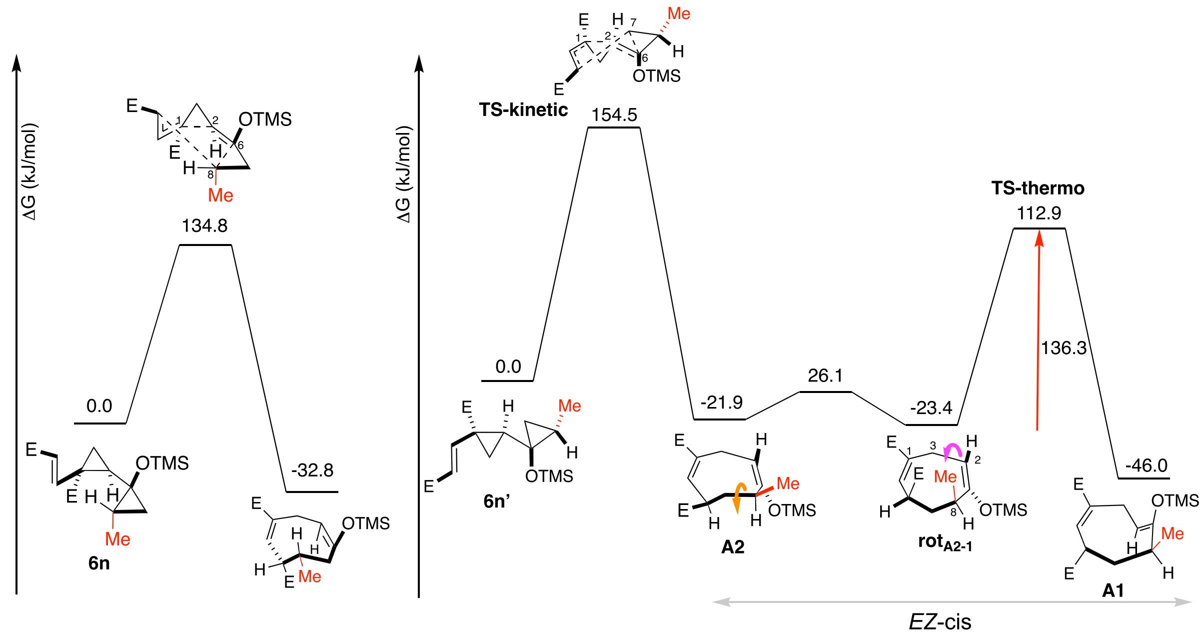

Figure 1. Mechanistic study of the alkyl pathway.

rationalized both the observed regioselectivity and diastereomeric mixtures.

In both cases, calculations show no feasible route to the *E*-configured enol ethers, consistently with experimental observations.

Through the rational design of DAC-based precursors, we have developed a robust and versatile method for constructing eight-membered carbocyclic systems under simple thermal conditions. This reaction achieved key transformations in a single

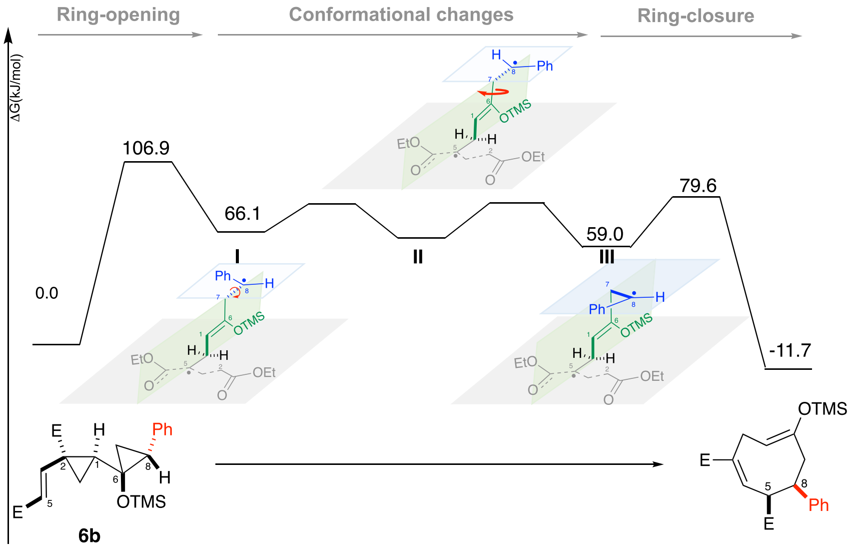

Figure 2. Mechanistic study of the phenyl pathway.

operation: ring opening of two cyclopropane moieties, formation of a new C–C bond, and generation of a medium-sized ring, all achieved in a catalyst-free, thermally driven process.

The transformation is regio- and stereoselective, and it accommodates a range of substituents. Two mechanistic pathways were identified, a concerted asynchronous route and a biradical stepwise one, depending on the electronic and steric nature of the donor part of the molecule.

This work demonstrates the powerful synergy between molecular design, experimental validation, and computational insight, offering new opportunities for the efficient and selective synthesis of challenging medium-sized ring systems.

2.2. *Rearrangement of DACs to benzocyclobutenes*

As part of our ongoing investigation into the reactivity of our DAC frameworks, we identified an unanticipated rearrangement pathway leading to the formation of benzocyclobutene derivatives [115].

Benzocyclobutenes are valuable synthetic species (for reviews on benzocyclobutenes, see [116–118]), notably due to their ability to generate *o*-quinodimethane (*o*QDM) intermediates [119] under thermal or photochemical conditions. They play a key role in natural product synthesis, medicinal chemistry [120–128], and polymer/material science [129–136]. While numerous synthetic methods have been reported (for seminal reports, see [137]; for selected examples, see [116–118,138–141]), a general and broadly applicable approach remains challenging. We believed that we could contribute to this effort by offering a complementary strategy.

Remarkably, this transformation originates from the same DAC precursors **5** that we previously employed in our annulation cascade strategy. In the presence of a fluoride anion, a skeletal reorganization occurred, but the product outcome differed significantly from our initial expectations. Upon refluxing DAC precursor **5a** (R = H) in THF for 16 h in the presence of a fluoride source (TBAF), benzocyclobutene product **8a** was obtained in 58% yield (Scheme 5).

Mechanistically, the reaction likely begins with fluoride-mediated deprotection of the tertiary alcohol, generating alkoxide intermediate **B**, which could undergo a hetero-Michael addition to the neighboring vinyl ester. Subsequent retro-Michael fragmentation of moiety **C** could induce ring expansion to a four-membered ring ketone **D**, reminiscent of known rearrangement of 1-silyloxy-1-vinylcyclopropanes. The resulting ketone **D** could undergo an intramolecular aldol-type condensation to form bicyclic intermediate **E**, followed by elimination and aromatization to yield the final benzocyclobutene scaffold **8a**. Crucially, the proposed mechanistic sequence

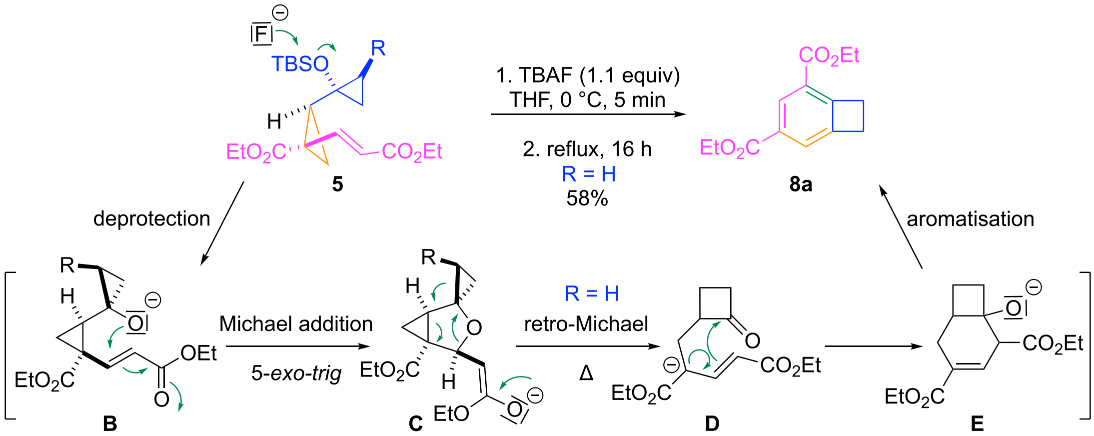

Scheme 5. Rearrangement of the DAC precursor in the presence of TBAF.

is not purely hypothetical. Each intermediate along this pathway was successfully isolated and fully characterized. These experimental findings provide direct validation for the stepwise mechanism.

However, this fluoride-mediated protocol showed limitations. When a substituent was present on the donor portion of DAC **5** (R ≠ H), the reaction either stalled at the formation of tetrahydrofuran **9k** (R = *i*Pr; 54% yield) (Scheme 6) or led to complete degradation of **5b** (R = Ph).

In response, we developed an alternative two-step route. Initial exposure of the precursor **5a** to MgI_2, used as a mild Lewis acid, rapidly (10 min only) triggered the formation of bicyclic product **10a** by a ring-expansion/ring-opening/ring-closure domino sequence (Scheme 7). This intermediate could then undergo a mild base-induced transetherification/elimination/aromatization step, ultimately affording the desired benzocyclobutene **8a** in 59% yield [142].

This sequence tolerated a range of substituents (R = primary and secondary alkyl, aryl) and could be applied to a broader set of substrates. As in the previous approach, regioselectivity was controlled by the relative configuration of the starting diastereomer.

For alkyl derivatives, each diastereoisomer led exclusively to a distinct regioisomer. For instance, compound **5n** (R = Me) underwent C6–C7 cleavage to furnish regioisomer **8a** (R = Me), while its diastereomer **5n**′ (R = Me) followed an alternate bond reorganization route (C6–C8 bond cleavage), yielding regioisomer **8a**′ (R = Me) (Scheme 8). This strict correspondence between initial stereochemistry and final regioisomer demonstrates a complete transfer of diastereoselectivity into regioselectivity, offering rare predictive control over the product distribution.

The nature of the substituent profoundly impacted the regioselectivity of the DAC ring opening. Aryl-substituted analogs consistently favored C6–C8 cleavage (Scheme 9).

These divergent behaviors echo isolated reports in related cyclopropyl ether systems [58,143] and also other cyclizations [144]. A concerted mechanism likely governs the alkyl series, minimizing steric repulsion in the transition state, whereas the aryl series appears to favor a stepwise pathway, enabled by stabilization of a benzyl carbocation intermediate. These findings demonstrate how fine-tuning the electronic profile of DACs can serve as a powerful tool to control reactivity and regioselectivity across mechanistically distinct pathways.

The elegance of this approach lies in its conciseness, a two-step sequence encompassing six elementary transformations, all initiated from a simple yet functionally rich cyclopropane framework. The method offers a direct and efficient route to benzocyclobutene scaffolds, with complete regio- and diastereocontrol, and compatible with a range of functional groups.

Taken together, these results not only unveil a new facet of DAC reactivity but also underscore the power of combining ring strain, stereoelectronic effects, and tailored reaction conditions to access otherwise challenging molecular architectures.

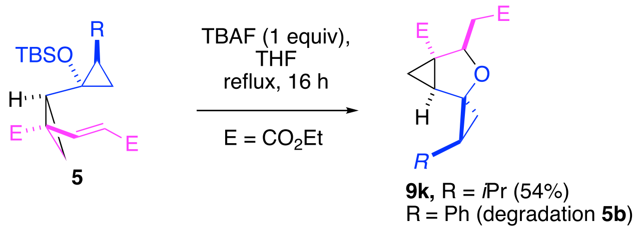

Scheme 6. A very limited scope.

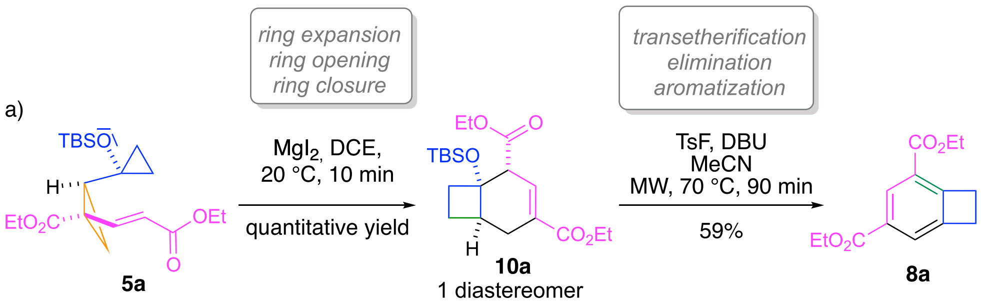

Scheme 7. An alternative two-step route.

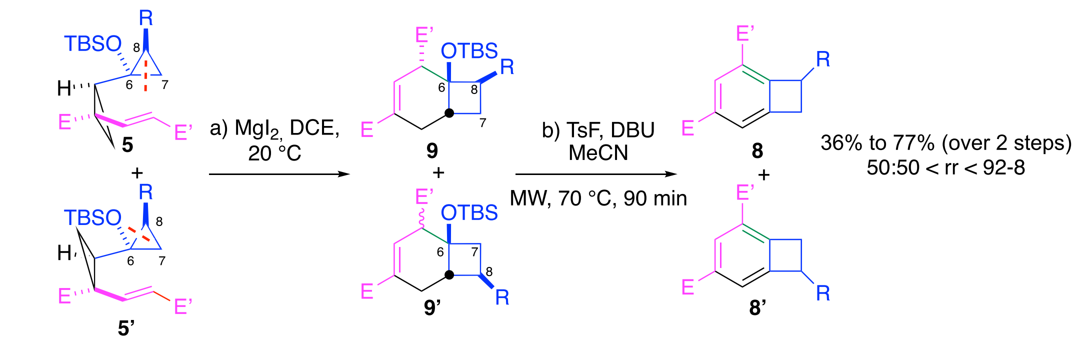

R = *i*Pr (**5k**), Cy (**5l/5l'**), Me (**5n/5n'**), *n*-Hex (**5o/5o'**), $CH_2(OBn)$ (**5p/5p'**), E = E' = CO_2Et.

Scheme 8. Alkyl derivatives—total transfer of diastereoselectivity into the regioselectivity.

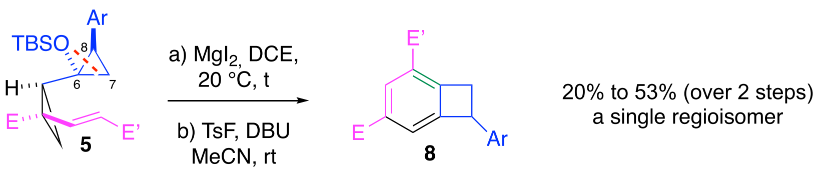

R = Ph (**5b**), *p*MeOPh (**5c**), *p*FPh (**5d**), *o*Tol (**5g**), E = E' = CO_2Et.

Scheme 9. Aryl derivatives—the opposite regioisomer.

3. Solid-state photopolymerization of donor–acceptor cyclopropanes

In our recent investigations of DACs, we identified an unexpected reactivity pathway occurring in the solid state, distinct from the thermal behavior observed in solution. While characterizing vinyl bis-cyclopropane compound **6a** (R^1 = *p*-F) by single-crystal X-ray diffraction (SCXRD), we unexpectedly found that even a short exposure (10 min) to Cu radiation triggered a notable transformation of the crystal packing, leading to the emergence of a layered structure composed of both intact monomers and newly generated polymer chains (Scheme 10, left side) [145]. Structural analysis indicated that polymerization proceeded via ring opening of both cyclopropane units, leading to covalent linkage between benzylic (C8) and vinyl carbons (C14) of adjacent monomers. The resulting polymeric chain **10** (Scheme 10, right side) displayed two non-conjugated Z-alkenes and two stereocenters per repeating unit, features difficult to access via conventional solution-phase methods.

To gain structural insight into the pre-reactive state of the crystal, we performed SCXRD analysis at 150 K, a temperature deliberately chosen to lie below the reaction threshold. Under these conditions, the system remains unreactive, allowing direct observation of the intact monomer. The structure revealed the presence of two closely related conformers, ***p*-F-m** and ***p*-F-p**, coexisting in the asymmetric unit (Scheme 11). These conformers were nearly superimposable, differing primarily by an approximate 65° rotation around the terminal ethyl group of the vinyl ester (Scheme 11, right side). Notably, only the ***p*-F-p** conformer adopted a spatial arrangement favorable for topochemical polymerization, with a distance of 4.324 Å between the reactive carbons C8 and C14i, allowing head-to-tail propagation along a crystallographic axis (Schmidt's rules say a distance < 4.2 Å is needed between reactive site for a topochemical reaction to occur [146] and see reference [46] but this can be overcome if there is enough void space in the crystal to allow molecular movement [147,148]). Due to the centrosymmetric packing of the crystal, polymer growth proceeds in a racemic fashion. This structural snapshot illustrates how small conformational variations and crystal symmetry elements govern the selectivity and outcome of solid-state transformations.

To explore the generality of the observed solid-state reactivity, we extended our study to a broader set of DAC derivatives. Among the compounds tested, only the *para*-chlorobenzene ***p*-Cl** and *meta*-fluorobenzene ***m*-F** analogs exhibited molecular arrangements compatible with topochemical reactivity. Measurements by SCXRD performed at 150 K revealed that each of these derivatives crystallized with a single conformer per asymmetric unit.

The ***p*-Cl** derivative underwent a temperature-dependent transformation that could be resolved into a series of well-defined intermediate states, ultimately leading to a topochemical polymerization. Upon warming to 250 K, two partially reacted species were detected in a 2:1 occupancy ratio. In the dominant species, the inner C–C bond of one cyclopropane stretched to 1.713(9) Å. In the minor species, full ring opening of the second cyclopropane was observed. This transformation progressed further at 270 K, with the reactive bond reaching 1.87(1) Å. These structural snapshots suggest a possible manifestation of push–pull polarization, as evidenced by progressive bond elongation prior to full cleavage. While this behavior aligns with expectations for DAC systems, it must be interpreted cautiously, since crystallographic data alone do not offer direct insight into electronic structure [149]. By 290 K, the crystals did not diffract anymore, reflecting the loss of crystalline integrity. In contrast, the ***m*-F** analog, despite its favorable preorganization, showed no signs of reactivity at any measurement temperature.

Molecular dynamics (MD) simulations revealed that favorable alignment of reactive centers must be coupled with sufficient molecular motion to allow bond reorganization. For ***p*-F**, such motions, especially perpendicular to the polymerization axis, were accommodated without compromising lattice coherence. In the case of ***p*-Cl**, movement was largely restricted to the direction of polymerization, resulting in mechanical stress and crystal collapse during the polymer growth. Despite its favorable packing and geometric preorganization, ***m*-F** remained unreactive. This lack of reactivity can be attributed to an insufficient number of internal degrees of freedom. There was not enough conformational flexibility to accommodate the structural rearrangements required for polymerization. Interestingly, the non-reactive conformers in ***p*-F** played a stabilizing role, possibly acting as molecular templates [150,151].

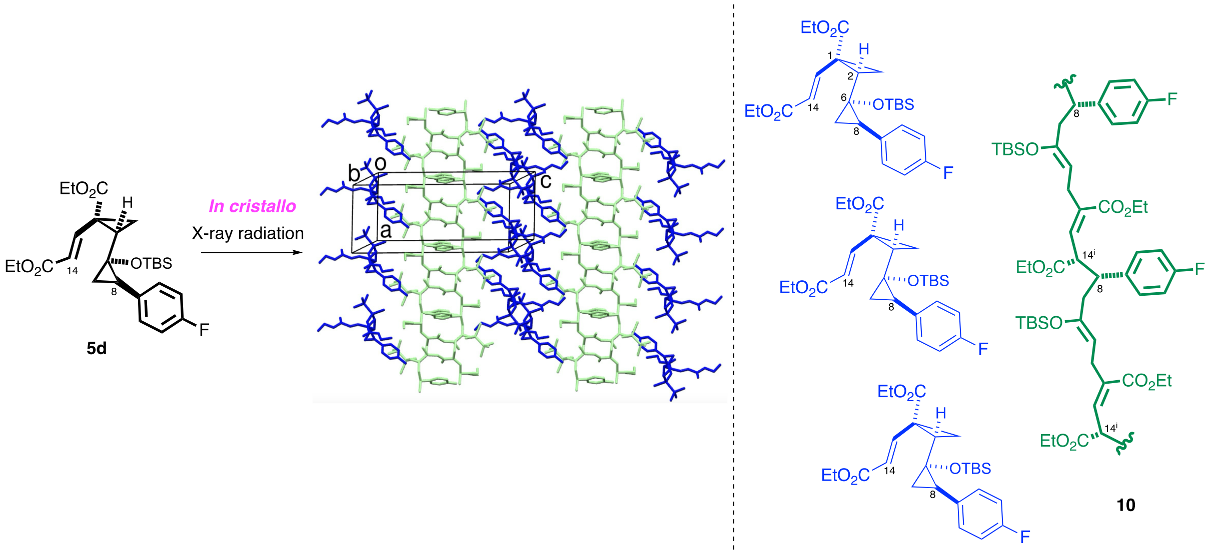

Scheme 10. Topochemical polymerization.

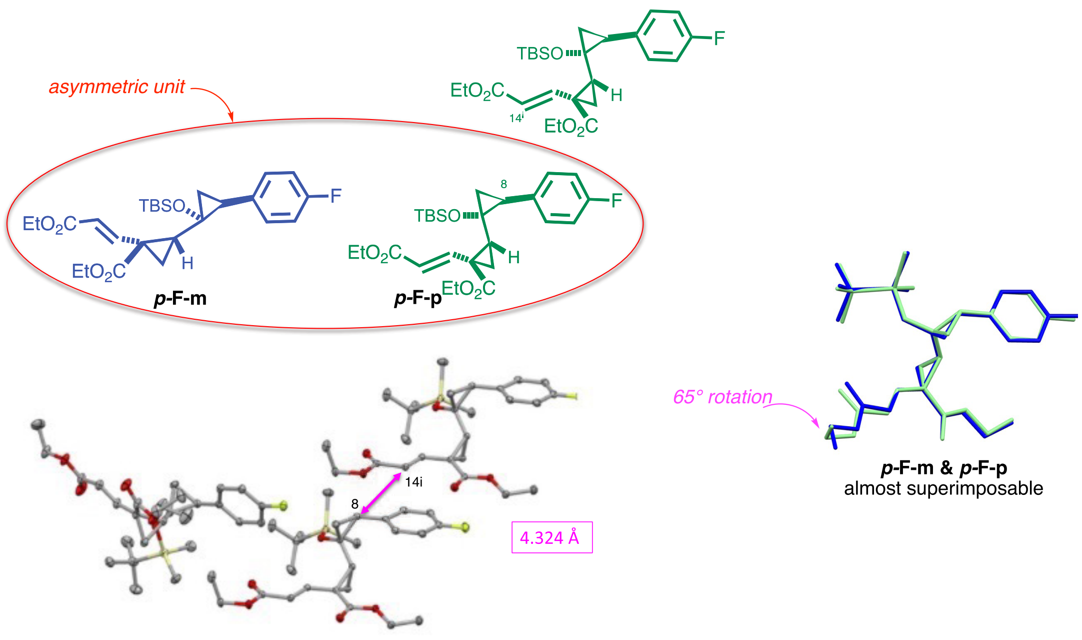

Scheme 11. Initial crystal packing of the monomer.

This divergence underscored the importance of not only geometric alignment, but also conformational flexibility and packing plasticity in enabling productive reactivity.

Collectively, these observations demonstrated that the crystalline environment acts as a true reaction variable, comparable to classical parameters such as temperature or pressure. It not only influences reaction rates, but also determines mechanistic pathways and enables access to product architectures that remain elusive in solution [55,56,152–156]. The topochemical constraints observed in DAC systems reveal a distinctive mode of reactivity, intimately tied to molecular packing and conformational freedom.

The combined use of SCXRD and molecular dynamics simulations [157–159][2] provided an atomically resolved view of this rare single-crystal-to-single-crystal polymerization. This approach allowed us to capture the interplay between molecular orientation, symmetry, and lattice plasticity with unprecedented clarity. Although predicting whether a given reaction will proceed in the solid state remains challenging, the introduction of ring strain and, more broadly, of built-in structural tension that seeks release, emerges as a promising strategy to bias systems toward reactivity under topochemical constraints.

4. Critical discussion

Beyond their distinct activation conditions, the contrasting reactivity profiles of donor–acceptor cyclopropanes (DACs) in solution and in the solid state emphasize the structural versatility and mechanistic richness in this class of compounds. In solution, DACs undergo cascade transformations such as ring expansion, rearrangement, and condensation, typically under mild thermal or basic conditions and often without the need for additional catalysts. These processes are largely governed by the intrinsic electronic polarization of the substrate and, critically, by the release of ring strain embedded in the cyclopropane core. This strain allows complex bond reorganizations to occur efficiently and selectively.

In the solid state, DACs display a fundamentally different mode of reactivity. The transformation is constrained by crystal packing, requiring precise preorganization of reactive units and sufficient lattice flexibility. Under these topochemical conditions, polymerization or bond cleavage occurs only when the spatial arrangement is favorable. Yet here too, ring strain plays a central role—facilitating the reaction by providing a thermodynamic incentive for bond rupture, even in the absence of molecular mobility. Although predicting whether a given transformation will proceed in the solid state remains inherently challenging, the deliberate incorporation of strain—and more generally, of structural tension that seeks release—emerges as a rational design element to bias systems toward productive reactivity.

However, a key limitation of this approach lies in its lack of scalability. To date, the solid-state transformations that we observe remain confined to single-crystal-to-single-crystal conversions, which require highly ordered materials and low-throughput handling. We have not yet identified operationally simple or bench-stable conditions that would enable these reactions to be performed in batch or on preparative scale. As such, while mechanistically instructive and structurally unique, the synthetic utility of these transformations is currently constrained by practical considerations.

Importantly, the reactivity principles traditionally associated with vinyl-cyclopropanol derivatives—well-known for undergoing ring opening and rearrangement—can be effectively transposed to biscyclopropanol systems. These more complex frameworks preserve the electronic and conformational features of their monosubstituted analogs but introduce new degrees of freedom and stereochemical control. In this context, the complete transfer of stereochemical information into regioselectivity, where each diastereomer leads unambiguously to a specific regioisomer, highlights the importance of geometric predisposition in steering divergent mechanistic pathways. This observation underscores how subtle differences in molecular orientation in strained systems can dictate not only product identity but also reaction trajectory.

Together, these insights consolidate DACs as uniquely powerful platforms for controlling molecular reorganization across environments. Whether in solution or in the solid state, they provide rare access to structurally complex, stereochemically defined products through mechanistically distinct yet conceptually unified strategies.

5. Conclusion and future directions

Taken together, these studies emphasize the synthetic potential of donor–acceptor cyclopropanes as highly versatile platforms for molecular construction. Whether activated in solution through

[2]To the best of our knowledge, molecular dynamics (MD) has rarely been used to study crystal-to-crystal transformations in organic systems.

well-orchestrated domino sequences or engaged in solid-state transformations dictated by lattice constraints, DACs enable access to diverse and otherwise challenging structural motifs. The capacity to translate reactivity patterns, such as ring expansion or rearrangement, from simpler vinyl-cyclopropanol systems to more elaborate bis-cyclopropane derivatives, further highlights the adaptability of this class of compounds. Beyond their synthetic utility, these transformations offer rare mechanistic insights into the interplay between strain release, stereoelectronic effects, and medium-dependent selectivity. This duality of behavior not only broadens the scope of DAC chemistry but also opens new avenues for rational design of reactivity, both in and beyond conventional solution-phase settings.

Acknowledgments

I would like to express my gratitude to my coworkers and collaborators who participated in this project: Dr. Bohdan Biletskyi, Dr. Sara Chentouf, Dr. Pierre Colonna, Professor Laurent Commeiras, Dr. Maxime Dousset, Dr. Virginie Héran, Dr. Kévin Masson, Dr. Jean-Valère Naubron, Dr. Paola Nava and Dr. Fabio Ziarelli. This work was supported by the computing facilities of the "Centre Régional de Compétences en Modélisation Moléculaire de Marseille" (CRCMM).

Declaration of interests

The authors do not work for, advise, own shares in, or receive funds from any organization that could benefit from this article, and have declared no affiliations other than their research organizations.

Funding

We gratefully acknowledge the Agence Nationale de la Recherche (project ANR-18-CE07-0005/Benz) for its financial support. We thank the French Ministère de l'Enseignement Supérieur et de la Recherche (MESR) for PhD fellowships. We also acknowledge institutional financial support from Aix-Marseille Université (AMU), the Centre National de la Recherche Scientifique (CNRS), and Centrale Méditerranée.

References

[1] E. Wenkert, M. E. Alonso, B. Buckwalter and K. J. A. Chou, "A method of synthesis of .beta.- methylfurans and .alpha.-methylene and .beta.-methylene .gamma.-lactones. Two menthofuran syntheses", *J. Am. Chem. Soc.* **99** (1977), pp. 4778–4782.

[2] H.-U. Reissig and E. Hirsch, "Donor–acceptor-substituted cyclopropanes: Synthesis and ring opening to 1,4-dicarbonyl compounds", *Angew. Chem. Int. Ed.* **19** (1980), pp. 813–814.

[3] E. Wenkert, "Oxycyclopropanes in organochemical synthesis", *Acc. Chem. Res.* **13** (1980), pp. 27–31.

[4] H. Reissig, "Lewis-acid-promoted additions of carbonyl compounds to donor–acceptor substituted cyclopropanes: A new synthesis of 2,3-dihydrofuran derivatives", *Tetrahedron Lett.* **22** (1981), pp. 2981–2984.

[5] C. Brückner and H.-U. Reissig, "Thiophene derivatives by novel rearrangements of siloxy-substituted cyclopropanecarboxylates", *Angew. Chem. Int. Ed.* **24** (1985), pp. 588–589.

[6] A. Kreft, A. Lücht, J. Grunenberg, P. G. Jones and D. B. Werz, "Kinetic studies of donor–acceptor cyclopropanes: The inuence of structural and electronic properties on the reactivity", *Angew. Chem. Int. Ed.* **58** (2019), pp. 1955–1959.

[7] H.-U. Reissig and R. Zimmer, "Donor–acceptor-substituted cyclopropane derivatives and their application in organic synthesis", *Chem. Rev.* **103** (2003), pp. 1151–1196.

[8] M. Yu and B. L. Pagenkopf, "Recent advances in donor–acceptor (DA) cyclopropanes", *Tetrahedron* **61** (2005), pp. 321–347.

[9] C. A. Carson and M. A. Kerr, "Heterocycles from cyclopropanes: applications in natural product synthesis", *Chem. Soc. Rev.* **38** (2009), pp. 3051–3060.

[10] T. F. Schneider, J. Kaschel and D. B. Werz, "A new golden age for donor–acceptor cyclopropanes", *Angew. Chem. Int. Ed.* **53** (2014), pp. 5504–5523.

[11] M. J. Di Grandi, "Nazarov-like cyclization reactions", *Org. Biomol. Chem.* **12** (2014), pp. 5331–5345.

[12] F. de Nanteuil, F. De Simone, R. Frei, F. Benfatti, E. Serrano and J. Waser, "Cyclization and annulation reactions of nitrogen-substituted cyclopropanes and cyclobutanes", *Chem. Commun.* **50** (2014), pp. 10912–10928.

[13] M. A. Cavitt, L. H. Phun and S. France, "Intramolecular donor–acceptor cyclopropane ring-opening cyclizations", *Chem. Soc. Rev.* **43** (2014), pp. 804–818.

[14] H. K. Grover, M. R. Emmett and M. A. Kerr, "Carbocycles from donor–acceptor cyclopropanes", *Org. Biomol. Chem.* **13** (2015), pp. 655–671.

[15] R. A. Novikov and U. V. Tomilov, "Dimerization of donor–acceptor cyclopropanes", *Mendeleev Commun.* **25** (2015), pp. 1–10.

[16] N. R. O'Connor, J. L. Wood and B. M. Stoltz, "Synthetic applications and methodological developments of donor–acceptor cyclopropanes and related compounds", *Isr. J. Chem.* **56** (2016), pp. 431–444.

[17] H.-U. Reissig and D. B. Werz, “Special issues: chemistry of donor–acceptor cyclopropanes and cyclobutanes”, *Isr. J. Chem.* **56** (2016), pp. 367–368.

[18] S. J. Gharpure and L. N. Nanda, “Application of oxygen/nitrogen substituted donor–acceptor cyclopropanes in the total synthesis of natural products”, *Tetrahedron Lett.* **58** (2017), pp. 711–720.

[19] B. L. Pagenkopf and N. Vemula, “Cycloadditions of donor–acceptor cyclopropanes and nitriles”, *Eur. J. Org. Chem.* **2017** (2017), pp. 2561–2567.

[20] E. M. Budynina, K. L. Ivanov, I. D. Sorokin and M. Y. Melnikov, “Ring opening of donor–acceptor cyclopropanes with N-nucleophiles”, *Synthesis* **49** (2017), pp. 3035–3068.

[21] O. A. Ivanova and I. V. Trushkov, “Donor–acceptor cyclopropanes in the synthesis of carbocycles”, *Chem. Rec.* **19** (2019), pp. 2189–2208.

[22] P. Singh, R. K. Varshnaya, R. Dey and P. Banerjee, “Donor–acceptor cyclopropanes as an expedient building block towards the construction of nitrogen-containing molecules: An update”, *Adv. Synth. Catal.* **362** (2020), pp. 1447–1484.

[23] D. B. Werz and A. T. Biju, “Uncovering the neglected similarities of arynes and donor–acceptor cyclopropanes”, *Angew. Chem. Int. Ed.* **59** (2020), pp. 3385–3398.

[24] A. U. Augustin and D. B. Werz, “Exploiting heavier organochalcogen compounds in donor–acceptor cyclopropane chemistry”, *Acc. Chem. Res.* **54** (2021), pp. 1528–1541.

[25] V. Pirenne, B. Muriel and J. Waser, “Catalytic enantioselective ring-opening reactions of cyclopropanes”, *Chem. Rev.* **121** (2021), pp. 227–263.

[26] Y. Xia, X. Liu and X. Feng, “Asymmetric catalytic reactions of donor–acceptor cyclopropanes”, *Angew. Chem. Int. Ed.* **60** (2021), pp. 9176–9288.

[27] K. Ghosh and S. Das, “Recent advances in ring-opening of donor acceptor cyclopropanes using C-nucleophiles”, *Org. Biomol. Chem.* **19** (2021), pp. 965–982.

[28] A. T. Biju and P. Banerjee (eds.), in *Donor–Acceptor Cyclopropanes in Organic Synthesis*, Wiley-VCH: Weinheim, 2024.

[29] M. Bao and M. P. Doyle, “Asymmetric [3+*n*]-cycloaddition reactions of donor–acceptor cyclopropanes”, *ChemCatChem* **15** (2023), article no. e202301090.

[30] S. J. Gharpure, L. N. Nanda and D. Kumari, “Enantiospecific total synthesis of (+)-3-epi-epohelmin a using a nitrogen-substituted donor–acceptor cyclopropane”, *Eur. J. Org. Chem.* **2017** (2017), pp. 3917–3920.

[31] C. Sparr and R. Gilmour, “Cyclopropyl iminium activation: Reactivity umpolung in enantioselective organocatalytic reaction design”, *Angew. Chem. Int. Ed.* **50** (2011), pp. 8391–8395.

[32] L. K. B. Garve, P. Barkawitz, P. G. Jones and D. B. Werz, “Ring-opening 1,3-dichlorination of donor–acceptor cyclopropanes by iodobenzene dichloride”, *Org. Lett.* **16** (2014), pp. 5804–5807.

[33] K. S. Halskov, F. Kniep, V. H. Lauridsen, E. H. Iversen, B. S. Donslund and K. A. Jørgensen, “Organocatalytic enamine-activation of cyclopropanes for highly stereoselective formation of cyclobutanes”, *J. Am. Chem. Soc.* **137** (2015), pp. 1685–1691.

[34] R. A. Novikov, K. V. Potapov, D. N. Chistikov, A. V. Tarasova, M. S. Grigoriev, V. P. Timofeev and Y. V. Tomilov, “Synthesis and structures of cyclopropanedicarboxylate gallium complexes”, *Organometallics* **34** (2015), pp. 4238–4250.

[35] K. S. Halskov, L. Næsborg, F. Tur and K. A. Jørgensen, “Asymmetric [3+2] cycloaddition of vinylcyclopropanes and α,β-unsaturated aldehydes by synergistic palladium and organocatalysis”, *Org. Lett.* **18** (2016), pp. 2220–2223.

[36] J. Blom, A. Vidal-Albalat, J. Jørgensen, C. L. Barløse, K. S. Jessen, M. V. Iversen and K. A. Jørgensen, “Directing the activation of donor–acceptor cyclopropanes towards stereoselective 1,3-dipolar cycloaddition reactions by Brønsted base catalysis”, *Angew. Chem. Int. Ed.* **56** (2017), pp. 11831–11835.

[37] I. A. Andreev, N. K. Ratmanova, A. U. Augustin, O. A. Ivanova, I. I. Levina, V. N. Khrustalev, D. B. Werz and I. V. Trushkov, “Protic ionic liquid as reagent, catalyst, and solvent: 1-methylimidazolium thiocyanate”, *Angew. Chem. Int. Ed.* **60** (2021), pp. 7927–7934.

[38] S. Kolb, M. Petzold, F. Brandt, P. G. Jones, C. R. Jacob and D. B. Werz, “Electrocatalytic activation of donor–acceptor cyclopropanes and cyclobutanes: An alternative C(sp^3)–C(sp^3) cleavage mode”, *Angew. Chem. Int. Ed.* **60** (2021), pp. 15928–15934.

[39] J. Turkowska, J. Durka, M. Ociepa and D. Gryko, “Reversal of regioselectivity in reactions of donor–acceptor cyclopropanes with electrophilic olefins”, *Chem. Commun.* **58** (2022), pp. 509–512.

[40] N. L. Ahlburg, O. Hergert, P. G. Jones and D. B. Werz, “Donor–acceptor cyclopropanes: Activation enabled by a single, vinylogous acceptor”, *Angew. Chem. Int. Ed.* **62** (2023), article no. e202214390.

[41] D. D. Borisov, D. N. Platonov, N. A. Sokolov, R. A. Novikov and Y. V. Tomilov, “Formal high-order cycloadditions of donor–acceptor cyclopropanes with cycloheptatrienes”, *Angew. Chem. Int. Ed.* **63** (2024), article no. e202410081.

[42] S. Maity, S. Mondal, S. Debnath and R. Lo, “Photoredox activation of donor–acceptor cyclopropanes: Distonic radical cation reactivity in [3+2] cycloaddition reactions”, *Angew. Chem. Int. Ed.* **63** (2024), article no. e202419426.

[43] S. Lan, Q. Cui, D. Luo, et al., “Copper-catalyzed asymmetric nucleophilic opening of 1,1,2,2-tetrasubstituted donor–acceptor cyclopropanes for the synthesis of α-tertiary amines”, *J. Am. Chem. Soc.* **147** (2025), pp. 1172–1185.

[44] C. F. Koelsch and W. H. Gumprecht, “Some diazine-N-oxides”, *J. Org. Chem.* **23** (1958), pp. 1603–1606.

[45] M. Hasegawa, “Photopolymerization of diolefin crystals”, *Chem. Rev.* **83** (1983), pp. 507–518.

[46] H.-G. Braun and G. Wegner, “New experiments concerning the mechanism of solid-state photopolymerization of 2,5-distyrylpyrazine”, *Makromol. Chem.* **184** (1983), pp. 1103–1119.

[47] G. M. J. Schmidt, “Photodimerization in the solid state”, *Pure Appl. Chem.* **27** (1971), pp. 647–678.

[48] A. Calderón-Díaz, L. Ordner, M. G. Bernbeck, M. Palesati, M. Weber, N. Stingelin and W. R. Gutekunst, "Topochemical ring-opening polymerization of an oxathianethione", *J. Am. Chem. Soc.* **147** (2025), pp. 21331–21338.

[49] C. Sun, J. J. Oppenheim, G. Skorupskii, L. Yang and M. Dincă, "Reversible topochemical polymerization and depolymerization of a crystalline 3D porous organic polymer with C–C bond linkages", *Chem* **8** (2022), pp. 3215–3224.

[50] K. Hema, C. Raju, S. Bhandary and K. M. Sureshan, "Tuning the regioselectivity of topochemical polymerization through cocrystallization of the monomer with an inert isostere", *Angew. Chem. Int. Ed.* **61** (2022), article no. e202210733.

[51] K. Hema, A. Ravi, C. Raju, J. R. Pathan, R. Rai and K. M. Sureshan, "Topochemical polymerizations for the solid-state synthesis of organic polymers", *Chem. Soc. Rev.* **50** (2021), pp. 4062–4099.

[52] R. Mohanrao, K. Hema and K. M. Sureshan, "Topochemical synthesis of different polymorphs of polymers as a paradigm for tuning properties of polymers", *Nat. Commun.* **11** (2020), pp. 865–872.

[53] Q.-H. Guo, M. Jia, Z. Liu, et al., "Single-crystal polycationic polymers obtained by single-crystal-to-single-crystal photopolymerization", *J. Am. Chem. Soc.* **142** (2020), pp. 6180–6187.

[54] V. Athiyarath and K. M. Sureshan, "Designed synthesis of a 1D polymer in twist-stacked topology via single-crystal-to-single-crystal polymerization", *Angew. Chem. Int. Ed.* **59** (2020), pp. 15580–15585.

[55] S. Kusaka, A. Kiyose, H. Sato, Y. Hijikata, A. Hori, Y. Ma and R. Matsuda, "Dynamic topochemical reaction tuned by guest molecules in the nanospace of a metal–organic framework", *J. Am. Chem. Soc.* **141** (2019), pp. 15742–15746.

[56] R. Medishetty, Z. Bai, H. Yang, M. W. Wong and J. J. Vittal, "Influence of fluorine substitution on the unusual solid-state [2+2] photo-cycloaddition reaction between an olefin and an aromatic ring", *Cryst. Growth Des.* **15** (2015), pp. 4055–4061.

[57] F. Hu, X. Bi, X. Chen, Q. Pan and Y. Zhao, "Single-crystal-to-single-crystal transformations for the preparation of small molecules, 1D and 2D polymers single crystals", *Chem. Lett.* **50** (2021), pp. 1015–1029.

[58] K. Masson, M. Dousset, B. Biletskyi, et al., "Designing donor–acceptor cyclopropane for the thermalsynthesis of carbocyclic eight-membered rings", *Adv. Synth. Catal.* **365** (2023), pp. 1002–1011.

[59] L. Yet, "Metal-mediated synthesis of medium-sized rings", *Chem. Rev.* **100** (2000), pp. 2963–3008.

[60] M. E. Maier, "Synthesis of medium-sized rings by the ring-closing metathesis reaction", *Angew. Chem. Int. Ed.* **39** (2000), pp. 2073–2077.

[61] G. A. Molander, "Diverse methods for medium ring synthesis", *Acc. Chem. Res.* **31** (1998), pp. 603–609.

[62] A. Hussain, S. K. Yousuf and D. Mukherjee, "Importance and synthesis of benzannulated medium-sized and macrocyclic rings (BMRs)", *RSC Adv.* **4** (2014), pp. 43241–43257.

[63] I. Shiina, "Total synthesis of natural 8- and 9-membered lactones: Recent advancements in medium-sized ring formation", *Chem. Rev.* **107** (2007), pp. 239–273.

[64] A. S. Kleinke, D. Webb and T. F. Jamison, "Recent progress in the synthesis of oxepanes and medium ring ethers", *Tetrahedron* **68** (2012), pp. 6999–7018.

[65] S. K. Chattopadhyay, S. Karmakar, T. Biswas, K. Majumdar, H. Rahaman and B. Roy, "Formation of medium-ring heterocycles by diene and enyne metathesis", *Tetrahedron* **63** (2007), pp. 3919–3952.

[66] L. Li, Z.-L. Li, Q.-S. Gu, N. Wang and X.-Y. Liu, "A remote C–C bond cleavage–enabled skeletal reorganization: Access to medium-/large-sized cyclic alkenes", *Sci. Adv.* **3** (2017), article no. e1701487.

[67] B. Kunze, R. Jansen, F. Sasse, G. Höfle and H. Reichenbach, "Apicularens A and B, new cytostatic macrolides from Chondromyces species (myxobacteria): production, physico-chemical and biological properties", *J. Antibiot.* **51** (1998), pp. 1075–1080.

[68] K. M. George, M.-C. Frantz, K. Bravo-Altamirano, et al., "Design, synthesis, and biological evaluation of PKD inhibitors", *Pharmaceutics* **3** (2011), pp. 186–228.

[69] K. R. Romines, K. D. Watenpaugh, P. K. Tomich, et al., "Use of medium-sized cycloalkyl rings to enhance secondary binding: Discovery of a new class of human immunodeficiency virus (HIV) protease inhibitors", *J. Med. Chem.* **38** (1995), pp. 1884–1891.

[70] T. P. Majhi, B. Achari and P. Chattopadhyay, "Advances in the synthesis and biological perspectives of benzannulated medium ring heterocycles", *Heterocycles* **71** (2007), pp. 1011–1052.

[71] F. Kopp, C. F. Stratton, L. B. Akella and D. S. Tan, "A diversity-oriented synthesis approach to macrocycles via oxidative ring expansion", *Nat. Chem. Biol.* **8** (2012), pp. 358–365.

[72] R. A. Bauer, T. A. Wenderski and D. S. Tan, "Biomimetic diversity-oriented synthesis of benzannulated medium rings via ring expansion", *Nat. Chem. Biol.* **9** (2013), pp. 21–29.

[73] C. Zhao, Z. Ye, Z.-X. Ma, S. A. Wildman, S. A. Blaszczyk, L. Hu, I. A. Guizei and W. Tang, "A general strategy for diversifying complex natural products to polycyclic scaffolds with medium-sized rings", *Nat. Commun.* **10** (2019), pp. 4015–4024.

[74] G. Illuminati and L. Mandolini, "Ring-closure reactions of bifunctional molecules", *Acc. Chem. Res.* **14** (1981), pp. 95–102.

[75] C. Galli and L. Mandolini, "The role of ring strain on the ease of ring closure of bifunctional chain molecules", *Eur. J. Org. Chem.* **2000** (2000), pp. 3117–3125.

[76] M. A. Casadei, C. Galli and L. Mandolini, "Ring-closure reactions. 22. Kinetics of cyclization of diethyl (.omega.-bromoalkyl)malonates in the range of 4- to 21-membered rings. Role of ring strain", *J. Am. Chem. Soc.* **106** (1984), pp. 1051–1056.

[77] K. C. Majumdar, "Regioselective formation of medium-ring heterocycles of biological relevance by intramolecular cyclization", *RSC Adv.* **1** (2011), pp. 1152–1170.

[78] A. Sharma, P. Appukkuttan and E. Van der Eycken, “Microwave-assisted synthesis of medium-sized heterocycles”, *Chem. Commun.* **48** (2012), pp. 1623–1637.

[79] A. K. Clarke and W. P. Unsworth, “A happy medium: the synthesis of medicinally important medium-sized rings via ring expansion”, *Chem. Sci.* **11** (2020), pp. 2876–2881.

[80] J. R. Donald and W. P. Unsworth, “Ring-expansion reactions in the synthesis of macrocycles and medium-sized rings”, *Chem. Eur. J.* **23** (2017), pp. 8780–8799.

[81] B. Biletskyi, P. Colonna, K. Masson, J.-L. Parrain, L. Commeiras and G. Chouraqui, “Small rings in the bigger picture: ring expansion of three- and four-membered rings to access larger all-carbon cyclic systems”, *Chem. Soc. Rev.* **50** (2021), pp. 7513–7538.

[82] D. J. Mack and J. T. Njardarson, “Recent advances in the metal-catalyzed ring expansions of three- and four-membered rings”, *ACS Catal.* **3** (2013), pp. 272–286.

[83] T. Seiser, T. Saget, D. N. Tran and N. Cramer, “Cyclobutanes in catalysis”, *Angew. Chem. Int. Ed.* **50** (2011), pp. 7740–7752.

[84] X. Cai, W. Liang and M. Dai, “Total syntheses via cyclopropanols”, *Tetrahedron* **75** (2019), pp. 193–208.

[85] P. Natho, L. A. T. Alle and P. J. Parsons, “Recent advances in the ring expansion of cyclobutanols, oxetanols, and azetidinols”, *Tetrahedron Lett.* **61** (2020), article no. 151695.

[86] J. Le Bras and J. Muzart, “Pd-catalyzed reactions of cyclopropanols, cyclobutanols and cyclobutenols”, *Tetrahedron* **76** (2020), article no. 130879.

[87] J. M. Wooton, J. K. F. Tam and W. P. Unsworth, “Cascade ring expansion reactions for the synthesis of medium-sized rings and macrocycles”, *Chem. Commun.* **60** (2024), pp. 4999–5009.

[88] C. J. Roxburgh, “Syntheses of medium sized rings by ring expansion reactions”, *Tetrahedron* **49** (1993), pp. 10749–10784.

[89] E. Vogel, “Kleine Kohlenstoff-ringe”, *Angew. Chem.* **72** (1960), pp. 4–26.

[90] T. Hudlicky, R. Fan, J. W. Reed and K. G. Gadamasetti, “Divinylcyclopropane–cycloheptadiene rearrangement”, *Org. React.* **4** (1992), pp. 1–133.

[91] S. Krüger and T. Gaïch, “Recent applications of the divinylcyclopropane–cycloheptadiene rearrangement in organic synthesis”, *Beilstein J. Org. Chem.* **10** (2014), pp. 163–193.

[92] H. M. L. Davies, D. G. Stafford, B. D. Doan and J. H. Houser, “Tandem asymmetric cyclopropanation/cope rearrangement. A highly diastereoselective and enantioselective method for the construction of 1,4-cycloheptadienes”, *J. Am. Chem. Soc.* **120** (1998), pp. 3326–3331.

[93] H. M. L. Davies and J. R. Denton, “Application of donor/acceptor-substituted rhodium carbenoids in organic synthesis”, *Chem. Soc. Rev.* **38** (2009), pp. 3061–3071.

[94] I. Özkan and M. Zora, “Transition structures, energetics, and secondary kinetic isotope effects for cope rearrangements of cis-1,2-divinylcyclobutane and cis-1,2-divinylcyclopropane: A DFT study”, *J. Org. Chem.* **68** (2003), pp. 9635–9642.

[95] K. V. Potapov, D. A. Denisov, V. V. Glushkova, R. A. Novikov and Y. V. Tomilov, “Donor–acceptor bicyclopropyls as 1,6-zwitterionic intermediates: synthesis and reactions with 4-phenyl-1,2,4-triazoline-3,5-dione and terminal acetylenes”, *J. Org. Chem.* **85** (2020), pp. 15562–15576.

[96] D. A. Denisov, R. A. Novikov, K. V. Potapov, V. A. Korolev, E. V. Shulishov and Y. V. Tomilov, “1,1′-bicyclopropyl-2,2-dicarboxylate and cyclopropylmethylidenemalonate as homovinylogs and vinylogs of donor–acceptor cyclopropanes”, *ChemistrySelect* **1** (2016), pp. 6374–6381.

[97] D. A. Denisov, R. A. Novikov and Y. V. Tomilov, “Donor-acceptor bicyclopropyl configuration-fixed by an additional trimethylene bridge: synthesis and Lewis acid-catalyzed tandem three-membered rings opening”, *Russ. Chem. Bull.* **70** (2021), pp. 1568–1574.

[98] A. Kreft, P. G. Jones and D. B. Werz, “The cyclopropyl group as a neglected donor in donor–acceptor cyclopropane chemistry”, *Org. Lett.* **20** (2018), pp. 2059–2062.

[99] G. A. Oliver and D. B. Werz, “Ring-opening 1,3-sulfonylation-fluorination of donor–acceptor cyclopropanes: Three-component access to γ-fluorosulfones”, *Org. Lett.* **25** (2023), pp. 3568–3572.

[100] H. F. von Köller, P. G. Jones and D. B. Werz, “A widely applicable and versatile method for the ring-opening 1,3-carbocarbonation of donor–acceptor cyclopropanes”, *Chem. Eur. J.* **29** (2023), article no. e202203986.

[101] G. A. Oliver, M. N. Loch, A. U. Augustin, et al., “Cycloadditions of donor–acceptor cyclopropanes and -butanes using S=N-containing reagents: access to cyclic sulfinamides, sulfonamides, and sulfinamidines”, *Angew. Chem. Int. Ed.* **60** (2021), pp. 25825–25831.

[102] B. Trost and A. Brandi, “Stereocontrolled 1,1,2-trialkylation of ketones”, *J. Am. Chem. Soc.* **106** (1984), pp. 5041–5043.

[103] B. M. Trost and D. C. Lee, “Cyclization terminators. Vinylcyclopropanol as a composite functional group”, *J. Am. Chem. Soc.* **110** (1988), pp. 6556–6558.

[104] B. M. Trost and D. W. C. Chen, “Vinylcyclobutanols: A composite functional group?”, *J. Am. Chem. Soc.* **118** (1996), pp. 12541–12554.

[105] B. M. Trost and P. H. Scudder, “Kinetics of the siloxyvinylcyclopropane rearrangement using a micro stirred flow reactor”, *J. Org. Chem.* **46** (1981), pp. 506–509.

[106] S. A. Monti, F. G. Cowherd and T. W. Mc Aninch, “Thermal rearrangement of trimethylsilyl enol ethers of cyclopropyl methyl ketones, a cyclopentanone annelation procedure”, *J. Org. Chem.* **40** (1975), pp. 858–862.

[107] B. M. Trost, “Strain and reactivity: Partners for selective synthesis”, *Top. Curr. Chem.* **133** (1986), pp. 3–82.

[108] J. R. Y. Salaün, “Synthesis and synthetic applications of 1-donor substituted cyclopropanes with ethynyl, vinyl and carbonyl groups”, *J. Top. Curr. Chem.* **144** (1988), pp. 1–71.

[109] R. C. Gadwood and R. M. Lett, “Preparation and rearrangement of 1,2-dialkenylcyclobutanols. A useful method for synthesis of substituted cyclooctenones”, *J. Org. Chem.* **47** (1982), pp. 2268–2275.

[110] B. B. Snider and A. J. Allentoff, "Synthesis of the bicyclo[5.3.1]undecane moiety (AB ring system) of taxane", *J. Org. Chem.* **56** (1991), pp. 321–328.

[111] N. Arichi, K.-I. Yamada, Y. Yamaoka and K. Takasu, "An arylative ring expansion cascade of fused cyclobutenes via short-lived intermediates with planar chirality", *J. Am. Chem. Soc.* **137** (2015), pp. 9579–9582.

[112] T. Ito, M. Tsutsumi, K.-I. Yamada, H. Takikawa, Y. Yamaoka and K. Takasu, "Synthesis of functionalized medium-sized trans-cycloalkenes by 4π electrocyclic ring opening/alkylation sequence", *Angew. Chem. Int. Ed.* **58** (2019), pp. 11836–11840.

[113] D. Sondag, L. Maartense, H. de Jong, et al., "Readily accessible strained difunctionalized trans-cyclooctenes with fast click and release capabilities", *Chem. Eur. J.* **29** (2023), article no. e202203375.

[114] I. Yavari, H. Kabiri-Fard and S. Moradi, "Conformational properties of (Z,Z)-, (E,Z)-, and (E,E)-cycloocta-1,4-dienes", *Monatsh. Chem.* **133** (2002), pp. 1459–1468.

[115] B. Biletskyi, M. Dousset, P. Colonna, V. Héran, Y. Carissan, L. Commeiras and G. Chouraqui, "Formation of substituted benzocyclobutenes starting from donor–acceptor cyclopropanes", *J. Org. Chem.* **90** (2025), pp. 4115–4120.

[116] S. Kotha, K. Lahiri and Y. Tangella, "Recent advances in benzocyclobutene chemistry", *Asian J. Org. Chem.* **10** (2021), pp. 3166–3185.

[117] G. Mehta and S. Kotha, "Recent chemistry of benzocyclobutenes", *Tetrahedron* **57** (2001), pp. 625–659.

[118] A. K. Sadana, R. K. Saini and W. E. Billups, "Cyclobutarenes and related compounds", *Chem. Rev.* **103** (2003), pp. 1539–1602.

[119] K. Adachi, S. Hirose, Y. Ueda, H. Uekusa and T. Hamura, "Thermodynamically stable o-quinodimethane: Synthesis, structure, and reactivity", *Chem. Eur. J.* **27** (2021), pp. 3665–3669.

[120] T. H. McLean, J. C. Parrish, M. R. Braden, D. Marona-Lewicka, A. Gallardo-Godoy and D. E. Nichols, "1-aminomethylbenzocycloalkanes: Conformationally restricted hallucinogenic phenethylamine analogues as functionally selective 5-HT_{2A} receptor agonists", *J. Med. Chem.* **49** (2006), pp. 5794–5803.

[121] A. Tsotinis, P. A. Afroudakis, P. J. Garratt, A. Bocianowska-Zbrog and D. Sugden, "Benzocyclobutane, benzocycloheptane and heptene derivatives as melatonin agonists and antagonists", *ChemMedChem* **9** (2014), pp. 2238–2243.

[122] J. Stieber, K. Wieland, G. Stöckl, A. Ludwig and F. Hofmann, "Bradycardic and proarrhythmic properties of sinus node inhibitors", *Mol. Pharmacol.* **69** (2006), pp. 1328–1337.

[123] Q. Zheng, S. Tang, X. Fu, et al., "Discovery and structure-activity-relationship study of novel conformationally restricted indane analogues for mutant isocitric dehydrogenase 1 (IDH1) inhibitors", *Bioorg. Med. Chem. Lett.* **27** (2017), pp. 5262–5266.

[124] M. J. Millan, A. Dekeyne, M. Papp, C. Drieu La Rochelle, C. MacSweeny, J.-L. Peglion and M. Brocco, "S33005, a novel ligand at both serotonin and norepinephrine transporters: II. Behavioral profile in comparison with venlafaxine, reboxetine, citalopram, and clomipramine", *Pharmacol. Exp. Ther.* **298** (2001), pp. 581–591.

[125] G.-H. Kuo, M. D. Gaul, Y. Liang, et al., "Synthesis and biological evaluation of benzocyclobutane-C-glycosides as potent and orally active SGLT1/SGLT2 dual inhibitors", *Bioorg. Med. Chem. Lett.* **28** (2018), pp. 1182–1187.

[126] J. P. Vilaine, "The discovery of the selective I_f current inhibitor ivabradine: A new therapeutic approach to ischemic heart disease", *J. Pharmacol. Res.* **53** (2006), pp. 424–434.

[127] M. Pascual Izco, G. L. Alonso Salinas, M. Sanmartín Fernández, H. Del Castillo Carnevalli, M. Jiménez Mena, A. C. Camino López and J. L. Zamorano Gómez, "Clinical experience with ivabradine in acute heart failure", *Cardiology* **134** (2016), pp. 372–374.

[128] P. G. Camici, S. Gloekler, B. I. Levy, E. Skalidis, E. Tagliamonte, P. Vardas and G. Heusch, "Ivabradine in chronic stable angina: from antianginal to anti-ischemic therapy", *Int. J. Cardiol.* **215** (2016), pp. 1–6.

[129] R. A. Kirchhoff and K. J. Bruza, "Benzocyclobutenes in polymer synthesis", *Prog. Polym. Sci.* **18** (1993), pp. 85–185.

[130] M. F. Farona, "Benzocyclobutenes in polymer chemistry", *Prog. Polym. Sci.* **21** (1996), pp. 505–555.

[131] Y. Cheng, S. Tian, Y. Shi, W. Chen, Z. Li, T. Zhu and Z. Zhang, "Benzocyclobutene organosiloxane resins prepared by alcoholysis of BCB functionalized chlorosilane for highly crosslinked low-k thermosets", *Eur. Polym. J.* **95** (2017), pp. 440–447.

[132] C. O. Hayes, P.-H. Chen, R. P. Thedford, C. J. Ellison, G. Dong and C. G. Willson, "Effect of ring functionalization on the reaction temperature of benzocyclobutene thermoset polymers", *Macromolecules* **49** (2016), pp. 3706–3715.

[133] Y. Huang, S. Zhang, H. Hu, X. Wei, H. Yu and J. Yang, "Photoactive polymers with benzocyclobutene/silacyclobutane dual crosslinked structure and low dielectric constant", *J. Polym. Sci. A* **55** (2017), pp. 1920–1928.

[134] L. Yang, K. Cao, Y. Huang, G. Chang, F. Zhu and J. Yang, "Synthesis and properties of cross-linkable polysiloxane via incorporating benzocyclobutene", *High Perform. Polym.* **26** (2014), pp. 463–469.

[135] S. Tian, J. Sun, K. Jin, J. Wang, F. He, S. Zheng and Q. Fang, "Postpolymerization of a fluorinated and reactive poly(aryl ether): An efficient way to balance the solubility and solvent resistance of the polymer", *ACS Appl. Mater. Interfaces* **6** (2014), pp. 20437–20443.

[136] K. S. Levchenko, K. A. Chudov, G. E. Adamov, N. O. Poroshin, P. S. Shmelin, E. P. Grebennikov and Y. G. Parshikov, "Photocurable and thermosetting polymer materials on the basis of benzocyclobutene and its derivatives for electronics", *Russ. J. Gen. Chem.* **88** (2018), pp. 2793–2812.

[137] H. Finkelstein, "Darstellung organischer Jodide aus den entsprechenden Bromiden und Chloriden", *Chem. Ber.* **43** (1910), pp. 1528–1532.

[138] M. Chaumontet, R. Piccardi, N. Audic, J. Hitce, J.-L. Peglion, E. Clot and O. Baudoin, "Synthesis of benzo-

cyclobutenes by palladium-catalyzed C–H activation of methyl groups: Method and mechanistic study", *J. Am. Chem. Soc.* **130** (2008), pp. 15157–15166.

[139] Z. Wu, D. Ma, B. Zhou, X. Ji, X. Ma, X. Wang and Y. Zhang, "Palladium-catalyzed alkylation with alkyl halides by C(sp^3)–H activation", *Angew. Chem. Int. Ed.* **56** (2017), pp. 12288–12291.

[140] J. Bezenšek, U. Grošelj, M. Počkaj, J. Svete and B. Stanovnik, "Formation of benzocyclobutenes from substituted oxocycloocta-2,8-diene-1,2-dicarboxylates", *Tetrahedron Lett.* **56** (2015), pp. 5705–5708.

[141] G.-A. Chen, A. Fang, Y. Wei, X.-Y. Tang and M. Shi, "Gold(I)-catalyzed dehydrogenative cycloisomerization of 1,5-enynes", *Chem. Commun.* **52** (2016), pp. 10799–10802.

[142] V. Gembus, F. Marsais and V. Levacher, "An efficient organocatalyzed interconversion of silyl ethers to tosylates using DBU and p-toluenesulfonyl fluoride", *Synlett* **2008** (2008), pp. 1463–1466.

[143] X. Cheng, Q. Yin, Y.-X. Jiang, et al., "Simple and versatile nitrooxylation: Noncyclic hypervalent iodine nitrooxylating reagent", *Angew. Chem. Int. Ed.* **62** (2023), article no. e202302521.

[144] Y.-Y. Li, S.-A. Zhang and X. Hong, "An asynchronous concerted mechanism and its origin in lewis acid-mediated carbonyl-olefin [2+2] cycloaddition", *Chem. Asian J.* **18** (2023), article no. e202300375.

[145] M. Giorgi, K. Masson, S. Chentouf, L. Commeiras, P. Nava and G. Chouraqui, "Template-directed in crystallo photopolymerization of a donor–acceptor cyclopropane: When everything falls into place!", *J. Am. Chem. Soc.* **146** (2024), pp. 17384–17392.

[146] M. D. Cohen, G. M. J. Schmidt and F. I. Sonntag, "384. Topochemistry. Part II. The photochemistry of trans-cinnamic acids", *J. Chem. Soc.* **1964** (1964), pp. 2000–2013.

[147] R. Khazeber, G. S. Kana and K. M. Sureshan, "Massive molecular motion in crystal leads to an unexpected helical covalent polymer in a solid-state polymerization", *Angew. Chem. Int. Ed.* **63** (2024), article no. e202316513.

[148] C. Raju, G. R. Ramteke, K. V. J. Jose and K. M. Sureshan, "Cascading effect of large molecular motion in crystals: A topotactic polymorphic transition paves the way to topochemical polymerization", *J. Am. Chem. Soc.* **145** (2023), pp. 9607–9616.

[149] D. Scheschkewitz, "Dimethylcyclobutadiene by confinement in a crystalline matrix", *Science* **330** (2010), pp. 1047–1048.

[150] M. Morimoto and M. Irie, "Photochromism of diarylethene single crystals: crystal structures and photochromic performance", *Chem. Commun.* **2005** (2005), pp. 3895–3905.

[151] S. Kobatake, Y. Matsumoto and M. Irie, "Conformational control of photochromic reactivity in a diarylethene single crystal", *Angew. Chem. Int. Ed.* **44** (2005), pp. 2148–2151.

[152] F. Cuccu, L. De Luca, F. Delogu, E. Colacino, N. Solin, R. Mocci and A. Porcheddu, "Mechanochemistry: New tools to navigate the uncharted territory of "impossible" reactions", *ChemSusChem* **15** (2022), article no. e202200362.

[153] T. Seo, N. Toyoshima, K. Kubota and H. Ito, "Tackling solubility issues in organic synthesis: Solid-state cross-coupling of insoluble aryl halides", *J. Am. Chem. Soc.* **143** (2021), pp. 6165–6175.

[154] G. M. J. Schmidt, "Photodimerization in the solid state", *Pure Appl. Chem.* **27** (1971), pp. 647–678.

[155] S. Ariel, S. Askari, J. R. Scheffer and J. Trotter, "Latent photochemical hydrogen abstraction reactions realized in crystalline media", *J. Org. Chem.* **54** (1989), pp. 4324–4330.

[156] S. Biswas, S. Banerjee, M. A. Shlain, A. A. Barfin, R. V. Ulijn, B. L. Nannenga, A. M. Rappe and A. B. Brauschweig, "Photomechanochemical control over stereoselectivity in the [2+2] photodimerization of acenaphthylene", *Faraday Discuss.* **241** (2023), pp. 266–277.

[157] L. Schmidt, D. van der Spoel and M.-M. Walz, "Probing phase transitions in organic crystals using atomistic MD simulations", *ACS Phys. Chem.* **3** (2023), pp. 84–93.

[158] A. Gavezzotti, L. L. Presti and S. Rizzato, "Molecular dynamics simulation of organic materials: structure, potentials and the MiCMoS computer platform", *CrystEngComm* **24** (2022), pp. 922–930.

[159] S. Rizzato, A. Gavezzotti and L. L. Presti, "Molecular dynamics simulation of molecular crystals under anisotropic compression: Bulk and directional effects in anthracene and paracetamol", *Cryst. Growth Des.* **20** (2020), pp. 7421–7428.

ACADÉMIE DES SCIENCES
INSTITUT DE FRANCE

Comptes Rendus. Chimie
2025, Vol. 28, p. 887-900
https://doi.org/10.5802/crchim.420

Review article

Cobalt-catalyzed cross-electrophile couplings: from electrosynthesis to conventional chemistry

Corinne Gosmini [a]

[a] Institut de Chimie Moléculaire et des Matériaux d'Orsay (ICMMO), CNRS UMR 8182, Université Paris-Saclay, Bâtiment Henri Moissan, 17 avenue des Sciences, 91400 Orsay, France

E-mail: corinne.gosmini@cnrs.fr

Abstract. Cobalt-catalyzed reductive cross-couplings, also known as cross-electrophile couplings (XECs), have emerged as a valuable and sustainable alternative to classical cross-coupling strategies. Unlike traditional methods relying on preformed organometallic reagents, cobalt catalysis enables the direct coupling of two electrophiles, offering broad functional group tolerance, access to diverse C(sp^2)–C(sp^2), C(sp^2)–C(sp^3), and C(sp^3)–C(sp^3) bonds, and compatibility with mild conditions. Building on early electrochemical studies, significant progress has been made in both electrosynthesis (eXEC) and conventional approaches (XEC), highlighting cobalt's cost-effectiveness, ecological advantages, and complementary reactivity compared to nickel. This account summarizes the development of cobalt-catalyzed reductive cross-couplings, from pioneering contributions to recent advances, with emphasis on mechanistic aspects and substrate scope.

Keywords. Cobalt catalysis, Reductive and electroreductive cross-coupling, C–C bond formation.

Note. Article submitted by invitation.

Manuscript received 2 September 2025, revised 5 September 2025, accepted 8 September 2025.

Nowadays, the formation of carbon–carbon (C–C) bonds via cross-electrophile coupling (XEC) or electrochemical cross-electrophile coupling (eXEC), catalyzed by transition metals, has emerged as a powerful and attractive strategy in synthetic chemistry [1–3]. The construction of C–C bonds is fundamental to the synthesis of a wide range of key molecules, including pharmaceuticals, agrochemicals, and basic organic materials. Compared to classic cross-coupling reactions involving the reaction of an organometallic (nucleophile) with an electrophile in the presence of a transition metal catalyst (notably palladium, as recognized by the 2010 Nobel Prize in Chemistry) [4], XEC or eXEC reactions offer several key advantages (Scheme 1). Notably, they eliminate the need for the preparation and handling of sensitive organometallic compounds in stoichiometric amount, simplify operations through one-step procedures, and exhibit broad functional group tolerance.

Although cobalt-catalyzed cross-couplings with organometallic reagents (e.g., Grignard reagents or zinc species) have been described, XECs (previously called reductive or direct couplings) have emerged as a robust and versatile alternative [5–8]. These reactions enable the formation of diverse carbon–carbon and carbon–heteroatom bonds—including Csp^2–Csp^2, Csp^2–Csp^3, Csp^3–Csp^3, and Csp–Csp^3 linkages—under mild conditions, using two electrophilic partners such as stable halides or pseudohalogenated substrates.

Prior to the emergence of modern XEC, eXEC of two electrophiles [9–11] had already been explored, particularly by Périchon and coworkers, predominantly using nickel catalysts [12]. These early contributions laid the foundation for the development of a wide range of nickel-catalyzed eXEC methods.

In an effort to replace nickel with a more cost-effective and environmentally benign alternative, we pioneered the use of cobalt in electroreductive C–C

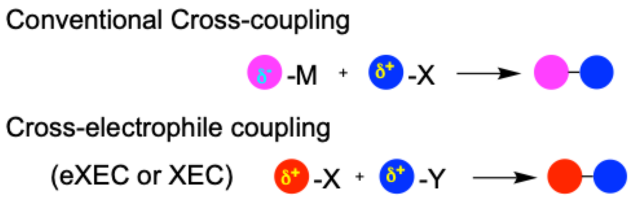

Scheme 1. Conventional cross-coupling vs cross-electrophile coupling.

bond formation via sacrificial anode processes [13]. Cobalt is particularly attractive due to its low cost, broad functional tolerance, and improved ecological footprint compared to nickel. Despite the increased accessibility of electrosynthesis in recent years—thanks in part to the advent of user-friendly equipment such as the IKA ElectraSyn—this technique was historically regarded as more complex and less practical than conventional synthetic methods, which significantly limited its adoption within the organic chemistry community.

It is worth noting that the concept of XEC dates back to the 19th century, with Wurtz's pioneering work using stoichiometric sodium metal at elevated temperatures [14]. However, such harsh conditions were incompatible with many functional groups, which curtailed its utility. To overcome the challenges associated with electrosynthesis or the use of palladium at high temperature [15,16], we reported in 2003 the first XEC of two distinct electrophiles under non-electrochemical conditions, employing a first-row transition metal catalyst, Co, in combination with metal reducers (Zn or Mn) [17]. This approach offered excellent functional group tolerance and operational simplicity.

Since 2010, the field of XEC has witnessed substantial growth, with many research groups initiating work in this area, primarily concentrating on nickel-catalyzed transformations [18–20]. These transformations typically use Ni(II) precursors along with either metallic reductants (Zn, Mn) or homogeneous reductants such as tetrakis(dimethylamino)ethylene (TDAE) [21] or bis(pinacolato)diboron (B_2pin_2) [22]. In contrast, examples involving other metals—such as Cu [23], Fe [24], or Cr [25]—remain comparatively rare. Photoredox catalysis has also emerged as a complementary strategy to minimize the use of stoichiometric metal reductants in XECs [26,27].

Despite being less extensively developed than nickel-catalyzed systems, cobalt-catalyzed XECs have shown interesting complementary reactivity and offer unique advantages in certain transformations [28]. Recognizing these advantages, we have pursued our studies on cobalt catalysis, particularly for the formation of Csp^2–Csp^2, Csp^2–Csp^3, and Csp^3–Csp^3 bonds.

This account highlights the contributions of our laboratory to the development of cobalt-catalyzed reductive cross-coupling reactions for the construction of C–C bonds from C–X (X = Cl, Br, I), C–O, C–N, and C–S bonds, using both electrochemical (eXEC) and conventional (XEC) approaches.

These methods are operationally simple and robust. In the case of eXEC, reactions are typically conducted in undivided cells equipped with an iron anode and a nickel foam cathode, with the choice of anode proving critical to the success of the reaction. Both electrochemical and classical approaches are carried out in solvents such as acetonitrile (CH_3CN) or dimethylformamide (DMF), with or without pyridine, under inert atmosphere (argon) at room temperature or moderate temperatures (up to 50 °C). The cobalt catalyst generally consists of commercially available $CoBr_2$ or $CoCl_2$, with negligible differences observed between these two salts. Additionally, the use of ancillary ligands (e.g., bipyridine or phosphines) is not always required, further simplifying the protocol.

1. Formation of $C(sp^2)$–$C(sp^2)$ bonds

1.1. *Biaryl formation*

Unsymmetrical biaryls are key structural motifs found in a broad range of biologically active compounds, including natural products, pharmaceuticals, functional materials, and agrochemicals [29–31]. Traditionally, their synthesis involves the transition-metal-catalyzed cross-coupling of an aryl halide with an organometallic reagent—such

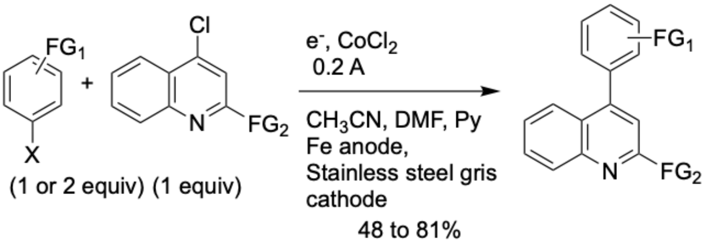

Scheme 2. Electroreductive cobalt-catalyzed cross-coupling of functionalized phenyl halides with 4-chloroquinoline derivatives.

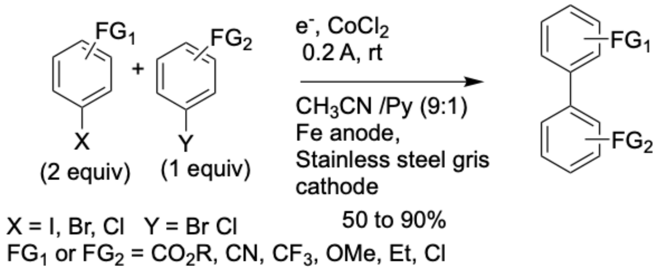

Scheme 3. Synthesis of unsymmetrical biaryls by electroreductive cobalt-catalyzed cross-coupling of aryl halides.

as arylboronic acids, arylzinc, stannane, or Grignard derivatives—typically mediated by palladium or nickel catalysts.

Pioneering work by Kharasch and coworkers has demonstrated that aryl Grignard reagents can undergo efficient homocoupling in the presence of catalytic amounts of first-row transition metal salts such as cobalt(II) chloride ($CoCl_2$) [32]. Beyond homocoupling, cobalt has also proven to be an effective catalyst for cross-coupling reactions between two different aryl partners. Notably, Nakamura et al. [33] and von Wangelin et al. [34] have independently showed that cobalt salts catalyze the cross-coupling between aryl Grignard reagents and aryl or heteroaryl halides, enabling the formation of unsymmetrical biaryls. This strategy has since been extended to include aryl tosylates as electrophilic partners by using a cobalt diisopropyl disubstituted bis(phosphino)pyridine pincer (^{iPr}PNP)-based catalyst [35].

In a complementary approach using commercially available precursors, cobalt precatalysts bearing N-heterocyclic carbene (NHC) ligands, have also been employed in Suzuki–Miyaura cross-coupling reactions of aryl chlorides and bromides with arylboronic pinacol esters, activated in situ with alkyllithium reagents [36].

To circumvent the need for stoichiometric organometallic reagents, the first cobalt-catalyzed eXEC was developed for biaryl synthesis. Initially, the method used aryl halides and 4-chloroquinolines as electrophilic partners (Scheme 2) [37]. This was later expanded to include couplings between two distinct aryl halides (Scheme 3) [38]. In both cases, the reactions were conducted in an undivided electrochemical cell equipped with an iron anode and required pyridine as a ligand to activate the cobalt catalyst.

The aromatic moiety involved in these transformations can accommodate a broad range of electron-donating and electron-withdrawing substituents. In 2008, the cobalt-catalyzed synthesis of biaryls via eXEC was successfully adapted to conventional chemical methods by changing some parameters (Scheme 4). These included reactions between two aryl halides or between an aryl halide and a heteroaryl halide with comparable reactivities [39]. In this protocol, manganese powder was employed as the reductant in a DMF/pyridine solvent system. The cobalt(II) bromide ($CoBr_2$) catalyst, ligated with

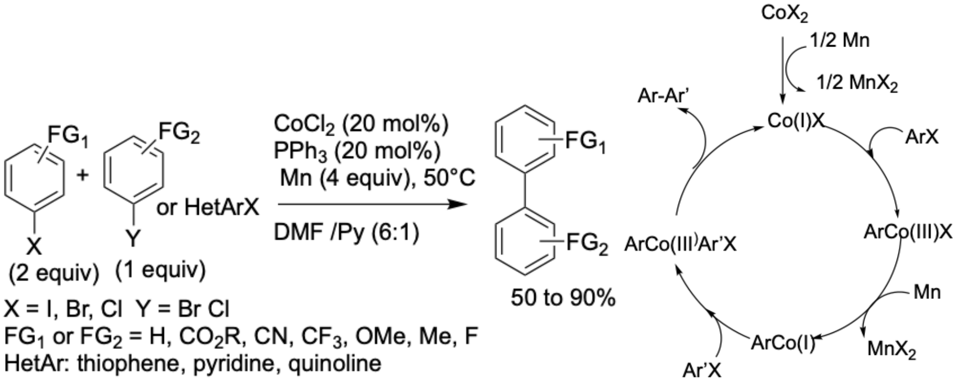

Scheme 4. Cobalt-catalyzed formation of unsymmetrical biaryl compounds and proposed mechanism.

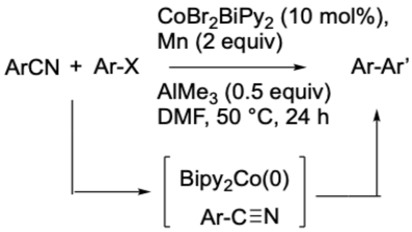

Scheme 5. Cobalt-catalyzed biaryl formation mediated by C(sp^2)–CN bond activation.

triphenylphosphine (PPh_3), enabled the efficient formation of unsymmetrical biaryls in good yields. With these adapted reaction conditions, the proposed mechanism proceeds via a non-radical pathway.

We applied this strategy to the synthesis of 2-(4-tolyl)benzonitrile, a key intermediate in the preparation of sartans—widely used antihypertensive agents. More recently, we demonstrated that cobalt catalysis could be extended to inert C–CN bond activation, thereby enabling the challenging formation of biaryls from aryl halides and benzonitriles—an approach that poses a greater synthetic challenge (Scheme 5) [40]. In this system, the addition of $AlMe_3$ to the reaction medium enhanced the reactivity of the aryl–CN bond.

Combined DFT calculations and experimental studies revealed that the reaction proceeds through the in situ generation of two low-valent cobalt species: a Co(I) species that activates the aryl halide, and a Co(0) species that facilitates the cleavage of the aryl–CN bond. Consistent with earlier findings by Chatani et al. in rhodium catalysis [41], an intramolecular version of this transformation was also shown to be feasible, albeit requiring prolonged reaction times.

1.2. *Formation of vinyl arenes*

Although Heck et al. initially reported the formation of styrene in low yield from vinyl acetate, via palladium catalysis, the first efficient XEC between an aryl and a vinyl compound was achieved through electrosynthesis using a sacrificial anode and cobalt catalysis. This approach enabled, for the first time, the use of vinyl acetates as reagents, compounds that are readily accessible from abundant carbonyl precursors, inexpensive, stable, and environmentally benign.

Although being considered highly attractive alkenyl reagents, vinyl acetates are rarely employed due to their low intrinsic reactivity. Daves and Arai described the first direct Pd-catalyzed vinylation starting from vinyl acetate and iodo compounds. However, poor yields were obtained [42,43]. Our group was the first to report a cobalt-catalyzed electrochemical vinylation of aryl halides using vinyl acetates (Scheme 6). This reaction was performed in an undivided cell equipped with an iron anode and a mixture of acetonitrile/pyridine [44]. This method afforded good to excellent yields, although it required a stoichiometric amount of bipyridine, which remains a notable limitation.

In 2005, we adapted this transformation to a conventional chemical method using manganese as the reductant, this time employing only a catalytic amount of bipyridine (Scheme 7) [45]. The proposed mechanism involves a six-membered transition state

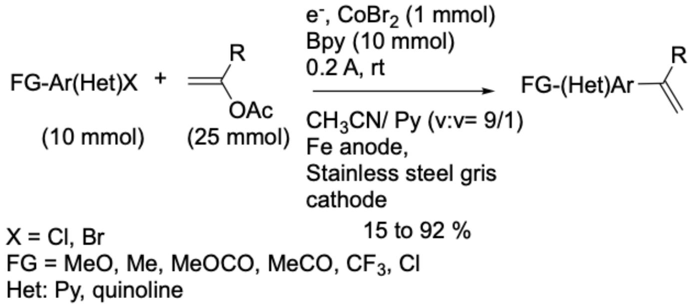

Scheme 6. Cobalt-catalyzed electrochemical vinylation of aryl halides using vinylic acetates.

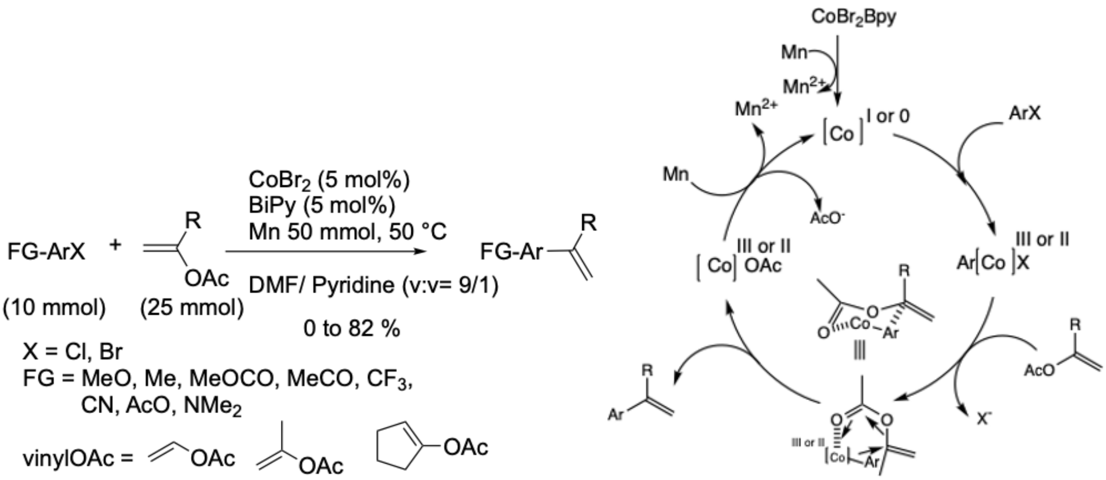

Scheme 7. Cobalt-catalyzed vinylation of functionalized aryl halides with vinyl acetates and proposed mechanism.

in which the aryl group adds to the more substituted carbon of the double bond.

Later, Shu et al. described several nickel-catalyzed XECs for C–C bond formation using alkenyl acetates as starting materials [46].

A similar strategy was applied to the synthesis of stilbenes from β-bromostyrenes and aryl halides (Scheme 8) [47]. These compounds are of significant interest due to their presence in the manufacture of industrial dyes, dye lasers, optical brighteners, scintillator, other materials, and a wide range of biologically active molecules, including resveratrol and combretastatin. Stilbenes can be obtained via XEC between aryl halides and bromostyrenes using cobalt catalysis. However, halostyrenes (X = Cl or Br) are more reactive than vinyl acetates and must be added dropwise to prevent dimerization.

Aryl bromides bearing electron-donating or electron-withdrawing groups in the *ortho*, *meta*, or *para* positions afforded good yields. Moreover, this method proceeds with complete retention of the double bond configuration, in contrast to reactions catalyzed by nickel.

1.3. *Formation of 1,3-dienes*

1,3-Dienes are a prominent class of functional molecules with diverse applications in materials science, natural product synthesis, and pharmaceuticals. Recent years have seen significant progress in both their synthesis and utilization. Beyond classic methods such as the Wittig and Julia reactions, 1,3-dienes can be accessed through elegant transition-metal-catalyzed coupling strategies. This includes

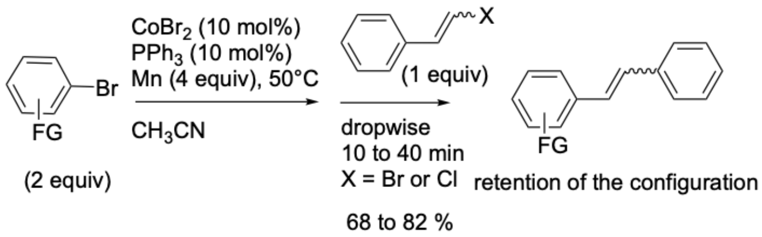

Scheme 8. Cobalt-catalyzed vinylation of aromatic halides using β-halostyrenes.

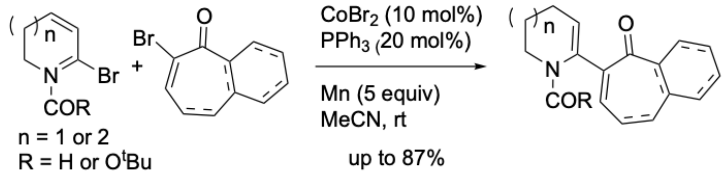

Scheme 9. Access to functionalized benzotropones, azepanes, and piperidines by reductive cross-coupling of α-bromo enones with α-bromo enamides.

palladium-catalyzed Suzuki, Stille, and Heck reactions involving vinyl halides, as well as transformations using alkynes, allenes, and carbenes. Moreover, ruthenium-, iridium-, and palladium-catalyzed processes offer straightforward access to 1,3-dienes as well.

Nickel-catalyzed XECs developed by Gong and Shu et al. allow the formation of vinyl–vinyl frameworks from vinyl halides and vinyl triflates, or between two vinyl halides [48,49]. While cobalt-catalyzed couplings using vinyl Grignard or vinyl zinc reagents with vinyl halides, triflates, or acetates have been reported, the only cobalt-catalyzed XEC between two vinyl compounds was described by Beng et al., involving α-bromo enones and α-bromo enamides for the synthesis of azepanes, piperidines, and benzotropones (Scheme 9) [50].

2. Formation of C(sp^2)–C(sp^3) bonds

The earliest cobalt-catalyzed XEC leading to a Csp^2–Csp^3 bond formation was achieved via electrosynthesis, similar to nickel-based systems.

2.1. *Coupling of aryl halides with allylic compounds*

This initial transformation involving aryl halides and allyl acetates was reported by electrosynthesis. Unlike nickel catalysis, which required dropwise addition of reactive allyl chlorides or acetate [51], the cobalt system allowed the addition of allyl acetates at the beginning of the reaction, simplifying the procedure. The reaction was conducted in an undivided cell with an iron anode, using cobalt bromide as the catalyst in acetonitrile/pyridine (Scheme 10) [52].

Aryl bromides bearing electron-donating or -withdrawing groups in *ortho*, *meta*, or *para* positions were well tolerated. In contrast, aryl chlorides required electron-withdrawing substituents. Heteroaryl substrates such as bromothiophenes or chloroquinaldines were also compatible. Remarkably, unlike many other methods, the major product was the linear isomer. This electrochemical synthesis was patented in 2001 [53]. Due to the perceived complexity of electrochemical methods at the time, we later developed a conventional chemical variant. Although this reaction was the first XEC involving a non-noble metal, yields were lower with substituted allyl acetates compared to the electrochemical approach [54]. Depending on the nature of the halide on aryl moiety, conditions are different (Scheme 11).

2.2. *Coupling of aryl halides with benzylic compounds*

Cobalt catalysis also enables coupling of aryl halides with benzylic compounds. Prior to exploring XECs,

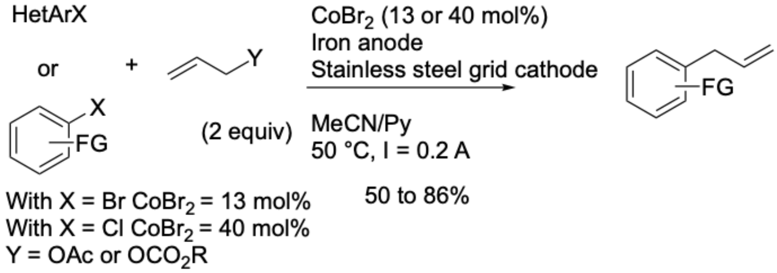

Scheme 10. Cobalt-catalyzed electrochemical coupling between aromatic halides and allylic acetates.

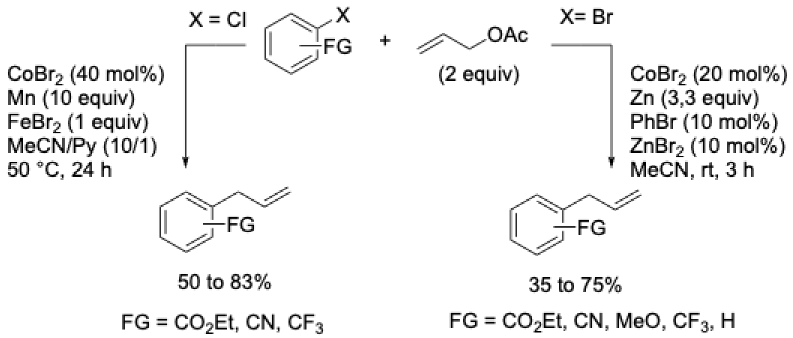

Scheme 11. Cross-coupling between aryl halides and allylic acetates using a cobalt catalyst.

Gosmini and Knochel jointly demonstrated that arylzinc [55] or benzylzinc [56] reagents could react with benzyl chlorides or aryl halides, respectively, under cobalt catalysis. However, these methods required the use of preformed organozinc species.

To overcome this limitation, a direct cobalt-catalyzed reductive arylation of benzyl chlorides with aryl halides was developed to synthesize diarylmethanes—key motifs in pharmaceuticals, agrochemicals, and supramolecular chemistry [57]. This protocol, which tolerates a wide range of functional groups, proceeds under mild conditions (rt to 35 °C) in acetonitrile without the need for ligands and uses pyridine as a cosolvent (Scheme 12). Heteroaryl bromides were also successfully employed.

Due to environmental concerns associated with halides, alternative electrophiles are being explored. Weix et al. reported a dual Ni/Co-catalyzed coupling of benzyl mesylates with aryl halides employing cobalt phthalocyanine as a radical precursor [58]. Inspired by this, our team demonstrated that benzyl mesylates—generated in situ from benzylic alcohols—could replace benzyl chlorides using simple cobalt bromide catalysis without ligands (Scheme 13) [59]. This method tolerates various functional groups on both benzyl and aryl moieties.

More recently, this strategy was extended to bench-stable benzyl sulfonium salts (Scheme 14) [60]. Under conditions similar to those optimized for mesylates, initial cross-coupling reaction yields were low but improved significantly upon addition of bipyridine. Mechanistic studies suggest that low-valent cobalt activates both aryl halides and C–S bonds via single-electron transfer, generating benzyl radicals.

2.3. *Coupling of aryl halides with non-activated alkyl halides*

Earlier studies primarily utilized activated alkyl electrophiles such as benzyl or allyl derivatives. Jacobi von Wangelin et al. used iron or cobalt catalysis in combination with magnesium as a reductant to expand the scope to non-activated alkyl halides. However, the underlying mechanism involves the in situ formation of Grignard reagents,

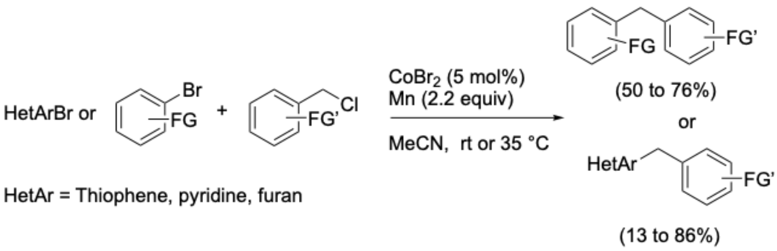

Scheme 12. Cross-electrophilic coupling benzyl chlorides and (Het)aryl bromides.

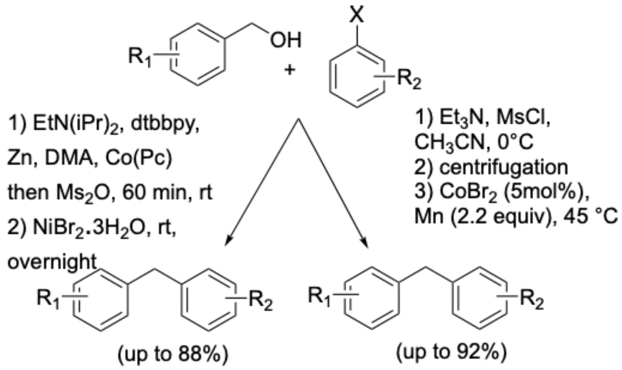

Scheme 13. Ni/Co or Co-catalyzed formation of functionalized diarylmethanes from benzyl alcohols and aryl halides.

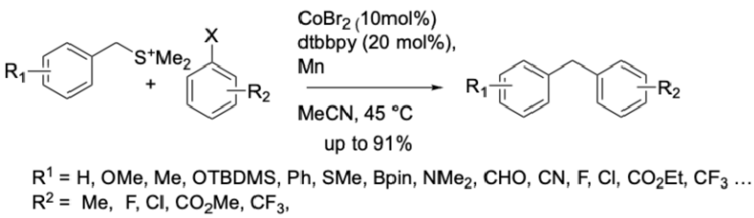

Scheme 14. Synthesis of diarylmethanes by cobalt-catalyzed reductive cross-coupling via Csp^3–S bond activation.

which inherently limits the functional group tolerance of the reaction [61].

Later, a more versatile system based on $CoBr_2$/iPr_2PhP/Mn in DMF/pyridine at 30 °C was developed (Scheme 15). This protocol tolerated functional groups and gave improved yields when using monodentate phosphine ligands, in contrast to bidentate nitrogen ligands. A slight excess of alkyl bromide was required, unlike the stoichiometric amounts typically sufficient for more reactive alkyl partners.

The mechanistic hypothesis is similar to other cobalt-catalyzed diarylmethane formation (Scheme 16). The initiating step is the reduction of the Co(II) precatalyst into the active low-valent Co(I) species by manganese. Subsequent oxidative addition to the aryl bromide forms an aryl Co(III) intermediate, which is reduced to arylcobalt(II). At the same time, the reduction of alkyl compound leads to the alkyl radical intermediate. Finally, the alkyl arylcobalt complex, generated from the combination of the alkyl radical and the arylcobalt complex, provides the cross-coupling product by reductive elimination together with the regeneration of the active species Co(I), closing the catalytic cycle.

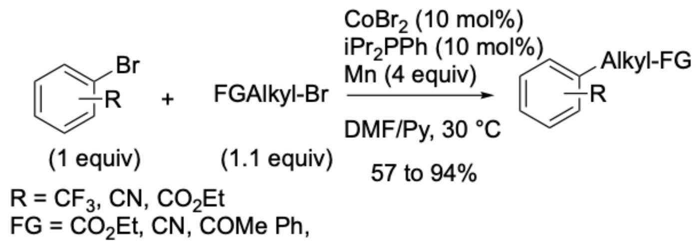

Scheme 15. Cobalt-catalyzed alkylation of aryl halides.

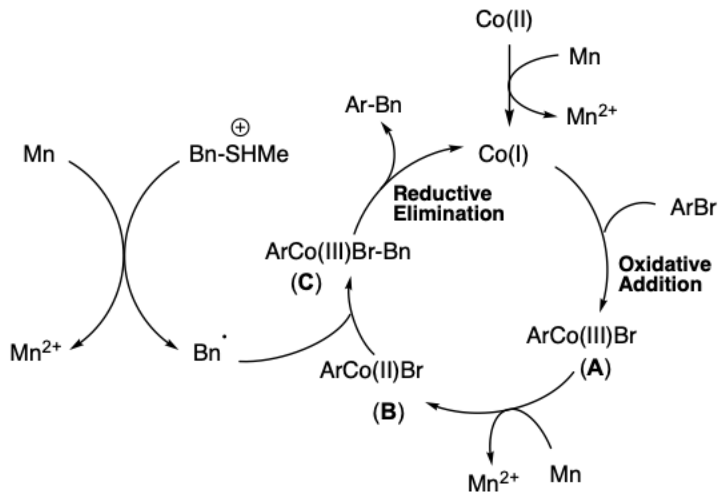

Scheme 16. Proposed mechanism.

2.4. *Coupling of vinyl compounds with benzyl chloride*

Beyond aryl partners, vinyl halides can also be coupled with benzyl chlorides. A cobalt/manganese system using $CoBr_2(PPh_3)_2$ was reported in acetonitrile with NaI as additive (Scheme 17). Electron-withdrawing groups required elevated temperatures (50 °C), while electron-donating groups allowed reactions at 0 °C to room temperature. Lipshutz et al. [62] previously described a similar transformation using palladium without organic solvents. More recently, Reisman and Cherney [63] developed an enantioselective nickel-catalyzed cross-coupling of secondary benzyl chlorides with styrenyl bromides. However, their method was not stereospecific: Z-alkenyl bromides yielded exclusively E-products. In contrast, the cobalt/manganese system preserved the stereochemistry of the starting material.

3. Formation of C(sp^3)–C(sp^3) bonds

Reductive cross-coupling between two alkyl electrophiles has emerged as a powerful strategy for constructing C(sp^3)–C(sp^3) bonds—a long-standing challenge in organic synthesis due to issues such as β-hydride elimination and the control of the selectivity. While nickel catalysis has traditionally dominated this field, cobalt has recently gained attention as a sustainable and versatile alternative, offering distinct reactivity profiles.

Historically, the Wurtz reaction was one of the earliest alkyl–alkyl coupling methods. However, it was limited to the synthesis of symmetrical alkanes due to uncontrolled radical formation. More modern approaches involve the cross-coupling of alkylmetals with alkyl halides, typically catalyzed by palladium or nickel. Yet, when using non-activated alkyl halides, undesired β-hydride elimination often occurs due to slow reductive elimination, especially in the absence

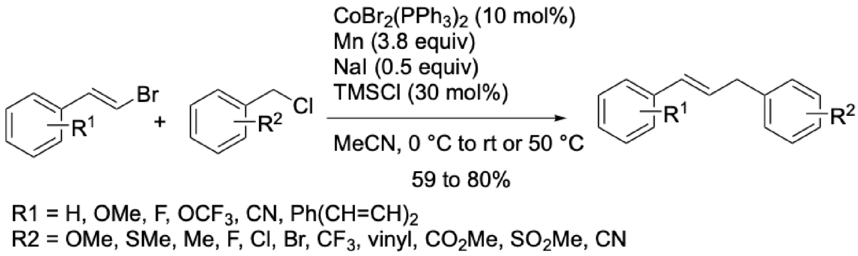

Scheme 17. Cobalt-catalyzed reductive cross-coupling between styryl and benzyl halides.

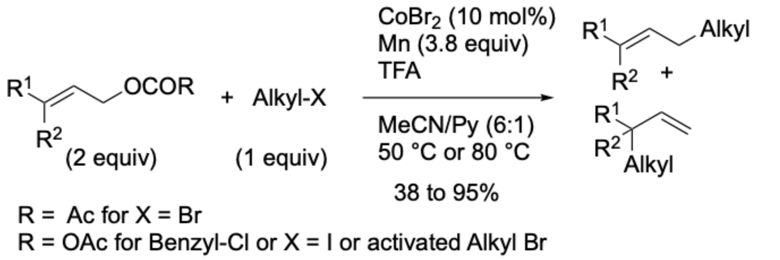

Scheme 18. Co-catalyzed reductive allylation of alkyl halides with allylic acetates and carbonates.

of bulky electron-rich phosphine or N-heterocyclic carbenes (NHC) ligands.

Nickel-catalyzed XECs have shown promise in suppressing β-hydride elimination by leveraging low-valent metal centers under reducing conditions [64]. However, cobalt catalysis offers complementary advantages, including broader functional group tolerance and enhanced radical reactivity.

Cobalt complexes stabilized by ligands such as bipyridines, phenanthrolines, or salen-type frameworks can mediate the coupling of two unactivated alkyl halides in the presence of external reductants like zinc or manganese. Alternatively, electrochemical reduction can generate low-valent cobalt species in situ, eliminating the need for sacrificial metals.

A key advantage of cobalt catalysis is its ability to suppress homocoupling and promote cross-coupling selectivity, particularly when using sterically or electronically differentiated electrophiles. Unlike palladium, cobalt catalysts are more effective in radical-mediated pathways and exhibit higher tolerance to functional groups.

3.1. *Coupling of alkyl halides with allyl acetates*

While cobalt-catalyzed homocoupling of non-activated alkyl halides has been reported [65], heterocoupling has also been achieved—either between an activated and a non-activated alkyl electrophile, or between two activated alkyl species such as benzyl or allyl compounds.

In 2011, we reported the first reductive cobalt-catalyzed Csp^3–Csp^3 formation by describing the allylation of alkyl halides using either allyl acetates or allyl carbonates, depending on the nature of the alkyl halide (Scheme 18) [66]. The reaction was effective with primary, secondary, and tertiary alkyl substrates and was conducted in a mixture of acetonitrile and pyridine.

For reactive alkyl halides such as benzyl chlorides, alkyl iodides, or alkyl bromides bearing β-electron-withdrawing groups, more reactive allyl carbonates were preferred over acetates, and the reaction temperature was lowered to 50 °C (versus 80 °C). With substituted allyl compounds, the linear product was consistently favored. Experimental evidence supported the involvement of alkyl radical intermediates.

3.2. *Coupling of activated alkyl compounds with allylic compounds*

More recently, the cobalt-catalyzed reductive alkylation was extended to other activated alkyl

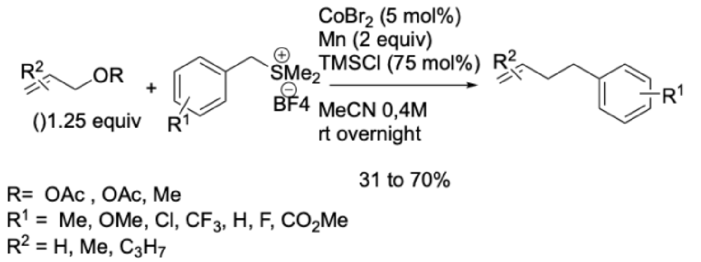

Scheme 19. Co-catalyzed cross-electrophile couplings of benzyl sulfonium salts with allyl esters or ethers.

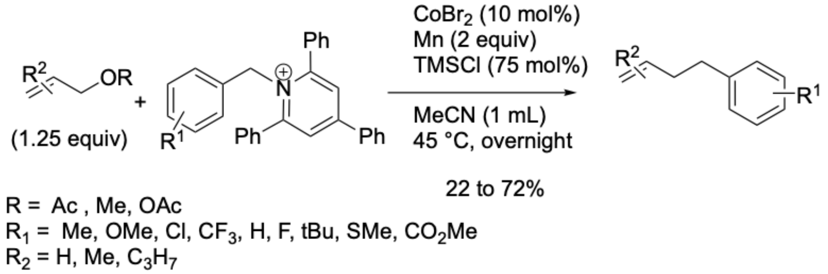

Scheme 20. Cobalt-catalyzed cross-electrophile couplings of benzyl Katritzky salts with allyl esters or ethers.

electrophiles, including benzyl sulfonium salts and Katritzky pyridinium salts, and XEC of benzyl sulfonium salts with *O*-allyl electrophiles, using simple $CoBr_2$ and Mn as reductant in acetonitrile without ligands, was demonstrated (Scheme 19) [67]. This system activated both C–S bonds (from sulfonium salts) and C–O bonds (from allyl esters or ethers), enabling the synthesis of functionalized alkyl–olefinic compounds in moderate to good yields. Notably, these reactions involved two non-halogenated electrophiles—a first in cobalt-catalyzed C–C bond formation.

While nickel-catalyzed cross-coupling reactions with Katritzky salts had been described by Watson et al., Ni et al., and Rueping et al. [68–70], they typically involved alkyl metals or aryl halides. The only cobalt-catalyzed variant was reported by Kojima and Matsunaga et al. via cobalt/organophotoredox dual catalysis, but it was limited to secondary alkyl pyridinium salts [71]. A similar transformation using benzylic Katritzky salts was also reported [72]. This method offers a simple and efficient alternative for synthesizing allyl–benzyl derivatives, using $CoBr_2$, under mild conditions (Scheme 20). The reaction was also applicable to allyl alkyl ethers, as previously shown with benzyl sulfonium salts. Mechanistic studies suggest the formation of benzyl radicals from pyridinium or sulfonium salts, and π-allylcobalt intermediates from allyl compounds.

Benzyl sulfonium salts were also shown to couple with benzyl chlorides or alkyl iodides, yielding functionalized alkyl derivatives [73] (Scheme 21). Preliminary mechanistic investigations suggest the involvement of two radical species—one from the sulfonium salt and the other from the alkyl halide.

4. Conclusion

Cobalt-catalyzed reductive cross-coupling, also known as cross-electrophile coupling (XEC), represents a powerful and sustainable approach for constructing $C(sp^2)$–$C(sp^2)$, $C(sp^2)$–$C(sp^3)$, and $C(sp^3)$–$C(sp^3)$ bonds from readily available precursors. This method stands out for its ability to activate non-halogenated electrophiles (e.g., C–O, C–S, or C–N bonds), its broad functional group tolerance, and its compatibility with mild conditions. Importantly, it circumvents the need for stoichiometric organometallic reagents that are typically required in traditional approaches. Although cobalt was the

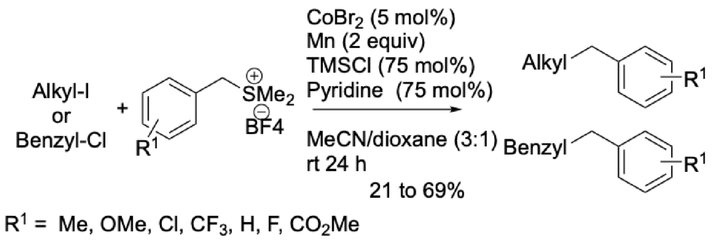

Scheme 21. Cobalt-catalyzed cross-electrophile couplings of benzyl sulfonium salts with alkyl iodides or benzyl chlorides.

first catalyst used to achieve efficient chemical XECs, its applications remain less explored than those of nickel. Continued advances in catalyst design, mechanistic insight, reaction scope, and integration with electrochemical and/or photochemical methods are expected to unlock the full potential of cobalt catalysis in modern synthetic chemistry.

Declaration of interests

The author does not work for, advise, own shares in, or receive funds from any organization that could benefit from this article, and has declared no affiliations other than their research organization.

References

[1] C. E. I. Knappke, S. Grupe, D. Gärtner, M. Corpet, C. Gosmini and A. von Wangelin, "Reductive cross-coupling reactions between two electrophiles", *Chem. Eur. J.* **20** (2014), pp. 6828–6842.

[2] L. E. Omar, M. Beleh, I. C. Priest, et al., "Cross-electrophile coupling: Principles, methods, and applications in synthesis", *Chem. Rev.* **124** (2024), pp. 13397–13569.

[3] S. Geng, C. Shi, B. Guo, H. Hou, Z. Liu and Z. Feng, "Recent progress in transition-metal-catalyzed reductive cross-coupling reactions using diboron reagents as reductants", *ACS Catal.* **13** (2023), pp. 15469–15480.

[4] C. C. Johansson Seechurn, M. O. Kitching, T. J. Colacot and V. Snieckus, "Palladium-atalyzed cross-oupling: a historical contextual perspective to the 2010 Nobel Prize", *Angew. Chem. Int. Ed. Engl.* **51** (2012), pp. 5062–5085.

[5] T. Shu and J. Cossy, "Enantioselective cross-couplings between halide derivatives and organometallics by using iron and cobalt catalysts: Formation of C–C bonds", *Chem. Eur. J.* **27** (2021), pp. 11021–11029.

[6] A. Guerinot and J. Cossy, "Cobalt-catalyzed cross-couplings between alkyl halides and Grignard reagents", *Acc. Chem. Res.* **53** (2020), pp. 1351–1363.

[7] F. H. Lutter, S. Graßl, L. Grokenberger, M. S. Hofmayer, Y.-H. Chen and P. Knochel, "Cobalt-catalyzed cross-couplings and electrophilic aminations using organozinc pivalates", *Chem. Cat. Chem.* **11** (2019), pp. 5188–5197.

[8] C. Gosmini and A. Moncomble, "Cobalt-catalyzed cross-coupling reactions of aryl halides", *Isr. J. Chem.* **50** (2010), pp. 568–576.

[9] Y. Liu, P. Li, Y. Wang and Y. Qiu, "Electroreductive cross-electrophile coupling (eXEC) reactions", *Angew. Chem. Int. Ed. Engl.* **62** (2023), article no. e202306679.

[10] M.-Y. Gao and C. Gosmini, "Transition metal catalyzed electroreductive cross-coupling for C–C bond formation", *Isr. J. Chem.* **64** (2024), article no. e202300074.

[11] S. D. Minteer and P. Baran, "Electrifying synthesis: Recent advances in the methods, materials, and techniques for organic electrosynthesis", *Acc. Chem. Res.* **53** (2020), pp. 545–546.

[12] M. Troupel, Y. Rollin, S. Sibille, J. Perichon and J.-F. Fauvarque, "Catalyse par des complexes σ-aryl-nickel de l'electroreduction en biaryles des halogénures aromatiques", *J. Organomet. Chem.* **202** (1980), pp. 435–446.

[13] P. Gomes, C. Gosmini, J.-Y. Nedelec and J. Périchon, "Cobalt bromide as catalyst in electrochemical addition of aryl halides onto activated olefins", *Tetrahedron Lett.* **41** (2000), pp. 3385–3388.

[14] A. Wurtz, "Coupling of two alkyl radicals by treating two moles of alkyl halides with two moles of sodium", *Ann. Chem. Pharm.* **96** (1855), pp. 364–375.

[15] J. Hassan, C. Hathroubi, C. Gozzi and M. Lemaire, "Synthesis of unsymmetrical biaryls via palladium-catalyzed coupling reaction of aryl halides", *Tetrahedron Lett.* **41** (2000), pp. 8791–8794.

[16] L. Wang, Y. Zhang, L. Liu and Y. Wang, "Palladium-catalyzed homocoupling and cross-coupling reactions of aryl halides in poly (ethylene glycol)", *J. Org. Chem.* **71** (2006), pp. 1284–1287.

[17] P. Gomes, C. Gosmini and J. Périchon, "New chemical cross-coupling between aryl halides and allylic acetates using a cobalt catalyst", *Org. Lett.* **5** (2003), pp. 1043–1045.

[18] C. Gosmini, C. Bassene-Ernst and M. Durandetti, "Synthesis of functionalized 2-arylpyridine from 2-halopyridines and various aryl halides via a nickel catalyst", *Tetrahedron* **65** (2009), pp. 6141–6146.

[19] D. A. Everson, R. Shrestha and D. J. Weix, "Nickel-catalyzed reductive cross-coupling of aryl halides with alkyl halides", *J. Am. Chem. Soc.* **132** (2010), pp. 920–921.

[20] T. Yang, S. Wang, H. Xu and H. Gong, "Nickel-catalyzed reductive cross-coupling of unactivated alkyl halides", *Org. Lett.* **13** (2011), pp. 2138–2141.

[21] L. L. Anka-Lufford, K. M. M. Huihui, N. J. Gower, L. K. G. Ackerman and D. J. Weix, "Nickel-catalyzed cross-electrophile coupling with organic reductants in non-amide solvents", *Chem. Eur. J.* **22** (2016), pp. 11564–11567.

[22] H. Xu, C. Zhao, Q. Qian, W. Deng and H. Gong, "Nickel-catalyzed cross-coupling of unactivated alkyl halides using bis(pinacolato)diboron as reductant", *Chem. Sci.* **4** (2013), pp. 4022–4029.

[23] J. Zhang, Z. Li, J. Zhuo, Y. Cui, T. Han and C. Li, "Tandem decarboxylative cyclization/alkenylation strategy for total syntheses of (+)-longirabdiol, (−)-longirabdolactone, and (−)-effusin", *J. Am. Chem. Soc.* **141** (2019), pp. 8372–8380.

[24] W. M. Czaplik, M. Mayer and A. Jacobi von Wangelin, "Domino iron catalysis: direct aryl-alkyl cross-coupling", *Angew. Chem., Int. Ed. Engl.* **48** (2009), pp. 607–610.

[25] J. Tang, L. L. Liu, S. Yang, X. Cong, M. Luo and X. Zeng, "Chemoselective cross-coupling between two different and unactivated C(aryl)–O bonds enabled by chromium catalysis", *J. Am. Chem. Soc.* **142** (2020), pp. 7715–7720.

[26] K. Prier, D. A. Rankic and D. W. C. MacMillan, "Visible light photoredox catalysis with transition metal complexes: Applications in organic synthesis", *Chem. Rev.* **113** (2013), pp. 5322–5363.

[27] N. A. Romero and D. A. Nicewicz, "Organic photoredox catalysis", *Chem. Rev.* **116** (2016), pp. 10075–10166.

[28] T. Wu, A. J. Castro, K. Ganguli, M. E. Rotella, N. Ye, F. Gallou, B. Wu and D. J. Weix, "Cross-electrophile coupling to form sterically hindered $C(sp^2)$–$C(sp^3)$ bonds: Ni and Co afford complementary reactivity", *J. Am. Chem. Soc.* **147** (2025), pp. 9449–9456.

[29] D. S. Ennis, J. McManus, W. Wood-Kaczmar, J. Richardson, G. E. Smith and A. Crastairs, "Multikilogram-scale synthesis of a biphenyl carboxylic acid derivative using a Pd/C-mediated Suzuki coupling approach", *Org. Process Res. Dev.* **3** (1999), pp. 248–252.

[30] J. P. Corbet and G. Mignani, "Selected patented cross-coupling reaction technologies", *Chem. Rev.* **106** (2006), pp. 2651–2710.

[31] J. Hassan, M. Sevignon, C. Gozzi, E. Schulz and M. Lemaire, "Aryl–aryl bond formation one century after the discovery of the ullmann reaction", *Chem. Rev.* **102** (2002), pp. 1359–1470.

[32] M. S. Kharasch and C. F. Fuchs, "Factors determining the course and mechanisms of grignard reactions. IV. The effect of metallic halides on the reaction of aryl grignard reagents and organic halides", *J. Am. Chem. Soc.* **63** (1941), pp. 2316–2320.

[33] T. Hatakeyama, S. Hashimoto, K. Ishizuka and M. Nakamura, "Highly selective biaryl cross-coupling reactions between aryl halides and aryl grignard reagents: A new catalyst combination of N-heterocyclic carbenes and iron, cobalt, and nickel fluoride", *J. Am. Chem. Soc.* **131** (2009), pp. 11949–11963.

[34] S. Gülak, O. Stepanek, J. Malberg, B. R. Rad, M. Kotora, R. Wolf and A. Jacobi von Wangelin, "Highly chemoselective cobalt-catalyzed biaryl coupling reactions", *Chem. Sci.* **4** (2013), pp. 776–784.

[35] J. M. Neely, M. J. Bezdek and P. J. Chirik, "Insight into transmetalation enables cobalt-catalyzed Suzuki–Miyaura cross coupling", *ACS Cent. Sci.* **2** (2016), pp. 935–942.

[36] S. Asghar, S. B. Tailor, D. Elorriaga and R. B. Bedford, "Cobalt-catalyzed Suzuki biaryl coupling of aryl halides", *Angew. Chem. Int. Ed. Engl.* **56** (2017), pp. 16367–16370.

[37] E. Le Gall, C. Gosmini, J.-Y. Nédélec and J. Périchon, "Cobalt-catalyzed electrochemical cross-coupling of functionalized phenyl halides with 4-chloroquinoline derivatives", *Tetrahedron Lett.* **42** (2001), pp. 267–269.

[38] P. Gomes, H. Fillon, C. Gosmini, E. Labbé and J. Périchon, "Synthesis of unsymmetrical biaryls by electroreductive cobalt-catalyzed cross-coupling of aryl halides", *Tetrahedron* **58** (2002), pp. 8417–8424.

[39] M. Amatore and C. Gosmini, "Efficient cobalt-catalyzed formation of unsymmetrical biaryl compounds and its application in the synthesis of a sartan intermediate", *Angew. Chem. Int. Ed. Engl.* **120** (2008), pp. 2119–2122.

[40] C. Dorval, M. Tricoire, J.-M. Begouin, V. Gandon and C. Gosmini, "Cobalt-catalyzed $C(sp^2)$–CN bond activation: Cross-electrophile coupling for biaryl formation and mechanistic insight", *ACS Catal.* **10** (2020), pp. 12819–12827.

[41] M. Tobisu, Y. Kita, Y. Ano and N. Chatani, "Rhodium-catalyzed silylation and intramolecular arylation of nitriles via the silicon-assisted cleavage of carbon–cyano bonds", *J. Am. Chem. Soc.* **130** (2008), pp. 15982–15989.

[42] I. Arai and G. D. Daves Jr., "Three isomeric 1, 3-dimethyl-5-(dihydropyran-2-yl)-2, 4-pyrimidinediones. Palladium-catalyzed synthesis and spectrometric properties", *Heterocycl. Chem.* **15** (1978), pp. 351–352.

[43] I. Arai and G. D. Daves Jr., "Palladium-catalyzed phenylation of enol ethers and acetates", *J. Org. Chem.* **44** (1979), pp. 21–23.

[44] P. Gomes, C. Gosmini and J. Périchon, "Cobalt-catalyzed electrochemical vinylation of aryl halides using vinylic acetates", *Tetrahedron* **59** (2003), pp. 2999–3002.

[45] M. Amatore, C. Gosmini and J. Périchon, "Cobalt-catalyzed vinylation of functionalized aryl halides with vinyl acetates", *J. Eur. J. Org. Chem.* **5** (2005), pp. 989–992.

[46] X. Pang, P.-F. Su and X.-Z. Shu, "Reductive cross-coupling of unreactive electrophiles", *Acc. Chem. Res.* **55** (2022), pp. 2491–2509.

[47] A. Moncomble, P. Le Floch, A. Lledos and C. Gosmini, "Cobalt-catalyzed vinylation of aromatic halides using β-halostyrenes: experimental and DFT studies", *J. Org. Chem.* **77** (2012), pp. 5056–5062.

[48] Y. Sha, J. Liu, L. Wang, D. Liang, D. Wu and H. Gong, "Nickel-catalyzed reductive 1,3-diene formation from the cross-coupling of vinyl bromides", *Org. Biomol. Chem.* **19** (2021), pp. 4887–4890.

[49] G.-L. Xu, C.-Y. Liu, X. Pang, X.-Y. Liu and X.-Z. Shu, "Nickel-catalyzed cross-electrophile vinyl–vinyl coupling: An approach to structurally versatile dienylboronates", *CCS Chem.* **4** (2022), pp. 864–871.

[50] T. K. Beng, K. Sincavage, A. W. V. Silaire, A. Alwali, D. P. Bassler, L. E. Spence and O. Beale, "Direct access to functionalized benzotropones, azepanes, and piperidines by reductive cross-coupling of α-bromo enones with α-bromo enamides", *Org. Biomol. Chem.* **13** (2015), pp. 5349–5353.

[51] M. Durandetti, J.-Y. Nédélec and J. Périchon, "Nickel-catalyzed direct electrochemical cross-coupling between aryl halides and activated alkyl halides", *J. Org. Chem.* **61** (1996), pp. 1748–1755.

[52] P. Gomes, C. Gosmini and J. Périchon, "Cobalt-catalyzed direct electrochemical cross-coupling between aryl or heteroaryl halides and allylic acetates or carbonates", *J. Org. Chem.* **68** (2003), pp. 1142–1145.

[53] H. Fillon, C. Gosmini and J. Périchon, Procédé d'hétérocouplage électrolytique entre un (pseudo) halogénure d'aryle et un ester d'allyle, utilisation du cobalt pour réaliser ledit couplage et composition pour ce faire, FR patent, no. 01/08808, July 3, 2001.

[54] P. Gomes, C. Gosmini and J. Périchon, "New chemical cross-coupling between aryl halides and allylic acetates using a cobalt catalyst", *Org. Lett.* **5** (2003), pp. 1043–1045.

[55] M. Amatore and C. Gosmini, "Synthesis of functionalised diarylmethanes via a cobalt-catalysed cross-coupling of arylzinc species with benzyl chlorides", *Chem. Commun.* **40** (2008), pp. 5019–5021.

[56] A. D. Benischke, I. Knoll, A. Rérat, C. Gosmini and P. Knochel, "A practical Cobalt-catalyzed cross-coupling of benzylic zinc reagents with aryl and heteroaryl bromides or chlorides", *Chem. Commun.* **52** (2016), pp. 3171–3174.

[57] S. Pal, S. Chowdhury, E. Rozwadowski, A. Auffrant and C. Gosmini, "Cobalt-catalyzed reductive cross-coupling between benzyl chlorides and aryl halides", *Adv. Synth. Catal.* **358** (2016), pp. 2431–2435.

[58] L. K. G. Ackerman, L. L. Anka-Lufford, M. Naodovic and D. J. Weix, "Cobalt co-catalysis for cross-electrophile coupling: diarylmethanes from benzyl mesylates and aryl halides", *Chem. Sci.* **6** (2015), pp. 1115–1119.

[59] B. R. P. Reddy, S. Chowdhury, A. Auffrant and C. Gosmini, "Cobalt-catalyzed formation of functionalized diarylmethanes from benzylmesylates and aryl halides", *Adv. Synth. Catal.* **360** (2018), pp. 3026–3026.

[60] M. Gao, M. Durandetti and C. Gosmini, "Synthesis of diarylmethanes by cobalt-catalyzed reductive cross-coupling via Csp^3–S bond activation", *Synthesis* **57** (2025), pp. 3179–3188.

[61] W. M. Czaplik, M. Mayer and A. J. von Wangelin, "Direct cobalt-catalyzed cross-coupling between aryl and alkyl halides", *Synlett* **8** (2009), pp. 2931–2934.

[62] V. Krasovskaya, A. Krasovskiy, A. Bhattacharjya and B. H. Lipshutz, ""On water" sp^3–sp^2 cross-couplings between benzylic and alkenyl halides", *Chem. Commun.* **47** (2011), pp. 5717–5719.

[63] A. H. Cherney and S. E. Reisman, "Nickel-catalyzed asymmetric reductive cross-coupling between vinyl and benzyl electrophiles", *J. Am. Chem. Soc.* **136** (2014), pp. 14365–14368.

[64] L.-X. You, L. Tian, C. L. Guo, S.-X. Li, Y.-C. Liu, Y.-L. Li and W. Shu, "Ni-catalyzed cross-electrophile alkyl–alkyl coupling reactions", *Sci. China Chem.* **68** (2025), pp. 3376–3400.

[65] Y. Cai, X. Qian and C. Gosmini, "Cobalt-catalyzed Csp^3–Csp^3 homocoupling", *Adv. Synth. Catal.* **358** (2016), pp. 2427–2430.

[66] X. Qian, A. Auffrant, A. Felouat and C. Gosmini, "Cobalt-catalyzed reductive allylation of alkyl halides with allylic acetates or carbonates", *Angew. Chem. Int. Ed. Engl.* **50** (2011), pp. 10402–10405.

[67] M. Gao and C. Gosmini, "Co-catalyzed reductive crosss-coupling of Csp^3–S with C-allyl-O electrophiles to form Csp^3–Csp^3 bonds", *Adv. Synth. Catal.* **365** (2023), pp. 3597–3602.

[68] S. Ni, C.-X. Li, Y. Mao, J. Han, Y. Wang, H. Yan and Y. Pan, "Ni-catalyzed deaminative cross-electrophile coupling of Katritzky salts with halides via C–N bond activation", *Sci. Adv.* **5** (2019), article no. eaaw9516.

[69] H. Yue, C. Zhu, L. Shen, Q. Geng, K. J. Hock, T. Yuan, L. Cavallo and M. Rueping, "Nickel-catalyzed C–N bond activation: activated primary amines as alkylating reagents in reductive cross-coupling", *Chem. Sci.* **10** (2019), pp. 4430–4435.

[70] S. Plunkett, C. H. Basch, S. O. Santana and M. P. Watson, "Nickel-catalyzed C–N bond activation: activated primary amines as alkylating reagents in reductive cross-coupling", *J. Am. Chem. Soc.* **141** (2019), pp. 2257–2262.

[71] T. Sekino, S. Sato, T. Yoshino, M. Kojima and S. Matsunaga, "Regioselective deaminative allylation of aliphatic amines via dual cobalt and organophotoredox catalysis", *Org. Lett.* **24** (2022), pp. 2120–2124.

[72] M. Gao and C. Gosmini, "Cobalt-catalyzed Csp^3–Csp^3 cross-coupling of benzyl Katritzky pyridinium salts with Callyl-O electrophiles", *Org. Chem. Front.* **11** (2024), pp. 3557–3561.

[73] M.-Y. Gao and C. Gosmini, "Co-catalyzed reductive cross-couplings to construct Csp^3–Csp^3 bonds via Csp^3–S and Csp^3–X bonds activation", *Org. Lett.* **25** (2023), pp. 7689–7693.

ACADÉMIE DES SCIENCES
INSTITUT DE FRANCE

Comptes Rendus. Chimie
2026, Vol. 29, p. 19-25
https://doi.org/10.5802/crchim.431

Research article

Electro-induced carbamoylation of arenes optimized by a machine learning model

Virgile Rouffeteau [a], Clara Perrier [a], Maximilian Fleck [b], Geoffrey Gontard [c], Maxime R. Vitale [*, a] and Laurence Grimaud [*, a]

[a] Chimie Physique et Chimie du Vivant (CPCV), Département de Chimie, École Normale Supérieure, PSL University, Sorbonne Université, CNRS, 75005 Paris, France

[b] Chimie ParisTech, Université PSL, CNRS, Institute of Chemistry for Life and Health Sciences, 75005 Paris, France

[c] Institut Parisien de Chimie Moléculaire, CNRS UMR 8232, Sorbonne Université, 75252 Paris Cedex 5, France

E-mails: virgile.rouffeteau@ens.psl.eu (V. Rouffeteau), maxime.vitale@ens.psl.eu (M. R. Vitale), laurence.grimaud@ens.psl.eu (L. Grimaud)

Abstract. In this article, we report the electro-induced C–H functionalization of aromatic compounds by isocyanides and water, to produce arylcarboxamides. This controlled oxidation of electron-rich aromatic compounds leads to an eco-efficient synthesis of secondary benzocarboxamides, along with cyanide group formation. The optimization process was guided by a Bayesian optimization-based model, and good yields were quickly obtained.

Keywords. Electrosynthesis, Multicomponent reaction, C(sp^2)–H functionalization, Carbamoylation, Bayesian optimization.

Funding. ENS-PSL, CNRS, ANR (ANR-20-CE07-0020), Ecole Polytechnique (AMX).

Note. Article submitted by invitation.

Manuscript received 20 October 2025, revised 28 October 2025, accepted 19 November 2025, online since 22 January 2026.

1. Introduction

Multicomponent reactions (MCRs) have seen a surge in interest due to their significant abilities of building complex scaffolds from easy-to-access starting materials, all the while respecting the principles of green chemistry [1]. A subclass of this field is the isocyanide-based multicomponent reactions (IMCRs), the Passerini [2] and Ugi [3] reactions being prime examples. They employ the unique properties of isocyanide moieties: they classically first react as nucleophiles, to generate nitrilium species, which can then be trapped by other nucleophiles, to efficiently construct complex patterns in one step [4].

Electrosynthesis can also be a major contributor to respecting green chemistry principles, by replacing costly and stoichiometric oxidants (often toxic and with poor atom-economy), or rare-earth-based catalysts [5,6]. In this endeavour, our group [7–10] and many others [11] merged the two concepts, electrosynthesis and IMCR, to avoid the use of unstable substrates, additives, or catalysts, toward the synthesis of Passerini and Ugi adducts among other structures. However, synthetizing a benzamide group from a non-substituted aromatic compound without using a metal-based catalysis and functionalization of the aromatic ring remained elusive. Inspired by previous electro-induced C(sp^2)–H bond functionalizations [12–15] (Scheme 1), we proposed a method merging

* Corresponding authors

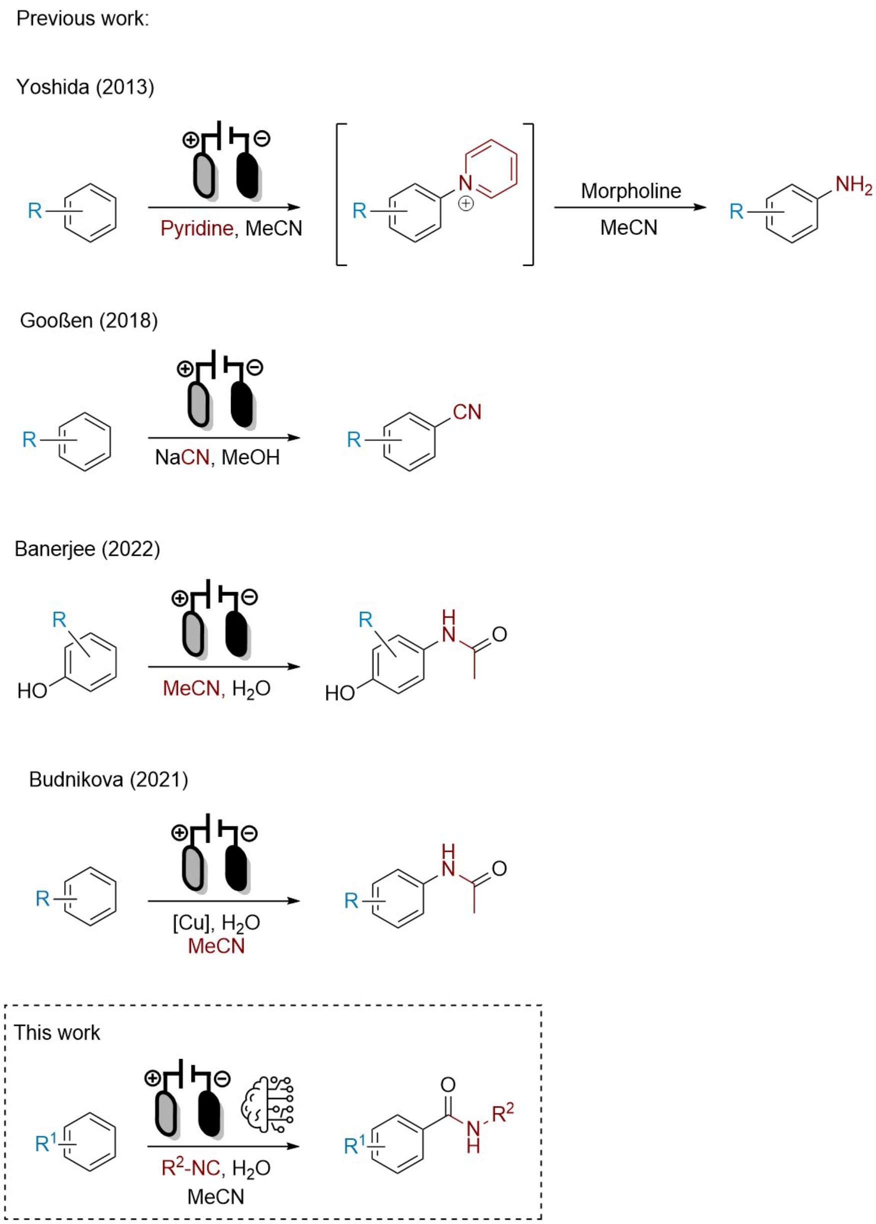

Scheme 1. Previous and current strategies for direct oxidative C(sp^2)–H functionalization.

electrosynthesis and IMCR toward the production of arylcarboxamides.

Indeed, building on the mechanistic studies of Gooßen et al. [13], we surmised that a radical cation, produced at the anode from the direct oxidation of an arene, could be trapped by an isocyanide and a water molecule to build arylcarboxamides. The released protons would in turn be converted into dihydrogen at the cathode, closing the electrical circuit (Scheme 2). This original carboxamide synthesis would avoid the use of catalyst and stoichiometric oxidants, using green energy (94% of low-carbon electricity in France's electricity mix in 2024, 96% in 2025) to convert available substrates into high-value products [16].

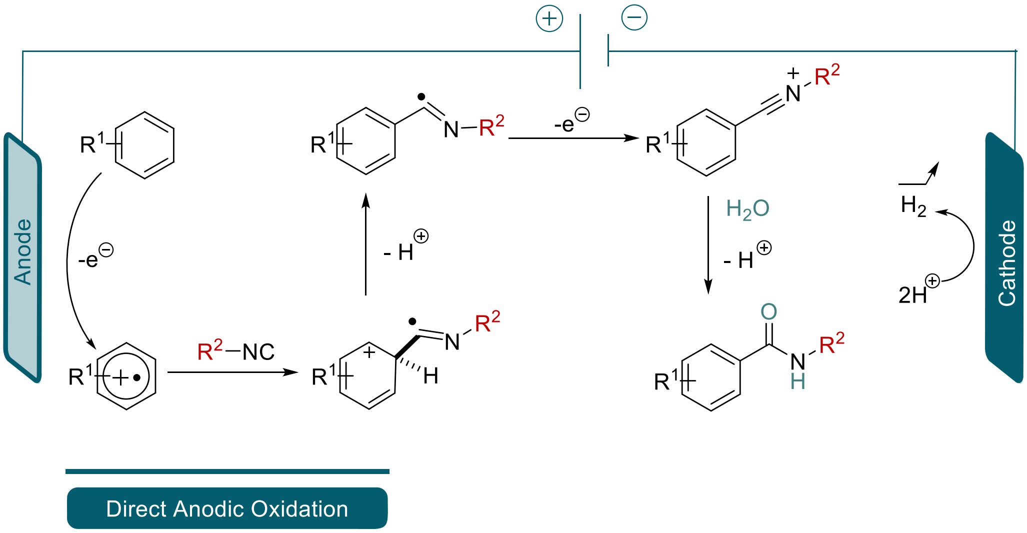

Scheme 2. Proposed mechanism.

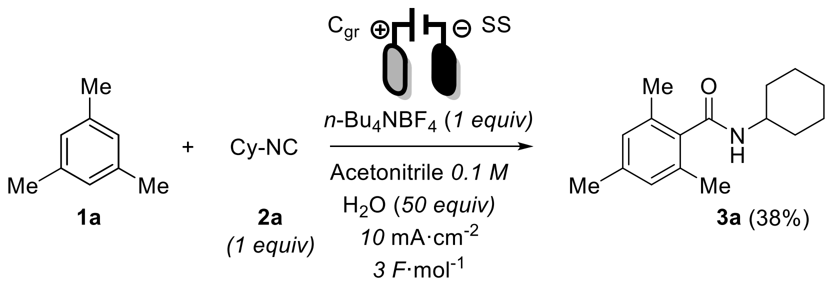

Scheme 3. Starting point.

2. Results and discussion

With this strategy in mind and using our in-house expertise on electro-induced IMCRs, we selected mesitylene **1a** as a prototypical oxidizable arene along with cyclohexyl isocyanide (Cy-CN) **2a** as partner in acetonitrile as solvent. A quick pre-optimization led to choose *N*-tetrabutylammonium tetrafluoroborate (n-Bu_4NBF_4) as supporting electrolyte, graphite as cathode and stainless steel as anode. These conditions led to the isolation of desired product **3a** in 38% yield, which constituted the starting point of the optimization process.

Subsequent tests fixed the temperature at 20 °C (a 41% yield at 60 °C was not significant enough to continue using high temperature) and showed that the stirring had no impact on the outcome. These observations fixed half of the reaction parameters (see Table S1 in Supplementary material), however, the rest of the parameters (in italic in Scheme 3) could hardly be optimized the usual way, one at a time, as they could be interdependent. Thus, we resorted to a machine learning model, as it was capable of optimizing several parameters at the same time [17–20]. The model chosen was EDBO, created by the Doyle group in 2021 [21] for its low resource cost and availability (https://edboplus.org/). While this work was in progress, the Ackerman group also used machine learning to optimize an electro-induced annulation via palladium catalysis [22], while the Sigman group reported using EDBO for the design of palladium catalyst for the fluorination of arylboronic acids [23], proving the usefulness of this strategy. In order to use this model, several questions needed to be answered:

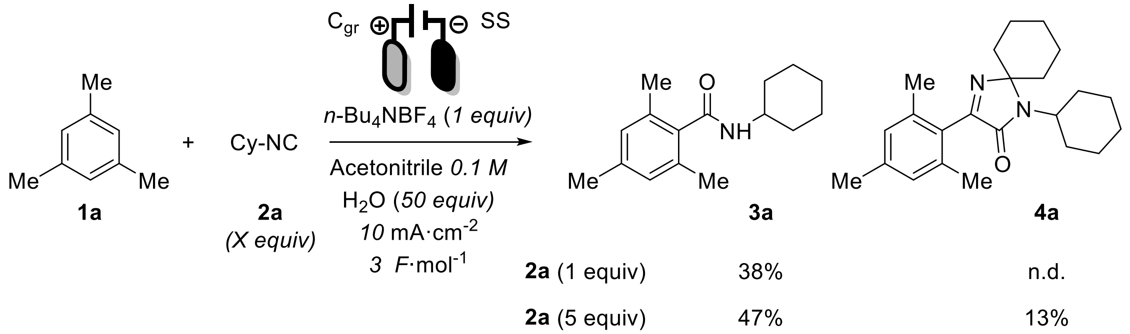

Scheme 4. Products formed according to isocyanide equivalents.

(1) Which outcome(s) is (are) of concern to us, and whether its maximization or minimization were desired? (2) How to measure the chosen outcome, and how to interact with the model? (3) What is the research space for the model to investigate? (4) What is (are) the stop condition(s)?

In our case, maximizing the yield was the main goal, which would be measured by ^{1}H NMR against an internal standard, the supporting electrolyte (it was proven to be stable with external standards). The research space was designed as neutral as possible, to avoid introducing human bias into the model (see Table 1). As an example, various amounts of the isocyanide led to different products, **3a** and **4a** (see Scheme 4, structure of **4a** was elucidated by X-ray analyses). Thus, the number of isocyanide equiv had to be limited between 0.33″ and 3 (0.33 experimentally means 1 equiv of isocyanide and 3 equiv of mesitylene).

Similarly, using more than 50 equiv of water was meaningless, so its limits were set at 1 and 50 equiv. Standard values often found in the literature for the supporting electrolyte were between 0.5 and 2 equiv; for the concentration of the reagents, they were above 0.05 M and below 0.5 M, and the current density was bounded between 5 and 25 mA·cm^{-2}. Finally, based on our proposed mechanism (see Scheme 2), this reaction would need at least 2 electrons per molecule of mesitylene. Using the same limits as for the isocyanide, the upper limit for the charge was set at 6 F·mol^{-1}. These studies led to the following research space (Table 1).

The resulting number of possible combinations was 10 500, and, as an example, a human would conduct 29 (0.3% of the research space) experiments with this table: one experiment for each value of each parameter, with all other parameters fixed, following the classical OFAT (one factor at a time) method [24]. For the purpose of this study, we decided to fix the total number of experiments to 15, which represents half the effort required with the OFAT method (below 0.15% of the research space). The results of this EDBO-led optimization are displayed in Figure 1.

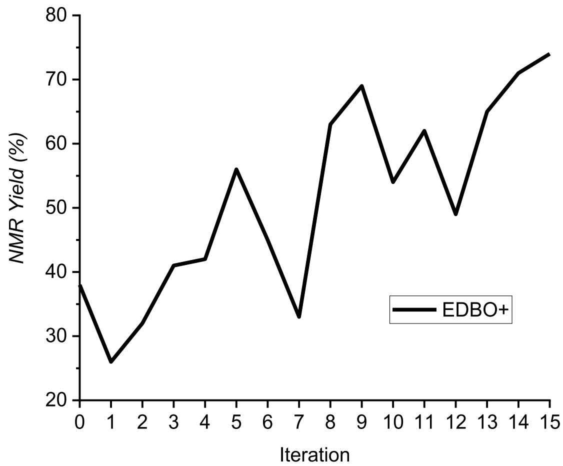

Figure 1. Evolution of yield with EDBO.

It became clear that EDBO was able to quickly increase the yield from the starting 38%, reaching 50% after 5 experiments, 70% at the 9th, and stopping at its 15th experiment, in which the starting yield of 38% was doubled to reach a high yield of 74%. The differences between the starting point (Scheme 3) and the best conditions found by EDBO (Scheme 5)

Table 1. Research space

Parameters	Values						
Cy-NC equiv	0.33	0.5	0.75	1	1.5	2	3
Water equiv	1	5	10	25	50		
n-Bu_4NBF_4 equiv	0.5	1	2				
Current density ($mA{\cdot}cm^{-2}$)	5	10	15	20	25		
Limiting reagent concentration (M)	0.05	0.1	0.15	0.2			
Charge ($F{\cdot}mol^{-1}$)	2	3	4	5	6		

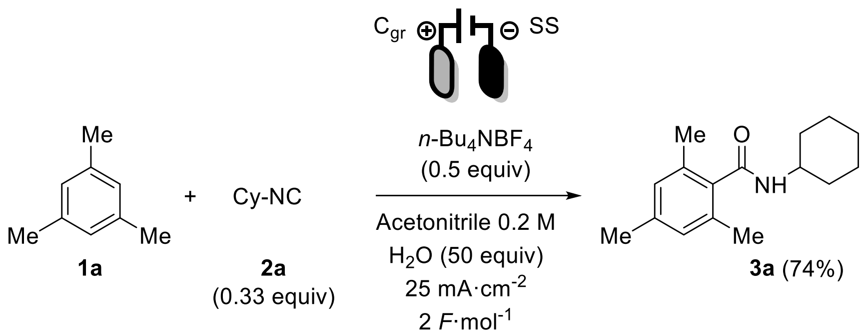

Scheme 5. Final conditions found by EDBO.

were counter-intuitive compared to commonly used values (isocyanide in default, high current density and concentration), highlighting the importance of an unbiased design of the research space.

With these optimized conditions, the scope of the reaction's applicability was then tested (Scheme 6).

Primary and secondary isocyanides were found to work under these conditions (74% for cyclohexyl isocyanide, 52% for 1-pentyl isocyanide, and 31% for benzyl isocyanide), while the aromatic isocyanide gave a low amount of the desired product (5%). Interestingly, tertiary isocyanides were found to fragment to give the cyano compound in good yield (up to 91% NMR yield, 52% isolated yield)[1]. Its formation is supposed to take place when the iminyl radical is produced: this structure may fragment to release a stabilized tertiary carbon-centered radical and the benzonitrile compound, favoring this elimination.

[1]This benzonitrile is prone to sublimation, which explains the difference between the two yields.

Alternative aromatic compounds were also tested, and *m*-xylene was functionalized with an acceptable 36% yield. Anisole was found to polymerize (black tar formation), resulting in low yield (17%), while *tert*-butylbenzene also gave the *para*-product in low yield (7%, also prone to polymerization). Several other aromatic compounds were tested, and none produced the desired amide in detectable amounts.

3. Conclusion

In this article, we report a previously unknown electro-induced isocyanide-based multicomponent reaction toward the synthesis of arylcarboxamides, with an AI-guided optimization. In respect with green chemistry objectives, this work avoids the use of chemical oxidants, coupling agents, or catalysts by relying on electrosynthesis. The optimization was conducted with a minimal number of experiments, thanks to guidance by a Bayesian optimization-based model (EDBO). Overall, this work opens a path toward more challenging electro-induced methods and the use of AI in the laboratory. Subsequent work

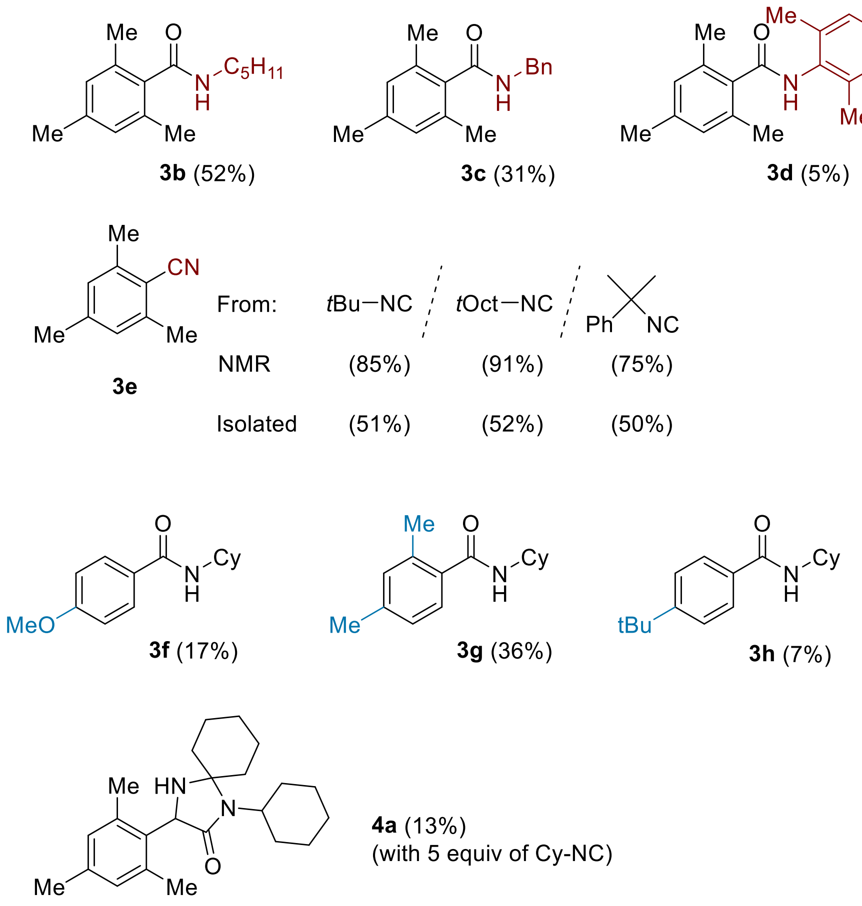

Scheme 6. Scope of the studied reaction.

on other electro-induced IMCRs is currently under investigation in our team.

CRediT authorship contribution statement

Virgile Rouffeteau: Data curation, Writing—original draft.
Clara Perrier: Data curation, Writing—review & editing.
Maximilian Fleck: Software, Writing—review & editing.
Geoffrey Gontard: Formal analysis, Writing—review & editing.
Maxime R. Vitale: Funding acquisition, Conceptualization, Supervision, Writing—review & editing.
Laurence Grimaud: Funding acquisition, Conceptualization, Supervision, Writing—review & editing.

Acknowledgments

Drs. A. Simon and S. Bachollet are thanked for early investigations.

Declaration of interests

The authors do not work for, advise, own shares in, or receive funds from any organization that could benefit from this article, and have declared no affiliations other than their research organizations.

Funding

ENS-PSL, CNRS, and the Agence Nationale de la Recherche (ANR-20-CE07-0020) are thanked for financial support. VR thanks Ecole Polytechnique for a PhD grant (AMX). CP thanks CNRS for a placement grant. MF acknowledges support under the Major Research Program of PSL Research University "ChemAI" launched by PSL Research University and implemented by ANR with the references ANR-10-IDEX-0001.

Supplementary materials

Supporting information for this article is available on the journal's website under https://doi.org/10.5802/crchim.431 or from the author.

Deposition Number CCDC 2492104 contain the supplementary crystallographic data for compound **4a**. These data can be accessed free of charge via the Cambridge Crystallographic Data Centre (CDCC).

References

[1] P. T. Anastas and J. C. Warner, *Green Chemistry: Theory and Practice*, Oxford University Press: Oxford, 2000.

[2] M. Passerini and L. Simone, "Sopra gli isonitrili (I). Composto del p-isonitril-azobenzolo con acetone ed acido acetico", *Gazz. Chim. Ital.* **51** (1921), pp. 126–129.

[3] I. Ugi, R. Meyr, U. Fetzer and C. Steinbrückner, "Versuche mit Isonitrilen", *Angew. Chem.* **71** (1959), p. 386.

[4] R. L. Mohlala and E. M. Coyanis, "The vital use of isocyanide-based multicomponent reactions (MCR) in chemical synthesis", *Phys. Sci. Rev.* **9** (2024), pp. 995–1032.

[5] Q. Sun, X. Xu and X. Xu, "Recent advances in rare-earth metal-catalyzed C–H functionalization reactions", *ChemCatChem* **14** (2022), article no. e202201083.

[6] K. Seth, "Recent progress in rare-earth metal-catalyzed sp^2 and sp^3 C–H functionalization to construct C–C and C–heteroelement bonds", *Org. Chem. Front.* **9** (2022), pp. 3102–3141.

[7] N. Pan, J. Ling, R. Zapata, J. P. Pulicani, L. Grimaud and M. R. Vitale, "Electrochemical TEMPO-catalyzed multicomponent C(sp^3)–H α-carbamoylation of free cyclic secondary amines", *Green Chem.* **21** (2019), pp. 6194–6199.

[8] N. Pan, M. X. Lee, L. Bunel, L. Grimaud and M. Vitale, "Electrochemical TEMPO-catalyzed oxidative Ugi-type reaction", *ACS Org. Inorg. Au* **1** (2021), pp. 18–22.

[9] S. Tang, R. Guillot, L. Grimaud, M. R. Vitale and G. Vincent, "Electrochemical benzylic CH functionalization with isocyanides", *Org. Lett.* **24** (2022), pp. 2125–2130.

[10] A. Simon, S. P. J. T. Bachollet, N. Pan, L. Grimaud and M. R. V. Vitale, "Electromediated alcohol-based Passerini-type reaction", *Synlett.* **36** (2025), pp. 2055–2059.

[11] Q. Gu, Z. Cheng, X. Qiu and X. Zeng, "Recent advances in the electrochemical functionalization of isocyanides", *Chem. Rec.* **23** (2022), article no. e202200177.

[12] T. Morofuji, A. Shimizu and J. I. Yoshida, "Electrochemical C–H amination: synthesis of aromatic primary amines via N-arylpyridinium ions", *J. Am. Chem. Soc.* **135** (2013), pp. 5000–5003.

[13] D. Hayrapetyan, R. K. Rit, M. Kratz, K. Tschulik and L. Gooßen, "Electrochemical C–H cyanation of electron-rich (hetero)arenes", *Chem. Eur. J.* **24** (2018), pp. 11288–11291.

[14] S. Strekalova, A. Kononov, I. Rizvanov and Y. Budnikova, "Acetonitrile and benzonitrile as versatile amino sources in copper-catalyzed mild electrochemical C–H amidation reactions", *RSC Adv.* **11** (2021), pp. 37540–37543.

[15] I. M. Taily, D. Saha and P. Banerjee, "Direct synthesis of paracetamol via site-selective electrochemical Ritter-type C–H amination of phenol", *Org. Lett.* **24** (2022), pp. 2310–2314.

[16] N. A. McGrath, M. Brichaeck and J. T. Njardarson, "A graphical journey of innovative organic architectures that have improved our lives", *J. Chem. Educ.* **87** (2010), pp. 1348–1349.

[17] G. Rebala, A. Ravi and S. Churiwala, *An Introduction to Machine Learning*, Springer International Publishing: Cham, 2019.

[18] M. Kubat, *An Introduction to Machine Learning*, Springer International Publishing: Cham, 2020.

[19] Z. H. Zhou and S. Liu, *Machine Learning*, Springer Singapore Publishing: Singapore, 2021.

[20] E. Alpaydin, *Machine Learning*, The MIT Press: Cambridge, MA, 2021.

[21] B. J. Shields, J. Stevens, J. Li, et al., "Bayesian reaction optimization as a tool for chemical synthesis", *Nature* **590** (2021), pp. 89–96.

[22] X. Hou, S. Li, X. Hong and L. Ackermann, "Machine learning-guided yield optimization for palladaelectrocatalyzed annulation reaction", *Chem* **10** (2024), pp. 2283–2294.

[23] S. Deolka, D. Dalmau, A. G. Roca, S. Vasylevskyi, M. H. Samha and M. S. Sigman, "Development of a heteroleptic palladium catalyst for the fluorination of arylboronic acids using data science tools", *J. Am. Chem. Soc.* **147** (2025), pp. 35705–35717.

[24] C. J. Taylor, A. Pomberger, K. C. Felton, et al., "A brief introduction to chemical reaction optimization", *Chem. Rev.* **123** (2023), pp. 3089–3126.

ACADÉMIE
DES SCIENCES
INSTITUT DE FRANCE

Comptes Rendus. Chimie
2026, Vol. 29, p. 53-69
https://doi.org/10.5802/crchim.433

Account

Metal-catalyzed enantioselective α-allylation of nitriles

Quentin Chevrier [a], **Cyril Nicolas** [a] and **Isabelle Gillaizeau** [*, a]

[a] Université d'Orléans, CNRS, UMR 7311, ICOA, 45067 Orléans, France
E-mail: isabelle.gillaizeau@univ-orleans.fr (I. Gillaizeau)

Abstract. α-Chiral nitriles are key structural motifs found in numerous natural products and pharmaceuticals. Nitriles play a central role in synthetic chemistry and industry as versatile intermediates for diverse functional groups. Considerable research has therefore been devoted to developing efficient strategies for preparing C^{α}-tetrasubstituted and α-quaternary chiral nitriles with varied architectures. This account highlights recent advances in the enantioselective synthesis of homoallylic and allylic nitriles achieved through transition-metal-catalyzed allylation. These catalytic systems deliver high levels of selectivity and accommodate a wide range of substrates, offering practical routes to complex nitrile derivatives. Transition-metal-mediated allylation remains one of the most powerful tools for forging C–C bonds under mild conditions. The discussion also provides key mechanistic insights showing how catalyst design and reaction dynamics control stereochemical outcomes. The synthetic applications presented illustrate how these methods expand access to intricate, stereochemically rich molecules relevant to pharmaceutical and materials chemistry. These advances greatly enrich the synthetic toolkit for the precise and efficient construction of α-chiral nitriles.

Keywords. Chiral nitrile, Metal-catalyzed allylation, Csp^3–Csp^3 bond, Quaternary or tertiary stereogenic center, Homoallylic nitrile, Allylic nitrile.

Funding. University of Orléans, Région Centre-Val de Loire, French National Research Agency (grant nos. ANR-20-CE07-0016-01 and ANR-23-CE07-0014-04).

Note. Article submitted by invitation.

Manuscript received 28 October 2025, revised 19 November 2025, accepted 20 November 2025, online since 2 February 2026.

1. Introduction

Recent studies have highlighted the crucial role of three-dimensional architecture in bioactive molecules, and many drugs featuring a quaternary chiral center are derived from natural products (Figure 1) [1]. However, building structures with vicinal tetrasubstituted stereocenters still remains elusive due to steric repulsions occurring at the Csp^3–Csp^3 bond formation [2–4]. α-Chiral nitriles are common structural motifs in natural products, pharmaceuticals, and bioactive compounds. Moreover, the cyano group serves as a highly versatile chiral building block, readily convertible into aldehydes, ketones, carboxylic acids, amides, amines, and N-heterocycles. In this context, significant progress has been achieved in developing innovative strategies for the synthesis of C^{α}-tetrasubstituted or α-quaternary chiral nitriles with diverse architectures. This account summarizes recent advances in this area, with particular emphasis on the formation of homoallylic and allylic nitriles.

2. Asymmetric allylic alkylation

Since its introduction several decades ago, metal-catalyzed asymmetric allylic alkylation (AAA) has proven remarkably powerful in enabling the enantioselective synthesis of carbon–carbon bonds,

* Corresponding author

ISSN (electronic): 1878-1543

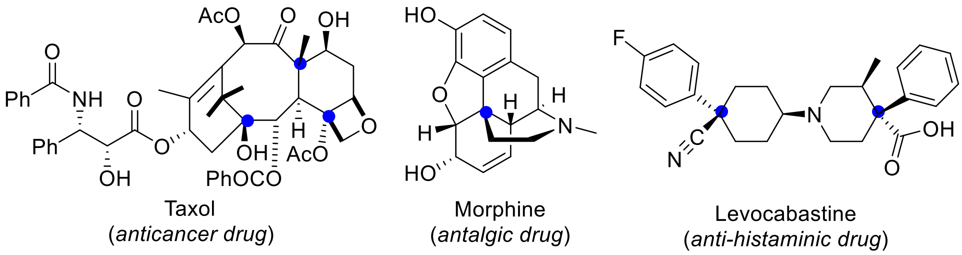

Figure 1. Examples of bioactive or natural compounds with quaternary stereogenic centers.

making it a cornerstone in modern organic synthesis [5–7]. Extensive efforts have since been devoted to expanding the scope of nucleophiles, with notable advances achieved using carbon-based nucleophiles [8–24]. While α-carbanions derived from ketones and carboxylic acid derivatives have been effectively employed in Pd-catalyzed AAA [25–31], reports on the use of nitrile-derived α-carbanions remain scarce. This limitation likely stems from the intrinsic "hardness" of such carbanions and their tendency to interconvert between C- and N-metalated forms [15–24]. As a result, several refined strategies have emerged that exploit electrophilic trapping of the N-metalated intermediate with silicon, affording axially chiral *N*-silyl ketene imines (SKIs) [32]. Despite these advances, the direct enantioselective alkylation of an α-metalated nitrile would represent a more straightforward and attractive approach. While diastereoselective alkylation [33] and enantiospecific acylation [34–37] of such anions have been documented, achieving a truly enantioselective variant has proven elusive, particularly in the case of asymmetric allylation, which is the focus of this Section.

Branch-selective allylic substitution catalyzed by iridium complexes was first disclosed by Takeuchi and Kashio in 1997 (Scheme 1) [38]. Building on this pioneering study, the Takeuchi group reported the enantioselective synthesis of chiral homoallylic nitriles via iridium-catalyzed allylation of cyanoacetates, followed by Krapcho demethoxycarbonylation. This strategy provided a broad array of homoallylic nitriles in excellent enantiomeric excess (>95–99% *ee*). The resulting products serve as valuable chiral building blocks, as further diversification can be achieved from either the nitrile moiety or the terminal alkene.

In 2005, Agbossou-Nidercorn demonstrated that Pd-catalyzed allylic substitution with aryl cyanoester pronucleophiles affords allylated products with significant enantioselectivity (*ee* up to 54%) (Scheme 2) [39]. Although the precise structure of the enolate involved in the addition step remains undefined, it seems to exert a critical influence on the stereocontrol. The noncyclic nature of the substrate likely accounts for the observed enantioselectivity, in line with precedents involving pronucleophiles that generate acyclic enolates. Among the chiral ligands examined, Trost-type "chiral pocket" ligands provided the highest selectivities. Notably, chiral alkylated cyanoesters bearing quaternary stereogenic centers constitute versatile building blocks for asymmetric synthesis.

In this context, Sauthier also reported a nickel-catalyzed α-allylation of phenyl- and α-alkyl phenyl acetonitriles using allylic alcohols (Scheme 3) [40]. The reaction proceeded under neutral conditions, using nickel complexes generated in situ from $Ni(cod)_2$ and dppf (1,1′-bis(diphenylphosphino) ferrocene).

In 2015, Evans et al. described a direct and highly enantioselective rhodium-catalyzed allylic alkylation of allyl benzoate with α-substituted benzyl nitrile pronucleophiles (Scheme 4) [22,41,42]. This protocol provided a new approach toward the synthesis of acyclic quaternary carbon stereogenic centers and is the first example of direct asymmetric alkylation of an α-cyanocarbanion. The process is driven by the ability to control the C- versus N-metalated equilibrium with a crown ether. The synthetic utility of the nitrile products is amply demonstrated through conversion to various functional groups and the asymmetric synthesis of the calcium channel blocker (*S*)-verapamil in three steps and 55% overall yield.

In 2017, Hou and Ding highlighted that the α-carbanion of acetonitrile ($pK_a \approx 31$ in DMSO) [43]

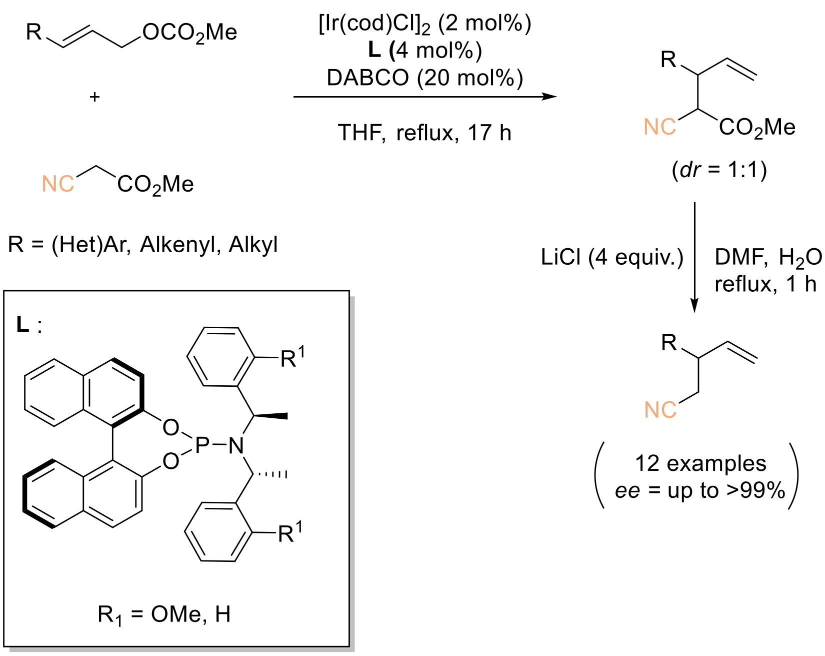

Scheme 1. Highly selective Ir-catalyzed allylic alkylation with a carbon nucleophile at the more substituted allylic terminus. Redrawn from Ref. [38].

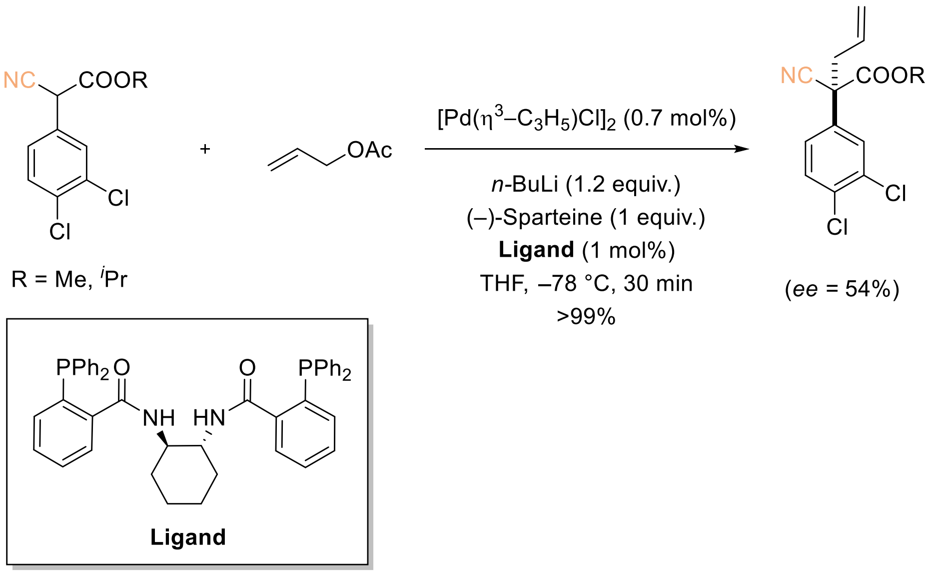

Scheme 2. Pd-catalyzed asymmetric allylic alkylation of prochiral aryl cyanoesters. Redrawn from Ref. [39].

was unreactive with allylic electrophiles [44], failing to yield the expected allylic-alkylation products, which instead underwent self-condensation to form β-enaminonitriles (Scheme 5). A novel nucleophilic species, the 3-imino nitrile carbanion, was subsequently generated in situ via the Thorpe reaction and employed in Pd-catalyzed asymmetric allylic alkylation of monosubstituted allyl reagents using the Pd/SIOCPHOX system. The resulting β-enaminonitriles isolated in high yields with high

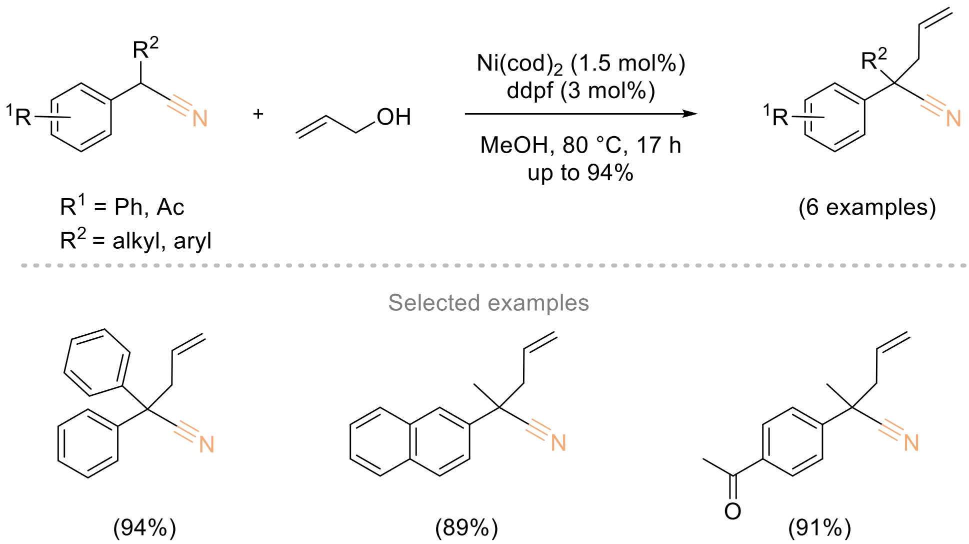

Scheme 3. Ni-catalyzed α-allylation of phenyl and α-alkyl phenyl acetonitrile with allylic alcohols. Adapted with permission from Ref. [40].

regio- and enantioselectivity constitute valuable building blocks for the synthesis of heterocycles, polymers, and pharmaceutical compounds. Regarding the reaction mechanism, the authors proposed that nitrile **VI** arises from the coupling of allyl reagent with nucleophile **III**, which is generated in situ through the attack of the acetonitrile α-carbanion **I** on a second acetonitrile molecule, followed by isomerization.

Cao and coworkers developed a method to overcome the side reactions associated with using nitrile α-carbanions as nucleophiles (Scheme 6). This strategy involved iridium-catalyzed enantioselective coupling between vinyl azides and allylic electrophiles [45]. Vinyl azides are cleverly employed as surrogates for acetonitrile carbanions, enabling the synthesis of γ,δ-unsaturated β-substituted nitriles with outstanding enantiomeric excess. These products can be efficiently converted to chiral nitrogen-containing building blocks and pharmaceutically relevant compounds. A mechanism has been proposed to account for the observed chemoselectivity of the coupling process (Scheme 6b). In the presence of a Lewis acid (e.g., $BF_3{\cdot}OEt_2$ or a Zn(II) salt), the chiral Ir(I) complex activates allylic carbonate **VII** through oxidative addition, giving Ir(III) intermediate **VIII** and $[LA–OtBu]^-$. An enantioselective C–C coupling between **VIII** and the vinyl azide then produces chiral iminodiazonium ion **IX**, which carries an α-2-hydroxypropan-2-yl group and then undergoes fragmentation to form **X**.

In 2022, a palladium(phosphinooxazoline)-catalyzed method for asymmetric allylic alkylation of α-aryl-α-fluoroacetonitriles was reported by Wolf and Sripada (Scheme 7) [46]. This reaction involves C–C bond formation and generates two contiguous chirality centers with moderate to good yields, high enantioselectivities, and up to 15:1 *dr*. The procedure is scalable, and it is worth noting that the brominated AAA products can be further derivatized using a Stille cross-coupling reaction without significant HF elimination.

Ito, Sawamura, and Sudoh reported an innovative strategy involving dual catalysis, in which each transition metal complex (Pd and Rh) activates its own substrate (Scheme 8) [47]. The resulting intermediates undergo an enantioselective coupling to afford optically active products. The allylation of diethyl (1-cyanoethyl)phosphonate proceeded with excellent enantioselectivity, yielding an optically active phosphonic acid derivative (*ee* = 92%). Notably, this remains the only reported example of dual catalysis applied to nitriles. However, in this case, the catalytic system is restricted to the formation of a single quaternary stereogenic center.

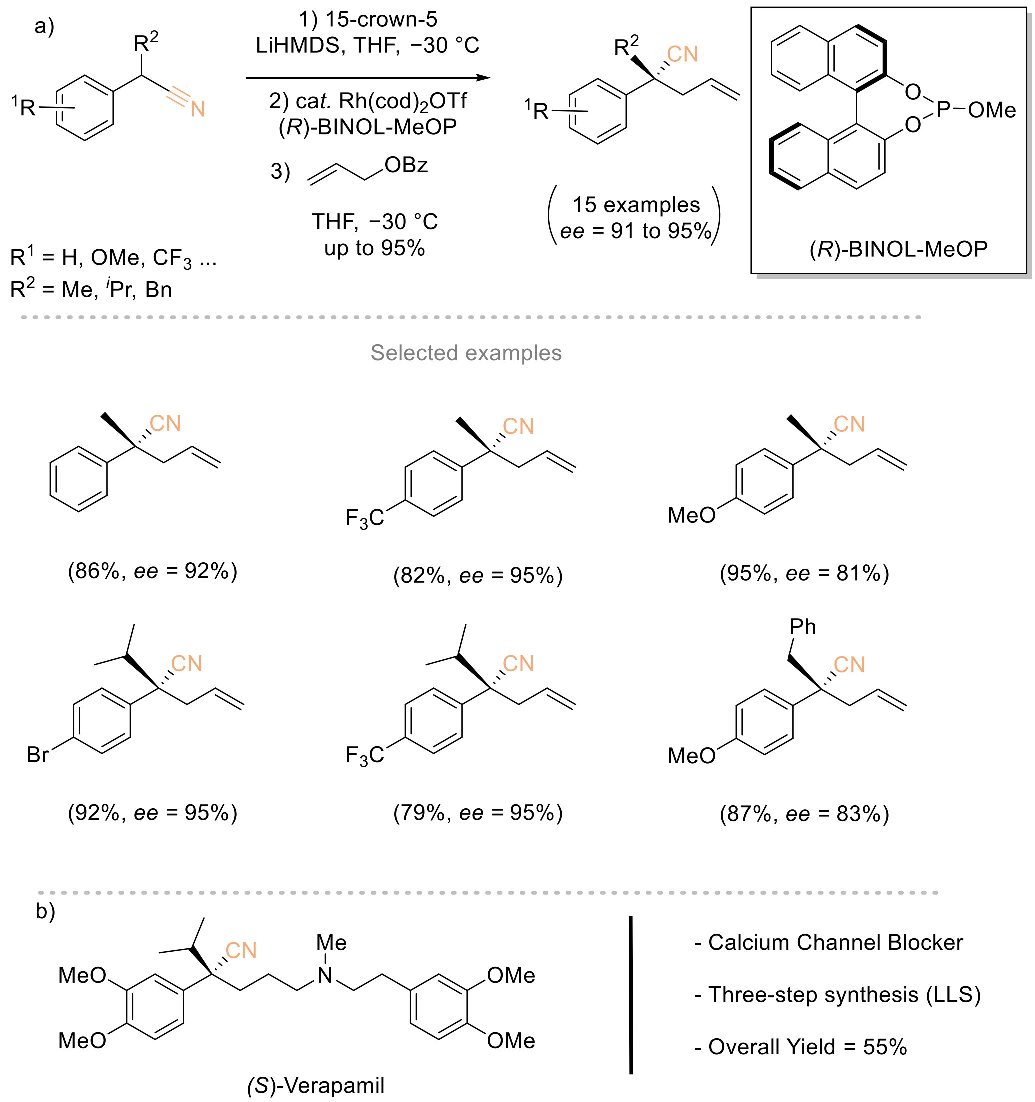

Scheme 4. (a) Enantioselective Rh-catalyzed allylic substitution. (b) Modular three-step synthesis of (*S*)-verapamil. Redrawn from Ref. [22,41,42].

Gillaizeau and Nicolas et al. established an enantioselective strategy for constructing unprecedented homoallylic nitriles bearing vicinal stereogenic centers through an allylic alkylation process (Scheme 9) [48]. This transformation relied on a dual catalytic system in which a palladium catalyst controls the configuration of the allylic electrophile, while a copper catalyst governs the stereochemistry of the nucleophilic carbon via an N-MKI (metal ketenimine) active species **XI**. This strategy delivers nitrile-substituted products bearing vicinal tertiary and quaternary centers in up to 99% yield and 91% *ee*. All four stereoisomers are accessible, underscoring independent stereocontrol at both reactive sites (Scheme 9b). The reaction is readily scalable without compromising efficiency. Computational studies highlighted the pivotal role of the copper catalyst and attributed the limited diastereoselectivity to an orthogonal alignment of the ketenimine and allyl moieties within the key intermediate.

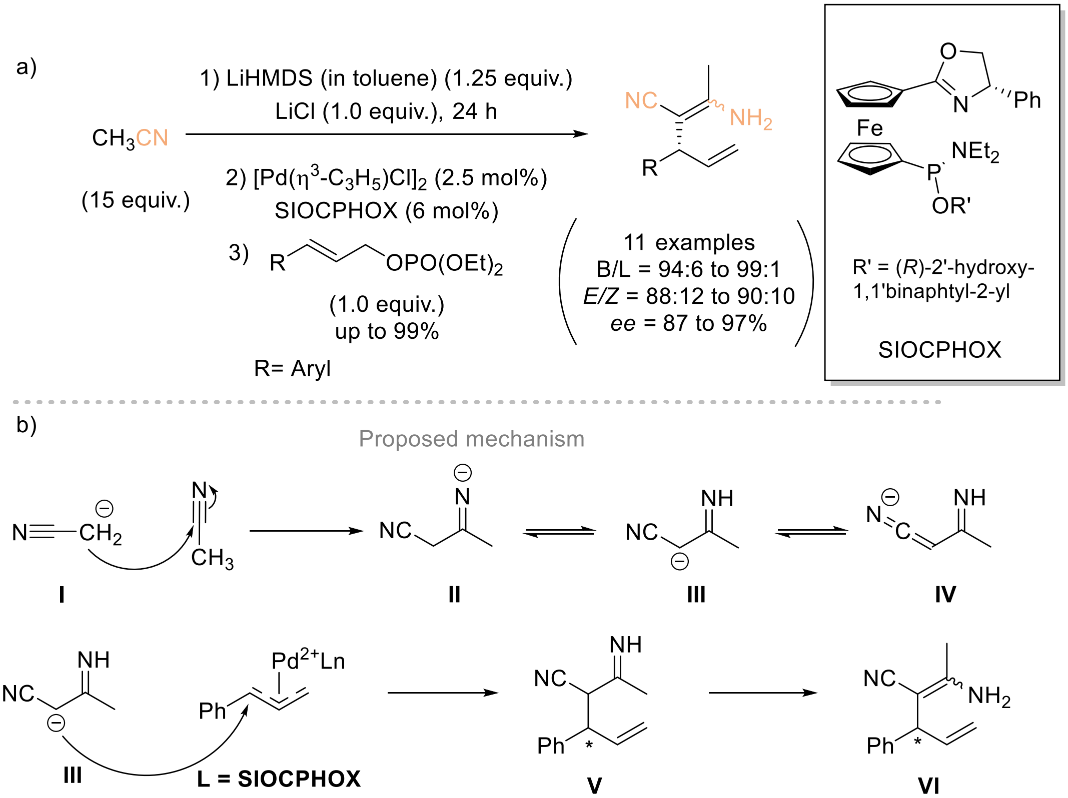

Scheme 5. (a) New type of nucleophile in Pd-catalyzed AAA. (b) Proposed mechanism. Adapted with permission from Ref. [44].

3. Metal-catalyzed conversion of allylic alcohols to nitrile

The transition-metal-catalyzed allylic substitution of diverse allylic substrates has emerged as a highly versatile transformation, particularly for constructing C–C bonds. This process typically relies on activated allylic precursors, such as acetates or carbonates, which promote the formation of η^3–M complexes. The direct use of allylic alcohols is particularly attractive, as it avoids the generation of stoichiometric waste and eliminates the need for hydroxyl protection [49,50]. In this regard, Tsuji and coworkers first established allylic cyanation using TMSCN as the cyanide donor and $Pd(PPh_3)_4$ as the catalyst [51]. Subsequent advances were made by Kawatsura et al., who employed CuI as the catalyst [52], and by Rousseaux et al., who developed a Ni(II)-based precatalyst in combination with $Zn(CN)_2$ as the cyanide source [53]. Koert et al. also reported that rhodium-catalyzed allylic cyanation of 3-fluoroallylic trifluoroacetates with TMSCN in the presence of a bulky phosphite ligand provides 3-fluoroallylic nitriles with a broad range of substrates and excellent Z/E selectivity [54]. In dialkyl-substituted substrates, the fluorine atom governs the regioselectivity, favoring the formation of the distal product. Investigation of selected scalemic substrates indicated stereocenter inversion during cyanation, accompanied by minimal or no stereochemical erosion. Despite extensive studies on asymmetric allylic substitution, the enantioselective synthesis of allylic cyanides remains underdeveloped. In 1998, Tsuji reported the catalytic enantioselective cyanation of cyclic allylic carbonates with TMSCN using 5 mol% of the (*S*)-MeO–MOP–Pd complex, yielding only two chiral allylic cyanides with 19% and 63% *ee*, respectively (Scheme 10, Equation (1)) [55]. Later, Hou and coworkers demonstrated an asymmetric kinetic resolution of racemic 1,3-disubstituted unsymmetrical

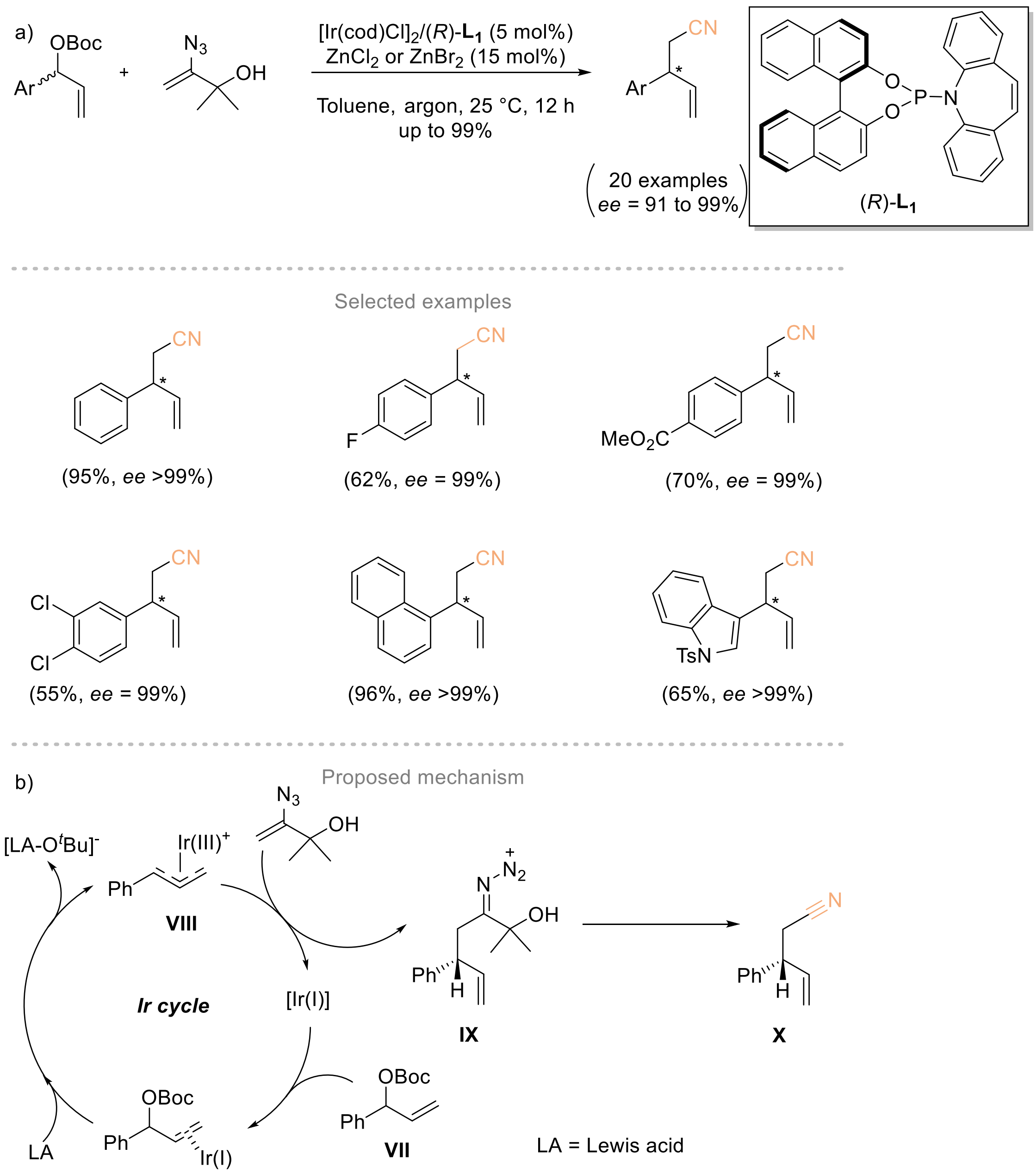

Scheme 6. (a) Enantioselective Ir-catalyzed coupling reaction of vinyl azides and racemic allylic carbonates. (b) Proposed mechanism. Adapted with permission from Ref. [45].

allylic carbonates by Pd-catalyzed allylic cyanation, affording allylic cyanides in 31–50% yields with 25–65% *ee*, alongside recovered chiral carbonates with an (*S*) configuration in 21–54% yields and with 24–99% *ee* (Scheme 10, Equation (2)) [31].

The Fang group described a one-pot conversion of allylic alcohols into chiral 1,3-dinitriles by merging allylic cyanation with asymmetric hydrocyanation through an auto-tandem catalysis strategy (Scheme 11) [56,57]. Using 5 mol% of a nickel

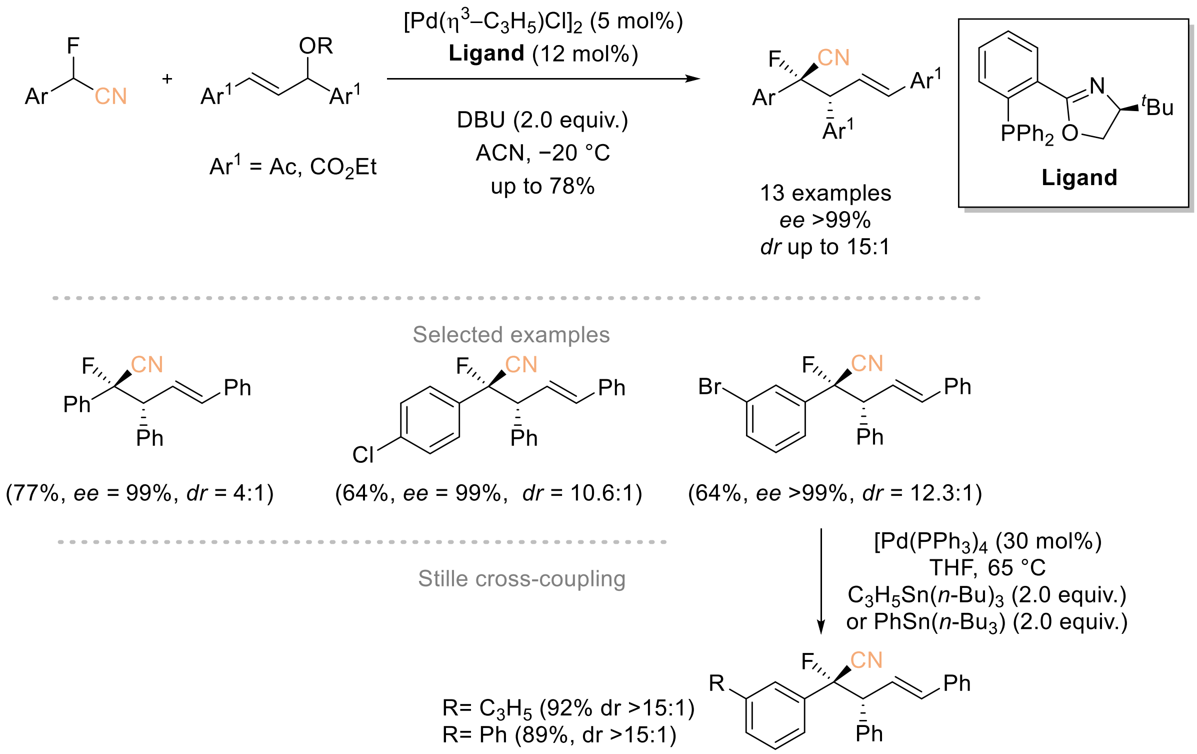

Scheme 7. Pd-catalyzed asymmetric allylic alkylation of α-aryl-α-fluoroacetonitriles. Adapted with permission from Ref. [46].

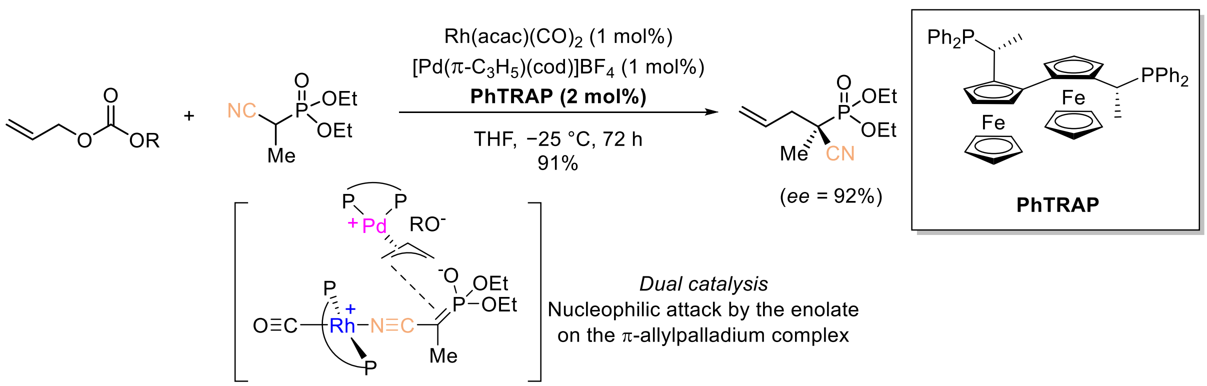

Scheme 8. Rh/Pd-Catalyzed allylic alkylation of activated nitriles. Adapted with permission from Ref. [47].

complex bearing a chiral bidentate phosphine ligand, a broad range of allylic alcohols reacted efficiently with acetone cyanohydrin as the cyanide donor to afford the corresponding enantioenriched 1,3-dinitriles in 37–89% yield and 65–94% *ee*. The proposed mechanism involves initial coordination of Ni(0)–L* species **XII** with the allylic alcohol to form a π-allyl–Ni(II)–OH intermediate **XIV**, which subsequently reacts with acetone cyanohydrin to generate intermediate **XV**. Reductive elimination delivers allyl nitrile **XVI**, which undergoes asymmetric hydrocyanation to furnish target dinitriles **XX** while regenerating active catalyst **XII**. These chiral dinitriles can be further transformed into piperidines **XXI**, a key step

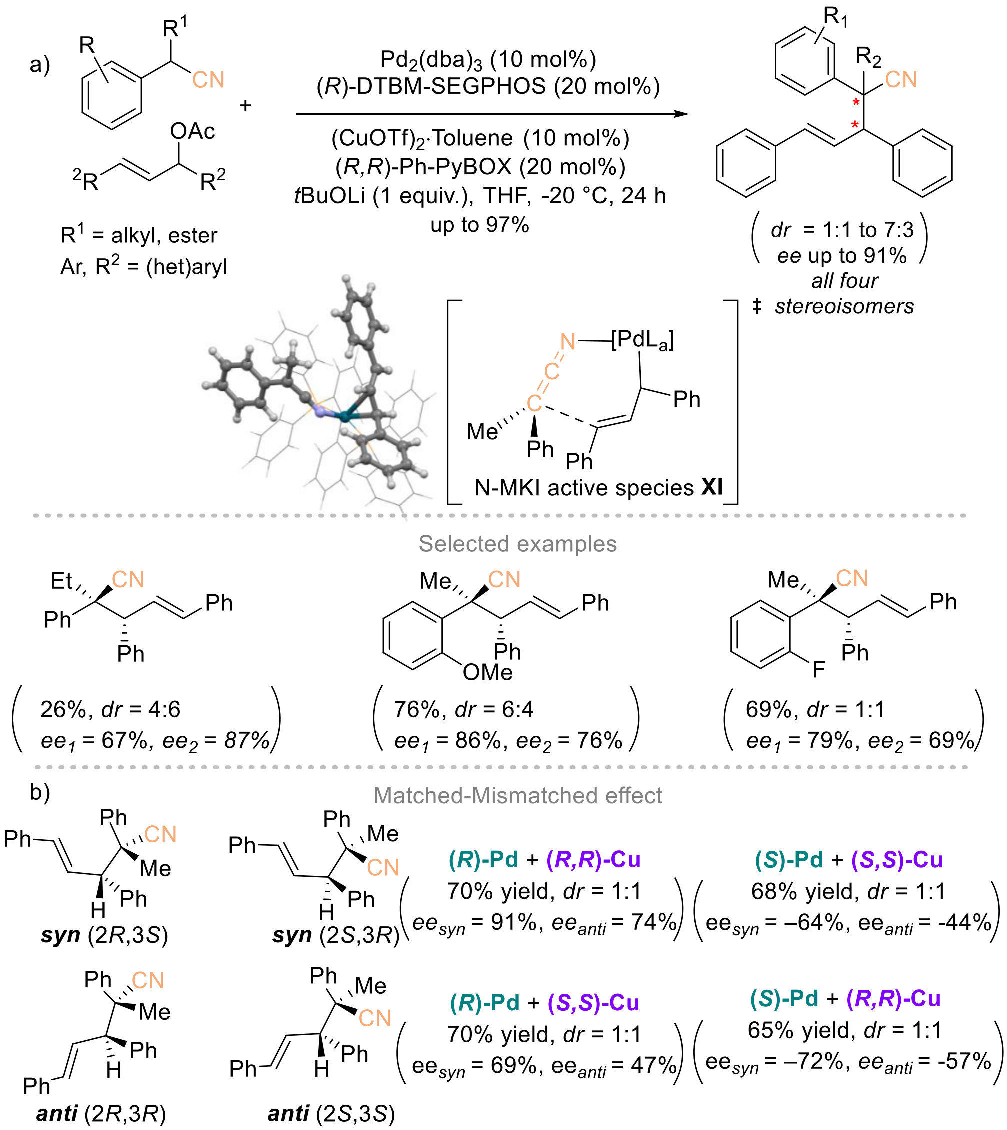

Scheme 9. Dual Pd/Cu-catalyzed enantioselective synthesis of chiral homoallylic nitriles bearing vicinal stereogenic centers. Redrawn from Ref. [48].

enabling the formal synthesis of the antidepressant (+)-paroxetine.

The same group reported a Ni-catalyzed asymmetric hydrocyanation of racemic allene- and methylene cyclopropanes (Scheme 12, Equation (1)). Using 10 mol% (*R*,*R*)-Ph-BPE with Ni(cod)$_2$, it delivered enantioenriched allylic nitriles in up to 78% yield and 98% *ee* with excellent regioselectivity. Subsequently, a nickel catalyst based on a TADDOL-derived diphosphate (**L$_1$**) enabled highly asymmetric hydrocyanation of disubstituted methylene cyclopropanes, providing chiral allylic nitriles in 82–99% *ee* (Scheme 12, Equation (2)) [58].

A nickel-catalyzed direct transformation of allylic alcohols with benzyl nitrile derivatives was also developed by Liu et al. in 2023, offering an efficient and racemic approach to access homoallylic nitriles featuring α-tertiary or quaternary carbon centers (Scheme 13) [59]. This protocol delivered good to excellent yields with high regioselectivity,

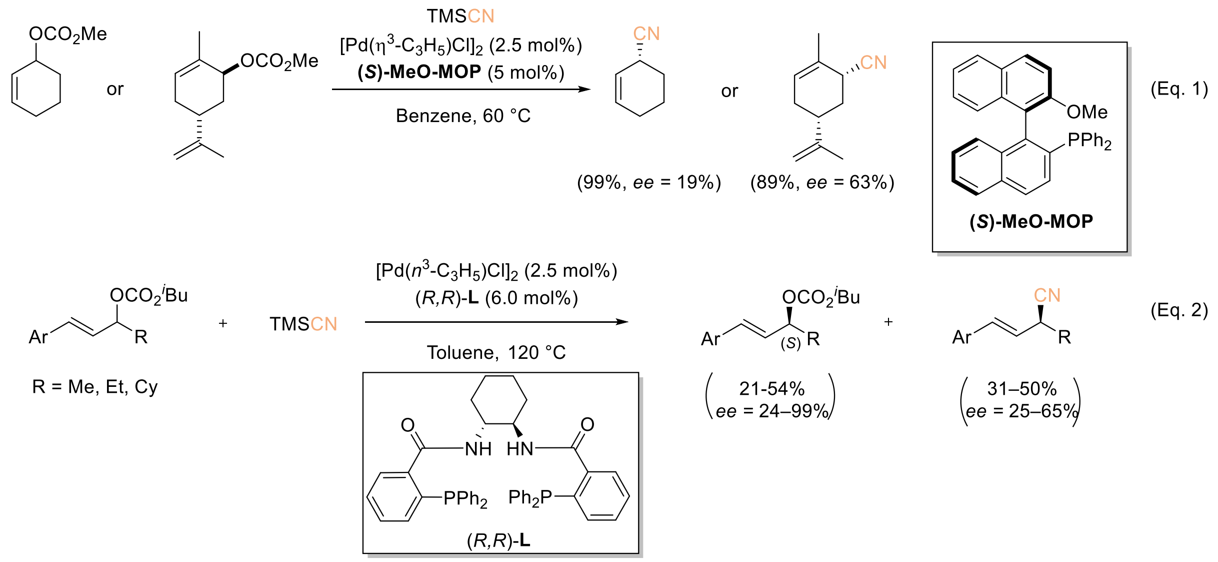

Scheme 10. Pd-Catalyzed asymmetric allylic cyanation of allylic carbonates using TMSCN. Adapted with permission from Ref. [55].

broad substrate applicability, and high tolerance toward diverse functional groups. Notably, *N*,*O*-bis(trimethylsilyl)-acetamide (BSA) was identified as a key additive that significantly promotes the coupling, particularly in reactions involving alkyl-substituted allylic alcohols.

4. Metal-catalyzed cyanofunctionalization of unsaturated bonds

Copper has been shown to mediate cyanation of the π-bond in nitriles through C–CN activation [60]. Procter and co-workers developed a regio- and enantioselective Cu-catalyzed borocyanation of dienes using bis(pinacolato)diboron (B_2pin_2) and electrophilic cyanamides (Scheme 14) [61]. With a *P*,*N*-ligated copper complex (10 mol%) and Cu(I) thiophene-2-carboxylate (CuTC) (10 mol%), allylic nitriles bearing a Bpin substituent were obtained in up to 90% yield and 94% *ee*. The reaction is proposed to proceed through selective borylcupration of the terminal alkene, isomerization to (*Z*)-allyl copper intermediate **XXIV**, and subsequent cyanamide insertion. Despite high efficiency with simple dienes, this led to a decrease in reactivity and selectivity with multisubstituted substrates.

5. Site-selective C(sp^3)–H cyanation of alkenes

While traditional asymmetric cyanation typically employs unsaturated substrates, recent advances have revealed that allylic C(sp^3)–H bonds can also serve as radical precursors suitable for enantioselective cyanation. In 2019, Li et al. further addressed the challenge of trapping allylic radical with chiral Cu(II) cyanide species, achieving site-selective and enantioselective allylic C(sp^3)–H cyanation of diverse di-, tri-, and tetrasubstituted alkenes via hydrogen atom transfer (HAT) pathways [62]. Using N-fluoroalkylsulfonamide (NFAS) as a precursor of the N-centered radical (NCR), the authors successfully realized allylic cyanation of trisubstituted alkenes bearing two distinct sets of allylic hydrogens. Under catalysis by 5 mol% of a chiral bisoxazoline L*/CuOAc complex, a diverse array of chiral allylic nitriles was obtained in yields of up to 91% and enantiomeric excesses as high as 99% (Scheme 15). Mechanistic studies suggested that the in situ—generated Cu(II)-bound NCR **XXVI** plays a decisive role in controlling site selectivity among multiple allylic C(sp^3)–H bonds with similar properties. This method features wide substrate generality and excellent chemo-, regio-, and enantioselectivity. Its synthetic utility was underscored by diverse downstream derivatizations.

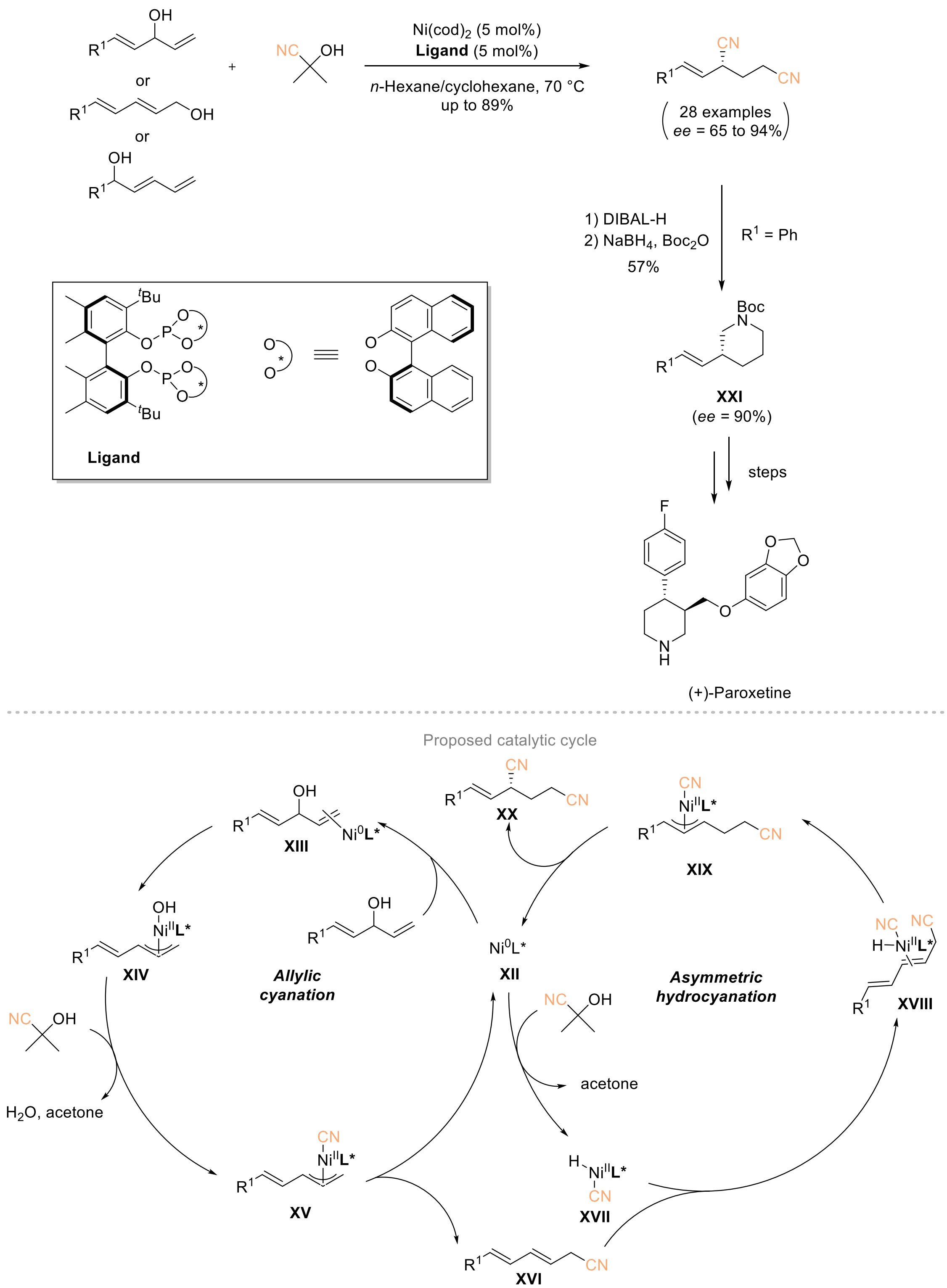

Scheme 11. One-pot conversion of allylic alcohols to chiral 1,3-dinitriles. Adapted with permission from Ref. [57].

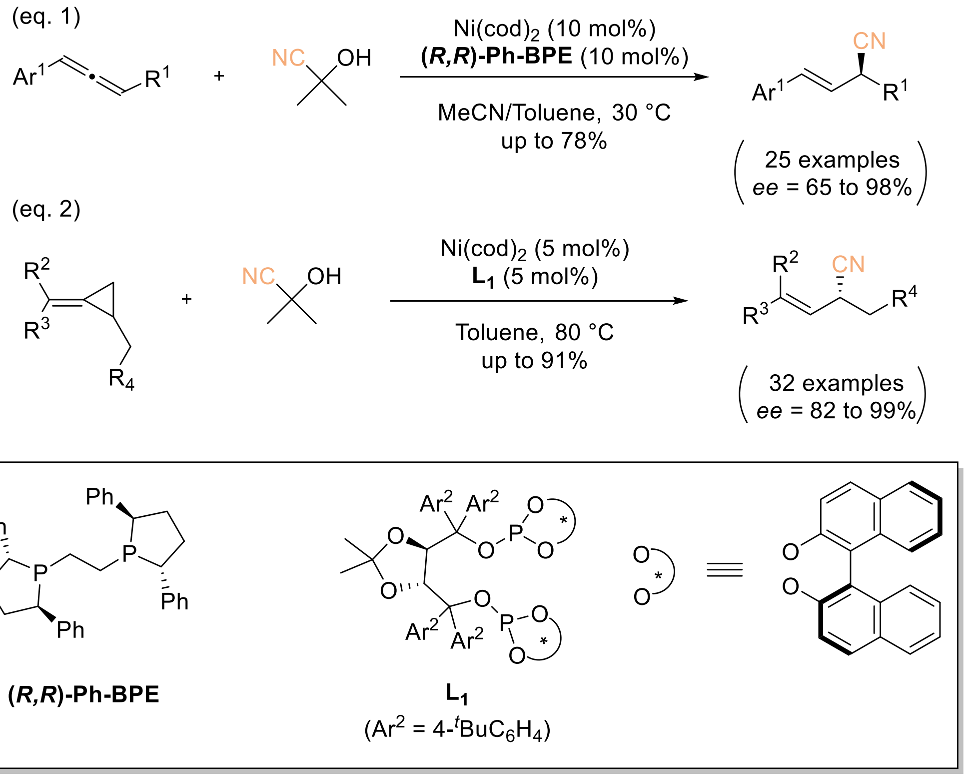

Scheme 12. Ni-catalyzed asymmetric hydrocyanation of allene- and methylene cyclopropanes. Adapted with permission from Ref. [58].

Scheme 13. Ni-Catalyzed allylation of nitriles with allylic alcohols. Adapted with permission from Ref. [59].

6. Intramolecular palladium-catalyzed decarboxylative allylic alkylation

Tan, Luan, and Ren outlined a practical strategy for the asymmetric synthesis of chiral acyclic nitriles bearing α-all-carbon quaternary stereocenters, employing a synergistic combination of palladium and phase-transfer catalysis on allyl 2-cyanoacetates under mild conditions (Scheme 16) [63]. This method provides an efficient and reliable route for the in-situ generation of tertiary α-cyano carbanions via an intramolecular palladium-catalyzed decarboxylative allylic alkylation. Moreover, it allows for exceptional enantioselective control of simple nitriles through ion-pairing interactions with chiral phase-transfer catalysts. The versatility of this approach was further

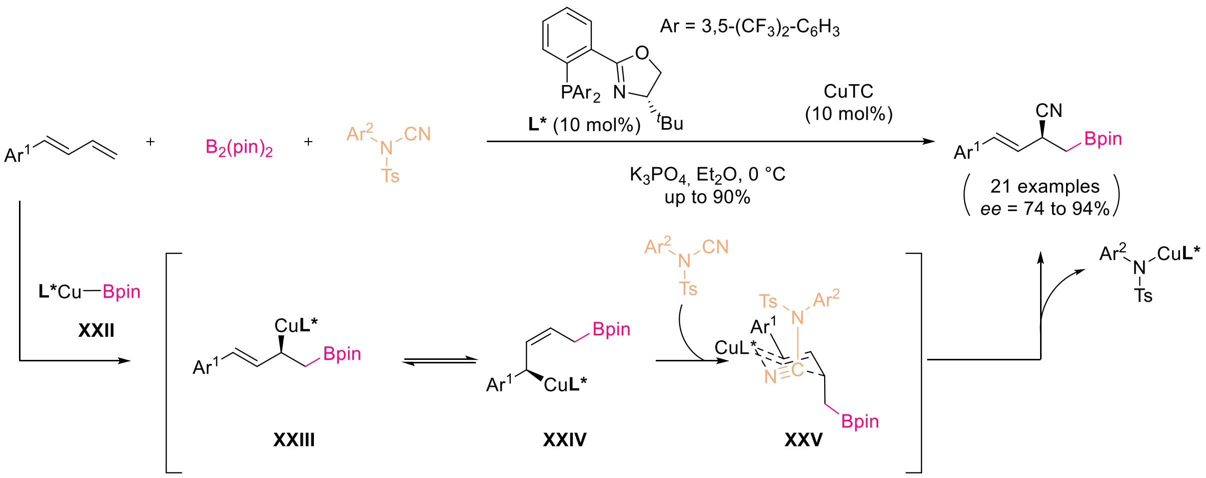

Scheme 14. Enantio- and regioselective Cu-catalyzed borocyanation of 1-aryl-1,3-butadienes. Adapted with permission from Ref. [61].

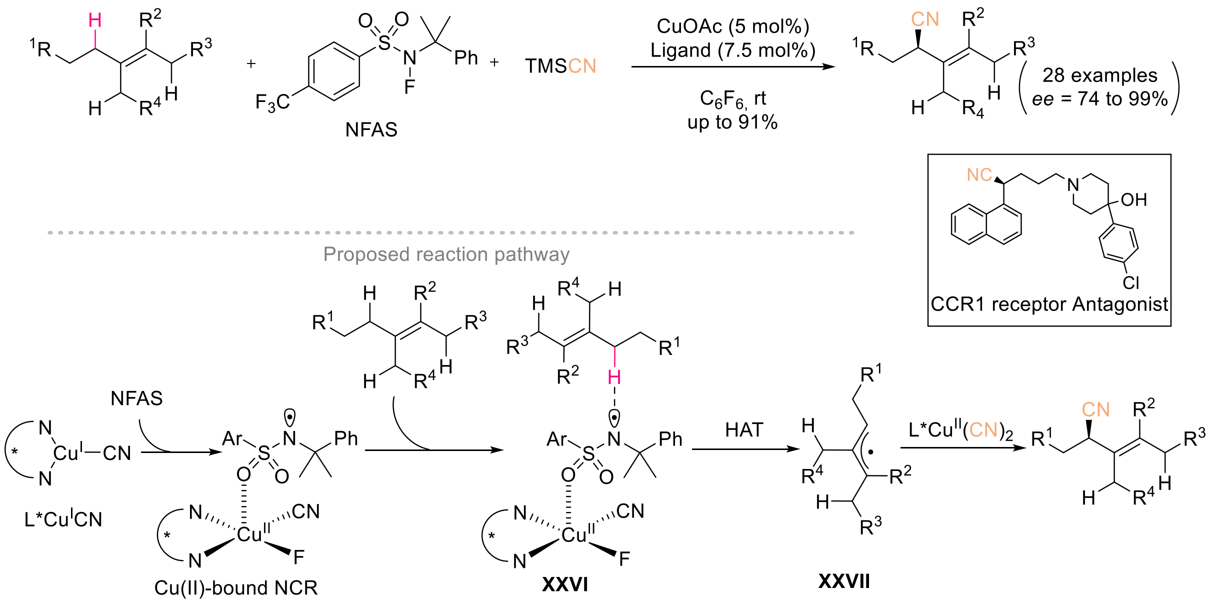

Scheme 15. Enantioselective allylic cyanation of alkenes. Redrawn from Ref. [62].

highlighted by its scalability to gram-scale synthesis and its subsequent conversion into a range of chiral functionalized molecules containing acyclic all-carbon quaternary stereocenters. A plausible reaction mechanism was proposed (Scheme 16). The starting substrate is first activated by Pd(0), releasing CO_2 and generating electrophilic $[\eta^3\text{-}\pi\text{-ally-PdLn}]^+$ species **XXVIII** and tertiary α-cyano carbanion **XXIX**, facilitated by Cs_2CO_3. Subsequently, tertiary α-cyano carbanion **XXIX** then associates with PN4 to form chiral ion pair **XXX**. Enantioselective nucleophilic attack by the α-cyano carbanion in **XXX** on the electrophilic species **XXVIII** furnishes the desired enantioenriched final homoallylic nitrile, while regenerating the palladium active catalyst for subsequent cycles.

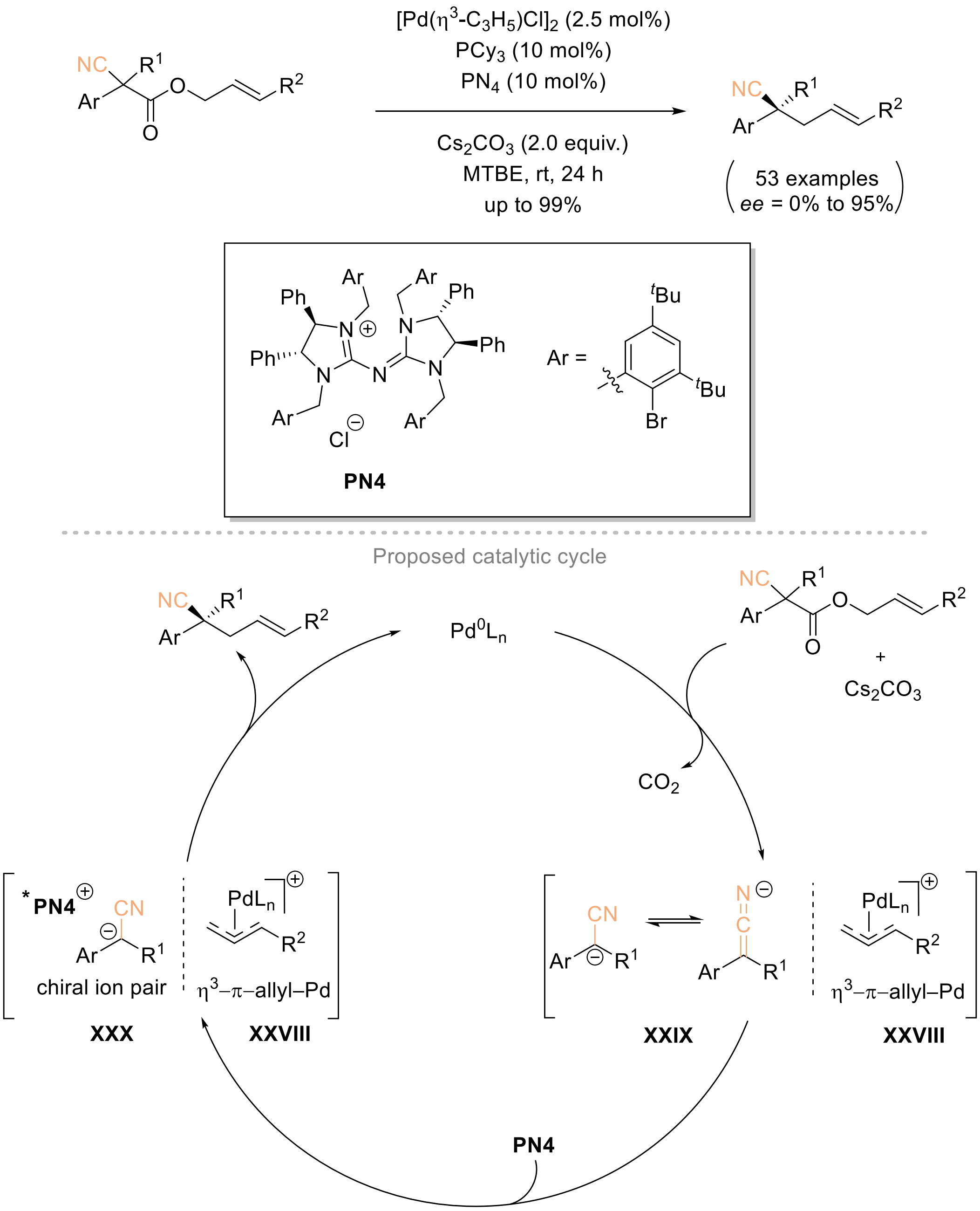

Scheme 16. Enantioselective construction of acyclic α-all-carbon quaternary nitriles via synergistic intramolecular Pd-catalyzed decarboxylative AAA and phase-transfer catalysis (PTC) from allyl 2-cyanoacetate substrates. Adapted with permission from Ref. [63].

7. Asymmetric deacylative allylation

The use of readily available prochiral or racemic quaternary carbons to generate enantioenriched counterparts offers an efficient alternative to conventional syntheses from tertiary or planar substrates. Unlike desymmetrization, which modifies an existing substituent of limited reactivity, functional-group

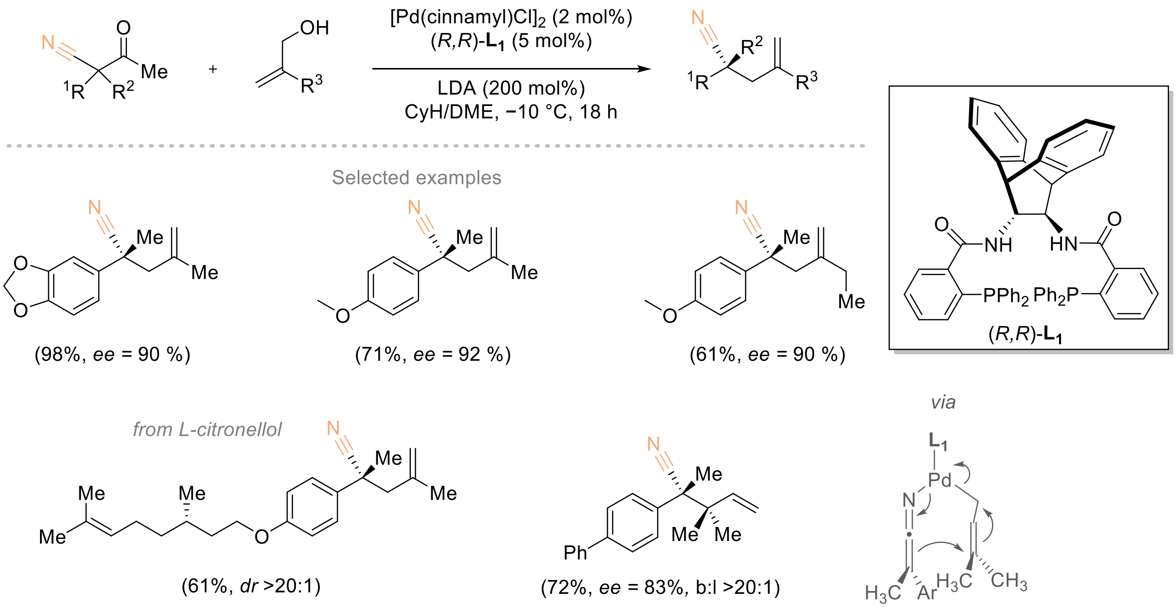

Scheme 17. Enantioconvergent deacylative functionalization toward α-quaternary nitriles. Redrawn from Ref. [64].

exchange introduces a new, structurally distinct motif. Achieving enantioconvergence in quaternary-to-quaternary transformations remains challenging, particularly for acyclic centers. Huang and coworkers reported a palladium-catalyzed deacylative allylation in which the acyl group of β-ketonitriles was stereoselectively replaced by an allyl fragment using simple alcohols as alkyl donors (Scheme 17) [64]. The transformation proceeded via a retro-Claisen-type elimination with alkoxide, and the absence of diastereoisomerism in the resulting ketenimine anion enabled highly selective asymmetric addition. The combination of α-substituents, retained nitrile, and introduced alkyl unit confers broad derivatization potential to the resulting enantioenriched quaternary stereocenters.

8. Conclusion

Over the years, significant progress has been made in the enantioselective synthesis of homoallylic and allylic nitriles through transition-metal-catalyzed allylation, enabling access to C^{α}-tetrasubstituted and α-quaternary chiral nitriles with diverse architectures. These advances have broadened the chemical space relevant to both academic and industrial research. Nevertheless, this account highlights the continuing need for enantioselective strategies capable of constructing chiral nitriles bearing vicinal tertiary or quaternary carbon centers.

Declaration of interests

The authors do not work for, advise, own shares in, or receive funds from any organization that could benefit from this article, and have declared no affiliations other than their research organizations.

Funding

This work was partially supported by University of Orléans, Région Centre-Val de Loire, and the French National Research Agency (ANR-20-CE07-0016-01 and ANR-23-CE07-0014-04).

References

[1] F. Lovering, “Escape from Flatland 2: complexity and promiscuity”, *Med. Chem. Commun.* **4** (2013), pp. 515–519.
[2] M. Büschleb, S. Dorich, S. Hanessian, D. Tao, K. B. Schenthal and L. E. Overman, “Synthetic strategies toward natural products containing contiguous stereogenic quaternary carbon atoms”, *Angew. Chem. Int. Ed.* **55** (2016), pp. 4156–4186.
[3] J. Christoffers and A. Baro, *Quaternary Stereocenters: Challenges and Solutions for Organic Synthesis*, Wiley-VCH: Weinheim, 2005.

[4] B. M. Trost and C. Jiang, "Catalytic enantioselective construction of all-carbon quaternary stereocenters", *Synthesis* **3** (2006), pp. 369–396.

[5] B. M. Trost and M. L. Crawley, "Asymmetric transition-metal-catalyzed allylic alkylations: Applications in total synthesis", *Chem. Rev.* **103** (2003), pp. 2921–2944.

[6] Z. Lu and S. Ma, "Metal-catalyzed enantioselective allylation in asymmetric synthesis", *Angew. Chem. Int. Ed.* **47** (2008), pp. 258–297.

[7] C.-H. Ding and X.-L. Hou, "Transition metal-catalyzed asymmetric allylation", *Top. Organomet. Chem.* **36** (2011), pp. 247–285.

[8] B. M. Trost and J. Xu, "Regio- and enantioselective Pd-catalyzed allylic alkylation of ketones through allyl enol carbonates", *J. Am. Chem. Soc.* **127** (2005), pp. 2846–2847.

[9] A. M. Johns, Z. Liu and J. F. Hartwig, "Primary tert- and sec-allylamines via palladium-catalyzed hydroamination and allylic substitution with hydrazine and hydroxylamine derivatives", *Angew. Chem. Int. Ed.* **46** (2007), pp. 7259–7261.

[10] É. Bélanger, K. Cantin, O. Messe, M. Tremblay and J.-F. Paquin, "Enantioselective Pd-catalyzed allylation reaction of fluorinated silyl enol ethers", *J. Am. Chem. Soc.* **129** (2007), pp. 1034–1035.

[11] J. Deska and U. Kazmaier, "Stereoselective syntheses and reactions of stannylated peptides", *Angew. Chem. Int. Ed.* **46** (2007), pp. 4570–4573.

[12] I. Usui, S. Schmidt and B. Breit, "Dual palladium- and proline-catalyzed allylic alkylation of enolizable ketones and aldehydes with allylic alcohols", *Org. Lett.* **11** (2009), pp. 1453–1456.

[13] Z. Hu, Y. Li, K. Liu and Q. Shen, "Bis (perfluoroalkyl) phosphino-oxazoline: a modular, stable, strongly π-accepting ligand for asymmetric catalysis", *J. Org. Chem.* **77** (2012), pp. 7957–7967.

[14] X. Wei, D. Liu, Q. An and W. Zhang, "Hydrogen-bond directed regioselective pd-catalyzed asymmetric allylic alkylation: The construction of chiral α-amino acids with vicinal tertiary and quaternary stereocenters", *Org. Lett.* **17** (2015), pp. 5768–5771.

[15] X. Wu, H.-C. Lin, M.-L. Li, L.-L. Li, Z.-Y. Han and L.-Z. Gong, "Enantioselective 1,2-difunctionalization of dienes enabled by chiral palladium complex-catalyzed cascade arylation/allylic alkylation reaction", *J. Am. Chem. Soc.* **137** (2015), pp. 13476–13479.

[16] J. Tsuji, I. Shimizu, I. Minami and Y. Ohashi, "Allylic carbonates. Efficient allylating agents of carbonucleophiles in palladium-catalyzed reactions under neutral conditions", *J. Org. Chem.* **50** (1985), pp. 1523–1529.

[17] B. M. Trost, J. R. Miller and C. M. Hoffman, "A highly enantio- and diastereoselective molybdenum-catalyzed asymmetric allylic alkylation of cyanoesters", *J. Am. Chem. Soc.* **133** (2011), pp. 8165–8167.

[18] J. Liu, G. Chen, J. Xing and J. Liao, "*tert*-Butanesulfinylthioether ligands: synthesis and application in palladium-catalyzed asymmetric allylic alkylation", *Tetrahedron: Asymmetry* **22** (2011), pp. 575–579.

[19] Y. Jin and D.-M. Du, "The synthesis of phosphine oxide-linked bis (oxazoline) ligands and their application in asymmetric allylic alkylation", *Tetrahedron* **68** (2012), pp. 3633–3640.

[20] M.-B. Li, H. Li, J. Wang, C.-R. Liu and S.-K. Tian, "Catalytic stereospecific alkylation of malononitriles with enantioenriched primary allylic amines", *Chem. Commun.* **49** (2013), pp. 8190–8192.

[21] T. Maji and J. A. Tunge, "Catalytic α-monoallylation of aryl acetonitriles", *Org. Lett.* **16** (2014), pp. 5072–5075.

[22] W.-H. Deng, F. Ye, X.-F. Bai, Z.-J. Zheng, Y.-M. Cui and L.-W. Xu, "Multistereogenic phosphine ligand-promoted palladium-catalyzed allylic alkylation of cyanoesters", *ChemCatChem* **7** (2015), pp. 75–79.

[23] S. Förster, O. Tverskoy and G. Helmchen, "Malononitrile as acylanion equivalent", *Synlett* **18** (2008), pp. 2803–2806.

[24] B. W. H. Turnbull and P. A. Evans, "Enantioselective rhodium-catalyzed allylic substitution with a nitrile anion: construction of acyclic quaternary carbon stereogenic centers", *J. Am. Chem. Soc.* **137** (2015), pp. 6156–6159.

[25] X.-X. Yan, C.-G. Liang, Y. Zhang, W. Hong, B.-X. Cao, L.-X. Dai and X.-L. Hou, "Highly enantioselective Pd-catalyzed allylic alkylations of acyclic ketones", *Angew. Chem. Int. Ed.* **44** (2005), pp. 6544–6546.

[26] K. Zhang, Q. Peng, X.-L. Hou and Y.-D. Wu, "Highly enantioselective palladium-catalyzed alkylation of acyclic amides", *Angew. Chem. Int. Ed.* **47** (2008), pp. 1741–1744.

[27] B.-L. Lei, C.-H. Ding, X.-F. Yang, X.-L. Wan and X.-L. Hou, "Kinetic resolution of 2,3-dihydro-2-substituted 4-quinolones by palladium-catalyzed asymmetric allylic alkylation", *J. Am. Chem. Soc.* **131** (2009), pp. 18250–18251.

[28] J.-P. Chen, C.-H. Ding, W. Liu, X.-L. Hou and L.-X. Dai, "Palladium-catalyzed regio-, diastereo-, and enantioselective allylic alkylation of acylsilanes with monosubstituted allyl substrates", *J. Am. Chem. Soc.* **132** (2010), pp. 15493–15495.

[29] B. H. Zheng, C.-H. Ding and X.-L. Hou, "Regio- and enantioselective Pd-catalyzed allylic amination of monosubstituted allylic substrates with BocNHOMe", *Synlett* **15** (2011), pp. 2262–2264.

[30] T.-G. Chen, P. Fang, X.-L. Hou and L.-X. Dai, "Palladium-catalyzed asymmetric allylic alkylation reaction of 2-mono-substituted indolin-3-ones", *Synthesis* **47** (2015), pp. 134–140.

[31] X.-H. Li, S.-L. Wan, D. Chen, Q.-R. Liu, C.-H. Ding, P. Fang and X.-L. Hou, "Enantioselective construction of quaternary carbon stereocenter via palladium-catalyzed asymmetric allylic alkylation of lactones", *Synthesis* **48** (2016), pp. 1568–1572.

[32] S. E. Denmark and T. W. Wilson, "Silyl ketene imines: Highly versatile nucleophiles for catalytic, asymmetric synthesis", *Angew. Chem. Int. Ed.* **51** (2012), pp. 9980–9992.

[33] A. H. Mermerian and G. C. Fu, "Nucleophile-catalyzed asymmetric acylations of silyl ketene imines: Application to the enantioselective synthesis of verapamil", *Angew. Chem. Int. Ed.* **44** (2005), pp. 949–952.

[34] S. E. Denmark, T. W. Wilson, M. T. Burk and J. R. Heemstra Jr., "Enantioselective construction of quaternary stereogenic carbons by the Lewis base catalyzed additions of

silyl ketene imines to aldehydes", *J. Am. Chem. Soc.* **129** (2007), pp. 14864–14865.

[35] S. E. Denmark and T. W. Wilson, "N-silyl oxyketene imines are underused yet highly versatile reagents for catalytic asymmetric synthesis", *Nat. Chem.* **2** (2010), pp. 937–943.

[36] G. T. Notte, J. M. Baxter Vu and J. L. Leighton, "Highly enantioselective Mannich reactions with α-aryl silyl ketene acetals and imines", *Org. Lett.* **13** (2011), pp. 816–818.

[37] J. Guin, G. Varseev and B. List, "Catalytic asymmetric protonation of silyl ketene imines", *J. Am. Chem. Soc.* **135** (2013), pp. 2100–2103.

[38] R. Takeuchi and M. Kashio, "Highly selective allylic alkylation with a carbon nucleophile at the more substituted allylic terminus catalyzed by an iridium complex: An efficient method for constructing quaternary carbon centers", *Angew. Chem. Int. Ed. Eng.* **36** (1997), pp. 263–265.

[39] A. Nowicki, A. Mortreux and F. Agbossou-Niedercorn, "Catalytic enantioselective allylation at the activated benzylic position of prochiral aryl cyano esters: access to quaternary stereogenic centers", *Tetrahedron Lett.* **46** (2005), pp. 1617–1621.

[40] B. Mouhsine, A. Karim, C. Dumont, I. Suisse and M. Sauthier, "Efficient and clean nickel catalyzed α-allylation reaction of nitriles", *Adv. Synth. Catal.* **363** (2021), pp. 1457–1462.

[41] M.-J. Tom and P. A. Evans, "Asymmetric rhodium-catalyzed allylic substitution reactions with nitrile-stabilized carbanions", *Synlett* **33** (2022), pp. 939–951.

[42] M.-J. Tom, B. W. H. Turnbull and P. A. Evans, "A concise and modular three-step synthesis of (*S*)-verapamil using an enantioselective rhodium-catalyzed allylic alkylation reaction", *Synthesis* **52** (2020), pp. 2185–2189.

[43] F. G. Bordwell, "Equilibrium acidities in dimethyl sulfoxide solution", *Acc. Chem. Res.* **21** (1988), pp. 456–463.

[44] D.-C. Bai, X.-Y. Liu, H. Li, C.-H. Ding and X.-L. Hou, "Tandem thorpe reaction/palladium catalyzed asymmetric allylic alkylation: Access to chiral β-enaminonitriles with excellent enantioselectivity", *Chem. Asian J.* **12** (2017), pp. 212–215.

[45] M. Han, M. Yang, R. Wu, et al., "Highly enantioselective iridium-catalyzed coupling reaction of vinyl azides and racemic allylic carbonates", *J. Am. Chem. Soc.* **142** (2020), pp. 13398–13405.

[46] A. Sripada and C. Wolf, "Catalytic asymmetric allylic alkylation with arylfluoroacetonitriles", *J. Org. Chem.* **87** (2022), pp. 11880–11887.

[47] M. Sawamura, M. Sudoh and Y. Ito, "An enantioselective two-component catalyst system: Rh–Pd-catalyzed allylic alkylation of activated nitriles", *J. Am. Chem. Soc.* **118** (1996), pp. 3309–3310.

[48] L. Mimoun, H. Sanaa, F. Heppner, et al., "Cu/Pd dual catalyzed stereoselective construction of vicinal tri- and tetrasubstituted stereocenters connected to chiral α-arylacetonitriles", *RSC Adv.* **15** (2025), pp. 30915–30920.

[49] J. Muzart, "Palladium-catalysed reactions of alcohols. Part B: Formation of C–C and C–N bonds from unsaturated alcohols", *Tetrahedron* **61** (2005), pp. 4179–4212.

[50] B. Sundararaju, M. Achard and C. Bruneau, "Transition metal catalyzed nucleophilic allylic substitution: activation of allylic alcohols via π-allylic species", *Chem. Soc. Rev.* **41** (2012), pp. 4467–4483.

[51] Y. Tsuji, N. Yamada and S. Tanaka, "Cyanation of allylic carbonates and acetates using trimethylsilyl cyanide catalyzed by palladium complex", *J. Org. Chem.* **58** (1993), pp. 16–17.

[52] D. Munemori, H. Tsuji, K. Uchida, T. Suzuki, K. Isa, M. Minakawa and M. Kawatsura, "Copper-catalyzed regioselective allylic cyanation of allylic compounds with trimethylsilyl cyanide", *Synthesis* **46** (2014), pp. 2747–2750.

[53] N. W. M. Michel, A. D. M. Jeanneret, H. Kim and S. A. L. Rousseaux, "Nickel-catalyzed cyanation of benzylic and allylic pivalate esters", *J. Org. Chem.* **83** (2018), pp. 11860–11872.

[54] C. Middel, L. Zygalski, J. Meinecke and U. Koert, "Rhodium-catalyzed regioselective 3-fluoroallylic cyanation", *Adv. Synth. Catal.* **363** (2021), pp. 1028–1032.

[55] Y. Tsuji, T. Kusui, T. Kojima, Y. Sugiura, N. Yamada, S. Tanaka, M. Ebihara and T. Kawamura, "Palladium-complex-catalyzed cyanation of allylic carbonates and acetates using trimethylsilyl cyanide", *Organometallics* **17** (1998), pp. 4835–4841.

[56] J. Long, S. Xia, T. Wang, G.-J. Cheng and X. Fang, "Nickel-catalyzed regiodivergent cyanation of allylic alcohols: Scope, mechanism, and application to the synthesis of 1,n-dinitriles", *ACS Catal.* **11** (2021), pp. 13880–13890.

[57] Y. Ding, J. Long, F. Sun and X. Fang, "Nickel-catalyzed isomerization/allylic cyanation of alkenyl alcohols", *Org. Lett.* **23** (2021), pp. 6073–6078.

[58] R. Yu and X. Fang, "Highly enantioselective nickel-catalyzed hydrocyanation of disubstituted methylenecyclopropanes enabled by TADDOL-based diphosphite ligands", *Org. Lett.* **22** (2020), pp. 594–597.

[59] M. Yang, H. Zhang and Y. Liu, "Nickel-catalyzed direct substitution of allylic alcohols with nitriles: A general tool for the construction of acyclic C2-tertiary or quaternary benzyl nitriles", *Org. Lett.* **25** (2023), pp. 1223–1228.

[60] Y. Nakao, "Metal-mediated C–CN bond activation in organic synthesis", *Chem. Rev.* **121** (2021), pp. 327–344.

[61] T. Jia, M. J. Smith, A. P. Pulis, G. J. P. Perry and D. J. Procter, "Enantioselective and regioselective copper-catalyzed borocyanation of 1-aryl-1,3-butadienes", *ACS Catal.* **9** (2019), pp. 6744–6750.

[62] J. Li, Z. Zhang, L. Wu, W. Zhang, P. Chen, Z. Lin and G. Liu, "Site-specific allylic C–H bond functionalization with a copper-bound N-centred radical", *Nature* **574** (2019), pp. 516–522.

[63] C. Guo, Y. Dong, Y. Wang, X. Du, R. Ma, C.-H. Tan, X. Luan and J. Ren, "Enantioselective synthesis of chiral acyclic nitriles containing α-all-carbon quaternary stereocenters via synergistic palladium and phase-transfer catalysis", *ACS Catal.* **14** (2024), pp. 18841–18850.

[64] M. Zhang and Z. Huang, "Enantioconvergent deacylative functionalization toward α-quaternary nitriles", *Angew. Chem. Int. Ed.* **64** (2025), article no. e202503149.

ACADÉMIE DES SCIENCES
INSTITUT DE FRANCE

Comptes Rendus. Chimie
2026, Vol. 29, p. 83-98
https://doi.org/10.5802/crchim.428

Account

High-pressure-driven cycloadditions: dearomatization of electron-deficient arenes

Nathan Noël [a], Rayhane Hammami [a], Laëtitia Chausset-Boissarie [a] and Isabelle Chataigner [*, a, b]

[a] Univ Rouen Normandie, CNRS, INSA Rouen Normandie, Univ Caen Normandie, ENSICAEN, Institut CARMeN UMR 6064, F-76000 Rouen, France

[b] Sorbonne Université, LCT, UMR 7616 CNRS, F-75005, Paris, France

E-mail: isabelle.chataigner@univ-rouen.fr (I. Chataigner)

Abstract. Dearomative cycloadditions transform planar structures into intricate three-dimensional polycyclic compounds. The scope of these reactions is limited however due to steric or electronic limitations. High-pressure conditions provide an effective way to overcome these challenges, often minimizing the formation of side products and eliminating the need for chemical catalysts. This article showcases recent advances from our group, revealing that high-pressure-induced cycloadditions facilitate the efficient transformation of electron-deficient arenes into complex molecules under conditions that promote sustainable chemistry.

Keywords. High pressure, Cycloadditions, Electron-poor arenes, Dearomatization.

Note. Article submitted by invitation.

Manuscript received 8 October 2025, revised 15 October 2025, accepted 20 October 2025, online since 24 February 2026.

1. Introduction

Pressure is a parameter frequently overlooked by the community of organic synthetic chemists, except in cases involving gases, such as hydrogenation or carbonylation, where it typically reaches values between 1 and 50 bars. In organic chemistry, reaction media are most often liquids, and compressing a liquid is generally considered challenging, if not impossible, especially when aiming to attain pressures above 1 kbar, such as those needed to significantly affect the reaction outcomes. For clarity, the term "high pressure" (HP) used in the following refers specifically to the 1–20 kbar range (i.e., 2000–20 000 atm or 0.2–2.0 GPa).

On the basis of the Evans–Polanyi transition state theory, it has been established that the influence of pressure on the activation energy of chemical reactions ($\Delta G^{\ddagger}$), and thus on their kinetic constants, is a function of the sign and absolute value of the activation volume ($\Delta V^{\ddagger}$), which corresponds to the volume of the transition state (V_{TS}) minus the volume of the substrate(s) (V_{SM}) ($\Delta V^{\ddagger} = V_{TS} - V_{SM}$). A chemical reaction characterized by a negative $\Delta V^{\ddagger}$ is accelerated when pressure increases, while in contrast it is decelerated when $\Delta V^{\ddagger}$ is positive [1–3].

Cycloadditions are among the most useful reactions in synthesis, giving rapid access to functionalized (poly)cyclic compounds from simple starting materials such as, for example, alkenes, dienes, or dipoles. As the cycloadducts incorporate the entire starting materials, the process generates no waste and exhibits high atom economy. However, the application of these reactions is often hampered by the unfavorable steric or electronic characteristics of the reagents. The typical activation methods used for promoting cycloadditions are thermal, microwave, or chemically catalyzed ones (acid, base, metal, or

* Corresponding author

ISSN (electronic): 1878-1543

organo-catalyst). Because cycloadditions are characterized by highly compact transition states, they are generally associated to negative activation volumes, comprised between -10 and -50 $cm^3{\cdot}mol^{-1}$, and are thus significantly accelerated when the pressure increases [4].

Under HP, deactivated and/or sterically hindered substrates can become good partners in cycloadditions, making HP a valuable alternative to conventional heating or chemical catalysis [5]. An increase in selectivity comes as an extra bonus since this activation mode disfavors uncontrolled side reactions, especially when they are characterized by a positive activation volume. For instance, HP tends to prevent retrocycloadditions or eliminations that are difficult to control under more classical conditions. Energy is required to compress the reaction medium, but HP remains constant once established, and the overall energy input remains low. Consequently, HP represents a sustainable and effective strategy to enhance the yields of sluggish or inefficient cycloadditions [6].

Electron-deficient aromatic compounds are easily accessible, through S_EAr reactions (electrophilic aromatic substitution) for example. Their involvement in dearomatizations is particularly attractive, facilitating a straightforward increase in the complexity of the molecular structure. In general, when electron-deficient aromatics interact with nucleophilic species, they undergo nucleophilic aromatic substitutions (S_NAr), which involve an addition/elimination sequence restoring the aromaticity of the original ring [7]. In some cases, the dearomatized Meisenheimer intermediate resulting from the nucleophilic addition step can be trapped intramolecularly, in a formal cycloaddition process, affording a dearomatized cycloadduct [8]. Complementarily, concerted cycloadditions between electron-poor aromatics and electron-rich dienes or dipoles can also deliver the dearomatized cycloadducts. Because the latter processes involve transition states that are more compact than the starting materials, they are efficiently accelerated under HP. At the same time, HP helps to prevent potentially competitive retroadditions or rearomatizations, which are typically associated with positive activation volumes.

Over the past two decades, our laboratory has explored dearomatizations of electron-deficient (hetero)arenes in different cycloaddition processes. While the involvement of the aromatics as electron-poor dipolarophiles in the presence of electron-rich 1,3-dipoles is typically performed at atmospheric pressure [9–14], HP activation has proven very useful to promote (4+2) dearomative cycloadditions. Two different types of reactions have been developed: the first one involves one double bond of the aromatic compound acting as an electron-poor dienophile, while the second exploits the C=C–N=O system of nitroarenes acting as an electron-poor heterodiene. Both approaches are described below.

2. Electron-deficient arenes as dienophiles in HP-promoted Diels–Alder cycloadditions

We have developed (4+2) dearomative cycloadditions in which the double bond of the aromatic bearing an electron-withdrawing substituent reacts as dienophile, through its lowest unoccupied molecular orbital (LUMO), with an electron-rich 1,3-diene involved through its highest occupied molecular orbital (HOMO). This typically leads to a polycyclic adduct bearing a tetrasubstituted carbon atom at the ring junction, with a relative *cis* stereochemistry of the junction due to the pericyclic character of the reaction (Scheme 1).

Different electron-poor (hetero)aromatics have been involved in these reactions with electron-rich dienes, and the cycloaddition conditions depend on the nature of the aromatic (indole, pyrrole, naphthalene, quinoline, or benzene), the electron-withdrawing group(s) (nitro, cyano, (alkoxy)carbonyl, or ketoamide) and the electron-rich diene. The following classification is based on the nature of the aromatic.

2.1. *Electron-depleted indoles as dienophiles in Diels–Alder cycloadditions*

Indoles are crucial structural frameworks present in a wide range of natural products, many of which display notable biological activities. From a reactivity perspective, indoles are widely recognized as moderate nucleophiles [15], and their reactivity with various electrophiles has been extensively studied in organic synthesis. Recently, in a complementary approach, the electrophilic reactivity of electron-deficient indoles has been largely

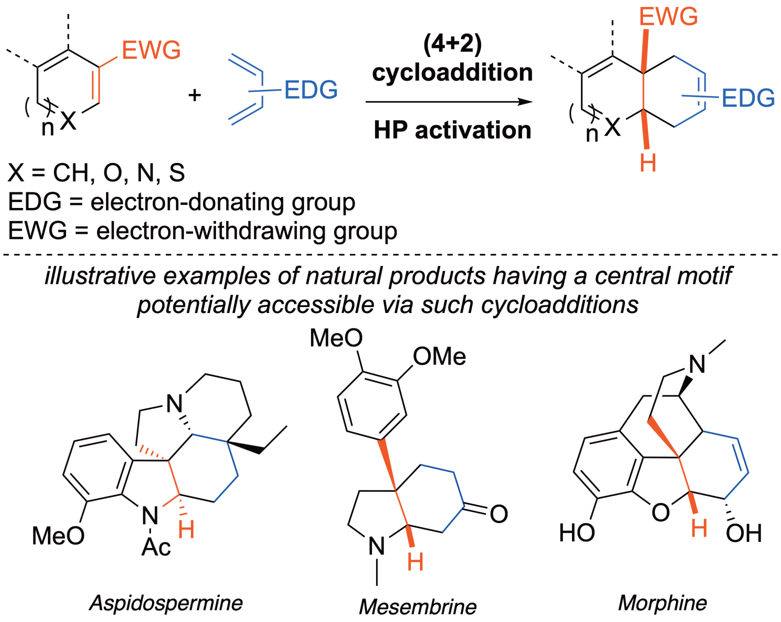

Scheme 1. Electron-deficient arenes as dienophiles in Diels–Alder cycloadditions.

investigated [16,17]. Intramolecular reactions have been developed some time ago, to generate interesting scaffolds [18,19]. In the case of the intermolecular version of the cycloadditions, it has been demonstrated that introducing a nitro group at the C3 position of this heterocycle decreases its aromaticity, thereby facilitating the addition of electron-rich species [20]. In this context, different research groups have contributed to exploit the "*umpolung*" reactivity of electron-depleted indoles and demonstrated that 3-nitroindoles can react as C2=C3 electron-poor dienophiles with electron-rich dienes in Diels–Alder cycloadditions (Scheme 2) [21]. Note that thermally activated processes generally lead to partial or complete rearomatization of the cycloadducts by nitrous acid elimination, a thermodynamically favored process [21–27].

Thanks to the relatively high electrophilic character of 3-nitroindoles bearing an electron-withdrawing group at the nitrogen position [20], the presence of the Danishefsky's diene **2a**, doubly activated by two oxy groups at positions N1 and C3, renders the cycloaddition possible at room temperature (r.t.) in the absence of any promoter. Under these smooth conditions, rearomatization is prevented and the indoline cycloadduct isolated in good yields [20]. Diastereoselectivities are low, probably because of the conflicting influences of the stabilizing secondary orbital interactions favoring the *endo* approach, and of the steric hindrance favoring the *exo* one. The reaction can also occur with thiourea- or squaramide-based organocatalysts, including chiral ones. However, the stereoselectivities observed with these catalysts are generally low, likely due to the competing non-catalyzed process [28].

With less reactive dienes such as 2-trimethylsilyloxycyclohexadiene **2b**, the reaction is not possible at atmospheric pressure. In such cases, HP activation proves efficient, and the reaction proceeds under 16 kbar at r.t. [29]. These smooth thermal and chemical conditions lead to the preservation of the three-dimensional nature of the dearomatized cycloadduct, which is isolated in good yields (Scheme 3). Notably, the diastereoselectivity of the cycloaddition is complete with this diene, leading to the exquisite formation of the *exo* cycloadduct. The corresponding approach is characterized by lower distortion of the substrates in a late transition state and by more favorable orbital interactions, presumably between the nitro group and the dienic part, explaining the stereoselectivity [29]. Under these conditions, 7-aza-3-nitroindoles also react well, leading to azaindolines in a similar manner.

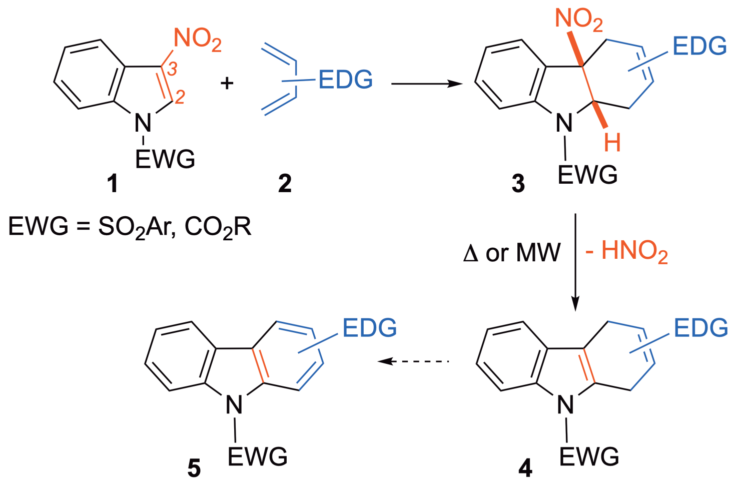

Scheme 2. 3-Nitroindoles as dienophiles in Diels–Alder cycloadditions.

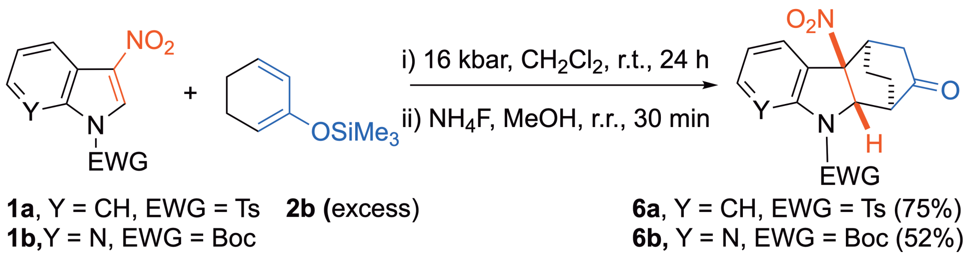

Scheme 3. HP-promoted Diels–Alder reaction of 3-nitro(aza)indoles with diene **2b**.

Other possible indolic dienophiles include 3-carbonylated substrates. In this case, the Diels–Alder (DA) reaction involving the C2=C3 double bond of the heteroaromatic competes with the hetero-Diels–Alder (HAD) reaction, where the carbonyl C=O bond acts as a competing dienophile. The reaction outcome depends on the carbonyl substituent, with tertiary ketoamide favoring the DA process, while formyl, ketoester, and secondary ketoamide favor the HDA one, all using Danishefsky's diene **2a** (Scheme 4) [30].

When less polarized, all-carbon dienes **2c** and **2d** are involved in the process with 3-formylindole **1c**, chemoselectivity favors the DA cycloadduct. Owing to the lower reactivity of these dienes, Lewis acid activation, such as zinc chloride catalysis, can be beneficial. However, this acidic catalyst also promotes competitive polymerization of the diene used in excess under HP, and this can sometimes complicate the isolation of the desired cycloadduct. Under thermal conditions (195 °C), cycloadduct **6c** is obtained in a good yield. However, when diene **2c** is used, HP activation triggers a subsequent reaction, leading to the formation of bis-cycloadduct **8** (Scheme 5) [30,31].

In contrast, when cyclohexa-1,3-diene **2d** is involved, the reaction leads to cycloadduct **6d** regardless of the reaction conditions (Scheme 6) [31]. The conversion, yield and diastereoselectivity of the reaction under HP conditions are greater than under thermal activation.

The type of electron-withdrawing substituent on the nitrogen atom of the indolic dienophile plays a crucial role in the cycloaddition. Although sulfonyl groups are known to be stronger electron-withdrawing groups than (alkoxy)carbonyl groups, the cycloaddition of 3-ketoamidic indoles with diene **2a** occurs more readily when the nitrogen atom is activated as an amide or carbamate rather than as a sulfonamide (Scheme 7) [32]. This fact is ascribed to a greater ability of the carbon-centered groups to

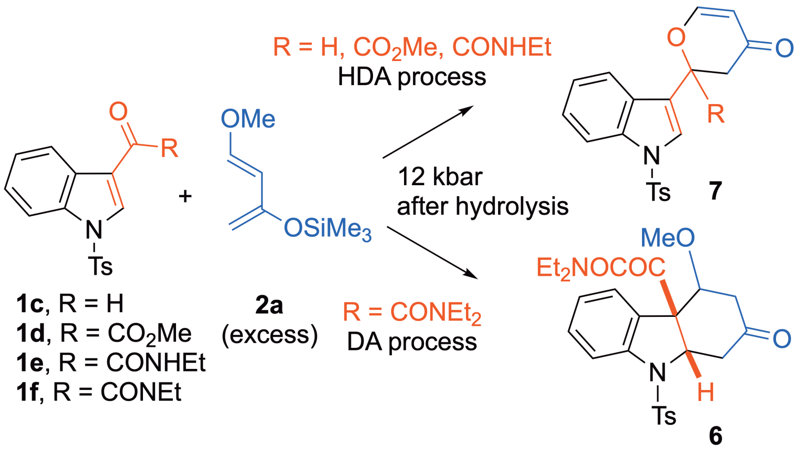

Scheme 4. HP-promoted Diels–Alder reaction of 3-carbonylated indoles with **2a**.

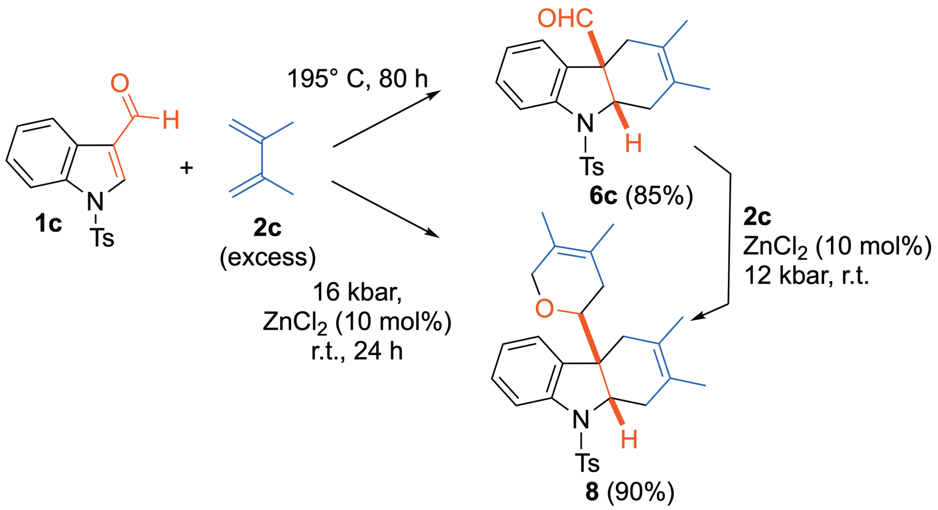

Scheme 5. Thermal versus HP-promoted Diels–Alder reaction of 3-formylindole with **2c**.

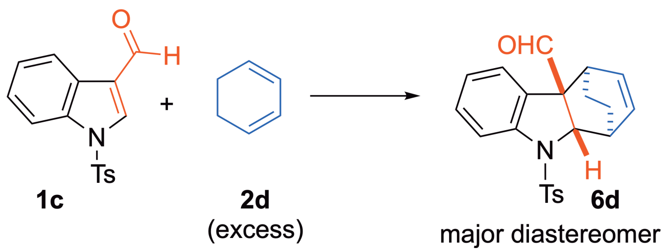

Reaction conditions	% Conversion	% Yield	*exo*/*endo* Ratio
195 °C, 72 h	25	25	80:20
16 kbar, $ZnCl_2$ cat., r.t., 48 h	100	62	>98:<2

Scheme 6. Thermal versus HP-promoted Diels–Alder reaction of 3-formylindole with **2d**.

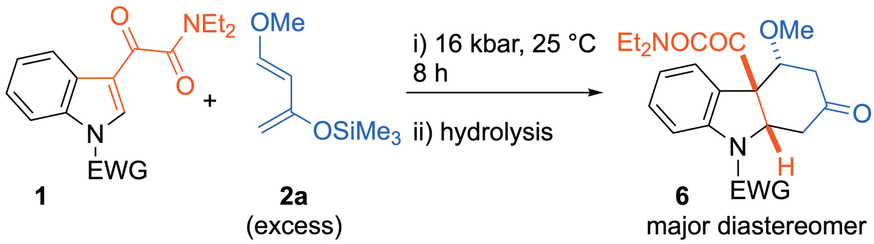

EWG	% Conversion	% Yield	*endo*/*exo* Ratio
Ms	18	nd[a]	75:25
Ts	31	nd[a]	75:25
Tf	66	60	90:10
Ac	88	87	90:10
Boc	87	75	90:10
Boc[b]	100	96	90:10

[a]not determined, [b]reaction carried out for 48h

Scheme 7. Influence of the nitrogen atom substituent on the cycloaddition.

achieve delocalization of the nitrogen's lone pair, resulting in stronger global withdrawing effects. The sulfur-centered functional group is less efficacious in decreasing electron density on the nitrogen atom, even when inductive effects are considered. This results in a lower aromaticity of the (alkoxy)carbonyl indoles and a higher reactivity at C2=C3 electron-poor dienophile [32].

2.2. *Electron-depleted benzofurans as dienophiles in Diels–Alder cycloadditions*

Other possible heteroarenic dienophiles include benzofuranic compounds, bearing an electron-withdrawing substituent at position C3. Here again, while 3-nitrobenzofurans react as C2=C3 dienophile at r.t. and ambient pressure with Danishefsky's diene **2a** to yield the corresponding cycloadduct [20], reactions with the less depleted 3-carbonylated substrates require a stronger activation. With 2,3-dimethylbuta-1,3-diene **2c** or cyclohexa-1,3-diene **2d**, the cycloadditions can be thermally activated. However, this activation mode is less efficient when more sensitive silyloxydienes are involved and HP conditions are then to be preferred (Scheme 8) [33]. Here again, competitive HDA processes, involving the carbonyl substituent at position C3 as heterodienophile, are observed with benzofurans bearing a ketoester group in the presence of Danishefsky's diene **2a** [33].

2.3. *Electron-depleted pyrroles as dienophiles in Diels–Alder cycloadditions*

When reacted under thermal conditions or Lewis acid activation, 3-nitro-*N*-tosylpyrrole **11** remains inert toward Danishesfky's diene **2a** and this sensitive diene is generally destroyed. In contrast, it reacts efficiently as an electron-poor dienophile with **2a** under HP activation [34]. The cycloadduct generated is unstable after decompression and leads to the corresponding carbazole **12**, resulting from a complete rearomatization (Scheme 9).

Cycloadditions with the less electron-depleted 3-acylpyrroles are also feasible under HP conditions, although Lewis acid catalysis is required alongside HP activation in this case. For example, cycloadditions between electron-poor pyrroles **13**, which contain electron-withdrawing groups at least at the N1 and C3 positions and a series of electron-rich dienes, result in the formation of cycloadducts **14** (Scheme 10) [35,36]. These products are obtained in

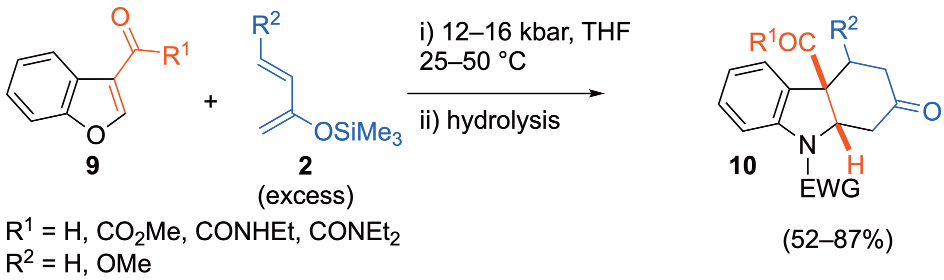

Scheme 8. 3-Carbonylated benzofurans as C2=C3 dienophiles under HP activation.

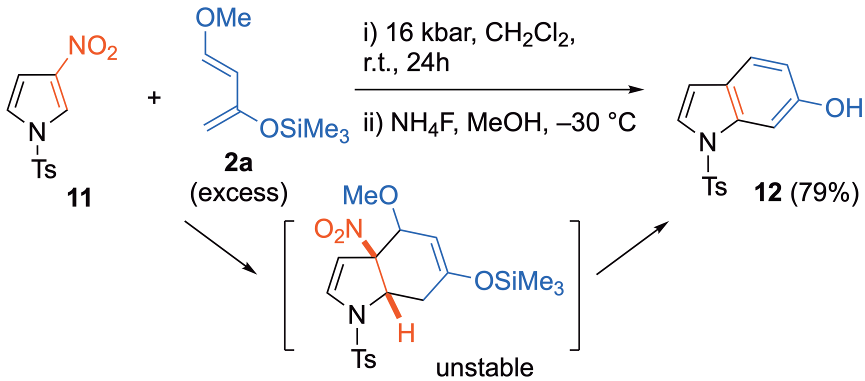

Scheme 9. 3-Nitropyrrole as C2=C3 dienophile under HP activation.

very low yields under thermal activation in the presence of $ZnCl_2$. Similarly, under HP and without a catalyst, this dienophile reacts poorly and enters a competitive polymerization process. However, combining HP and Lewis acid ($ZnCl_2$) activations significantly improves the efficiency of the cycloaddition and the expected *syn*-tetrahydroindole **14** is recovered in good to excellent yields.

2.4. *Other electron-depleted five-membered-ring heteroaromatics as dienophiles in Diels–Alder cycloadditions*

Other nitrated five-membered-ring heteroaromatics can be dearomatized under HP in the presence of Danishefsky's diene **2a**, among which benzothiophene, pyrazole, or furan. The reaction does not require any additional chemical activation and smooth hydrolysis of the pressurized mixture leads to preservation of the three-dimensional structure of the dearomatized cycloadduct in these cases (Scheme 11) [34].

2.5. *Six-membered-ring (hetero)aromatics as dienophiles in Diels–Alder cycloadditions*

HP–promoted DA reactions may also involve highly aromatic six-membered rings, such as nitroquinolines or nitronaphthalenes and nitrobenzenes in the presence of Danishefsky's diene **2a** (Scheme 12) [34]. The reaction proceeds at r.t. in the absence of any chemical promoter and affords in good yields the hydrolyzed cycloadducts with their three-dimensional structures intact. Here again, the *endo*/*exo* diastereoselectivities are low with this diene, because of compensation between the stabilizing secondary orbital interactions favoring the *endo* approach and steric hindrance favoring the *exo* one. The diastereoselectivity is slightly enhanced with structurally similar but sterically more hindered dienes, especially those bearing bulky groups at position C1 or C3, but this comes at the expense of reactivity [34]. Notably, when two nitro groups are positioned on the same ring of the original aromatic substrate, two cycloadditions occur, resulting in the formation of polycyclic

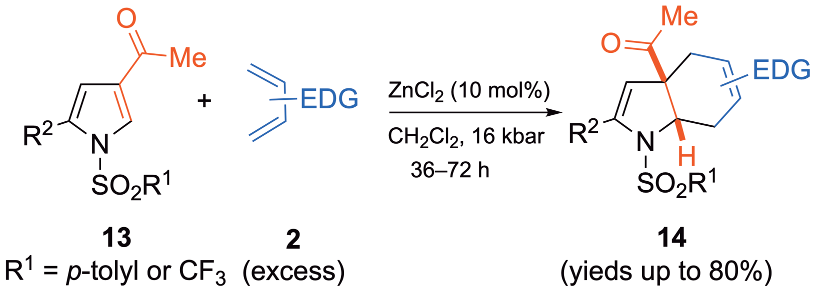

Scheme 10. 3-Acylpyrrole **13** as C2=C3 dienophile under HP activation combined with Lewis acid catalysis.

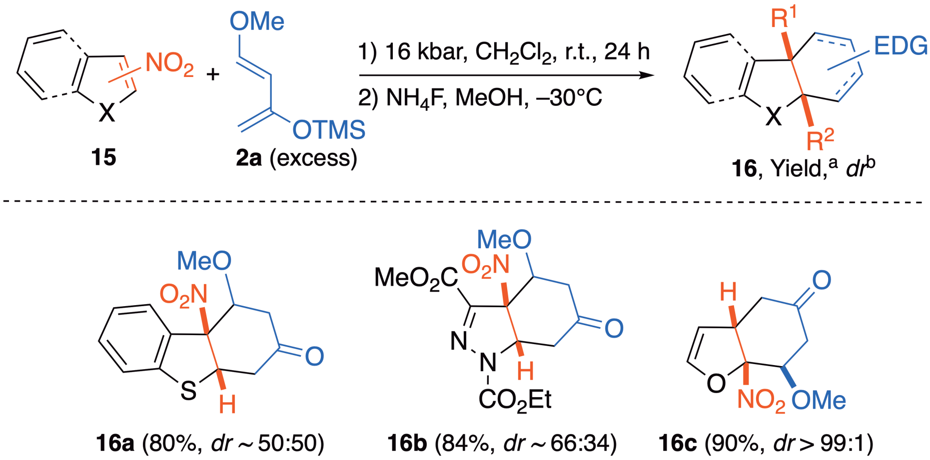

a. Isolated yield. b. Diastereomeric ratio determined by ^{1}H NMR.

Scheme 11. Nitrated five-membered-ring heteroaromatics as dienophiles under HP activation.

bis-cycloadducts **19** from 1,3-dinitronaphthalene or 1,3-dinitrobenzene.

As suggested by DFT computations performed on a model reaction between 1-nitronaphthalene and Danishefsky's diene **2a**, the cycloaddition occurs in a stepwise fashion, the silylenol ether first adding at position C2 of the aromatic. The formation of an elusive zwitterionic primary adduct (**PA**) is quickly followed by cyclization via a Michael addition to furnish the cycloadduct (**CA**), prior to hydrolysis of the silyl enol ether moiety (Scheme 13). The initial dearomatization addition is associated with a significantly higher energy barrier than that of the subsequent cyclization step (~27 versus ~4 kcal·mol^{-1}), making it the rate-determining step. Assuming that the **PA** undergoes no conformational change before cyclization, the diastereoselectivity of the overall cycloaddition is governed by the stereochemical outcome of the initial addition. Consistent with the experimental data, the small energy difference between the *endo* and *exo* transition states ($\Delta\Delta G^\ddagger = 0.4$ kcal·mol^{-1}) accounts for the low diastereoselectivity observed in the resulting cycloadducts.

With the less reactive 2-trimethylsilyloxycyclohexadiene **2b**, the reaction is still possible at r.t. under 16 kbar in the absence of a catalyst (Scheme 14) [29]. As observed with 3-nitroindoles, diastereoselectivity with this cyclic diene is now totally controlled and the exquisite formation of the sole *exo*-cycloadduct is observed. As suggested by DFT computations, the *exo* approach is associated with reduced substrate distortion in a late transition state, along with more favorable orbital interactions, likely between the nitro group and the diene moiety. The propensity for the cycloadducts to rearomatize by loss of nitrous acid is higher here, causing a slight lowering of the

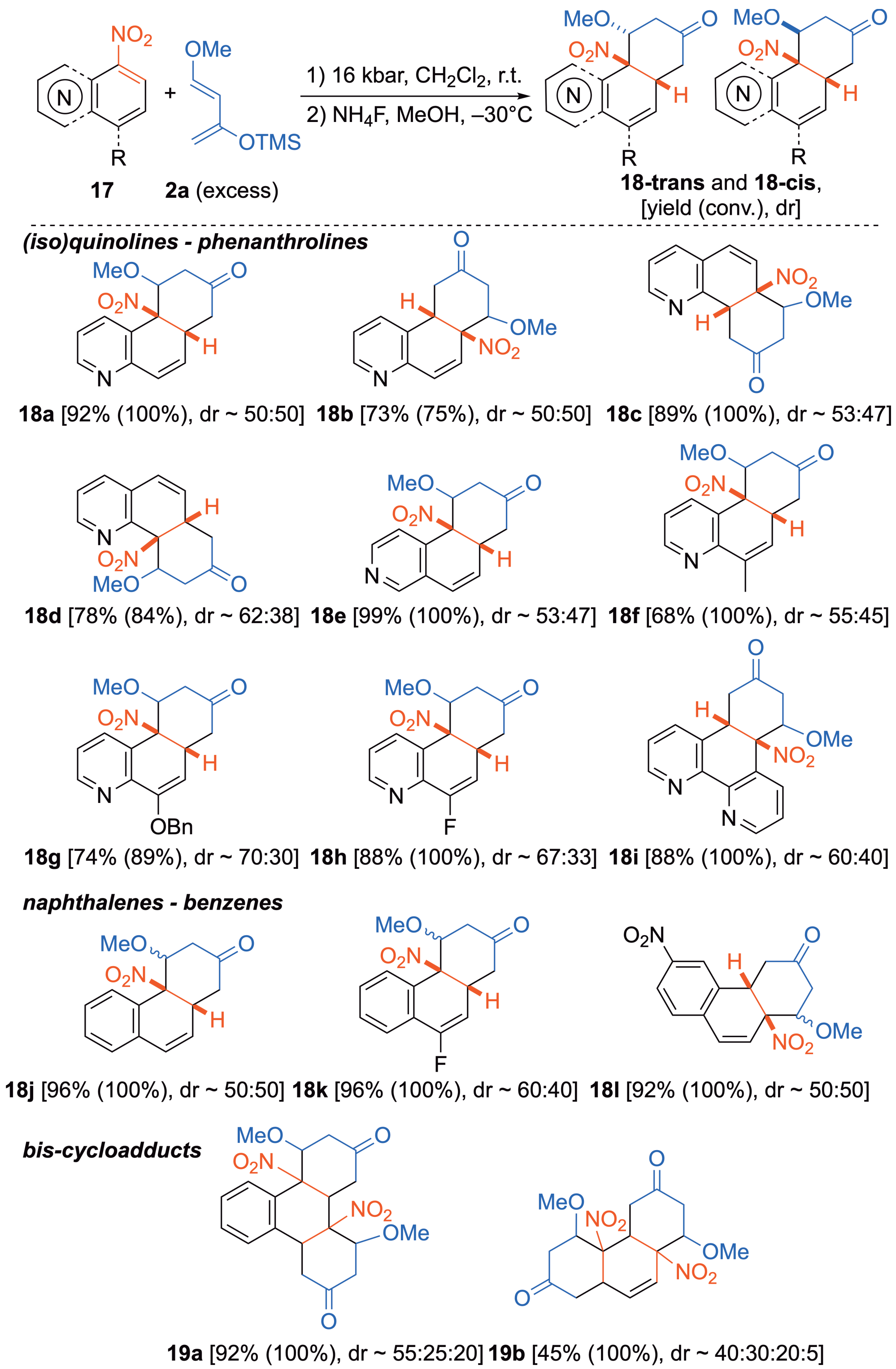

Scheme 12. Cycloadditions of nitrated six-membered-ring (hetero)aromatics as dienophiles with Danishefsky's diene **2a** under HP activation.

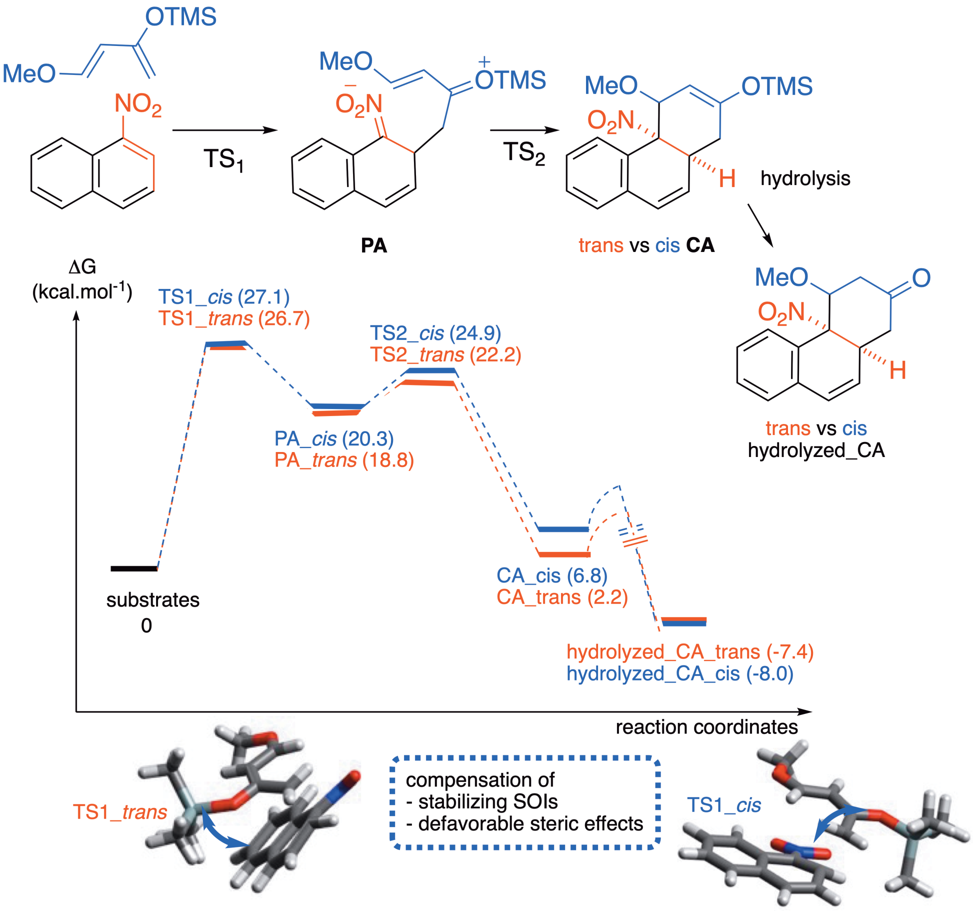

Scheme 13. Energy profiles for the cycloadditions between 1-nitronaphthalene and diene **2a** ; *trans* (*endo*) approach (red); *cis* (*exo*) approach (blue), computed at the (SMD:CH_2Cl_2) M062X/6-31+G(d,p) level of theory.

isolated yields. Here again, when two nitro groups are positioned on the same ring of the initial aromatic compound, two cycloadditions occur, resulting in the formation of the *bis*-cycloadduct **21** from 1,3-dinitro-naphthalene in a completely diastereoselective way.

3. Nitroarenes as heterodienes in HP-promoted domino (4+2)-/(3+2)-cycloadditions

Over the years, domino processes have proven to be powerful and efficient strategies for the rapid construction of complex molecules in a minimal number of synthetic steps. Notably, Denmark et al. described a series of (4+2)-/(3+2)-cycloadditions involving nitroalkenes, and these processes have proven highly valuable for the synthesis of a wide range of nitrogen-containing compounds [37]. In these domino transformations, the nitroalkene partner **22** initially acts as a heterodiene in an inverse electron-demand (4+2)-cycloaddition, forming the intermediate nitronate **23**. This species then undergoes a subsequent (3+2)-cycloaddition to afford a nitrosoketal derivative **24** (Scheme 15). Such compounds provide useful synthetic intermediates, giving an easy access to nitrogenated motifs, after selective cleavage of the N–O bonds for instance.

It turns out that both (4+2)- and (3+2)-cycloaddition processes are promoted under HP [4]. Hence, Scheeren et al. have demonstrated that such (4+2)-/(3+2)-reactions using nitrostyrenes as heterodienes can be efficiently promoted under HP [38]. Given the comparable electrophilic character of

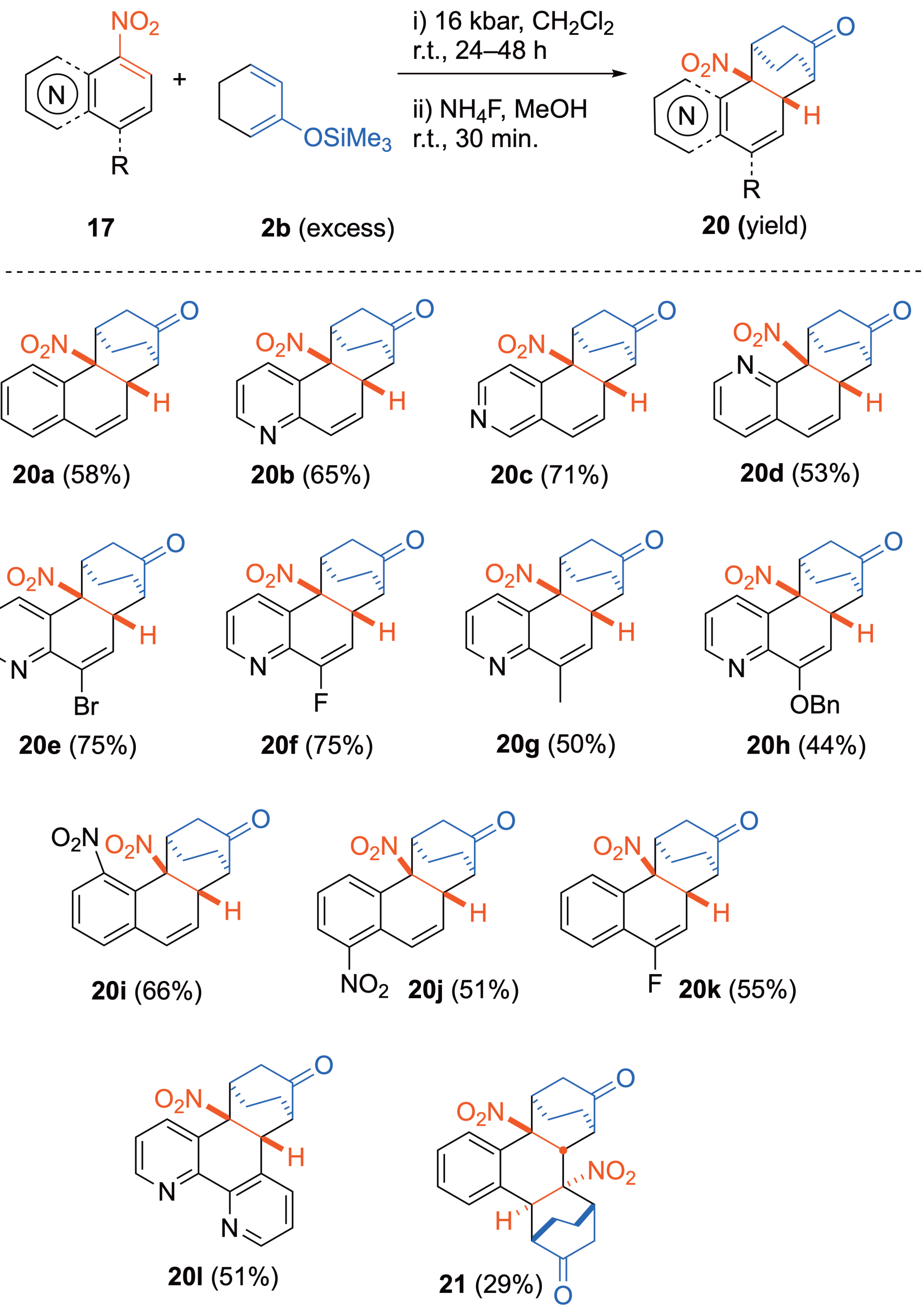

Scheme 14. Cycloadditions of nitrated six-membered-ring (hetero)aromatics as dienophiles with **2b** under HP activation.

nitrostyrenes and 3-nitroindoles [20], we sought to explore the participation of these nitro heteroarenes in similar domino processes. If such a synthetic endeavor could be impeded by the aromaticity of the substrate, it would offer the advantage of relying on readily accessible starting materials to generate partially dearomatized polycyclic structures bearing a tetrasubstituted center at the ring junction, a feature generally difficult to control. In the first (4+2)-cycloaddition, the nitroalkene moiety is expected

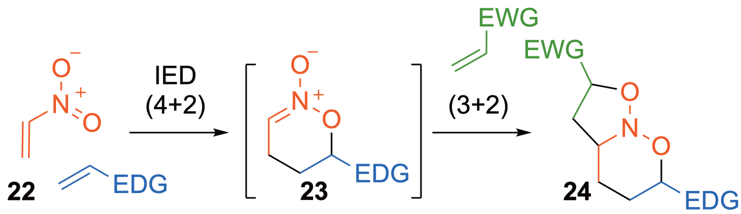

Scheme 15. (4+2)-/(3+2)-Domino cycloadditions involving nitroalkenes.

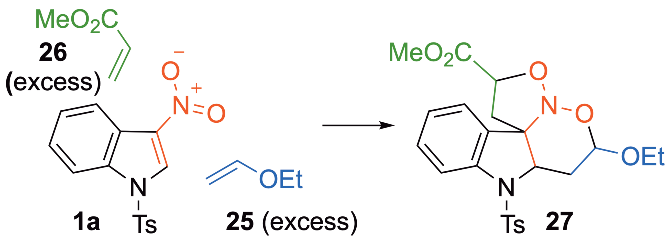

Conditions	% Conversion	% Yield	d.r.[a]
CH_2Cl_2, r.t., 168 h	42	20	50:50:0:0
$Cu(OTf)_2$, CH_2Cl_2, r.t.	0	n.d.[b]	n.d.[b]
Toluene, 110 °C, 60 h	100	83	45:45:5:5
120W,[c] Toluene, 130 °C, 1h	100	75	35:35:15:15
12 kbar,[d] THF, r.t., 24 h	100	83	55:45:0:0

[a] *diastereomeric ratio evaluated by ^1H NMR,* [b] *not determined,* [c] *microwave irradion,* [d] *high pressure activation*

Scheme 16. (4+2)/(3+2)-Domino cycloadditions involving 3-nitroindole **1a**, ethyl vinyl ether **25**, and methylacrylate **26**.

to react via its LUMO as an electron-deficient heterodiene, favoring interaction with an electron-rich dienophile in an inverse electron-demand (4+2)-cycloaddition. Ethyl vinyl ether was selected as a model electron-rich dienophile. In contrast, the nitronate dipole intermediate is expected to react more effectively via its HOMO with an electron-deficient dipolarophile, such as an acrylate. The complementary reactivities of these two alkene species make them excellent candidates for the design of a multicomponent domino process enabling the efficient synthesis of nitroso ketals.

Indeed, the reaction of indole **1a** with ethyl vinyl ether **25** and methyl acrylate **26** in dichloromethane at r.t. successfully affords the expected nitroso ketal **27** [39]. Comparing different activation modes shows that HP is the most efficient one, leading to the expected tetracyclic adduct in good yield and with superior diastereoselectivities (Scheme 16). The reaction can also occur with thiourea- or squaramide-based organocatalysts, including chiral ones. However, the enantioselectivities observed with these catalysts are low, likely due to the competing non-catalyzed process [28].

In this process, two of the eight possible diastereomer couples are formed under HP. As shown by X-ray diffraction analyses on the two separated compounds resulting from the same reaction, but involving *n*-butyl vinyl ether instead of ethyl vinyl ether, the difference stems from the relative stereochemistry at the methoxycarbonyl alpha position. This suggests that the initial (4+2)-cycloaddition proceeds in a purely *endo* mode, determining the relative configurations of both $C7_a$ at the ring junction and C6 alpha to the alkoxy group. A complete facial differentiation for the subsequent (3+2)-process, with an approach of the dipolarophile from the more accessible bottom face sets the relative stereochemistry of quaternary

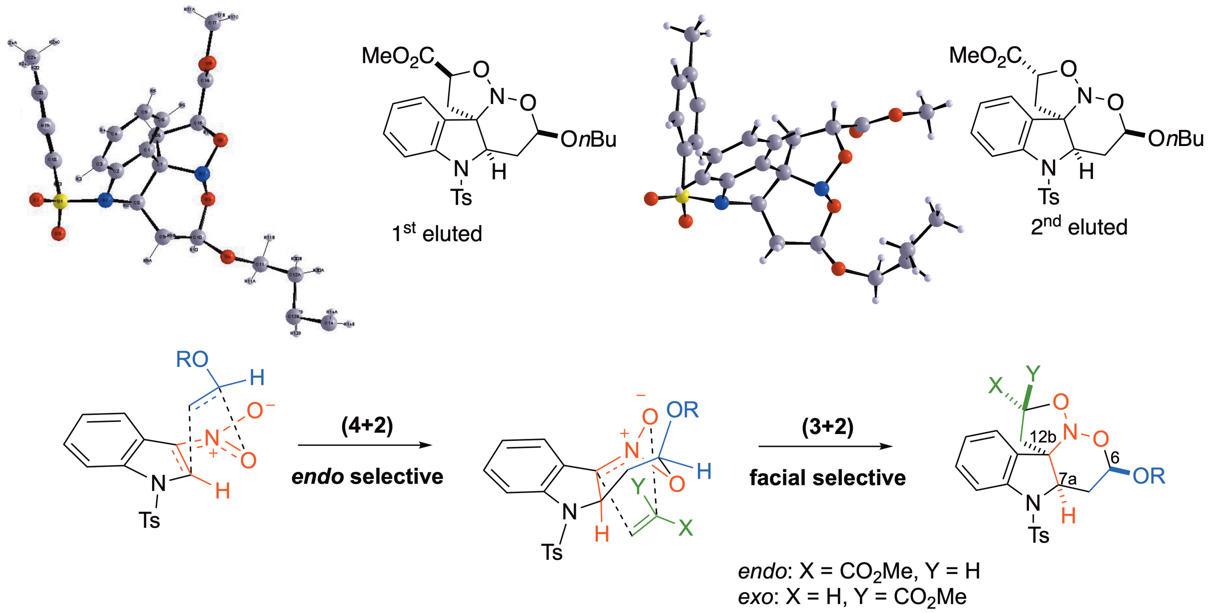

Scheme 17. Proposed pathways for the (4+2)-/(3+2)-sequence accounting for the observed diastereoselectivity.

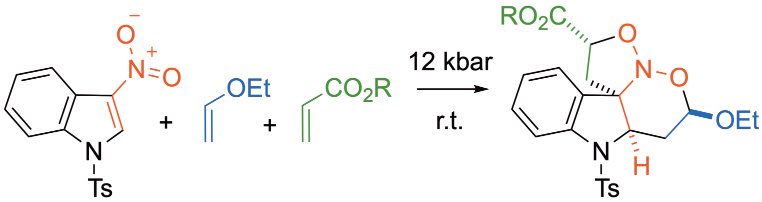

R	% Yield	*endo*/*exo*
CO_2tBu	83	60:40
CO_2Ph	92	66:34
CO_2Tol	95	70:30
$CO_2Naphth$	99	90:10
CO-NPh-CO-	85	85:15

Scheme 18. Influence of the dipolarophile on the diastereoselectivity of the (4+2)-/(3+2)-process.

carbon $C12_b$ at the ring junction. This second cycloaddition, however, shows little or no *endo*/*exo* selectivity for the acrylate approach (Scheme 17) [40].

The diastereoselectivity is improved when other dipolarophiles are employed, notably when they bear an aromatic moiety (Scheme 18) [39].

One of the key strengths of this method is the straightforward and efficient conversion of the resulting nitroso ketals. Therefore, the simple catalytic reduction of ***endo*-27** under 15 bar hydrogen using Raney nickel® for 48 h results in the formation of pyrrolizidone **28**, isolated in 98% yield, with the original characteristics of the stereogenic centers completely retained (Scheme 19). Most likely, this product results from the sequential cleavage of two N–O bonds, formation, and subsequent reduction of an imine intermediate to construct ring D, followed by lactamization to complete ring C. Similarly,

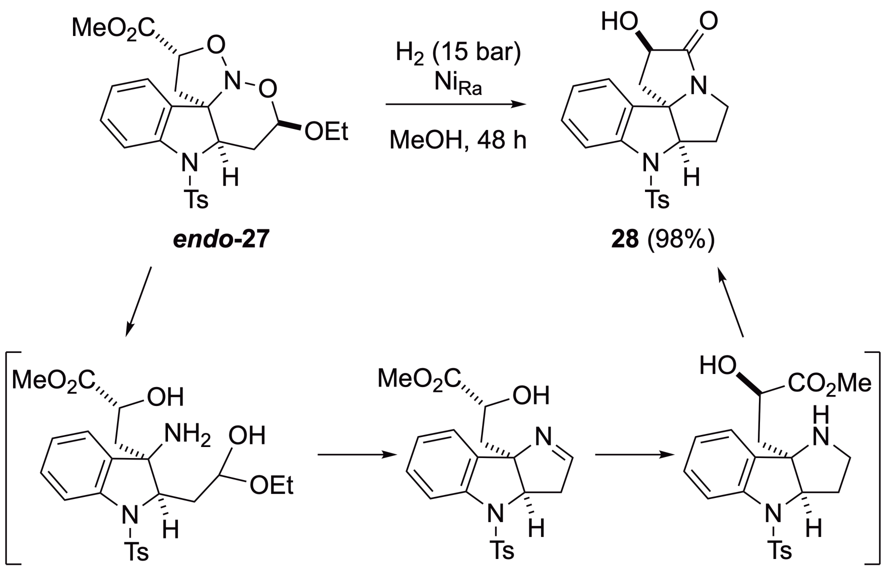

Scheme 19. Reduction of nitroso ketal **27**.

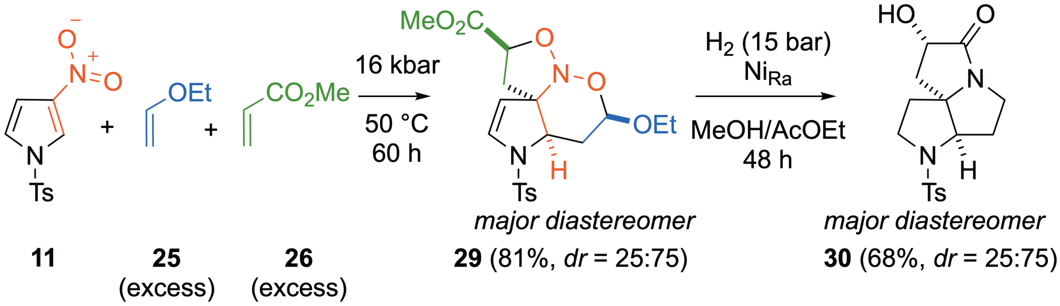

Scheme 20. (4+2)/(3+2)-Domino cycloadditions involving 3-nitropyrrole **11**, ethyl vinyl ether **25,** and methyl acrylate **26** and subsequent reduction of nitroso ketal **29**.

reduction of the diastereomer ***exo*-27** led to the formation of the corresponding diastereomeric tetracyclic lactam.

Extension of this process to other ring systems has been achieved with 3-nitropyrrole (Scheme 20). As expected, this more aromatic substrate requires a higher pressure of 16 kbar and heating to 50 °C to react. It leads to the corresponding nitroso ketal obtained in a 25:75 *endo*/*exo* ratio and isolated in an overall 81% yield. Note that this smaller heterocycle leads to a stereoselectivity different from that above. Here again, the nitroso ketal can be efficiently reduced into the corresponding tricyclic compound under similar hydrogenation conditions and the tricyclic amine is obtained in 68% isolated yield.

Although these tetra- or tricyclic structures are not commonly found in natural products, they certainly exhibit functional and three-dimensional topological characteristics that could contribute to the development of novel pharmacological scaffolds.

4. Conclusion

In conclusion, dearomative cycloadditions involving electron-deficient (hetero)arenes are strongly favored by high-pressure conditions. These easily available aromatic compounds can act as dienophiles or heterodienes, in reaction with electron-rich dienes or dienophiles, providing an efficient access to the corresponding three-dimensional polycyclic adducts. High-pressure conditions primarily promote these reactions by overcoming the high energy barrier required to disrupt aromaticity, thereby enabling more efficient and selective transformations. High pressure favors forward cycloadditions over retroreactions, which is a key point since dearomatization is often endergonic and reversible under normal thermal conditions. High pressure can indeed shift equilibria toward product formation since cycloadditions are characterized by highly negative activation volumes, associated to a decrease in volume from reactants to the transition state and products. They also stabilize tightly packed transition states and intermediates. High pressure (HP) simultaneously disfavors the retrocycloadditions involving an elimination reaction, which are characterized by a positive activation volume. Because these dearomative cycloadditions proceed at lower temperatures under HP, the side reactions and decomposition processes are limited. In many cases, HP conditions also help improving selectivity and stereocontrol as the pressurized confined environment can favor specific diastereomers or regioisomers, thus improving the stereochemical outcome of cycloadditions. In summary, acting as a physical promoter, HP facilitates cycloadditions that disrupt aromaticity and enables the access to strained or unusual polycyclic structures. In doing so, HP helps in building complex three-dimensional polycyclic scaffolds with a high sp^3 character that are important in pharmaceutics and materials science.

Declaration of interests

The authors do not work for, advise, own shares in, or receive funds from any organization from this article, and have declared no affiliations other than their research organizations.

References

[1] F.-G. Klärner and R. van Eldik (eds.), *High Pressure Chemistry: Synthetic, Mechanistic, and Supercritical Applications*, Wiley-VCH: Weinheim, 2002.

[2] D. Margetic, *High Pressure Organic Synthesis*, De Gruyter: Berlin; Boston, MA, 2019.

[3] M. Malacria, *Activation Methods: Sonochemistry and High Pressure*, John Wiley & Sons Inc.: Newark, 2020.

[4] K. Matsumoto, H. Hamana and H. Iida, "Compendium of cycloaddition reactions under high pressure", *Helv. Chim. Acta* **88** (2005), pp. 2033–2234.

[5] N. Noël, R. Hammami, L. Chausset Boissarie, R. Spezia and I. Chataigner, "Recent developments in high-pressure promoted cycloaddition reactions: experimental and theoretical perspectives", *Chem. Commun.* **61** (2025), pp. 15953–15971.

[6] G. Xie, V. Wright, A. Lazarev, G. Smejkal, V. Gross and B. Török, "Green synthesis of building blocks, drug candidates and fine chemicals by barochemistry: application of high pressure in organic synthesis", *Green Chem.* **27** (2025), pp. 7096–7113.

[7] F. Terrier, *Modern Nucleophilic Aromatic Substitution*, Wiley-VCH: Weinheim, 2013.

[8] F. López Ortiz, M. J. Iglesias, I. Fernández, C. M. Andújar Sánchez and G. Ruiz Gómez, "Nucleophilic dearomatizing (D_NAr) reactions of aromatic C,H-Systems. A mature paradigm in organic synthesis", *Chem. Rev.* **107** (2007), pp. 1580–1691.

[9] S. Lee, I. Chataigner and S. R. Piettre, "Facile dearomatization of nitrobenzene derivatives and other nitroarenes with *N*-benzyl azomethine ylide", *Angew. Chem. Int. Ed.* **50** (2011), pp. 472–476.

[10] S. Lee, S. Diab, P. Queval, M. Sebban, I. Chataigner and S. R. Piettre, "Aromatic C=C bonds as dipolarophiles: Facile reactions of uncomplexed electron-deficient benzene derivatives and other aromatic rings with a non-stabilized azomethine ylide", *Chem. Eur. J.* **19** (2013), pp. 7181–7192.

[11] L. Birbaum, L. Gillard, H. Gérard, H. Oulyadi, G. Vincent, X. Moreau, M. De Paolis and I. Chataigner, "Dearomatization of 3-nitroindoles with highly γ-functionalized allenoates in formal (3+2) cycloadditions", *Chem. Eur. J.* **25** (2019), pp. 13688–13693.

[12] M. Manneveau, S. Tanii, F. Gens, J. Legros and I. Chataigner, "Dearomatization of 3-cyanoindoles by (3 + 2) cycloaddition: from batch to flow chemistry", *Org. Biomol. Chem.* **18** (2020), pp. 3481–3486.

[13] M. Manneveau, B. Rkein, D. Cahard, J. Legros and I. Chataigner, "Flow dearomatization of electron-poor 3-fluoromethylthioindoles by 1,3-dipolar cycloaddition", *J. Flow Chem.* **12** (2022), pp. 141–145.

[14] B. Rkein, M. Manneveau, H. Gérard, J. Legros and I. Chataigner, "1,3-dipolar cycloadditions of cyanoheteroarenes with non-stabilized azomethine ylides: C≡N *vs* aromatic C=C reactivity", *ChemistrySelect* **7** (2022), article no. e202203628.

[15] S. Lakhdar, M. Westermaier, F. Terrier, R. Goumont, T. Boubaker, A. R. Ofial and H. Mayr, "Nucleophilic reactivities of indoles", *J. Org. Chem.* **71** (2006), pp. 9088–9095.

[16] M. Bandini, "Electrophilicity: the "dark-side" of indole chemistry", *Org. Biomol. Chem.* **11** (2013), pp. 5206–5212.

[17] A. Cerveri and M. Bandini, "Recent advances in the catalytic functionalization of "electrophilic" indoles", *Chin. J. Chem.* **38** (2020), pp. 287–294.

[18] G. A. Kraus, J. Raggon, P. J. Thomas and D. Bougie, "Intramolecular Diels–Alder reactions of indoles", *Tetrahedron Lett.* **29** (1988), pp. 5605–5608.

[19] G. A. Kraus, D. Bougie, R. A. Jacobson and Y. Su, "The urea connection. Intramolecular Diels–Alder reactions of ureas", *J. Org. Chem.* **54** (1989), pp. 2425–2428.

[20] B. Rkein, M. Manneveau, L. Noël-Duchesneau, K. Pasturaud, M. Durandetti, J. Legros, S. Lakhdar and I. Chataigner, "How electrophilic are 3-nitroindoles? Mechanistic investigations and application to a reagentless (4+2) cycloaddition", *Chem. Commun.* **57** (2021), pp. 10071–10074.

[21] B. Rkein, A. Bigot, L. Birbaum, M. Manneveau, M. De Paolis, J. Legros and I. Chataigner, "Reactivity of 3-nitroindoles with electron-rich species", *Chem. Commun.* **57** (2021), pp. 27–44.

[22] E. Wenkert, P. D. R. Moeller and S. R. Piettre, "Five-membered aromatic heterocycles as dienophiles in Diels–Alder reactions. Furan, pyrrole, and indole", *J. Am. Chem. Soc.* **110** (1988), pp. 7188–7194.

[23] B. Biolatto, M. Kneeteman and P. Mancini, "Diels–Alder reactions of *N*-tosyl-3-nitroindole and dienamides: synthesis of intermediates of *Aspidospermine* alkaloids", *Tetrahedron Lett.* **40** (1999), pp. 3343–3346.

[24] B. Biolatto, M. Kneeteman, E. Paredes and P. M. E. Mancini, "Diels–Alder reactions of *N*-tosyl-3-nitroindole and dienamides: synthesis of intermediates of *Aspidospermine* alkaloids", *J. Org. Chem.* **66** (2001), pp. 3906–3912.

[25] T. L. S. Kishbaugh and G. W. Gribble, "Diels–Alder reactions of 2- and 3-nitroindoles. A simple hydroxycarbazole synthesis", *Tetrahedron Lett.* **42** (2001), pp. 4783–4785.

[26] M. Victoria Gómez, A. I. Aranda, A. Moreno, F. P. Cossío, A. de Cózar, Á. Díaz-Ortiz, A. de la Hoz and P. Prieto, "Microwave-assisted reactions of nitroheterocycles with dienes. Diels–Alder and tandem hetero Diels–Alder/[3,3] sigmatropic shift", *Tetrahedron* **65** (2009), pp. 5328–5336.

[27] Y. Li, F. Tur, R. P. Nielsen, H. Jiang, F. Jensen and K. A. Jørgensen, "Enantioselective formal [4+2] cycloadditions to 3-nitroindoles by trienamine catalysis: Synthesis of chiral dihydrocarbazoles", *Angew. Chem. Int. Ed.* **55** (2016), pp. 1020–1024.

[28] M. Andreini, M. De Paolis and I. Chataigner, "Thiourea-catalyzed dearomatizing [4+2] cycloadditions of 3-nitroindole", *Catal. Commun.* **63** (2015), pp. 15–20.

[29] M. Powderly, M. Roseau, G. Frison, R. Hammami, L. Chausset-Boissarie, D. Harrowven, J. Legros and I. Chataigner, "Controlling diastereoselectivity in dearomatizing Diels–Alder reactions of nitroarenes with 2-trimethylsilyloxycyclohexadiene", *Chem. Euro. J.* **30** (2024), article no. e202303697.

[30] A. Chrétien, I. Chataigner, N. L'Hélias and S. R. Piettre, "Complete and remarkable reversal of chemoselectivity in [4 + 2] cycloadditions involving electron-poor indoles as dienophiles. Diels–Alder versus hetero-Diels–Alder processes", *J. Org. Chem.* **68** (2003), pp. 7990–8002.

[31] I. Chataigner, E. Hess, L. Toupet and S. R. Piettre, "Activation of the dienophilicity of indoles in normal electron demand [4 + 2] cycloadditions under high pressure", *Org. Lett.* **3** (2001), pp. 515–518.

[32] I. Chataigner, C. Panel, H. Gérard and S. R. Piettre, "Sulfonyl vs. carbonyl group: which is the more electron-withdrawing?", *Chem. Commun.* (2007), pp. 3288–3290.

[33] N. Chopin, H. Gérard, I. Chataigner and S. R. Piettre, "Benzofurans as efficient dienophiles in normal electron demand [4 + 2] cycloadditions", *J. Org. Chem.* **74** (2009), pp. 1237–1246.

[34] B. Rkein, R. Coffinier, M. Powderly, et al., "High pressure promoted dearomatization of nitroarenes by [4+2] cycloadditions with silyloxydienes", *Chem. Commun.* **58** (2022), pp. 11807–11810.

[35] A. Chrétien, I. Chataigner and S. R. Piettre, "1-Triflylpyrroles as efficient dienophiles in normal electron demand [4+2] cycloaddition reactions under pressure", *Chem. Commun.* (2005), pp. 1351–1353.

[36] A. Chrétien, I. Chataigner and S. R. Piettre, "Tuning the reactivity and chemoselectivity of electron-poor pyrroles as dienophiles in cycloadditions with electron-rich dienes", *Tetrahedron* **61** (2005), pp. 7907–7915.

[37] S. E. Denmark and A. Thorarensen, "Tandem [4+2]/[3+2] cycloadditions of nitroalkenes", *Chem. Rev.* **96** (1996), pp. 137–166.

[38] R. W. M. Aben, R. De Gelder and H. W. Scheeren, "High-pressure promoted cycloadditions of enol ethers and 3-aryl-2-cyano-2-propenoates", *Eur. J. Org. Chem.* **2002** (2002), pp. 3126–3132.

[39] I. Chataigner and S. R. Piettre, "Multicomponent domino [4+2]/[3+2] cycloadditions of nitroheteroaromatics: An efficient synthesis of fused nitrogenated polycycles", *Org. Lett.* **9** (2007), pp. 4159–4162.

[40] H. Gérard and I. Chataigner, "Selectivities of multicomponent [4 + 2]/[3 + 2] cycloadditions of 3-nitroindole with substituted alkenes: A DFT analysis", *J. Org. Chem.* **78** (2013), pp. 9233–9242.

ACADÉMIE
DES SCIENCES
INSTITUT DE FRANCE

Comptes Rendus. Chimie
2025, Vol. 28, p. 901-910
https://doi.org/10.5802/crchim.427

Review article

Chiral phosphorescent derivatives from molecular engineering between helicenic *N*,*N*-type ligands and rhenium(I) metal centers

Debsouri Kundu [a, b] and Jeanne Crassous [*, a]

[a] Institut des Sciences Chimiques de Rennes, University of Rennes, CNRS, ISCR, UMR 6226, F-35000 Rennes, France

[b] ICBMS, UMR 5246, Univ Lyon, Université Lyon 1, CNRS, INSA, CPE-Lyon, 1 rue Victor Grignard, 69622 Villeurbanne, France

E-mail: jeanne.crassous@univ-rennes.fr (J. Crassous)

Dedicated to the memory of Bertrand Carboni.

Abstract. The incorporation of rhenium atoms within an extended helical π-conjugated *N*,*N*-type (bipyridine or phenanthroline) system impacts the chiroptical and photophysical properties of the resulting neutral or cationic complexes, leading to rhenium-based phosphorescent derivatives that exhibit circularly polarized luminescence. In this short review, we describe key results that have been obtained by our group in this field in the past decade.

Keywords. Helicenes, Rhenium, Stereochemistry, Circularly polarized luminescence, *N*,*N* ligands.

Funding. Ministère de l'Education Nationale, de la Recherche et de la Technologie, Centre National de la Recherche Scientifique (CNRS), Rennes Métropole, French National Agency (ANR, LumoMat-E project, 18-EURE-0012), European Commission Research Executive Agency (Grant Agreement number: 859752 – HEL4CHIROLED – H2020-MSCA-ITN-2019).

Note. Article submitted by invitation.

Manuscript received 28 September 2025, revised 2 October 2025, accepted 10 October 2025.

1. Introduction

Rhenium(I) tricarbonyl d^6 complexes are well-known emissive complexes, notably for their efficient visible-light and long-lived luminescence [1]. Owing to the strong spin–orbit coupling of the heavy rhenium atom, these complexes exhibit efficient room-temperature (rt) phosphorescence. They have been investigated for diverse applications, including photoredox chemistry [2,3], chemo- and electro-chemiluminescence [4,5], chemical and biological sensing [6,7], bioconjugation [8,9], and as dopants in organic light-emitting diodes (OLEDs) [10]. They can be easily synthesized by refluxing in toluene a rhenium(I) source (commonly $ReX(CO)_5$, where X = Cl, Br) with a bidentate *N*,*N* or *C*,*N* ligand (such as a 2,2′-bipyridine, terpyridine, or pyridyl-*N*-substituted heterocyclic carbene), yielding complexes of general formula $ReL_2X(CO)_3$, with L_2 representing the bidentate ligand. An attractive research direction involves the introduction of chirality into L_2, for instance helical chirality, and combination with chirality at the rhenium center. Helicenes are helically chiral molecules obtained from the *ortho*-fusion of aromatic rings [11]. Over the past two decades, our group has focused on synthesizing helicenic structures, incorporating coordinating units to produce helically chiral ligands and a broad range of chiral metal complexes upon subsequent

* Corresponding author

coordination [12,13]. This approach enables the combination of the chirality-driven properties of the ligand with the intrinsic photophysical, chiroptical, and magnetic characteristics of the chosen metal ion, thereby generating unique functional molecular materials. In this short account, the main results on rhenium complexes bearing helicenic ligands functionalized with 2,2′-bipyridine or phenanthroline-type coordinating units are reviewed. These complexes exhibited intense electronic circular dichroism, and circularly polarized long-lived phosphorescence, appealing properties for the development of chiral photoactive materials. The specific stereochemical features that significantly influence the properties of these chiral emitters are also highlighted.

2. Results and discussion

2.1. *Synthesis and characterization of helicenic N,N ligands*

2,2′-Bipyridine (bipy) units are widely used ligands in coordination chemistry, enabling access to a broad range of luminescent metal-based molecular materials [14]. Our group was the first to prepare helical bipy ligands, i.e., bipy units fused with a helicenic moiety, actually consisting of 4-aza[n]helicenes 3-substituted by a 2-pyridyl unit. As described in Scheme 1, we developed in a systematic fashion [4]helicene **3a** [15,16], [6]helicene **3b** [15,16], with a single bipyridine unit at one end, along with [6]helicene **3c** [17] containing a bipyridine unit at both termini. We started our two-step synthesis from 2,2′-bipyridine-6-carboxaldehyde **1**, by a Wittig reaction with either 2-naphthyl phosphonium bromide **2a**, 2-methylbenzophenanthrene phosphonium bromide **2b**, or naphtyl-2,7-dimethyl-diphosphonium bromide **2c**, respectively, followed by a Mallory reaction (photocyclization under oxidative conditions) [18]. Regarding [4]helicene-pyrazino[2,3-*f*][1,10]phenanthroline (**6**), incorporating a dppz unit (dppz = benzo[*h*]dipyrido[3,2-*a*:2′,3′-*c*]phenazine) [19], it was obtained from condensation of a 1,2-[4]helicene-diamine **4** with 1,10-phenanthroline-5,6-dione **6** (Scheme 1) using catalytic para-toluene sulfonic acid [20]. A similar strategy was recently utilized by others to generate pyrazino-phenanthryl-based helicenic systems displaying high photoconductive properties [21].

The photophysical properties of ligands **3b**, **3c**, and **6** were studied in detail. These three compounds exhibited absorption spectra in the UV–visible (UV–Vis) region between 270 and 500 nm. Furthermore, helicene derivatives **3b** and **3c** were found to display vibronically structured blue fluorescence with moderate quantum yields. For instance, in CH_2Cl_2 solution at rt, ligand **3b** exhibited a structured blue fluorescence at 421 nm, with a vibronic progression of 1400 cm^{-1} (quantum yield $\Phi = 8.4\%$) (Table 1). Ligand **6** was found to emit redshifted fluorescence centered at 515 nm, which appeared broad and unresolved as a result of the presence of charge transfer (CT), and with a higher quantum yield of 29%. Interestingly, long-lived phosphorescence signals emerging around 530 nm were observed for **3b**,**c** and at 560 nm for **6** when cooling down to low temperature (77 K) (Figure 3d).

While benzophenanthryl system **3a** was found to be configurationally unstable, hexahelicenic enantiopure (*M*)- and (*P*)-**3b**, and (*M*)- and (*P*)-**3c** could successfully be obtained by HPLC over chiral stationary phases. Unfortunately, due to very poor solubility, attempts to separate the enantiomers of **6** proved unsuccessful. (*M*) and (*P*) enantiomers of **3b** and **3c** displayed the typically strong electronic circular dichroism (ECD) responses, which are very typical of helicenic organic derivatives [22]. For instance, enantiomer (*P*)-**3b** exhibited a very strong negative band at 265 nm and a very strong positive band at 335 nm along with weaker positive bands between 380 and 430 nm (Figure 2a).

3. Coordination to rhenium(I)

3.1. *Monometallic helicene–bipy–Re(I) complexes*

The coordination of **3a** and **3b** to rhenium(I) was then performed under classical conditions, i.e., by reacting them with $Re(CO)_5Cl$ in refluxing toluene and isolating the complexes by simple filtration thanks to their low solubility in toluene (Scheme 2). Specifically, the neutral Re(I) complexes **7a** and **7b** were synthesized from 4-(2-pyridyl)-5-aza[4]helicene **3a** and 4-(2-pyridyl)-5-aza[6]helicene **3b**, respectively. In contrast to the starting ligands, Re(I) complexes **7a** and **7b** displayed red phosphorescence at ~673–678 nm in CH_2Cl_2 at rt, but with very low quantum

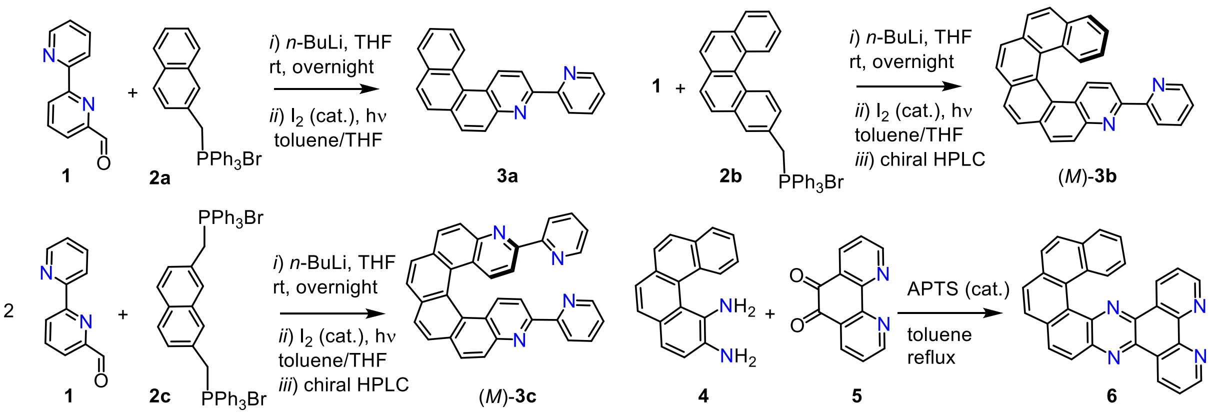

Scheme 1. Synthetic procedures used to prepare helicenic *N,N* ligands **3a**–**3c** and **6** [15,17,20].

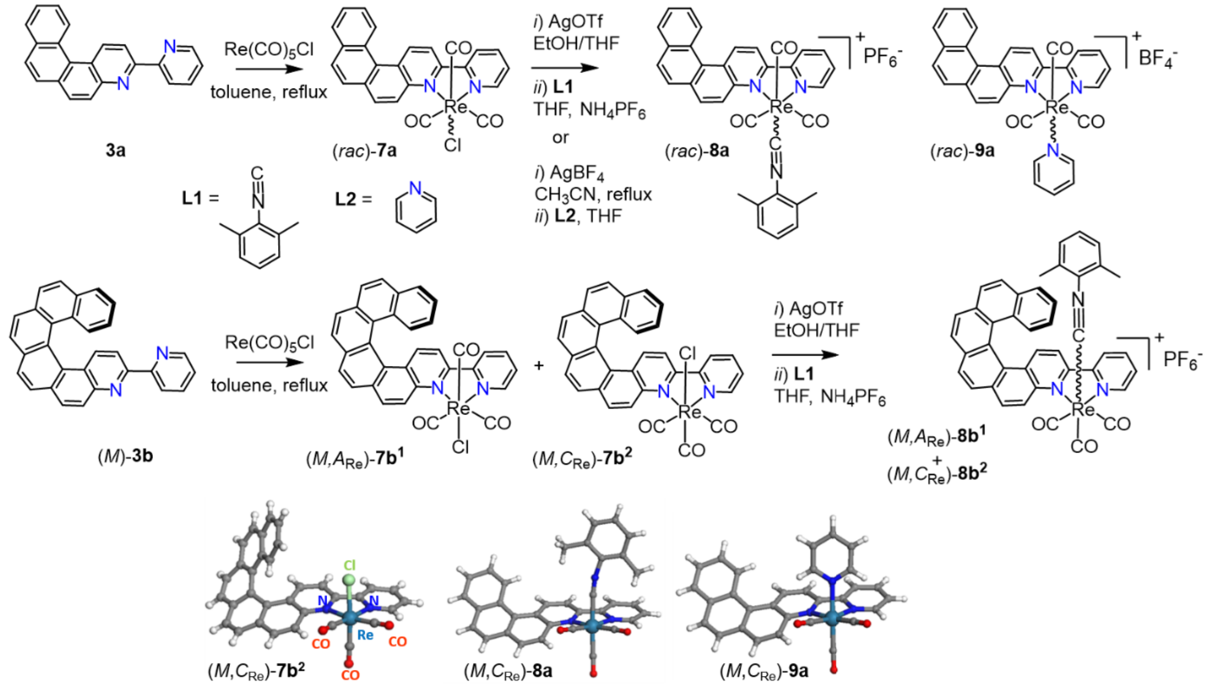

Scheme 2. Synthesis of neutral and charged rhenium complexes **7a**–**9a** and enantioenriched (M, A_{Re})-$\mathbf{7b^1}$, (M, C_{Re})-$\mathbf{7b^2}$ and (M, CA_{Re})-$\mathbf{8b^{1,2}}$ from, respectively, [4]helicene-bipy **3a** and [6]helicene-bipy (*M*)-**3b**. X-ray crystallographic structures of racemic $\mathbf{7b^2}$, **8a**, and **9a** (only (M, C_{Re}) stereoisomers are shown). Adapted with permission from Ref. [16].

yields (Φ = 0.11–0.13%, Table 1). In order to improve efficiency, charged complexes **8a**/$\mathbf{8b^{1,2}}$ and **9a**, were readily prepared by direct substitution of the chloride ligand with pyridine or isocyanide. Satisfyingly, these were found to exhibit red phosphorescence with markedly higher quantum yields (6–16%) (Table 1) and much longer lifetimes. From the stereochemical viewpoint, ligand **3a** is in average planar and achiral, while ligand **3b** adopts helical (*P*) or (*M*) chirality. Due to the dissymmetric nature of the bipy ligands, the slightly distorted octahedral rhenium center also becomes chiral,

Table 1. Absorption data, emission maxima, quantum yields, lifetimes and emission dissymmetry factors of the compounds described. In dichloromethane at 298 ± 3 K, except otherwise indicated

Compound	Absorption λ_{max} (nm) (ε ($\times 10^3$ $M^{-1}\cdot cm^{-1}$))	Emission λ_{max} (nm)	Φ (%)	τ (ns)[a]	CPL g_{lum}
3b	240 (35.0), 266 (55.8), 322 (27.0), 353 (14.4), 372 (10.2), 393 (2.63), 417 (1.80)	421, 445, 473sh	8.4	6.6	$+3.4 \times 10^{-3}$ [(*P*)-**3b**] [15]
3c	242 (35.1), 272 (60.3), 286 (65.3), 344 (26.5), 366sh (20.2), 398 (3.50), 420 (2.75)	422, 448, 476, 513sh	8.6	5.1	$+8.6 \times 10^{-3}$ [(*P*)-**3c**] [15]
6	260 (85), 288 (67), 350 (33), 435 (13), 410 (16)	515 (CH_2Cl_2) 560 (77 K)	29	5.8, 2.8	n.d.
7a	243 (34.5), 273 (30.3), 318 (30.3), 330 (43.2), 398 (12.7)	678	0.11	25	n.d.
8a	251 (54.9), 273 (51.9), 326sh (35.9), 337 (46.6), 403 (14.6), 422 (15.2)	585, 618	16	67 000	n.d.
9a	248 (35.7), 280 (34.2), 327sh (27.3), 338 (37.7), 408 (13.5), 422 (13.9)	595, 623	8.3	11 500	n.d.
7b^1	236 (45.9), 277 (49.9), 307 (28.2), 339 (21.3), 420 (7.96), 444 (7.30)	680	0.13	27	n.d.
7b^2	237 (59.8), 278 (65.0), 305sh (36.3), 344 (26.3), 418 (11.0), 445 (10.2)	673	0.16	33	$+3.1 \times 10^{-3}$ [(P, A_{Re})-**7b^2**] [16]
8b^{1,2}	272 (48.0), 339 (17.6), 444 (5.6)	598	6	79 000	$+1.3 \times 10^{-3}$ [(P, AC_{Re})-**8b^{1,2}**] [16]
10-1	283 (46.5), 299 (51.4), 361 (15.5), 387 (15.4), 450 (6.08)	664	0.20	38	$+3.4 \times 10^{-3}$ [(P, A_{Re}, A_{Re})-**10-1**] [17]
10-2	283 (33.7), 299 (37.9), 359 (12.7), 389 (11.3), 450 (5.09)	678	0.15	32	n.d.
11	267 (77), 304 (40), 353 (29), 460 (12)	518 (CH_2Cl_2) 560 (77 K)	2.0	1.2, 7.6	$+2.3 \times 10^{-3}$ at rt $+2.9 \times 10^{-2}$ at 77 K [(P, AC_{Re})-**11**] [20]

[a] In degassed solution. n.d. not determined.

with its configuration described as anticlockwise (A_{Re}) or clockwise (C_{Re}) [23,24]. Consequently, complex **7a** can exist as (A_{Re})/(C_{Re}) enantiomers, whereas **7b** forms two diastereomeric pairs of enantiomers: (P, A_{Re})/(M, C_{Re}) and (P, C_{Re})/(M, A_{Re}). In the charged complexes, the Re center readily isomerized, thus yielding inseparable racemic mixtures (**8a**) or epimeric mixtures (**8b^{1,2}**). In contrast, enantiomerically and diastereomerically pure samples of **7a** and **7b^{1,2}** were successfully isolated by chiral HPLC. Having these species in hand allowed a detailed investigation of their chiroptical properties. For instance, Figure 1a represents the comparison of the ECD spectra of pure stereoisomers of **3b** with those of **7b^1** and **7b^2**, while Figure 1c shows the comparison of the calculated ECD spectra

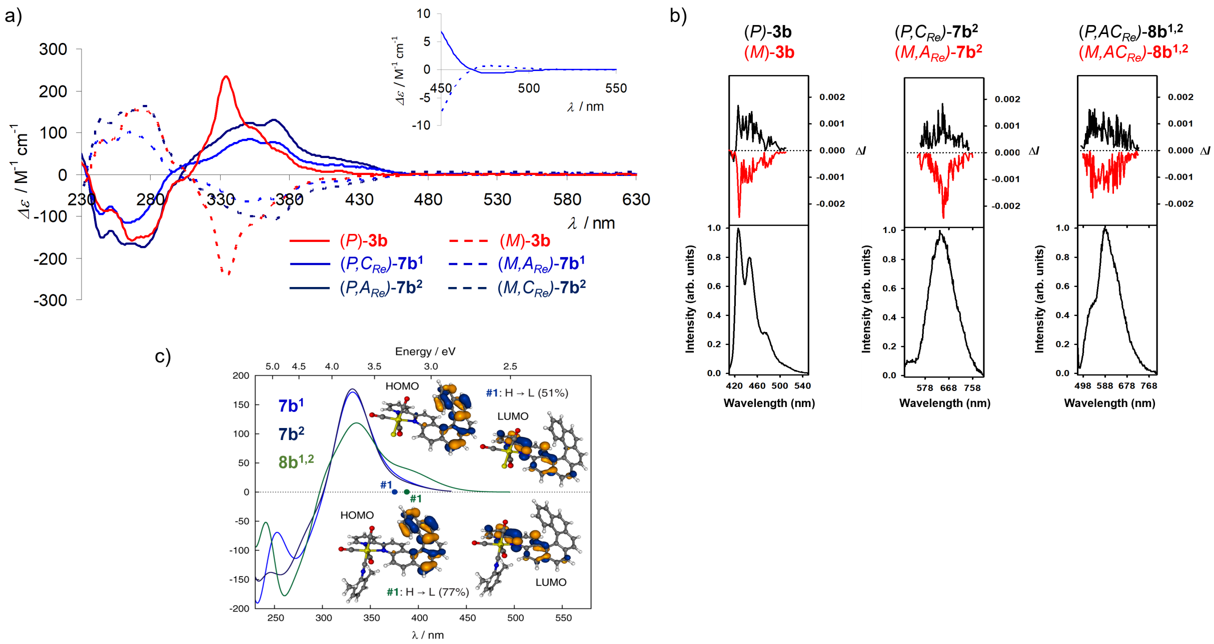

Figure 1. (a) Experimental ECD spectra of enantiopure (M) and (P)-**3b** and their corresponding enantiopure Re^{I} complexes (M, A_{Re})-**7b**^{1}, (P, C_{Re})-**7b**^{1}, (M, C_{Re})-**7b**^{2}, and (P, A_{Re})-**7b**^{2}. Inset: ECD spectra of **7b**^{1} enantiomers between 450 and 550 nm. (b) CPL (upper curves within each panel) and total luminescence (lower curves within each panel) spectra of (M)-**3b**, (P)-**3b**, (M, C_{Re})-7b^{2}, (P, A_{Re})-**7b**^{2}, (M, AC_{Re})-**8b**^{1,2}, (P, AC_{Re})-**8b**^{1,2} in degassed CH_2Cl_2 at rt. (c) Calculated ECD spectra of (P, C_{Re})-**7b**^{1}, and (P, A_{Re})-**7b**^{2} and Boltzmann-averaged spectrum for (P)-**8b**^{1,2} conformers. View of HOMO and LUMO of **7b**^{1} and **8b**^{1}. First excitation energies indicated by dots on the abscissa. Adapted with permission from Ref. [16].

of **7b**^{1} and **7b**^{2} with the epimeric mixture of **8b**^{1,2}, and Figure 1b presents their CPL (circularly polarized luminescence) responses. The ECD spectra of **7b**^{1,2} and **8b**^{1,2} feature a new low-energy band which was absent in **3b**. The calculated ECD spectra revealed that this transition mainly corresponded to the HOMO→LUMO excitation and arose from the π-helical ligand system in the HOMO and the bipy–rhenium fragment, with partial π-extension into the helicenic core in the LUMO. Importantly, ligand **3b**, complex **7b**^{2}, and complex **8b**^{1,2} were found CPL-active, with emission dissymmetry factors (g_{lum}) on the order of 10^{-3} (Table 1). Theoretical calculations indicated that the emission process involves Re orbitals, enabling the formally spin-forbidden $T_1 \rightarrow S_0$ phosphorescence transitions via spin–orbit coupling. The reduced metal-orbital participation (lower metal-to-ligand CT [MLCT] character) in the T_1 state of **8b**^{1,2} compared with **7b**^{1,2} explained the higher emission efficiency of the charged complexes.

3.2. *Bimetallic helicene–bis-bipy–Re(I) complexes*

Using the same strategy, the dinuclear Re(I) complexes **10-1** and **10-2** were synthesized from 3,14-bis(2-pyridyl)-4,13-diaza[6]helicene **3c** incorporating two bipy units (Scheme 3). Similarly to mono-Re complexes, each Re center in **10-1** and **10-2** adopts a distorted octahedral geometry with *fac*-oriented carbonyl groups. In **10-1**, both chlorides point toward the helicene core, giving C_2 symmetry with identical C or A configurations at the two Re centers and a helical angle of 39.13°. In **10-2**, one chloride points inward (C) and the other outward (A), breaking the symmetry (C_1) and increasing the helical angle to 46.39°. The isomer with both chlorides pointing outward was not observed. X-ray diffraction established the absolute configurations as $(M, C_{Re}, C_{Re})/(P, A_{Re}, A_{Re})$ for **10-1** and $(M, C_{Re}, A_{Re})/(P, A_{Re}, C_{Re})$ for **10-2**, consistent with

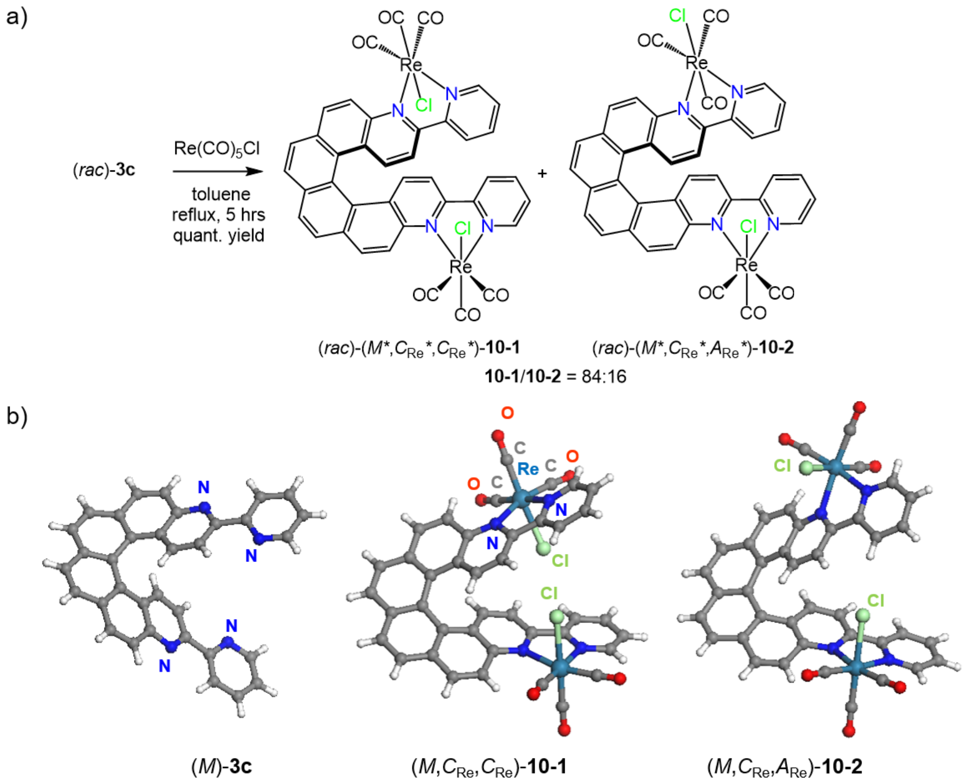

Scheme 3. (a) Synthesis of dinuclear rhenium(I) complexes (*rac*)-**10-1** and (*rac*)-**10-2** from racemic diaza [6]helicene-bis-bipyridine ligand **3c**. (b) X-ray crystallographic molecular structures of **3c**, **10-1**, and **10-2** (racemic structures, only one enantiomer shown). Adapted with permission from Ref. [17].

their respective C_2 and C_1 symmetry. Incorporation of two Re centers into the helicenic ligand induced a marked redshift of the lowest-energy bands and increased molar absorptivity beyond 375 nm (Table 1). The nature of these excitations in **10-1** and **10-2** was investigated in detail by TDDFT calculations. Bands around 299 nm are assigned to intraligand π–π^* transitions, while the lower-energy bands corresponded to intra-ligand CT (ILCT) excitations with MLCT contributions. In CH_2Cl_2 at rt, **10-1** and **10-2** displayed weak, broad red phosphorescence (λ_{max} = 673 and 687 nm; Φ = 0.20% and 0.15%; τ = 38 and 32 ns), typical of ^{3}MLCT emission in $Re(CO)_3(N,N)Cl$ complexes. At 77 K, the complexes exhibited structured phosphorescence blueshifted by over 100 nm relative to rt, with τ over 40 µs. This low-temperature emission closely resembled that of ligand **3c** suggesting that a ligand-centered $^3\pi$–π^* state lies below the ^{3}MLCT state under these conditions, with metal coordination slightly stabilizing the π^* orbitals and accelerating the $T_1 \rightarrow S_0$ transition.

Enantiopure dinuclear Re(I) complexes were prepared from enantiopure ligands. Interestingly, only one diastereomer was formed from each ligand, namely (M, C_{Re}, C_{Re}) and (P, A_{Re}, A_{Re})-**10-1** from (M)- and (P)-**3c**, respectively, while enantiopure **10-2** was not detected. This selectivity most likely originated from the lower stability of enantiopure **10-2**, which under refluxing toluene isomerized to the thermodynamically more stable **10-1**. This interpretation was supported by DFT calculations. Figure 2a compares the experimental ECD spectra of the ligand and its complexes. The enantiomers of **10-1** exhibited mirror-image spectra featuring several bands between 272 and 459 nm. The MOs involved in the low-energy intense excitations of **3c** and **10-1** are shown in Figure 2c. Transitions of the ligands are dominated

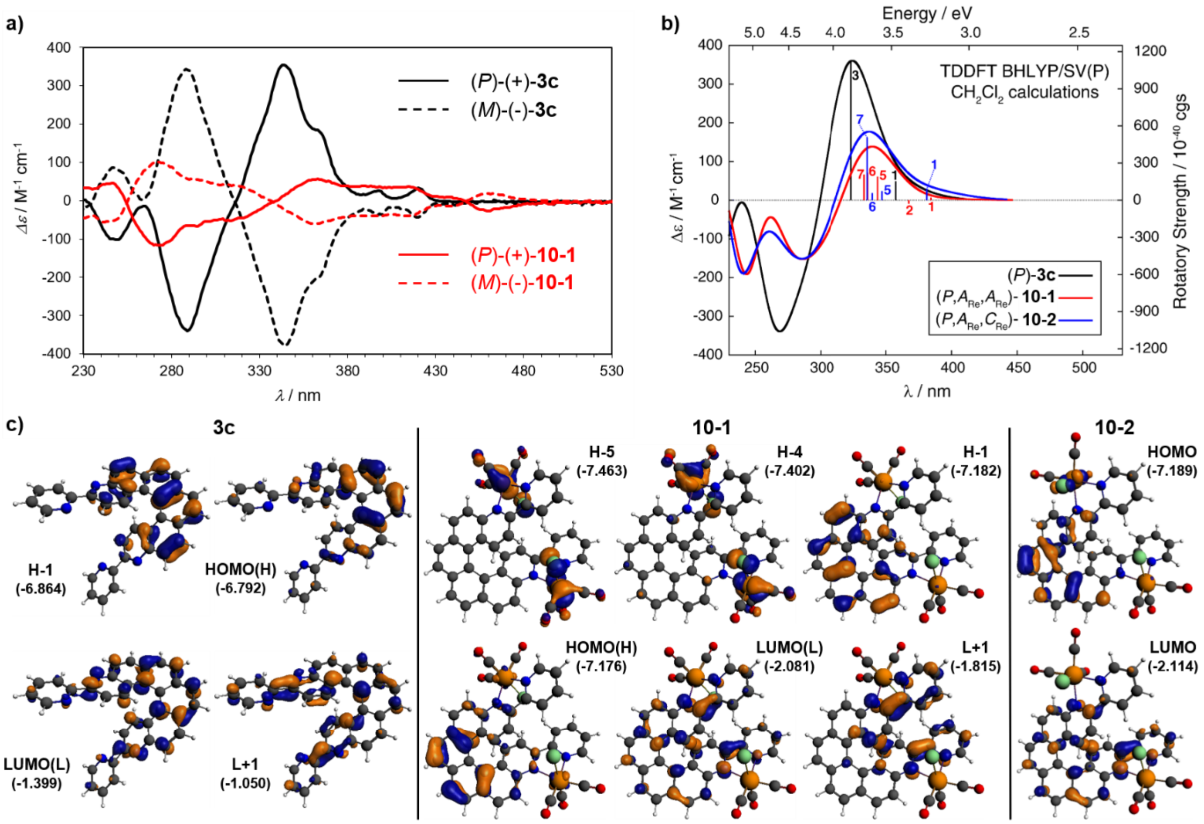

Figure 2. (a) Experimental ECD spectra of (*P*)- and (*M*)-**3c** and (*P*)- and (*M*)-**10-1** in CH_2Cl_2 at rt. (b) Simulated ECD spectra of (*P*)-**3c**, (*P*, A_{Re}, A_{Re})-**10-1**, and (*P*, A_{Re}, C_{Re})-**10-2** with selected calculated excitation energies and rotatory strengths indicated as "stick" spectra. (c) Isosurfaces of selected molecular orbitals for **3c**, **10-1**, and **10-2**. Adapted with permission from Ref. [17].

by π–π^* ones, with extended conjugation through the whole system. In complex **10-1**, the strong ECD bands mainly arise from metal and halogen to helicene–bis-bipyridine charge transfers (MLCT and halogen-to-ligand CT [XLCT]), with additional helicene ILCT and π–π^* transitions. Finally, nearly mirror-image CPL spectra were recorded in degassed CH_2Cl_2 solutions at rt, with g_{lum} values of $+8.6 \times 10^{-3}$ at ~450 nm for (*P*)-**3c** and $+3.4 \times 10^{-3}$ at ~630 nm for (*P*, A_{Re}, A_{Re})-**10-1**. The latter value is similar to the one of complex **7b²** (see Table 1). It is worth mentioning that complex **10-1** displayed a CPL sign which was opposite to that of the lowest-energy ECD band ($g_{abs} = -3.4 \times 10^{-3}$ for (*P*, A_{Re}, A_{Re})-**10-1**), suggesting that absorption and emission involve different electronic states and/or the transition is not Franck–Condon-allowed [25].

3.3. *Monometallic helicene–DPPZ–Re(I) complexes*

Coordination of Re(I) to helical DPPZ-type ligand **6**, using $Re(CO)_5Cl$ in refluxing toluene, yielded complex **11**. Contrary to ligand **6**, it was possible to obtain enantiomerically enriched samples of **11** on an analytical scale using the chiral HPLC separation technique [20]. The (*P*) and (*M*) helical configurations were confirmed by (TD)DFT calculations. However, these systems may exist in two octahedral diastereomeric forms differing in rhenium-centered chirality ((*P*, C_{Re})-**11-1** and (*P*, A_{Re})-**11-2** and their mirror images), but they could not be clearly distinguished in this particular case. This outcome suggested either a weak differentiation between both diastereomers, a potential dynamic equilibrium in solution,

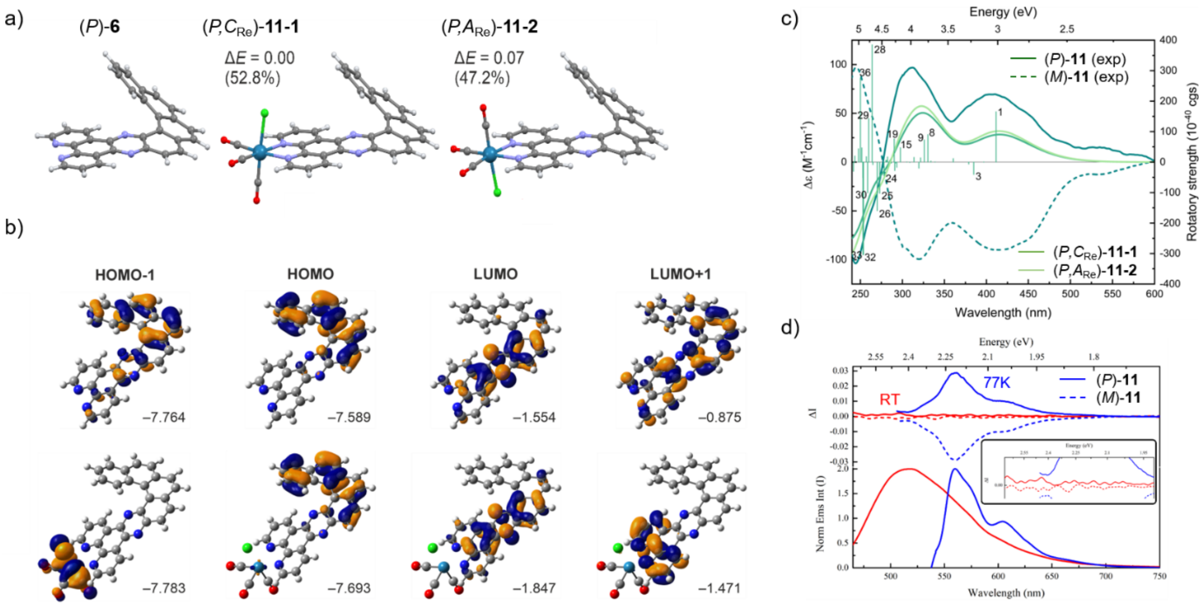

Figure 3. (a) Optimized structures of (P)-**6**, (P, C_{Re})-**11-1**, and (P, A_{Re})-**11-2** with relative electronic energy ΔE values (in kcal/mol) and respective Boltzmann populations at 298 K. (b) FMOs of (P)-**6** and (P, C_{Re})-**11** obtained based on LC-PBE0*/def2-TZVP/PCM(CH_2Cl_2) calculations. Values listed are the corresponding orbital energies (in eV). (c) Experimental ECD spectra of **11** enantiomers in CH_2Cl_2 at rt, along with the corresponding simulated (TDDFT-LC-PBE0*/def2-TZVP/PCM(CH_2Cl_2)) spectral envelopes obtained for (P, C_{Re})-**11-1** and (P, A_{Re})-**11-2**. Selected numbered excitation energies and the corresponding rotatory strengths obtained for (P, C_{Re})-**11-1** indicated as "stick". (d) Experimental photoluminescence spectra of **11** in CH_2Cl_2 at rt and in 2-MeTHF at 77 K. Inset: Enlarged spectra. Adapted with permission from Ref. [20].

or a preferential formation of one stereoisomer under the synthetic conditions, as already seen in the complexes described above. Complex **11** exhibited very similar UV–Vis absorption in the higher-energy region as for the ligand (Figure 3 and Table 1) but with an additional tail of absorption going down to 575 nm due to the presence of the rhenium atom. TDDFT calculations and MO analysis of **6** highlighted the presence of strong charge-transfer transitions ([4]helicene→pyrazino-phenanthroline) in addition to the classical π–π^* transitions (Figure 3b), while for **11** they revealed similar electronic characteristics corresponding to almost pure HOMO→LUMO ILCT transition with some helicene-centered π–π^* signature but with additional Metal-to-Ligand CT (MLCT) component due to the involvement of the metal orbital. The emission spectra of **11** recorded in CH_2Cl_2 at rt and in 2-MeTHF at 77 K (Figure 3d) were nevertheless found to be mainly influenced by the ligand scaffold with rather minimal impact of the metal center on the photophysical properties but with a quantum yield (Φ = 2%) which was found one order of magnitude higher than for the previously reported neutral mononuclear rhenium–bipyridine–helicene complexes (0.1–0.3%, see above) although lower than for the charged systems (8.3–16%, see above) and the rhenium–NHC–helicene complexes also described by our group (5–13%) [26,27]. Similarly to **6**, emission decay of **11** was found bi-exponential, with a faster lifetime component at 1.2 ns (87%) and a more extended lifetime component of 7.6 ns (13%). The observed lifetime was much shorter than that reported for rhenium–bipyridine–helicene complexes (25–38 ns) (Table 1) indicating again that the emission predominantly originated from the ligand itself with small contribution of the rhenium. Regarding the chiroptical properties, complex **11** exhibited mirror-image ECD and CPL spectra (Figures 3c, d).

In ECD, (*P*)-**11** enantiomer exhibited mainly four bands, a negative one around 240 nm, and three positive ones between 311 and 540 nm. The (*P*) and (*M*) assignments were based on theoretical calculations. However, calculations showed similar ECD spectra for (P, C_{Re})-**11-1** and (P, A_{Re})-**11-2** preventing any further assignment about the rhenium stereochemistry. CPL signals of **11** were examined both at rt in CH_2Cl_2 and at 77 K in 2-MeTHF. At rt, the CPL signal correlated with the ECD signals, and (*P*)-**11** showed a positive CPL signal and a g_{lum} value of $+2.3 \times 10^{-3}$ at 507 nm. Notably, the CPL signal was significantly increased at 77 K, with a g_{lum} value of $+2.9 \times 10^{-2}$ at 560 nm and displayed a clear vibrational progression. Noteworthy, the g_{lum} was found to be stable throughout the band suggesting that the emission at 77 K originated from a single excited state, which was not the case at rt, as also indicated by the presence of bi-exponential decay.

4. Conclusion

In this review, we have described helicenic organic bipy- or phen-type fluorophores and their use as efficient *N*,*N* ligands for coordination to rhenium(I) heavy transition metal centers. This strategy enabled us to generate enantiopure or enantioenriched *fac*-ReX(bpy)$(CO)_3$-type complexes for which the structure and stereochemical features were carefully analyzed. Furthermore, this gave access to helically chiral absorbers and phosphorescent derivatives with strong experimental ECD responses, substantial CPL activity, and long-lived emission. Their photophysics and chiroptics were studied in detail by theoretical calculations, allowing characterization of CT/π–π^* transitions in the ligands, and additional MLCT, XLCT, and ligand-to-ligand CT (LLCT) in the complexes. Further molecular engineering enabled access to optimized chiral phosphorescent compounds. Indeed, going from neutral to charged complexes led to significantly improved photophysical characteristics, especially improved quantum yields and much longer-lived emission, while lowering the temperature significantly improved the CPL response, with emission dissymmetry factors increasing by one order of magnitude (from $\sim 10^{-3}$ to $\sim 10^{-2}$). Overall, we think that such specific features in these unique helically shaped heavy-metal complexes provide potentially important future applications, notably in the domain of photoactive catalysts such as in the use of rhenium tricarbonyl bipy complexes for CO_2-to-CO reduction [28–30]. This work is currently ongoing in our group.

Acknowledgements

All collaborators and students involved in this work reviewed in this article are warmly thanked for their precious contributions.

Declaration of interests

The authors do not work for, advise, own shares in, or receive funds from any organization that could benefit from this article, and have declared no affiliations other than their research organizations.

Funding

We acknowledge the Ministère de l'Education Nationale, de la Recherche et de la Technologie, the Centre National de la Recherche Scientifique (CNRS), Rennes Métropole and the French National Agency (ANR, LumoMat-E project, 18-EURE-0012). The European Commission Research Executive Agency (Grant Agreement number: 859752 – HEL4CHIROLED – H2020-MSCA-ITN-2019) is thanked for financial support.

References

[1] M. Wrighton and D. L. Morse, "Nature of the lowest excited state in tricarbonylchloro-1,10-phenanthrolinerhenium (I) and related complexes", *J. Am. Chem. Soc.* **96** (1974), pp. 998–1003.

[2] H. Tsubaki, A. Sekine, Y. Ohashi, K. Koike, H. Takeda and O. Ishitani, "Control of photochemical, photophysical, electrochemical, and photocatalytic properties of rhenium(I) complexes using intramolecular weak interactions between ligands", *J. Am. Chem. Soc.* **127** (2005), pp. 15544–15555.

[3] D. Beck, J. Brewer, J. Lee, D. McGraw, B. A. DeGraff and J. N. Demas, "Localizing molecular probes: Inclusion of Re(I) complexes in β-cyclodextrin", *Coord. Chem. Rev.* **251** (2007), pp. 546–553.

[4] M. M. Richter, "Electrochemiluminescence (ECL)", *Chem. Rev.* **104** (2004), pp. 3003–3036.

[5] S. Y. Reece, M. R. Seyedsayamdost, J. Stubbe and D. G. Nocera, "Electron transfer reactions of fluorotyrosyl radicals", *J. Am. Chem. Soc.* **128** (2006), pp. 13654–13655.

[6] K. K.-W. Lo, W.-K. Hui, C.-K. Chung, K. H.-K. Tsang, D. C.-M. Ng, N. Zhu and K.-K. Cheung, “Biological labelling reagents and probes derived from luminescent transition metal polypyridine complexes”, *Coord. Chem. Rev.* **249** (2005), pp. 1434–1450.

[7] V. Fernández-Moreira, F. L. Thorp-Greenwood and M. P. Coogan, “Application of d^6 transition metal complexes in fluorescence cell imaging”, *Chem. Commun.* **46** (2010), pp. 186–202.

[8] K. K.-W. Lo, K. H.-K. Tsang and N. Zhu, “Luminescent tricarbonylrhenium(I) polypyridine estradiol conjugates: synthesis, crystal structure, and photophysical, electrochemical, and protein-binding properties”, *Organometallics* **25** (2006), pp. 3220–3227.

[9] K. K.-W. Lo, W.-K. Hui, C.-K. Chung, K. H.-K. Tsang, T. K.-M. Lee, C.-K. Li, J. S.-Y. Lau and D. C.-M. Ng, “Luminescent transition metal complex biotin conjugates”, *Coord. Chem. Rev.* **250** (2006), pp. 1724–1736.

[10] N. J. Lundin, A. G. Blackman, K. C. Gordon and D. L. Officer, “Synthesis and characterization of a multicomponent rhenium(I) complex for application as an OLED dopant”, *Angew. Chem. Int. Ed.* **45** (2006), pp. 2582–2584.

[11] J. Crassous, I. G. Stará and I. Starý (eds.), *Helicenes—Synthesis, Properties and Applications*, Wiley-VCH: Weinheim, 2022.

[12] J.-K. Ou-Yang and J. Crassous, “Chiral multifunctional molecules based on organometallic helicenes: recent advances”, *Coord. Chem. Rev.* **376** (2018), pp. 533–547.

[13] E. S. Gauthier, R. Rodríguez and J. Crassous, “Metal-based multihelicenic architectures”, *Angew. Chem. Int. Ed.* **59** (2020), pp. 22840–22856.

[14] H.-L. Kwong, H.-L. Yeung, C.-T. Yeung, W.-S. Lee, C.-S. Lee and W.-L. Wong, “Chiral pyridine-containing ligands in asymmetric catalysis”, *Coord. Chem. Rev.* **251** (2007), pp. 2188–2222.

[15] N. Saleh, B. Moore II, M. Srebro, et al., “Acid-base triggered switching of circularly polarized luminescence and electronic circular dichroism in organic and organometallic helicenes”, *Chem. Eur. J.* **21** (2015), pp. 1673–1681.

[16] N. Saleh, M. Srebro, T. Reynaldo, et al., “Enantio-enriched CPL-active helicene-bipyridine-rhenium complexes”, *Chem. Commun.* **51** (2015), pp. 3754–3757.

[17] N. Saleh, D. Kundu, N. Vanthuyne, et al., “Dinuclear rhenium complexes with a bridging helicene-bis-bipyridine ligand: synthesis, structure, and photophysical and chiroptical properties”, *ChemPlusChem* **85** (2020), pp. 2446–2454.

[18] F. B. Mallory and C. W. Mallory, “Photocyclization of stilbenes and related molecules”, *Org. React.* **30** (1984), pp. 1–456.

[19] J. A. Smith, M. W. George and J. M. Kelly, “Transient spectroscopy of dipyridophenazine metal complexes which undergo photo-induced electron transfer with DNA”, *Coord. Chem. Rev.* **255** (2011), pp. 2666–2675.

[20] D. Kundu, D. Jelonek, N. Del Rio, N. Vanthuyne, M. Srebro-Hooper and J. Crassous, “Photophysical and chiroptical properties of pyrazino-phenanthroline-helicene derivative and its rhenium(I) complex”, *Chem. Asian J.* **20** (2025), article no. e202401735.

[21] Z. Zhang, W. Hu, Z. Liu, Y. Tsutsui, Y. Murata, S. Seki and T. Hirose, “Face-to-face helical columns with permanent polarity consisting of homochiral end-functionalized helicenes”, *J. Am. Chem. Soc.* **147** (2025), pp. 25978–25989.

[22] K. Dhbaibi, L. Favereau and J. Crassous, “Enantioenriched helicenes and helicenoids containing main-group elements (B,Si,N,P)”, *Chem. Rev.* **119** (2019), pp. 8846–8953.

[23] A. von Zelewsky, *Stereochemistry of Coordination Compounds*, J. Wiley & Sons: Chichester, 1996.

[24] H. Amouri and M. Gruselle, *Chirality in Transition Metal Chemistry. Molecules, Supramolecular Assemblies and Materials*, John Wiley & Sons: Hoboken, 2008.

[25] Y. Liu, J. Cerezo, G. Mazzeo, N. Lin, X. Zhao, G. Longhi, S. Abbate and F. Santoro, “Vibronic coupling explains the different shape of electronic circular dichroism and of circularly polarized luminescence spectra of hexahelicenes”, *J. Chem. Theory Comput.* **12** (2016), pp. 2799–2819.

[26] E. S. Gauthier, L. Abella, N. Hellou, et al., “Long-lived circularly-polarized phosphorescence in helicene-NHC-rhenium(I) complexes: the influence of helicene, halogen and stereochemistry on emission properties”, *Angew. Chem. Int. Ed.* **59** (2020), pp. 8394–8400.

[27] E. S. Gauthier, L. Abella, E. Caytan, et al., “N-(aza[6]helicenyl)-NHC-rhenium(I) complexes: modulation of chiroptical and photophysical properties in helicenic rhenium(I) systems”, *Chem. Eur. J.* **29** (2023), article no. e202203477.

[28] N. Elgrishi, M. B. Chambers, X. Wang and M. Fontecave, “Molecular polypyridine-based metal complexes as catalysts for the reduction of CO_2”, *Chem. Soc. Rev.* **46** (2017), pp. 761–796.

[29] N. W. Kinzel, C. Werlé and W. Leitner, “Transition metal complexes as catalysts for the electroconversion of CO_2: an organometallic perspective”, *Angew. Chem. Int. Ed.* **60** (2021), pp. 11628–11686.

[30] A. M.-H. Yip and K. K.-W. Lo, “Luminescent rhenium(I), ruthenium(II), and iridium(III) polypyridine complexes containing a poly(ethylene glycol) pendant or bioorthogonal reaction group as biological probes and photocytotoxic agents”, *Coord. Chem. Rev.* **361** (2018), pp. 138–163.

ACADÉMIE
DES SCIENCES
INSTITUT DE FRANCE

Comptes Rendus. Chimie
2026, Vol. 29, p. 27-51
https://doi.org/10.5802/crchim.429

Research article

From deprotometalation of ferrocenyl ketones to fused ferrocene structures

Madani Hedidi [a,b], William Erb [*,a], Sirine Boussandel [a,c], Yury Siarheevich Halauko [*,d], Vadim Edvardovich Matulis [d], Jean-Pierre Hurvois [a], Marielle Blot [a], Thierry Roisnel [a], Ali Samarat [c] and Florence Mongin [*,a]

[a] Univ Rennes, CNRS, ISCR (Institut des Sciences Chimiques de Rennes) – UMR 6226, F-35000 Rennes, France

[b] Laboratoire de Chimie des Matériaux, Catalyse et Réactivité, Département de Chimie, Faculté des Sciences Exactes et d'Informatique, Université Hassiba Benbouali de Chlef, Ouled Fares Chlef, BP 78C, 02180 Chlef, Algérie

[c] University of Carthage, Faculty of Sciences of Bizerte, Laboratory of Hetero-Organic Compounds and Nanostructured Materials (LR18ES11), Zarzouna, 7021 Bizerte, Tunisia

[d] Department of Chemistry, Belarusian State University, 14 Leningradskaya St., 220030 Minsk, Belarus

E-mails: william.erb@univ-rennes.fr (W. Erb), hys@tut.by (Y. S. Halauko), florence.mongin@univ-rennes.fr (F. Mongin)

Abstract. Although ferrocene ketones have been known since the early days of ferrocene chemistry, their behavior in deprotometalation has never been studied in detail. Here, we have optimized this reaction using lithium 2,2,6,6-tetramethylpiperidide in tetrahydrofuran containing $ZnCl_2 \cdot N,N,N',N'$-tetramethylethylenediamine as an in-situ trap. Numerous 2-iodoferrocene derivatives were obtained, while a change in regioselectivity was observed for certain aroyl- and heteroaroylferrocenes, in good agreement with our DFT calculations. The development of an enantioselective deprotometalation was also attempted using lithium di[(*S*)-1-phenylethyl]amide, affording the desired compounds in up to 60% enantiomeric excess (*ee*). A selection of iodinated derivatives was finally subjected to post-functionalizations, leading to original ferrocene-fused heterocycles, including an enantiopure tetracyclic derivative. A selection of compounds was studied in both electrochemical reduction and oxidation, and weak interactions such as halogen–halogen, halogen–oxygen and chalcogen–chalcogen bonds were identified in the solid state for some new derivatives.

Keywords. Ferrocene, Ketone, Deprotometalation, Selectivity, Polycyclic compounds.

Funding. Algerian Direction Générale de la Recherche Scientifique et du Développement Technologique, Rennes Métropole, University of Carthage, Tunisian Ministry of Higher Education and Scientific Research, Fonds Européen de Développement Régional, Université de Rennes, Centre National de la Recherche Scientifique, BASF, Thermofisher.

Note. Article submitted by invitation.

Manuscript received 22 September 2025, revised 17 October 2025, accepted 20 October 2025, online since 22 January 2026.

* Corresponding authors

1. Introduction

Since the discovery and the structure determination of the parent molecule [1–4], ferrocenes have attracted considerable interest from synthetic chemists due to their numerous applications [5–13], such as catalysis [14–17], materials science [18,19], molecular sensing [20,21], and bioorganometallic chemistry [22–25]. In addition to monosubstituted ferrocenes, which can be synthesized from ferrocene via aromatic electrophilic substitution [26] or deprotometalation/trapping sequences [27,28], polysubstituted structures may be required for targeted applications [29–33]. Among the most commonly used motifs, 1,1′-disubstituted derivatives are often obtained by double deprotolithiation of ferrocene [34], while 1,2-disubstituted derivatives are typically prepared by directed functionalization of monosubstituted ferrocenes [35–38].

As a bulky electron-rich aromatic, ferrocene tends to reduce the electrophilicity of the attached functional group [39,40]. However, although ferrocene ketones are readily accessible by Friedel–Crafts acylation of ferrocene [41], exploiting this change in reactivity to promote their functionalization by deprotometalation/trapping sequences has rarely been explored. In 2000, Enders and coworkers converted ferrocene ketones to enantiopure hydrazones (e.g., using (*S*)-1-amino-2-methoxymethylpyrrolidine, SAMP) in order to achieve their diastereoselective functionalization by deprotolithiation/trapping sequences [42]. A similar approach was later developed by Top and coworkers using chiral imines derived from ferrocene ketones [43].

To our knowledge, the only study concerning the direct functionalization of ferrocene ketones using lithium bases was reported by Enders and coworkers, who subjected enantiopure diferrocenyl ketones to *s*-BuLi in the presence of N,N,N',N'-tetramethylethylenediamine (TMEDA) in toluene at −78 °C for 9 h, prior to interception with various electrophiles [44]. However, the reactivity of the function toward nucleophiles was probably affected by the presence of the two organometallic cores, and the behavior of this particular substrate may not reflect the behavior of aroylferrocenes in general. Thus, when benzoylferrocene was treated with sodium zincate (TMEDA)Na(TMP)Zn(t-Bu)$_2$ [TMP = 2,2,6,6-tetramethylpiperido] in hydrocarbon solvents at room temperature, mixtures of products were observed, some resulting from deprotonation (mediated by TMP) of the ferrocene core at the site adjacent to the ketone, others from competitive 1,2- and 1,6-addition reactions [45].

In 2010, we reported a synthesis of 1-benzoyl-2-iodoferrocene in 36% yield using a base generated in tetrahydrofuran (THF) from LiTMP (1.5 equiv) and $CdCl_2$·TMEDA (0.50 equiv) [46]. Here, our goal is to evaluate an approach using the less toxic $ZnCl_2$·TMEDA for the functionalization of ferrocene ketones and to investigate the development of an enantioselective version.

2. Results and discussion

2.1. *Preliminary considerations*

Our aim in this study was twofold: firstly, to identify suitable conditions to functionalize ferrocene ketones by deprotometalation, and secondly, to understand the regioselectivity observed during this reaction. Indeed, most of the ferrocene ketones studied here have two to four sites that can be functionalized in the presence of organometallic bases.

Our approach involved the use of a hindered lithium amide, LiTMP, in THF containing $ZnCl_2$·TMEDA as an in-situ trap [47]. While many deprotometalations using lithium dialkylamides are under thermodynamic control [48], those using the strong base LiTMP can also lead to derivatives functionalized next to a coordinating element, probably via pre-metalation complexes (complex-induced proximity effect) [49,50] or/and rate-limiting transition states (kinetically enhanced metalation) [51,52], or benefiting from favorable hydrogen charges (overriding base mechanism) [53–56]. This is particularly true when using an in-situ trap, as we intended to do.

Therefore, to get an idea of the kinetic acidity of the ferrocene ketones selected for the present study, we calculated (see computational details in Supplemantary material) the atomic charges of a few representative examples by natural population analysis (NPA), with and without oxygen coordination to lithium of $LiNMe_2$ chosen as model base. For benzoylferrocene (**1-Ph**), the most acidic hydrogens were found on the substituted cyclopentadienyl ring of ferrocene, on either side of the benzoyl group (Figure 1, **1-Ph**). Further calculations of NPA charges

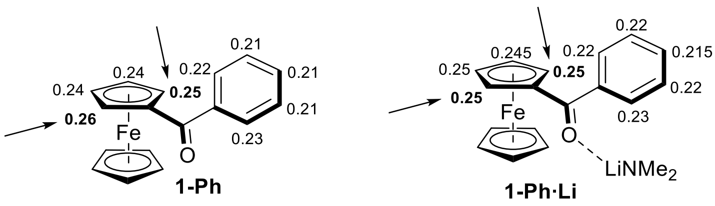

Figure 1. Natural-population-analysis charges on hydrogen atoms in the isolated molecule of benzoylferrocene (**1-Ph**) and impact of coordination to lithium on these charges (complex of **1-Ph** with $LiNMe_2$).

for all hydrogen atoms of the two substituted rings of the complex **1-Ph·Li** showed comparable results (Figure 1, **1-Ph·Li**). A similar tendency was observed for the other substrates (Figure S1, in Supplementary material).

However, formation of the thermodynamic product can also be observed in reactions using strong lithium dialkylamides such as LiTMP [57–59]. We therefore also calculated significant pK_a values for several aroyl ketones in THF within the DFT framework [60–63] (see Figure S2 in Supplementary material for a complete list). As shown on Figure 2a, the lowest pK_a value for **1-Ph** corresponds to the ferrocene site next to the carbonyl group. Coordinating the ketone to $LiNMe_2$ (**1-Ph·Li**, to mimic the stabilizing effect that the function exerts on the lithiated derivative formed) also seemed to show that the most stable lithium species was the one deprotonated next to the carbonyl group on the ferrocene side (Figure 2a, **1-Ph·Li**).

The introduction of electron-withdrawing substituents such as Br or CF_3 on the phenyl group (with compounds **1-*p*BrPh** and **1-*p*CF$_3$Ph**) significantly decreased the pK_a values at their adjacent positions (Figure 2b). However, coordination to $LiNMe_2$ restored the desired reactivity, and the species deprotonated on the ferrocene side appeared to be the most stable. A similar, although less pronounced, effect can be noticed for **1-*p*OMePh** (Figure 2c). Finally, in the case of (2-pyridoyl)- and (2-benzothienoyl)ferrocenes (**1-2Py** and **1-2BTh**), the calculations showed different behaviors, with lithium derivatives being more stable when deprotonation occurs on the heterocycle side (Figure 2d). Furthermore, unlike the other benzoylferrocene compounds considered, the conformation adopted by these heterocyclic compounds has a clear impact on their computed pK_a values (see Figures S3 and S4 in Supplementary material).

All these data suggest that it should be possible to functionalize most of these derivatives next to the ketone on the ferrocene core, while (heteroaroyl)ferrocenes could afford derivatives functionalized on the heterocycle side. With these predictions in mind, we then subjected our selected compounds to the planned deprotometalation/trapping sequences.

2.2. *Functionalization of ferrocene ketones*

Various ferrocene ketones have been prepared in the frame of this study (for details, see Supplementary material). Most of the aroylferrocenes were obtained by Friedel–Crafts acylation, by adapting reported procedures [64–66]. A few other ferrocene ketones were synthesized either by action of lithioferrocene onto the Weinreb 2,2,2-trifluoroacetamide (compound **1-CF$_3$**; see Scheme 7) [67] or by reacting heteroarylmetals with the Weinreb amide of ferrocene [68] (compounds **1-2Py** and **1-2BTh**).

Benzoylferrocene (**1-Ph**) was chosen to optimize the reaction using LiTMP in the presence of an in-situ trap [47]. We first tested the use of the putative $Zn(TMP)_2$ (generated from 1 equiv of $ZnCl_2$·TMEDA and 2 equiv of LiTMP) as an in-situ trap [69] in the reaction of **1-Ph** with LiTMP (1.1 equiv) in THF at −20 °C. After subsequent trapping with iodine, the expected product **2-Ph** was obtained in a moderate 55% yield although almost complete conversion was obtained (<4% **1-Ph** recovered). Replacing $Zn(TMP)_2$ with $ZnCl_2$·TMEDA (1.1 equiv) favored the formation of **2-Ph**, isolated in 72% yield (91% using 2.2 equiv of LiTMP) (Scheme 1, Equation (1)). The intermediate ferrocenylzinc was also engaged in a Negishi cross-coupling [70,71] with 2-chloropyridine. Thus, the use of catalytic amounts of $PdCl_2$ and 1,1′-bis(diphenylphosphino)ferrocene

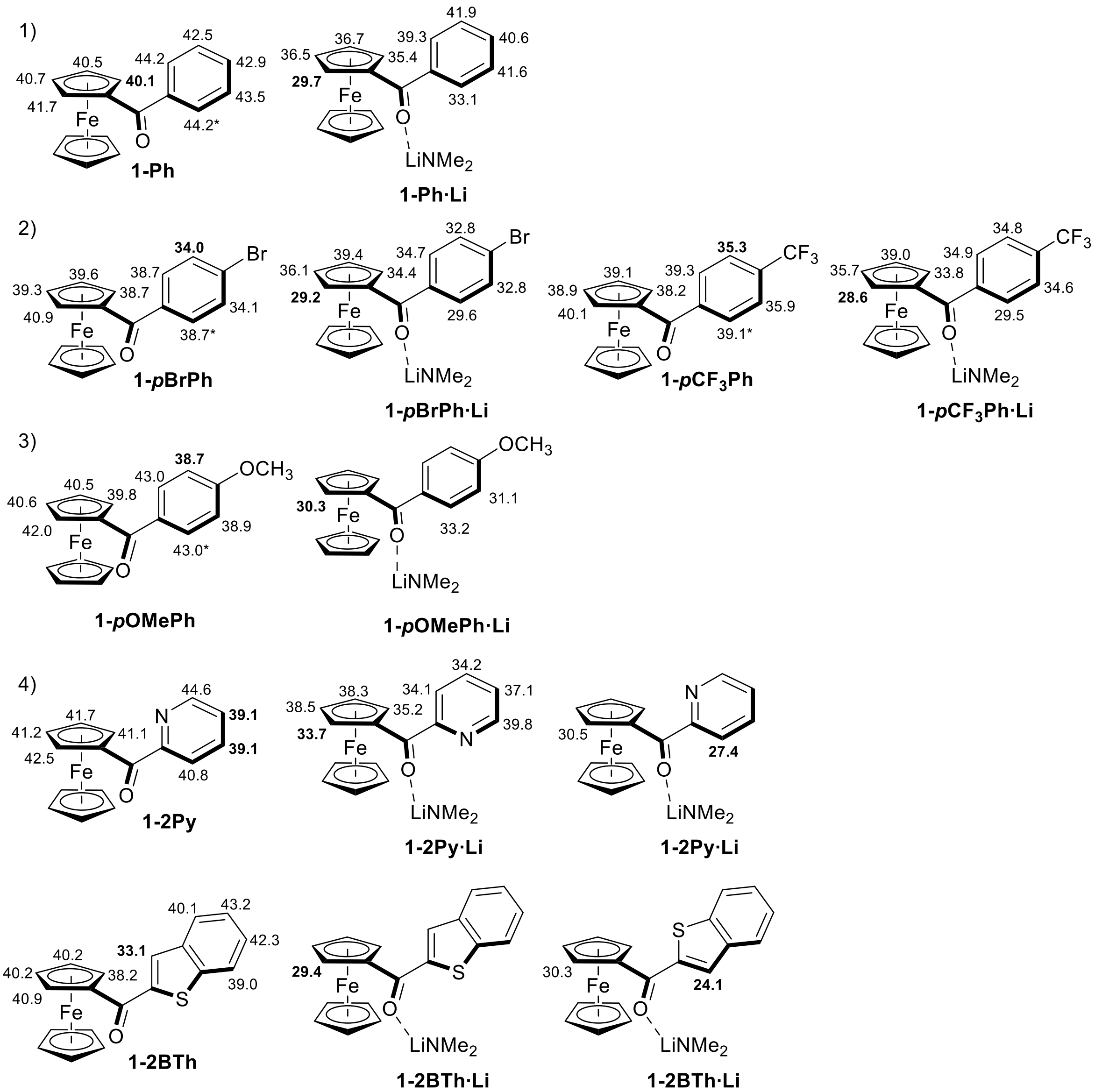

Figure 2. Values of pK_a calculated for ferrocene ketones in THF (an asterisk means that deprotonation in the corresponding position is predicted to lead to interring rotation in order to reduce electron repulsion), and impact of coordination to lithium on these values (complexes with $LiNMe_2$).

(dppf) [72] led to the expected heteroarylated product **3-Ph** (37% yield) (Scheme 1, Equation (2)).

We next attempted to use chlorotrimethylsilane instead of $ZnCl_2$·TMEDA as the in-situ trap, but we failed to observe the formation of the expected ferrocenylsilane under these conditions. We also tried to replace benzoylferrocene (**1-Ph**) by (phenylcarbonothioyl)ferrocene (**4-Ph**), prepared by reacting the former with Lawesson's reagent [73]. However, as already observed in the case of thionoesters [74], the iodinated derivative was not detected, while we recovered 20% of **4-Ph** and 29% of **1-Ph**.

Functionalization at position C-2 of aroylferrocenes was then carried out starting from three different (methoxybenzoyl)ferrocenes, e.g., **1-*o*OMePh**, **1-*m*OMePh**, and **1-*p*OMePh**. As shown in Scheme 2,

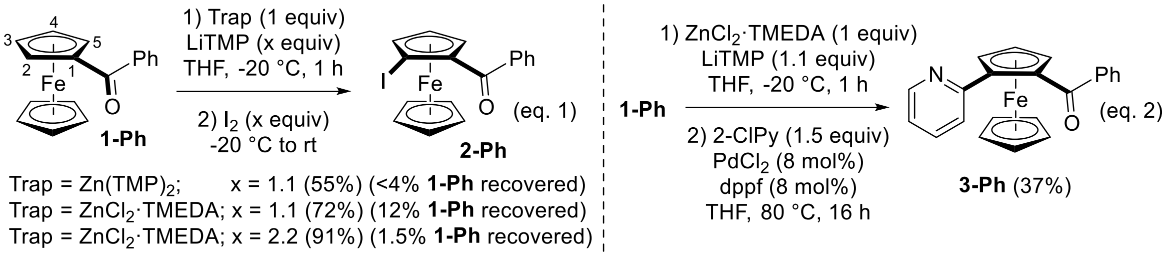

Scheme 1. Functionalization of benzoylferrocene (**1-Ph**) by deprotolithiation with in-situ trap, followed by either iodination or Negishi cross-coupling.

the amount of base was advantageously increased from 1.1 to 1.5 equiv, enabling the isolation of iodides **2-*o*OMePh**, **2-*m*OMePh**, and **2-*p*OMePh** in yields ranging from 82 to 94%. Functionalization of (methoxybenzoyl)ferrocenes at C-2 is therefore consistent with the calculated pK_a values of **1-*p*OMePh** after coordination to lithium (Figure 2c). In the case of (4-*tert*-butylbenzoyl)ferrocene (**1-*pt*BuPh**), derivative **2-*pt*BuPh** was produced in a high 94% yield using 2 equiv of base. Even for the (chlorobenzoyl)ferrocenes **1-*o*ClPh**, **1-*m*ClPh**, and **1-*p*ClPh**, the functionalization took place at the ferrocene site next to the carbonyl group, producing iodides **2-*o*ClPh**, **2-*m*ClPh**, and **2-*p*ClPh** in yields of 51–64%.

The results were different for the other (halo)benzoylferrocenes. In the (bromoaroyl)ferrocene series, all the derivatives obtained resulted from the functionalization next to the ketone function. However, the iodoferrocenes were formed less efficiently (**2-*o*BrPh** > **2-*m*BrPh** > **2-*p*BrPh**), and iodination of the aryl ring was even mainly observed in the case of **2-*p*BrPh** (**2′-*p*BrPh**, >50% yield; Scheme 3). This outcome could be rationalized by the combined effects of the ketone function, which promotes deprotolithiation at its neighboring sites, and bromine, which exerts a long-range acidifying effect [75]. This is consistent with the pK_a values calculated for **1-*p*BrPh·Li**, which are similar for positions C-2 and C-2′ (Figure 2b). A similar trend was noticed in the (trifluoromethyl)ferrocene series, which probably results from the acidifying properties of the trifluoromethyl group in the *ortho*, *meta*, and *para* positions [56,76] (Scheme 3). For **1-*p*CF$_3$Ph·Li**, the pK_a difference between positions C-2 and C-2′ is slightly greater than in the case of **1-*p*BrPh·Li** (Figure 2b), which could explain the predominance of **2-*p*CF$_3$Ph**, functionalized on the ferrocene side.

In contrast to bromine and trifluoromethyl, fluorine is known to be a short-range acidifying group [76,77]. As a consequence, when (2-fluorobenzoyl)ferrocene (**1-*o*FPh**) was treated under the same conditions, the expected product **2-*o*FPh** functionalized on the ferrocene ring (41% yield) was accompanied by (2-fluoro-3-iodobenzoyl)ferrocene (**2′-*o*FPh**, 6% yield) and 1-(2-fluoro-3-iodobenzoyl)-2-iodoferrocene (**2″-*o*FPh**, 18% yield), both due to competitive reactions next to the halogen (Scheme 4).

Coordination of (2-pyridoyl)- and (2-benzothienoyl)ferrocenes (**1-2Py** and **1-2BTh**) to lithium decreases their pK_a values at position C-3′ by several units, making these sites more prone to deprotometalation than those in position C-2 (Figure 2d). For ferrocene **1-2Py**, the calculated pK_a difference is about three units, while it reaches six units for ferrocene **1-2BTh**. As a result, in these two cases, the main products obtained are iodinated on the heterocycle with **2′-2Py** (26% yield) and above all **2′-2BTh** (>50% yield). Products monoiodinated on ferrocene were not observed, but the diiodides **2″-2Py** and **2″-2BTh**, probably resulting from double deprotometalation/trapping, were isolated in ∼10% yield (Scheme 5).

Cinnamoyl- and (phenylpropioloyl)ferrocenes (**1-CH=CHPh** and **1-C≡CPh**) were also involved in the reaction for the purpose of comparison with **1-Ph**. The expected products were obtained in both cases, but with lower yields than those observed with **1-Ph**. Compound **2-C≡CPh** was produced in a higher yield (48%) than **2-CH=CHPh** (only 25%), probably due to higher sensitivity of **1-CH=CHPh** (only 17% recovered) to nucleophilic attacks, leading to unidentified decomposition products (Scheme 6).

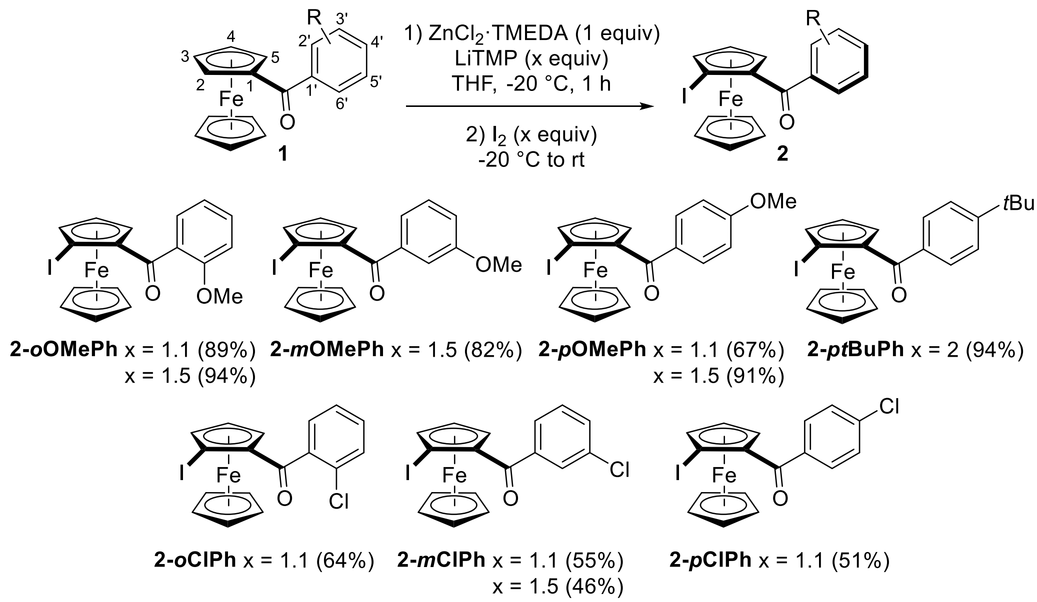

Scheme 2. Regioselective functionalization of aroylferrocenes at C-2 by deprotolithiation with in-situ trap, followed by iodination.

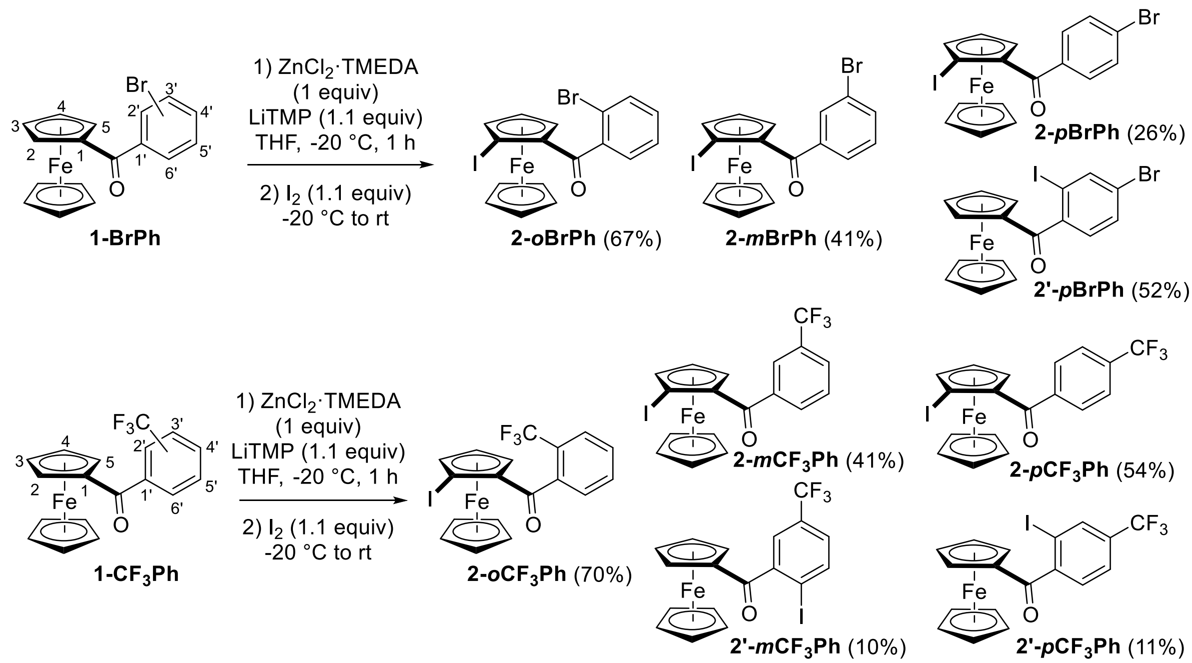

Scheme 3. Functionalization of (bromobenzoyl)- and [(trifluoromethyl)benzoyl]ferrocenes by deprotolithiation with in-situ trap, followed by iodination.

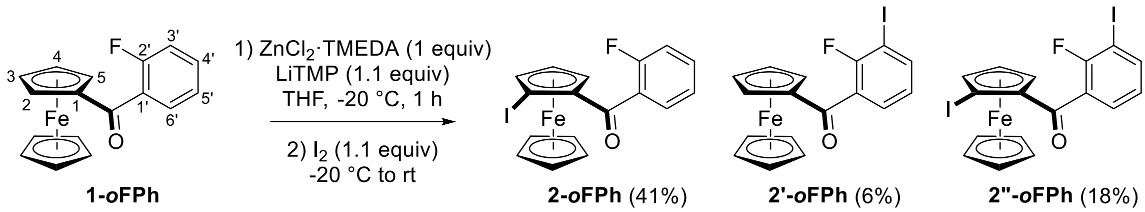

Scheme 4. Functionalization of (2-fluorobenzoyl)ferrocene by deprotolithiation with in-situ trap, followed by iodination.

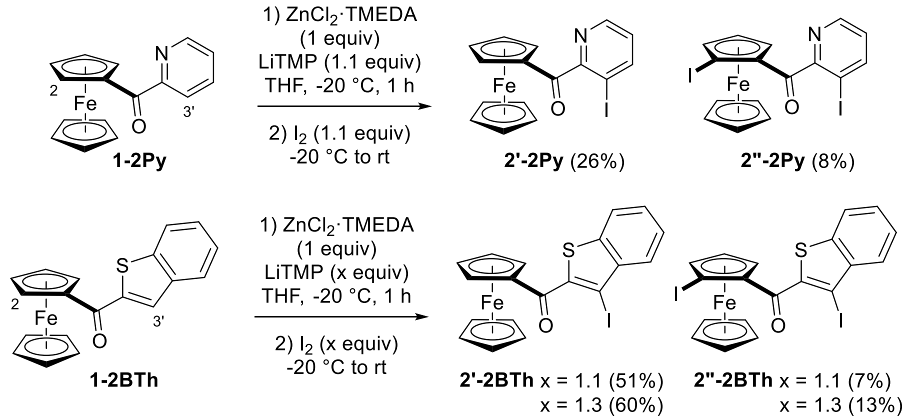

Scheme 5. Functionalization of (2-pyridoyl)- and (2-benzothienoyl)ferrocenes by deprotolithiation with in-situ trap, followed by iodination.

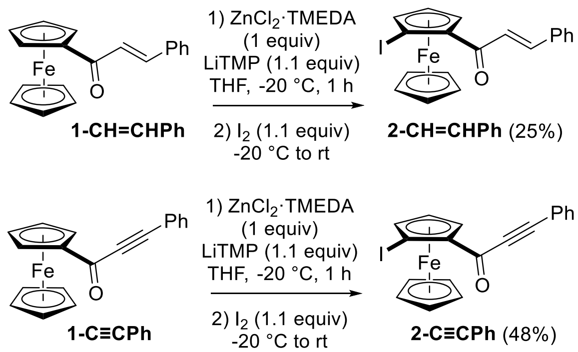

Scheme 6. Functionalization of cinnamoyl- and (phenylpropioloyl)ferrocenes by deprotolithiation with in-situ trap, followed by iodination.

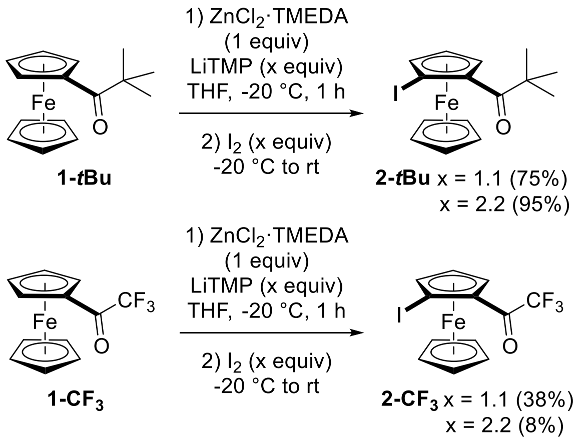

Scheme 7. Functionalization of [(trifluoromethyl) carbonyl]- and (*tert*-butylcarbonyl)ferrocenes by deprotolithiation with in-situ trap, followed by iodination.

Finally, we compared the reactivities of [(trifluoromethyl)carbonyl]ferrocene (**1-CF$_3$**) and (*tert*-butylcarbonyl)ferrocene (**1-*t*Bu**) under these conditions. As the question of regioselectivity does not arise, **1-*t*Bu** was treated with 1.1 or 2.2 equiv of LiTMP to provide, after subsequent trapping, the expected iodide **2-*t*Bu** in high yield (75–95%). However, while the use of 1.1 equiv of LiTMP on **1-CF$_3$** afforded **2-CF$_3$** (as an inseparable mixture with **1-CF$_3$**) in an estimated 38% yield, using an excess of base was detrimental to the reaction outcome (Scheme 7).

Ferrocene ketones being prochiral substrates, their enantioselective functionalization is expected to deliver enantio-enriched 1,2-disubstituted derivatives [78]. Enantioselective deprotolithiation of ferrocenes substituted by aminomethyl [79,80] and dimethylamino [81,82] groups, as well as hindered tertiary carboxamide [83–86] or even triflone [87], using alkyllithium-chiral ligand chelates (e.g., *n*-BuLi-sparteine), represents an important achievement in this field. However, as such chiral nucleophilic bases would be barely compatible with a sensitive ketone, we evaluated another approach involving a chiral, non-nucleophilic lithium dialkylamide {lithium di[(*S*)-1-phenylethyl]amide, (*S*)-PEALi} in the presence of an in-situ trap, as initially documented by Simpkins [88] and later extended to sensitive ferrocene carboxamides and esters [74,89,90]. Regarding the nature of the in-situ trap [91], we selected $ZnCl_2$·TMEDA as well as the putative zinc diamide $\{(S)\text{-PEA}\}_2Zn$, obtained in situ from (*S*)-PEALi and $ZnCl_2$·TMEDA in a 2:1 ratio, given their superiority in studies already carried out in the group [87,92].

To optimize the reaction, a solution of ketone **1-Ph** and $ZnCl_2$·TMEDA (1 equiv) in THF was treated with (*S*)-PEALi (2.2 equiv) at various temperatures (0, −20, −50, and −80 °C) before iodolysis (Scheme 8, Equation (1)). Whereas lower yields of **2-Ph** were recorded at −50 °C and even lower at −80 °C, the best enantioselectivities were observed at 0 or −20 °C but did not exceed 38% enantiomeric excess (*ee*) in favor of the R_P enantiomer, as revealed by the growing of crystals suitable for X-ray diffraction (XRD) analysis (Figure 3). No change in *ee* was noticed by using either (*R*)-PEALi instead of (*S*) or a shorter contact time. We next attempted the reaction using our alternative in-situ trap, $\{(S)\text{-PEA}\}_2Zn$, instead of $ZnCl_2$·TMEDA (Scheme 8, Equation (2)). The reactions were thus repeated at −20 and −80 °C, affording the major R_P enantiomer in a slightly improved 44% *ee* and yields of 60 and 35%, respectively, due to important recovery of **1-Ph** at the lowest temperature. In a last attempt to improve the enantioselectivity, THF was replaced by 2-methyltetrahydrofuran (2-MeTHF), which was found helpful in processes involving sensitive species in asymmetric transformations [93]. However, whether using $ZnCl_2$·TMEDA at −20 °C or $\{(S)\text{-PEA}\}_2Zn$ at −80 °C as an in-situ trap, significantly lower yields (from 69 to 40% and from 35 to 3%, respectively) and enantioselectivities (from 38 to 18% *ee* and from 44 to 4% *ee*, respectively) were recorded.

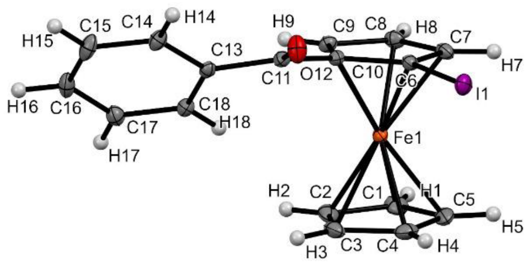

Figure 3. Molecular structure of compound ***R*P-2Ph** in the solid state. Thermal ellipsoids shown at the 30% probability level. Selected bond lengths (Å) and angles (°): C10–C11 = 1.475(3), C6–I1 = 2.082(2), C10–Cg2···Cg1–C3 = 2.74 (Cg1 being the centroid of the C1–C2–C3–C4–C5 ring and Cg2 the one of the C6–C7–C8–C9–C10 ring), Cg2–C6–I1 = 175.62, C6–C10–C11–O12 = 15.8(4), O12–C11–C13–C14 = 25.9(3).

Reactions using $ZnCl_2$·TMEDA as an in-situ trap, being considerably easier to implement, were performed at −20 °C to explore the behavior of a selection of ferrocene ketones in asymmetric deprotolithiation (Scheme 9). The yields recorded for these reactions using (*S*)-PEALi were generally lower than those obtained with the same amount of LiTMP, which can be explained in most cases by the lower reactivity of (*S*)-PEALi. Using these conditions, ketones **1-CH=CHPh** and **1-C≡CPh** only afforded mixtures of unidentified products. The ferrocenyl versus aryl deprotonation selectivities were the same, notably with the competitive formation of derivatives iodinated on the aryl group in the case of **1-*p*BrPh**, **1-*o*FPh**, **1-*m*CF$_3$Ph**, and **1-*p*CF$_3$Ph**. The enantioselectivities remained modest at best, ranging from 0% for the sterically hindered ketone **1-*o*CF$_3$Ph** to 60% for the trifluoromethylketone **1-CF$_3$**. Pleasingly, crystallization of **2-*o*BrPh** afforded an enantiopure product (see Supplementary material), and XRD analysis validated the expected R_P configuration.

Slightly disappointed by these results, we next turned our attention to a diastereoselective approach and prepared the enantiopure ferrocene ketone ***R*P-5** from [(*S*)-1-(dimethylamino)ethyl]ferrocene (Ugi's amine) [94,95] (Scheme 10). Further treatment of ***R*P-5** with LiTMP (2 equiv) in THF containing $ZnCl_2$·TMEDA (1 equiv) at −20 °C before iodolysis afforded the expected iodoferrocene ***R*P-6** as a single diastereoisomer, albeit in a low 20% yield due

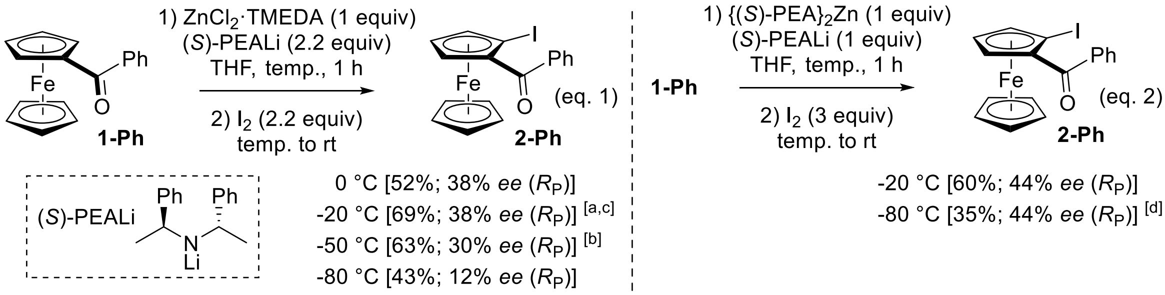

Scheme 8. Enantioselective functionalization of benzoylferrocene (**1-Ph**) by deprotolithiation using the lithium di(1-phenylethyl)amide (*S*)-PEALi with zinc-based in-situ traps. (a) 67% yield and 38% *ee* (S_P) using (*R*)-PEALi. (b) 62% yield and 30% *ee* (R_P) after 5 min time. (c) 40% yield and 18% *ee* (R_P) using 2-MeTHF. (d) 3% yield and 4% *ee* (R_P) using 2-MeTHF.

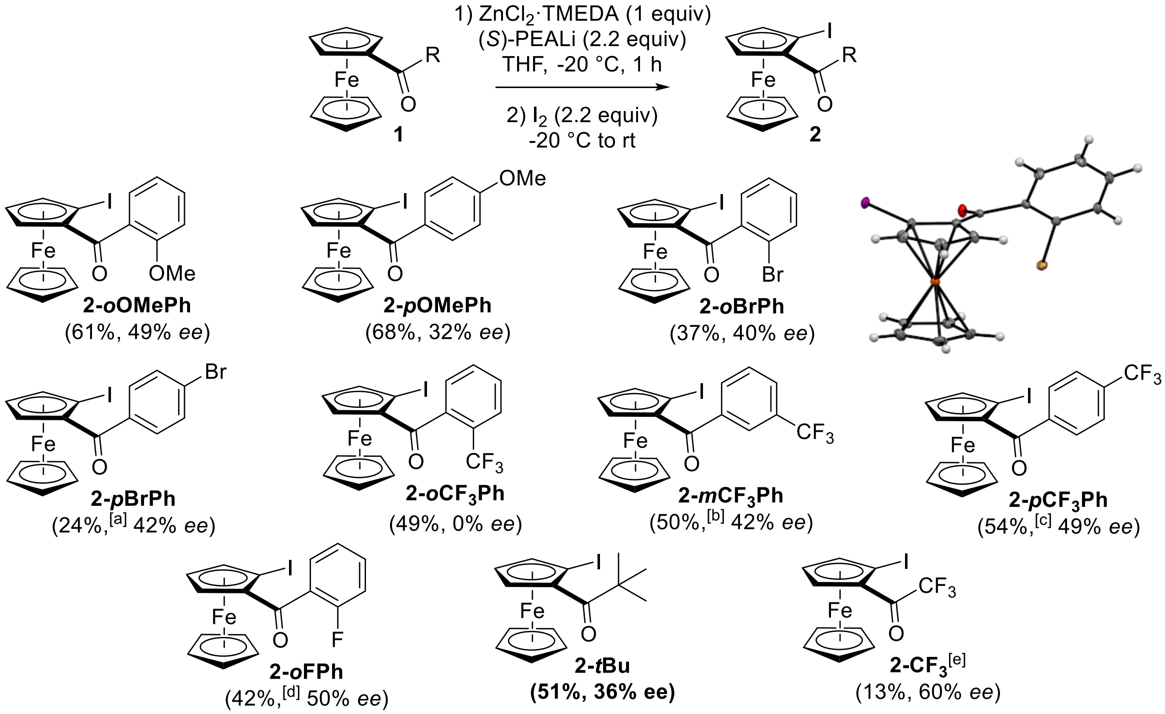

Scheme 9. Enantioselective functionalization of ferrocene ketones by deprotolithiation using the lithium di(1-phenylethyl)amide (*S*)-PEALi with $ZnCl_2$·TMEDA as an in-situ trap. (a) **2′-*p*BrPh** also obtained in 50% yield. (b) **2′-*m*CF$_3$Ph** also formed in 8% yield. (c) **2′-*p*CF$_3$Ph** also formed in 16% yield. (d) **2′-*o*FPh** (23% yield) and **2″-*o*FPh** (15% yield, 28% *ee*) also formed. (e) Reaction carried out by using (*S*)-PEALi (1.1 equiv) and I_2 (1.1 equiv).

to recovery of ***R*$_P$-5** (about 20%) and formation of unidentified byproducts (Scheme 10).

In 1991, Olah and co-workers reported the ring *tert*-butylation of benzophenones by successive action of *t*-BuLi in THF at very low temperature and $SOCl_2$ [96]. Inspired by these results, we similarly treated ***R*$_P$-5** with *t*-BuLi at −80 °C for 15 min before addition of I_2 to either intercept a deprotometalated species or oxidize a 1,6-adduct. Pleasingly, we were able to isolate the 1,6-addition/rearomatization product ***R*$_P$-7** in 61% yield (Scheme 11, Equation (1)). A similar result was recorded from benzoylferrocene (**1-Ph**), with **1-*pt*BuPh** obtained in 80% yield (Scheme 11, Equation (2)).

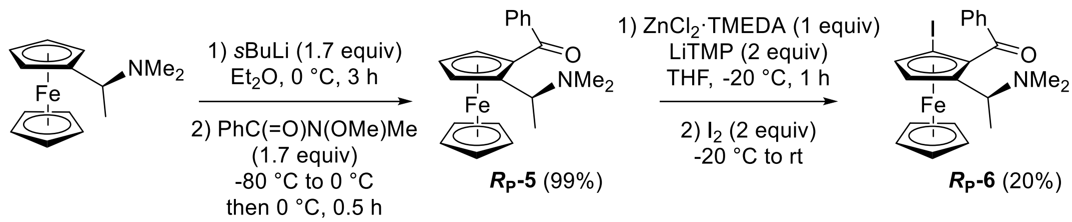

Scheme 10. Diastereoselective conversion of Ugi's amine to the ketone ***R*P-5** and further conversion to the enantiopure iodoketone ***R*P-6**.

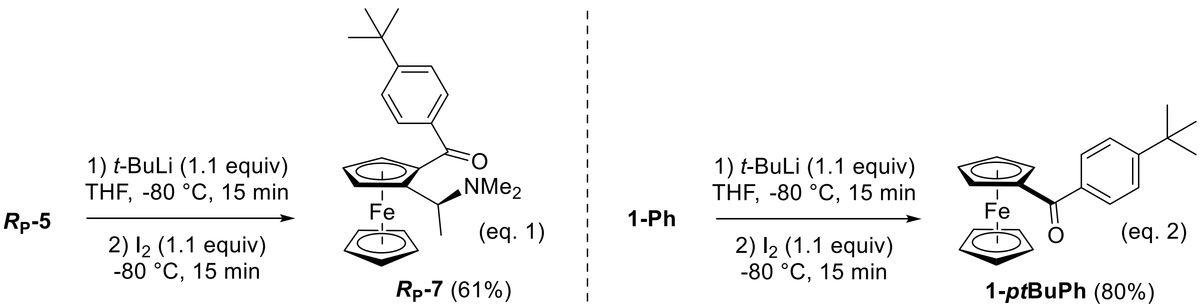

Scheme 11. Ring *tert*-butylation of ***R*P-5** and **1-Ph**.

In the course of their studies on the reactivity of organolithium compounds toward ketones, Yamataka and coworkers obtained both the products coming from the 1,2-addition (65%) and the 1,6-addition/rearomatization (28%) by reacting benzophenone with *t*-BuLi in Et_2O at 0 °C [97]. The use of various *tert*-butylzinc species in order to achieve *para*-selective *tert*-butylation of benzophenone [98–100] and other (hetero)aromatic ketones [101] has also been extensively studied. In our case, the major 1,6-addition observed by simply using *t*-BuLi could be explained by the lower electrophilicity of the ketone and the higher steric hindrance generated by the ferrocene core when compared with benzophenone.

Whether using *t*-BuLi [97] or *tert*-butylzinc species [102], all the studies of this reaction have pointed out a single electron transfer mechanism from the alkylmetal to the ketone. Applied to **1-Ph**, the formation of **1-*pt*BuPh** could unfold as depicted in Scheme 12.

2.3. *Post-functionalization toward polycyclic compounds*

Some of our iodinated ferrocene ketones were next engaged in metal-promoted transformations, and post-functionalization by Suzuki–Miyaura cross-coupling [103,104] was first considered from **2-Ph**. The reactions were carried out with 4-methoxyphenyl- and 3-thienylboronic acid, under conditions previously tested [105,106] (2 equiv CsF [107], 5 mol% $Pd(dba)_2$ (dba = dibenzylideneacetone) and 20 mol% SPhos (2-(dicyclohexylphosphino)-2′,6′-dimethoxybiphenyl) [108] in refluxing toluene), to afford the derivatives **8a** and **8b** (Scheme 13, Equation (1) and (2)). A Sonogashira cross-coupling [109] was next attempted with (trimethylsilyl)acetylene, under conditions previously reported [40,110] [4 mol% $Pd(PtBu_3)_2$ and 4 mol% CuI in THF-iPr_2NH at rt]. Although the expected product **9** was obtained in a low 21% yield due to 55% recovery of **2-Ph** (Scheme 13, Equation (3)), it could be a promising substrate for accessing biologically active ferrocene derivatives such as prostaglandin analogues [111].

In the last decade, ferrocenes fused with heterocycles such as pyridine [112], 4-pyridone [112], and 4-piperidinone [113] have appeared as privileged structures for different applications [114]. With the aim of preparing a sulfur-containing related compound and inspired by similar reaction in the benzene series [115], we reacted

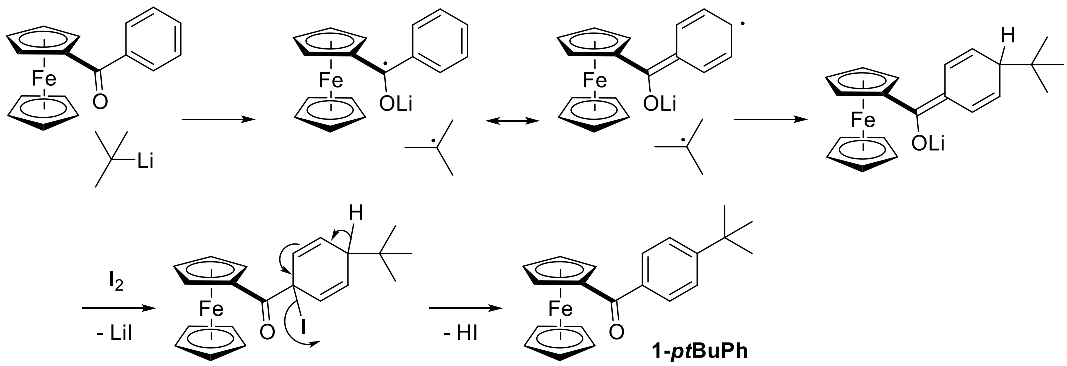

Scheme 12. Proposed mechanism for the *tert*-butylation of **1-Ph**.

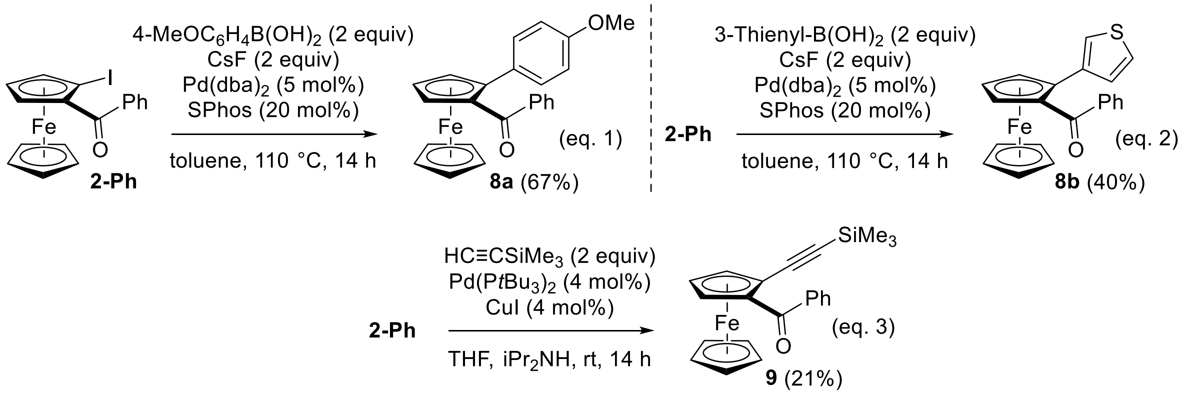

Scheme 13. Suzuki–Miyaura and Sonogashira cross-coupling reactions from **2-Ph**.

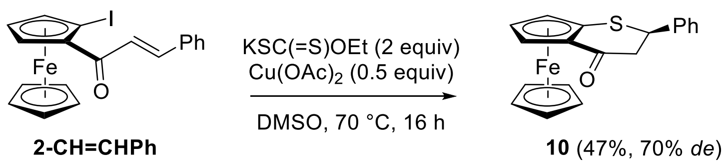

Scheme 14. Conversion of **2-CH=CHPh** to the 2,3-dihydrothiopyrano[2,3]ferrocen-4-one **10**.

(*E*)-1-cinnamoyl-2-iodoferrocene (**2-CH=CHPh**) with potassium ethyl thioxanthate in the presence of $Cu(OAc)_2$ in dimethylsulfoxide (DMSO) at 70 °C. Pleasingly, we were able to isolate the expected 2,3-dihydrothiopyrano[2,3]ferrocen-4-one **10** in 47% yield and 70% *de* (Scheme 14).

Ferrocene-fused quinoline derivatives are also documented, and notably ferroceno[*c*]quinolines, which can be synthesized from 2-iodoferrocene carboxaldehyde [116]. As starting from a ketone would provide a substituent in position C-6 of this building block, we were keen to prepare such derivatives from the iodinated ketone **2-*p*CF$_3$Ph**. Inspired by previous results, it was treated with 4 equiv of 2-aminophenylboronic acid, 5 mol% $Pd(dba)_2$, 20 mol% PPh_3, and 2 equiv of CsF [107], to which 2 equiv of Cs_2CO_3 were added for subsequent cyclization in refluxing dioxane. This afforded the original compound **11** in high yield (Scheme 15).

Condensed systems in which the cyclopentadienyl ring of the ferrocene is annulated with a (hetero)aromatic moiety have seen renewed interest with

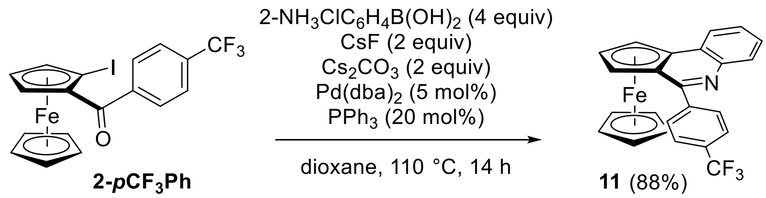

Scheme 15. Suzuki–Miyaura cross-coupling from **2-*p*CF$_3$Ph** and subsequent cyclization into ferroceno[*c*]quinoline.

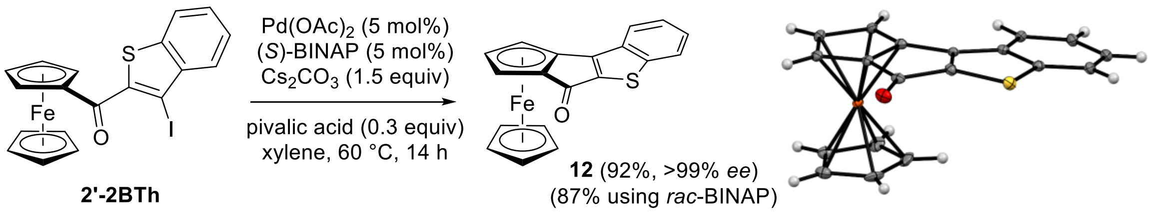

Scheme 16. Conversion of **2′-2BTh** to the polycyclic compound **12** by CH-functionalization.

the advent of palladium-catalyzed enantioselective C–H bond activation [114]. Inspired by the synthesis of ferrocene analogues of fluorenone documented by You and coworkers [117], we finally attempted the synthesis of the original thiophene-containing derivative **12** from the iodinated compound **2′-2BTh**. To this purpose, our substrate was treated with 5 mol% Pd(OAc)$_2$, 5 mol% (*S*)-BINAP [BINAP = 2,2′-bis(diphenylphosphino)-1,1′-binaphthyl], 1.5 equiv of Cs$_2$CO$_3$, and 0.3 equiv of pivalic acid in xylene at 60 °C. Pleasingly, the expected tetracyclic compound **13** was isolated in 92% yield and >99% *ee*, the R_P absolute configuration being confirmed by XRD analysis (Scheme 16).

2.4. *Electrochemical characterization of selected compounds*

Although ferrocene ketones have been known since the early days of ferrocene history [41], and indeed helped Woodward and his team to coined the name ferrocene [118,119], they have been scarcely studied from an electrochemical point of view. Kutal et al. reported an in-depth study of the link between the spectroscopic properties and their electronic structure [120], while Gao et al. reported third-order non-linear optical properties of some benzoylferrocenes, supported by DFT calculations [121]. However, electrochemical analyses were not included in these studies. The redox potential of a few ferrocene ketones has been reported from time to time [122–124], most of the work on benzoylferrocenes coming from the work of Kleinberg et al. [125]. We were therefore interested in investigating the electrochemical properties of some ferrocene ketones prepared during this work, initially focusing our attention on the ketone reduction. Cyclic voltammetry (CV) and differential pulse voltammetry (DPV) were therefore realized in dry, oxygen-free, dimethylformamide, using *n*-Bu$_4$NPF$_6$ (0.1 M) as the supporting electrolyte with a glassy carbon disk as working electrode, an Ag/AgCl reference electrode, and a glassy carbon rod as counter electrode (Table 1).

From benzophenone to **1-Ph**, **1-*p*OMePh**, and **1-*t*Bu**, the monoelectronic reduction of the ketone, forming the radical anion species, was found reversible and increasingly difficult to achieve, in agreement with the increased electron-donating properties of the group attached to the ketone. Regarding the effect of electron-withdrawing groups, reduction is easier from the 2-pyridyl derivative **1-2Py** than from the compounds **1-*p*CF$_3$Ph** and **1-Ph**, as one can have expected regarding the electronic properties of these aromatics. We also attempted to push the reduction of **1-*p*CF$_3$Ph** forward to form the corresponding dianion species. However, although we did observe a second reduction in DPV (see Supplementary material), it did not appear to be the expected formation of the dianion species, but rather the reduction of the trifluoromethyl group,

Table 1. Electrochemical data (in V) for the monoelectronic reduction of selected ferrocene ketones

Compound	E_{pc} [a]	E_{pa} [a]	i_{pc}/i_{pa} [a]	$E_{1/2}$ [b]
Benzophenone	−1.74	−1.64	1.00	−1.68
1-Ph	−1.88	−1.79	0.99	−1.84
1-*p*OMePh	−2.00	−1.87	1.36	−1.95
1-*p*CF$_3$Ph	−1.67	−1.51	nd[(c)]	−1.75
1-2Py	−1.68	−1.60	1.43	−1.64
1-*t*Bu	−2.29	−2.15	1.20	−2.23
2-Ph	−1.70	nd[(d)]	nd[(d)]	−1.68
12	−1.36	−1.26	0.92	−1.30

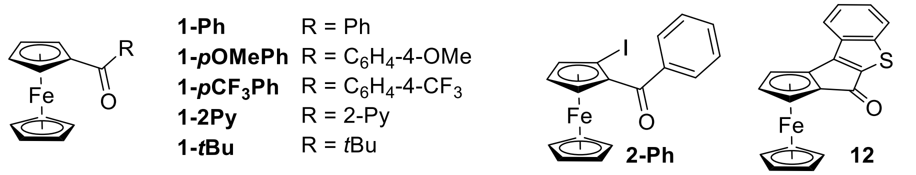

Potential values given relative to Ag/AgCl, scan rate = 100 mV·s^{-1}. [a]From CV experiments. [b]From DPV experiments. [c]A complex reduction process was observed. [d]An irreversible dielectronic reduction process was observed.

as reported by Perichon et al. and Savéant et al. [126,127]. Due to the inductive effect of iodine, **2-Ph** was more easily reduced than benzoylferrocene (**1-Ph**) by 0.16 V. However, the first dielectronic irreversible process was immediately followed by a second reduction at −1.84 V versus FcH/FcH$^+$, corresponding to that of **1-Ph**. We suggest that the initial formation of the radical anion of **2-Ph** was followed by the cleavage of the carbon–iodine bond toward the neutral radical **1-Ph$^\bullet$**, which was more easily reduced than the parent compound **2-Ph** (Scheme 17). The resulting anion **1-Ph$^-$** would then be protonated in situ to generate **1-Ph**, which exhibited the expected monoelectronic reduction at −1.84 V. The fused tetracycle **12** was found to undergo an easy and reversible monoelectronic reduction first, followed by two irreversible reduction peaks, which might be attributed to the reduction of the radical anion to the corresponding dianion and to the reduction of the benzothiophene core [128].

We next investigated the oxidation of the organometallic core for the same compounds but working in dichloromethane this time, in line with our previous studies [92,129] (Table 2). The redox potential of **1-Ph** was measured first, and the 0.25 V value versus FcH/FcH$^+$ was found in good agreement with the results of Herberhold and Jahn, although their measurements were done in acetonitrile instead of dichloromethane [123,124]. As expected, the redox potential of **1-Ph** falls between the ones of **1-*p*OMePh** and **1-*p*CF$_3$Ph** due to their respective electron-donating and electron-withdrawing groups attached to the phenyl ring. The thioketone **4-Ph** was more easily oxidized than the parent ketone ($E_{1/2}$ 0.22 versus 0.25 V), probably due to the stronger electron-withdrawing properties of the former [130]. Surprisingly, the redox potential of the pyridyl derivative (**1-2Py**) was 50 mV lower than that of benzoylferrocene (**1-Ph**). Indeed, due to the more pronounced electron-withdrawing properties of the pyridine ring, the reverse order was expected. However, electronic repulsion between the lone pairs of the ketone and the pyridine's nitrogen might promote a conformation similar to the one observed for **2-2Py** (see below), avoiding the full transmission of the pyridine's electronic effect to the ferrocene core. The ferroceno[*c*]quinolines **11** was found easier to oxidize than any of the ferrocene ketones studied, probably due to the planar structure of the tricyclic core and to the presence of an imine instead of a ketone. In the ferrocene series, it is usually possible to link the $E_{1/2}$ value of monosubstituted derivatives with the Hammett's parameter α_p [122,131,132] and the $E_{1/2}$ of polysub-

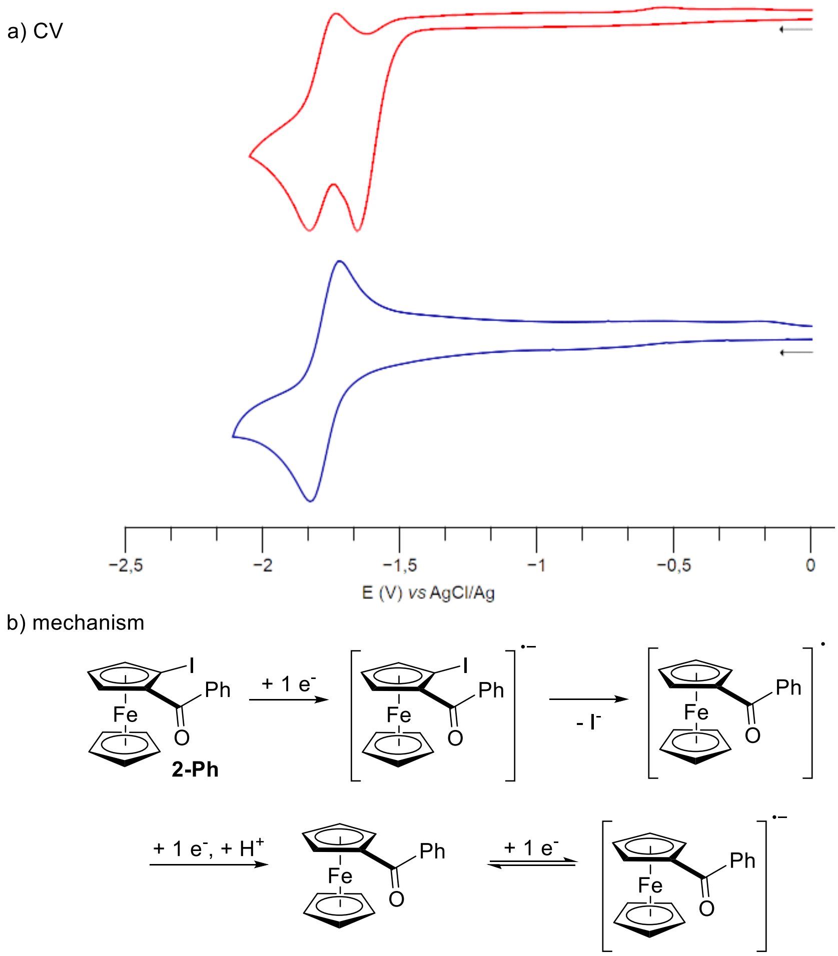

Scheme 17. (a) Cyclic voltammetry of compounds **2-Ph** (red) and **1-Ph** (blue). (b) Putative mechanism for the electrochemical conversion of **2-Ph** into **1-Ph**.

stituted compounds with the sum of α_p or $\alpha_p + \alpha_m$, depending on the substation pattern [133–135]. Unfortunately, only a limited number of Hammett's parameters is known for ketones [130]. However, it was still possible to find a correlation between the recorded $E_{1/2}$ values and the sum of α_p parameters for compounds **1-*t*Bu**, **1-Ph**, **2-Ph**, and **1-CF$_3$** with the equation $E_{1/2} = 1.8466\ \Sigma\alpha_p - 0.026$ ($R^2 = 0.9857$) (see Supplemtary material).

2.5. *Solid-state structures and weak interactions of some ferrocenyl ketones*

In the frame of this work, many ferrocene ketone derivatives were found to produce crystals suitable for XRD analysis, some of them deserving additional comments. Regarding unsubstituted ferrocene ketones, an eclipsed conformation of the ferrocene core was identified in most cases and the substitution pattern of the phenyl ring was found to have an impact on the solid-state structure. For *para-* and *meta*-substituted aromatics, the C=O bond was found tilted above the substituted cyclopentadienyl (Cp) ring while the phenyl ring was slightly inclined compared to the C=O bond. However, for *ortho*-substituted aromatics, the carbonyl was found aligned with the Cp ring while the aromatic was much more tilted, probably to reduce the steric clash between the carbonyl group and the *ortho* substituent. The case of the three trifluoromethylated derivatives is especially representative of this general trend (Figure 4).

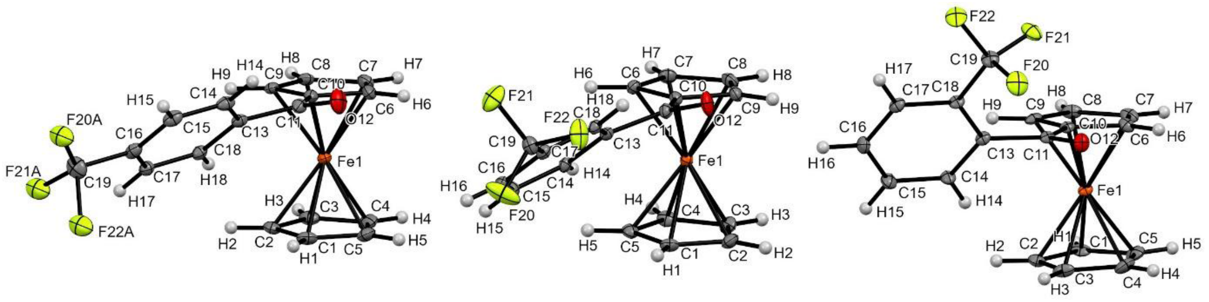

Figure 4. Molecular structure of compounds **1-*p*CF$_3$Ph** (left), **1-*m*CF$_3$Ph** (middle), and **1-*o*CF$_3$Ph** (right) in the solid state. Thermal ellipsoids shown at the 30% probability level. Selected bond lengths (Å) and angles (°) for **1-*p*CF$_3$Ph**: C10–C11 = 1.469(4), C10–Cg2···Cg1–C1 = 4.71 (Cg1 being the centroid of the C1–C2–C3–C4–C5 ring and Cg2 the one of the C6–C7–C8–C9–C10 ring), C6–C10–C11–O12 = 12.9(4), O12–C11–C13–C14 = 27.7(4); for **1-*m*CF$_3$Ph**: C10–C11 = 1.469(3), C10–Cg2···Cg1–C1 = 3.19, C9–C10–C11–O12 = 18.0(3), O12–C11–C13–C18 = 20.2(3); for **1-*o*CF$_3$Ph**: C10–C11 = 1.471(8), C10–Cg2···Cg1–C3 = 7.58, C6–C10–C11–O12 = 2.5(8), O12–C11–C13–C18 = 53.0(7).

Table 2. Electrochemical data (in V) for the oxidation of selected ferrocene ketones

Compound	E_{pa} [a]	E_{pc} [a]	i_{pa}/i_{pc} [a]	$E_{1/2}$ [b]
1-Ph	0.30	0.20	0.88	0.25
1-*p*OMePh	0.27	0.17	0.84	0.21
1-*p*CF$_3$Ph	0.34	0.24	0.75	0.29
1-2Py	0.26	0.17	0.89	0.20
1-*t*Bu	0.25	0.16	0.90	0.22
1-CF$_3$	0.50	0.40	0.81	0.44
4-Ph	0.29	nd[(c)]	nd[(c)]	0.22
2-Ph	0.38	0.29	0.84	0.33
10	0.30	0.20	0.89	0.25
11	0.24	0.14	0.97	0.17
12	0.37	0.28	0.86	0.33

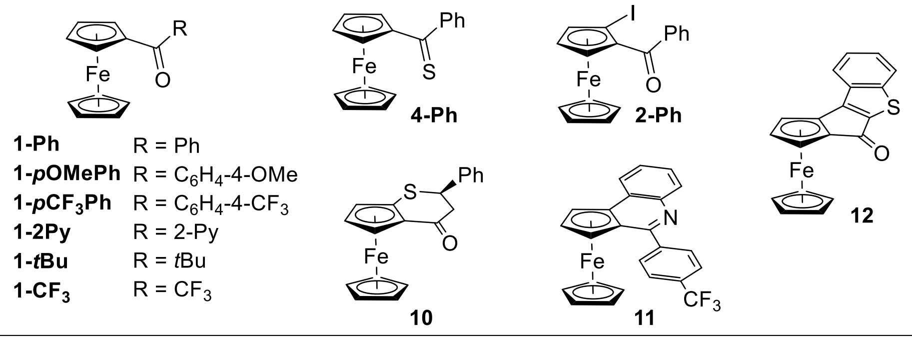

Potential values given relative to FcH/FcH$^+$, scan rate = 100 mV·s^{-1}. [a]From CV experiments. [b]From DPV experiments. [c]Irreversible oxidation was observed.

The iodinated derivative **2′-2Py** further features an intermolecular halogen–oxygen bond resulting from the interaction between the region of positive electrostatic potential (σ-hole) of iodine, acting as the donor, and a lone pair of the oxygen of the ketone, acting as the acceptor [136]. While such interactions

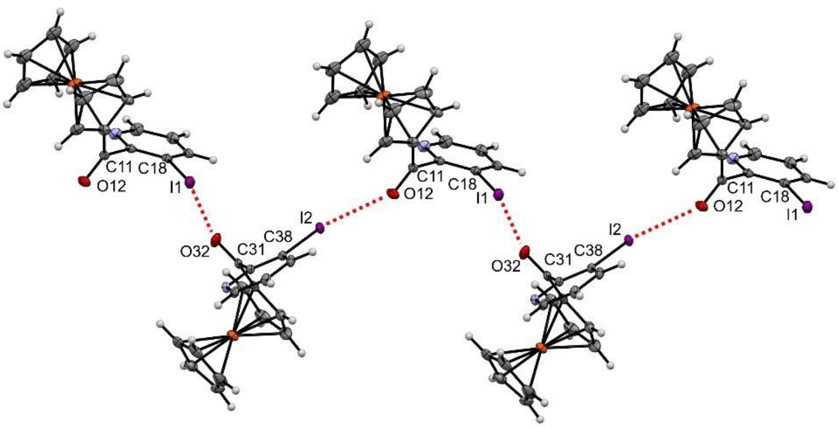

Figure 5. Halogen–oxygen bond observed in the solid state for compound **2′-2Py**. Thermal ellipsoids shown at the 30% probability level. Selected bond lengths (Å) and angles (°) O12···I2 = 3.051, O32···I1 = 3.061, C11–O12···I2 147.99, C31–O32···I1 146.03, O12···I2–C38 156.03, O32···I1–C18 160.76.

are not usually observed with bare iodopyridines, they are more common from iodopyridinium derivatives in which the electron-withdrawing pyridinium ring increases the electrostatic potential of the iodine and thus the strength of the interaction [137,138]. In **2′-2Py**, the ketone adjacent to the iodine atom is expected to have a similar effect, leading to a zigzag halogen-bond network connecting all the molecules in the solid state (Figure 5).

As expected, the introduction of the iodine next to the ketone induced some structural changes in the solid state, as observed between **1-*p*CF$_3$Ph** and **2-*p*CF$_3$Ph** (Figure 6). Indeed, to accommodate the iodine atom, which was inclined by 4.9° above the Cp ring, the C=O bond was forced to move from its tilted position to be aligned with the Cp ring. A large change in the orientation of the phenyl ring was also observed between the two structures.

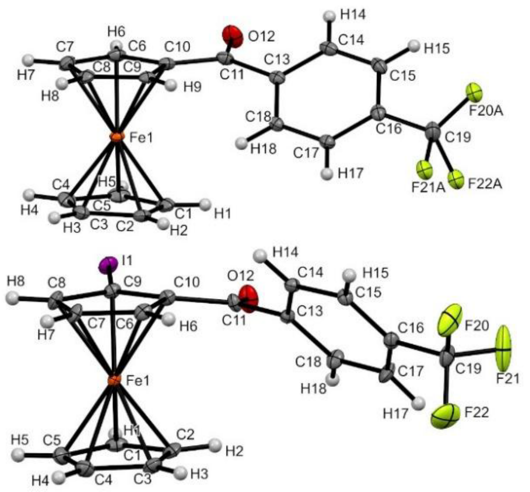

Figure 6. Molecular structure of compounds **1-*p*CF$_3$Ph** (top) and **2-*p*CF$_3$Ph** (bottom) in the solid state. Thermal ellipsoids shown at the 30% probability level. Selected bond lengths (Å) and angles (°) for **2-*p*CF$_3$Ph**: C10–C11 = 1.49(1), C9–I1 = 2.082(7), C10–Cg2···Cg1–C2 = 3.35 (Cg1 being the centroid of the C1–C2–C3–C4–C5 ring and Cg2 the one of the C6–C7–C8–C9–C10 ring), Cg2–C9–I1 = 175.11, C9–C10–C11–O12 = −3(1), O12–C11–C13–C14 = −138.0(8).

The substitution pattern of the phenyl ring was also found to influence the solid-state structures of the iodoferrocene ketones. Indeed, except for derivative **2-*p*CF$_3$Ph**, the C=O bond was found tilted from the Cp ring but aligned with the phenyl ring for all the *para*-substituted derivatives, while the contrary was identified for all the *ortho*-substituted derivatives, probably for steric encumbrance reasons. The **2-*p*OMePh** and **2-*o*OMePh** structures depicted in Figure 7 nicely illustrate this trend. The opposite behavior of **2-*p*CF$_3$Ph** might be rationalized in terms of substituent effects. Indeed, due to its strong electron-withdrawing inductive effect, the trifluoromethyl group might favor the resonance between the Cp ring of the organometallic and the C=O bond, which therefore need to be aligned. For the other *para*-substituted aryl derivatives studied, all substituents have a positive mesomeric effect which might override the donating effect of the ferrocene

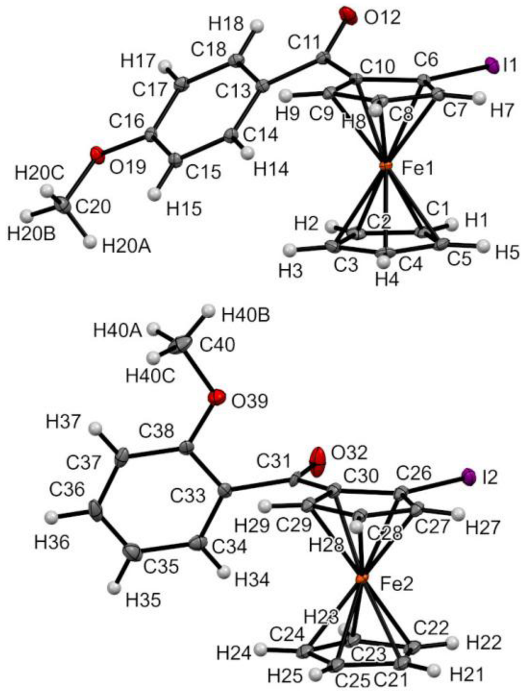

Figure 7. Molecular structure of compounds **2-*p*OMePh** (top) and **2-*o*OMePh** (bottom) in the solid state. Thermal ellipsoids shown at the 30% probability level. Selected bond lengths (Å) and angles (°) for **2-*p*OMePh**: C10–C11 = 1.490(3), C6–I1 = 2.089(2), C10–Cg2···Cg1–C2 = 3.12 (Cg1 being the centroid of the C1–C2–C3–C4–C5 ring and Cg2 the one of the C6–C7–C8–C9–C10 ring), Cg2–C6–I1 = 178.23, C6–C10–C11–O12 = −33.5(3), O12–C11–C13–C18 = −1.1(3); for **2-*p*OMePh**: C30–C31 = 1.492(7), C26–I2 = 2.096(4), C30–Cg4···Cg3–C23 = 22.47 (Cg3 being the centroid of the C21–C22–C23–C24–C25 ring and Cg4 the one of the C26–C27–C28–C29–C30 ring), Cg4–C26–I2 = 176.92, C26–C30–C31–O32 = −10.1(8), O32–C31–C33–C38 = −105.7(7).

core, explaining why the C=O bond is therefore aligned with the phenyl ring.

From racemic **2-*o*ClPh**, preferential crystallization of the enantiopure S_P enantiomer was pleasingly observed [139], allowing us to identify the formation of a halogen–oxygen bond in the solid state (Figure 8). Due to the electron-richness of the organometallic core, iodoferrocenes are usually not able to develop such interactions. However, the presence of electron-withdrawing substituents can substantially increase the positive electrostatic potential of iodine's σ-hole. As a result, halogen bond networks have been recently identified for various iodoferrocenes substituted with sulfonamides [140], sulfonates [92], sulfoxides [141], sulfonyl fluoride [134], and triflones [87]. Similar bonds were also observed for ferrocene iodoalkyne derivatives [142]. In the case of ***S*$_\mathbf{P}$-2-*o*ClPh**, having the iodine and the ketone groups in a same plane and pointing in the same direction led to a zigzag chain of halogen–oxygen bonds with bonds lengths and angles being in the range of classical values [136].

We were pleased to identify the two types of halogen–halogen interactions in three of our iodoferrocene ketones [143,144]. In the solid state, both enantiomers of **2-*p*ClPh** were identified in the crystal structure, with the R_P enantiomer interacting with the S_P enantiomer via a type II iodine–iodine interaction, characterized by two different C–I···I angle values (Figure 9a). However, while the two enantiomers of **2″-2BTh** crystallized together in a similar manner, a type I iodine–iodine interaction with similar C–I···I angles was observed between the iodine atoms attached to the benzothiophene moiety and not between those linked to the ferrocene core (Figure 9b).

From racemic **2-*o*BrPh**, spontaneous resolution was observed and the two enantiomers were separately isolated as conglomerates. As expected, single molecules of each enantiomer were almost similar in the solid state, both crystallizing in the same tetragonal system, although in different space groups. However, the most interesting characteristics were observed having a closer look at intermolecular halogen–halogen bonds for each enantiomer. Indeed, the bromine of one molecule was found to develop a type I interaction with the iodine atom of another molecule, leading to the helix arrangement of all molecules. While ferrocene derivatives have previously been involved in the formation of such structures [145–148], the involvement of halogen–halogen interactions to structure the arrangement is pretty unusual. The planar chirality of the ferrocene core was further found to influence the axial chirality of the helix, the R_P enantiomer giving rise to a *M* helix (Figure 10a), while a *P* helix was observed for the S_P enantiomer (Figure 10b).

It was finally possible to grow crystals of the enantiopure tetracycle **12** suitable for XRD analysis (Figure 11). Not only the solid-state structure validated the expected R_P configuration of the compound but it also allowed the identification of chalcogen–chalcogen interactions [149,150]. Indeed, a sulfur···sulfur interaction between two

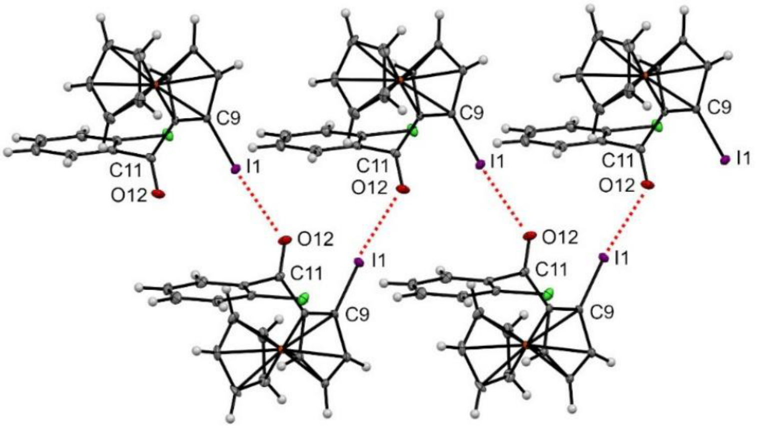

Figure 8. Halogen–oxygen bonds observed in the solid state for compound ***S*P-2-*o*ClPh**. Thermal ellipsoids shown at the 30% probability level. Selected bond lengths (Å) and angles (°) O12···I1 = 2.999, C11–O12···I1 139.63, O12···I1–C9 173.64.

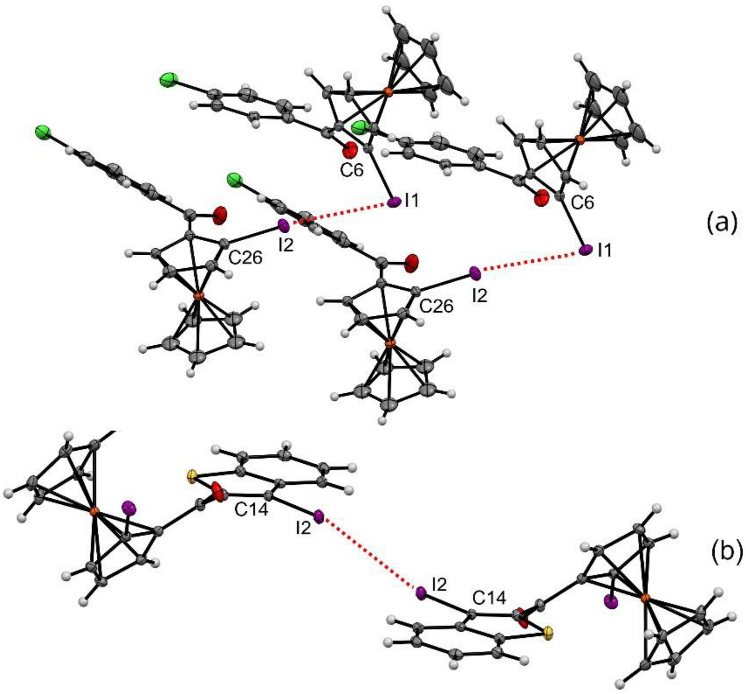

Figure 9. Iodine–iodine interaction network observed in the solid state for compounds **2-*p*ClPh** (top) and **2′′-2BTh** (bottom). Thermal ellipsoids shown at the 30% probability level. Selected bond lengths (Å) and angles (°) for **2-*p*ClPh**: I1···I2 = 3.882, I1···I2–C26 173.07, C6–I1···I2 73.43; for **2-*p*ClPh**: I2···I2 = 3.772, I2···I2–C14 137.38, C14–I2···I2 137.38.

molecules was likely to happen due to the S1···S2 distance below the van der Waals radii (3.54 versus 3.60 Å) [151], although the various C–S···S angles are shorter than expected, probably due to the rigid fused-thiophene unit. The tetracyclic systems of the two molecules composing the dimer were found perpendicular and, although this arrangement is not usual, it was previously identified in other benzothiophene derivatives [152].

3. Conclusion

Here we have presented the first in-depth study of the deprotolithiation of ferrocene ketones using a

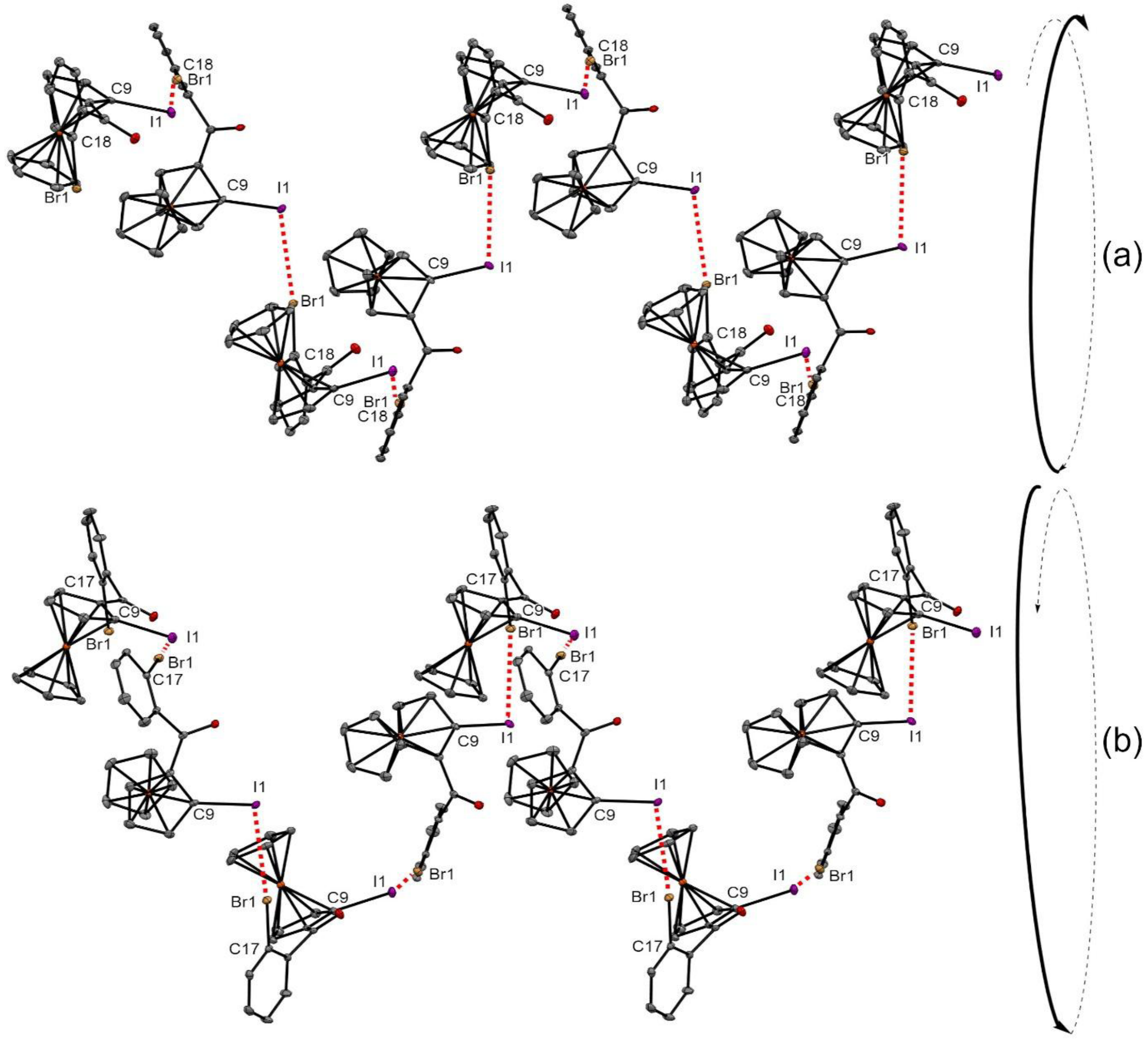

Figure 10. Iodine–bromine bond network observed in the solid state for compounds ***R*P-2-*o*BrPh** (a) and ***S*P-2-*o*BrPh** (b) and sense of the helix formed. Thermal ellipsoids shown at the 30% probability level; hydrogen atoms omitted for clarity. Selected bond lengths (Å) and angles (°) for ***R*P-2-*o*BrPh**: Br1···I1 = 3.594, C18–Br1···I1 171.16, C9–I1···Br1 98.79; for ***S*P-2-*o*BrPh**: Br1···I1 = 3.599, C17–Br1···I1 170.96, C9–I1···Br1 99.35.

bulky, non-nucleophilic lithium amide, as well as an in-situ trap to prevent nucleophilic attack of the function by the ferrocenyllithium formed. The expected iodoferrocene derivatives were obtained in most cases although the presence of electron-acceptor substituents on the aryl moiety was found to reroute the functionalization on this cycle, in agreement with our DFT calculations (pK_a values after coordination to lithium).

The development of an enantioselective version of the reaction was next attempted using a chiral lithium amide. Although our best *ee* did not exceed 60%, the feasibility of this approach was demonstrated. Finally, we took advantage of the installation of the iodine on the (hetero)aryl ring to reach original ferrocene-fused heterocycles, including a tetracycle obtained by enantioselective C–H functionalization.

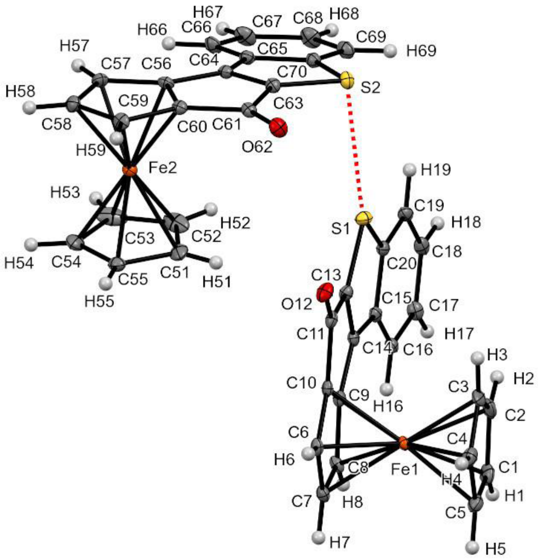

Figure 11. Chalcogen–chalcogen bond observed in the solid state for compound ***R*P-12**. Thermal ellipsoids shown at the 30% probability level. Selected bond lengths (Å) and angles (°): S1···S2 = 3.547, C13–S1···S2 124.90, C20–S1···S2 144.94, C63–S2···S1 105.11, C70–S2···S1 76.54, angle plane (C9–C8–C7–C6–C10–C11–C13–S1–C20–C19–C18–C17–C16–C15–C14)-(C56–C57–C58–C59–C60–C61–C63–S2–C70–C69–C68–C67–C66–C65–C64) 89.24.

Given the significant potential of both ferrocene ketones [65] and ferrocene-fused heterocycles [153], the current study is expected to pave the way for future work toward such compounds to promote their application in various fields.

Acknowledgments

We acknowledge BASF (generous gift of di[(*S*)-1-phenylethyl]amine and di[(*R*)-1-phenylethyl]amine) and Thermofisher (generous gift of 2,2,6,6-tetramethylpiperidine). We acknowledge Olivier Perez, Carmelo Prestipino and Jean-François Lohier (CRISMAT, UMR CNRS 6508) and well as Magali Allain (Moltech-Anjou, UMR CNRS 6200) for their help in X-ray data collection.

Declaration of interests

The authors do not work for, advise, own shares in, or receive funds from any organization that could benefit from this article, and have declared no affiliations other than their research organizations.

Funding

This work was supported by the Direction Générale de la Recherche Scientifique et du Développement Technologique (MH), Rennes Métropole (WE), the University of Carthage and the Tunisian Ministry of Higher Education and Scientific Research (SB), the Fonds Européen de Développement Régional (FEDER; D8 VENTURE Bruker AXS diffractometer), the Université de Rennes and the Centre National de la Recherche Scientifique (WE, J-PH, MB, TR, FM).

Supplementary materials

Supporting information for this article is available on the journal's website under https://doi.org/10.5802/crchim.429 or from the author.

The CCDC files 2490197 (**1-*o*OMePh**), 2490198 (**1-*p*ClPh**), 2490199 (**1-*m*BrPh**), 2490200 (**1-*o*CF$_3$Ph**), 2490201 (**1-*m*CF$_3$Ph**), 2490202 (**1-*p*CF$_3$Ph**), 2490203 (**1-*o*FPh**), 2490204 (**1-2BTh**), 2490205 (**1-C≡CPh**), 2490206 [***R*P-2-Ph**], 2490207 (**2-*o*OMePh**), 2490208 (**2-*p*OMePh**), 2490209 (**2-*o*ClPh**), 2490210 (**2-*p*ClPh**), 2490211 [***R*P-2-*o*BrPh**], 2490212 [***S*P-2-*o*BrPh**], 2490213 (**2-*p*BrPh**), 2490214 (**2-*p*CF$_3$Ph**), 2490215 (**2′-2Py**), 2490216 (**2′-2BTh**), 2490217 (**2″-2BTh**) and 2490218 (**12**) contain the supplementary crystallographic data. These data can be obtained free of charge from the Cambridge Crystallographic Data Center via www.ccdc.cam.ac.uk/structures.

References

[1] T. J. Kealy and P. L. Pauson, "A new type of organo-iron compound", *Nature* **168** (1951), pp. 1039–1040.

[2] S. A. Miller, J. A. Tebboth and J. F. Tremaine, "Dicyclopentadienyliron", *J. Chem. Soc.* **1952** (1952), pp. 632–635.

[3] G. Wilkinson, M. Rosenblum, M. C. Whiting and R. B. Woodward, "The structure of iron biscyclopentadienyl", *J. Am. Chem. Soc.* **74** (1952), pp. 2125–2126.

[4] E. O. Fischer and W. Pfab, "Cyclopentadiene-metallic complex, a new type of organo-metallic compound", *Z. Naturforsch.* **7b** (1952), pp. 377–379.

[5] G. G. A. Balavoine, J. C. Daran, G. Iftime, E. Manoury and C. Moreau-Bossuet, "Selective synthesis of ferrocenes", *J. Organomet. Chem.* **567** (1998), pp. 191–198.

[6] C. J. Richards and A. J. Locke, "Recent advances in the generation of non-racemic ferrocene derivatives and their application to asymmetric synthesis", *Tetrahedron Asymmetry* **9** (1998), pp. 2377–2407.

[7] R. C. J. Atkinson, V. C. Gibson and N. J. Long, "The syntheses and catalytic applications of unsymmetrical ferrocene ligands", *Chem. Soc. Rev.* **33** (2004), pp. 313–328.

[8] I. R. Butler, “The simple synthesis of ferrocene ligands from a practitioner’s perspective”, *Eur. J. Inorg. Chem.* **15** (2012), pp. 4387–4406.

[9] F. A. Larik, A. Saeed, T. A. Fattah, U. Muqadar and P. A. Channar, “Recent advances in the synthesis, biological activities and various applications of ferrocene derivatives”, *Appl. Organomet. Chem.* **31** (2017), article no. e3664.

[10] D. Astruc, “The numerous paths of ferrocene”, *Nat. Chem.* **15** (2023), p. 1650.

[11] A. Straube, L. Useini and E. Hey-Hawkins, “Multi-ferrocene-based ligands: From design to applications”, *Chem. Rev.* **125** (2025), pp. 3007–3058.

[12] H. Qi, N.-N. Hang and J. Ming, “Synthesis of planar chiral ferrocenes by catalytic desymmetrization reactions”, *ChemCatChem* **16** (2024), article no. e202400736.

[13] S. E. Park, S. Park, W. Lee and J. M. Joo, “Recent strategies for the synthesis of ferrocene derivatives and their applications to electrochemistry”, *Synthesis* **57** (2025), pp. 2411–2422.

[14] T. J. Colacot, “A concise update on the applications of chiral ferrocenyl phosphines in homogeneous catalysis leading to organic synthesis”, *Chem. Rev.* **103** (2003), pp. 3101–3118.

[15] R. Gómez-Arrayás, J. Adrio and J. C. Carretero, “Recent applications of chiral ferrocene ligands in asymmetric catalysis”, *Angew. Chem. Int. Ed.* **45** (2006), pp. 7674–7715.

[16] In, *Chiral Ferrocenes in Asymmetric Catalysis: Synthesis and Applications*, Wiley-VCH: Weinheim, 2010.

[17] K. Yoshida and R. Yasue, “Planar-chiral ferrocene-based N-heterocyclic carbene ligands”, *Chem. Eur. J.* **24** (2018), pp. 18575–18586.

[18] In, *Ferrocenes: Ligands, Materials and Biomolecules*, Wiley: Chichester, 2008.

[19] G. Roy, R. Gupta, S. Ranjan Sahoo, S. Saha, D. Asthana and P. Chandra Mondal, “Ferrocene as an iconic redox marker: From solution chemistry to molecular electronic devices”, *Coord. Chem. Rev.* **473** (2022), article no. 214816.

[20] S. K. Sahoo, “Fluorescent chemosensors containing redox-active ferrocene: a review”, *Dalton Trans.* **50** (2021), pp. 11681–11700.

[21] A. A. J. Torriero, A. M. Torriero, K. T. Miller and A. K. V. Mruthunjaya, “Beyond cations: Expanding the horizons of ferrocene-based electrochemical sensors for neutral and anionic molecules”, *Inorganics* **13** (2025), article no. 3.

[22] D. R. van Staveren and N. Metzler-Nolte, “Bioorganometallic chemistry of ferrocene”, *Chem. Rev.* **104** (2004), pp. 5931–5985.

[23] M. Patra and G. Gasser, “The medicinal chemistry of ferrocene and its derivatives”, *Nat. Rev. Chem.* **1** (2017), article no. 0066.

[24] B. Sharma and V. Kumar, “Has ferrocene really delivered its role in accentuating the bioactivity of organic scaffolds?”, *J. Med. Chem.* **64** (2021), pp. 16865–16921.

[25] V. Tomar, P. Kumar, D. Sharma, R. K. Joshi and M. Nemiwal, “Anticancer potential of ferrocene-containing derivatives: Current and future prospective”, *J. Mol. Struct.* **1319** (2025), article no. 139589.

[26] L. Ezell, D. H. LaVoy, T. Sasaki and L. M. Goldman, “Solvent-free acylation of ferrocene: Crowdsourcing student data to evaluate reaction conditions”, *J. Chem. Educ.* **102** (2025), pp. 2422–2428.

[27] F. Rebière, O. Samuel and H. B. Kagan, “A convenient method for the preparation of monolithioferrocene”, *Tetrahedron Lett.* **31** (1990), pp. 3121–3124.

[28] R. Sanders and U. T. Mueller-Westerhoff, “The lithiation of ferrocene and ruthenocene: a retraction and an improvement”, *J. Organomet. Chem.* **512** (1996), pp. 219–224.

[29] D. Astruc, “Why is ferrocene so exceptional?”, *Eur. J. Inorg. Chem.* **20** (2017), pp. 6–29.

[30] E. Lerayer, L. Radal, T. A. Nguyen, et al., “Highly functionalized ferrocenes”, *Eur. J. Inorg. Chem.* **23** (2020), pp. 419–445.

[31] P. Štepnička, “Forever young: the first seventy years of ferrocene”, *Dalton Trans.* **51** (2022), pp. 8085–8102.

[32] M. Korb and H. Lang, “Rearrangements and migrations along the ferrocene periphery: On the way to planar-chiral and (multi)substitution patterns”, *Eur. J. Inorg. Chem.* **25** (2022), article no. e202100946.

[33] C. Guchhait, V. Suriyaa, N. Sahu, S. D. Sarkar and B. Adhikari, “Ferrocene: an exotic building block for supramolecular assemblies”, *Chem. Commun.* **59** (2023), pp. 14482–14496.

[34] W. Erb and F. Mongin, “Twofold ferrocene C–H lithiations for one-step difunctionalizations”, *Synthesis* **51** (2019), pp. 146–160.

[35] B. Ferber and H. B. Kagan, “Metallocene sulfoxides as precursors of metallocenes with planar chirality”, *Adv. Synth. Catal.* **349** (2007), pp. 493–507.

[36] V. Mamane, “The diastereoselective ortho-lithiation of Kagan’s ferrocenyl acetal. Generation and reactivity of chiral 2-substituted ferrocenecarboxaldehydes”, *Tetrahedron Asymmetry* **21** (2010), pp. 1019–1029.

[37] D. Schaarschmidt and H. Lang, “Selective syntheses of planar-chiral ferrocenes”, *Organometallics* **32** (2013), pp. 5668–5704.

[38] C.-X. Liu, Q. Gu and S.-L. You, “Asymmetric C–H bond functionalization of ferrocenes: New opportunities and challenges”, *Trends Chem.* **2** (2020), pp. 737–749.

[39] W. Erb, M. Wen, T. Roisnel and F. Mongin, “Synthesis of ferrocenesulfonyl chloride, key intermediate toward ferrocenesulfonamides”, *Synthesis* **53** (2021), pp. 2612–2620.

[40] W. Erb and T. Roisnel, “The chemistry of ferrocenesulfonyl fluoride revealed”, *Dalton Trans.* **50** (2021), pp. 16483–16487.

[41] R. B. Woodward, M. Rosenblum and M. C. Whiting, “A new aromatic system”, *J. Am. Chem. Soc.* **74** (1952), pp. 3458–3459.

[42] D. Enders, R. Peters, R. Lochtman and J. Runsink, “Enantioselective synthesis of planar chiral ortho-functionalized ferrocenyl ketones”, *Eur. J. Org. Chem.* **3** (2000), pp. 2839–2850.

[43] B. Ferber, S. Top, P. Herson and G. Jaouen, “New ortho-directing group for lithiation: Use of a methoxy-imino auxiliary for the synthesis of chiral ortho-substituted acetyl- and propionylferrocenes”, *Organometallics* **26** (2007), pp. 1686–1691.

[44] D. Enders, E. A. Jonas and T. Klumpen, “Efficient asymmetric synthesis of planar-chiral bisferrocenes”, *Eur. J. Org. Chem.* **12** (2009), pp. 2149–2162.

[45] E. Hevia, A. R. Kennedy and M. D. McCall, “Assessing the reactivity of sodium zincate $[(TMEDA)Na(TMP)Zn^{t}Bu_2]$ towards benzoylferrocene: deprotonative metalation vs. alkylation reactions”, *Dalton Trans.* **41** (2012), pp. 98–103.

[46] G. Dayaker, A. Sreeshailam, F. Chevallier, T. Roisnel, P. Radha Krishna and F. Mongin, “Deprotonative metallation of ferrocenes using mixed lithium-zinc and lithium-cadmium combinations”, *Chem. Commun.* **46** (2010), pp. 2862–2864.

[47] N. Mokhtari Brikci-Nigassa, G. Bentabed-Ababsa, W. Erb and F. Mongin, “In situ ‘trans-metal trapping’: An efficient way to extend the scope of aromatic deprotometalation”, *Synthesis* **50** (2018), pp. 3615–3633.

[48] C. Bastien, W. Erb, Y. S. Halauko, V. E. Matulis, T. Roisnel, Y. Sarazin and F. Mongin, “Functionalisation of chromane by deprotonative metallation”, *Eur. J. Org. Chem.* **27** (2024), article no. e202400566.

[49] M. C. Whisler, S. MacNeil, V. Snieckus and P. Beak, “Beyond thermodynamic acidity: A perspective on the complex-induced proximity effect (CIPE) in deprotonation reactions”, *Angew. Chem. Int. Ed.* **43** (2004), pp. 2206–2225.

[50] P. Beak and A. I. Meyers, “Stereo- and regiocontrol by complex induced proximity effects: reactions of organolithium compounds”, *Acc. Chem. Res.* **19** (1986), pp. 356–363.

[51] N. J. R. van Eikema Hommes and P. v. R. Schleyer, “Mechanisms of aromatic lithiation. Influence of aggregation and directing groups”, *Tetrahedron* **50** (1994), pp. 5903–5916.

[52] A. Abbotto, S. S.-W. Leung, A. Streitwieser and K. V. Kilway, “The role of monomer in alkylation reactions of the lithium enolate of p-phenylisobutyrophenone in tetrahydrofuran”, *J. Am. Chem. Soc.* **120** (1998), pp. 10807–10813.

[53] In, *Organometallics in Synthesis: A Manual*, John Wiley & Sons: New York, 1994.

[54] M. Schlosser, “The 2 ∗ 3 toolbox of organometallic methods for regiochemically exhaustive functionalization”, *Angew. Chem. Int. Ed.* **44** (2005), pp. 376–393.

[55] R. Maggi and M. Schlosser, “Rate enhancing and rate retarding effects of methoxy substituents on arene metalation”, *Tetrahedron Lett.* **40** (1999), pp. 8797–8800.

[56] M. Schlosser, F. Mongin, J. Porwisiak, W. Dmowski, H. H. Buker and N. M. M. Nibbering, “Bis- and oligo(trifluoromethyl)benzenes: Hydrogen/metal exchange rates and gas-phase acidities”, *Chem. Eur. J.* **4** (1998), pp. 1281–1286.

[57] D. A. Evans, V. J. Cee, T. E. Smith and K. J. Santiago, “Selective lithiation of 2-methyloxazoles. Applications to pivotal bond constructions in the phorboxazole nucleus”, *Org. Lett.* **1** (1999), pp. 87–90.

[58] N. Sharma, J. S. Dhau, A. Singh, S. Abbat, P. V. Bharatam, A. K. Malik and A. Singh, “Selective lithiation of 2,4-lutidine: Role of transition states of lithium dialkylamides”, *J. Organomet. Chem.* **936** (2021), article no. 121691.

[59] M. Hasyeoui, P. M. Chapple, F. Lassagne, T. Roisnel, M. Cordier, A. Samarat, Y. Sarazin and F. Mongin, “Lateral deprotometallation-trapping reactions on methylated pyridines, quinolines and quinoxalines using lithium diethylamide”, *Eur. J. Org. Chem.* **26** (2023), article no. e202300555.

[60] V. E. Matulis, Y. S. Halauko, O. A. Ivashkevich and P. N. Gaponik, “CH acidity of five-membered nitrogen-containing heterocycles: DFT investigation”, *J. Mol. Struct.: Theochem* **909** (2009), pp. 19–24.

[61] R. R. Kadiyala, D. Tilly, E. Nagaradja, et al., “Computed CH acidity of biaryl compounds and their deprotonative metalation by using a mixed lithium/Zinc-TMP base”, *Chem. Eur. J.* **19** (2013), pp. 7944–7960.

[62] M. Hedidi, W. Erb, F. Lassagne, et al., “Functionalization of pyridyl ketones using deprotolithiation-in situ zincation”, *RSC Adv.* **6** (2016), pp. 63185–63189.

[63] M. Hedidi, J. Maillard, W. Erb, et al., “Fused systems based on 2-aminopyrimidines: Synthesis combining deprotolithiation-in situ zincation with N-arylation reactions and biological properties”, *Eur. J. Org. Chem.* **20** (2017), pp. 5903–5915.

[64] A. C. Bényei, C. Glidewell, P. Lightfoot, B. J. L. Royles and D. M. Smith, “Functionalized acyl ferrocenes: crystal and molecular structures of 4-aminobenzoylferrocene, 4-hydroxybenzoylferrocene and 1,1’-bis(4-hydroxybenzoyl)ferrocene”, *J. Organomet. Chem.* **539** (1997), pp. 177–186.

[65] E. A. Hillard, P. Pigeon, A. Vessières, C. Amatore and G. Jaouen, “The influence of phenolic hydroxy substitution on the electron transfer and anti-cancer properties of compounds based on the 2-ferrocenyl-1-phenyl-but-1-ene motif”, *Dalton Trans.* **36** (2007), pp. 5073–5081.

[66] D. Plazuk and J. Zakrzewski, “Friedel-Crafts acylation of ferrocene with alkynoic acids”, *J. Organomet. Chem.* **694** (2009), pp. 1802–1806.

[67] P. Švec, O. V. Petrov, J. Lang, et al., “Fluorinated ferrocene moieties as a platform for redox-responsive polymer 19F MRI theranostics”, *Macromolecules* **55** (2022), pp. 658–671.

[68] S. Masi, S. Top, L. Boubekeur, G. Jaouen, S. Mundwiler, B. Spingler and R. Alberto, “Direct synthesis of tricarbonyl(cyclopentadienyl)rhenium and tricarbonyl(cyclopentadienyl)technetium units from ferrocenyl moieties - Preparation of 17α-ethynylestradiol derivatives bearing a tricarbonyl(cyclopentadienyl)technetium group”, *Eur. J. Inorg. Chem.* **7** (2004), pp. 2013–2017.

[69] A. Seggio, M.-I. Lannou, F. Chevallier, D. Nobuto, M. Uchiyama, S. Golhen, T. Roisnel and F. Mongin, “Ligand-activated lithium-mediated zincation of n-phenylpyrrole”, *Chem. Eur. J.* **13** (2007), pp. 9982–9989.

[70] E. Negishi, A. O. King and N. Okukado, “Selective carbon-carbon bond formation via transition metal catalysis. 3.

A highly selective synthesis of unsymmetrical biaryls and diarylmethanes by the nickel- or palladium-catalyzed reaction of aryl- and benzylzinc derivatives with aryl halides", *J. Org. Chem.* **42** (1977), pp. 1821–1823.

[71] E. Negishi, "Palladium- or nickel-catalyzed cross coupling. A new selective method for carbon-carbon bond formation", *Acc. Chem. Res.* **15** (1982), pp. 340–348.

[72] D. R. Gauthier Jr, R. H. Szumigala Jr, P. G. Dormer, J. D. Armstrong III, R. P. Volante and P. J. Reider, "Synthesis of 5-pyridyl-2-furaldehydes via palladium-catalyzed cross-coupling with triorganozincates", *Org. Lett.* **4** (2002), pp. 375–378.

[73] G. Mloston, R. Hamera and H. Heimgartner, "Synthesis of ferrocenyl thioketones and their reactions with diphenyldiazomethane", *Phosph. Sulfur Silicon Relat. Elem.* **190** (2015), pp. 2125–2133.

[74] G. Dayaker, W. Erb, M. Hedidi, et al., "Enantioselective deprotometalation of alkyl ferrocenecarboxylates using bimetallic bases", *New J. Chem.* **45** (2021), pp. 22579–22590.

[75] F. Mongin, "Long-range effect of bromine in the deprotonative metalation of aromatic compounds", *Chimia* **70** (2016), pp. 48–52.

[76] F. Mongin, C. Curty, E. Marzi, F. R. Leroux and M. Schlosser, "Substituent effects on the relative rates and free energies of ortho-lithiation reactions: families of fluorobenzenes as the substrates", *ARKIVOC* **2015** (2015), pp. 48–65.

[77] E. Castagnetti and M. Schlosser, "The trifluoromethoxy group: - a long-range electron-withdrawing substituent", *Chem. Eur. J.* **8** (2002), pp. 799–804.

[78] T. Čarný and R. Šebesta, "Comparison of diastereoselective ortho-metalations and C–H activations of chiral ferrocenes", *Synlett* **35** (2024), pp. 165–182.

[79] Y. Nishibayashi, Y. Arikawa, K. Ohe and S. Uemura, "Enantioselective ortho-lithiation of substituted ferrocenes", *J. Org. Chem.* **61** (1996), pp. 1172–1174.

[80] P. Steffen, C. Unkelbach, M. Christmann, W. Hiller and C. Strohmann, "Catalytic and stereoselective ortho-lithiation of a ferrocene derivative", *Angew. Chem. Int. Ed.* **52** (2013), pp. 9836–9840.

[81] C. Metallinos, J. Zaifman and L. Dodge, "Aminoferrocene lithiation by boron trifluoride activation", *Org. Lett.* **10** (2008), pp. 3527–3530.

[82] C. Metallinos, J. Zaifman, T. Dudding, L. Van Belle and K. Taban, "Asymmetric lithiation of boron trifluoride-activated aminoferrocenes: An experimental and computational investigation", *Adv. Synth. Catal.* **352** (2010), pp. 1967–1982.

[83] M. Tsukazaki, M. Tinkl, A. Roglans, B. J. Chapell, N. J. Taylor and V. Snieckus, "Direct and highly enantioselective synthesis of ferrocenes with planar chirality by (-)-sparteine-mediated lithiation", *J. Am. Chem. Soc.* **118** (1996), pp. 685–686.

[84] C. Metallinos, H. Szillat, N. J. Taylor and V. Snieckus, "(-)-Sparteine-mediated directed ortho-metalation of N-cumyl-N-ethylferrocenecarboxamide. Versatile routes to functionalized planar chiral ferrocenecarboxamides, amines, esters and phosphines", *Adv. Synth. Catal.* **345** (2003), pp. 370–382.

[85] C. Genet, S. J. Canipa, P. O'Brien and S. Taylor, "Catalytic asymmetric synthesis of ferrocenes and P-stereogenic bisphosphines", *J. Am. Chem. Soc.* **128** (2006), pp. 9336–9337.

[86] W. Erb, T. Roisnel and V. Dorcet, "Practical chromatography-free synthesis of 2-iodo-N,N-diisopropylferrocenecarboxamide and further transformations", *Synthesis* **51** (2019), pp. 3205–3213.

[87] M. Wen, W. Erb, F. Mongin, et al., "Enantioselective synthesis of planar chiral ferrocene triflones", *Adv. Synth. Catal.* **366** (2024), pp. 4984–4993.

[88] D. Price and N. S. Simpkins, "Concerning the asymmetric metalation of ferrocenes by chiral lithium amide bases", *Tetrahedron Lett.* **36** (1995), pp. 6135–6136.

[89] M. Hedidi, G. Dayaker, Y. Kitazawa, et al., "Enantioselective deprotometalation of N,N-dialkyl ferrocenecarboxamides using metal amides", *New J. Chem.* **43** (2019), pp. 14898–14907.

[90] G. Dayaker, D. Tilly, F. Chevallier, G. Hilmersson, P. C. Gros and F. Mongin, "Enantioselective metalation of N,N-diisopropylferrocenecarboxamide and methyl ferrocenecarboxylate using lithium-metal chiral bases", *Eur. J. Org. Chem.* **2012** (2012), pp. 6051–6057.

[91] N. M. Brikci-Nigassa, G. Bentabed-Ababsa, W. Erb and F. Mongin, "In situ 'trans-metal trapping': An efficient way to extend the scope of aromatic deprotometalation", *Synthesis* **50** (2018), pp. 3615–3633.

[92] W. Erb, M. Wen, J.-P. Hurvois, F. Mongin, Y. S. Halauko, O. A. Ivashkevich, V. E. Matulis and T. Roisnel, "*O*-isopropylferrocenesulfonate: Synthesis of polysubstituted derivatives and electrochemical study", *Eur. J. Inorg. Chem.* **24** (2021), pp. 3165–3176.

[93] S. Monticelli, L. Castoldi, I. Murgia, et al., "Recent advancements on the use of 2-methyltetrahydrofuran in organometallic chemistry", *Monatsh. Chem.* **148** (2017), pp. 37–48.

[94] D. Marquarding, H. Klusacek, G. Gokel, P. Hoffmann and I. Ugi, "Stereoselective syntheses. VI. Correlation of central and planar chirality in ferrocene derivatives", *J. Am. Chem. Soc.* **92** (1970), pp. 5389–5393.

[95] L. F. Battelle, R. Bau, G. W. Gokel, R. T. Oyakawa and I. K. Ugi, "Stereoselective synthesis. VIII. Absolute configuration of a 1,2-disubstituted ferrocene derivative with planar and central elements of chirality and the mechanism of the optically active α-ferrocenyl tertiary amines", *J. Am. Chem. Soc.* **95** (1973), pp. 482–486.

[96] G. A. Olah, A.-h. Wu and O. Farooq, "Synthetic methods and reactions. 168. Ring tert-butylation of benzophenones and benzaldehyde with tert-butyllithium and thionyl chloride", *Synthesis* **23** (1991), pp. 1179–1182.

[97] H. Yamataka, Y. Kawafuji, K. Nagareda, N. Miyano and T. Hanafusa, "Electron transfer in the additions of organolithium reagents to benzophenone and benzaldehyde", *J. Org. Chem.* **54** (1989), pp. 4706–4708.

[98] E. Hevia, G. W. Honeyman, A. R. Kennedy and R. E. Mulvey, "Trapping, stabilization, and characterization of an enolate anion of a 1,6-adduct of benzophenone chelated

by a sodium alkylamidozincate cation", *J. Am. Chem. Soc.* **127** (2005), pp. 13106–13107.

[99] D. R. Armstrong, J. A. Garden, A. R. Kennedy, R. E. Mulvey and S. D. Robertson, "Modifying alkylzinc reactivity with 2,2′-dipyridylamide: Activation of tBu–Zn bonds for para-alkylation of benzophenone", *Angew. Chem. Int. Ed.* **52** (2013), pp. 7190–7193.

[100] D. R. Armstrong, E. V. Brouillet, A. R. Kennedy, J. A. Garden, M. Granitzka, R. E. Mulvey and J. J. Trivett, "Donor-activated alkali metal dipyridylamides: co-complexation reactions with zinc alkyls and reactivity studies with benzophenone", *Dalton Trans.* **43** (2014), pp. 14409–14423.

[101] J. J. Crawford, B. J. Fleming, A. R. Kennedy, J. Klett, C. T. O'Hara and S. A. Orr, "Remote functionalization via sodium alkylamidozincate intermediates: access to unusual fluorenone and pyridyl ketone reactivity patterns", *Chem. Commun.* **47** (2011), pp. 3772–3774.

[102] D. R. Armstrong, L. Balloch, J. J. Crawford, et al., "Single electron transfer (SET) activity of the dialkyl-amido sodium zincate [(TMEDA)·Na(μ-TMP)(μ-tBu)Zn(tBu)] towards TEMPO and chalcone", *Chem. Commun.* **48** (2012), pp. 1541–1543.

[103] N. Miyaura, K. Yamada and A. Suzuki, "A new stereospecific cross-coupling by the palladium-catalyzed reaction of 1-alkenylboranes with 1-alkenyl or 1-alkynyl halides", *Tetrahedron Lett.* **20** (1979), pp. 3437–3440.

[104] N. Miyaura and A. Suzuki, "Palladium-catalyzed cross-coupling reactions of organoboron compounds", *Chem. Rev.* **95** (1995), pp. 2457–2483.

[105] M. Tazi, W. Erb, Y. S. Halauko, O. A. Ivashkevich, V. E. Matulis, T. Roisnel, V. Dorcet and F. Mongin, "From 2- to 3-substituted ferrocene carboxamides or how to apply halogen "dance" to the ferrocene series", *Organometallics* **36** (2017), pp. 4770–4778.

[106] W. Erb, L. Kadari, K. Al-Mekhlafi, T. Roisnel, V. Dorcet, P. Radha Krishna and F. Mongin, "Functionalization of 3-iodo-N,N-diisopropylferrocene-carboxamide, a pivotal substrate to open the chemical space to 1,3-disubstituted ferrocenes", *Adv. Synth. Catal.* **362** (2020), pp. 832–850.

[107] S. W. Wright, D. L. Hageman and L. D. McClure, "Fluoride-mediated boronic acid coupling reactions", *J. Org. Chem.* **59** (1994), pp. 6095–6097.

[108] T. E. Barder, S. D. Walker, J. R. Martinelli and S. L. Buchwald, "Catalysts for Suzuki–Miyaura coupling processes: Scope and studies of the effect of ligand structure", *J. Am. Chem. Soc.* **127** (2005), pp. 4685–4696.

[109] K. Sonogashira, Y. Tohda and N. Hagihara, "Convenient synthesis of acetylenes. Catalytic substitutions of acetylenic hydrogen with bromo alkenes, iodo arenes, and bromopyridines", *Tetrahedron Lett.* **16** (1975), pp. 4467–4470.

[110] M. S. Inkpen, A. J. P. White, T. Albrecht and N. J. Long, "Rapid Sonogashira cross-coupling of iodoferrocenes and the unexpected cyclo-oligomerization of 4-ethynylphenylthioacetate", *Chem. Commun.* **49** (2013), pp. 5663–5665.

[111] N. Kausch-Busies, J. M. Neudörfl, P. Wefelmeier, A. Prokop, H. Kühn and H.-G. Schmalz, "Stereoselective synthesis and biological evaluation of ferrocene-containing 5-hydroxyeicosatetraenoic acid analogues", *Eur. J. Org. Chem.* **2011** (2011), pp. 4634–4644.

[112] K. Yoshida, Q. Liu, R. Yasue, S. Wada, R. Kimura, T. Konishi and M. Ogasawara, "Versatile and enantioselective preparation of planar-chiral metallocene-fused 4-dialkylaminopyridines and their application in asymmetric organocatalysis", *ACS Catal.* **10** (2020), pp. 292–301.

[113] C. Duro, T. Jernei, K. J. Szekeres, et al., "Synthesis and SAR analysis of novel 4-hydroxytamoxifen analogues based on their cytotoxic activity and electron-donor character", *Molecules* **27** (2022), article no. 6758.

[114] O. Bernardo, S. González-Pelayo and L. A. López, "Synthesis and applications of ferrocene-fused nitrogen heterocycles", *Eur. J. Inorg. Chem.* **2022** (2022), article no. e202100911.

[115] S. Sangeetha, P. Muthupandi and G. Sekar, "Copper-catalyzed domino synthesis of 2-arylthiochromanones through concomitant C–S bond formations using xanthate as sulfur source", *Org. Lett.* **17** (2015), pp. 6006–6009.

[116] J. Wang, Z.-H. Zhu, M.-W. Chen, Q.-A. Chen and Y.-G. Zhou, "Catalytic biomimetic asymmetric reduction of alkenes and imines enabled by chiral and regenerable NAD(P)H models", *Angew. Chem. Int. Ed.* **58** (2019), pp. 1813–1817.

[117] D.-W. Gao, C. Zheng, Q. Gu and S.-L. You, "Pd-Catalyzed highly enantioselective synthesis of planar chiral ferrocenylpyridine derivatives", *Organometallics* **34** (2015), pp. 4618–4625.

[118] M. C. Whiting, "Recollections of the arrival of ferrocene", *J. Organomet. Chem.* **637–639** (2001), pp. 16–17.

[119] M. Rosenblum, "The early ferrocene days-a personal recollection", *J. Organomet. Chem.* **637–639** (2001), pp. 13–15.

[120] Y. Yamaguchi, W. Ding, C. T. Sanderson, M. L. Borden, M. J. Morgan and C. Kutal, "Electronic structure, spectroscopy, and photochemistry of group 8 metallocenes", *Coord. Chem. Rev.* **251** (2007), pp. 515–524.

[121] J. Jia, Y. Cui, L. Han, W. Sheng, Y. Li and J. Gao, "Syntheses, third-order optical nonlinearity and DFT studies on benzoylferrocene derivatives", *Dyes Pigm.* **104** (2014), pp. 137–145.

[122] W. F. Little, C. N. Reilley, J. D. Johnson and A. P. Sanders, "Chronopotentiometric studies of ferrocene derivatives. II. Directly substituted ferrocenes", *J. Am. Chem. Soc.* **86** (1964), pp. 1382–1386.

[123] W. E. Britton, R. Kashyap, M. El-Hashash, M. El-Kady and M. Herberhold, "The anomalous electrochemistry of the ferrocenylamines", *Organometallics* **5** (1986), pp. 1029–1031.

[124] D. A. Khobragade, S. G. Mahamulkar, L. Pospíšil, I. Císařová, L. Rulíšek and U. Jahn, "Acceptor-substituted ferrocenium salts as strong, single-electron oxidants: Synthesis, electrochemistry, theoretical investigations, and initial synthetic application", *Chem. Eur. J.* **18** (2012), pp. 12267–12277.

[125] G. L. K. Hoh, W. E. McEwen and J. Kleinberg, "Substituent effects in the chronopotentiometric oxidation of ferrocenes", *J. Am. Chem. Soc.* **83** (1961), pp. 3949–3953.

[126] C. Saboureau, M. Troupel, S. Sibille and J. Perichon, "Electroreductive coupling of trifluoromethylarenes with electrophiles: synthetic applications", *J. Chem. Soc. Chem. Commun.* **25** (1989), pp. 1138–1139.

[127] C. P. Andrieux, C. Combellas, F. Kanoufi, J.-M. Savéant and A. Thiebault, "Dynamics of bond breaking in ion radicals. Mechanisms and reactivity in the reductive cleavage of carbon-fluorine bonds of fluoromethylarenes", *J. Am. Chem. Soc.* **119** (1997), pp. 9527–9540.

[128] R. I. Pacut and E. Kariv-Miller, "Birch-type reductions in aqueous media. Benzo[b]thiophene and diphenyl ether", *J. Org. Chem.* **51** (1986), pp. 3468–3470.

[129] W. Erb, N. Richy, J.-P. Hurvois, P. J. Low and F. Mongin, "From ferrocene to 1,2,3,4,5-pentafluoroferrocene: halogen effect on the properties of metallocene", *Dalton Trans.* **50** (2021), pp. 16933–16938.

[130] C. Hansch, A. Leo and R. W. Taft, "A survey of Hammett substituent constants and resonance and field parameters", *Chem. Rev.* **91** (1991), pp. 165–195.

[131] M. S. Inkpen, S. Du, M. Hildebrand, A. J. P. White, N. M. Harrison, T. Albrecht and N. J. Long, "The unusual redox properties of fluoroferrocenes revealed through a comprehensive study of the haloferrocenes", *Organometallics* **34** (2015), pp. 5461–5469.

[132] D. M. Evans, D. D. Hughes, P. J. Murphy, P. N. Horton, S. J. Coles, F. F. de Biani, M. Corsini and I. R. Butler, "Synthetic route to 1,1′,2,2′-tetraiodoferrocene that avoids isomerization and the electrochemistry of some tetrahaloferrocenes", *Organometallics* **40** (2021), pp. 2496–2503.

[133] S. D. Waniek, J. Klett, C. Förster and K. Heinze, "Polysubstituted ferrocenes as tunable redox mediators", *Beilstein J. Org. Chem.* **14** (2018), pp. 1004–1015.

[134] W. Erb, J.-P. Hurvois, Y. S. Halauko, V. E. Matulis and T. Roisnel, "Exploring the boundaries of ferrocenesulfonyl fluoride chemistry", *Inorg. Chem. Front.* **9** (2022), pp. 5862–5883.

[135] M. Wen, W. Erb, F. Mongin, et al., "From ferrocene to decasubstituted enantiopure ferrocene-1,1′-disulfoxide derivatives", *Dalton Trans.* **52** (2023), pp. 3725–3737.

[136] G. Cavallo, P. Metrangolo, R. Milani, T. Pilati, A. Priimagi, G. Resnati and G. Terraneo, "The halogen bond", *Chem. Rev.* **116** (2016), pp. 2478–2601.

[137] L. Fotović, N. Bedeković and V. Stilinović, "Evaluation of halogenopyridinium cations as halogen bond donors", *Cryst. Growth Des.* **21** (2021), pp. 6889–6901.

[138] K. Raatikainen, M. Cametti and K. Rissanen, "The subtle balance of weak supramolecular interactions: the hierarchy of halogen and hydrogen bonds in haloanilinium and halopyridinium salts", *Beilstein J. Org. Chem.* **6** (2010), pp. 1–13.

[139] G. Levilain and G. Coquerel, "Pitfalls and rewards of preferential crystallization", *CrystEngComm* **12** (2010), pp. 1983–1992.

[140] M. Wen, W. Erb, F. Mongin, Y. S. Halauko, O. A. Ivashkevich, V. E. Matulis, T. Roisnel and V. Dorcet, "Functionalization of N,N-dialkylferrocenesulfonamides toward substituted derivatives", *Organometallics* **40** (2021), pp. 1129–1147.

[141] M. Wen, W. Erb, F. Mongin, Y. S. Halauko, O. A. Ivashkevich, V. E. Matulis and T. Roisnel, "Synthesis of polysubstituted ferrocenesulfoxides", *Molecules* **27** (2022), article no. 1798.

[142] V. Mamane, P. Peluso, E. Aubert, R. Weiss, E. Wenger, S. Cossu and P. Pale, "Disubstituted ferrocenyl iodo- and chalcogenoalkynes as chiral halogen and chalcogen bond donors", *Organometallics* **39** (2020), pp. 3936–3950.

[143] S. Scheiner, "Characterization of type I and II interactions between halogen atoms", *Cryst. Growth Des.* **22** (2022), pp. 2692–2702.

[144] B. K. Saha, R. V. P. Veluthaparambath and V. Krishna G, "Halogen$\cdots$halogen interactions: Nature, directionality and applications", *Chem. Asian J.* **18** (2023), article no. e202300067.

[145] T. Moriuchi, "Helical chirality of ferrocene moieties in cyclic ferrocene-peptide conjugates", *Eur. J. Inorg. Chem.* **2022** (2022), article no. e202100902.

[146] M. Fellert, R. Hein, A. Ryabchun, Y. Gisbert, C. N. Stindt and B. L. Feringa, "A multiresponsive ferrocene-based chiral overcrowded alkene twisting liquid crystals", *Angew. Chem. Int. Ed.* **64** (2025), article no. e202413047.

[147] Y. Wang, W. Qi, R. Huang, X. Yang, M. Wang, R. Su and Z. He, "Rational design of chiral nanostructures from self-assembly of a ferrocene-modified dipeptide", *J. Am. Chem. Soc.* **137** (2015), pp. 7869–7880.

[148] H. Yamagishi, T. Fukino, D. Hashizume, T. Mori, Y. Inoue, T. Hikima, M. Takata and T. Aida, "Metal-organic nanotube with helical and propeller-chiral motifs composed of a c10-symmetric double-decker nanoring", *J. Am. Chem. Soc.* **137** (2015), pp. 7628–7631.

[149] R. Gleiter, G. Haberhauer, D. B. Werz, F. Rominger and C. Bleiholder, "From noncovalent chalcogen–chalcogen interactions to supramolecular aggregates: Experiments and calculations", *Chem. Rev.* **118** (2018), pp. 2010–2041.

[150] A. S. Lundemba, D. D. Bibelayi, P. A. Wood, J. Pradon and Z. G. Yav, "σ–hole interactions in small-molecule compounds containing divalent sulfur groups R1-S-R2", *Acta Crystallogr.* **B76** (2020), pp. 707–718.

[151] A. Bondi, "van der Waals volumes and radii", *J. Phys. Chem.* **68** (1964), pp. 441–451.

[152] S. Jin, S.-J. Li, X. Ma, J. Su, H. Chen, Y. Lan and Q. Song, "Elemental-sulfur-enabled divergent synthesis of disulfides, diselenides, and polythiophenes from β-CF3-1,3-enynes", *Angew. Chem. Int. Ed.* **60** (2021), pp. 881–888.

[153] L. A. Casper, K. L. Deuter, A. Rehse and R. F. Winter, "Dimerization of 9-phenyl-ferroceno[2,3]indenylmethyl radicals: Electrochemical and spectroelectrochemical studies", *ACS Org. Inorg. Au* **4** (2024), pp. 395–409.

ACADÉMIE
DES SCIENCES
INSTITUT DE FRANCE

Comptes Rendus. Chimie
2026, Vol. 29, p. 131-144
https://doi.org/10.5802/crchim.430

Research article

Tuning gas-phase photocatalytic CO_2 reduction activity and selectivity on bimetallic copper-based titanium-dioxide-supported photocatalysts

Clément Marchal [a], Eliane Khoury [a] and Valérie Keller [*, a]

[a] ICPEES, Institut de Chimie et des Procédés pour l'Energie, l'Environnement et la Santé UMR 7515 CNRS/Université de Strasbourg 25, rue Becquerel 67087 Strasbourg cedex 2, France

E-mail: vkeller@unistra.fr (V. Keller)

Abstract. This study explores various approaches to enhancing the activity and selectivity of gas-phase photocatalytic CO_2 reduction under humid conditions by implementing and optimizing bimetallic M–Cu systems (M = Pt, Pd, Au, Ag) supported on titanium dioxide (TiO_2). By tuning the total metal content, the molar ratio between M and Cu, the deposition method, and the nature of the TiO_2 support, it is possible to create a synergy between copper and the secondary metal, each contributing its own advantages while minimizing drawbacks. This strategy also improves the stability of the systems by increasing their resistance to Cu oxidation. These results offer a promising pathway for the development of efficient photocatalysts for solar-driven gas-phase CO_2 conversion into chemical fuels.

Keywords. Photocatalysis, Sustainable CO_2 reduction, Artificial photosynthesis, Solar energy, TiO_2, Bimetallic systems.

Funding. PEPR PowerCO2, ECOCHEM projects.

Note. Article submitted by invitation.

Manuscript received 17 October 2025, revised 23 October 2025, accepted 24 October 2025, online since 9 March 2026.

1. Introduction

Instead of being an undesired waste, CO_2 can be considered as feedstock to be transformed into sustainable fuels replacing fossil fuels, which could be an interesting alternative to limit both global warming and depletion of fossil fuels. Because of high chemical stability, the photocatalytic reduction of CO_2 is thermodynamically unfavorable under direct solar light irradiation. Consequently, CO_2 photocatalytic reduction has been considered for a few years as a promising technology for converting CO_2 into light-driven C-based compounds, as reported in several reviews summing up the state of the art on that topic [1,2]. Another important aspect of the solar-driven conversion of CO_2 into liquid or gaseous fuels is the high-density storage of solar energy in the form of chemical bonds, mainly C–H bonds. Thus, the non-intermittent energy storage capacity of solar fuels has become a very attractive solution.

The photocatalytic reduction of CO_2 can be achieved in gas phase using solar energy at low temperature. During photocatalysis, CO_2 and H_2O in humified air are utilized as initial reactants allowing to simultaneously reduce CO_2 and oxidize H_2O to produce renewable fuel products without secondary pollution [3,4]. Furthermore, water is considered as being the most suitable hydrogen donor (mainly implied as H^+ donor in CO_2 reduction steps).

[*] Corresponding author

Among the different reaction products that could be obtained from CO_2 photocatalytic reduction and knowing also that the energy content of oxygenated compounds decreases as the oxygen content increases (due to the relative decrease in C–H bonds storing energy), methane (CH_4) is one of the most interesting products, as well as methanol. Nonetheless, as methanol's photoreactivity is much higher than that of CO_2, leading to easy over-oxidation to formaldehyde and formic acid, high selectivity toward methane formation is preferred [5].

Amongst the huge variety of semiconductors and composite materials investigated for CO_2 photocatalytic reduction in gas phase, TiO_2 often prevails due to its chemical stability, moderate cost and resistance toward corrosion [6–8]. However, its relative fast recombination rate of electron–hole pairs and limited visible-light harvesting capacity (mainly in the UV region, <5% of the solar spectrum) are considered the main limitations for solar light-driven gas-phase CO_2 photocatalytic reduction in presence of water. In recent years, several strategies have been carried out in order to overcome these limitations, including modification of the morphology of TiO_2 [9,10], combination with other semiconductors [11–13] or elements by means of mono-doping [14,15] or co-doping approaches [16,17], or loading with metal nanoparticles (NPs), acting as electron sinks, cocatalyst or inducing surface plasmon (SP) phenomena [8,18,19]. Between the different metal NPs used as cocatalysts and exhibiting surface plasmon resonance (SPR) properties in the visible range, gold nanoparticles (Au NPs) can be considered as among the most interesting NPs for driving CH_4 production from CO_2 gas-phase photocatalytic reduction in presence of water vapor as reducing agent. Indeed, in addition to high inertness in numerous environments, Au NPs exhibit a high quality factor in visible light [20]. Moreover, Pt NPs, because of their large work function (5.64 eV vs. E_{vacuum}), have also been considered as efficient cocatalysts, the deposition of Pt promoting the migration of photoinduced electrons from TiO_2 to Pt thus improving the photocatalytic reduction steps [21]. However, finding a cocatalyst with a low price, abundant reserves (typically non-noble metals), and excellent catalytic performance is a crucial concern.

As an alternative, cocatalytic phases, earth-abundant copper-based heterogeneous photocatalysts have received increasing attention for CO_2 reduction, since copper is an inexpensive element with multiple oxidation states, meaning that metal and oxide particles can be formed and also contribute positively to the photocatalytic process. Copper oxide (CuO) and cuprous oxide (Cu_2O) have narrow band gaps of 1.7 eV [22] and 2.2 eV [23], respectively, and can additionally act as photoactive phases under visible light. Moreover, the introduction of metallic Cu can improve the photocatalytic activity when it is in contact with other semiconductors, acting as CO_2 adsorption sites or as catalytic reduction ones, and also achieving limitation of charge carrier recombination by adding electron traps, yielding the formation of a Schottky barrier [24]. Another beneficial impact to be mentioned is the generation of a SPR effect in visible light, knowing that SPR of metallic Cu extends from UV–visible to near-infrared (NIR) regions of the optical spectrum [25]. It is thus necessary to maintain a good balance between the different oxidation states of Cu, the main difficulty consisting in keeping a sufficient proportion of Cu in its metallic state. To do this, the development of approaches designed to mitigate oxidation, such as the formation of bimetallic M–Cu NPs may be a promising solution. Moreover, it is fully admitted that Cu-based bimetallic systems significantly promote activation of the very stable CO_2 molecule. Although it is known (by means of electrocatalysis or thermal catalysis) that bimetallic Cu-based systems can efficiently improve CO_2 catalytic reduction, and that the second metal plays various roles (morphological, electronic transfer, reactant transfer, generation of supplementary actives sites, intermediates adsorption/desorption) [26,27], these bimetallic systems have been only scarcely studied in heterogeneous photocatalysis for gas-phase CO_2 photoreduction in presence of H_2O.

Herein, M–Cu (M = Ag, Pt, Pd, Au)/TiO_2 bimetallic samples were prepared by impregnation/chemical reduction methods, characterized and compared toward gas-phase photocatalytic CO_2 reduction in humid atmosphere under artificial solar- and visible-light illumination.

2. Results and discussion

2.1. *Chemical composition*

The real chemical compositions of Pt-, Cu-, Au-, Pd- and Ag-monometallic as well as related bimetallic

Table 1. Determination of total metal content, deposition yield, and bi-metallic composition from ICP-AES measurements

Sample	Nominal tot. metal wt%	Real total metal wt%	Deposition yield %	Nominal M–Cu mol. composition	Real M–Cu mol. composition
Pt/TiO_2 P25	2	1.99	99		
Pd/TiO_2 P25	2	2.00	100		
Au/TiO_2 P25	2	1.69	85		
Ag/TiO_2 P25	2	1.81	90		
Cu/TiO_2 P25	2	1.46	73		
$Pt–Cu/TiO_2$ P25	2	1.72	86	50–50	59–41
$Pd–Cu/TiO_2$ P25	2	1.69	85	50–50	47–53
$Au–Cu/TiO_2$ P25	2	1.53	77	50–50	60–40
$Ag–Cu/TiO_2$ P25	2	1.62	81	50–50	49–51
Pt/TiO_2 UV-100 350 °C	1	1.00	100		
Cu/TiO_2 UV-100 350 °C	1	0.70	70		
$Pt_x–Cu_y/TiO_2$ UV-100 350 °C	1	0.99	99	20–80	21–79
	1	0.93	93	50–50	53–47
	1	0.97	90	80–20	81–19
$Pt_x–Cu_y/TiO_2$ UV-100 350 °C*	1	0.90	99	20–80	20–80
	1	0.99	99	50–50	57–43
	1	0.99	99	80–20	82–18

*stands for $Pt–Cu/TiO_2$ UV-100 350 °C obtained by successive reduction method. The relative error is estimated at 5%.

systems obtained by coreduction are reported in Table 1. First, by considering the TiO_2 P25 support, one can observe that on monometallic samples, the deposition yield changed from 73 to 100%. The two noble metals Pd and Pt showed the highest yield among all. Ag deposition was also achieved with a very good yield of 90%. It is worth mentioning that Cu exhibited the lowest yield, close to 70%. Regarding the bimetallic materials, Pt- and Pd-containing materials led to 77–86% yields, the lowest ones being obtained for Au– and $Ag–Cu/TiO_2$ photocatalysts, already identified as more difficult to deposit as monometallics. It is worth noting that the presence of Cu and the difficulty to deposit it onto the TiO_2 surface is detrimental to the deposition of a second metal. Nevertheless, even if Cu deposition is more difficult as a monometallic system, the M–Cu molar composition however was close to the expected one, assuming that M–Cu interaction using a codeposition method happened before deposition onto the support.

Globally, except for the Cu monometallic sample, the total deposition yield onto the TiO_2 UV-100 350 °C support was very important, higher than 90%. As well as what was observed above for the TiO_2 P25 support, in terms of bimetallic molar composition, the real compositions are close to the targeted ones, meaning that despite the weaker interaction of Cu with TiO_2 UV-100 350 °C when alone, this metal takes advantage of the simultaneous presence of Pt.

2.2. *Photocatalytic activity under simulated solar light*

From the photocatalytic activity of the $M_{0.5}$–$Cu_{0.5}/TiO_2$ P25 bimetallic systems, one can underline that the association with Pt resulted in the best performance, considering both the reaction rate and selectivity toward C-based products, namely CH_4 formation (more than 40 $\mu mol \cdot h^{-1} \cdot g^{-1}$) (Figure 1). With a production rate for CH_4 formation

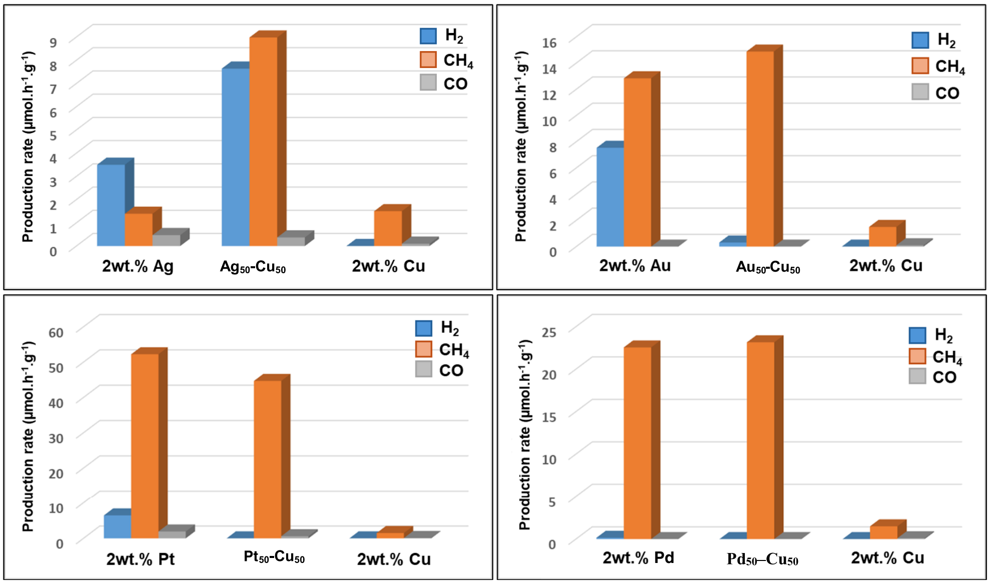

Figure 1. Gas-phase photocatalytic CO_2 reduction on (top left) 2 wt% $Ag_{0.5}$–$Cu_{0.5}$/TiO_2 P25 (top right) 2 wt% $Au_{0.5}$–$Cu_{0.5}$/TiO_2 P25 (bottom left) 2 wt% $Pt_{0.5}$–$Cu_{0.5}$/TiO_2 P25 (bottom right) 2 wt% $Pd_{0.5}$–$Cu_{0.5}$/TiO_2 P25. Comparison with the monometallic counterparts.

of ca. 23 $\mu mol \cdot h^{-1} \cdot g^{-1}$, and despite a selectivity close to 100%, the $Pd_{0.5}$–$Cu_{0.5}$/TiO_2 P25 photocatalyst exhibited a reaction rate almost twice lower than the Pt–Cu-based one. The activity on $Au_{0.5}$–$Cu_{0.5}$/TiO_2 P25, although accompanied by almost total selectivity toward CH_4, was decreased to less than 15 $\mu mol \cdot h^{-1} \cdot g^{-1}$. The lowest performance was observed when associating Ag and Cu, in parallel with a drastic decrease in selectivity. Among all the M–Cu bimetallic systems, one has to underline that, except for $Pt_{0.5}$–$Cu_{0.5}$/TiO_2 P25, enhanced activity was obtained compared to the monometallic counterparts, even if the monometallic Cu/TiO_2 reference resulted in poor activity. Beside this observation, we can note that the Ag/TiO_2 and Cu/TiO_2 monometallics led to very low activity and selectivity towards C-containing molecules compared to the noble-metal monometallic systems.

The two 2 wt% $Pd_{0.5}$–$Cu_{0.5}$/TiO_2 P25 and 2 wt% $Pt_{0.5}$–$Cu_{0.5}$/TiO_2 P25 samples previously identified as the most active in terms of production rate and selectivity toward CH_4 were further chosen to study the influence of total metal content, molar composition, and TiO_2 support. Looking at the effect of metal content varying from 1 to 3 wt%, a common general trend emerged, while keeping the electronic selectivity close to 100% (Figure 2). It was observed that doubling total metal loading from 1 to 2 wt% resulted in doubling the active sites that contribute the most strongly to the rate-determining steps, without impacting the reaction routes. However, increasing further to 3 wt% led to a deviation with a non-proportional increase in the reaction rate but, above all, detrimental to selectivity toward the formation of C-based compounds.

The evolution of both CH_4 production rate and selectivity as a function of molar composition (keeping the metal content constant at 2 wt%) showed an optimum close to 80–20 between Pd (or Pt) and Cu (Figure 3). For this optimal composition, the resulting performance regarding CH_4 production rate exceeded the one of the corresponding Pd (or Pt) activity. Increasing further Cu content yielded a strong decrease in activity, without impacting the selectivity, however.

Whether for Pd–Cu or Pt–Cu bimetallic system, a UV-100 support resulted in slightly higher activity, and lower selectivity than for TiO_2 P25. This first feature can probably be attributed to the larger surface area of the UV-100 photocatalyst, compared to the P25 one. Moreover, it is worth mentioning that the CH_4 reaction rate notably increased

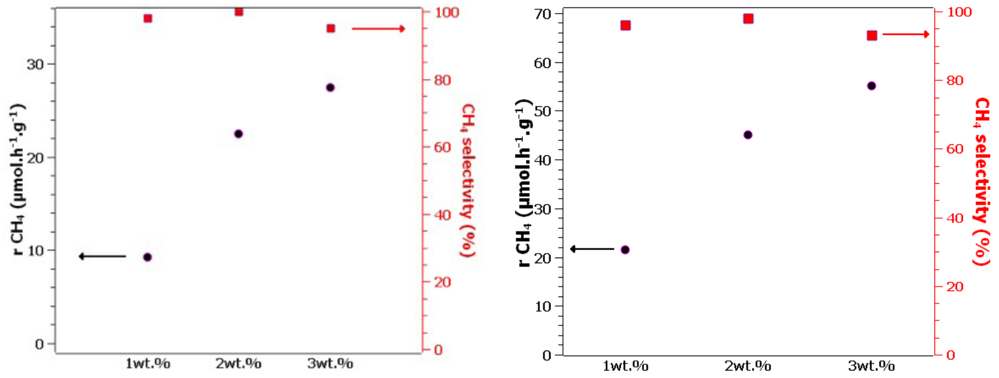

Figure 2. Gas-phase photocatalytic CO_2 reduction on (left) $Pd_{0.5}$–$Cu_{0.5}/TiO_2$ P25 and (right) $Pt_{0.5}$–$Cu_{0.5}/TiO_2$ P25 for 1, 2, and 3 wt%.

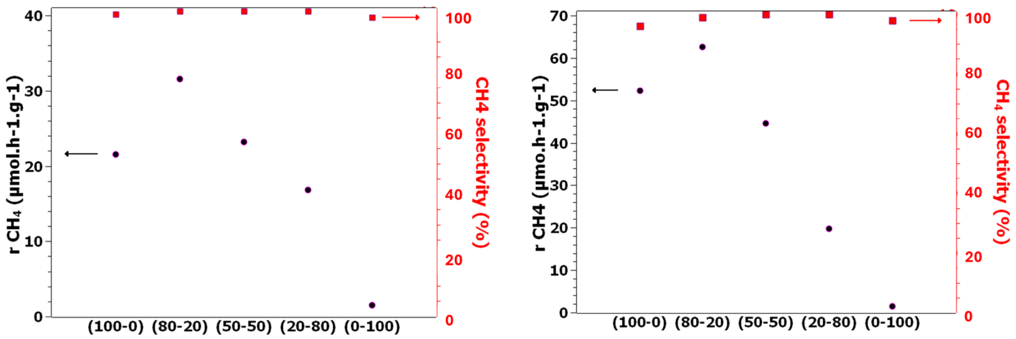

Figure 3. Gas-phase photocatalytic CO_2 reduction on (left) 2 wt% Pd_x–Cu_y/TiO_2 P25 and (right) 2 wt% Pt_x–Cu_y/TiO_2 P25, $x = 0.2$, 0.5, and 0.8.

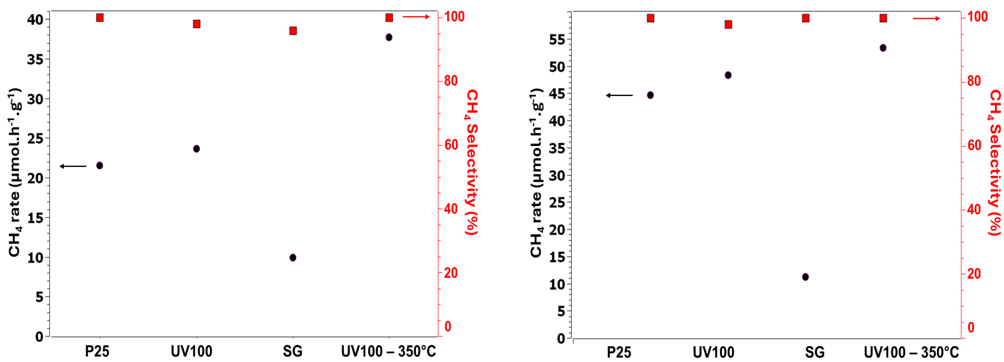

Figure 4. Gas-phase photocatalytic CO_2 reduction on (left) 2 wt% $Pd_{0.5}$–$Cu_{0.5}/TiO_2$ P25 and (right) 2 wt% $Pt_{0.5}$–$Cu_{0.5}/TiO_2$, using various TiO_2 supports (x-axes).

with the UV-100 350 °C substrate, accompanied by full selectivity. Knowing the lower surface area (ca. 140 $m^2 \cdot g^{-1}$) of TiO_2 UV-100 350 °C, compared to 315 $m^2 \cdot g^{-1}$ for bare UV-100, this important enhancement in activity is thus not correlated to this parameter, but probably to the better crystallinity of TiO_2, which might be beneficial for charge carrier dynamics (Figure 4).

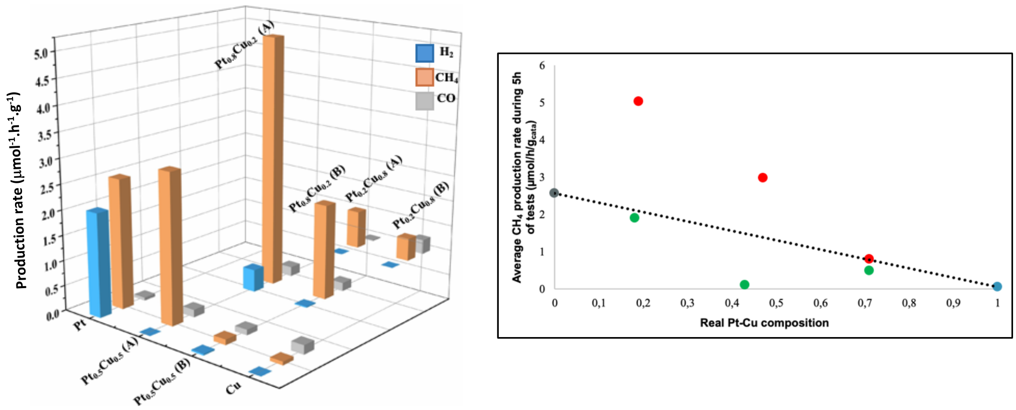

Figure 5. Gas-phase photocatalytic CO_2 reduction on 1 wt% Pt_x–Cu_y/TiO_2 UV-100 350 °C, x = 0.2, 0.5, and 0.8. Effect of (A) simultaneous- and (B) successive-reduction deposition methods.

2.3. *Photocatalytic activity under simulated visible light on 1 wt% Pt_xCu_y/TiO_2 UV-100 350 °C*

Subsequently, given that amongst the studied materials, 2 wt% $Pt_{0.5}$–$Cu_{0.5}$/TiO_2 UV-100 350 °C sample yielded the best photocatalytic activity and selectivity for CH_4 formation, further investigations were undertaken with 1 wt% of total metal content, analyzing in more details the Pt_xCu_y molar composition, i.e., $Pt_{0.8}$–$Cu_{0.2}$, $Pt_{0.5}$–$Cu_{0.5}$, and $Pt_{0.2}$–$Cu_{0.8}$, the deposition method, and targeting visible-light illumination (Figure 5).

Comparing the effect of the addition order of the metal precursors revealed the superiority of the coreduction method (labeled A) over the successive one (labeled B) (Figure 5). It must also be underlined that all the synthesized Pt–Cu bimetallic samples showed improved activity compared to their monometallic counterparts under visible light activation. Looking at the best 1 wt% coreduced bimetallics, the $Pt_{0.8}$–$Cu_{0.2}$ material showed by far the highest performance, amongst all compositions.

Looking further into the experimental CH_4 production rate in relation with the weighted combination of the respective activities of the monometallic counterparts (Figure 5-right), it must be highlighted that the Pt–Cu bimetallics exhibited a real synergy provided that the composition was not too rich in Cu. In addition, it should also be noted that on those Pt–Cu/TiO_2 UV-100 350 °C materials, electronic selectivity higher than 90% was obtained under visible-light activation, unlike their monometallic counterparts (83% for 1 wt% Pt/TiO_2 and 61% for 1 wt% Cu/TiO_2, with the production of non-negligible CO amounts).

2.4. *Optical properties*

2.4.1. *On the TiO_2 P25 support*

From the UV–Vis absorption spectra of the 2% $M_{0.5}Cu_{0.5}$/TiO_2 P25 bimetallic samples (Figure 6), one can observe that beside the contribution in the UV region due to anatase TiO_2, additional absorption occurred in the visible spectrum, extending from 400 nm to NIR, whose intensity and extent depend on the metal associated to Cu.

The two noble-metal-based bimetallic systems exhibited a continuous increase in the visible spectrum as also observed on the monometallic Pt and Pd references (Figure 6-right), which can be attributed mainly to their intraband absorption [28]. Nevertheless, by comparing with the Cu/TiO_2 counterpart, this broad signal might also include contributions from Cu species, namely from plasmonic Cu(0) inter- and intraband transitions located at ca. 380–450 and 580 nm, respectively [29]. Moreover, knowing the low resistance to oxidation of Cu(0), CuO_x species probably also contribute to this signal. Indeed, it is admitted that Cu_2O [30] and CuO [31] semiconductor NPs show absorption from ca. 600 and 700 nm corresponding to their band-edge position, a feature that becomes more prominent in NP forms.

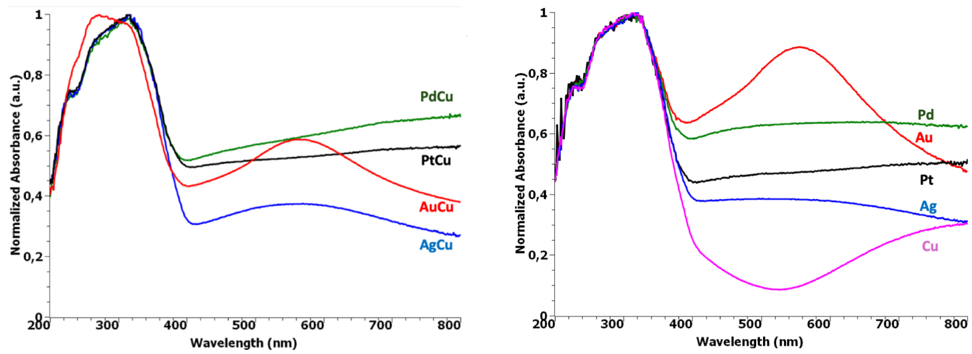

Figure 6. UV–Vis absorption spectra of (left) 2 wt% $M_{0.5}$–$Cu_{0.5}$/TiO_2 P25 samples and (right) corresponding monometallic references.

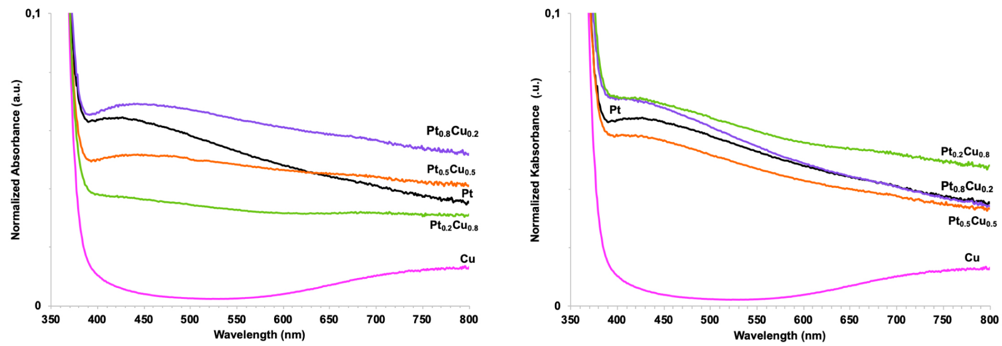

Figure 7. UV–Vis absorption spectra of 1 wt% Pt_x–Cu_y/TiO_2 UV-100 350 °C (x = 0.2, 0.5, 0.8) samples prepared by (left) coreduction and (right) successive reduction.

With regard to the Au–Cu samples, in addition to Cu species absorption, d–d interband transitions from Au NPs were observed centered approximatively around 570 nm, characteristic of SPR fingerprint of Au NPs as confirmed with the monometallic reference. It is currently admitted that the intensity and position of this SPR strongly depend on the Au NP size, shape, and interaction with the support [32,33].

Looking at the very broad and extended Ag–Cu/TiO_2 visible-light signal and comparing with the monometallic counterparts, one can suppose that it encompasses optical behaviors of the different (above-mentioned) Cu and Ag species. It should indeed be noted that, depending on the size and shape of Ag(0) NPs, the corresponding SPR peak position can be extended from 390 to 460 nm, in addition to the presence of contributions from the Ag_2O semiconductor (maximum absorption at ca. 550 nm that can extend up to 800 nm) [34], as Ag(0) is likely to easily undergo surface oxidation.

2.4.2. *On the TiO_2 UV-100 350 °C support*

Focusing on the Pt–Cu bimetallic system immobilized onto the TiO_2 UV-100 350 °C support, optical properties were investigated by simultaneously varying the molar composition between the two metals and the addition order of the precursors (coreduction or successive reduction) (Figure 7). The general shape of the absorption curve was similar to that already noted for the $Pt_{0.5}$–$Cu_{0.5}$ system deposited onto the TiO_2 P25 support, with the relative intensity increasing with Pt content in case of coreduction (Figure 7-left). However, for successive reduction (Figure 7-right), the trend was reversed for molar content in Pt greater than 50%.

2.5. *Transmission electronic microscopy (TEM) of $Pt_xCu_yTiO_2$ UV-100 350 °C*

We consequently performed TEM analyses on the 1 wt% Pt_x–Cu_y/TiO_2 UV-100 350 °C (coreduction)

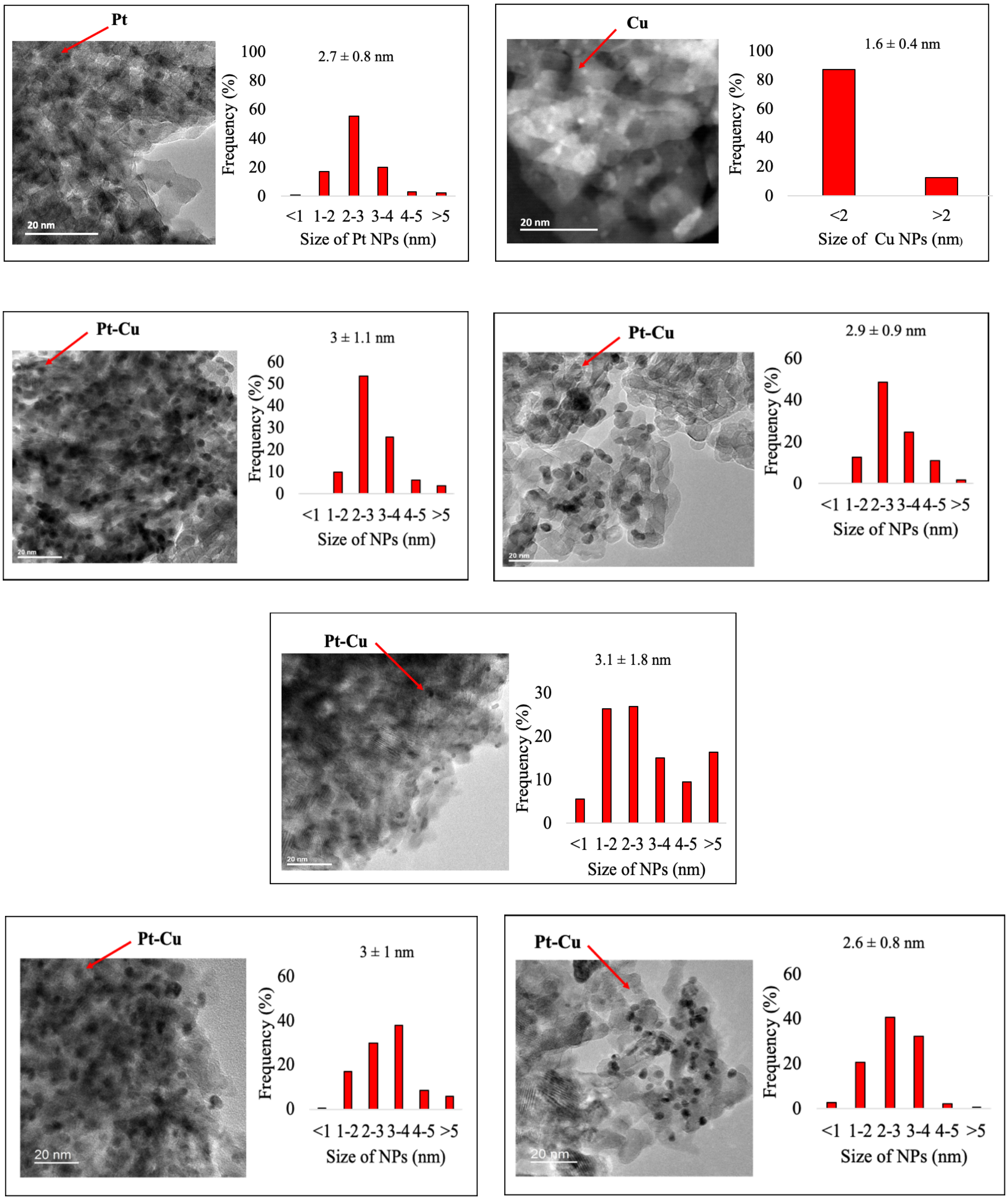

Figure 8. Transmission electronic microscopy micrographs and particle size distribution of (top left) 1 wt% Pt/TiO_2 UV-100 350 °C (top right) 1 wt% Cu/TiO_2 UV-100 350 °C (middle) 1 wt% $Pt_{0.2}$–$Cu_{0.8}$/TiO_2 UV-100 350 °C, 1 wt% $Pt_{0.5}$–$Cu_{0.5}$/TiO_2 UV-100 350 °C, and 1 wt% $Pt_{0.8}$–$Cu_{0.2}$/TiO_2 UV-100 350 °C obtained by coreduction (top left) 1 wt% $Pt_{0.2}$–$Cu_{0.8}$/TiO_2 UV-100 350 °C and 1 wt% Pt_{05}–$Cu_{0.5}$/TiO_2 UV-100 350 °C obtained by successive reduction.

series (Figure 8). Independently of the mono- or bimetallic material, the NPs appeared to be rather homogeneously deposited onto the TiO_2 UV-100 350 °C substrate. Looking first at the monometallic references, one can observe that Cu NPs exhibited a small and narrowly distributed average particle size of 1.6 nm, whereas Pt exhibited a broader distribution centered around 2.7 nm, both with moderate standard deviation. On bimetallic systems, it must be underlined that regardless of the molar composition and addition order of the metallic precursors, their average particle size was always greater than that of the monometallic counterparts, also accompanied by larger standard deviation. Thus, one can assume that the differences observed in optical properties and photocatalytic CO_2 reduction activity do not originate either from discrepancies in metal loading or composition or from particle size and/or dispersion disparities (Figure 8).

2.6. *XPS analysis on the TiO_2 UV-100 350 °C support*

The surface and bulk Cu/(Cu+Pt) atomic ratios of the 1 wt% Pt_xCu_y/TiO_2 UV-100 350 °C samples varying in their molar composition and deposition method A (coreduction) or B (successive reduction) displayed two main features (Figure 9). Regarding samples resulting from coreduction and regardless of the Cu–Pt molar composition, the Cu/(Cu+Pt) surface atomic ratio was larger than the total one, consistent with a surface enrichment in Cu, all the more important as the composition in Cu increased. Nevertheless, it seems that this behavior did not happen in the case of successive reduction, even if the measurements were performed only on one Pt–Cu composition. From these observations, it may be assumed that the addition order of the Pt and Cu precursors impacts the surface enrichment in Cu particles. More precisely, the photocatalytic materials exhibiting the best performances seems to be those showing an optimal surface enrichment in Cu, without being too important however. Complementary detailed XPS analysis (to be published elsewhere) revealed that Cu(0) and/or Cu(+1) surface species are the predominant Cu oxidation states, apparently excluding the presence of other Cu oxidation states.

It is well known that noble-metal NPs, such as Au, Pt, Pd are able to absorb visible light thanks to surface plasmonic resonance (SPR), which may contribute to visible light activation of TiO_2. In addition to this beneficial SPR feature that would help extend the response of TiO_2 from UV to visible light, the presence of a noble metal would also result in improving charge carrier separation thanks to the formation of a Schottky barrier at the metal/semiconductor (SC) interface and also be helpful in supplying cocatalytic function. Because of their large work function (5.64 eV vs. E_{vacuum}), Pt NPs have been considered an efficient cocatalyst for TiO_2. However, more recently, non-noble plasmonic metals such as copper Cu, Bi, Ni, etc. have been proposed as alternatives to plasmonic noble metals, also considering their massive Earth abundance, low cost, and promising SPR tunable from UV to NIR [35,36]. Non-metal-based plasmonic materials often exhibit plasmonic properties comparable to those of noble metals, but they can outperform their noble-metal counterparts in some cases. There are several recent studies showing that Cu is used to replace Au, which is considered as the most widely researched metal in the plasmonic field. Moreover, as the work function of Cu (4.65 eV) is smaller than that of Au (5.1 eV), it can form a lower Schottky barrier with TiO_2. It is usually admitted that intraband transitions are characterized by the creation of hot electrons above the Fermi level more suitable for reductive catalytic pathways, whereas interband transitions mainly lead to the generation of hot d-band holes below the Fermi level, thus better for oxidative catalytic pathways. However, as the

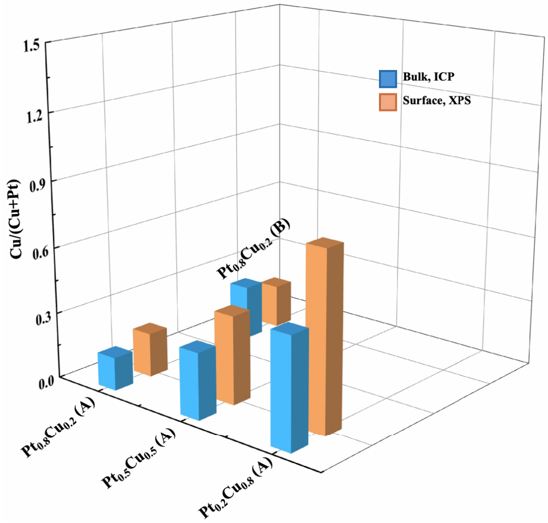

Figure 9. Cu/(Cu+Pt) surface (determined from XPS) and bulk (determined from ICP-AES) atomic ratios as a function of molar composition and deposition method (A and B stand for coreduction and successive reduction deposition, respectively) for 1 wt% Pt_xCu_y TiO_2 UV-100 350 °C samples.

interband transition energy level of Cu is also lower than that of Au, it is possible to produce hot electrons with higher energy, thus allowing hot electrons excited from both intraband and interband transitions to be extracted more efficiently [30]. As CO_2 is also a very stable linear molecule, CO_2 activation is a key step for its further reduction. For this purpose, a Cu-based metallic catalyst is considered to significantly promote CO_2 activation. Indeed, it has already been demonstrated that the presence of Cu atoms on the surface of TiO_2 significantly stabilizes the adsorption of curved CO_2, meaning that Cu can effectively stabilize the CO_2 adsorbed on the catalyst [37]. Thus, loading Cu onto TiO_2 leads to increase CO_2 adsorption but also to inhibit the competitive H_2 evolution [38]. In addition, as a conductive substance, Cu can be associated with TiO_2 to form a metal–semiconductor Schottky junction allowing effective inhibition of the charge carrier recombination.

However, despite their low cost and Earth abundance, Cu NPs are easily oxidized and can exist in different oxidation states where metallic Cu and CuO_x can be present at the same time. More precisely, copper oxide (CuO) and cuprous oxide (Cu_2O) can be formed exhibiting narrow band gaps of 1.7 eV and 2.2 eV, respectively, which may permit visible-light absorption. It is worth mentioning that, in addition to their band-gap energy smaller than that of TiO_2, they also exhibit higher conduction band values facilitating CO_2 reduction. Many works have reported the use of CuO_x with different morphologies [39,40] for photocatalytic reduction of CO_2, overcoming the rapid charge carrier recombination by formation of (hetero)junction with another material. However, for longer-term stability, keeping an optimal balance between the different Cu oxidation states remains a tricky concern, especially in the case where O_2 production occurs as a result of the first H_2O oxidation step (essential for providing H^+ to further advance CO_2 reduction) and can thus be considered as one of the key-point that can be satisfied by designing M–Cu bimetallic systems.

Cu–Pt/TiO_2 bimetallic photocatalysts with optimized Cu–Pt molar composition were identified as the best materials for CO_2 reduction due to the synergistic effects where each metal complements the role of the other one. Indeed, Cu is an excellent cocatalyst for CO_2 activation by lowering the energy barrier required to break the stable linear C=O bond. Pt enhances transfer of the photogenerated electrons from the TiO_2 semiconductor to the CO_2 molecule, a crucial step in the reduction pathway. Moreover, optimized interface between Cu and Pt domains can lead to the formation of specific active sites promoting CO_2 reduction and driving toward the desired products. Within the Cu–Pt bimetallic system, specific electronic interactions between the two metals result in preventing too important an oxidation of Cu(0) NPs, allowing stabilization of the optimal balance between Cu(0) and Cu(+1) (Cu_2O) oxidation species, also resulting both in the formation of TiO_2/Cu_2O heterojunctions for increased charge carrier separation and visible light photosensitization of the TiO_2 semiconductor. In addition to all those positive effects deriving from the optimal association between Pt and Cu, it is worth mentioning the ones related to SPR effects. Hot electrons from Cu can be injected into Pt thus lowering the energy barrier for the kinetically slow steps of CO_2 reduction, thus accelerating the reaction. This electron injection can also influence the reaction pathway. For instance, an increased concentration of electrons at the active Pt sites can favor the reduction of specific intermediates, thereby inhibiting competing pathways like hydrogen evolution.

3. Conclusion

Tuning and elaboration of M–Cu bimetallic phases supported on TiO_2 semiconductors can be considered an interesting strategy considering that photocatalysts based on non-noble plasmonic metals may be a promising alternative to noble-metal-based ones due to their advantages like Earth abundance, effectiveness, and thus large-scale application possibility. However, despite their low cost and Earth abundance, Cu NPs are easily oxidized. As a consequence, the development of approaches to mitigate oxidation represents a key point. Amongst them, the intimate association, in an optimized way, of Cu and noble metals can result in synergistic effects on photocatalytic properties compared to the monometallic catalysts. Overall, Pt–Cu bimetallic catalysts—benefiting from catalytic synergy, plasmonic enhancement, tailored electronic interactions, and optimized balance between the different Cu species—represent a promising direction for the development of efficient, stable, and solar-driven systems for CO_2 conversion.

4. Experimental section

4.1. *Materials*

Commercial TiO_2 P25 (surface area of 50 $m^2 \cdot g^{-1}$) and UV100 Hombikat (315 $m^2 \cdot g^{-1}$) were purchased from Evonik and Sachtleben Chemie, respectively. UV 100 is used either as received or after calcination in air at 350 °C for 4 h (named UV-100 350 °C) in a muffle furnace to obtain a pure-phase anatase, nanocrystalline, without amorphous phase and with well-defined crystallites of 13 nm, exhibiting a surface area of 140 $m^2 \cdot g^{-1}$. $H_2PtCl_6 \cdot xH_2O$, Na_2PdCl_6, $HAuCl_4 \cdot 3H_2O$, $AgNO_3$, and $NaBH_4$ were purchased from Sigma-Aldrich and used without further purification. $Cu(NO_3)_2 \cdot xH_2O$ was purchased from Alfa Aesar & used without further purification.

4.2. *Photocatalyst preparation*

The TiO_2 support (1 g) was dispersed and stirred at 1000 rpm for 5 min in distilled water (400 mL). For all bi-metallic M–Cu systems, the *codeposition/chemical reduction* protocol was carried out. For this, two aqueous solutions of metal (Pt, Pd, Au, or Ag) precursor, and $Cu(NO_3)_2 \cdot xH_2O$ (0.25 M) were added simultaneously to the suspended TiO_2 support under vigorous stirring for 45 min. A freshly prepared solution of $NaBH_4$ ($n(NaBH_4)/n_{metal} = 5$) was added and left to react for 15 min. The resulting powder in suspension was isolated by filtration under vacuum, washed with distilled water (1 L), and dried under air for 24 h at 100 °C. The final photocatalyst was recovered after a calcination at 200 °C for 2 h.

Nevertheless, in the case of UV-100 350 °C support, *sequential chemical reduction* was also applied in order to assess whether there was an influence of the addition order of the metal precursors. To do this, in a first step, the aqueous solution of the metal precursor was added to the medium, and the synthesis was then pursued as described above to obtain the M/TiO_2 catalyst. Secondly, the aqueous solution of $Cu(NO_3)_2 \cdot xH_2O$ was added, and the same synthesis was performed yielding M–Cu/TiO_2 catalyst.

Different series of M–Cu/TiO_2 materials were targeted. Series of 1, 2, and 3 wt% Pd_xCu_y/TiO_2 P25, Pt_xCu_y/TiO_2 P25, Au_xCu_y/TiO_2 P25 and Ag_xCu_y/TiO_2 P25 (with y = nominal content of Cu = 0, 0.5, 1; $x = 1 - y$), and of 2 wt% Au_xCu_y/TiO_2 P25, 2 wt% Au_xCu_y/TiO_2 P25 (with y = 0, 0.2, 0.5, 0.8, 1) were prepared in order to investigate the impact of bimetallic composition and total metal loading. Additionally, a series of 1 wt% Pt_xCu_y/TiO_2 UV-100 350 °C (with y = 0, 0.2, 0.5, 0.8, 1) was also investigated in order to study the influence of the TiO_2 support.

4.3. *Material characterization*

Elemental analyses of the composites were performed using inductively coupled plasma atomic emission spectroscopy (ICP-AES). The detection threshold of the instrument is 0.1 $mg \cdot L^{-1}$ for Au, Cu, Pd, Pd and Ag. Analysis of the metal component in the composites allowed us to calculate deposition yields, which are defined as the ratio between the real deposited mass of Au (deduced from ICP-AES analysis) and the mass of Au introduced during the deposition step. High-resolution transmission electron microscopy (HRTEM) was performed on a Jeol 2100F microscope equipped with a lanthanum hexaboride cathode (LaB6) operating at 200 kV. The sample was sonicated in EtOH, and then a drop of the suspension was deposited on a carbon membrane placed on a copper grid. The size of M NPs was determined by HRTEM, and consequently the size distribution was obtained by measuring particle size for more than 100 particles using the ImageJ software. UV–Vis absorption spectra were recorded on a Perkin Elmer 950 spectrophotometer fitted with a Labsphere RSA ASSY 100 nm integrating sphere. The spectra were acquired in reflection mode (diffuse reflectance).

The surface of the catalysts was studied by X-ray photoelectron spectroscopy (XPS). The spectrometer used was an ultrahigh vacuum (UHV) one with an incident X-ray source such as a dual anode Al Kα (1486.6 eV). The electron analyzer was a VSW Class WA hemi-sphere. The spectra, survey and high resolution, were recorded in constant pass energy mode, 90 eV for survey scan and 20 eV for high resolution spectra. The % surface atomic ratios were calculated using the corresponding core level peaks, which were normalized to the photoemission cross-section, and assuming a homogeneous distribution arrangement.

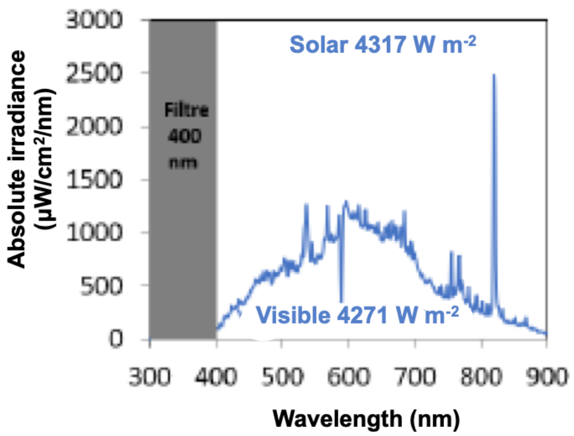

Figure 10. Emission spectra of the 150 W ceramic metal-halide Hg lamp with and without Schott GG 400 optical filter.

4.4. *Photocatalytic evaluation*

Photocatalytic setup has already been described in detail elsewhere [41]. During the test, the continuous reaction mixture (CO_2+H_2O, CO_2/H_2O = 97/43) flow (0.3 mL·min^{-1}) passes through a light-transparent photoreactor (6 mL) equipped with a ventilator-cooled Hg lamp simulating artificial solar light (150 W ceramic metal-halide Hg lamp). Note that, to do the tests under visible light, a Schott GG 400 optical filter (Edmund Optics) was placed between the photoreactor and the lamp to cut all wavelengths below 400 nm. Total irradiance was 4317 W/m^2 for the whole lamp spectrum (from 300–900 nm) and 4271 W/m^2 with the 400 nm optical filter (simulated visible light) (Figure 10). The irradiated surface was 19.65 cm^2. For photocatalytic tests, materials (50 mg) were dispersed in EtOH and deposited on a 50 mm diameter glass disk by evaporation at 100 °C. The surface concentration of the photocatalyst on the glass disc was 25 g·m^{-2}. The glass disk was then placed in the reactor and the setup was purged for 5 min with CO_2 flow (>100 mL·min^{-1}) to remove air and other gas impurities. As a blank test, the setup was run without CO_2 gas flow under illumination to control the absence of gaseous products that may result from conversion of carbon-based contaminants [42]. Products from the reactor were analyzed by an online micro-GC (Agilent 3000A SRA instrument). Finally, the lamp was switched on and the duration of test went from 5 h to 10 h.

Production rates were calculated according to the following equation:

$$r_X(\text{mol}\cdot\text{h}^{-1}\cdot\text{g}^{-1}) = \frac{[X]\times 10^{-6}\times(\text{flow rate})\times 60}{V_m \times m_{\text{photocat}}}$$

where $[X]$ is the concentration in ppm, m_{photocat} the mass of photocatalyst, $S_{\text{irradiated}}$ the irradiated surface (0.001965 m^2), flow rate was 0.0003 L·min^{-1} and V_m = 24.79 L·mol^{-1} (STP conditions).

Electronic selectivity was calculated by these equations:

$$CH_4 \text{ Selectivity} = \frac{8[CH_4]}{8[CH_4]+2[H_2]} \quad (1)$$

$$H_2 \text{ Selectivity} = 1 - CH_4 \text{ Selectivity} \quad (2)$$

Acknowledgments

Vasiliki Papaefthimiou (ICPEES, Strasbourg France) is acknowledged for XPS analyses and discussion.

Declaration of interests

The authors do not work for, advise, own shares in, or receive funds from any organization that could benefit from this article, and have declared no affiliations other than their research organizations.

Funding

The authors acknowledge PEPR PowerCO2 and ECOCHEM projects for financial support of Eliane Khoury's PhD and Clément Marchal's postdoctoral fellowship.

References

[1] K. Li, X. An, K. H. Park, M. Khraisheh and J. Tang, "Photocatalytic CO_2 reduction over TiO_2-based catalysts: A review", *Catal. Today* **224** (2014), pp. 3–12.

[2] B. T. Barrocas, N. Ambrozova and K. Koci, "Photocatalytic reduction of CO_2: A review of materials and mechanisms", *Materials* **15** (2022), pp. 967–1000.

[3] J. Albero, Y. Peng and H. García, "Photocatalytic CO_2 reduction to $C2^+$ products", *ACS Catal.* **10** (2020), pp. 5734–5749.

[4] S. Nahar, M. Zain, A. A. H. Kadhum, H. A. Hasan and M. Hasan, "Advances in photocatalytic CO_2 reduction with water: A review", *Materials* **10** (2017), article no. 629.

[5] S. Neatu, J. A. Marcia-Agullo and H. Garcia, "Heterogeneous photocatalysis for CO_2 conversion", *Int. J. Mol. Sci.* **15** (2014), pp. 5246–5262.

[6] A. Dhakshinamoorthy, S. Navalon, A. Corma and H. Garcia, "Metal organic frameworks as heterogeneous catalysts for CO_2 reduction", *Energy Environ. Sci.* **5** (2012), pp. 9217–9233.

[7] Z. Yuan, X. Zhu, X. Gao, et al., "Advanced photocatalytic systems for environmental applications", *Environ. Sci. Ecotechnol.* **20** (2024), pp. 100368–100384.

[8] S. N. Habisreutinger, L. Schmidt-Mende and J. K. Stolarczyk, "Carbon dioxide reduction by photocatalysis", *Angew. Chem. Int. Ed.* **52** (2013), pp. 7372–7408.

[9] P. Renones, A. Maya, F. Fresno, L. Lollado, J. J. Vilatela and V. A. de la Pena O'Shea, "CO_2 Photoreduction using carbon-based materials", *J. CO_2 Util.* **15** (2016), pp. 24–31.

[10] C. Hiragond, S. Ali, S. Sorcar and S.-I. In, "Hierarchical nanostructured photocatalysts for CO_2 photoreduction", *Catalysts* **9** (2019), pp. 370–381.

[11] K. Li, C. Teng, S. Wang and Q. Min, "Recent advances in photocatalytic CO_2 reduction", *Front. Chem.* **9** (2021), pp. 637501–637525.

[12] L. Hammoud, C. Marchal, C. Colbeau-Justin, J. Toufaily, T. Hamieh, V. Caps and V. Keller, "Photocatalytic CO_2 conversion over engineered materials", *Energy Technol.* **11** (2023), article no. 2201363.

[13] J. Low, J. Yu, M. Jaroniec, S. Wageh and A. A. Al-Ghamdi, "Artificial photosynthesis for solar fuel production", *Adv. Mater.* **29** (2017), article no. 1601694.

[14] V. P. Indrakanti, J. D. Kubicki and H. H. Schobert, "Photocatalytic reduction of CO_2 to fuels", *Energy Environ. Sci.* **2** (2009), pp. 745–758.

[15] K. K. Ghuman and C. C. Singh, "Electronic structure effects in CO_2 reduction catalysis", *J. Phys. Condens. Matter* **25** (2013), article no. 475501.

[16] Z. Xiong, Z. Lei, S. Ma, et al., "Enhanced visible-light photocatalytic CO_2 reduction", *Appl. Catal. B: Environ.* **219** (2017), pp. 412–424.

[17] M. Wen, M. Benabdesselam and C. Beauger, "High-performance photocatalytic CO_2 conversion systems", *J. CO_2 Util.* **81** (2024), pp. 102719–102731.

[18] S. Linic, U. Aslam, C. Boerigter and M. Morabito, "Plasmonic-metal nanostructures for efficient conversion of solar to chemical energy", *Nat. Mater.* **14** (2015), pp. 567–576.

[19] V. P. Indrakanti, J. D. Kubicki and H. H. Schobert, "Recent advances in photocatalytic CO_2 reduction", *Energy Environ. Sci.* **2** (2009), pp. 745–758.

[20] Y. Zhang, S. He, W. Guo, Y. Hu, J. Huang and J. R. Mulcahy, "Design of advanced photocatalysts for CO_2 reduction", *Chem. Rev.* **118** (2018), pp. 2927–3031.

[21] A. Meng, L. Zhang, B. Cheng and J. Yu, "Photocatalytic CO_2 reduction over graphitic carbon nitride: Surface engineering and mechanistic insights", *Adv. Mater.* **31** (2019), article no. 1807660.

[22] M. G. Mendez-Medrano, E. Kowalska, B. Ohtani, D. B. Uribe, C. Colbeau-Justin, S. Rau, J. Rodriguez-Lopez and H. Remita, "Surface modification of TiO_2 for enhanced photocatalytic activity: A combined experimental and theoretical study", *J. Chem. Phys.* **153** (2020), pp. 034705–034713.

[23] Y. Song and M. Ichimura, "Photocatalytic reduction of CO_2 over nitrogen-doped TiO_2", *Int. J. Photoenergy* **2013** (2013), pp. 1–6.

[24] I. Shown, H.-C. Hsu, Y.-C. Chang, et al., "Highly efficient visible light photocatalytic reduction of CO_2 using graphene-based composites", *Nano Lett.* **14** (2014), pp. 6097–6103.

[25] P. Zhang, H. Liu, H. Liu and X. Li, "Enhanced charge separation in modified TiO_2 for photocatalytic CO_2 conversion", *Appl. Surf. Sci.* **535** (2021), pp. 147720–147732.

[26] J. Dean, Y. Yang, N. Austin, G. Veser and G. Mpourmpakis, "Mechanistic insights into CO_2 hydrogenation on metal catalysts", *ChemSusChem* **11** (2018), pp. 1169–1178.

[27] Q. Shao, P. Wang and X. Huang, "Single-atom catalysts for CO_2 reduction: Structure–activity relationships", *Adv. Funct. Mater.* **29** (2019), pp. 1806419–1806441.

[28] P. Lyu, R. Espinoza and S. C. Nguyen, "Electronic structure tuning in metal catalysts for selective CO_2 conversion", *J. Phys. Chem. C* **127** (2023), pp. 15685–15698.

[29] Y. Wang, P. Gao, B. Li, Z. Yin, L. Feng, Y. Liu, Z. Du and L. Zhang, "Photocatalytic degradation and CO_2 conversion using modified semiconductor catalysts", *Chemosphere* **291** (2022), article no. 133007.

[30] Q. Su, C. Zuo, M. Liu and X. Tai, "Recent advances in photocatalytic CO_2 reduction materials", *Molecules* **28** (2023), article no. 5576.

[31] M. I. Said, A. A. Othman and E. M. Abd elhakeem, "Synthesis and characterization of nanostructured photocatalysts for CO_2 reduction", *RCS Adv.* **11** (2021), pp. 37801–37813.

[32] A. Amirjani, N. B. Amlashi and Z. S. Ahmadiani, "Nanostructured catalysts for enhanced photocatalytic performance", *ACS Appl. Nanomater.* **6** (2023), pp. 9085–9123.

[33] E. Kowalska, O. O. P. Mahaney, R. Abe and B. Ohtani, "Effect of metal modification on TiO_2 photocatalytic activity", *Phys. Chem. Chem. Phys.* **12** (2010), pp. 2344–2355.

[34] A. J. Varkey and A. F. Fort, "Semiconductor photocatalysts for solar energy conversion", *Sol. Energy Mater. Sol. Cells* **29** (1993), pp. 253–259.

[35] M. Luo, A. Ruditskiy, H.-C. Peng, J. Tao, L. Figueroa-Cosme, Z. He and Y. Xia, "Shape-controlled metal nanocrystals for catalytic applications", *Adv. Funct. Mater.* **26** (2016), pp. 1209–1216.

[36] X. Lv, Y. Sun, Z. Zhao, W. Zhang, Y. Zhang and F. Dong, "Visible-light-driven photocatalytic CO_2 reduction over modified semiconductors", *Environ. Sci. Nano.* **3** (2016), pp. 1306–1317.

[37] C. Liu, S. K. Iyemperumal, N. A. Deskins and G. Li, "Photonic enhancement of semiconductor-based CO_2 reduction", *J. Photon. Energy* **7** (2016), pp. 012004–0120018.

[38] Y. Lan, J. Xie, Z. Chen, D. Hu and D. Cui, "Efficient CO_2 photoreduction over engineered catalysts", *Chem. Commun.* **55** (2019), pp. 8068–8071.

[39] M. E. Aguirre, R. Zhou, A. J. Eugene, M. I. Guzman and M. A. Grela, "Efficient CO_2 photoreduction over engineered catalysts", *Appl. Catal. B: Environ.* **217** (2017), pp. 485–493.

[40] Q. Zheng, Y. Wei, X. Zeng, W. Xia, Q. Lu, J. Sun and Z. Li, "Nanostructured photocatalysts for enhanced CO_2 conversion", *Nanotechnology* **31** (2020), article no. 425402.

[41] S. Bardey, A. Bonduelle-Skrzypczak, A. Fécant, C. Zhzn-pznq, C. Colbeau-Justin, V. Caps and V. Keller, "Advanced materials for photocatalytic CO_2 conversion: Mechanistic and spectroscopic insights", *Faraday Discuss.* **214** (2019), pp. 417–439.

[42] Y. Zhang, D. Yao, B. Xia, M. Jaroniec, J. Ran and S.-Z. Qiao, "Recent progress in photocatalytic CO_2 reduction for solar fuel production", *ACS Energy Lett.* **7** (2022), pp. 1611–1617.

Comptes Rendus

Chimie

Objet de la revue

Les *Comptes Rendus Chimie* sont une revue électronique évaluée par les pairs, de niveau international, qui couvre l'ensemble des domaines des sciences chimiques.
Ils publient des numéros thématiques, des articles originaux de recherche, des articles de synthèse, des mises au point, des mises en perspective historiques, des textes à visée pédagogique, ou encore des actes de colloque, en anglais ou en français, sans limite de longueur et dans un format aussi souple que possible (figures, données associées, etc.).

Depuis 2020, les *Comptes Rendus Chimie* sont publiés avec le centre Mersenne pour l'édition scientifique ouverte, selon une politique vertueuse de libre accès diamant, gratuit pour les auteurs (pas de frais de publication) comme pour les lecteurs (accès libre, immédiat et pérenne).

Depuis 2026, les *Comptes Rendus* sont co-édités par l'Académie des sciences et le CNRS.

À propos de la revue

Les *Comptes Rendus Chimie* sont exclusivement publiés au format électronique. Toutes les informations sur la revue, ainsi que le texte intégral de l'ensemble des articles, sont disponibles sur son site internet, à l'adresse https://comptes-rendus.academie-sciences.fr/chimie.

Informations pour les auteurs

Pour toute question relative à la soumission d'un manuscrit, merci de consulter le site internet de la revue : https://comptes-rendus.academie-sciences.fr/chimie.

Contact

Académie des sciences
23 quai de Conti
75006 Paris (France)
cr-chimie@academie-sciences.fr

Pour citer ce numéro :
Janine Cossy (éd.). Women Chemists in France in 2026. *Comptes Rendus. Chimie* (2026). https://doi.org/10.5802/crchim.sp.3

Comptes Rendus
de l'Académie des sciences

Chimie

Women Chemists in France in 2026 / *Femmes chimistes en France en 2026*

Contents / *Sommaire*

Please note that the page numbers indicated are those of the electronic file of the issue (212 pages). Each article also has its own pagination, linked to its publication date.

Cover illustration: The authors of the articles in this issue. Photograph taken by Julien Desmarets at the Women Chemists Breakfast organized by the Academy of Sciences on March 3, 2026.

1878-1543 (electronic)

Académie des sciences / CNRS — Paris

Comptes Rendus | *Chimie*

Femmes chimistes en France en 2026